Development and performance of robust particle image velocimetry algorithms and investigation of a model tornado-like vortex: Kinematics and proper orthogonal decomposition

Benjamin Jamie Pelc
The University of Leeds
School of Mechanical Engineering

Submitted in accordance with the requirements for the degree of
Doctor of Philosophy

June 2014

Declaration

The candidate confirms that the work submitted is his own and that appropriate credit has been given where reference has been made to the work of others. This copy has been supplied on the understanding that it is copyright material and that no quotation from the thesis may be published without proper acknowledgement.

Acknowledgements

I would like to acknowledge Prof. David Towers and Dr. Catherine Towers for their invaluable help, patience and guidance throughout the duration of my studies. Without their keen and constant help and advice none of the following work would have been possible.

I would also like to thank Dr Natalia Angarita-Jaimes for her help and assistance whenever I got stuck developing algorithms and for generally helping around the lab.

Dr Diego Angarita-Jaimes is also owed my gratitude for having the patience to introduce me to many of aspects of working with much of the experimental equipment I used during my studies from lasers to cameras to general bits of apparatus.

None of the experimental work would have been possible without the brilliant work of Paul Banks and other members of the technical staff who repeatedly built impeccable experimental rigs and other apparatus often from the most incomplete of drawings.

Finally I would like to thank my parents for putting up with me (financially & otherwise) and for being an infinite source of support throughout the duration of my studies.

Abstract

In the study of fluid flows experimentally obtained data is of importance due to the complex nature of modelling complex fluid flows computationally. Most flows of academic or industrial interest are turbulent, requiring complex experimental methods to capture meaningful data. Currently the dominant method of experimentally obtaining fluid flow data is Particle Image Velocimetry (PIV).

The first part of this study focuses on evaluating cross-correlation based PIV vector calculation algorithms. Algorithms are tested against synthetic images depicting Oseen vortex flow enabling calculated and exact displacements to be compared. Image parameters are varied to investigate the sensitivities of each algorithm to each parameter. The methods evaluated are standard cross-correlation, multigrid (MGRID), the products of adjacent correlation functions (CBC), particle image deformation (PID) and an original method combining PID methods and CBC methods. The new method is shown to return displacement vectors with a reduced level of error compared to existing methods, especially in regions of high spatial velocity gradients.

The second part of this study focuses on recording and evaluating experimentally obtained fluid flow data. One of the most important flow features within turbulence is the vortex, to investigate vortex flow a laboratory tornado-like vortex generator was created from which PIV data could be obtained. Velocity vectors were extracted for varying flow configurations showing the impact of swirl ratio on vortex characteristics such as variability and precession of the vortex as well as the internal vortex structure. The methods developed for quantifying this variability give a greater ability to understand the bulk and internal vortex dynamics for swirling flows.

Proper Orthogonal Decomposition, a correlation based method for extracting coherent structures is applied to the tornado-like flow to further show the underlying dynamics of the variations within the vortex flow and its spatial precession. Temporal characteristics of the tornado-like vortex are also investigated using velocity vectors obtained from high-speed PIV.

Contents

List of Figures

List of Tables

Nomenclature

Roman Symbols

A	image area
$\mathbf{a}$	acceleration vector
a_0	tornado vortex chamber aspect ratio
$a_i^{(n)}$	proper orthogonal decomposition coefficient for mode n and snapshot i
B	correlation function
$\mathbf{C}$	autocovariance matrix
C	two-dimensional PIV image cross-correlation function
C_a	two-dimensional PIV image auto-correlation function
C_d	dissipation rate scalling constant
C_S	Smagorinski constant
d_λ	wavelength normalised diameter
d_p	particle diameter
d_v	distance between POD mode vortices
E	turbulent energy-wavenumber spectrum
e_{ij}	strain rate component
$\mathscr{F}$	Fourier transform
F	turbulent energy-frequency spectrum
$\mathscr{F}^{-1}$	inverse Fourier transform
f	frequency
f_0	peak frequecy

f_s	sampling frequency
g	acceleration due to gravity
h_0	height of tornado vortex chamber
I	turbulence intensity
I_l	local turbulence intensity
i	index value
j	index value
k	turbulent kinetic energy
k_c	turbulent kinetic energy without the effect of vortex precession
$\mathscr{L}$	characteristic length scale
L	correlation length
M	total number of vector grid points
m	index value
N_c	proper orthogonal decomposition truncation mode number
N_p	number of particle images
N_s	number of snapshots (total number of of vector fields)
N_v	total number of velocity vector components
N_W	interrogation region linear dimension
N_x	total number of vector grid points in the x-direction
N_y	total number of vector grid points in the y-direction
n	index value
N_{Γ_1}	total number of vortex cores
P	coordinate point
p	modified pressure including body force pressure
Q	second invariant of the velocity gradient tensor
Q_V	volumetric flow rate
q	digital image pixel intensity

R	mean instantaneous vortex radius (without the effect of precession)
R_3	radius of POD mode 3 vortex
R_a	radius of vortex in the temporal average of instantaneous velocity vectors
R_D^2	coefficient of determination
Re	Reynolds number
Re_r	radial Reynolds number
r	radial coordinate
r_0	tornado vortex chamber updraft orifice radius
$\mathbf{S}$	strain rate tensor
S	swirl ratio
$\mathbf{s}$	displacement vector
s_{ij}	strain rate tensor
T	time period
T_{Int}	integral time scale
t	time
t_v	computation time per velocity vector
t_v'	normalised computation time per velocity vector
$\mathscr{U}$	characteristic velocity scale
U	velocity magnitude
$\hat{\mathbf{u}}$	incoherent component of fluctuating velocity vector
$\mathbf{u}$	velocity vector
$\tilde{\mathbf{u}}$	coherent component of fluctuating velocity vector
u	velocity vector component
$\mathbf{u}'$	velocity fluctuation vector
$\overline{\mathbf{u}}$	time average velocity vector
$\langle \mathbf{u} \rangle$	spatial average velocity vector
$\mathbf{u}_{rms}$	root-mean-square velocity fluctuation vector

$\mathbf{u}_p$	particle velocity vector
u_r	radial velocity component
$u_{rms_{uv}}$	root mean square velocity fluctuation over all velocity components
$\mathbf{u}_s$	Stokes drag velocity lag vector
u_θ	tangential velocity component
V_Γ	tornado vortex simulator circulation fan supply voltage
v	velocity vector component
W	normalised out of plane particle image displacement
w	velocity vector component
$\mathbf{x}$	position vector
x	coordinate position
x'	x coordinate with origin at vortex centre
y	coordinate position
x'	y coordinate with origin at vortex centre
z	coordinate position

Greek Symbols

α	angle between two vectors
α_v	Oseen vortex scaling parameter
β_v	Oseen vortex scaling parameter
Γ	circulation
Γ_1	Graftieaux vortex identification function
γ	Oseen vortex radius scaling constant
Δx	vector grid spatial resolution in the x-direction
Δy	vector grid spatial resolution in the y-direction
δ_{ij}	Kronecker delta
δ_W	correlation based correction spatial translation of interrogation windows
ε	dissipation rate

ε_d	vortex core location error
ε_{Oseen}	difference between measured velocity and Oseen vortex profiles
ε_{thresh}	threshold value
ε_u	velocity error
η	Kolmogorov length scale
κ	wavenumber
Λ	integral length scale
λ	wavelentgth
$\lambda^{(n)}$	n^{th} proper orthogonal decomposition eigenvalue
λ_T	Taylor micro-scale
μ	fluid dynamic viscosity
μ_p	particle image density
ν	fluid kinematic viscosity
π	$\simeq 3.141\ldots$
ρ	normalised radial coordinate
ρ_f	fluid density
ρ_p	particle density
σ_c	vortex spatial stability
σ_l	laser sheet half thickness
σ_p	standard deviation of particle image diameters
θ	angular coordinate
τ_{ij}	stress tensor
τ_s	fluid relaxation time
ϕ	proper orthogonal decomposition spatial mode
Ψ	body force per unit mass
$\mathbf{\Omega}$	vorticity tensor
ω_{ij}	vorticity component

Acronyms / Abbreviations

CBC	Correlation Based Correction
CCD	Charged Couple Device
CCF	Cross Correlation Function
CNN	Cellular Neural Network
CVD	Combinatorial Vortex Detection
DNS	Direct Numerical Simulation
ENMT	Enhanced Normalised Median Test
FFT	Fast Fourier Transform
HPIDCBC	Hybrid Particle Image Distortion Correlation Based Correction
HPIV	Holographic Particle Image Velocimetry
LES	Large Eddy Simulation
MGRID	Multigrid
MVM	Maximum Vorticity Method
Nd:YAG	Neodymium-yttrium aluminium garnet
NMT	Normalised Median Test
PCA	Principle Component Analysis
PID	Particle Image Distortion
PIV	Particle Image Velocimetry
POD	Proper Orthogonal Decomposition
SCC	Standard Cross Correlation
SVD	Singular Value Decomposition
WAM	Winding Angle Method

Chapter 1

Particle Image Velocimetry

1.1 Overview

Particle image velocimetry (PIV) is a non-intrusive optical full-field method for the measurement of velocities in a fluid. Due to the optical non-intrusive nature there are clear advantages over other methods such as rakes of hotwires or pressure probes as the flow is not disturbed. The method involves imaging seed particles (or droplets) that follow the flow sufficiently and then calculating the displacement of the particles between two subsequent frames. In most applications the seed particles are illuminated by a laser light sheet and imaged using a charged couple device (CCD) camera, a typical modern two-dimensional PIV system diagram can be seen in Figure 1.1.

Once the images have been captured there are a number of ways in which the velocity vector field can be extracted, the most common method is to divide the recorded image into small interrogation windows, the cross-correlation between two interrogation regions from two subsequent frames is then taken. The displacement vector, ds, is then calculated from the location of the largest peak in the correlation plane and when divided by the time between frames, dt, the average velocity of particles in the interrogation region is then calculated as ds/dt.

1.2 Historical Background

The idea behind modern PIV can be traced back to the work carried out by Ludwig Prandtl at the turn of the century, he developed a water tunnel to study the unsteady flow behind objects submerged in the flow. Mica particles were suspended on the surface of the water and from this the flow structures could be observed, though only qualitatively as quantitative methods had not yet been developed (Raffel et al., 1998).

It was later recognised that photographing a set of particle tracers in a flow field generated a faithful reproduction of the particle distribution (rather than a speckle pattern) and from a multiply exposed image, particle and thereby flow velocities can be inferred. This realisation led to the expression particle image velocimetry (PIV) in 1984 (Pickering and Halliwell, 1984).

In early applications prior to the availability of digital cameras film cameras were used in

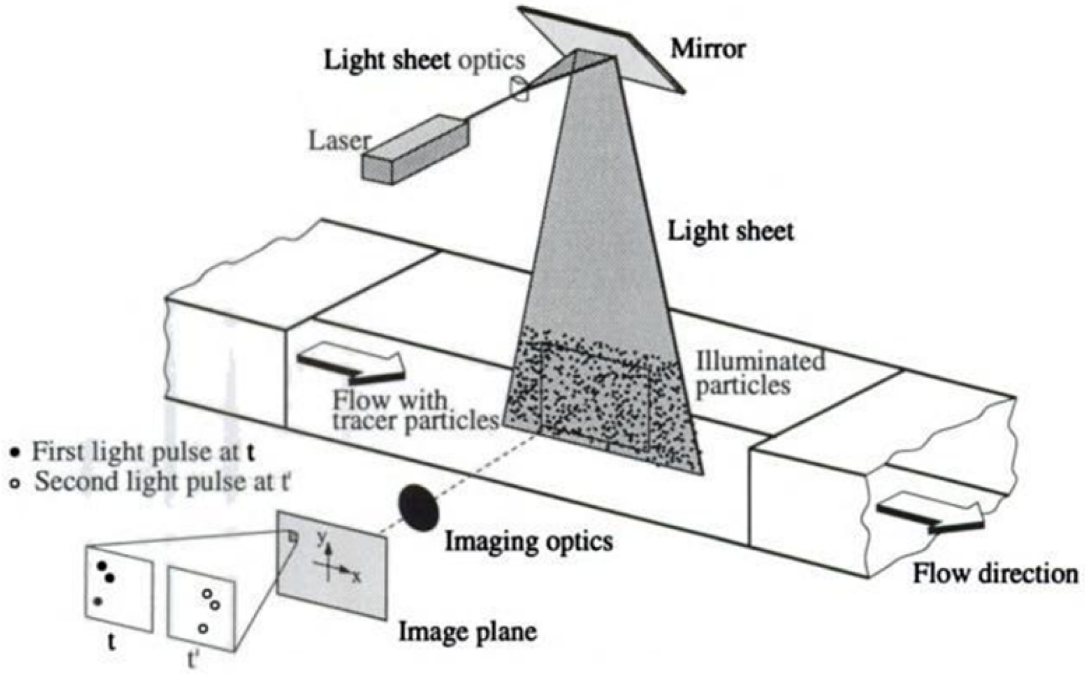

Fig. 1.1 Basic PIV setup, from (Raffel et al., 1998).

which case two frames were imaged onto the same sheet of film giving a double exposed image. This presented difficulty in determining the direction of the flow in complex flows (for example, turbulent flows) as it could not be distinguished whether particle images belonged to the first or second exposure. It was Adrian (1988) who laid down the groundwork for modern PIV theory by outlining a method for calculating the auto-correlation function for a double-exposure PIV image, this method though did not overcome the directional ambiguity as when the auto-correlation is taken there is a peak value at zero displacement with lower magnitude peaks at positive and negative positions corresponding to the actual particle displacement in the correlation plane.

With the development of digital CCD cameras digital PIV was developed (Willert and Gharib, 1991) with particle images now recorded on separate frames and analysed using cross-correlation analysis. See §1.8 for a detailed review.

1.3 General considerations of PIV

PIV has developed considerably during the last twenty years and considerable research has been done and published (Adrian, 1991; Raffel et al., 1998); some of the general considerations concerning PIV are mentioned below

- PIV is a non-intrusive technique as opposed to conventional techniques which use probes, pressure tubes etc. Therefore, PIV can be applied to high speed flows, boundary layers which may be disturbed and modified by the presence of a probe or in multi-phase systems such as a fuel spray where the atomisation processes will not be affected by the measurements.

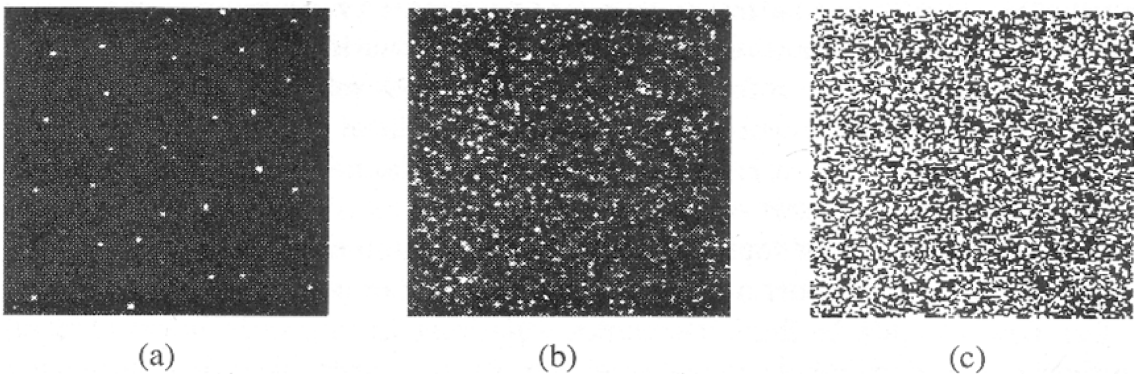

Fig. 1.2 Levels of seeding density of PIV images, (a) low density, (b) medium density and (c) high density. Image from (Raffel et al., 1998).

- Velocities using PIV are measured indirectly; these are calculated by measuring the velocities of tracer particles which, in most of the cases, have been previously added to the flow.
- Unlike most of the available diagnostics techniques, PIV is a whole field technique. It is possible to record images of large parts of the flow giving a high spatial resolution with a temporal resolution limited by technical restrictions; on the other hand, most of the conventional techniques for velocity measurement (such as hot wire anemometry) provide measurements at a single point with high temporal resolution.
- The choice and distribution of the tracer particles is of fundamental importance; seeding particles must follow the flow accurately and the seeding level should be of medium density and homogeneously distributed in the flow.
- The selection of the illumination source is equally important and dependant on the particular application; in gas applications a high power laser source is usually required due to the need of using small particles (~2μm), which will scatter less light, so that they follow the flow accurately. On the other hand, in liquid flows larger particles (~20μm), which scatter more light, can be used and therefore a lower power laser source may be used.
- The time delay between the two laser pulses must be long enough to determine the displacement of the tracer particles and short enough to avoid tracer particles leaving the laser sheet between consecutive illuminations due to in-plane or out of plane displacement.
- Although the density of the particle images vary according to different applications, three types of images can be distinguished as shown in Figure 1.2.

Low density images, as presented in Figure 1.2a require tracking methods for evaluation and this method is normally referred to as particle tracking velocimetry; images with medium image density (Figure 1.2b) require statistical evaluation techniques and this case is referred to as particle image velocimetry (PIV); images with high particle density are referred to as laser speckle velocimetry (Figure 1.2c).

Different factors have influenced the development of PIV during the last two decades such as the use of digital techniques which have replaced conventional analogue recording and evaluation techniques; there have also been other important landmarks on the development of PIV and can be grouped as follows (Raffel et al., 1998):

- The use of Nd:YAG lasers with doubled frequency (wavelength of 532nm of green visible light achieved) and double oscillator allowed the illumination of a plane with laser pulses of the same energy with any delay between the two laser pulses at repetition frequencies of around 10Hz.

- Initial efforts on image recording did not allow separate recordings of the first and second illumination so the temporal sequence of the images could not be obtained. Different methods were developed to overcome the limitations of directional ambiguity including image shifting. It was also very important that there was a considerable improvement in computer hardware (memory size and processors) allowing for a faster and more reliable image handling and processing of PIV data.

- Similarly, recording devices have also improved considerably in the last 20 years; today's progressive scan video cameras allows for the recording on separate frames of different illumination images with exposure separations of <1 microsecond.

1.4 Acquisition of PIV Data

1.4.1 Light Scattering of Small Particles

PIV recordings are generated by capturing the light scattered by tracer particles from an illumination source with the recorded image contrast directly proportional to the power of the scattered light (Raffel et al., 1998). For particles with a diameter greater than the wavelength of the illuminating light Mie's scattering theory can be applied (Hulst, 1957; Stanislas and Monnier, 1997; Willert and Gharib, 1991). Mie scattering is characterised using a normalised diameter, d_λ, and is defined as:

$$d_\lambda = \frac{\pi d_p}{\lambda} \tag{1.1}$$

Where d_p is the particle diameter and λ the wavelength of the light (Raffel et al., 1998; Stanislas and Monnier, 1997). Figure 1.3 shows the light scatter intensity for 10μm oil particles in air (Raffel et al., 1998). The data is from the Lorenz-Mie solution to the Maxwell equations of electromagnetism with illumination at 532nm (Hulst, 1957), it can be seen that scatter is greatest for forward and backward angles (0° and 180° respectively) however for practical reasons owing to limited depth of field recording at 90° is most often used (Raffel et al., 1998).

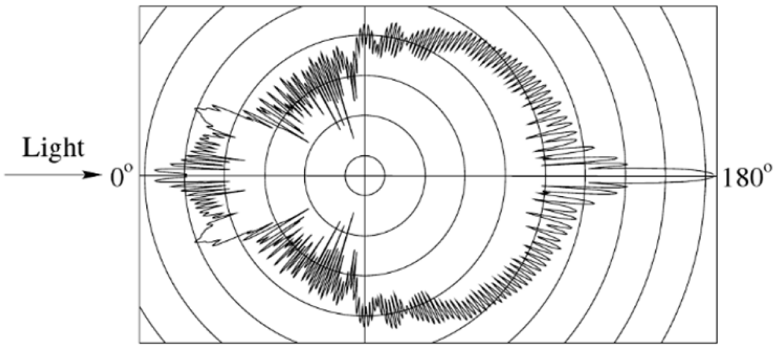

Fig. 1.3 Mie scatter light (λ = 532nm) intensity against scatter angle for a 10μm oil particle in air (Raffel et al., 1998).

1.4.2 Light Sources

Two of the overriding requirements of PIV are that a) the time between the capturing of subsequent image frames is very short (usually on the order of 10-100μs) to ensure that the displacement of the tracer particles between images remains low and b) the exposure time of the image is also low (nanoseconds) as the target images are not stationary long exposures will result in streaked particle images with indeterminate location.

Taking into account the short exposure times the tracer particles need to reflect enough light through Mie scattering for the recording device to be able to detect the particles. In modern PIV the most common light sources are lasers owing to their ability to "output a large amount of light in a very small solid angle and then it is quite easy to transform the laser beam into a thin sheet of light" (Stanislas and Monnier, 1997). Pulsed lasers are most commonly used over continuous output lasers as short light pulses are required so that particle images do not become blurred, pulse lasers can fire short nano-second scale pulses whereas continuous lasers require a high speed mechanical shuttering system to emit short pulses.

Pulsed lasers come in two varieties, single pulse and repetitive. Single pulse lasers, of which a ruby laser is an example have a very low repetition rate but are capable of emitting high energy pulses at 694.3nm (Stanislas and Monnier, 1997).

Many pulsed lasers, specifically designed for applications to PIV are equipped with two laser cavities enabling two pulses to be separated by an arbitrary time whilst both pulsing at a rate for the continuous capture of PIV image pairs. If single cavity laser heads are used then it is often required to use two laser heads to get the required time separation between pulses which adds extra complications in that the two beams have to be aligned to follow the exact same path after they have exited their individual laser heads. This tends to be more complex to setup and maintain alignment than when the two laser cavities are housed within a single laser head. A comprehensive review of helium-neon (He-Ne), argon-ion (Ar+), ruby (Cr 3+), semiconductor and Nd:YAG lasers and applications to PIV is provided in (Raffel et al., 1998) with a further detailed evaluation of Nd:YAG lasers provided in (Stanislas and Monnier, 1997).

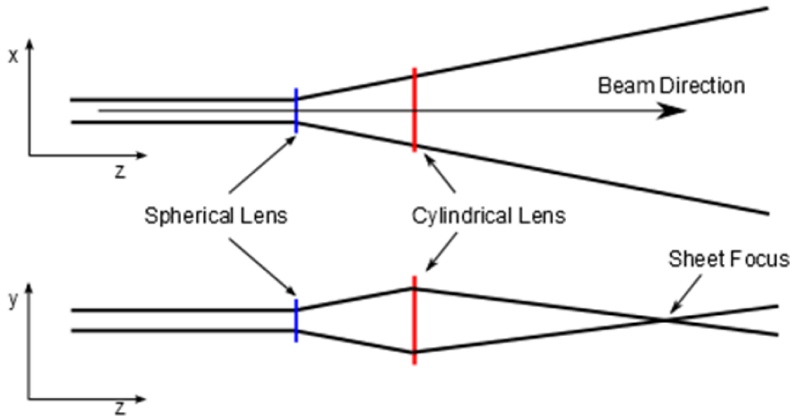

Fig. 1.4 Formation of a laser light sheet using a combination of spherical and cylindrical lenses.

Neodymium-YAG Laser

The most commonly used laser for PIV experiments is the Nd:YAG (neodymium-yttrium aluminium garnet) solid-state laser (Raffel et al., 1998; Stanislas and Monnier, 1997). Nd:YAG lasers emit light at 1064nm generated by Nd3+ ions which are incorporated in YAG crystals (Raffel et al., 1998). The natural output wavelength of 1064nm lies outside the visible range and the absorption range of silicon detectors and is hence not suitable for PIV but by using a frequency doubler the output wavelength can be halved to 532nm (Stanislas and Monnier, 1997) which also happens to be in the optimum region of most CCD cameras. Short pulse durations of the order approximately 5–10ns are also ideal for fulfilling the requirement of short exposure times to avoid blurring of particle images.

Nd:YAG lasers can be configured to output beams with a Gaussian energy profile. Before using an Nd:YAG laser, the cavity has to reach a thermal equilibrium as beam quality and output power are all finely tuned to the laser rod (Stanislas and Monnier, 1997).

1.4.3 Beam Shaping

When emitted from a Nd:YAG laser the beam is approximately Gaussian profiled and normally collimated with a small cross-sectional area (of the order of millimetres), two dimensional PIV requires a sheet of illumination in the measurement plane. The most common way of shaping a collimated beam of laser light into a flat sheet is through the use of a cylindrical lens. Unlike spherical lenses a cylindrical lens is only curved in one axis causing light to converge in only that axis as show in Figure 1.4. Owing to the small profile of the laser beam a spherical lens (with negative focal length) is used to expand the beam first before hitting the cylindrical lens to increase the effect.

For planar PIV a thin light sheet is required to increase the energy incident on the particles, this means arranging the optical setup so the focus of the light sheet is in the centre of the measurement plane.

Certain considerations have to be taken into account when creating a light sheet for use in

PIV experiments, mainly that the more the sheet is expanded in the x-direction (see Figure 1.4) the energy density of the light is reduced as it is spread over a larger area meaning that less light will be available to illuminate the tracer particles. The light sheet intensity is at a maximum at the y-direction focus of the light sheet, it is important to make sure the distance between the cylindrical lens and the light sheet focus is not too small to ensure the thickness of the sheet in the measurement area does not diverge too much and reduce particle image contrast.

1.4.4 Image Acquisition

As previously stated the first PIV experiments were carried out using photographic film but modern digital PIV is now the state of the art with vast improvements in digital camera technology over the last 20 years.

The most commonly used typed of camera for capturing particle images is a charge coupled device (CCD) camera. A CCD is essentially a device which converts light into an electronic signal. A CCD sensor works using the photoelectric effect, a silicone crystal at its rest state has its electrons mostly in a low energy state, when excited by impacting photons electrons jump to a higher energy state creating a potential well. These excited electrons are stored as a charge for the duration of the exposure, during this time the more photons that hit the CCD the greater the charge. Each CCD has a maximum charge it can store, if more photons hit above this the stored charge does not increase and this is what leads to overexposure (Raffel et al., 1998). A CCD Camera has a sensor that is made up of a two-dimensional array of detector elements with each representing an image pixel. It is typical for modern PIV to have sensors containing 1 to 4 megapixels although with advancing technology higher resolution sensors are available. When the exposure is complete the charge is converted to a digital signal which is stored in the camera memory before it is transferred to a computer as a digital image.

CCD sensors are only able to detect photons for a given band of wavelengths from ultraviolet to near infrared. The efficiency of the CCD to detect photons reduces at the extremes with typical maximum efficiencies in the region of 450-700nm (Raffel et al., 1998) giving the greatest light sensitivity in the visible region. A typical light efficiency spectrum for a given CCD is shown in Figure 1.5.

1.4.5 Tracer Particles

As the point behind PIV is to measure fluid by tracing the movement of particles within the flow, some form of seed particles have to be used. Suitable tracer particles must meet two main requirements:

1. They must scatter enough of the illumination source light to be detected by the imaging device.

2. They must follow the flow as accurately as possible without modifying the nature of the

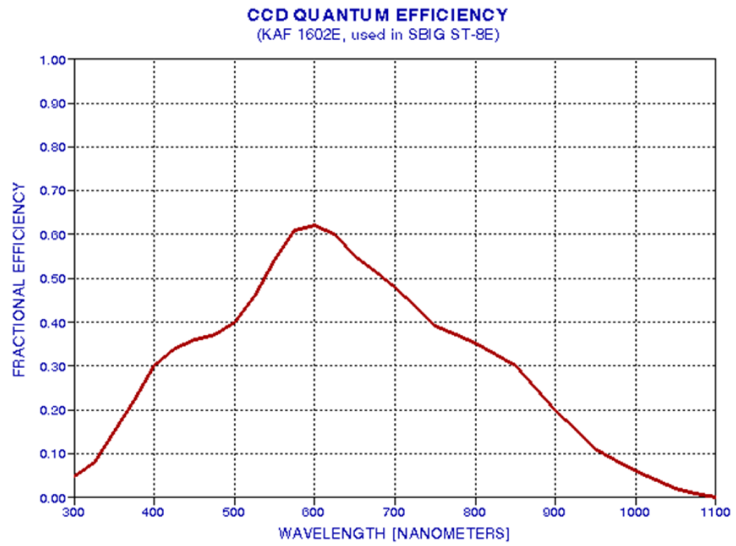

Fig. 1.5 CCD quantum efficiency as a function of photon wavelength (taken from www.brucegary.net).

measured flow.

The major source of error by particles not accurately following the measured flow arises from the inertia of the particle due to difference in the densities of the fluid and the tracer particles (Raffel et al., 1998). A particle's behaviour under acceleration can be described using Stokes drag law, the velocity lag of a particle under continuous acceleration in a viscous fluid is described as (Raffel et al., 1998):

$$\mathbf{u}_s = \mathbf{u}_p - \mathbf{u} \tag{1.2}$$

$$\mathbf{u}_s = d_p^2 \left(\frac{\rho_p - \rho_f}{18\mu} \right) \mathbf{a} \tag{1.3}$$

Where $\mathbf{u}_s$ is the velocity lag, $\mathbf{u}_p$ is the particle velocity, $\mathbf{u}$ the fluid velocity d_p the particle diameter, ρ_p and ρ_f the particle and fluid densities respectively, μ the dynamic viscosity of the fluid and $\mathbf{a}$ the acceleration the particle is undertaking (Raffel et al., 1998). It can be seen from (1.3) that the velocity lag can be minimised when the density of tracer particles is equal to that of the fluid, this is not always achievable in practice so the aim should be to match the tracer particle density as closely as possible.

In situations where the density of the tracer particles is much greater than that of the fluid the step response of the particle velocity $\mathbf{u}_p$ to a step change in flow velocity can be modelled as follows:

$$\mathbf{u}_p(t) = \mathbf{u} \left[1 - \exp\left(\frac{t}{\tau_s} \right) \right] \tag{1.4}$$

Where the relaxation time τ_s is defined by (Raffel et al., 1998):

$$\tau_s = d_p^2 \frac{\rho_p}{18\mu} \tag{1.5}$$

By combining (1.4) and (1.5) it can be seen that the time response of the particles increases with particle diameter and particle density meaning they will react to changes in the flow more slowly.

As light scattering increases with particle diameter but particle velocity lag also increases with diameter a compromise has to be reached where the particles accurately follow the flow but remain large enough to scatter the required amount of light for imaging.

1.5 Analysis Methods

The nature of PIV images which contain anywhere between thousands and millions of particle images implies that manual analysis of the displacement between pairs of particle images between one frame and another is impossible, therefore automated algorithms have to be applied. The aim of PIV is to statistically calculate the average displacement of a number of particles in a particular region (interrogation region) of the full image between the two image frames. The way this is achieved is by using cross-correlation image-matching algorithms which can be calculated in either the spatial or frequency domain, the two approaches are described subsequently.

1.5.1 Direct Spatial Domain Cross-Correlation

When subsequent particle images are contained on separate image frames cross-correlation can be applied to analyse the data (Keane and Adrian, 1992). The continuous cross correlation function (CCF), C, of two images q_1 and q_2 which are sub-images of the whole image frames and known as interrogation regions is defined as (Grant, 1997; Keane and Adrian, 1992):

$$C(m,n) = \int_{-\infty}^{\infty} q_1(x,y)\, q_2^*(x+m, y+n)\, \mathrm{d}x\mathrm{d}y \tag{1.6}$$

where $q_{1,2}(x,y)$ are the greyscale light intensity value in the image plane at the location (x,y) with values ranging from zero (black) to 255 (white) for 8-bit images, q_2^* denotes the complex conjugate of q_2, (x,y) is a spatial coordinate and (m,n) is a coordinate in the CCF relating to the spatial offset between q_1 and q_2. Once the cross correlation has been carried out, within the CCF there is a peak at some coordinate (m,n), this is the mean displacement of particle images between frames 1 and 2. The main advantage of using the cross-correlation compared to auto-correlation is that there is no self-correlation peak relating to no image shift and there is only one main peak at the particle displacement as the temporal order of the particle images is known.

When using digital images it is not practical to use the continuous cross-correlation so instead the discrete version is utilised:

$$C(m,n) = \sum_i \sum_j q_1(i,j)\, q_2(i+m, j+n) \tag{1.7}$$

Where (i, j) is an integer pixel coordinate in the image q and is summed over the dimensions of the image. The above equation is very sensitive to fluctuations in the intensity values q_1 and q_2, to overcome this it is common to normalise the equation in the following manner (Huang et al., 1997):

$$C(m,n) = \frac{\sum_i \sum_j [q_1(i,j) - \bar{q}_1][q_2(i-m, j-n) - \bar{q}_2]}{\sqrt{\sum_i \sum_j [q_1(i,j) - \bar{q}_1][q_2(i,j) - \bar{q}_2]}} \tag{1.8}$$

Where, $\bar{q}$ is the mean pixel intensity of the overlapping regions and the summations are only calculated over the overlapping regions (Gonzalez and Woods, 2001; Huang et al., 1997). Shavit et al. (2007) present a method to further reduce sensitivity to variations in particle brightness by capping all intensity values at a certain intensity.

1.5.2 Frequency Domain Cross-Correlation

The above spatial cross-correlation is computationally intensive, to save processing time the cross-correlation can be calculated in the frequency domain implementing the Fast Fourier Transform (FFT) and the Wiener-Khinchin theorem. The Wiener-Khinchin theorem states that the auto-correlation function (C_A) is equal to the inverse Fourier transform, $\mathscr{F}^{-1}$ of the Fourier transform, $\mathscr{F}$ of the original function squared (Hariharan, 1984):

$$C_A = \mathscr{F}^{-1}\left[\left(\mathscr{F}(q)\right)^2\right] \tag{1.9}$$

(1.9) can easily be modified to implement the cross-correlation, C by taking the inverse Fourier transform of the product of the Fourier transforms of the two images q_1 and q_2:

$$C = \mathscr{F}^{-1}\left[\mathscr{F}(q_1)\mathscr{F}(q_2)\right] \tag{1.10}$$

which reduces to the convolution between the two input images, q_1 and q_2

$$C = q_1 \otimes q_2 \tag{1.11}$$

Implementing FFT correlation the number of computations is reduced from order O$[N_W^4]$ using direct spatial cross-correlation to order O$[N_W^2 \log 2 N_W]$ (Pratt, 2001; Raffel et al., 1998) making it much more efficient, where N_W is the linear dimension of the interrogation region. There are a number of studies that have shown that the FFT implementation of the correlation function is less accurate than that of the direct normalised spatial cross-correlation (Gui and Merzkirch, 2000; Pust, 2000) with Pust showing that peak locking (of which a description is provided in § 1.5.5) effect is more pronounced when the FFT method is used.

Windowing

Problems arise when using the FFT method as the FFT is taken over a finite domain which in most cases is very small, i.e. 16x16pix^2, 8x8pix^2 etc, but for the transform to work effectively the function that is to be transformed must be periodic, this can be assumed to be true in the case where there are no particle images on the boundary of the interrogation window giving an ideal value (greyscale intensity) of zero at every point on the boundary. In the alternate case where a particle image or part particle image is present on the boundary the image (the transformed function) is no longer periodic causing leakage of the energy present in the spectral power density and hence a loss of information when inverting the transform. One solution to this problem is to apply a window-function (i.e. Hanning, Hamming, Gaussian, zero-padding etc...) (Eckstein and Vlachos, 2009a; Gui and Merzkirch, 2000; Nogueira et al., 1999; Scarano, 2003). In a detailed review of windowing techniques Eckstein and Vlachos (2009b) show how windowing can reduce the error in estimating particle displacement by 30%-50% when compared to no windowing, there is however no information regarding the extra computations and how much more processing time it takes as the aim of the FFT correlation is to decrease processing time.

Zero-padding (Raffel et al., 1998) which extends the sample size to four times the original by filling in zeros has proved to perform poorly as the original image usually contains a noisy, non-zero background causing the spectra of the image to become contaminated with the high frequencies present at the edge where the noisy background meets the padding zeros. Fore et al. (2005) show how this effect can be reduced through background scaling and noise removal.

Previously when implementing the FFT the interrogation window had to have sides of a length of a power of two limiting the range of velocities that could be effectively resolved but Gui (1998) devised a method in which interrogation regions of any size can be used.

It is assumed that the FFT-based correlation transforms a periodic function resulting in the correlation function also being periodic, this creates problems when the particle displacement exceeds more than half the interrogation region size as the correlation peak will appear on the other side of the correlation plane. This arises due to a breach of the Nyquist theorem resulting in aliasing of the data. To overcome this one would have to increase the interrogation window size or reduce the time between frames, dt (Raffel et al., 1998).

1.5.3 Correlation Function Peak Fitting

Once the cross correlation has been carried out the average particle displacement is at the location of the highest peak in the correlation plane but as the data is digitised correlation values only exist at integer displacements giving an accuracy of only $\pm$1/2pix. To get a more accurate measure of the particle displacement to sub-pixel accuracy a function can be fitted to the correlation peak values. The most common peak fitting estimator is the Gaussian peak fit as the correlation peaks tend to be approximately Gaussian in shape. The Gaussian peak fit is typically a three-point estimator, using three points in each direction to fit a Gaussian curve to the peak location gives a

Table 1.1 The-point subpixel correlation function fitting functions. Reproduced from (Raffel et al., 1998).

Fitting function	Estimators
Peak centroid	$x_0 = \frac{(m-1)C_{(m-1,n)}+mC_{(m,n)}+(m+1)C_{(m+1,n)}}{C_{(m-1,n)}+C_{(m,n)}+C_{(m+1,n)}}$
$f(x) = \frac{\text{first order moment}}{\text{zero order moment}}$	$y_0 = \frac{(n-1)C_{(m,n-1)}+nC_{(m,n)}+(n+1)C_{(m,n+1)}}{C_{(m,n-1)}+C_{(m,n)}+C_{(m,n+1)}}$
Parabolic peak fit	$x_0 = m + \frac{C_{(m-1,n)}-C_{(m+1,n)}}{2C_{(m-1,n)}-4C_{(m,n)}+2C_{(m+1,n)}}$
$f(x) = \alpha x^2 + \beta x + \gamma$	$y_0 = n + \frac{C_{(m,n-1)}-C_{(m,n+1)}}{2C_{(m,n-1)}-4C_{(m,n)}+2C_{(m,n+1)}}$
Gaussian peak fit	$x_0 = m + \frac{\ln C_{(m-1,n)}-\ln C_{(m+1,n)}}{2\ln C_{(m-1,n)}-4\ln C_{(m,n)}+2\ln C_{(m+1,n)}}$
$f(x) = \gamma \exp\left[\frac{-(x_0-x)^2}{k}\right]$	$y_0 = n + \frac{\ln C_{(m,n-1)}-\ln C_{(m,n+1)}}{2\ln C_{(m,n-1)}-4\ln C_{(m,n)}+2\ln C_{(m,n+1)}}$

more accurate particle displacement. Other methods of peak detection include finding the centroid of the peak and fitting a parabolic curve, the three methods are summarised in Table 1.1. The following process can be used to detect correlation peaks to sub-pixel accuracy:

1. Scan the correlation plane C to find the maximum value $C(m,n)$ at the location (m,n).

2. Record the four adjoining correlation values: $C(m-1,n), C(m+1,n), C(m,n-1), C(m,n+1)$.

3. Use three points in each direction to apply a three point estimator, see Table 1 1.

1.5.4 Errors

There are two main types of error present in PIV measurement; random and bias errors. Random errors arise due to electrical camera noise and errors associated with identifying the sub-pixel displacement (Christensen, 2004). Random errors can be reduced by statistical analysis using a sufficiently large ensemble set of data in either space or time (Chen and Katz, 2005; Christensen, 2004).

Bias errors are more problematic as they arise due to uncertainties with the fill ratio of the CCD camera, interrogation algorithm and most significantly peak locking (pixel locking) errors (Christensen, 2004). Sources of and means of reducing bias errors are discussed in the following sections.

1.5.5 Peak Locking

The peak-locking effect arises due to the biasing of particle displacements towards integer pixel values. The scale of the peak locking is effected by a number of factors such as particle image diameter (Adrian, 1991), particle displacement (Adrian, 1991; Raffel et al., 1998), the sampling of the particle images. The sub-pixel locator used with Westerweel (1997) showing that the Gaussian fit outperforms both centroid and parabolic fitting in terms of minimising peak lock errors and where Pust (2000) shows that a normalised direct spatial cross-correlation has reduced peak locking error when compared to an FFT based correlation. Gui and Wereley (2002) and Cholemari (2007) present studies into the peak locking effect and a methods by which it can be reduced.

There are many methods for reducing the effect of peak locking (Gui and Wereley, 2002) such as the use of correlation mapping as done by Chen and Katz (2005), the use of discrete window shifts (Westerweel et al., 1997) to name but a couple.

The diameter of captured particle images plays an important role in the effect of peak locking, ideally particle images should have a diameter of 2-3pix. Particle images with a diameter of 1 pixel or less leads to a high peak locking effect as the centre of the particle image will be located at the centre of the pixel when calculated using curve fitting functions giving bias towards integer values. Conversely particles with a diameter greater than two pixels can be located more accurately as when applying a curve fitting function the location of maximum intensity can be calculated to sub-pixel accuracy.

To minimise the effect of peak locking it is therefore necessary when setting up a PIV experiment to choose appropriate optics and carefully selected tracer particles to ensure that the captured particle images are of an optimum size. Further it is important to choose algorithms such as Gaussian sub-pixel peak detection when processing the PIV data to further minimise the effects of peak locking.

1.5.6 Discrete window shifting and multigrid algorithms

Various studies show that errors in displacement vector calculations are at a minimum when the particle displacements are less than 0.5pix (Cameron, 2011; Raffel et al., 1998). This fact can be taken advantage of by introducing an iterative window offset method (Westerweel et al., 1997). An initial displacement field is calculated using cross-correlation and vector validation to remove erroneous displacement vectors. Using the discrete displacement value from the initial cross-correlation function a second iteration is carried out only this time the interrogation window in the second image, I_2, is displaced by the discrete displacement calculated in the first iteration, ds as shown in Figure 1.6. The particle image displacement is then given as the sum of the discrete offset from the first iteration and the sub-pixel displacement from the subsequent iteration. This helps to reduce the effect of loss-of-pairs between images (reducing bias towards low levels of particle displacement) and reduces errors in the calculated displacements as all further displacements of particle images between the two new windows are in the range -0.5pix to 0.5pix.

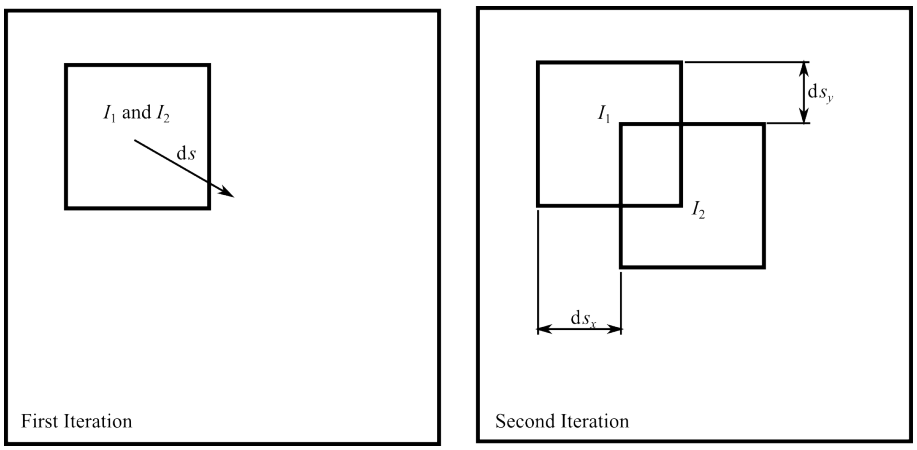

Fig. 1.6 Interrogation region arrangement for first and second iterations when using discrete window shifting.

Experiments carried out by Westerweel et al. (1997) show that a measurement error of only 0.5% can be obtained when evaluating grid-turbulence when using a discrete window shift. Scarano and Riethmuller (1999) further develop this method into an iterative procedure where the particle displacement is iteratively predicted and corrected with vector validation carried out after each iteration to further increase accuracy. The multigrid method allows for an increase in spatial resolution of the vector field by increasing the detectable particle displacement, Adrian (1991) established the general rule that a particle displacement should not exceed more than one quarter of the size of the interrogation window due to increasing error with displacement due to the 'loss of pairs' where particle images move outside the interrogation window resulting in lower correlation peaks and consequently a lower signal to noise ratio. The errors due to the loss of pairs can almost wholly be eliminated using window offsets as the displacement of particle images is followed by the interrogation windows and using this method the window size can be iteratively decreased further increasing spatial resolution as shown in Figure 1.7. In Figure 1.7 the first iteration is carried out with two interrogation regions, I_1 and I_2 with the same coordinates in the first and second images. In the second iteration the interrogation window size is reduced (by half in this case) giving four new interrogation windows; $I_{1,1}$, $I_{1,2}$, $I_{1,3}$ and $I_{1,4}$ in the first image and $I_{2,1}$, $I_{2,2}$, $I_{2,3}$ and $I_{2,4}$ in the second. CCFs are then calculated between corresponding interrogation windows ($I_{1,n}$ and $I_{2,n}$) where the second frame interrogation windows, $I_{2,n}$ are translated by the displacement calculated in the first iteration as in Figure 1.6.

Applying the iterative multigrid method to flow over a backward facing step Scarano and Riethmuller (1999) show that the minimum resolvable displacement is reduced by approximately a third and the maximum amplified by up to a factor of four when compared to the method without any offset. This is an increase in the dynamic range (the ratio of measurable displacements to window size) allowing larger displacements to be measured using smaller window sizes and thus increasing spatial resolution.

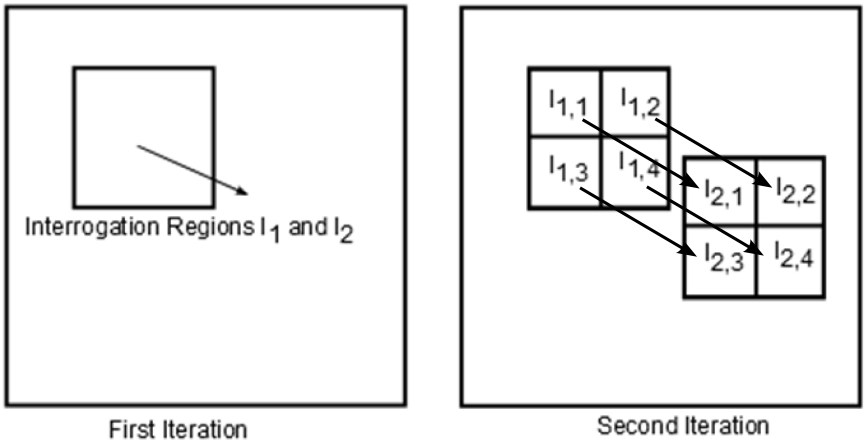

Fig. 1.7 Interrogation region arrangement for first and second iterations when using discrete multi-gridding.

1.5.7 Continuous Window Deformation

As in most practical fluids experiments velocity gradients are present within the flow field resulting in non-uniform particle displacement within an interrogation region (Westerweel, 2008). In cases where these spatial velocity gradients are high the cross-correlation function can fail to provide a dominant displacement peak resulting in spurious data or less accurate displacement vectors due to the stretching of the cross-correlation peak. Iterative multi-gridding with a discrete offset can reduce the effect up to a point by reducing the window size and hence reducing the difference in particle image displacements within the window due to gradients.

First proposed by Huang et al. (1993) particle image distortion (PID) or iterative image deformation methods (Scarano, 2002), apply a continuous offset to each pixel in the second interrogation window based on the displacement field calculated in the first iteration using standard cross-correlation (SCC) (see § 1.5.1). Huang et al (Huang et al., 1993) state that fluid motion can be described as the summation of three components; convection (translation), stretch and rotation. The first of these, translation is dealt with in the previous section using a discrete offset of the second interrogation window, but in this case a continuous sub-pixel translation is applied. The stretch and rotation terms are calculated from the various spatial derivatives of the displacements. By using an image interpolation scheme the displacement at each pixel between each vector grid point can be calculated, these individual displacements are then applied to each pixel in the second interrogation window to deform it in such a way as that it follows the local velocity distribution across the interrogation region.

Since the second image is translated by a sub-pixel amount an image interpolation algorithm has to be applied to calculate the correct grey levels in the deformed window. The choice of interpolation algorithm has a large effect on the quality of the calculated vectors (Astarita, 2008; Astarita and Cardone, 2005; Duncan et al., 2009; Kim and Sung, 2006; Roesgen, 2003) and a trade-off between computation time and the accuracy of the reconstructed image has to be made.

Jambunathan et al. (1995) proposed a method where the second interrogation window is offset by a fractional amount and a linear deformation applied. Latterly more complex transformations are introduced such as sinc interpolation (Scarano and Riethmuller, 2000), spline and third order Lagrange interpolation (Fincham and Delerce, 2000) and quadratic and fourth-order Lagrange interpolations (Stanislas et al., 2003). Astarita (2008) and Kim and Sung (2006) provide a detailed evaluation of a number of deformation methods with the latter concluding that the sinc and Lagrange interpolations performed best with sinc interpolation optimal in terms of both performance and computation time for small particle images and Lagrange interpolation for larger particle images.

1.5.8 Other Vector Calculation Algorithms

Local field correction (Nogueira et al., 1999, 2001) is able to resolve flow structures smaller than the interrogation window and is almost indifferent to the effect of particles with differing brightnesses as the field is first estimated using the brighter particles but then the deformation of particles is compensated and fainter particles are considered to finish the correlation. Other advanced methods include adaptive space resolution (Astarita, 2009), reverse hierarchical processing (Rohály et al., 2002), phase correlation (Eckstein et al., 2008; Eckstein and Vlachos, 2009b), phase only filtering (Awwal et al., 2000; Wernet, 2005) and the use of weighting windows with significantly increased computation time and some improvements in particle displacement resolution (Astarita, 2007; Nogueira et al., 2002).

Another more advanced correlation based vector calculation algorithm is Hart's 'correlation based correction' (CBC) (Hart, 2000) which aims to reduce the amount of spurious vectors calculated whilst improving the accuracy in measured velocity, especially in regions of high velocity gradients through the multiplication of adjacent correlation functions. The CBC method is investigated in detail in § 5.

1.6 High-Speed Time-Resolved PIV

High-Speed Time-resolved PIV (TR-PIV) is a rapidly developing implementation of PIV in which the temporal evolution of flows can be evaluated by capturing PIV image pairs at a high temporal frequency. This is an important development as highly resolved temporal data is crucial for the analysis of the smaller structures present in turbulence as will be discussed in the following chapter. The three major limiting factors with TR-PIV are laser repetition rate, camera framing rates and camera memory capacity (Wernet, 2007). However, with the use of modern equipment PIV data can be captured at rates of 50 kHz (25 kHz for frame pairs) for low spatial resolutions (640x80 pixels) (Wernet, 2007). Towers and Towers use high speed TR-PIV to capture data at 14kHz in three orthogonal planes in an optical gasoline direct injection (GDI) engine cylinder and isolate high-frequency turbulence from bulk-flow components, this evaluation of high frequency

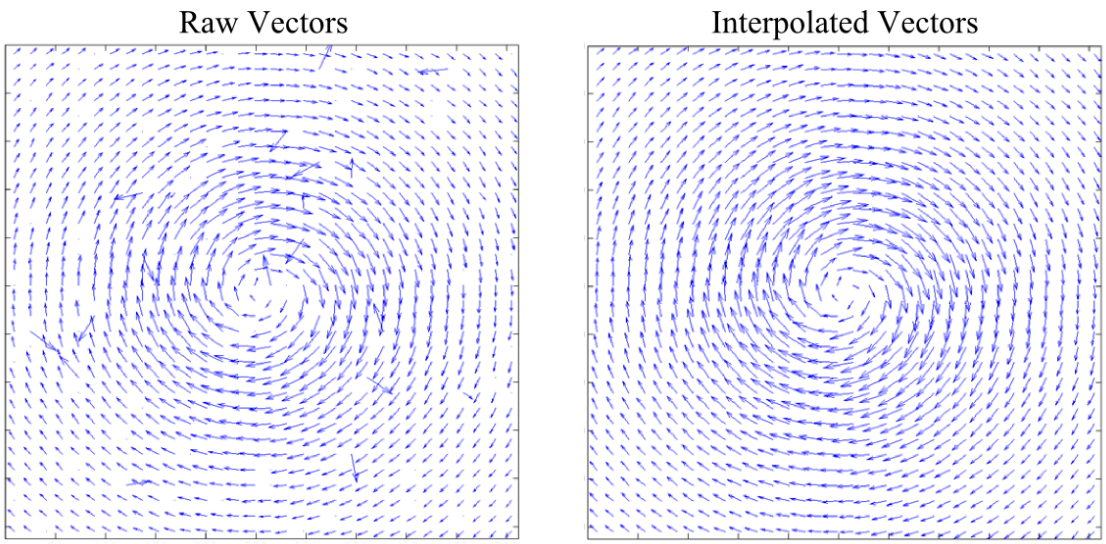

Fig. 1.8 (*left*) Raw velocity vector field containing spurious data and (*right*) the same vector field after spurious vectors are removed and replaced with interpolated vectors.

temporal structures is possible using standard, low repetition rate PIV (Towers and Towers, 2004, 2008). With TR-PIV data techniques such as proper orthogonal decomposition (presented in § 3) can be used to investigate turbulent flow evolution (Cosadia et al., 2007).

Using multiple lasers and cameras Timmerman et al. (2009) present a method where temporally resolved high resolution (2048 x 2048 pixel square images) PIV data can be recorded at megahertz frequencies. Using six cameras and five lasers Timmerman et al were able to capture up to six consecutive 4MP images at a temporal resolution of 2MHz from which both spatial and temporal flow structures can be evaluated.

1.7 Spurious Vector Detection

1.7.1 Introduction

In every PIV experiment, no matter how well designed, especially when investigating flows with complex structures when it comes to calculating the vector field there are more often than not vectors that do not fit in with the flow and can clearly be seen to be erroneous, these are referred to as spurious vectors, an example of which can be seen in Figure 1.8. A spurious vector can be identified as having a substantially different magnitude or direction to the surrounding data (Raffel et al., 1998). Spurious vectors arise due to interrogation windows having insufficient particle image pairs or a low signal to noise ratio (Nogueira et al., 1997), bad seeding, poor illumination, over exposure of images just to name a few and it is of interest to find, remove and replace these spurious vectors with interpolated values. Figure 1.8 shows the same vector field before and after data validation.

Due to very large data sets (thousands of vector fields each containing tens of thousands of vectors) the process has to be highly automated and has to be highly robust as individually checking

each vector field qualitatively is impossible.

The algorithm used to detect spurious vectors has to be robust as it is used in the intermediate stages when calculating the predictor fields during iterative vector calculation (multigrid). Due to this if any spurious vectors that are not identified, removed and replaced at each stage the predicted particle image displacement and resulting window shift deformation for the next iteration will be wrong leading to spurious or no vectors being calculated in the next iteration. Also it is important in the final vector field that all spurious data is removed from a data-set as further calculated properties such as divergence or vorticity based on raw velocity vector fields containing spurious vectors will greatly affect the quality of the results. After a vector validation algorithm has been applied the result is a vector grid with data missing at points where spurious vectors were present (Nogueira et al., 1997). In most cases it is desirable to fill in these gaps using interpolation methods, of which there are many including linear and bilinear interpolation of surrounding data, the median value of surrounding data or the mean value of the surrounding data (Raffel et al., 1998).

A spurious vector detection must meet two main criteria (Raffel et al., 1998):

- Detection of all spurious data.
- Rejection of the data if it cannot be decided whether the data is valid or not.

There are many methods for the detection of spurious vectors in a vector field, most of which are based on statistical methods. Westerweel (1994) presents a purely statistical method of detecting spurious vectors by comparing each displacement vector with nearby vectors. This was a key development as detection of spurious vectors by visual inspection is time consuming and subjective, for large data-sets a person carrying out the inspection will easily become fatigued and not all spurious vectors will be detected, or valid vectors will be detected as spurious (Raffel et al., 1998). Westerweel further develops this algorithm into a robust and efficient process for the detection of spurious vectors in fields and is described below in detail along with a number of other detection algorithms.

1.7.2 Global Histogram Operator

The global histogram operator (Raffel et al., 1998) is a basic spurious vector detection algorithm based on the difference in magnitude of a central vector to those surrounding it. It assumes that if the length scale of the flow is much greater than the distance between vectors then if a vector is spurious the difference in magnitude to its neighbours is above some threshold ε_{thresh}. The difference U_{diff} is calculated as the magnitude of the difference in vectors:

$$U_{diff_n} = |\mathbf{u}_i - \mathbf{u}_0| \tag{1.12}$$

Where $\mathbf{u}_i$ is a neighbouring vector and $\mathbf{u}_0$ is the vector under inspection. If $U_{diff} > \varepsilon_{thresh}$ the the vector is identified as spurious. The main limitation of this algorithm is that the threshold level

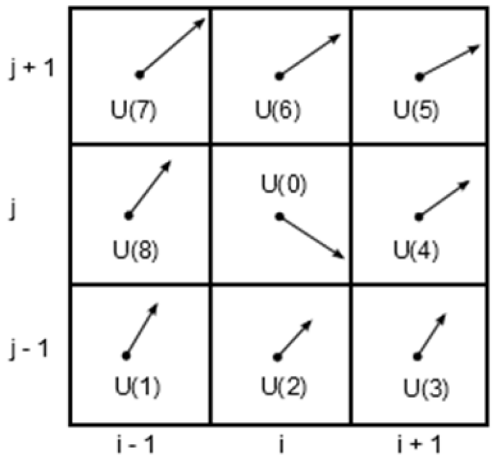

Fig. 1.9 Grid of a neighbouring 8 vectors centred around the spurious vector $\mathbf{u}(0)$.

chosen is sensitive to the velocity magnitudes present in the flow, if a threshold is chosen to be sensitive to spurious data in regions of high velocity spurious vectors in regions of low velocity may not be detected.

1.7.3 Normalised Median Test

A common and robust spurious vector detection algorithm is the normalised median test (NMT) as presented by Westerweel and Scarano (2005) an adaptation of the original and widely used median test by Westerweel (1994). The algorithm works by comparing the vector of interest to the local median of the nearest eight or 24 vectors, see Figure 1.9. At each point the local median is normalised by a specific value to enable a single threshold value to be used for the entire flow field making it more suitable to large area images where both high and low velocities are present.

In the case when a 3 x 3 vector filter is applied the nearest eight neighbouring vectors centred about the vector of interest, $\mathbf{u}_0$ are denoted by $\mathbf{u}_i$ where i = 1, 2,..., 8. The local median of the neighbouring vectors, $\mathbf{u}_{1-8}$ is denoted $\mathbf{u}_m$. From the local median and for each neighbouring vector a residual value, r_i is calculated as the modular difference between each vector $\mathbf{u}_i$ and the median vector $\mathbf{u}_m$:

$$r_i = |\mathbf{u}_i - \mathbf{u}_m| \tag{1.13}$$

A normalising value is next calculated, this is the median of the above residual values, r_i and is denoted r_m. The normalised residual, r'_0 of the vector $\mathbf{u}_0$, is then calculated by dividing the residual r_i by the normalising residual r_m:

$$r'_0 = \frac{|\mathbf{u}_0 - \mathbf{u}_m|}{r_m} \tag{1.14}$$

This value r'_0 is then compared to a predefined threshold value, ε_{thresh} and if r'_0 is greater than the threshold value the vector is flagged as spurious.

1.7.4 Cellular Neural Network Algorithm

Liang et al. (2003) devised a method for the detection of spurious vectors using an artificial neural network. Neural networks are composed of simple elements operating in parallel so named as they are inspired by biological neural systems. The cellular neural network (CNN) is a single layer, local feedback network, composed of m x n neurons in the two-dimensional case. The neurons are then linked between all other neurons within a radius r, if $r = 1$ then each neuron is connected only to the nearest eight neighbours and to the nearest 24 if $r = 2$. Each neuron in the network corresponds to a vector in the velocity field and has either a value of one or zero representing valid and spurious vectors respectively. In the two-dimensional case each flow field corresponds to two neural networks, one each for the u and v components of the velocity field. The vector is then marked as spurious if either one, or both, of these components is shown to be erroneous. The algorithm works for each vector component (initially set to a value of one) the weight of the neuron with it's neighbours is calculated and if this is above a defined threshold level the vector is marked as spurious, the method is iterative and is repeated until no more vectors are detected as spurious.

1.7.5 Variable Threshold Algorithm

The variable threshold method introduced by Shinneeb et al. (2004) first uses an aggressive spurious vector detection algorithm such as CNN (Liang et al., 2003) or local-median testing (Westerweel and Scarano, 2005) to first remove any vector suspected of being an outlier. The vectors detected as spurious in this first pass are then replaced by a Gaussian-weighted average of their neighbours whilst vectors not initially detected as spurious are unmodified at this stage. From this new provisional field the 'expected' difference between a velocity vector and its immediate neighbours is calculated, this expected deviation then has a Gaussian filter applied to give a local threshold for each point in the flow field. Whilst this method shows improved detection of spurious vectors against the local-median and CNN methods it is much more computationally intensive than the normalised median test method and is based on a similar principle of varying the threshold criterion for each point in the flow.

1.7.6 Other Spurious Vector Detection Algorithms

There are a number of other methods presented in the literature by which spurious vectors can be detected and each have their advantages and disadvantage. Methods include model-based validation by Young et al. (2004), flow-adaptive data validation by Liu et al. (2008), rule based fuzzy logic by Sapkota and Ohmi (2008) and mode ratio bootstrapping by Pun et al. (2007). Whilst improved performance can be obtained, the computational 'cost' can be significant; furthermore, careful optimisation of the PIV experimental system can reduce the number of outliers to less than a few percent.

1.7.7 Other Considerations for Vector Post-Processing

For iterative vector calculation algorithms, e.g. multigrid it is sometimes beneficial to smooth the vector field before proceeding with subsequent iterations. PIV data sets usually contain noise and it can be beneficial to reduce the noise levels by applying a smoothing kernel such as replacing each vector with the median of the neighbouring vectors. For final vector calculations smoothing should be treated with caution as it can have the effect of filtering out very small scale flow structures or purely turbulent fluctuations.

Chapter 2

Turbulence and Vortex Identification

2.1 What is turbulence?

> *"Observe the motion of the surface of the water, which resembles that of hair, which has two motions, of which one is caused by the weight of the hair, the other by the direction of the curls; thus the water has eddying motions, one part of which is due to the principal current, the other to random and reverse motion."*
>
> Leonardo da Vinci, 1452-1519

Reportedly, on his deathbed the great physicist Werner Heisenberg, one of the pioneers of quantum theory said he would ask God two questions, "*Why relativity and why turbulence? I really think he may have an answer for the first one*". This hints towards the complex nature of turbulent flow.

Most flows, whether naturally occurring or present in a mechanical system are turbulent. Turbulence is a feature of everyday life, wind is turbulent, the flow of water over a waterfall is turbulent, the smoke exiting the chimney of a steam train is turbulent. What these all have in common is that when looked at closely it becomes apparent that there is a chaotic, stochastic nature to these flows which appear to have no structure and rapidly change with time. The study of and an understanding of turbulence is required in a lot of fields, for example, predictive weather models used in weather forecasting depend heavily on turbulence models as the movement of air in the atmosphere which dictates the weather is turbulent. Mixing, an everyday process depends heavily on turbulence, without it the quality of mixing would be greatly reduced affecting the quality of products from medicines to paint to chemicals. Combustion, for example in an internal combustion engine is heavily dependent on turbulence to control the quality of combustion and hence the performance of the engine. Turbulence has applications in astrophysics as it governs the formation of galaxies and the dynamics of supernova.

In his book on turbulence Cebeci collates the two following early definitions of turbulence by Hinze and von Karman (Cebeci, 2004):

von Kármán (1937) gave the following definition:

> *"Turbulance is an irregular motion which in general makes its appearance in fluids, gaseous or liquid, when they flow past solid surface or even when neighbouring streams of the same fluid flow past or over one another"*

Hinze, in 1959 gives the following definition of what he believes to be turbulent flow (Hinze, 1975):

> *"Turbulent fluid motion is an irregular condition of the flow in which the various quantities show a random variation with time and space co-ordinates, so that statistically distinct average values can be discerned."*

And in 1985 Chapman and Tobak (1985) go on to give a more formal definition of turbulence:

> *Turbulence is any chaotic solution to the 3-D Navier-Stokes equations that is sensitive to initial data and which occurs as a result of successive instabilities of laminar flows as a bifurcation parameter is increased through a succession of values*

Tennekes and Lumley (1972) list a number of characteristics of turbulent flows:

- **Irregularity**: The stochastic nature of turbulence renders analytical solutions impossible meaning statistical methods have to be used to describe turbulent flows.
- **Diffusivity**: Diffusivity of turbulence causes rapid mixing and increased rates of momentum, heat and mass transfer; as far as applications are concerned Tennekes and Lumley describe this as the most important feature.
- **Large Reynolds Numbers**: All turbulent flows occur when the flow is dominated by inertial forces rather than internal viscous forces.
- **Three-Dimensional Vorticity Fluctuations**: Turbulence is defined by fluctuating vorticity, vortex stretching is an essential feature of turbulence and is not present in two dimensional flow.
- **Dissipation**: Viscous shear stresses cause an increase in the internal energy of the fluid, this energy is passed down from the inertial energy of the turbulence. If the application of energy to the flow ceases all turbulent energy will dissipate due to viscous forces and the turbulence will be impossible to maintain.
- **Turbulent flows are flows**: Turbulence is not a feature of fluids but of fluid flows and most of the dynamics of turbulence are the same for both liquid and gas phase flows.

When making observations of turbulent flows at a fixed point (an Eulerian reference frame) one notices that the measured quantity, for example, velocity fluctuates both in direction and speed with time and it is the magnitude of these fluctuations away from the average flow that give a measure of the scale of the turbulence. These fluctuations arise from "the sensitivity of the flow to

uncontrollable perturbations in the initial and boundary conditions" (Bernard and Wallace, 2002). Bernard and Wallace go on to suggest that the defining feature of turbulence is the ability of the flow to take minute fluctuations in boundary and initial conditions caused by such things as changes in small scale surface roughness or slight variations in the driving mechanism and amplify them in a chaotic nature to a measurable scale. Whilst always present, if the flow is laminar viscous forces damp out these slight perturbations and the flow remains constant not changing with time.

2.2 The Navier-Stokes Equations of Fluid Motion

Developed in the 1840s by Claude-Louis Navier and George Gabriel Stokes the Navier-Stokes equations describe the motion of fluid elements and are derived by applying Newton's Second law to a fluid element (Navier, 1823; Stokes, 1848).

2.2.1 The Convective Derivative

Introduced by Stokes, the operator $\mathrm{D}(\cdot)/\mathrm{D}t$ represents the rate of change of a quantity associated with a given fluid element as opposed to $\partial(\cdot)/\partial t$ which represents the rate of change of a quantity associated at a fixed point in space (Davidson, 2004). $\mathrm{D}(\cdot)/\mathrm{D}t$ has a Lagrangian reference frame (moves with the fluid) whereas $\partial(\cdot)/\partial t$ has an Eulerian reference frame (velocities related to this fixed frame). In the case of the velocity vector u we have (Davidson, 2004):

$$\frac{\mathrm{D}u}{\mathrm{D}t} = \frac{\partial u}{\partial t} + (u \cdot \nabla) u \tag{2.1}$$

Where ∇ is the three dimensional gradient opperator:

$$\nabla = \frac{\partial}{\partial x_i} + \frac{\partial}{\partial x_j} + \frac{\partial}{\partial x_k} \tag{2.2}$$

2.2.2 Derivation of Navier-Stokes Equations from the Momentum Equation

Using Newton's second law one can relate the acceleration of a fluid element to the surface and body forces acting upon it with the following, the momentum equation (Pope, 2000):

$$\rho_f \frac{\mathrm{D}u_j}{\mathrm{D}t} = \frac{\partial \tau_{ij}}{\partial x_i} - \rho_f \frac{\partial \Psi}{\partial x_j} \tag{2.3}$$

Where τ_{ij} is the stress tensor which contributes the surface forces acting on the fluid element and Ψ is the gravitational potential which gives rise to the body forces. The body force per unit mass is defined as:

$$g = -\nabla\Psi \tag{2.4}$$

where g is the acceleration due to gravity. For flows of constant-property Newtonian fluids the stress tensor is:

$$\tau_{ij} = -P\delta_{ij} + \mu\frac{\partial u_i}{\partial x_j} + \frac{\partial u_j}{\partial x_i} \tag{2.5}$$

where P is pressure, μ the viscosity and δ_{ij}, the Kronecker delta defined as:

$$\delta_{ij} = \begin{cases} 1, & \text{if } i = j, \\ 0, & \text{if } i \neq j. \end{cases} \tag{2.6}$$

Substituting (2.5) into (2.3) we can derive the Navier-Stokes equations:

$$\frac{\mathrm{D}u_j}{\mathrm{D}t} = \mu\frac{\partial^2 u_j}{\partial x_i^2} - \frac{\partial P}{\partial x_j} - \rho_f\frac{\partial \Psi}{\partial x_j} \tag{2.7}$$

The body force and pressure terms can be combined by defining the modified pressure, p:

$$p = P + \rho_f \Psi \tag{2.8}$$

If in place of the dynamic viscosity, μ the kinematic viscosity, ν where $\nu = \mu/\rho_f$ is used in conjunction with the modified pressure term, p as defined in (2.8) the the Navier-Stokes equation presented in (2.7) reduces to:

$$\frac{\mathrm{D}u}{\mathrm{D}t} = -\frac{1}{\rho_f}\nabla p + \nu\nabla^2 u \tag{2.9}$$

Looking at (2.9) one can see that the Navier-Stokes equations are a series of second-order partial differential equations and they describe the motion of a fluid element for both laminar and turbulent flow regimes. Due to the complex nature of the equations analytical solutions are only attainable for the most simple of flows in the laminar flow region with non-complex boundary geometry. One analytical solution is the Oseen vortex which is described in detail in §5. For more complex flows analytical solutions do not yet exist and it is unsure whether analytical solutions will ever be found so modelling is reduced to numerical solutions of the equations.

2.2.3 Reynolds Number

Whether a flow is in the turbulent or laminar flow regime is dependent on the dimensionless number, the Reynolds number, Re. The Reynolds number is a measure of the ratio of inertial forces to viscous surface forces and is defined as:

$$\mathrm{Re} = \frac{\rho_f u l}{\mu} \tag{2.10}$$

$$\mathrm{Re} = \frac{u l}{\nu} \tag{2.11}$$

where ρ_f is the fluid density, u the velocity of the flow, l the characteristic length scale of the flow. What do (2.10) and (2.11) tell us about the flow regime? The Reynolds number will be high if the inertial forces are dominant over the viscous forces, this is the case when the flow velocity is high, the viscosity of the fluid is low or a combination of the two. Turbulent flows are typical of high Reynolds numbers, it can be seen that for low Reynolds numbers the viscosity term dominates over the inertial term meaning any disturbances in the flow caused by inertial forces are damped out through viscosity resulting in a laminar flow regime.

Derivation of Reynolds Number from Navier-Stokes Equations

The Navier-Stokes equations as presented in (2.9) can be made non-dimensional by using the characteristic velocity, $\mathscr{U}$ and length, $\mathscr{L}$ scales to define the independent dimensionless variables $\nabla = \nabla'/\mathscr{L}$ and $t = t'(\mathscr{L}/\mathscr{U})$ and the dependent variables $u = u'\mathscr{U}$ and $p = p'\mathscr{U}^2\rho_f$. Substituting these variables into (2.9) and expanding the convective derivative we have (Bruno and Carbone, 2005):

$$\frac{\partial u'}{\partial t'} + \left(u' \cdot \nabla'\right) u' \quad = \quad -\nabla' p' + \frac{\nu}{\mathscr{U}\mathscr{L}} \nabla'^2 u' \tag{2.12}$$

Recognising in (2.11) that $\mathrm{Re} = \mathscr{U}\mathscr{L}/\nu$ and dropping the prime notation for clarity we end up with the following non-dimensional representation of the Navier-Stokes equations:

$$\frac{\partial u}{\partial t} + (u \cdot \nabla) u \quad = \quad -\nabla p + \frac{1}{\mathrm{Re}} \nabla p^2 u \tag{2.13}$$

(2.13) shows that the Reynolds number is the only parameter of the flow (Bruno and Carbone, 2005) and as the Navier-Stokes equations govern all fluid motion it can be assumed that flows with similar Reynolds numbers behave in the same manner. (2.13) also shows that for high Reynolds numbers the viscous term becomes negligible meaning the flow is essentially inviscid and is dominated by the inertial forces.

2.3 Statistical Methods in Turbulence Analysis

2.3.1 Reynolds Decomposition

Due to the stochastic nature of turbulent flows looking at only instantaneous data is not very helpful when attempting to describe the flow as a whole, so averaged values are used. The most commonly used quantity when trying to describe the overall structure of a turbulent flow is to use Reynolds decomposition. A turbulent flow when observed over time can display certain bulk features which appear to remain relatively constant but upon closer inspection it can be seen that this bulk motion contains temporal fluctuations.

For the three-dimensional velocity vector $\mathbf{u}(\mathbf{x},t)$ where $\mathbf{u} = (u,v,w)$ and $\mathbf{x} = (x,y,z)$ is the position vector the time averaged velocity, $\overline{\mathbf{u}}$ over a period T and beginning at t_0 is calculated as

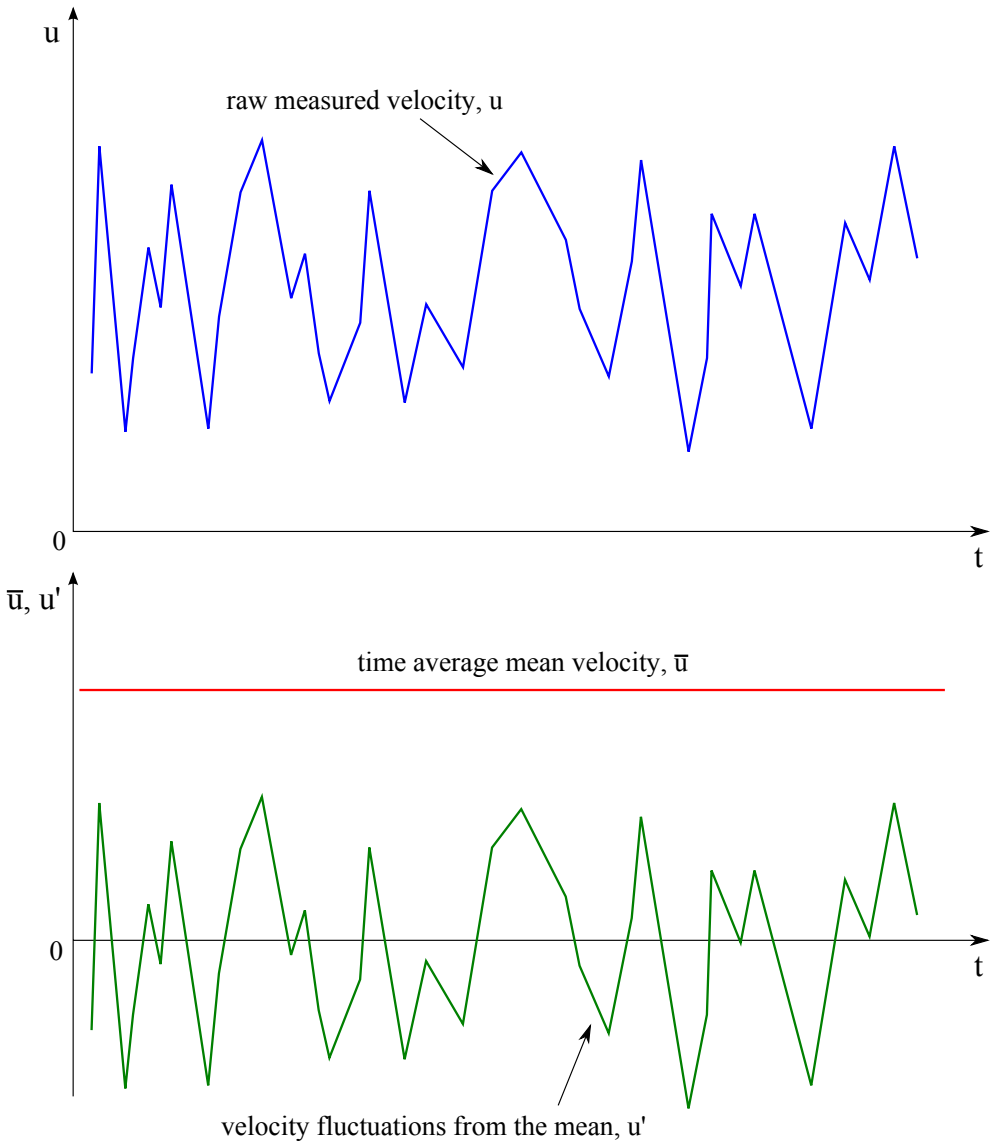

Fig. 2.1 (*top*) Raw velocity time series containing random fluctuations, u and (*bottom*) velocity fluctuations, u' after subtracting the mean velocity through Reynolds decomposition.

follows (Pope, 2000):

$$\bar{\mathbf{u}} = \lim_{T\to\infty} \frac{1}{T} \int_{t_0}^{t_0+T} \mathbf{u} \mathrm{d}t \tag{2.14}$$

The above equation assumes continuous velocity data. While useful in mathematical models of fluid flows experimental data is obtained at discrete time intervals, when this is the case the average velocity vector is calculated as the summation of all instantaneous velocity vectors at times t_n divided by the total number of velocity measurements, N:

$$\bar{\mathbf{u}} = \frac{1}{N} \sum_{n=1}^{N} \mathbf{u}(t_n) \tag{2.15}$$

A time average only makes sense if the mean flow is steady, i.e. does not vary with time meaning

the following condition has to be met (Pope, 2000):

$$\frac{\partial \overline{\mathbf{u}}}{\partial t} = 0 \tag{2.16}$$

Using the time-average velocity calculated in (2.15) one can decompose the instantaneous velocity vector, $\mathbf{u}$ into mean, $\overline{\mathbf{u}}$, and fluctuating, $\mathbf{u}'$, velocity components by subtracting the mean velocity from the instantaneous velocity:

$$\mathbf{u}' = \mathbf{u} - \overline{\mathbf{u}} \tag{2.17}$$

and finally, for completeness, instantaneous velocities can be represented as the sum of the mean flow and the instantaneous fluctuation from the mean:

$$\mathbf{u} = \overline{\mathbf{u}} + \mathbf{u}' \tag{2.18}$$

From the above it can be seen that the time-average of the fluctuating values is equal to zero. Figure 2.1 shows this graphically. Reynolds decomposition, by subtracting the time-average centres the fluctuating velocities around zero making it easier to spot smaller scale features of the flow which are often hidden by the average flow, though it is not uncommon for the fluctuating values to be greater than the mean value.

2.3.2 Turbulent Kinetic Energy and Turbulence Intensity

It is useful to have a way of quantifying the magnitude of the turbulence present in a flow, this is done using the related quantities of turbulent kinetic energy and turbulence intensity. In the above section it was stated that the time average of the fluctuating velocity components is equal to zero however, when taking the mean of the squares of the fluctuating values a positive value is obtained (Cebeci, 2004):

$$\overline{\mathbf{u}}' = \frac{1}{N}\sum_{n=1}^{N} \mathbf{u}'_n = 0 \tag{2.19}$$

$$\overline{\mathbf{u}'^2} = \frac{1}{N}\sum_{n=1}^{N} \mathbf{u}'^2_n \tag{2.20}$$

Where $\mathbf{u}'_n = \mathbf{u}'(t_n)$. It can be seen in (2.20) that the mean of the squares of the fluctuating values is only equal to zero when the fluctuating values are equal to zero, in this case the instantaneous velocity at each time is equal to the mean velocity meaning the flow is laminar and steady and hence has no turbulent fluctuations. Taking the square root of (2.20) gives the strength of the turbulence (i.e. the average magnitude of velocity fluctuations from the mean) and is defined as

the root-mean-square of the fluctuating velocity values, $\mathbf{u}_{rms}$ as follows:

$$\mathbf{u}_{rms} = \sqrt{\frac{1}{N}\sum_{n=1}^{N}\mathbf{u}_n'^2} \tag{2.21}$$

(2.21) shows that the greater the magnitude of the velocity fluctuations the greater the turbulence strength, $\mathbf{u}_{rms}$ is. This means that the strength of the turbulence is greater the more the fluctuations deviate from the mean; in low turbulence systems fluctuations deviate little from the mean velocity and conversely in highly turbulent systems the fluctuations deviate from the mean by a much greater amount.

Whilst the turbulence strength is a useful quantity it is often non-dimensionalised by normalising by the mean velocity, this quantity is referred to as the turbulence intensity, I and is defined by the three quantities (one each for the three velocity components, u, v and w) (Cebeci, 2004):

$$I_{u,v,w} = \frac{u_{rms}}{\overline{u}}, \frac{v_{rms}}{\overline{v}}, \frac{w_{rms}}{\overline{w}} \tag{2.22}$$

Turbulence kinetic energy, k, is defined as the mean kinetic energy per unit mass in a turbulent flow and is defined as follows (Cebeci, 2004; Davidson, 2004; Pope, 2000):

$$k = \frac{1}{2}\left(u_{rms}^2 + v_{rms}^2 + w_{rms}^2\right) \tag{2.23}$$

As can be seen with the previously defined quantities the greater the RMS fluctuation values the greater the turbulence kinetic energy. This turbulence kinetic energy is associated with the energy contained within the larger eddies of the flow and is subsequently transferred through the smaller scales until dissipated at the Kolmogorov scale (Pope, 2000) as will be introduced next.

2.3.3 Homogeneity and Isotropy

Turbulence is considered to be *homogeneous* if statistics relating to velocity fluctuations such as intensity, energy, length scales (introduced later), etc... are invariant across the measurement domain (Pope, 2000), i.e. statistics measured at a point $\mathbf{x}$ are the same at the point $\mathbf{x}+\boldsymbol{\zeta}$ where $\boldsymbol{\zeta} = (\zeta_1, \zeta_2, \zeta_3)$ is the spatial translation vector where ζ_1,ζ_2 and ζ_3 are translations in the x, y and z coordinate directions respectively.

If the turbulence statistics are invariant under rotations or reflections of the coordinate system, i.e. independent of orientation, then the turbulence is said to be *isotropic* (Pope, 2000). For example, in isotropic turbulence the turbulence intensity is the same for each velocity component, $I_u = I_v = I_w$.

2.4 Scales of Turbulence

To fully understand the properties of turbulent flows length scales have to be investigated. Length scales give a measure of the size of structures present in turbulent flows and govern the mixing

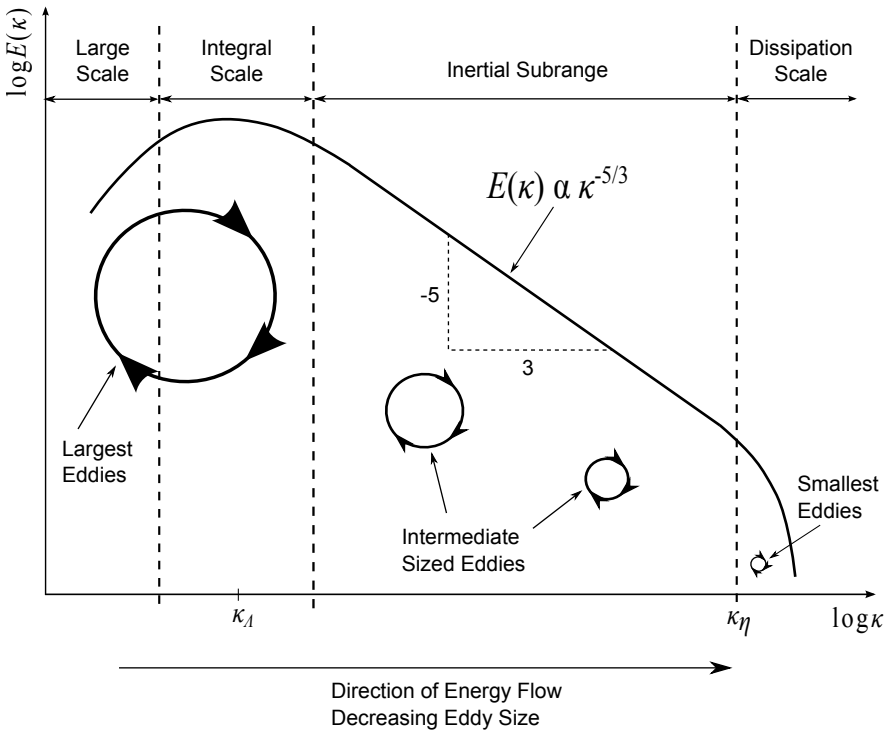

Fig. 2.2 One dimensional turbulent energy-wavenumber spectrum.

process in heat and mass transfers (Thacker et al., 2010).

2.4.1 Kolmogorov Energy Cascade

Much of modern turbulence theory can be said to be based on the work carried out in the mid-20th Century by A. N. Kolmogorov, specifically his two publications of 1941 where he outlines the notion of the local isotropy of turbulence (Kolmogorov, 1941a) and the cascade of energy from large eddies to smaller ones (Kolmogorov, 1941b).

In turbulent flows the largest eddies contain the majority of the turbulence kinetic energy as previously discussed, these large eddies are however unstable and break up transferring their energy into smaller eddies which in turn break up and transfer energy to yet smaller eddies. This energy cascade continues until the length scale reaches a point where eddies no longer break down into smaller ones but their energy is dissipated to heat through molecular viscosity (Tennekes and Lumley, 1972), the order of the scale at which dissipation occurs is referred to as the Kolmogorov micro-scale. The process of the energy cascade is nicely described by the following verse by Richardson (1922):

Big whirls have little whirls
Which feed on their velocity;
And little whirls have lesser whirls,
And so on to viscosity.

Kolmogorov describes in the first of his 1941 papers (Kolmogorov, 1941a) that at the smallest scales the forces driving the main large scale turbulence are of little influence and that at these

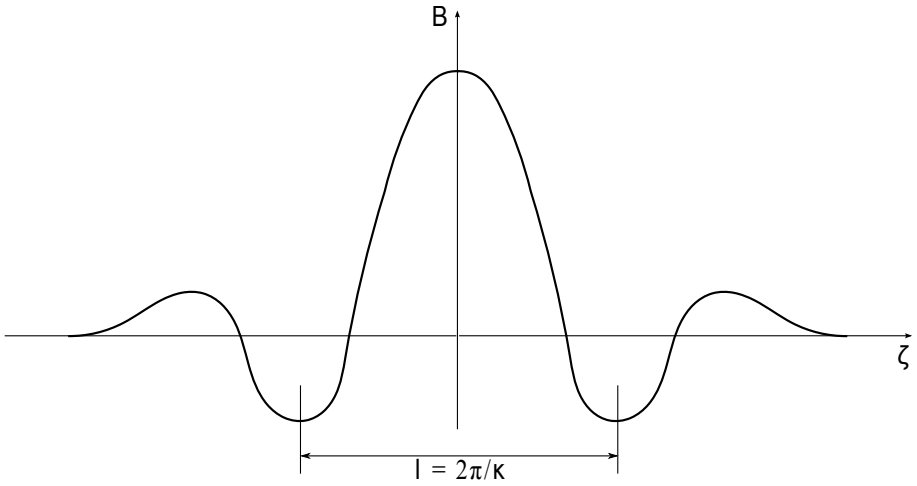

Fig. 2.3 Autocorrelation function of an eddy of wavenumber κ and wavelength $2\pi\kappa$.

smallest scales the flow turbulence is homogeneous and isotropic meaning that at scales approaching the Kolmogorov microscale the turbulent motions are statistically independent of those at the scale of the largest eddies and that at these scales the fluid motion is universal for all high Reynolds number fluid flows and is governed only by the viscosity of the fluid and the dissipation rate (Pope, 2000). This holds true even though at the larger scales in general the flow turbulence is inhomogeneous and anisotropic containing directional properties (also referred to as 'shape') owing to factors such as geometrical bounds (Tennekes and Lumley, 1972). Following from the hypotheses that at the smallest scales the flow is isotropic and homogeneous Kolmogorov then goes on to hypothesise that at very high Reynolds numbers, at these small scales the statistics of the turbulence are the same for all turbulent flows, only depending on the viscosity of the fluid and the dissipation rate (Kolmogorov, 1941a).

The variation of energy at the different scales of turbulent flow is shown in Figure 2.2 in the form of the turbulent energy spectrum, $E(\kappa)$. The different scales at which energy is contained are defined by wavenumber, κ which is a measure of the spatial frequency of an eddy of a particular scale l where spatial eddy size and wavenumber are linked as follows:

$$\kappa = \frac{2\pi}{l} \tag{2.24}$$

Figure 2.3 shows the autocorrolation function, B of a eddy of wavenumber κ and spatial wavelength l, the corresponding energy spectrum, $E(\kappa)$ of this eddy is presented in Figure 2.4 showing that the energy content of the eddy is centred on wavenumber κ with the majority of the energy contained between 0.6κ and 1.6κ (Tennekes and Lumley, 1972).

As stated the turbulent kinetic energy contained within a flow is distributed among eddies of varying scale (size). Figure 2.4 shows the energy spectrum $E(\kappa)$ of a single eddy of wavenumber κ and the total energy spectrum for eddies of all scales contained within a flow is presented in Figure 2.2. The normalised energy contained at each wavenumber, $\tilde{B}(\kappa)$ is obtained by taking the Fourier transform of the autocorrelation function, B (Equation (2.29)) of the fluctuating velocities

as follows Batchelor (1953):

$$\tilde{B}(\kappa) = \int_{-\infty}^{\infty} B(\zeta) e^{i\kappa\zeta} \mathrm{d}\zeta \tag{2.25}$$

The correlation function B is normalised as presented in Equation (2.29) with the result that the energy spectrum $\tilde{B}$ provides a normalised energy content at each wavenumber, κ with the total energy integrated over each wavenumber equalling 1. The total turbulent energy contained within the flow, k as previously stated in (2.23) is equal to half the square of the RMS velocity fluctuations, this same energy must also be contained in the energy spectrum $E(\kappa)$:

$$k = \frac{1}{2} u_{rms}^2 = \int_0^{\infty} E(\kappa) \mathrm{d}\kappa \tag{2.26}$$

From (2.26) and the fact that the energy contained within the normalised energy spectrum, $\tilde{B}$ is equal to 1 it can be seen that in order for the energy content of $E(\kappa)$ to be equal to k, $\tilde{B}$ needs to be scaled by a factor $2u_{rms}^2$ as follows:

$$E(\kappa) = 2u_{rms}^2 \tilde{B}(\kappa) \tag{2.27}$$

Turbulent flow can be broken down as containing four main flow scales as are highlighted in Figure 2.2 which will now be discussed further:

1. The large scale, governed by the geometry of the system.

2. The integral scale, the scale of the largest eddies contained within the flow.

3. The Taylor microscale, an intermediate scale corresponding to Kolmogorov's inertial subrange.

4. The Kolmogorov scale which contains the smallest scale flow structures.

2.4.2 Integral Length Scale

The integral length scale (also known as the Taylor macro-scale) (Taylor, 1935), Λ is "characteristic of the larger eddies" (Pope, 2000) and these largest eddies contain most of the turbulence kinetic energy (Li et al., 2002) and is also used in the calculation of the Reynolds number (Pope, 2000). For contained flows such as pipe flow the integral length scale is a feature of the physical constraints of the system such as the diameter of the pipe as no eddies can be larger than this (O'Neill et al., 2004). In systems which are not enclosed the largest length scales are not immediately apparent. Taylor proposes a relationship between the integral length scale and the distance or time over which velocity fluctuations become uncorrelated; mathematically the integral length scale, Λ is defined as the integral of the longitudinal autocorrelation function of the fluctuating velocity component (Benedict and Gould, 1998; Chanson and Carosi, 2007; Li et al., 2002; O'Neill

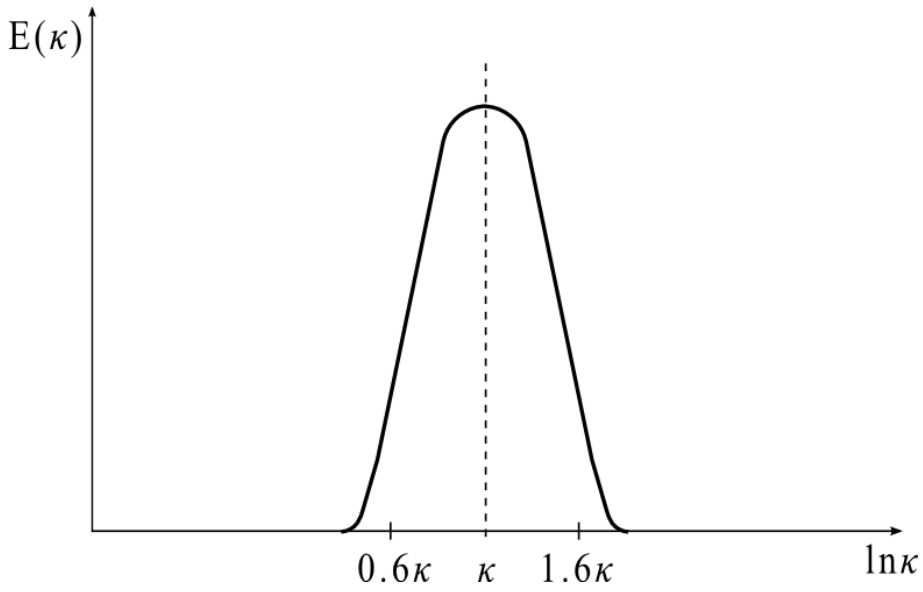

Fig. 2.4 Energy spectrum $E(\kappa)$ of single eddy of wavenumber κ.

et al., 2004; Pope, 2000; Swamy et al., 1979; Tritton, 1988):

$$\Lambda = \int_0^\infty B_{ii}(\zeta,t)\mathrm{d}\zeta \tag{2.28}$$

Where $B_{ii}(\zeta)$ is the longitudinal autocorrelation function of the i^{th} fluctuating velocity component, $\mathbf{u}' = (u',v',w') = (u'_1,u'_2,u'_3)$ and ζ is the distance, in the direction of the i^{th} velocity component, between two points in the flow. The longitudinal autocorrelation function of the i^{th} fluctuating velocity component is defined as:

$$B_{ii}(\zeta,t) = \frac{\langle u'_i(x_i,t)u'_i(x_i+\zeta,t)\rangle}{\langle u'^2_i\rangle} \tag{2.29}$$

$B_{ii}(\zeta)$ shows that when the distance between points is zero ($\zeta = 0$) the flow is fully correlated with a value of 1 and this decreases with increasing r until the flow is no longer correlated. Using this formulation of the integral length scale it is possible to calculate this quantity directly from PIV data as only the velocity fluctuations are required.

It must be noted in (2.28) the length scale is calculated as an integral between zero and infinity, in practice however the integral is limited to the size of the domain. For situations where the turbulence is homogeneous the turbulent length scale when measured over the whole measurement domain will be the same at each point in the flow field. In inhomogeneous turbulence where the scale of the present structures varies spatially care has to be taken in the selection of the size of the integration domain as the integral length scale varies spatially and can be different in different directions (Bewley et al., 2012). Spatial variation in the calculation of the integral length scale are presented in numerous studies, for example when looking at the swirling flow inside an internal combustion engine (Breuer et al., 2005; Li et al., 2002) or when looking at boundary layer flows (Saddoughi and Veeravalli, 1994). O'Neill et al. (2004) shows that the size of the integral domain have an effect on the calculated integral length scale. When calculating the integral length scale

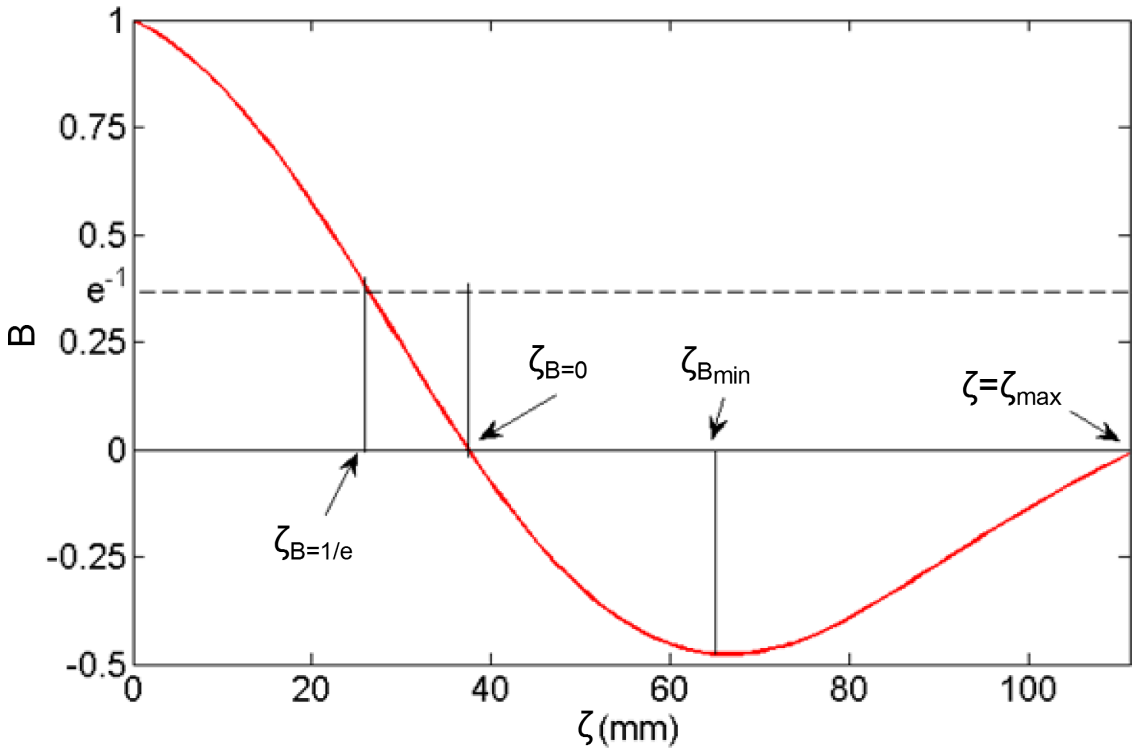

Fig. 2.5 Fluctuating velocity component autocorrelation function and commonly used integral limits for the calculation of the integral length scale.

using the fluctuating velocity autocorrelation function the limits of the integration domain can be defined in a number of ways, the four most common of which are shown in Figure 2.5 and are described here (O'Neill et al., 2004):

1. Integrate over the whole of the available domain (between zero and $\zeta = \zeta_{max}$ in Figure 2.5).
2. If the autocorrelation function has a negative region, integrate between zero and the first minimum point ($\zeta_{B_{min}}$ in Figure 2.5).
3. Integrate up to the first point the autocorrelation crosses zero (if it crosses zero).
4. Integrate between zero and the point where the autocorrelation value falls to e^{-1}.

In the practical analysis of autocorrelation values the above conditions quite often do not exist, most commonly the autocorrelation function does not have a negative region so integrating between zero and the first minimum point or zero and the first zero-crossing cannot be evaluated leaving integrating over the entire domain and to the value where the autocorrelation value reaches a value of e^{-1} as the most commonly used.

Looking at Figure 2.5 it can be seen that when integrating between zero and the point where the autocorrelation function reaches a value of e^{-1} a large portion of the information contained within the autocorrelation function is disregarded, this can have the effect of giving an underestimate of the integral length scale (O'Neill et al., 2004).

Pope (2000) shows that the majority of the energy containing eddies exist in the range of length scales of between 6Λ and $\Lambda/6$ where the turbulence is generally anisotropic. Below length scales

of $\Lambda/6$ (the inertial subrange and dissipation range) the turbulence tends to be isotropic.

2.4.3 The Taylor Micro-Scale and Inertial Subrange

The Taylor micro-scale, λ_T is an intermediate length scale in the turbulence energy cascade, it is the largest scale at which fluid viscosity has a considerable effect on the dynamics of turbulent eddies contained within the flow (Tennekes and Lumley, 1972). At length scales smaller than this viscosity is dominant and kinetic energy is dissipated rather than cascaded down to the production of smaller eddies, these lie in the dissipation range in Figure 2.2. The Taylor micro-scale inhabits the inertial subrange in the energy cascade (Figure 2.2), in this range the net energy coming from the energy-containing eddies is in equilibrium with the net energy cascading to smaller eddies where it is dissipated (AMS, 2012). The gradient of the energy spectrum in this region is -5/3 (Kolmogorov, 1941b).

2.4.4 The Kolmogorov Scale and the Dissipation Range

As previously stated, at length-scales shorter than the Taylor micro-scale viscous forces dominate over inertial forces and the flow kinetic energy at these scales is dissipated as heat rather than cascading down to the production of smaller eddies. At this scale the turbulence is isotropic (Tennekes and Lumley, 1972). The Kolmogorov length-scale, η is defined as:

$$\eta = \left(\frac{\nu^3}{\varepsilon}\right)^{\frac{1}{4}} \tag{2.30}$$

where ν is the kinematic viscosity and η the dissipation rate. When the Reynolds number is calculated at this scale to fully resolve the spatial and temporal behaviour of turbulence the spatial and temporal resolution of the measurements should be less than or equal to the the Kolmogorov length and time scales. Saarenrinne et al show that to account for 65% and 95% of the total turbulent kinetic energy the spatial resolution of the velocity measurements should be of the order 90η and 20η respectively (Saarenrinne et al., 2001) showing that the majority of the flow turbulence can be measured without having to resolve all the way down to the Kolgmogorov length or time scales.

2.4.5 Dissipation Rate

The dissipation of turbulent energy from the larger to the smaller scales is governed by the dissipation rate, ε of the flow and determines the efficiency of many industrial processes (Saarenrinne and Piirto, 2000). Experimental evidence suggests that this rate is dictated by the energy of the large eddies and their corresponding timescale and can be estimated as (Saarenrinne and Piirto, 2000; Stelmach and Kuncewicz, 2012; Tennekes and Lumley, 1972):

$$\varepsilon = C_d \frac{u_{rms}^3}{\Lambda} \tag{2.31}$$

Where C_d a numerical constant which for isotropic flows is equal to 1 but otherwise should be determined experimentally. In practice the integral length scale, Λ, for complex flows varies over different regions of the flow meaning one value cannot be chosen to give an accurate estimation of the dissipation rate using this method (Sheng et al., 2000).

Alternatively to (2.31) the dissipation rate can be calculated directly from the energy spectrum, $E(\kappa)$ (as in (2.27)) by integrating the product of $E(\kappa)$ and κ^2 over all wavenumbers and then multiplying by twice the kinematic viscosity, ν as follows (Pope, 2000):

$$\varepsilon = 2\nu \int_0^\infty \kappa^2 E(\kappa) \mathrm{d}\kappa \tag{2.32}$$

For PIV data where spatial derivatives of the velocity field are available the dissipation rate for a two-dimensional velocity field can be calculated directly from the strain rate tensor, s_{ij} as defined in (2 3) (Saarenrinne and Piirto, 2000; Sheng et al., 2000; Tennekes and Lumley, 1972):

$$\varepsilon = 2\nu\overline{\langle s_{ij}s_{ij}\rangle} = \frac{\nu}{2}\overline{\left(\frac{\partial u'}{\partial y} + \frac{\partial v'}{\partial x}\right)^2} \tag{2.33}$$

The above definition requires highly spatially resolved velocity fields with a resolution less than the Kolmogorov scale in order to get an accurate estimation of the dissipation rate (Sheng et al., 2000). The error introduced by a lack of spatial resolution can be countered by applying a correction to (2.33) to model the sub-grid-scale turbulence (Stelmach and Kuncewicz, 2012):

$$\varepsilon = (C_S \Delta l)^2 \overline{\left[\frac{1}{2}\left(\frac{\partial u'}{\partial y} + \frac{\partial v'}{\partial x}\right)^2\right]^{\frac{3}{2}}} \tag{2.34}$$

where Δl is the spatial resolution of the velocity vector grid and C_S is the Smagorinski constant and usually has a value ranging from 0.11 to 0.21 and often taking the value 0.17 (Sheng et al., 2000; Stelmach and Kuncewicz, 2012). (Sheng et al., 2000) give a detailed evaluation of the difficulties in obtaining the dissipation rate from experimental PIV data, in the majority of cases either the spatial or temporal measurement resolution is the limiting factor.

2.5 Vortex Identification from PIV Data

2.5.1 Introduction

It is impossible to study turbulent flows in an empirical nature without studying the structures that characterise the flow. The study of these structures, known as coherent structures and their properties are key to understanding the dynamics of a turbulent flow such as the transfer of energy from different flow scales. Whilst turbulent flows appear random and chaotic to the naked eye it has been shown that there are, contained within the flow, organised complex structures which are known as coherent structures (Cantwell, 1981; Jeong and Hussain, 1995; Vincent and Meneguzzi, 1991).

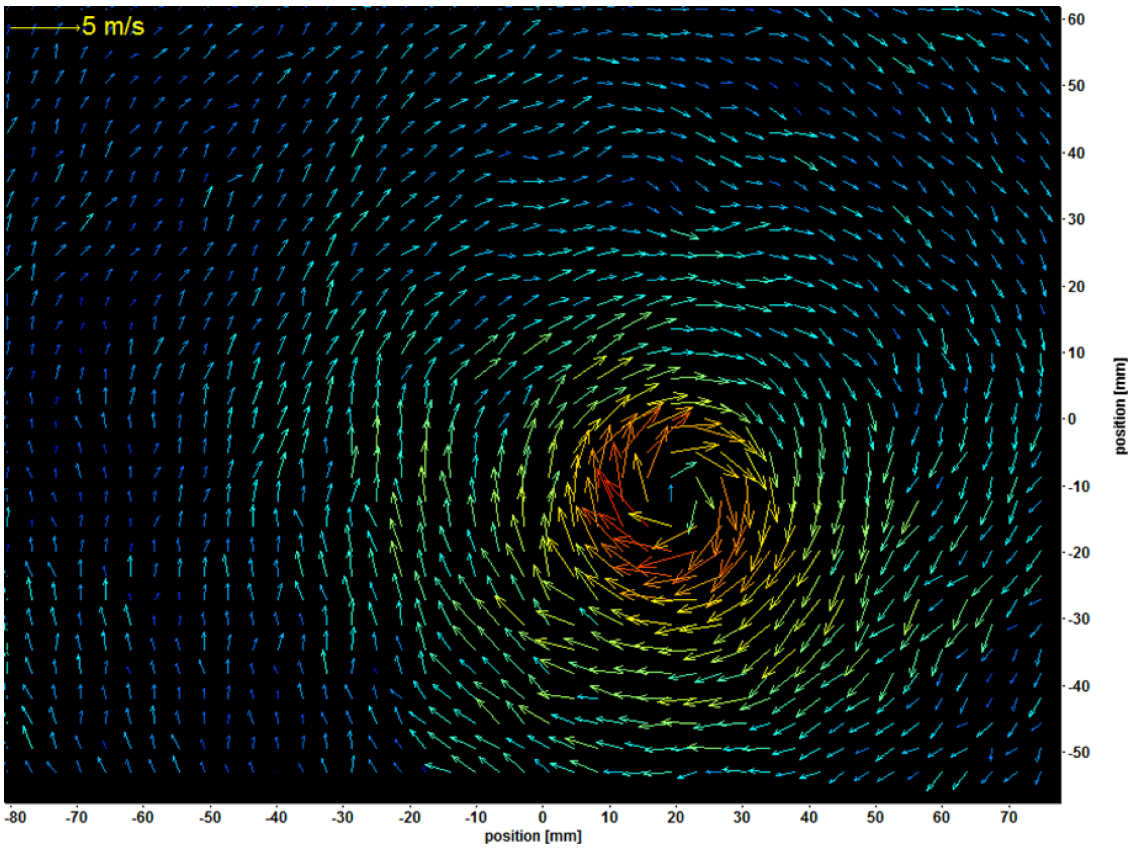

Fig. 2.6 Example of a vortex as captured using PIV on a tornado-like flow.

2.5.2 What is a vortex?

A vortex is a flow pattern which in general exhibits a swirling motion around a central point (Figure 2.6) and of all coherent structures in turbulent flows it is vortices that receive the most attention with Prandtl stating that "vortices are the muscles of the flow" and "vortices are the voices of the flow" (Müller and Obermeier, 1988). Lugt (1972) defines a vortex as:

> *"A vortex is the rotating motion of a multitude of material particles around a common centre."*

And Robinson (1991) goes on to describe a vortex in a three-dimensional flow as:

> *"A vortex exists when instantaneous streamlines mapped onto a plane normal to the vortex core exhibit a roughly circular or spiral pattern, when viewed from a reference frame moving with the centre of the vortex core."*

A more formal mathematical definition of a vortex is provided by Chong et al. (1990) but even taking into account various definitions of a vortex from the literature currently available no consensus on a definitive definition has yet been reached.

In order to study the vortex structures present in a turbulent flow methods are required to identify them from the measured velocity data, a number of methods for which are now discussed.

2.5.3 Identification of Vortex Structures in Turbulent Flows

Velocity Gradient, Strain Rate and Vorticity Tensors

The velocity gradient tensor, $\nabla\mathbf{u}$ of a flow field $\mathbf{u} = (u,v,w)$ is a measure of the rate of change of the three components of the velocity vector in the three spatial directions $\mathbf{x} = (x,y,z)$ and is defined as:

$$\nabla\mathbf{u} = \frac{\partial u_i}{\partial x_j} = \begin{pmatrix} \frac{\partial u}{\partial x} & \frac{\partial v}{\partial x} & \frac{\partial w}{\partial x} \\ \frac{\partial u}{\partial y} & \frac{\partial v}{\partial y} & \frac{\partial w}{\partial y} \\ \frac{\partial u}{\partial z} & \frac{\partial v}{\partial z} & \frac{\partial w}{\partial z} \end{pmatrix} \tag{2.35}$$

For two-component velocity data as is the case in the work carried out in this thesis (2.35) reduces to:

$$\nabla\mathbf{u} = \begin{pmatrix} \frac{\partial u}{\partial x} & \frac{\partial v}{\partial x} \\ \frac{\partial u}{\partial y} & \frac{\partial v}{\partial y} \end{pmatrix} \tag{2.36}$$

Decomposing the velocity gradient tensor, $\nabla\mathbf{u}$ into its symmetric and anti-symmetric parts one obtains the strain-rate and vorticity tensors. The strain rate tensor, $\mathbf{S}$ is defined as the symmetric part of the velocity gradient tensor (Jeong and Hussain, 1995):

$$\mathbf{S} = \frac{1}{2}\left[\nabla\mathbf{u} + (\nabla\mathbf{u})^{\mathrm{T}}\right] \tag{2.37}$$

Which can be expanded in two dimensions as:

$$\mathbf{S} = e_{ij} = \begin{pmatrix} e_{11} & e_{12} \\ e_{21} & e_{22} \end{pmatrix} \tag{2.38}$$

With individual strain components e_{ij} defined as:

$$e_{ij} = \frac{1}{2}\left(\frac{\partial u_i}{\partial x_j} + \frac{\partial u_j}{\partial x_i}\right) \tag{2.39}$$

Similarly, the vorticity tensor $\mathbf{\Omega}$, is defined as the anti-symmetric part of the velocity gradient tensor:

$$\mathbf{\Omega} = \frac{1}{2}\left[\nabla\mathbf{u} - (\nabla\mathbf{u})^{\mathrm{T}}\right] \tag{2.40}$$

Which in two dimensions expands as:

$$\mathbf{\Omega} = \begin{pmatrix} 0 & \omega_{12} \\ \omega_{21} & 0 \end{pmatrix} \tag{2.41}$$

With individual vorticity components ω_{ij} defined as:

$$\omega_{ij} = \frac{1}{2}\left(\frac{\partial u_j}{\partial x_i} - + \frac{\partial u_i}{\partial x_j}\right) \tag{2.42}$$

Vortex Identification: Maximum Vorticity Method

Probably the simplest of analytical vortex identification methods is the maximum vorticity method (MVM) where the existence of a vortex core can be identified as a local maximum in the vorticity magnitude field as calculated by (2.41). Vorticity magnitude is used as vorticity is directional and can take positive or negative values (Bussiere et al., 2012; Strawn et al., 1999). The main downfall in using this method is that vorticity not only occurs in regions where vortices exist but also in regions of shear meaning that other algorithms have to be employed in conjunction with the MVM in order to distinguish between regions of vorticity caused by shear and regions caused by vortex motion (Bussiere et al., 2012; Jeong and Hussain, 1995; Strawn et al., 1999). Bussiere et al. (2012) go on to use the MVM as a means of identifying regions where vortex cores could potentially be located and then proceed to investigate these highlighted regions of interest with further algorithms to identify vortex cores as part of their combinatorial vortex detection algorithm (CVD). It is also worth noting that when applying MVM to real data (such as that obtained using PIV) it is often necessary to apply a low pass filter such as a Gaussian filter to remove noise from the data or high frequency spatial fluctuations; this is important as vorticity is calculated by taking the spatial derivatives of velocity data and high frequency changes can create spikes in the vorticity field which may be wrongly identified as vortices (Bussiere et al., 2012).

As a way of alleviating the problem of high vorticity values being present in shear flow regions Jiang et al. (2005) suggest searching for a local maximum in the vorticity field where the spatial derivative of the vorticity field is zero, this is useful as shear flows do not contain a peak-like local maxima as vortices do.

Vortex Identification: Winding Angle Method

The winding angle method (WAM) is a numerical interpretation of the description of a vortex as having looping streamlines and was first proposed by Portela in 1998 (Bussiere et al., 2012; Portela, 1998; Sadarjoen and Post, 1999). The winding angle, α_w belonging to a streamline, S is defined as the sum of all the angles between N_α streamline segments connected at points P_i as in Figure 2.7:

$$\alpha_w = \sum_{i=1}^{N_\alpha - 1} \angle(P_{i-1}, P_i, P_{i+1}) \tag{2.43}$$

where $\angle(a,b,c)$ denotes the angle between the line segment connected by points a and b and the segment connected by points b and c, positive angles defining a counterclockwise rotation. Sadarjoen and Post (1999) state two criteria that must be met to be considered part of a vortex:

1. The streamline must form a closed loop meaning the winding angle $\alpha_w \geq 2\pi$.
2. Since it is possible the winding angle may be large enough without the streamlines forming a closed loop the start and endpoint of the streamline must be sufficiently close.

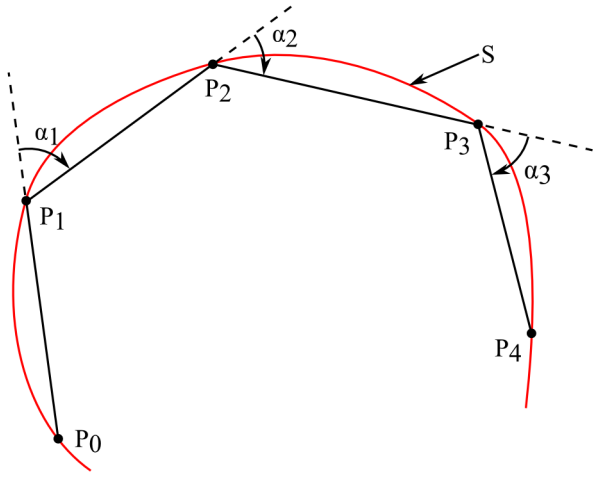

Fig. 2.7 Schematic showing how the winding angle, α_w of the streamline S is calculated.

Vortex Identification: λ_2-Criterion

Using the definitions of the strain-rate (2.37) and vorticity (2.40) tensors Jeong and Hussain (1995) go on to identify a vortex as the region where the symmetrical tensor $(\Omega^2 + \mathbf{S}^2)$ has two negative eigenvalues λ_1 and λ_2. Since the eigenvalues λ are arranged in increasing order $(\lambda_1 \geq \lambda_2 \geq \lambda_3)$, λ_2 must be negative for this condition to be met. For a two-dimensional incompressible flow it can be shown that the second eigenvalue λ_2 is:

$$\lambda_2 = \left(\frac{\partial u}{\partial x}\right)^2 + \left(\frac{\partial u}{\partial y}\right)\left(\frac{\partial v}{\partial x}\right) \tag{2.44}$$

This measures the excess of rotation rate over the strain rate magnitude in the specific plane (Alim, 2006). In the centre of the vortex region the magnitude of λ_2 reaches a maximum and this is used to define the location of the vortex.

Vortex Identification: Q-Criterion

Hunt et al. (1988) define a vortex as a region in which the second invariant, Q, of the velocity gradient tensor $\nabla\mathbf{u}$ is positive and that the pressure in this region is lower than that of the ambient pressure of the flow field in question. The second invariant of $\nabla\mathbf{u}$ is:

$$Q = \frac{1}{2}\left[(\nabla\cdot\mathbf{u})^2 - \mathrm{tr}(\nabla\mathbf{u}^2)\right] \tag{2.45}$$

Where $\mathrm{tr}(\cdot)$ is the trace operator. (2.45) is the same as:

$$Q = -\frac{1}{2}\left(\frac{\partial u_i}{\partial x_j}\right)\left(\frac{\partial u_j}{\partial x_i}\right) \tag{2.46}$$

Using the definitions for the strain-rate and vorticity tensors Q becomes

$$Q = \frac{1}{2}\left(\left\|\mathbf{\Omega}^2\right\| - \left\|\mathbf{S}^2\right\|\right) \tag{2.47}$$

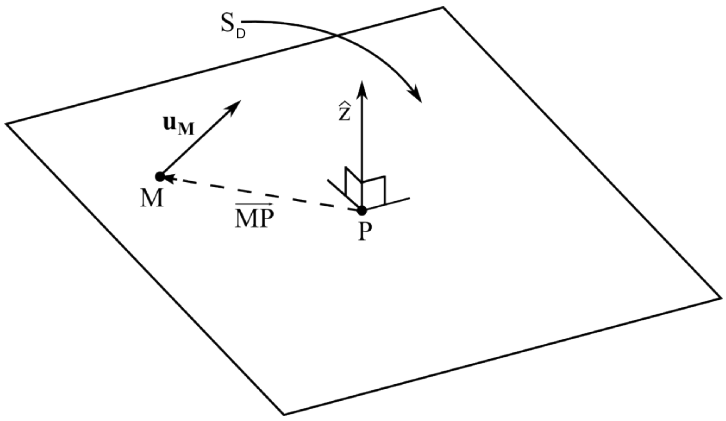

Fig. 2.8 Schematic of Γ_1 function variables.

Where

$$\left\|\mathbf{\Omega}^2\right\| = \mathrm{tr}\left(\mathbf{\Omega}\mathbf{\Omega}^{\mathrm{T}}\right) \tag{2.48}$$

$$\left\|\mathrm{S}^2\right\| = \mathrm{tr}\left(\mathbf{S}\mathbf{S}^{\mathrm{T}}\right) \tag{2.49}$$

This shows that when $Q = 0$ the strain-rate and the vorticity magnitude are in balance therefore, when $Q > 0$ the local rotational component of the flow exceeds the local strain-rate suggesting there is a vortical flow pattern.

Vortex Identification: Γ_1-Criterion

Graftieaux et al. (2001) introduced the Γ_1 function as a means of identifying vortices. The algorithm is especially suited to identifying the centre point of large scale turbulent vortices as it is dependent only on the topology of the flow field and not the magnitude and depending on the size of the domain of the integration employed it removes small scale fluctuations resulting in the bulk centre of rotation being identified. The function is defined as:

$$\Gamma_1(P) = \frac{1}{S_D}\int_{M\in S_D} \frac{(\overrightarrow{PM}\wedge\mathbf{u}_M)\cdot\hat{z}}{\left\|\overrightarrow{PM}\cdot u_M\right\|}\mathrm{d}S_D \tag{2.50}$$

where S_D is the domain surrounding the point P and the velocity vector $\mathbf{u}_M$ at point M lies in S with $\hat{z}$ the normal vector to the measurement plane as depicted in Figure 2.8. Γ_1 is calculated for all P in the measurement plane $(x,y) \in S_D$ and gives a maximum or minimum approaching 1 or -1 depending on the direction of rotation. In the remainder of the work in this thesis the Graftieaux Γ_1 method will be employed as it returns normalised values for the strength of vortices enabling one to identify the location of the main vortex structures from datasets comprising of multiple vortices of varying scale.

Chapter 3

The Proper Orthogonal Decomposition

3.1 Introduction

Proper Orthogonal Decomposition (POD) is a method commonly used in the analysis of turbulent flows to develop reduced-order models of the flow for use in prediction and analysis of the flow. POD decomposes a flow onto a set of basis functions (known as modes) that represent the flow optimally in the energy norm (Holmes et al., 1998; Prabhu et al., 2001). POD as it is referred to when applied to turbulent flows (POD also goes under a number of other titles depending on the application, including Principle Component Analysis (PCA), Karhunen-Loeve Decomposition or Expansion, Singular Value Decomposition (SVD), Principle Factor Analysis and Hotelling Transform (Tropea et al., 2007; Uruba, 2012) is a powerful tool which is used extensively in the analysis of two dimensional velocity data obtained experimentally using PIV and for the analysis of 3-Dimensional data as obtained by direct numerical simulation (DNS), large eddy simulation (LES) or holographic PIV (HPIV) (Adrian et al., 2000). Whilst Reynolds decomposition as introduced in § 2.3.1 is ample for investigating the mean flow field or for analysing various turbulent statistics such as turbulence intensity it is insufficient if one wishes to focus solely on either the large scale coherent structures or the smaller scale turbulent vortices present within the flow. By decomposing the flow information on the basis of energy contained at different levels POD is able to identify structures in the flow at a range of energy scales (Adrian et al., 2000). It can be shown that the basis functions (modes) generated by POD are optimal in the sense that they converge to the instantaneous data sets quicker than any other basis (e.g. Fourier Decomposition) meaning that the flow can be represented to a specified accuracy with the fewest possible modes (Liang et al., 2002). The aim of POD is to represent a realisation of the flow u_i (of N_s total realisations of the flow) as a linear combination of basis functions or modes, ϕ in the form:

$$u_i = \sum_{n=1}^{N_s} a_i^{(n)} \phi^{(n)} \tag{3.1}$$

Where a_i are the POD coefficients which will later be more formally introduced. The power of POD comes from the ability to extract flow features from a series of realisations of a flow based

on the content of their energy. The larger scale, coherent structures present in the flow account for the majority of the flow energy whilst the smaller unorganised turbulent flow structures contain less energy. Using the information present in the high energy containing modes it is possible to rebuild a model of the flow using a combination of these modes or coherent structures, this lower dimensional modelling is useful if one is only concerned with the large scale flow structures present in the flow rather than the small scale turbulence (Druault et al., 2005a; Holmes et al., 1998; Kourentis and Konstantinidis, 2012; Shinneeb, 2006; Shinneeb et al., 2008)

3.2 Mathematical Formulation of the Proper Orthogonal Decomposition

3.2.1 Direct Method

As introduced by Lumley (1967) POD is the problem of finding the orthonormal set of basis functions that maximise the mean square energy of a set of realisations of a flow (Druault et al., 2005b). Lumley (1967) and Druault et al. (2005b) propose that a coherent structure is a structure that has the largest mean square projection of the velocity field.

The basis functions are optimal in the sense that they have the smallest error out of all possible orthogonal basis functions and hence for any number $N_c \leq N_s$ the error, ε, is a minimum where $u_i^{N_c}$ is a reconstruction of the i^{th} velocity field using the first N_c basis functions (Rowley et al., 2000) ($\|\cdot\|$ denotes the standard L^2 norm and $\langle\cdot\rangle$ the spatial average over all $M = N_x N_y$ vector grid points where N_x and N_y are the number of vectors in the x and y directions respectively):

$$\varepsilon = \left\| u_i - u_i^{N_c} \right\| \tag{3.2}$$

Where ||.|| is the discrete two-dimensional norm defined as (Meyer et al., 2007):

$$\|y\| = \sqrt{y_1^2 + y_2^2 + \ldots + y_M^2} \tag{3.3}$$

The set of basis functions $\mathbf{\Phi}$ are calculated by solving the following Fredholm integral eigenvalue problem (Druault et al., 2005b; Prabhu et al., 2001):

$$\sum_{j=1}^{N_v} \int_D \overline{u_i(\mathbf{x}) u_j(\mathbf{x}')} \phi_j^{(n)}(\mathbf{x}') d\mathbf{x} = \lambda^{(n)} \phi_i^{(n)}(\mathbf{x}) \tag{3.4}$$

Where $\mathbf{x} = (x, y, z)$ is a spatial coordinate vector, N_v is the total number of velocity components (which is 2 in the case of planar PIV, the u and v velocity components). $\overline{u_i(\mathbf{x}) u_j(\mathbf{x}')}$ is the time-average spatial cross-correlation tensor and $\phi^{(n)}(\mathbf{x})$ and $\lambda^{(n)}$ are the n^{th} eigenfunction and eigenvalue respectively. D represents the domain of interest and in the case of PIV is generally taken as the field of view of the vector field.

In practice (3.4) is discretised as all data from experiments or numerical simulations is in a

discrete form and the cross-correlation tensor becomes (Alan et al., 2010):

$$u_i(\mathbf{x})u_j(\mathbf{x}') = \frac{1}{N_s}\sum_{k=1}^{N_s} u_i(\mathbf{x},t_k)u_j(\mathbf{x}',t_k) \tag{3.5}$$

Using (3.5), the Fredholm integral eigenvalue problem (3.4) can be solved for ϕ and λ. Since the basis functions $\phi^{(n)}$ are orthonormal, the vector product of any two modes of differing order is zero and those of equal order unity. Letting δ_{nm} be equal to the Kronecker delta and (a,b) denote the vector product (Borée, 2003) the following shows the orthogonality of the basis functions:

$$\left(\phi^{(n)},\phi^{(p)}\right) = \delta_{np} = \begin{cases} 1, & \text{if } n = p, \\ 0, & \text{if } n \neq p. \end{cases} \tag{3.6}$$

The method of calculating the eigenfunctions and eigenvalues demonstrated here is often computationally very expensive so a more efficient algorithm is used and is detailed below.

3.2.2 Snapshot Method

The direct method of calculating the POD is computationally very expensive. Instead when there are a large number of realisations of the velocity field, known as snapshots, the snapshot method can be used. Introduced by Sirovich (1987) the method of snapshots is applicable when the number of spatial data points in the measurement domain, M, is much larger than the number of realisations, N_s (snapshots) captured of the flow field. In this thesis this condition is met as the minimum spatial resolution of individual velocity vectors is $N_x = 128, N_y = 128$ vectors giving a total of $M = 16384$ vectors compared to a longest data set of $N_s = 2700$ snapshots.

Snapshot POD is carried out on the fluctuating component of the velocity vector field, this is calculated by subtracting the time average velocity field from each velocity field snapshot as defined in (2.17). By arranging the fluctuating velocity components in a column vector from the entire dataset of all snapshots can be represented by the matrix $\mathbf{U}$ as follows (Meyer et al., 2007):

$$\mathbf{U} = \left[\mathbf{u}^1,\mathbf{u}^2,\ldots,\mathbf{u}^{N_s}\right] = \begin{bmatrix} u_1^1 & u_1^2 & \ldots & u_1^{N_s} \\ \vdots & \vdots & \vdots & \vdots \\ u_M^1 & u_M^2 & \ldots & u_M^{N_s} \\ v_1^1 & v_1^2 & \ldots & v_1^{N_s} \\ \vdots & \vdots & \vdots & \vdots \\ v_M^1 & v_M^2 & \ldots & v_M^{N_s} \end{bmatrix} \tag{3.7}$$

Where N_s is the total number of snapshots and $M = N_x \times N_y$ is the number of vectors in each snapshot. Using the above representation of the velocity data the autocovariance matrix $\mathbf{C}$ is calculated as:

$$\mathbf{C} = \mathbf{U}^{\mathrm{T}}\mathbf{U} \tag{3.8}$$

When calculated this way the autocovariance matrix, $\mathbf{C}$ has dimension $N_s \times N_s$ and is symmetrical. It can be seen that calculating the autocovariance matrix in this manner the problem reduces to solving an $N_s \times N_s$ matrix eigenvalue problem as opposed to a $M \times M$ matrix $(M = N_x \times N_y)$ eigenvalue problem as with the direct method (Druault et al., 2005b). From the autocovariance matrix the following eigenvalue problem is solved:

$$\mathbf{C}\mathbf{A}^{(n)} = \lambda^{(n)}\mathbf{A}^{(n)} \tag{3.9}$$

The symmetry of $\mathbf{C}$ implies that all eigenvalues are real and positive and can be ordered as:

$$\lambda^{(1)} > \lambda^{(2)} > \ldots > \lambda^{(N_s)} = 0 \tag{3.10}$$

The individual spatial POD modes $\phi^{(n)}$ are generated by projecting the POD coefficient matrix $\mathbf{A}$ onto the velocity vector snapshots and normalising:

$$\phi^{(n)} = \frac{\sum_{i=1}^{N_s} A_i^{(n)} u_i}{\left\| \sum_{i=1}^{N_s} A_i^{(n)} u_i \right\|} \tag{3.11}$$

Where $A_i^{(n)}$ is the i^{th} component of the eigenvector corresponding to the eigenvalue $\lambda^{(n)}$ (Meyer et al., 2007).

As with any decomposition individual snapshots must be able to be represented from the calculated basis functions, in the case of POD a velocity vector snapshot is a linear combination of individual modes $\phi^{(n)}$ multiplied by the corresponding POD coefficient a^n. The coefficients $\mathbf{a}_i$ for the i^{th} velocity vector snapshot are calculated by projecting the fluctuating velocity onto the POD modes (Meyer et al., 2007):

$$\mathbf{a}_i = \mathbf{\Phi}^{\mathrm{T}}\mathbf{u}^i \tag{3.12}$$

Where $\mathbf{\Phi}$ is a matrix containing all POD modes arranged as such:

$$\mathbf{\Phi} = \left[\phi^1 \phi^2 \ldots \phi^{N_s}\right] \tag{3.13}$$

Taking (3.12) it can be seen that the POD coefficient for the n^{th} mode and the i^{th} velocity snapshot, a_i^n is the projection of the n^{th} mode onto the i^{th} velocity field:

$$a^{(n)} = \phi^{(n)} u_i \tag{3.14}$$

Similarly, as with the basis functions ϕ as shown by (3.6) the orthogonality (zero-correlation) of the POD coefficients can also be shown (Borée, 2003; Tamura et al., 1999):

$$\overline{a_i^{(n)} a_i^{(p)}} = \lambda^{(n)} \delta_{np} \tag{3.15}$$

This leads to the result showing that the energy contained in the n^{th} mode is equal to the mean

square of the n^{th} POD coefficients (Tamura et al., 1999):

$$\overline{\left(a_i^{(n)}\right)^2} = \lambda^{(n)} \tag{3.16}$$

Furthermore, as one would expect the total energy contained in the eigenvalues $\lambda^{(n)}$is equal to the fluctuating kinetic energy of the flow (Borée, 2003):

$$\overline{(u_i, u_i)} = \sum_{n=1}^{N_s} \lambda^{(n)} \tag{3.17}$$

Finally, for completeness, with all eigenvalues, modes and coefficients calculated the scaling of ϕ is as follows (Borée, 2003):

$$\phi^{(n)} = \frac{\overline{a_i^{(n)} u_i}}{\lambda^{(n)}} \tag{3.18}$$

3.3 Reconstruction of Velocity Snapshots from POD Modes

As previously stated any individual snapshot velocity field can be approximated using a linear combination of a number of POD modes, since the decomposition is carried out on the fluctuating velocity component to reproduce the full flow field the modes have to be added to the ensemble average. Thus each full snapshot velocity field, u_i, is recreated as the sum of the ensemble average $\overline{u}$ and a linear combination of each of the N_s (number of snapshots) modes $\phi^{(n)}$ and the corresponding POD coefficient $a_i^{(n)}$ (Sirovich, 1987):

$$u_i = \overline{u} + \sum_{n=1}^{N_s} a_i^{(n)} \phi^{(n)} \tag{3.19}$$

The above representation, as the summation represents the full fluctuating component of the snapshot and is equivalent to the classical Reynolds decomposition:

$$u_i = \overline{u} + u_i' \tag{3.20}$$

For completeness it can be seen that by combining (3.19) and (3.20) that:

$$u_i' = \sum_{n=1}^{N_s} a_i^{(n)} \phi^{(n)} \tag{3.21}$$

As an extension to the Reynolds decomposition as shown in (3.20) Roudnitzky et al. (2006) show that the fluctuating velocity component u_i' can be further decomposed into a large scale coherent fluctuating component, $\tilde{u}$ and incoherent small scale turbulence, $\hat{u}$:

$$u_i' = \tilde{u}_i + \hat{u}_i \tag{3.22}$$

Thus giving the total flow field snapshot as a triple decomposition:

$$u_i = \overline{u} + \tilde{u}_i + \hat{u} + i \tag{3.23}$$

The representation of u in (3.19) since it includes all N_s modes contains the full flow information. If one needs only to consider the large scale flow structures, neglecting the small scale incoherent turbulence the summation to N_s in (3.19) can be truncated to a cut-off mode number, N_c since it is the first N_c modes that contain the majority of the flow energy associated with the large scale coherent structures, the POD approximation then becomes:

$$u_i^{(N_c)} = \overline{u} + \sum_{n=1}^{N_c} a_i^{(n)} \phi^{(n)} \tag{3.24}$$

Further, the full flow snapshot can be recreated as follows:

$$u_i^{(N_s)} = \overline{u} + \sum_{n=1}^{N_c} a_i^{(n)} \phi^{(n)} + \sum_{n=N_c+1}^{N_s} a_i^{(n)} \phi^{(n)} \tag{3.25}$$

Where the coherent fluctuating velocity component is the summation of the first N_c modes:

$$\tilde{u}_i^{(N_c)} = \sum_{n=1}^{N_c} a_i^{(n)} \phi^{(n)} \tag{3.26}$$

And the incoherent turbulent fluctuating component is the summation of the modes from $N_c + 1$ to N_s:

$$\hat{u}_i^{(N_s)} = \sum_{n=N_c+1}^{N_s} a_i^{(n)} \phi^{(n)} \tag{3.27}$$

Using a truncated number of modes to recreate the velocity snapshots means that only an approximation is being modelled since not all of the flow information is included but due to the nature of the decomposition the most important, dominant flow structures are contained in the earlier modes (since $\lambda^{(n)} > \lambda^{(n+1)}$) whereas the higher modes contain the smaller scale coherent structures and the even smaller scale incoherent turbulence.

3.4 Applications to Turbulence

One area in the analysis of turbulent flows where POD features heavily is in the analysis of the swirling flow in internal combustion engines as with the rise in the number of research engines giving optical access more and more PIV is being carried out for which POD is a perfect analysis tool. The POD has been applied to in-cylinder flows in many studies (Bizon et al., 2010; Cosadia et al., 2006, 2007; Druault et al., 2005b; Fogleman et al., 2004; Graftieaux et al., 2001; Kostas et al., 2005; Roudnitzky et al., 2006; Vu and Guibert, 2012). Cosadia et al. (2006) also apply the POD to circulation data calculated from the vector fields to study modes which contribute to the fluctuations of the circulation, it is shown that the fluctuations of circulation converge using

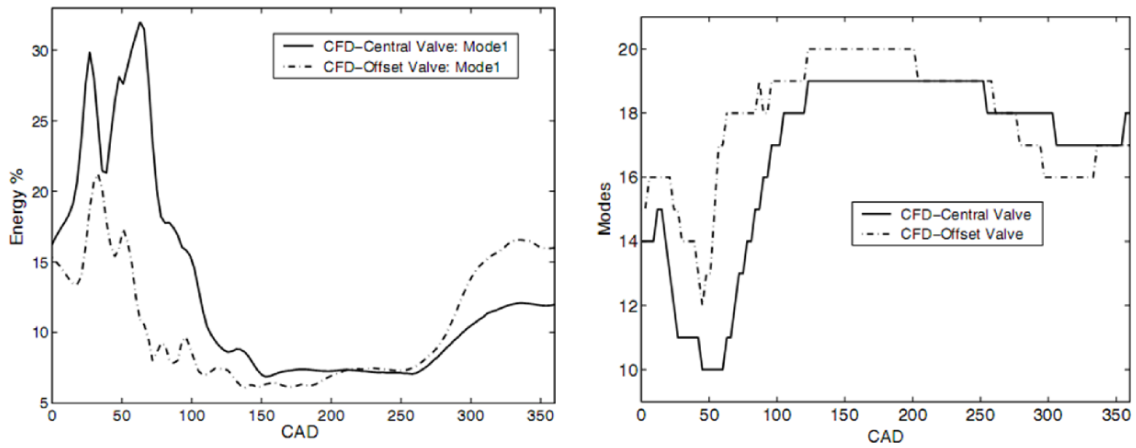

Fig. 3.1 (*left*) Energy content of the first POD mode for varying crank angle degree of the flow in an engine cylinder and (*right*) the number of POD modes required to account for 75% of the total energy for varying crank angle degree. Reproduced from (Fogleman et al., 2004).

less modes at a radius further away from the centre of the vortex than those close to the centre suggesting that variability is higher and structure more complex closer to the vortex core.

Recent developments in the application of the POD to flow variables other than velocity such as the vorticity field have been investigated. Kostas et al. (2005) show that coherent structure identification in the case of flow over a backward facing step captured using 2D PIV is more efficient when POD is carried out on the out of plane vorticity field rather than when using the velocity decomposition in the sense that the energy contained in the modes converges quicker. For POD carried out on vorticity fields also see Gurka et al. (2006); Regert et al. (2005).

Fogleman et al. (2004) were among the first to obtain fully three-dimensional POD modes from a three-dimensional velocity field (CFD) and the first in relation to in-cylinder flows, in this case in the tumble plane. The CFD data was generated using a large eddy simulation model (Haworth and Jansen, 2000; Lumley, 2001) and was simulated over 33 consecutive engine cycles giving 32 instantaneous vector fields for each crank angle degree (the first cycle was discarded to avoid contamination by the initial conditions). It is shown that for PIV data the energy present in the POD modes converges quicker than for CFD generated data owing to the larger number of snapshots present for PIV. The percentage of energy present in the first POD mode (the mode containing the highest energy) varies significantly at differing crank angle degrees (CAD) Figure 3.1, for the CAD where the first mode contains a high proportion of the energy the flow is of a more simple (more organised) nature compared to CAD at the end of the intake stroke where only a low proportion of energy is contained in the first mode which suggest a more complex structure and more modes are required to model the flow.

Maurel et al. (2001) and Borée (2003) introduced a variant on POD known as Extended-POD to investigate inhomogeneous flows where certain areas of the measurement domain contain a small proportion of the turbulent kinetic energy. The benefit of this method is that traditional POD extracts coherent structures present in the full measurement domain whereas in reality for flows with localised features these structures are also highly localised; a mathematical description of

extended POD is provided in (Borée, 2003) and an example of Extended-POD as applied to a jet/vortex interaction in (Maurel et al., 2001). More recently Duwig and Iudiciani (2010) applied Extended-POD to the analysis of unsteady flames in combustion.

There are numerous studies where POD is used as a tool for the direct extraction of coherent structures in a number of differing turbulent flows such as turbulent wakes (Kourentis and Konstantinidis, 2012), vortex shedding behind cylinders of various shapes (Chong et al., 2013; Feng et al., 2011; Huera-Huarte and Vernet, 2010; Liu et al., 2011), free jets (Patte-Rouland et al., 2001; Schram and Riethmuller, 2001; Shinneeb et al., 2008) and the analysis of mixing in stirred tanks which are used heavily in the chemical industry (Doulgerakis et al., 2011; Hasal et al., 2000; Kim et al., 2012; Liné et al., 2013) to name but a few flow types POD has been applied to.

The literature at present does not contain a POD analysis of either a tornado vortex flow or laboratory tornado-like vortex flow though the work carried out by Graftieaux et al. (2001) on a vortex in a wall bounded circular cylinder with water shows similarities to the work carried out in this thesis and will be referred to in later chapters.

3.5 Phase-Invariant POD

Fogleman et al. (2004) present a method for the application of the POD to time resolved PIV (TRPIV) for in-cylinder flows. During the intake and compression strokes in an IC cylinder the size of the flow domain parallel to the cylinder axis evolves as the piston moves, the aim of the phase-invariant POD is to remove the dependency on phase of standard POD so that flows with a temporally evolving domain can be studied. This is carried out by manipulation of the instantaneous velocity fields through stretching and normalising so that all flow phases are equally weighted. Through the projection of these phase-invariant POD modes a model for the temporal breakdown of flow structures parallel to the cylinder axis can be produced. It is also shown that the phase-invariant POD modes converge quicker than the phase-dependant modes, possibly due to the increased number of realisations used (all velocity fields at all phases rather than all velocity fields at a certain phase).

Cosadia et al. (2007) use a phase-invariant POD method on time-resolved PIV with a low temporal resolution to study the temporal evolution of the in-cylinder flow in the swirl plane. In this case the spatial domain decreases as early in the compression phase the flow is able to fill the full bore of the cylinder whereas at the top of the compression stroke the flow is confined to the piston bowl. It is shown that fluctuations in intensity and displacement of the swirling motion increase in the latter stages of the compression stroke, especially during transfer to the piston bowl. An interpolation method is also presented based on the phase-invariant POD modes to generate a continuous time-resolved flow field for the compression stroke between the first and last phases. A similar approach is presented by Druault et al. (2005b) also in the plane perpendicular to the cylinder axis.

Chapter 4

Laboratory Generated Tornado-Like Vortices

4.1 Introduction

Tornadoes produce the highest naturally occurring wind speeds on earth and in the USA on average are the cause of 80 fatalities and 1500 injuries annually and US$850 million in damage according to statistics provided by the Wind Hazard Reduction Coalition. In 2011 alone there were 553 recorded deaths from tornadoes (NOAA, 2012).

A tornado, according to Glickman (2000) is:

> *"a violently rotating column of air, pendant from a cumuliform cloud or underneath a cumuliform cloud, and often (but not always) visible as a funnel cloud."*

Tornadoes form within a parent thunderstorm with a large circulation known as a mesocyclone where the mesocyclone is two orders of magnitude greater in horizontal dimension than the resulting tornado and contains a vastly great amount of energy and circulation (Davies-Jones, 1986; Glickman, 2000). Ying and Chang (1970) list the main features of tornado as being:

1. A huge votex column with a low pressure core that travels along the ground with very large rotational velocity and centrifugal force.

2. The circulation of the tornado vortex is maintained by the parent storm.

3. A large buoyant updraft is present in the vortex core arising from warm humid air of low density next to the ground with the visual vortex column forming from the reverse flow of the condensing air.

4. The ground boundary layer is occupied by a spiral inflow of the warm air into the base of the vortex core where there is an appreciable pressure drop.

5. Prevailing winds at usually mid-tropospheric level drives the precession of the parent storm causing the tornado vortex to lean and be stretched.

In terms of fluid mechanics a tornado is a vortex with an axis perpendicular to the ground with an overall upward axial velocity. As one can see looking at video footage of tornadoes the vortex does not remain stationary in space but precesses with a bulk motion as well as exhibiting more random fluctuations in their movement.

4.2 Historical Notes on Laboratory Generated Tornado-Like Vortices

Due to the size of naturally occurring tornadoes and the lack of ability to accurately predict where and when a tornado would form, in the late 1960's work moved towards generating laboratory scale tornadoes using apparatus that would generate tornado-like vortices that provide accurate scaled down representations of full scale naturally occurring tornadoes.

Ying and Chang (1970) were among the first to publish on laboratory generated tornado-like vortices, they identified four criteria that were necessary to be fulfilled:

1. A single stationary vortex column touching the ground.
2. A pressure drop and updraft within the vortex core.
3. A ground boundary layer with flow spiraling in towards the vortex core.
4. The vortex flow should be turbulent.

It became apparent that to generate a tornado-like vortex two separate flow components are required, a rotating flow with axis perpendicular to the ground plane and an exhaust vertical flow component. In this early model Ying and Chan produced the circulation through means of a rotating mesh screen of diameter 198cm through which air could flow through and the axial flow was provided by use of an exhaust fan, a schematic of this tornado vortex simulator is show in Figure 4.1. The fan generating the updraft is separated from the main flow region by a hood with an updraft orifice of diameter 21.6cm allowing the flow to escape toward the fan. This design enabled Ying and Chan to independently control the circulation and updraft parameters allowing them to study a wide range of tornado-like vortices.

Ying and Chan using anemometers and pressure transducers in their simulator recorded tangential and radial velocity profiles, they show that the pressure drop on the ground increases with circulation and the pressure drop on the hood decreases with increasing circulation as the axial fan becomes less efficient with increased circulation. It is shown that in the ground boundary layer pressure remains almost constant aside from the vortex core region, this leads to a drop in tangential velocity and hence centrifugal force which is no longer able to balance the radial pressure gradient leading to the inward radial flow. However, at this stage accurate measurement of the flow further away from the floor within the boundary layer was not possible without introducing large interference errors due to the presence of probes. It is also shown that above the boundary layer the

radial inflow is very small compared to the tangential flow velocities. The main findings of their work however was that a scaled down tornado-like vortex which exhibits similar characteristics to natural tornadoes can be created in a lab environment. These are all key findings which remain consistent with the evolution of future studies and tornado-like vortex simulators. Wan and Chang (1972) show that this model tornado-like vortex generator provides a reasonable similarity to the 1957 Dallas Tornado (Hoecker, 1960).

Ward (1972) improves on the design of Chang's simulator by adding a honeycomb at the top of the chamber to straighten the flow and remove vertically oriented vorticity from the generated vortex simulating more closely the conditions present at the top of an atmospheric vortex, a schematic of the Ward tornado vortex simulator is shown in Figure 4.2. Also differing from the Chang model the inflow of air is restricted to the region close to the chamber floor while the circulation is as with the Chang model provided by a rotating mesh screen and the updraft by an exhaust fan. It is this Ward type simulator that provides the basis of the majority of tornado-like vortex simulators that follow. Using this simulator Ward was the first to report multi-celled tornadoes in a laboratory simulator. Multi-celled tornadoes are tornadoes which contain a number of individual vortex cores inside of the main tornado vortex.

Jischke and Parang (1974) show that for a tornado-like vortex simulator three dimensionless numbers define the size and structure of the vortex; swirl ratio, aspect ratio and radial Reynolds number. The swirl ratio, S is defined as the ratio of axial to angular momentum of the vortex as follows:

$$S = \frac{\Gamma R}{2Q_V} \tag{4.1}$$

Where Q_V is the volumetric flow rate through the system and is usually measured as the flow rate through the axial fan or blower. R is the vortex radius defined as the radius from the centre of the vortex to where the tangential velocity is greatest, i.e. the radius of maximum wind and Γ is the circulation around the circular path at radius R from the centre of the vortex. The aspect ratio, a_r is defined as the ratio of the height of the vortex chamber, h_0 to the radius of the updraft orifice, r_0 as follows:

$$a_0 = \frac{h_0}{r_0} \tag{4.2}$$

The radial Reynolds number, Re_r is defined as:

$$\mathrm{Re}_r = \frac{Q_V}{h_0 \nu} \tag{4.3}$$

Where ν is the kinematic viscosity of air at lab temperature.

Davies-Jones (1973) shows, using the Ward (1972) simulator that it is the swirl ratio alone that controls the radius of the tornado vortex core and that similar vortex radii can be created using different combinations of circulation intensity and updraft to create the same swirl ratio. These

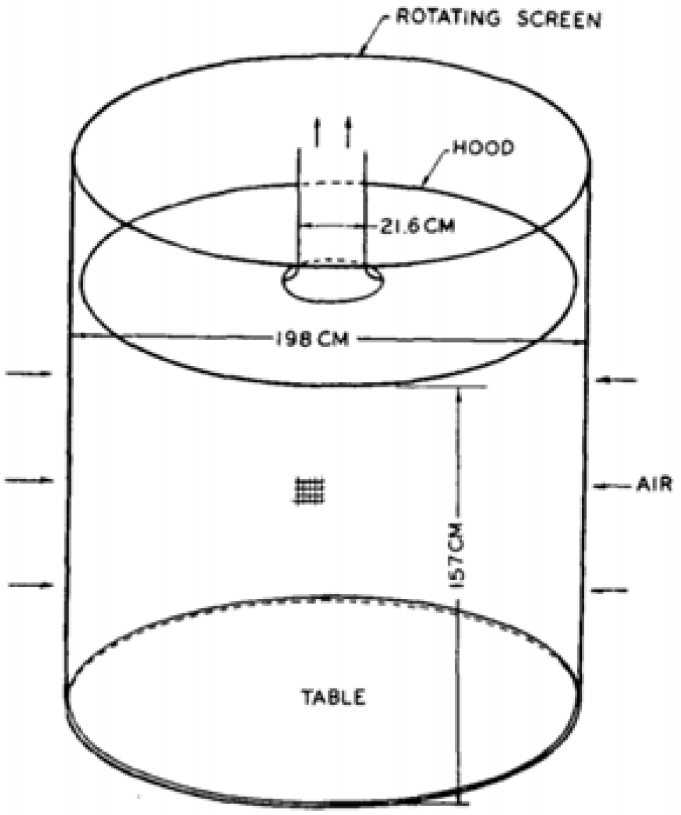

Fig. 4.1 Schematic of the Ying and Chen tornado vortex simulator. Reproduced from (Ying and Chang, 1970).

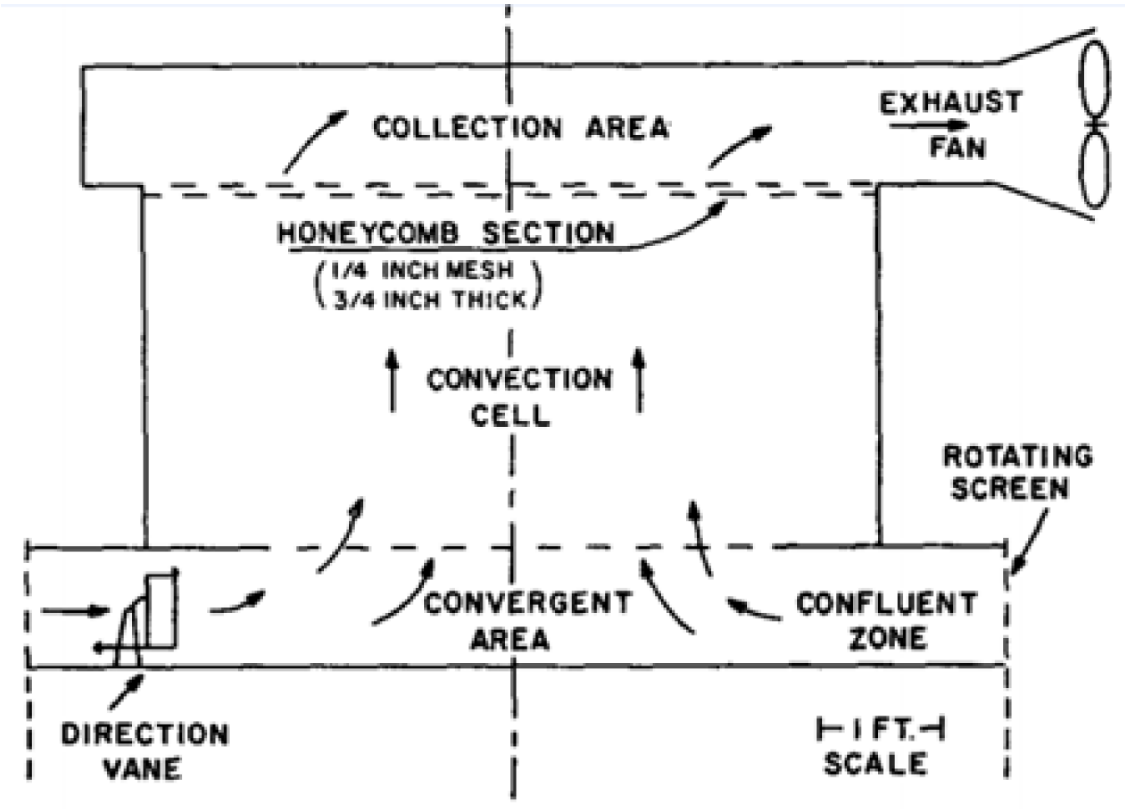

Fig. 4.2 Schematic of the Ward Tornado Vortex Simulator. Reproduced from (Ward, 1972).

results are backed up by numerical calculations carried out on the Ward simulator by Rotunno (1979). Davies-Jones goes on to show that volumetric flow rate and not the radial momentum flux is the important factor in the production of atmospheric vortices as for constant flow rate, circulation, updraft radius and the in-draft height did not alter the size of the core radius.

Church et al. (1977) constructed a large scale Ward type simulator at Purdue University measuring 4m wide and 7m tall, a schematic of which is presented in Figure 4.3 and a photograph in Figure 4.4, again using a rotating mesh to create the circulation. The research emphasised the nature of the vortex structure as a function of swirl ratio and demonstrated that they could achieve vortex breakdown and multiple vortices. Church et al. (1979) define five different flow regimes based on swirl ratio, in order of increasing swirl ratio:

1. Single laminar vortex.
2. A single vortex with an upper turbulent region separated from the lower laminar region by a separation bubble.
3. Fully developed turbulent vortex core where breakdown bubble penetrates to the chamber floor.
4. Transition to two intertwined helical vortices.
5. Higher order multiple-vortex configurations that form in the core region.

Church et al. (1979) showed that as the angular momentum in the vortex increased, relating to an increase in the swirl ratio, the vortex evolves from a single-celled vortex to a two-celled vortex before moving onto higher multiple core vortex. They came to the conclusion that it is the swirl ratio that is the dominant parameter in defining vortex configuration and that aspect ratio and Reynolds number have a much smaller influence on the overall configuration of the tornado-like vortex.

The overall design of laboratory tornado vortex simulators has evolved very little from these original steps described above. Lund and Snow (1993) adapted their TVS at Purdue University to enable them to take flow measurements using laser Doppler velocimetry (LDV) rather than using hotwires as most previous research relied on. The advantage of this is that they were able to increase the spatial resolution of their measurements however they were only able to measure one velocity component at a time meaning instantaneous information regarding the tangential and radial velocity components were not available.

In 2008 Mishra et al at Texas Tech State University, USA, present a new type of TVC, the Texas Tech University vortex simulator II (TTU-VSII) (Mishra et al., 2008a,b). TTU-VSII is based on a Ward type TVC. Axial flow is provided by sucking air through the chamber from the updraft orifice and circulation is provided by 16 slotted jets made out of PVC pipe with axial slits cut in each. A schematic of the TTU-SVII is shown in Figure 4.5. They show that flow velocity data obtained via hotwire probes is in strong agreement with real atmospheric tornado

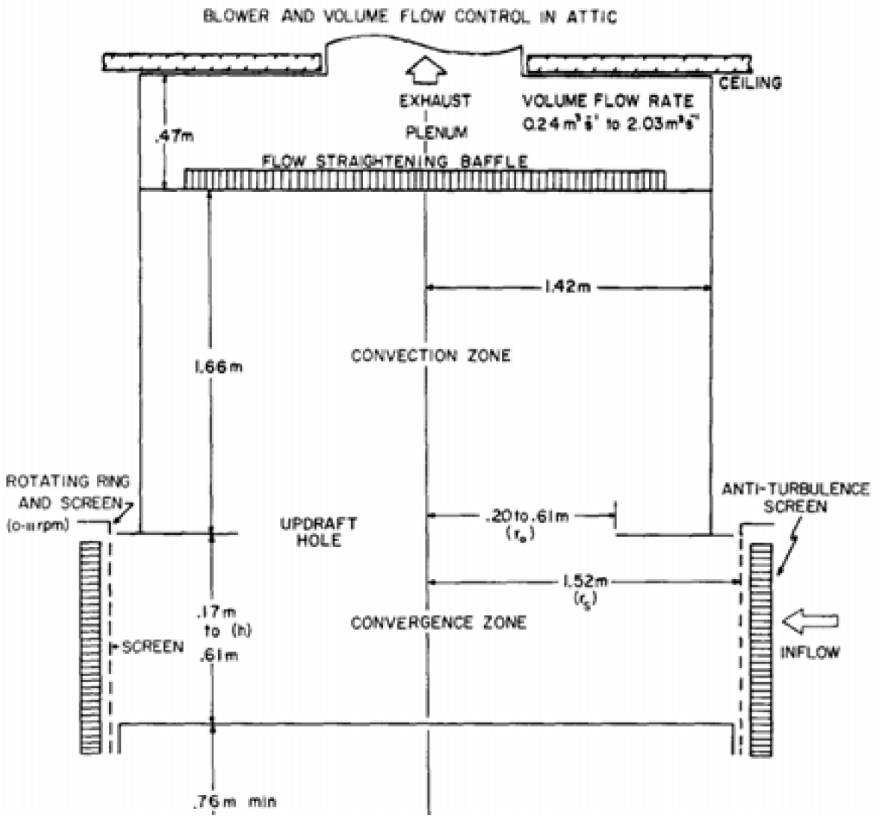

Fig. 4.3 Schematic of the Purdue University tornado vortex simulator. Reproduced from (Church et al., 1977).

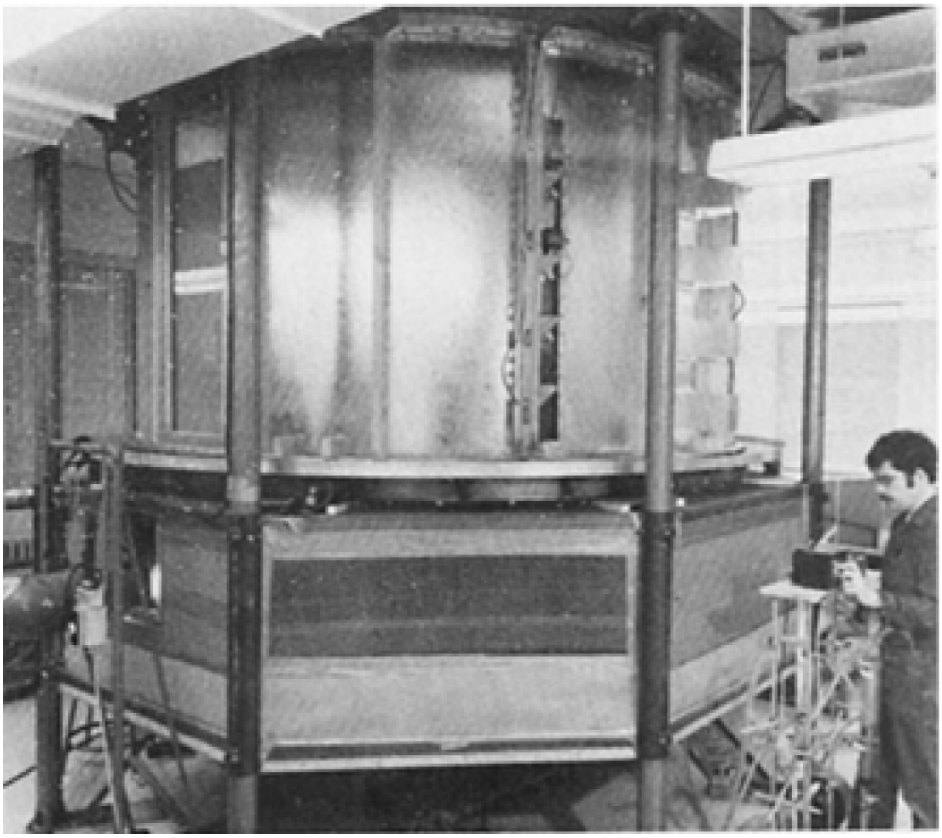

Fig. 4.4 Photograph of the Purdue University tornado vortex simulator. Reproduced from (Church et al., 1977).

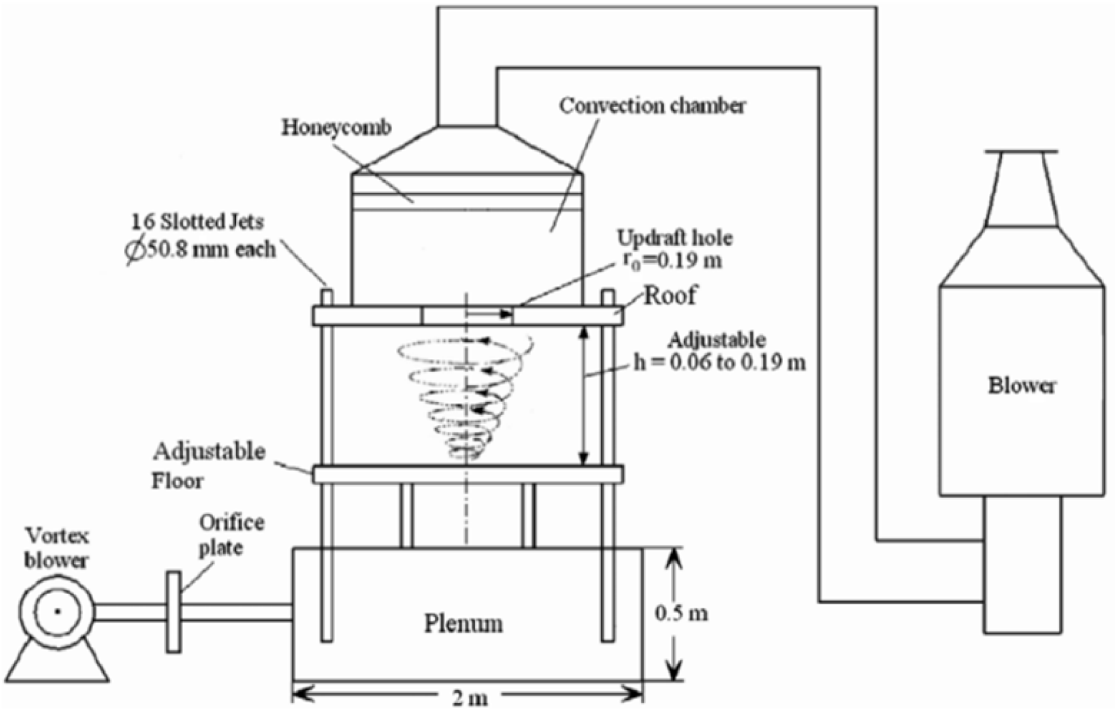

Fig. 4.5 Texas Tech University vortex simulator II (TTU-VSII). Diagram from (Mishra et al., 2008a).

measurements, showing that this modified TVC design provides a good model for the study of tornado-like vortices.

4.3 PIV and Laboratory Generated Tornado-Like Vortices

With the development of PIV as detailed in § 1 a means of whole field, non-intrusive, quantitative flow measurement became available without disturbing the flow using single point, intrusive measurement probes such as hotwire probes as were used in many of the experiments detailed in the previous section. Even with the wide adoption of PIV as a flow measurement technique in many academic and industrial outposts a review of the available literature returned a relatively low number of PIV measurements of laboratory generated tornado-like vortices.

Among the earliest work on a tornado vortex simulator providing full optical access to the flow perpendicular to the swirl axis is that at Iowa State University (ISU), USA (Haan Jr et al., 2008; Sarkar et al., 2005). The TVC is a large modified Ward type TVC mounted so the chamber is able to translate relative to the ground plane enabling a travelling tornado-like vortex to be modelled. Their initial results show that measurements of this type of vortex bear a strong resemblance to real atmospheric tornado measurements obtained with Doppler radar.

In 2008 Hangan et al presented velocity vectors measured in the vertical plane using PIV in order to benchmark CFD simulations of laboratory generated tornado-like vortices (Hangan et al., 2008).

Using a 1:3 scale ISU TVC Zhang and Sarkar (2012) use PIV to record velocity measurements

in both the vertical and horizontal planes obtaining clear full field instantaneous velocity vector fields showing compact single cell vortices at low swirl ratios and large multi-cellular vortices at high swirl ratios. In the same study Zhang et al go on to show, through identifying the vortex core location in instantaneous velocity fields, that the degree of vortex wondering/precession are considerably greater at low swirl ratios.

Hashemi-Tari et al. (2010) designed and built a TVC enabling full optical access in both the horizontal and vertical planes allowing PIV measurements to be taken and over a wide range of swirl ratios from 0.08 to 1 showing that the radius of the vortex core increases with swirl ratio and in the near core region the tangential velocity profiles closely fit a Rankin vortex model. By investigating the turbulent flow characteristics Hashemi-Tari et al show that both normal and shear stresses contained within the flow increase with increasing swirl ratio.

More recently Yang et al again using the ISU TVC use PIV to study the flow characteristics and wind loads of a tornado-like vortex interacting with a model high-rise building showing that the flow patterns in the wake of and the resultant wind loads on the model building were considerably different to those observed in conventional head on winds. It is shown that the wind loading on the building model were at their greatest when the building model was mounted at the outer boundary of the tornado-like vortex core (Yang et al., 2011). Making use of the ISU TVC once again Hu et al conducted an investigation similar to the previously mentioned study but this time on gable-roofed building models (Hu et al., 2011).

Chapter 5

Evaluation of PIV Vector Calculation Algorithms

5.1 Introduction

The work in this study is an evaluation and expansion of the Correlation Based Correction (CBC) PIV vector calculation algorithm as presented by Hart (Hart, 2000).The implementation of CBC aims to reduce errors in vector calculation by reducing noise levels in the correlation function and increasing the signal strength of the displacement peak by multiplying spatially adjacent correlation functions.

When a correlation function is calculated using a correlation based algorithm aside from the main displacement peak other peaks are present due to correlations between particles other than their pair between the two frames, image noise as well as other factors as discussed in the literature review. It is also possible for the correlation peak to become splintered due to the presence of velocity gradients across the interrogation region (Huang et al., 1997). In some cases the magnitude of the noise peaks are larger than the displacement peak resulting in an erroneous vector being calculated for that interrogation region. The CBC algorithm aims to overcome this by multiplying adjacent correlation functions value by value. Through multiplication of adjacent correlation functions random noise peaks are eliminated or significantly reduced as it is highly improbable that exactly the same noise peaks will be present in adjacent correlation functions.

5.1.1 Implementation of the Correlation Based Correction Algorithm

Figure 5.1 shows a schematic of the arrangement of individual interrogation regions, I_i, $\{i = 0, 1, 2, 3, 4\}$ used to calculate the vector located at the centre of interrogation region I_0. Interrogation regions $1 - 4$ are translated from the location of I_0 by a distance δ_W in the up, right, down and left directions respectively. Correlation functions, C_i are then generated using a correlation based algorithm such as the normalised cross-correlation algorithm as presented in § 1.5 for each of the five interrogation regions. The final cross-correlation function, C is then calculated as the

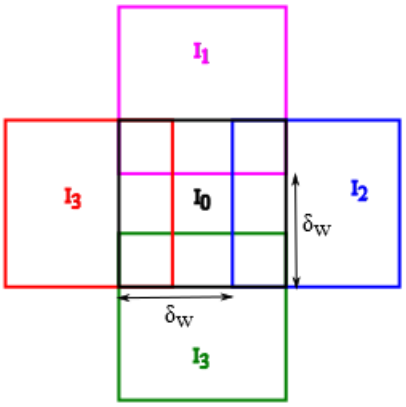

Fig. 5.1 Arrangement of individual interrogation windows, I_{0-4} for the implementation of CBC with a window offset δ_W for the calculation of the vector centred on the central (black) interrogation region I_0

element-wise product of each correlation function as follows:

$$C = \prod_{i=0}^{4} C_i \tag{5.1}$$

Figure 5.2 shows individual correlation functions C_i and their product C as calculated using CBC and the interrogation region arrangement presented in Figure 5.1. It can be seen that each correlation function C_i contains a strong displacement peak of approximately similar size and location and a number of smaller noise peaks which vary between each correlation function. As seen in the product, C the displacement peak is maintained and all noise peaks are reduced to a near zero value increasing the signal to noise ratio of the displacement peak by many orders of magnitude.

5.1.2 Previous Findings and Outline of Present Study

When originally presenting CBC Hart applies the technique to both synthetic and experimentally obtained images (Hart, 2000). The major part of the work presented by Hart focuses on large window offsets of δ_W = 32pix and individual interrogation regions of size 64 x 64 pix^2 and shows that CBC leads to increased accuracy in the measurement of sub-pixel displacements when compared to standard single cross-correlation vector calculation (SCC). Hart also goes on to show how the implementation of CBC can reduce the amount of spurious vectors (caused by loss-of-pairs, out of plane motion, inter-particle correlations and electrical and optical image noise) almost entirely and in some cases completely when compared to SCC.

Developing the original findings of Hart the present work aims to expand on this by conducting a thorough evaluation of the performance, measured by evaluating the accuracy of calculated vectors and the amount of spurious data through the use of Monte Carlo simulations using synthetically generated particle image pairs with a deterministic imposed flow field. All image parameters

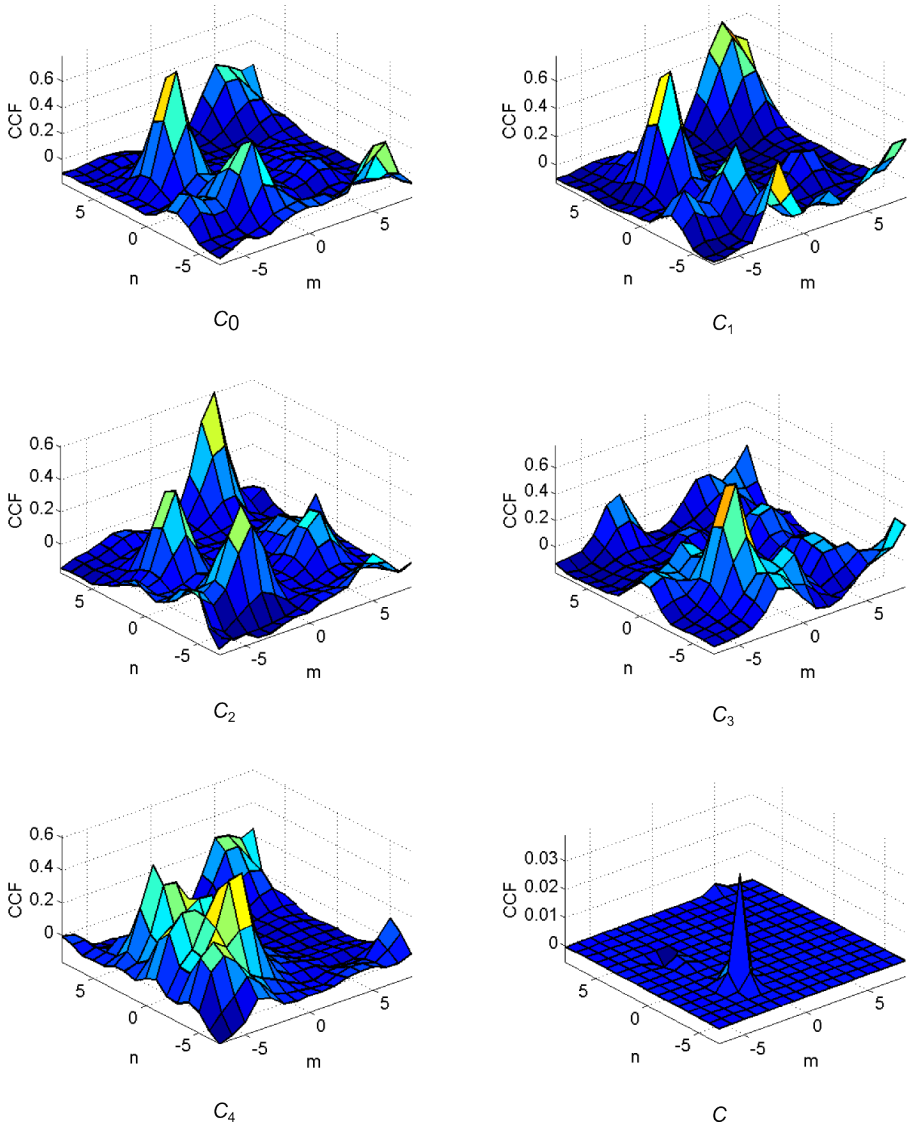

Fig. 5.2 Correlation function noise reduction (C) by applying CBC as the product of five individual correlation functions (C_i).

used in the construction of the synthetic images, such as particle image diameter and the degree of out of plane displacement are varied to model varying aspects of PIV experiment design. Then the effect of each parameter on the performance of the CBC algorithm can be independently investigated with the aim of identifying an optimum set of experimental parameters in order to minimise measurement error. This work also sets out to investigate CBC performance with smaller spatial offsets, δ_W values, which are important in flows with strong spatial gradients.

In order to evaluate the amount of spurious data returned through the implementation of various vector calculation algorithms an enhanced implementation of the Westerweel normalised median test (Westerweel and Scarano, 2005) algorithm is presented.

The CBC algorithm is then applied in conjunction with and against other well established vector calculation algorithms such as discrete iterative multigridding (MGRID) and particle image distortion (PID) to evaluate the performance on synthetic images containing a range of flow

conditions such as high and low spatial gradients and velocity magnitudes.

Finally a new hybrid PID/CBC algorithm (HPIDCBC) is presented which is shown to utilise the optimum performance of each of the two individual algorithms under differing flow conditions.

5.2 Synthetic Flow Field

In order to evaluate the accuracy of various vector calculation algorithms a deterministic flow field is required where the exact velocity is known at each point. For this study the time-independent Oseen vortex was chosen as it closely models naturally occurring fluid vortices and only has a tangential velocity component, u_θ with the radial velocity component, u_r equal to zero at all points, such that the flow field is defined by the following equations:

$$u_\theta = \frac{\Gamma}{2\pi r}\left[1-\exp\left(\frac{-r^2}{\gamma}\right)\right] \tag{5.2}$$

$$u_r = 0 \tag{5.3}$$

Where Γ is the strength of the vortex circulation and is directly related to the magnitude of the displacement of particle images between image pairs and r is the radial distance from the vortex centre. The variable γ relates to the vortex size and thus controls the magnitude of spatial velocity gradients within the flow. The constant variables Γ and γ were assigned values based on the parameters of the experiment, namely images pairs of size 512 x 512 pix^2 and 16 x 16 pix^2 vector calculation interrogation regions. Γ was assigned a value of 1200π pix^2 resulting in a maximum displacement of 5.41pix as can be seen in Figure 5.3. This is approximately equal to one third of the size of the interrogation regions used and was chosen to be greater than the maximum ideal displacement of one quarter the size of the interrogation region as discussed in the literature review in order to test the limits of the algorithm. A value of 5000 pix^2 was assigned to γ giving a wide range of spatial displacement gradients and displacement magnitudes over the 512 x 512 pix^2 image area. Referring to Figure 5.3 it can be seen that the flow contains a region, close to the origin, of high displacement gradient presenting a tough challenge for vector calculation algorithms whereas the outer regions of the images contain regions of small displacement and low gradient enabling the effectiveness of various algorithms to be evaluated under different flow conditions.

5.3 Generation of Synthetic Particle Image Images

Synthetic image pairs were generated following the method of Raffel et al. (1998) using randomly distributed 256-greyscale Gaussian particle images. Particle intensity q, is modelled by a two-dimensional Gaussian function; for a particle image of diameter d_p (which may be selected from

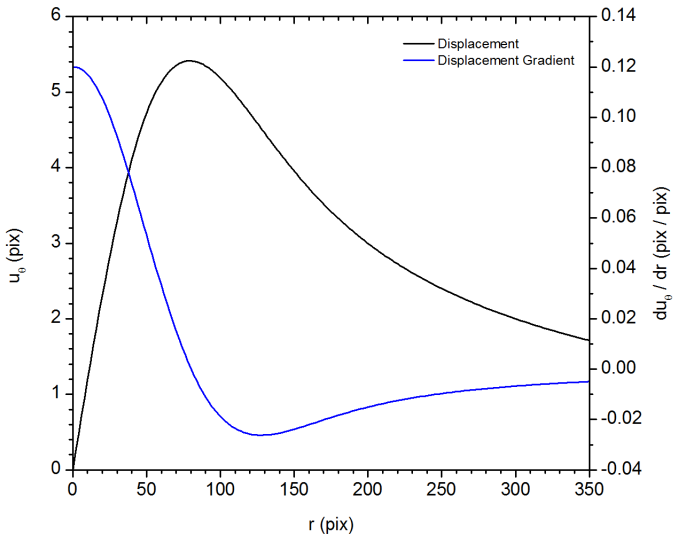

Fig. 5.3 Oseen vortex profiles of tangential displacement u_θ (black curve) and radial displacement gradient (blue curve).

a statistical distribution) and centre located at (x_0, y_0) the pixel intensity at (x, y) is given by:

$$q(x,y) = q_0 \exp\left[-\frac{(x-x_0)^2+(y-y_0)^2}{(d_p/2)^2}\right] \tag{5.4}$$

Where q_0 is the maximum particle brightness based on its location z, within the Gaussian profile laser sheet of thickness Z defined as:

$$q_0(z_0) = q_{max} \exp\left[-\frac{(z-z_0)^2}{(2\sigma_l)^2}\right] \tag{5.5}$$

Where q_{max} is the maximum greyscale intensity. To generate the image each pixel (i, j) is assigned a value by integrating (5.4) over the image area $A = IxJ$ for each individual particle.

$$q(i,j) = \iint_A q_0 \exp\left[-\frac{(x-x_0)^2+(y-y_0)^2}{(d_p/2)^2}\right] \mathrm{d}A \tag{5.6}$$

Where particle images overlap the pixel greyscale intensity value is calculated as the sum of the greyscale levels of the overlapping particle images at that pixel. The number of particle images, N_p distributed over the whole image area, A, can be calculated from the desired particle density μ_p (pix^{-2}) using the following equation:

$$\mu_p = \frac{N_p}{A} \tag{5.7}$$

Once the first image in an image pair is generated as above the second image is created by displacing individual particle images by a distance as calculated from its spatial location using the Oseen vortex displacement field as presented in (5.2). Using the above method to generate synthetic im-

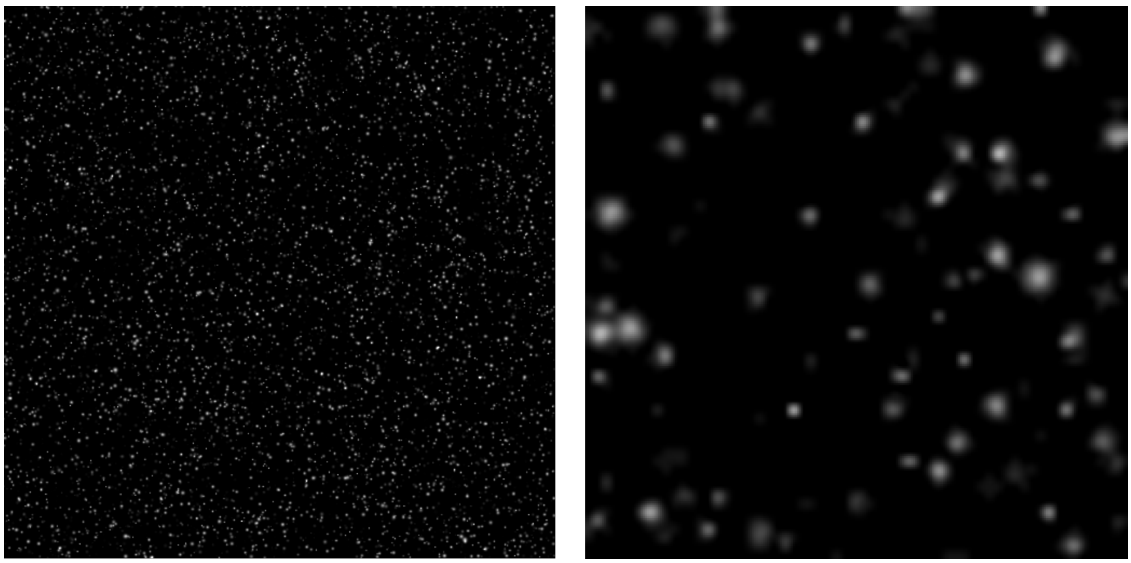

Fig. 5.4 (*left*) Full 512 x 512pix^2 synthetic particle image image constructed using the default parameters and (*right*) a zoomed in 64 x 64pix^2 region.

age pairs the following parameters are modified to create different sets of images to analyse the effects of varying image parameters on the accuracy of the vector calculation algorithms.

- Mean particle image diameter, d_p
- Particle image density, μ_d
- Magnitude of out of plane displacement, W
- Particle image brightness, q_{max}
- Image background noise level, q_{bg}
- Standard deviation of particle image diameters, σ_p

The default image set (for which a 64 x 64 pix^2 region of a particular image is shown in Figure 5.4) has the parameters listed below with each additional set only varying one of the above parameters.

- Image size, $A = IxJ$ = 512 $\times$ 512 pix^2
- Particle density, μ_d = 0.04 pix2 (10 particles / interrogation region for 16 x 16 pix2 interrogation regions)
- Particle diameter, d_p = 2.5 pix
- Standard deviation of particle diameters (Gaussian distribution), σ_p = 0.5 pix
- Light sheet thickness, $2\sigma_l$ = 20 pix
- Maximum particle image intensity value, q_{max} = 200

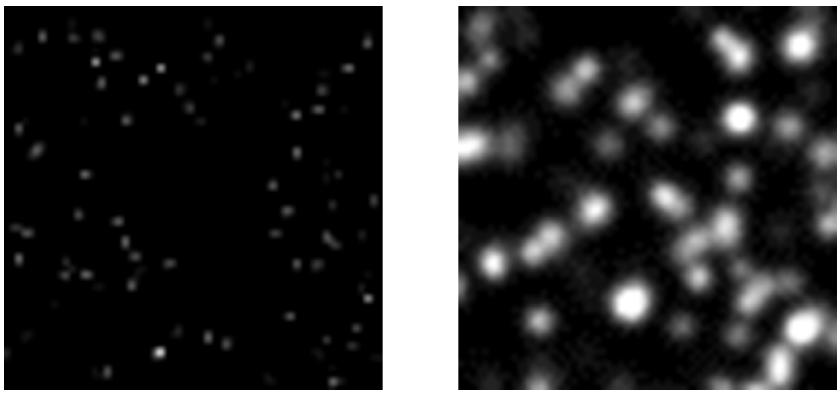

Fig. 5.5 64 x 64 pix^2 region of a synthetic image with mean particle image diameters of (*left*) d_p = 0.5 pix and (*right*) d_p = 7 pix.

- No background image noise
- No out of plane displacement

5.3.1 Details of Image Parameter Variation

Particle Image Diameter

Particle image diameter, d_p is an important parameter to control when designing a PIV experiment as it has an impact on the shape of the peaks in the cross-correlation function as discussed in the literature review. To simulate a range of particle image diameters the mean diameter was varied from 0.5 pix to 7.0 pix at 0.5 pix intervals (see Figure 5.5), the standard deviation of diameters remains constant at 0.5 pix as per the default images.

Particle Image Density

One of the more important considerations when designing a PIV experiment is the density of seed particles, if the seeding density is too low then in any given interrogation region too few particle images will be present to calculate an accurate displacement, too high and individual particle images become indistinguishable and deteriorate the quality of the displacement peak in the correlation function. In this analysis 16 x 16 pix^2 interrogation windows were used and the average number of particle images per interrogation region was varied between 2 and 20 at an interval of 2 giving a range of particle densities of 0.0078 to 0.078 particles/pix^2, see Figure 5.6.

Out of Plane Displacement

The out of plane displacement is modelled as a normalised parameter W, where $W = w/2\sigma_l$. Where $2\sigma_l$ is the light sheet thickness and w is the out of plane displacement in pixels. In the tests carried out the maximum magnitude of W was varied between 0 and 0.5 at intervals of 0.1 which for a sheet thickness of 20 pix gives a maximum out of plane displacement of 10 pix. It was chosen not to go higher than this as when using a 16 x 16 pix^2 interrogation window the

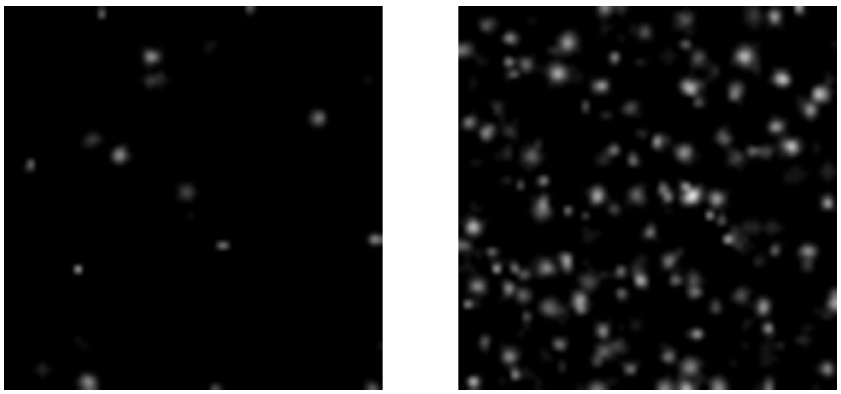

Fig. 5.6 64 x 64 pix^2 region of a synthetic image with particle image densities of (*left*) $\mu_p = 0.0078$ pix^2 and (*right*) $\mu_p = 0.078$ pix^2.

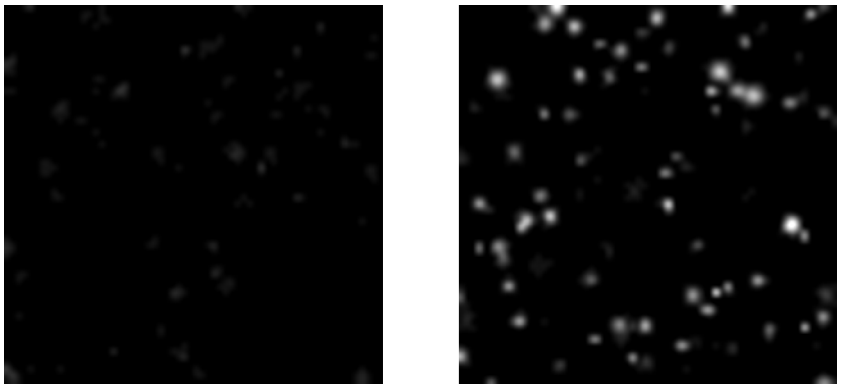

Fig. 5.7 64 x 64 pix^2 region of a synthetic image with maximum particle image brightness of (*left*) $q_max = 50$ greyscales and (*right*) $q_{max} = 250$ greyscales.

maximum resolvable displacements are approximately 1/3 x 16 = 5.33 pix With a value of W = 0.5 any particle which starts in the centre of the light sheet will have disappeared by the second image.

Particle Image Brightness

To model the effect that particle brightness has on the accuracy of the vector calculation algorithms the maximum particle image greyscale intensity value (when located in the middle of the light sheet) was varied between 50 and 250 at intervals of 50 greyscales to simulate a full range of particle image intensities, see Figure 5.7.

Image Background Noise Level

In experimental PIV images the background greyscale level is not zero due to non-optimal light conditions, electrical noise in the camera CCD chip and other factors relating to the design of the experiment as discussed in the literature review. In order to model background noise a set of images was created with nonzero background image intensity. Four image sets were created with mean background greyscale levels of 0, 20, 40 and 60 and 10% Gaussian noise. As can be seen in Figure 5.8 X when the mean background greyscale is set to 60 the individual particle

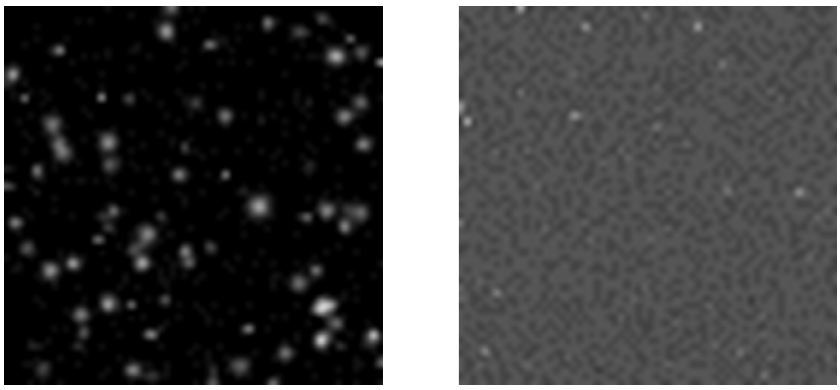

Fig. 5.8 64 x 64 pix^2 region of a synthetic image with average background noise brightness of (*left*) q_{bg} = 0 greyscales and (*right*) q_{bg} = 60 greyscales.

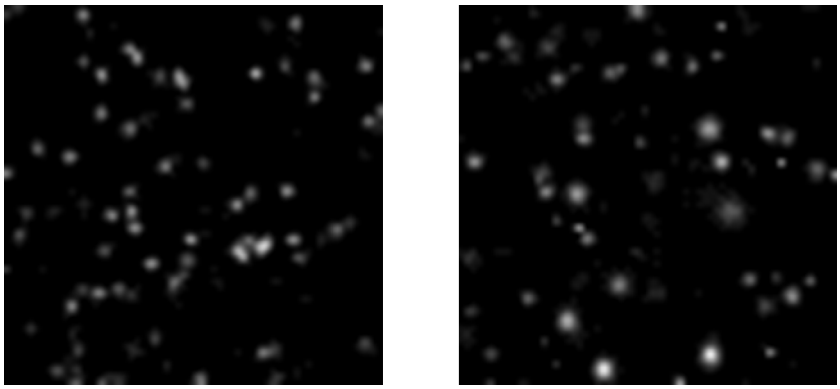

Fig. 5.9 64 x 64 pix^2 region of a synthetic image with standard deviation of particle image diameters of (*left*) σ_p = 0 pix and (*right*) σ_p = 2.5 pix.

images become much less distinguished making it more difficult for a clear displacement peak to be identified from a cross-correlation function.

Standard Deviation of Particle Image Diameters

To simulate variation in particle image diameters as a result of non-uniformity of tracer particle diameters the standard deviation of the synthetic particle image diameters was varied. Using a mean diameter of 2.5 pixels the standard deviation of the normal distribution of particle image diameters was varied in the range 0 to 2.5 pix at 0.25 pix intervals, see Figure 5.9.

5.4 Algorithms

Along with the previously introduced CBC algorithm several other algorithms discussed in the literature review are evaluated as a comparison with and in conjunction with the CBC algorithm. The standard cross-correlation (SCC), multigrid (MGRID) and particle image distortion (PID) algorithms are briefly recapped below.

5.4.1 Standard Spatial Cross-Correlation

The control vector calculation algorithm used to measure the performance of all other algorithms against is the normalised spatial (as opposed to Fourier space) standard cross-correlation (SCC) algorithm as outlined in the literature review (§ 1.5.1). The cross-correlation function, C is calculated as follows:

$$C(m,n) = \frac{\sum_i \sum_j [q_1(i,j) - \bar{q}_1][q_2(i-m, j-n) - \bar{q}_2]}{\sqrt{\sum_i \sum_j [q_1(i,j) - \bar{q}_1][q_2(i,j) - \bar{q}_2]}} \tag{5.8}$$

Where $q(i,j)$ is the greyscale intensity at pixel coordinates (i,j) and m and n are coordinates in the cross-correlation function. The mean intensities $\bar{q}_1$ and $\bar{q}_2$ are determined over the over-lapping region of the two images. In the following analysis 16 x 16 pix^2 interrogation windows are used (unless specifically stated) resulting in cross-correlation functions of the same dimension. As spatial resolution of the final vector grid is not important in this analysis and to reduce computational time there is no overlap between adjacent interrogation regions.

5.4.2 Discrete Iterative Multigrid

Later analysis makes use of discrete iterative multigridding (MGRID) as outlined in § 1.5.6. The multigrid technique is applied using either SCC or CBC to calculate CCFs, in each case two iterations are used, the first iteration, the predictor phase, employs 32 x 32 pix^2 interrogation windows with 50% window overlap. Following this spurious vectors are removed and replaced with interpolated vectors using the modified universal outlier detection algorithm as described in § 1.7.3. The second (final) iteration employs 16 x 16 pix^2 interrogation regions (no overlap between adjacent regions) with the second interrogation region offset by the nearest integer value to the displacement calculated in the first iteration.

When the multigrid algorithm is used in conjunction with CBC the first and second iterations both employ CBC in the calculation of correlation function. Results are denoted in the form 'MGRID δ_W = #' where '#' is the spatial pixel offset between CBC correlation functions as presented in Figure 5.1, when $\delta_W = 0$ this indicates that the SCC algorithm is used and 'MGRID δ_W = 8' denotes that CBC with a correlation function offset of 8 pix is used in each iteration.

5.4.3 Particle Image Distortion

The particle image distortion algorithm (PID) is a continuous extension of the discrete multigrid method detailed above where the second interrogation region for the second iteration is distorted on a pixel by pixel basis taking into account local spatial displacement gradients calculated from vectors calculated in the first iteration as opposed to a single integer valued displacement over the whole interrogation region as with the discrete multigrid algorithm.

Unlike the discrete multigrid method this is a continuous transformation (sub-pixel offsets) meaning an interpolation algorithm has to be applied to calculate the discrete pixel intensity in

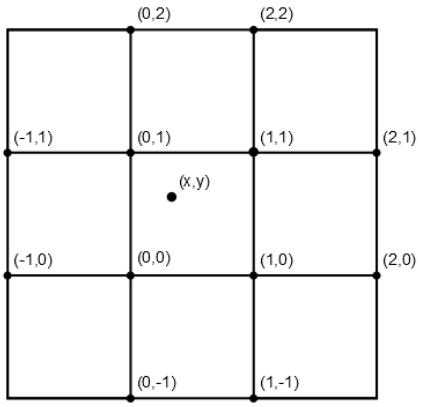

Fig. 5.10 Interpolation grid for 12 point simplex interpolation algorithm.

the second interrogation region. A 12 point simplex interpolation algorithm was selected as it was shown (Astarita and Cardone, 2005) that this offers a good trade-off between the accuracy of the reconstructed image and computational complexity.

The intensity value q, located at the sub-pixel coordinate (x,y) is calculated as a weighted average of the intensity values of the 12 nearest points (as arranged in Figure 5.10) as follows:

$$q(x,y) = q_{(0,0)} + \frac{x^2}{8}a_1 + \frac{y^2}{8}a_2 + xya_3 + \frac{x}{8}a_4 + \frac{y}{8}a_5 \tag{5.9}$$

with the coefficients a_i defined as follows:

$$a_1 = q_{(0,-1)} - q_{(0,0)} - q_{(0,1)} + q_{(0,2)} + q_{(1,-1)} - q_{(1,0)} - q_{(1,1)} + q_{(1,2)} \tag{5.10}$$

$$a_2 = q_{(-1,0)} + q_{(-1,1)} - q_{(0,0)} - q_{(0,1)} - q_{(1,0)} - q_{(1,1)} + q_{(2,0)} + q_{(2,1)} \tag{5.11}$$

$$a_3 = q_{(0,0)} - q_{(0,1)} - q_{(1,0)} + q_{(1,1)} \tag{5.12}$$

$$a_4 = -q_{(0,-1)} - 7q_{(0,0)} + 9q_{(0,1)} - q_{(0,2)} - q_{(1,-1)} + q_{(1,0)} + q_{(1,1)} - q_{(1,2)} \tag{5.13}$$

$$a_5 = -q_{(-1,0)} - q_{(-1,1)} - 7q_{(0,0)} + q_{(0,1)} + 9q_{(1,0)} + q_{(1,1)} - q_{(2,0)} - q_{(2,1)} \tag{5.14}$$

5.4.4 Spurious Vector Detection Algorithm

Original Normalised Median Test Algorithm

The algorithm used to detect spurious vectors is an enhanced version of the 'normalised median test', NMT (Westerweel and Scarano, 2005) as presented in the literature review § 1.7.3. An example of a grid of raw vectors containing erroneous vectors and grid points where no vectors are calculated is presented in Figure 5.11. Erroneous vectors are located at the grid locations $(2,2)$, $(0,1)$, $(-1,-1)$ and $(0,-2)$ and the grid points $(1,2)$, $(1,1)$, $(-2,0)$ and $(0,-1)$ represent grid

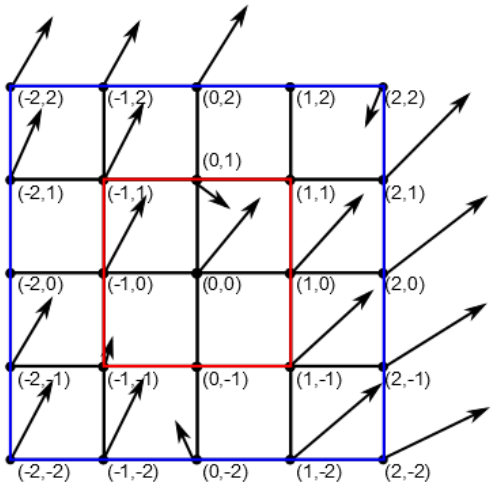

Fig. 5.11 Grid of vectors used when implementing the normalised median test utilising the nearest eight neighbouring vectors (red square) and the nearest 24 vectors (blue square).

locations where the PIV vector calculation algorithm was unable to calculate a vector.

The NMT algorithm as presented by Westerweel and Scarano identifies a vector as spurious if the normalised residual, r'_0 is above a certain threshold and is calculated as follows (this example uses a window of size 3 x 3 vectors for simplicity, depicted by the red square in Figure 5.11):

1. For the vector under inspection at grid location $(0,0)$ the local median, $\mathbf{u}_m$ of the eight surrounding vectors $\mathbf{u}_i$, $i = 1...8$ is calculated.

2. For each surrounding vector $\mathbf{u}_i$ the residual value r_i is calculated as the modular difference between that vector and the median vector $\mathbf{u}_m$ calculated in step 1:

$$r_i = |\mathbf{u}_i - \mathbf{u}_m| \tag{5.15}$$

3. Calculate the normalising value, r_m by finding the median of the r_i values.

4. Calculate the normalised residual of the vector $\mathbf{u}_0$:

$$r'_0 = \frac{|\mathbf{u}_0 - \mathbf{u}_m|}{r_m} \tag{5.16}$$

5. If the value r'_0 is greater than a predefined threshold, ε_{thresh} mark the vector $\mathbf{u}_0$ as spurious.

For two component velocity vectors the value r'_0 is calculated individually for both vector components and the final residual value is calculated as the magnitude of the two using Pythagoras' theorem. In some circumstances the above algorithm may be applied over a larger window, for example a 5 x 5 vector window as depicted by the blue box in Figure 5.11 in which case the surrounding 24 vectors are used in calculating the residual r'_0 rather than the nearest 8 as with a 3 x 3 vector window.

Enhanced Normalised Median Test Algorithm

Whilst the NMT algorithm is robust in detecting spurious vectors and is used in commercial packages such as LaVision DaVis (as used in later chapters) for this work the algorithm was extended (referred to as ENMT) to further increases its robustness.

The first refinement to the algorithm is to crudely pre-filter the surrounding vectors $\mathbf{u}_i$ of obviously spurious data. The algorithm as originally presented does not discriminate against outlying data points contained within the surrounding vectors when calculating the local median value Um and hence the residual, r'_0, thereby decreasing the sensitivity to detect spurious data at the vector under inspection $\mathbf{u}_0$. The new adapted algorithm calculates the local median of the surrounding non-zero vectors as in step 1 of the original algorithm, but the standard deviation, σ_m of the surrounding vectors is also calculated. Following calculation of the local median all vectors that were used to calculate it are tested to see if they lie within a certain threshold of the calculated median value. In the work carried out the threshold used is $\pm 2\sigma_m$, any surrounding vectors that lie outside of this range centred on the median are rejected for use in the remainder of the algorithm. In the example vector grid presented in Figure 5.11 this would result in the vectors located at (0,1) and (-1,-1) being rejected. The residual r'_0 is then calculated using the remaining surrounding vectors.

The second refinement is to specify how many vectors as a minimum are required to carry out the test, using the example shown in Figure 5.11 for a 3 x 3 vector window only 4 surrounding vectors are available due to the fact that no vectors were calculated at the grid points $(0,-1)$ and $(1,1)$ and the crude filtering of the surrounding vectors described in the previous paragraph rejects two more vectors. If it is decided that more than 4 surrounding vectors are required to carry out the test the new algorithm automatically increases the radius of the window by a value of 1 to use a 5 x 5 vector window and so on until the threshold of minimum number of vectors available for use for each filter size (5x5, 7x7, etc...) in calculating the residual is met.

By removing obviously spurious data from the surrounding vectors the normalising value r_m in (5.16) is reduced as larger values of r_i which are associated with vectors far away from the local median are discounted. The lower value of r_m then increases the sensitivity of the r'_0 value enabling a more reliable spurious / non-spurious threshold value to be selected which reduces the possibility of valid vectors being detected as spurious and also reduces the possibility of spurious data being overlooked as positive.

5.5 Analysis Methods

For each set of N = 100 image pairs displacement vectors were calculated using SCC and CBC with spatial shifts, δ_W, of 2pix, 4pix and 8pix giving four sets of displacement vectors for each image pair. After vector calculation two tests were carried out; the percentage of spurious data and the accuracy of the calculated displacement vectors.

In order to measure the amount of spurious data returned, the ENMT spurious vector detection

algorithm was applied to identify erroneous data as previously described. A threshold value of 2 was selected and residual values, with a residual threshold, r'_0 greater than this were identified as spurious. The total number of spurious data points in the n^{th} $(n = 1...100)$ vector field, S_n is then calculated as the sum of the number of spurious displacement vectors identified using the ENMT algorithm, S_{n_A}, and grid points where no vector was calculated, S_{n_0}:

$$S_n = S_{n_A} + S_{n_0} \tag{5.17}$$

The average number of spurious data points, s as a percentage of the total number of vector grid points in each vector field, N_M across each of the $N = 100$ vector fields is then calculated as:

$$s = \frac{100}{N} \sum_{n=1}^{N} \frac{S_n}{N_M} \tag{5.18}$$

After spurious vectors were identified they were removed and replaced with interpolated vectors equal to the median of the nearest surrounding 24 vectors.

Once all spurious data points were removed and replaced by interpolated vectors the magnitude of the errors between the two components of the calculated displacement vectors, u, and the analytic displacement, u_a, as calculated by (5.2) is calculated. The displacement vector at grid location (i, j) for the n^{th} image pair, $u_n(i, j)$ has orthogonal components in the x and y directions u_x and u_y respectively. The displacement error magnitude $\varepsilon_n(i, j)$ is then calculated as the resultant of the magnitudes of the individual component errors as follows:

$$\varepsilon_{n_x}(i, j) = |u_{n_x}(i, j) - u_{a_x}(i, j)| \tag{5.19}$$

$$\varepsilon_{n_y}(i, j) = \left|u_{n_y}(i, j) - u_{a_y}(i, j)\right| \tag{5.20}$$

$$\varepsilon_n(i, j) = \sqrt{\varepsilon_{n_x}^2(i, j) + \varepsilon_{n_y}^2(i, j)} \tag{5.21}$$

After displacement errors were calculated at each grid point for each of the $N = 100$ vector fields the ensemble average error at each grid location, $\overline{\varepsilon(i, j)}$ is calculated as:

$$\overline{\varepsilon_n(i, j)} = \frac{1}{N} \sum_{n=1}^{N} \varepsilon_n(i, j) \tag{5.22}$$

And finally the spatially averaged error $\langle \bar{\varepsilon} \rangle$ is calculated over each grid point where I and J are the total number of grid points in the x and y directions:

$$\langle \bar{\varepsilon} \rangle = \frac{1}{IJ} \sum_{i=1}^{I} \sum_{j=1}^{J} \overline{\varepsilon_n(i, j)} \tag{5.23}$$

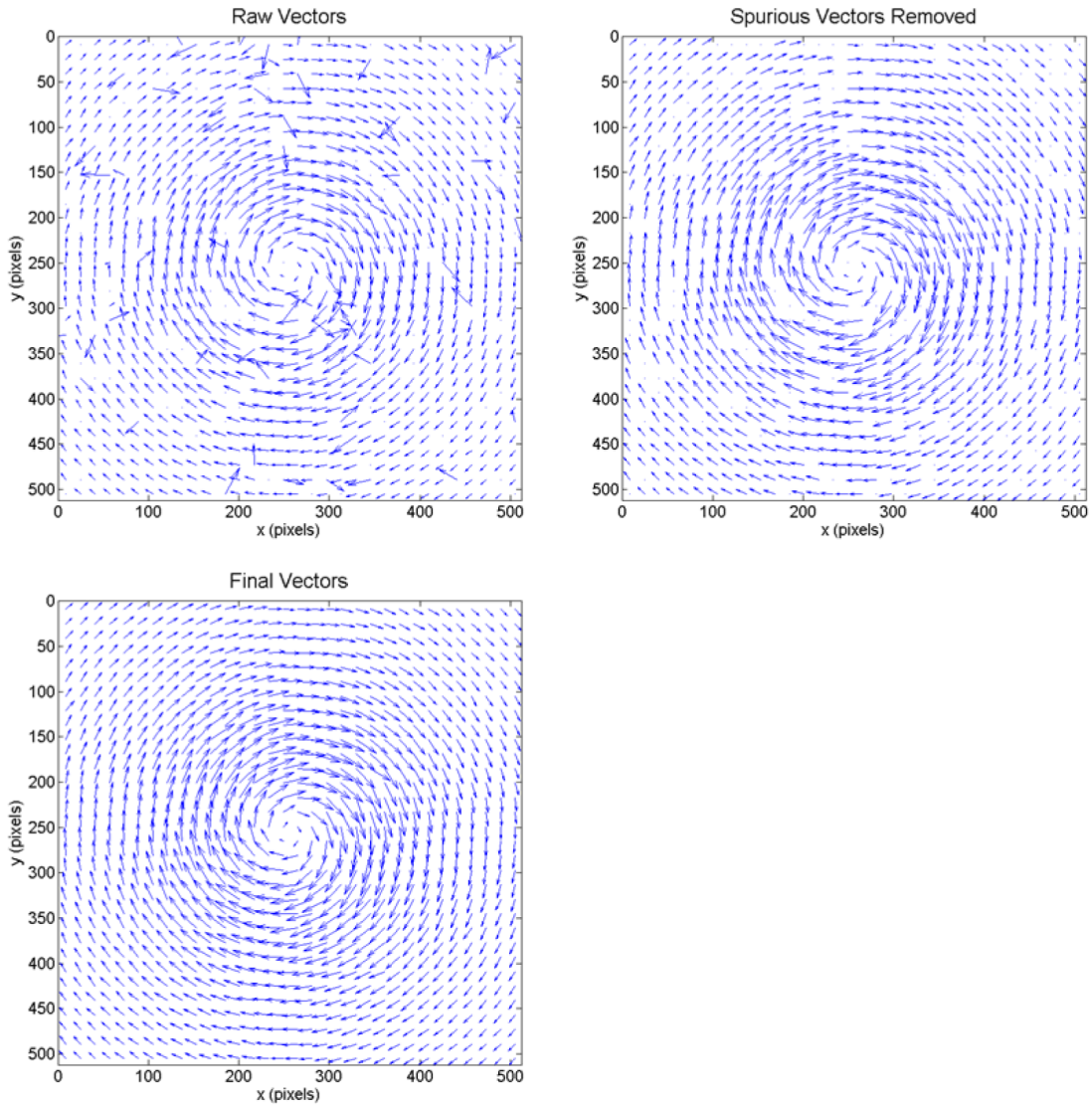

Fig. 5.12 (*Top left*) Initial vector field calculated using standard cross correlation (SCC), (*top right*) detection and removal of spurious vectors and (*bottom*) final vector field with missing vectors interpolated.

5.6 Results and Discussion

5.6.1 Spurious Vector Detection, Removal and Replacement

Figure 5.12 shows the results of implementing the spurious vector detection algorithm for the vectors calculated using SCC; it shows that all spurious vectors are identified and removed with no valid data identified as spurious and when interpolation is applied to gird points with removed vectors the result is a complete grid.

Figure 5.13 shows four displacement vector fields for the same image pair generated with a normalised out of plane displacement $W = 0.2$ equating to an out of plane displacement of 4 pixels based on the simulated laser sheet thickness of 20 pixels. The four displacement vector fields were generated using the SCC algorithm and CBC with window offsets of δ_W = 2, 4 and 8 pixels. For the vector grids presented the total number of spurious data points, s (erroneous vectors and grid

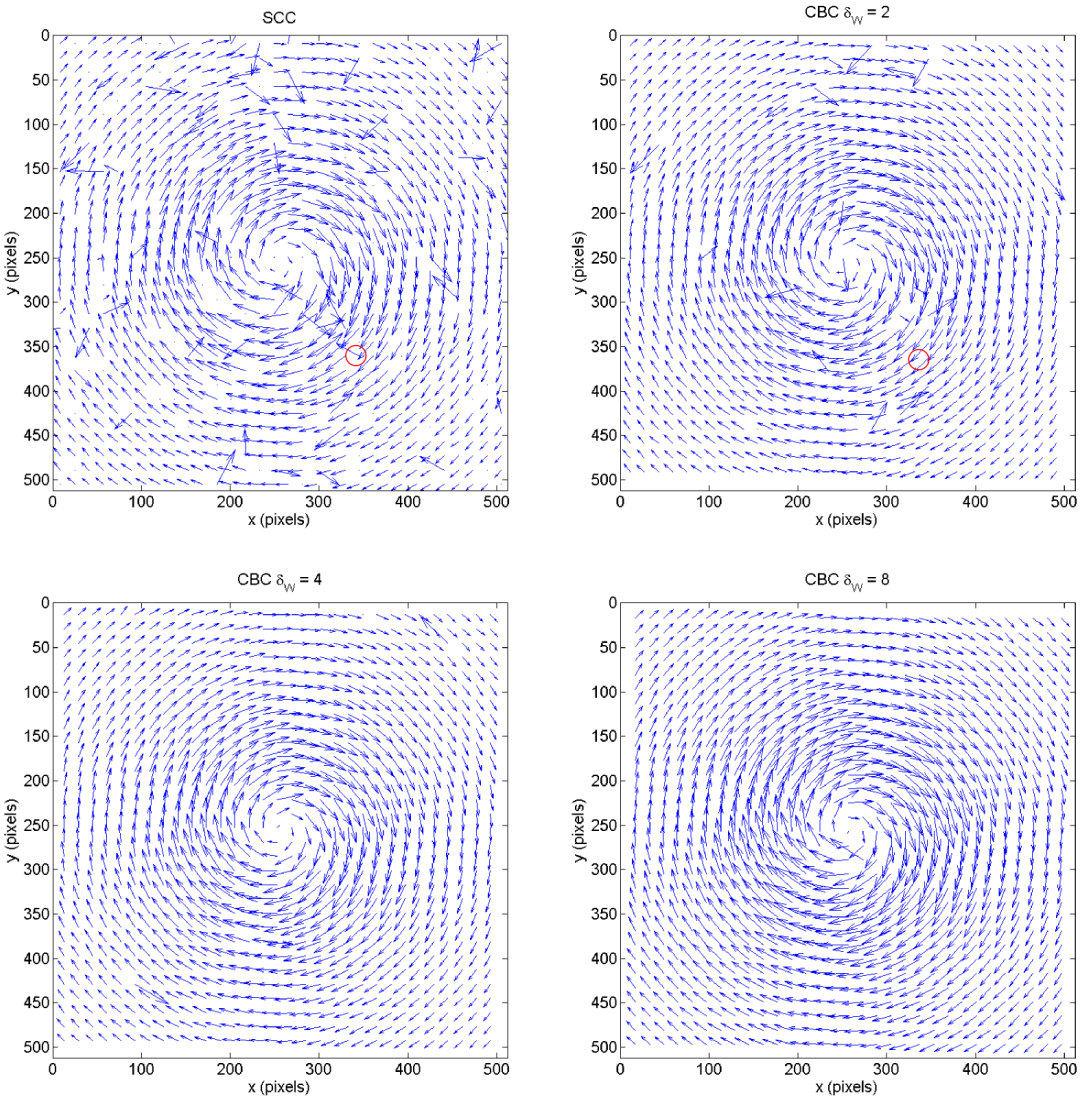

Fig. 5.13 Vector fields for a flow field with a normalized out of plane motion of 0.2 and no vector validation for (*top left*) SCC and for CBC with window offsets of (*top right*) δ_W = 2pix, (*bottom left*) δ_W = 4pix and (*bottom right*) δ_W = 8pix.
. The red circles indicate the vectors calculated from the correlation functions in Figure 5.14.

points where no vector is calculated) is greatly reduced when CBC is applied, even for a window offset of 2 pixels. When SCC is applied to this pair of images $S_n = 155$ spurious data points are returned, when applying CBC with an offset of 2 pixels this reduces to $S_n = 33$, a reduction of 78.7%. Increasing the window offset to 4 and 8 pixels further reduces the number of erroneous data points to $S_n = 14$ and $S_n = 6$ respectively, reductions of 91.0% and 96.1% respectively.

Correlation functions for the vectors calculated at grid point $(345, 361)$ in Figure 5.13 using SCC and CBC with a window offset of 2 pixels are presented in Figure 5.14. The single correlation function generated when using SCC (Figure 5.14 top left) is equal to the central correlation function, C_0 when using CBC. It can be seen that the vector at this location is clearly spurious by having a positive displacement in the y direction whereas valid vectors at this location have a negative y-displacement. The correlation function C_0 shows a large well defined peak located at $(-4, 4)$ in the correlation function plane and a second peak of lower magnitude located at $(-3, -4)$. The

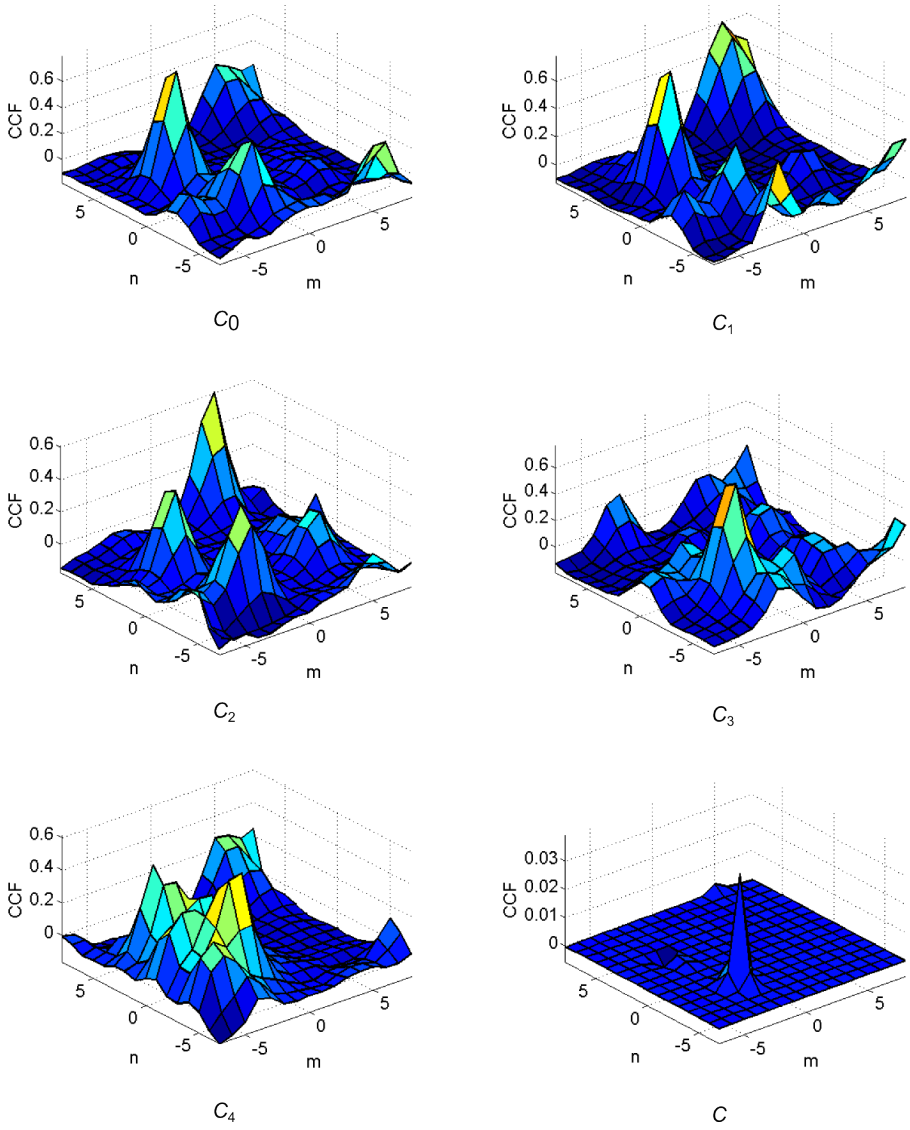

Fig. 5.14 Individual cross-correlation functions C_{0-4} and their CBC product, C, for the vector at grid point $(345, 361)$.

imposed displacement for the vector at this grid location is (-3.25pix, -2.75pix), from this it is clear that it is the second lesser peak that identifies the correct displacement of the particle images and not the larger peak that is used instead. Looking at the correlation functions C_1 to C_4 in Figure 5.14 generated by applying CBC (δ_W = 2pix) with individual correlation functions calculated from interrogation regions arranged as in Figure 5.1 it can be seen that each contain a peak in the region of the correct displacement which in the case for C_1 and C_2 (as with C_0) is not the largest peak, however the product of the five correlation functions, C shows a very clearly defined peak located at $(-3, -3)$ with the correlation function approximately equal to zero at all other locations. This demonstrates very clearly how CBC, even with a very small window offset of 2pix is very effective at removing noise signals from individual correlation functions leaving only a peak associated with the mean displacement of the particle image pairs within that interrogation window.

5.6.2 Spurious Vectors And Displacement Error

As has already been shown for an individual vector field the CBC algorithm greatly reduces the total number of spurious data points compared to SCC, Figure 5.15 shows that for all image parameter variations when CBC is utilised the percentage of spurious vectors is reduced by between a factor of approximately 10 to 100 and in the case of high particle density images by a factor of 1000.

Particle Image Diameter

Figure 5.15a and Figure 5.16a show that for SCC the optimum particle image diameter, d_p is located at different values for reducing the number of spurious vectors and minimising the displacement error. A particle image diameter of 1.5pix returns the highest proportion of valid vectors with only 6.3% spurious, for diameters above this the percentage of spurious vectors increases to 84.5% for a particle image diameter of 7pix using 16 x 16 pix^2 interrogation regions. Applying CBC δ_W = 2, 4 and 8pix the percentage of spurious vectors is for all particle diameters less than 3% compared to a minimum of 6.3% for standard cross-correlation. The optimum particle image diameter for reducing spurious data when using CBC increases with the degree of window displacement, δ_W. With δ_W = 2pix the optimum particle image diameter is 4pix resulting in 0.5% spurious data, for window offsets of 4 and 8 pixels the optimum diameter increases to 4.5 and 5 pixels respectively with 0.019% and 0.016% spurious data respectively.

To minimise the spatially averaged error, $\langle\bar{\varepsilon}\rangle$ the optimum particle image diameter when using SCC is 2.5-3pix where the error is approximately 0.12pix, this diameter is consistent with the findings of previous studies (Raffel et al., 1998). For particle images with diameter greater than three pixels the average error begins to rapidly increase up to a magnitude of 0.65pix for a particle image diameter of 7pix. When using CBC, unlike for reducing the number of spurious vectors, the optimum particle image diameter for reducing displacement error occurs at a diameter of 4 pixels for all window offsets (which is consistent with the findings presented by Hart (Hart, 2000)) with spatially averaged errors of 0.096pix, 0.088pix and 0.08pix for window offsets of 2, 4 and 8pix respectively. Under optimum conditions for particle image diameter the CBC method when applied with a window offset of 8pix reduces the displacement error by 33.3% when compared to SCC under optimum conditions.

Figure 5.17 shows the correlation function generated using SCC with a 16x16pix^2 interrogation region with a mean particle image diameter corresponding to the CBC optimum of 4pix which is considerably larger than the SCC optimum of 2.5pix. For this interrogation region the imposed displacement is 0pix in y-direction and 1pix in the x-direction. It can clearly be seen that the displacement peak is very wide (approximately 10px) owing to the large size of the particle images which leads to reduced accuracy when calculating the sub-pixel displacement using a three-point Gaussian fit. The measured displacement for this interrogation region was 0.961pix in the x-direction and 0.080pix in the y-direction giving a total error of ε = 0.089pix. Figure 5.18

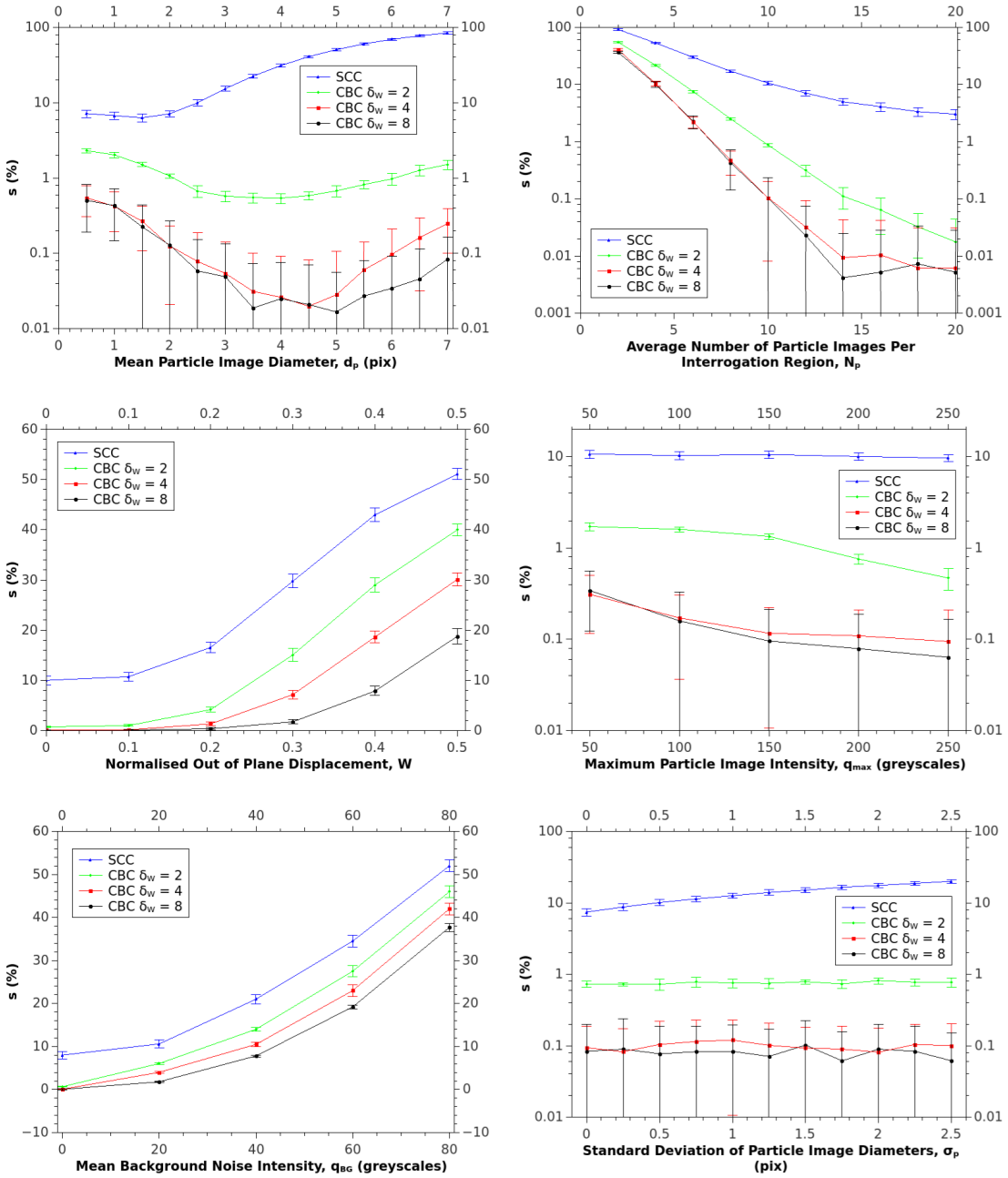

Fig. 5.15 Percentage spurious data, s for variation of synthetic image parameters. Error bars indicate $\pm$ one standard deviation of the percentage of spurious vectors.

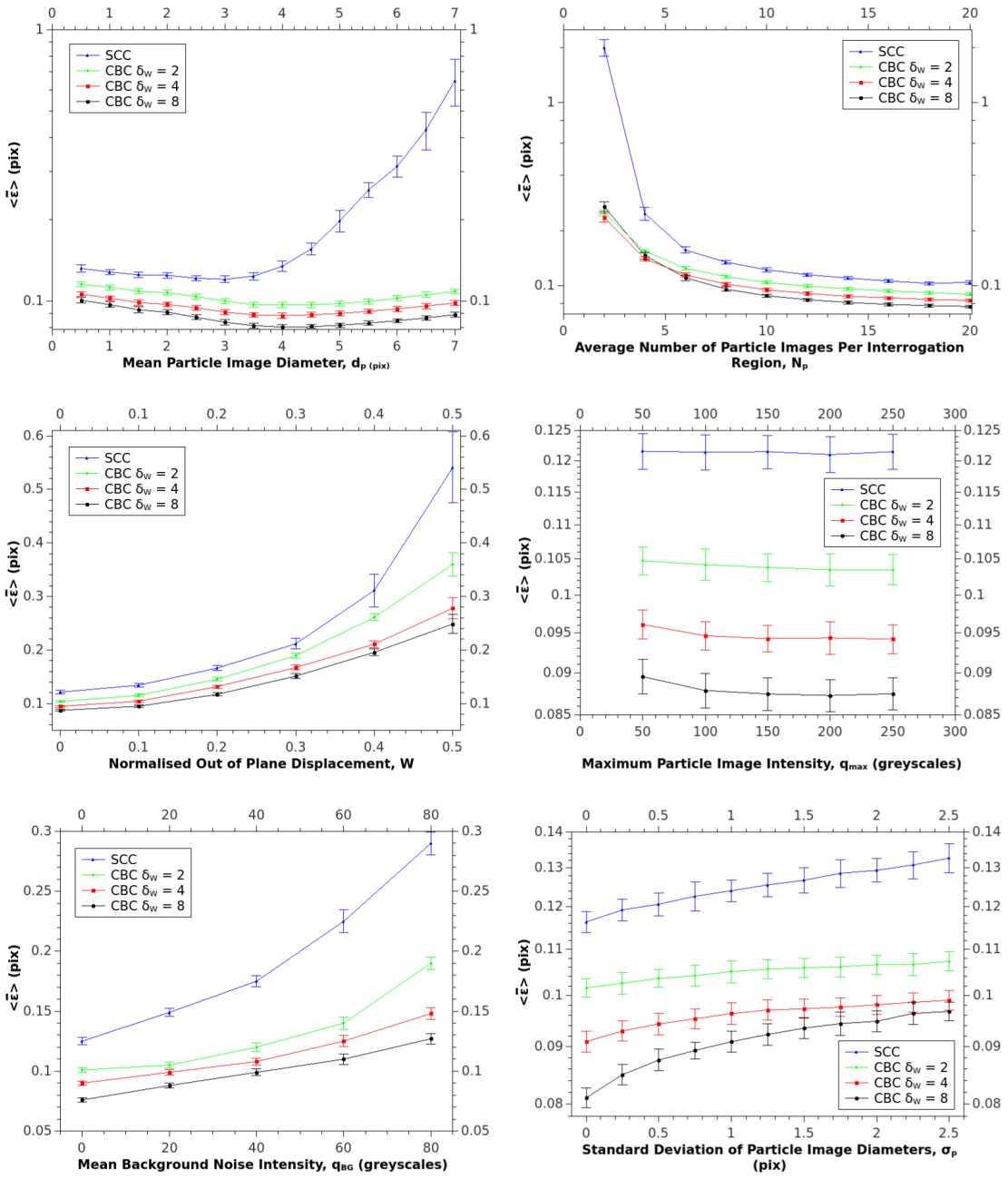

Fig. 5.16 Spatial average displacement vector error, $\langle\bar{\varepsilon}\rangle$ for variation of image parameters. Error bars indicate $\pm$ one standard deviation of displacement errors.

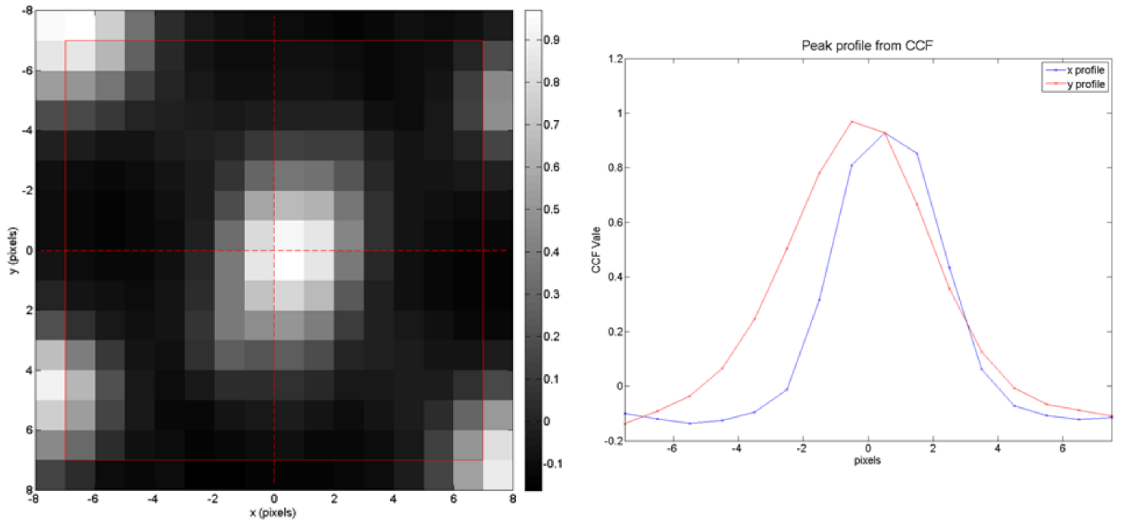

Fig. 5.17 Correlation function of a 16 x 16pix^2 interrogation region for particle diameter of 4pix using standard cross-correlation. The peak profiles are taken along the dashed lines shown on the full correlation function.

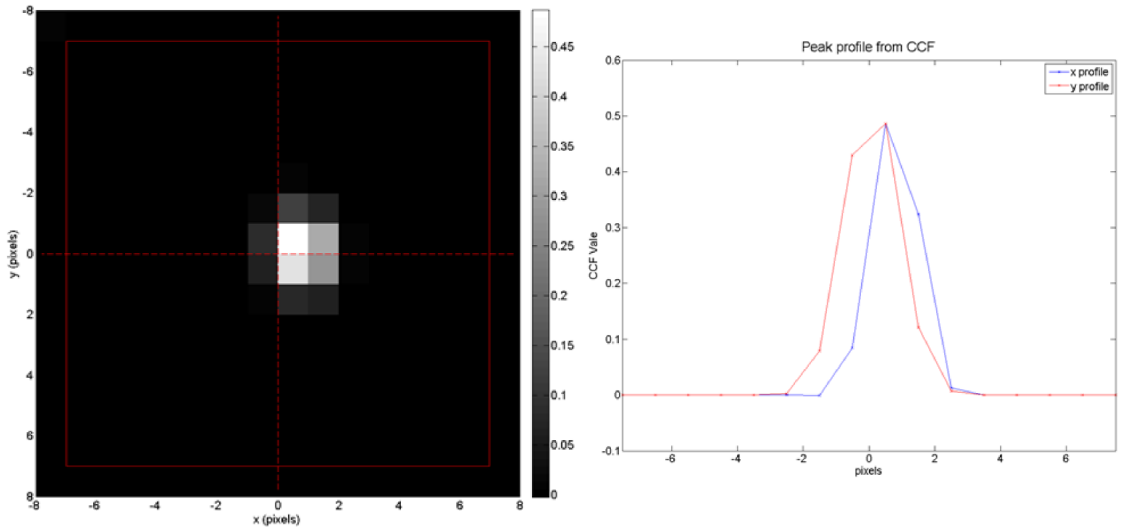

Fig. 5.18 Correlation function of a 16x16pix^2 interrogation region for particle diameter of 4pix using CBC with a shift of 8pix. The peak profiles are taken along the dashed lines shown on the full correlation function.

shows the correlation function calculated using CBC with δ_W = 8pix for the same image pair used in Figure 5.17 and it is instantly noticeable that the correlation peak is much more well defined (approximately 4px wide) than is the case when using SCC. The sharpening of the peak can be explained by the fact that the points surrounding the peak maximum when multiplied by their corresponding values in adjacent individual correlation functions are reduced by a greater amount than the central peak value. The displacement vector calculated from this correlation function is 0.983pix in the x-direction and 0.013pix in the y-direction resulting in a total error, ε = 0.021pix, an improvement of 76% on the error when using SCC.

Particle Image Density

As can be seen in Figure 5.15b and Figure 5.16b increasing the particle density (number of particle images per interrogation window, N_p) reduces both the amount of spurious data and the error in measured displacement. With N_p = 2 particle images per 16x16pix^2 interrogation region the amount of spurious data is very high with 91.9% of all data points containing either spurious or no vectors when SCC is applied, at this low density CBC offers significant improvements in reducing the amount of spurious data with spurious percentages of 55.1%, 40.9% and 36.7% for δ_W = 2, 4 and 8pix respectively. Even in the best case scenario of δ_W = 8pix this is over one third of all the data and as such is not suitable. For SCC and CBC with all three degrees of window offset the amount of spurious data decreases with increasing particle image density. It is not until there are on average 10 particle images per interrogation region that the amount of spurious data drops to 10% when using SCC whereas to reach the same level of valid vectors using CBC approximately 5, 4 and 4 particle images per interrogation are required for δ_W = 2, 4 and 8pix, respectively, showing that CBC greatly outperforms the SCC algorithm for reducing the amount of spurious data calculated at low particle image densities. The rate at which the amount of spurious data reduces with increasing image density is much greater when using CBC. At a density of 20 particle images per interrogation region the amount of spurious data when using SCC is at 3.0% reducing to 0.02% when CBC is applied with a window offset of 2pix. For window offsets of 4 and 8pix the amount of spurious data decreases as particle image density increases to 14 particle images per interrogation region to a value of approximately 0.003% where increasing particle image density beyond this appears to have no further effect on the amount of spurious data. The improvement in the amount of spurious data when using CBC can partly be attributed to the greater total number of particle images available to calculate the average displacement due to the increased sample area of the images used as well as the suppressing of noise signals as previously discussed.

As with the amount of spurious data the spatially averaged displacement error, $\langle\bar{\varepsilon}\rangle$ decreases with increasing particle image density for SCC and CBC with each of the window offsets. At a density of 2 particle images per interrogation region the average displacement error was not calculated as 91.9% of the data returned was spurious and thus of no use for calculating displacement vectors. Using a density of 4 particle images per interrogation region the average error is 0.25pix with SCC which is approximately the same as when CBC is used with all degrees of window offset. The minimum error for each case occurs at the highest tested density of 20 particle images per interrogation region with errors of 0.1pix for SCC and 0.09pix, 0.08pix and 0.07pix when CBC is used for δ_W = 2, 4 and 8pix respectively.

Out of Plane Displacement

When particle images undergo zero displacement in the out of plane direction the amount of spurious data and average displacement error are consistent with the results of the default image set and both increase with increasing out of plane displacement due to the loss of pairs between im-

age frames as shown in Figure 5.15c and Figure 5.16c. Both the increase in spurious data and displacement error are reduced when CBC is applied with greater reductions when a higher degree of window offset is applied. When the normalized out of plane displacement $W = 0.5$ (10pix based on the laser sheet thickness of 20pix) any particle image in the centre of the light sheet in the first frame will have disappeared by the second. At this level when using SCC the amount of spurious data 51.0% compared to 18.8% when CBC is applied with a window offset of 8pix which, while a reduction in erroneous data of over a half, is still a significant proportion. When using SCC for all levels of out of plane displacement above zero the amount of spurious data is greater than 10% whereas the amount of spurious data does not exceed 10% until $W \approx 0.25$ when CBC is applied with δ_W = 2pix further increasing to $W \approx 0.32$ and 0.42 for δ_W = 4pix and 8pix respectively showing a greater robustness in calculating valid vectors for higher degrees of out of plane displacement. As the out of plane displacement increases the average displacement error $\langle \bar{\varepsilon} \rangle$ likewise increases. However the amount the error increases is much reduced when CBC is utilised, the error for SCC when $W = 0.5$ is 0.54pix, this error is more than halved to 0.25pix when CBC with δ_W = 8pix is applied thus CBC can give quarter pixel accuracy despite approximately half of the particle images moving out of the light sheet between frames.

As very few flows with strictly two-dimensional flow exist in the real world the improvements provided by using CBC over SCC both in terms of the reduction in spurious data and the increase in vector accuracy are to be welcomed as when looking at a specific fluid flow this can be much harder to control than the other parameters varied here such as particle image diameter and density.

Particle Image Brightness

Maximum particle image brightness, q_{max} (Figure 5.15d and Figure 5.16d) has little effect on either the amount of spurious data or the displacement error which can be explained by the fact that the cross-correlation algorithm (5.8) used to calculate the SCC correlation function and the individual cross-correlation functions for CBC is normalized reducing the effect of changes in particle image brightness (Willert and Gharib, 1991). The amount of spurious data resulting from the SCC algorithm for all particle image brightnesses remains at approximately 10% whereas this reduces from approximately 0.33% to approximately 0.08% for values of q_{max} of 50 and 250 respectively when CBC is applied with δ_W = 4pix and 8pix from which it can be drawn brighter particles reduce the number of erroneous vectors for CBC but have negligible effect when using SCC.

Background Noise

As one would expect increasing the level of background noise, q_{BG} in the images increases both the amount of spurious data and the error as is shown in Figure 5.15e and Figure 5.16e. As the background noise level increases particle images further away from the centre of the light sheet become less well defined or completely drowned out by the noise resulting in fewer particle images

in the interrogation region. When q_{BG} = 80 greyscales (with 10% Gaussian noise) the amount of spurious vectors is 52.0% for the SCC algorithm and falls to 37.7% when CBC is applied with δ_W = 8pix. For all algorithms $\langle\bar{\varepsilon}\rangle$ rapidly increases at approximately the same rate when q_{BG} is above 20 greyscales with values of 0.28pix and 0.13pix when q_{BG} = 80 greyscales for SCC and CBC with δ_W = 8pix respectively, a reduction in the calculated displacement error of 55.0%.

Uniformity of Particle Image Diameter

As the standard deviation of particle image diameters, σ_p increases the amount of spurious data for the SCC algorithm increases from 7.4% to 20.0% for σ_p = 0pix and σ_p = 2.5pix respectively (see Figure 5.15f). When CBC is applied the amount of spurious data remains approximately constant for all σ_p at 0.1%, 0.09% and 0.08% for δ_W = 2pix, 4pix and 8pix respectively showing that the variation in particle image diameters has negligible effect on the amount of spurious data for CBC.

Unlike with the amount of spurious data when using CBC increasing the variation in particle image diameters increases the error in the calculated displacement vectors as shown in Figure 5.16f, with lower errors for greater degrees of window offset and the increase in error slowing as σ_p further increases with $\langle\bar{\varepsilon}\rangle$ = 0.09pix for δ_W = 8pix. The error when SCC is used increases approximately linearly with σ_p up to 0.13pix when σ_p = 2.5pix, only a 12% increase in error over completely uniform particle image diameters when σ_p = 0pix ($\langle\bar{\varepsilon}\rangle$ = 0.12pix).

5.6.3 Displacement error Against Radius

Whilst the spatially averaged measured displacement errors presented in Figure 5.16 show the overall accuracy of the CBC and SCC algorithms over the whole displacement field no information is provided about the effect of local displacement gradients on the measured displacement. In order to quantify the errors due to displacement gradient radial profiles of the displacement error are investigated. The centre of the Oseen vortex in the flow field is chosen as the zero radius point (r = 0) (see Figure 5.3). In the following radial plots of measured displacement error the error values presented are an azimuthal average of all displacement errors of vectors at that radial location. The dataset used for the radial error analysis presented here is the default image set with zero out of plane displacement and a particle image density of 0.078 particle images per pix^2.

The previous section discussing the results of the spatially averaged velocity errors for all datasets focused on the CBC algorithm and SCC as a control, the following results also incorporate a number of more advanced algorithms as previously discussed.

The graph presented in Figure 5.19 shows that for the SCC and CBC algorithms the error in calculated displacement is significantly higher in the centre of the vortex where the displacement gradients are at a maximum which for the SCC algorithm is consistent with previous findings in the literature (Huang et al., 1993). The SCC algorithm is the worst performing returning the highest displacement errors at each radial location with a maximum error of 0.35pix at the vortex origin. It can be seen that the CBC algorithm makes considerable improvements in the displacement error

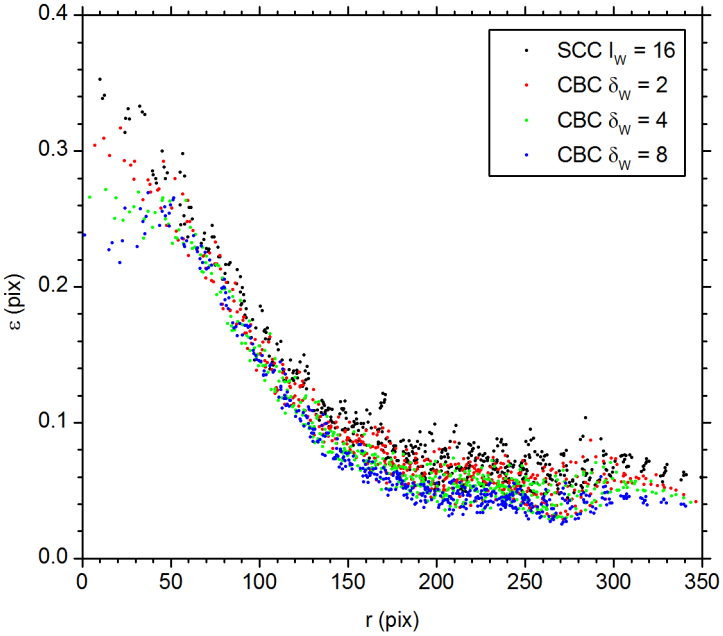

Fig. 5.19 Azimuthally averaged displacement error against radial position for the SCC algorithm and CBC algorithm with window displacements of 2pix, 4pix and 8pix.

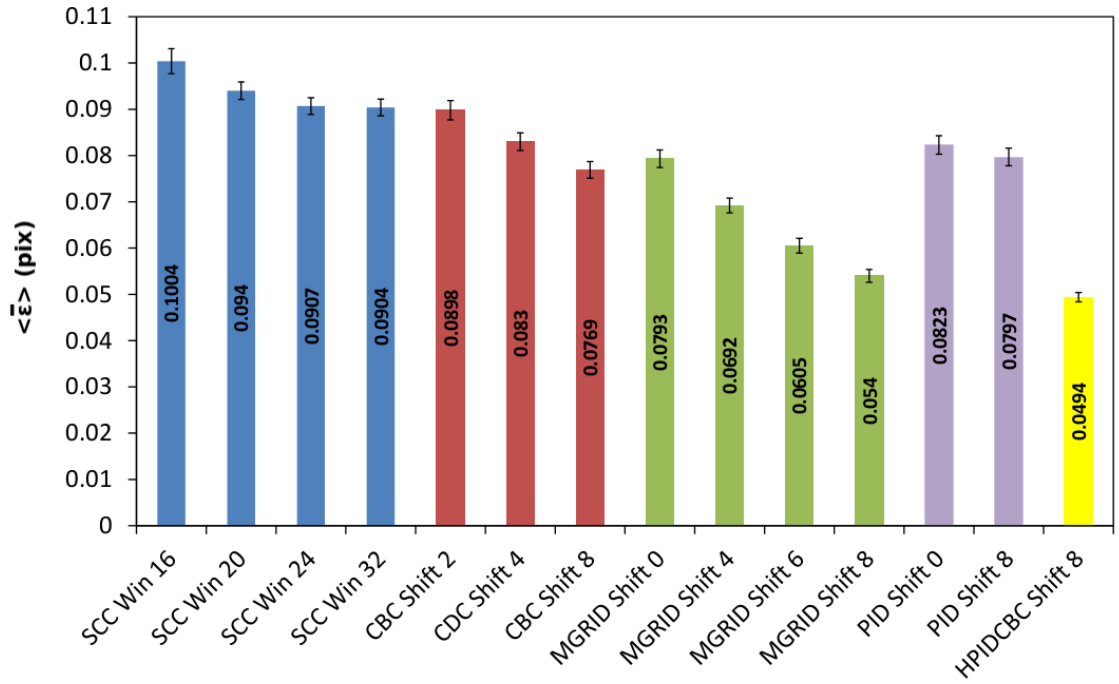

Fig. 5.20 Spatially averaged displacement vector errors for all tested algorithms. Error bars indicate +/- one standard deviation of error values.

in both regions of high and low gradients, in the case where CBC is applied with a window offset of 8pix the displacement error in the centre of the vortex is reduced to approximately 0.24pix, an improvement of 32%. Figure 5.20 shows the spatially averaged displacement error (average over each vector in the flow field) for each of the applied vector calculation algorithms and it can be

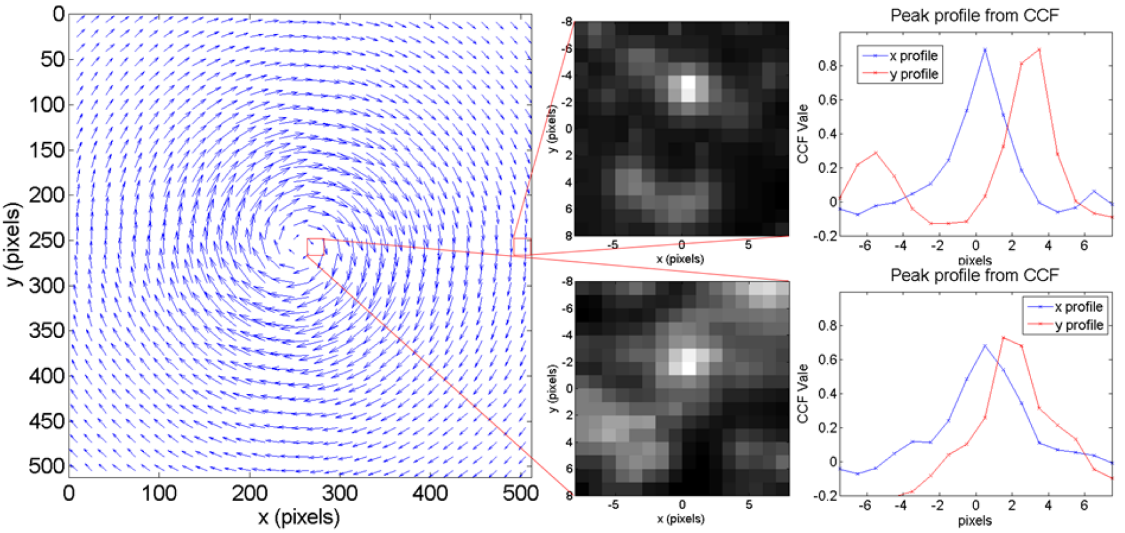

Fig. 5.21 Correlation functions for low gradient region (*top*) and high gradient region (*bottom*) for vector field calculated using standard cross-correlation. The correlation function peak profiles are taken through the correlation function origin.

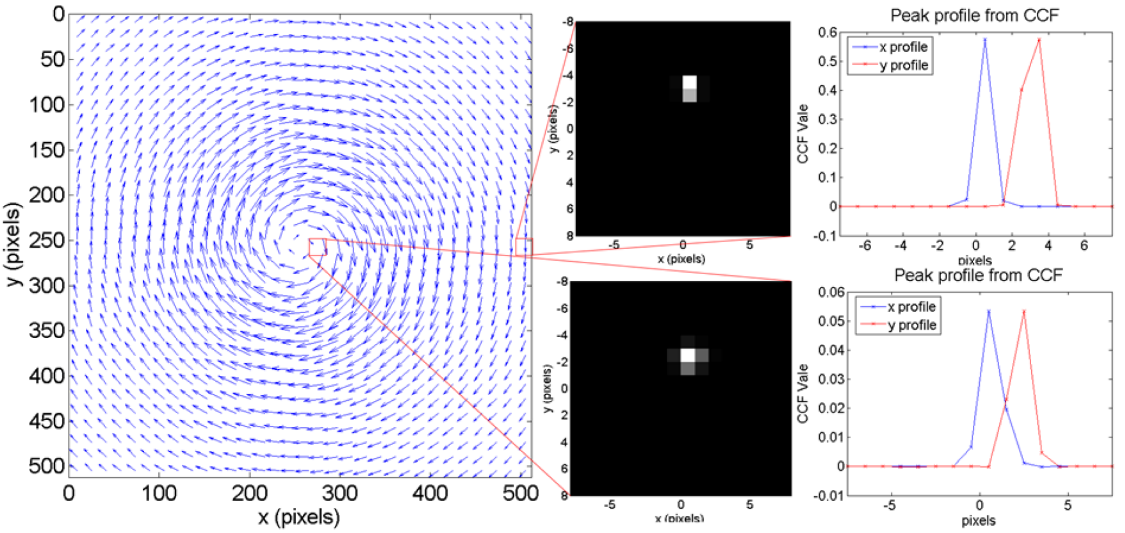

Fig. 5.22 Correlation functions for low gradient region (*top*) and high gradient region (*bottom*) for vector field calculated using correlation based correction with δ_W = 8pix. The correlation function peak profiles are taken through the correlation function origin.

seen that when CBC is applied with a window offset of 8pix the average displacement error is reduced by 23% compared to the SCC algorithm. Combining the results presented in Figure 5.19 and Figure 5.20 it can be seen that the CBC increases the accuracy of calculated displacements and the most significant improvements in accuracy are to be found in the inner region of the vortex where displacement gradients are at a maximum.

It has been shown in literature that large velocity gradients stretch the correlation function (Hart, 2000; Huang et al., 1993; Raffel et al., 1998) this effect is shown in Figure 5.21. The two highlighted correlation functions are chosen so that the displacement values are approximately the same but one is in a location of high velocity gradient (near the core) and a velocity gradient close to zero (near the edge). The two plots of the correlation functions clearly show that the peak is

much more clearly defined in the low gradient region and in the high gradient region it is much more spread out which leads to larger errors when applying the sub-pixel Gaussian fit.

Figure 5.22 shows that by using CBC the effect of local velocity gradients on the spread of the correlation peak is negated giving very well defined peaks for both high and low gradient regions leading to a much more accurate sub-pixel fit. It should be noted that when using the CBC the overall peak value decreases, this is due to multiplying several peak values with sub-unity magnitude. Whilst the overall peak value is reduced the signal-to-noise ratio is considerably larger as all other peaks in the correlation function tend to zero.

When applying the CBC algorithm with a fixed individual interrogation window size the effective area of image used to calculate each vector is increased due to the shifting of the interrogation regions over which individual correlation functions are calculated before taking their product. The degree of offset between the windows dictates the total image area used in calculating the displacement vector. For example when CBC is applied using the standard individual interrogation region window size of 16x16pix^2 and δ_W = 2pix the size of the interrogation window encompassing all five individual interrogation windows (see Figure 5.1) becomes 20x20pix^2 (neglecting the small number of pixels in the corners between interrogation regions, see see Figure 5.1). As the results presented show the calculated displacement error reduces with increasing window shift it is useful to compare the results with the SCC algorithm over larger window size to investigate whether the increased accuracy is due to the increased area over which each vector is calculated.

Comparisons between CBC and SCC with the SCC interrogation window size chosen based on the degree of offset of the windows used in CBC are presented in Figure 5.23 for offsets of 2pix, 4pix and 8pix. It can clearly be seen that the improved accuracy of CBC when applied with larger window shifts is not exhibited when the SCC interrogation window size is increased. As one would expect in regions of high gradient increasing the size of the SCC interrogation window decreases the accuracy of the calculated displacements as the variation of individual particle image displacements within each window becomes greater as the size of the window is increased thus distorting the peak in the correlation function by a greater amount. This shows that applying CBC with greater window offsets has the opposite effect of increasing the individual interrogation region size in SCC by reducing calculated displacement errors rather than increasing them in regions of high gradient. In low gradient regions (large r) it is shown in Figure 5.23 that CBC and SCC using a window size based on the CBC window shift perform approximately equally.

Figure 5.24 shows the displacement error against radius when CBC is applied combined with iterative multigridding using two iterations, the first using a window size of 32x32pix^2 and the final vectors calculated using 16x16pix^2 windows. It is observed that the application of multigridding without CBC ($\delta_W = 0$) reduces the calculated displacement error compared to single iteration SCC as is predicted in the literature due to the second iteration only having to calculate the subpixel displacement as the first iteration calculates the total displacement to the nearest integer and thus reducing the effect of loss-of-pairs. Further improvements are achieved when CBC is applied

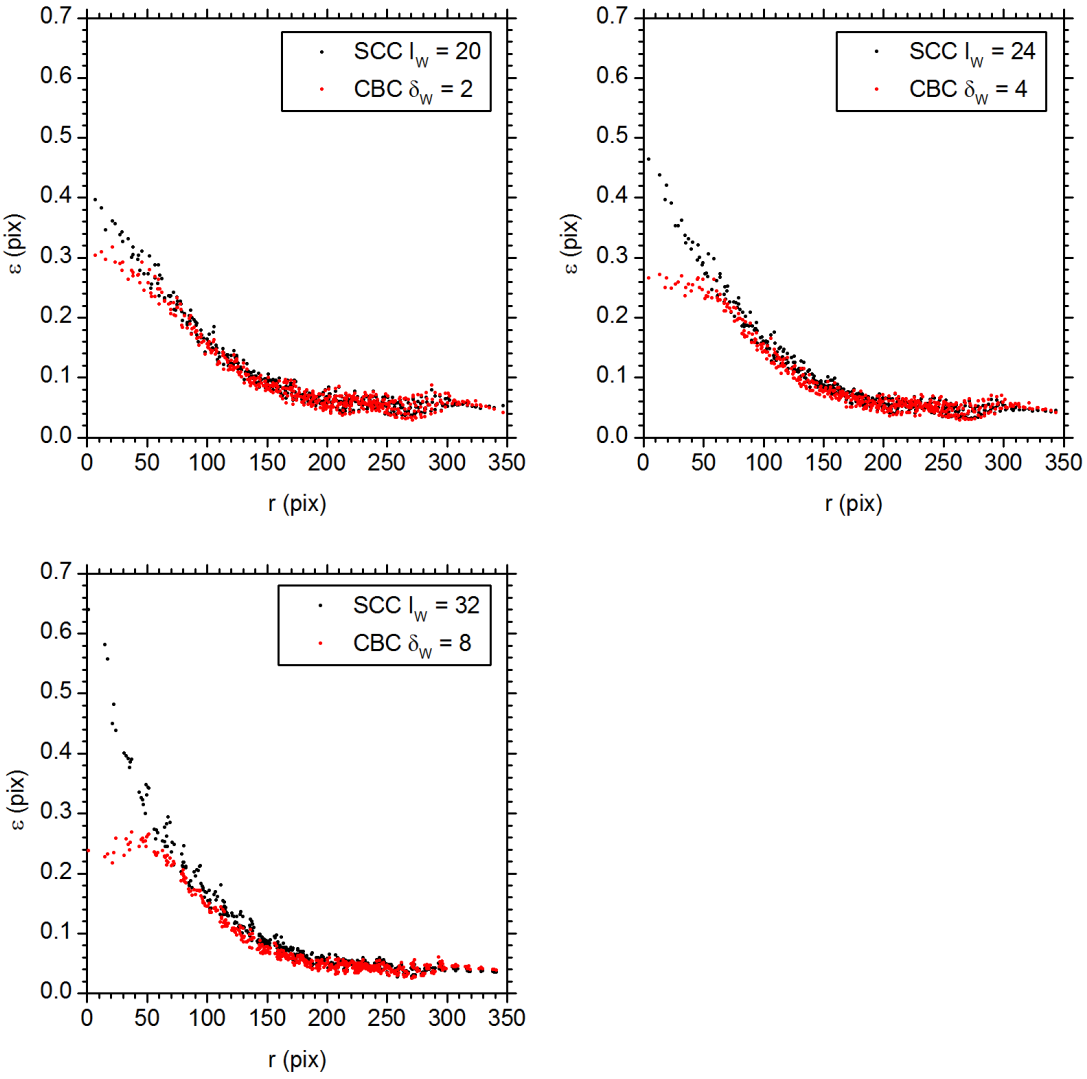

Fig. 5.23 Comparisons of SCC and CBC algorithms where interrogation region used in SCC is equal to the area over which CBC correlation functions are generated.

to each iteration of the multigrid process with increasing accuracy as the CBC window offset is increased. In the region very close to the centre of the vortex even with the application of CBC multigrid the displacement errors are greater than those when single iteration CBC is applied (see Figure 5.19). This can be explained by the greater error returned by the muligrid first iteration due to the larger 32x32pix^2 interrogation window as shown in Figure 5.23. However, still in a high gradient region (r is approximately greater than 25pix) the errors using multigrid CBC are much lower than those observed by single iteration CBC. When multigrid CBC is applied with a window offset of 8pix the spatial average displacement error is 0.054pix compared to 0.077pix for single iteration CBC, an improvement of 30% and 46% on the SCC algorithm.

The displacement error against radial location when using the PID algorithm is presented in Figure 5.25. In the two PID cases presented the first iteration is carried out using a 32x32pix^2 window with SCC for the case PID δ_W = 0pix and CBC with a window shift of 8pix for the case PID δ_W = 8pix. The utilisation of CBC in the predictor phase has minimal effect on the final

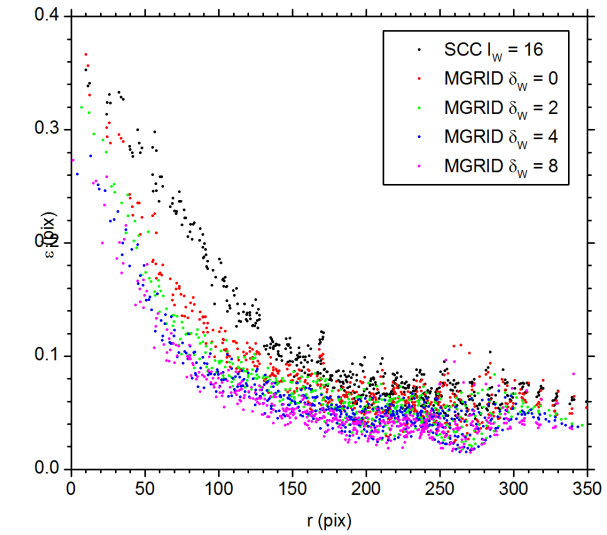

Fig. 5.24 Displacement error against radial location for CBC applied using iterative multigridding.

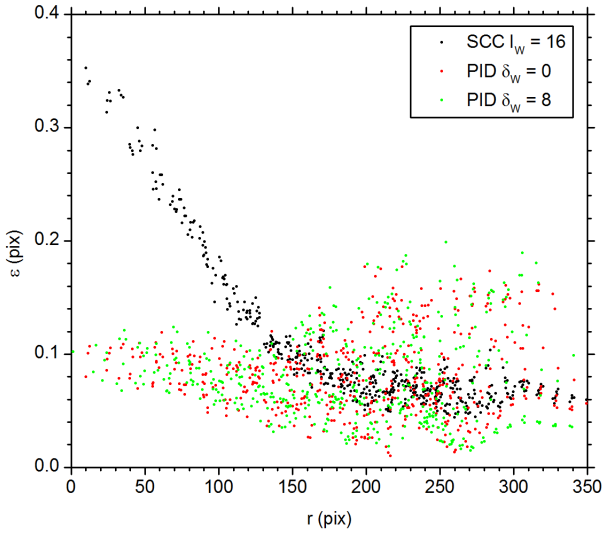

Fig. 5.25 Displacement error against radius for the particle image distortion algorithm.

calculated error. The results clearly show that the PID algorithm is superior to each of the previously tested algorithms in regions of high gradient where errors due to high gradients observed with each previous algorithm are almost entirely removed. The error level in the high gradient regions is much closer (though still greater) to those observed in low gradient regions for the other algorithms. This is explained by the application of PID removing the velocity gradients from subsequent interrogation region pairs as discussed in the literature review (§ 1.5.7). Whilst significant error reduction is observed in the high gradient region the spread of displacement errors in low gradient regions is much greater than for other algorithms. A possible explanation of this is the degradation in image quality of the reconstructed image due to the applied interpolation method.

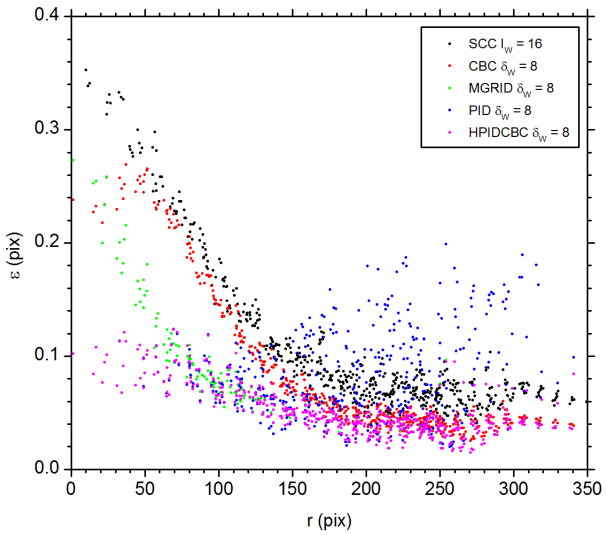

Fig. 5.26 Comparison of of displacement errors of various vector calculation algorithms and the new HPIDCBC algorithm.

Due to the greater spread of displacement errors in the low gradient regions and despite the large improvements in the high gradient region the overall spatially averaged displacement error is approximately 0.08pix as can be seen in Figure 5.20.

Combining the results presented it can be seen that the optimum algorithm for the vortex core region where spatial gradients are high is PID and in the low gradient region the optimum algorithm is multigrid CBC with a window shift of 8pix. Using these results the Hybrid PID CBC (HPIDCBC) algorithm is applied. Local displacement gradients are calculated during a first iteration using CBC with a window size of 32x32pix^2 and a window offset of 8pix, with vectors calculated in the second iteration if the local displacement gradient is above a certain threshold (in this case 0.05pix/pix) using the PID algorithm and if below this threshold the CBC algorithm is used with a window offset of 8pix (and a 16x16pix^2 interrogation region).

The results of the best performing algorithm in each category, SCC, CBC, MGRID, PID and HPIDCBC are presented in Figure 5.26 showing that the HPIDCBC algorithm is optimum in terms of the accuracy of calculated displacement vectors at each point in the displacement field with the low gradient region accuracy of the multigrid CBC algorithm and the high gradient region accuracy of the PID algorithm. The spatially average displacement error for the HPIDCBC algorithm is 0.049pix which is a 9.3% improvement on the multigrid CBC (δ_W = 8pix) algorithm and a 51% improvement on the SCC algorithm.

5.6.4 Computational Expense and Overall Cost Benefit Analysis

In order to measure the computational expense of the various algorithms the vector calculation process was timed using MATLAB's inbuilt timing function. The average total time to calculate all vectors for each of the 100 image pairs, T_v is calculated and then divided by the number of

vectors, N_M to give the processing time per vector, t_v for each of the algorithms. As the absolute values of t_v are hardware dependent the normalized time per vector t'_v is calculated by normalizing t_v by the time per vector of the 16x6 pix^2 interrogation region SCC algorithm, $t_{v_{SCC}}$:

$$t'_v = \frac{t_v}{t_{v_{SCC}}} \tag{5.24}$$

The calculation time per vector for the SCC algorithm using a 16x16pix^2 interrogation region, $t_{v_{SCC}}$ was calculated to be 1.47ms which for the total number of vectors calculated for each image pair, N_M = 1024 gives a total processing time of 1.5s per image pair.

For each of the algorithms applied with different parameters presented in Figure 5.20 the spatially average error $\langle\bar{\varepsilon}\rangle$ is plotted against the normalised vector calculation time in Figure 5.27 showing that improved displacement vector accuracy comes with the cost of increased computation time. The most accurate algorithm, the new HPIDCBC algorithm is also the most computationally expensive with t'_v = 9.47 which translates to it taking approximately 9.5 times longer to calculate each vector for a 50.8% reduction in average measured displacement error than when the SCC algorithm is applied with a 16x16pix^2 interrogation region.

Increasing the size of the interrogation region used for SCC increases the computational expense with 32x32pix^2 interrogation regions taking t'_v = 2.24 times longer than 16x16pix^2 interrogation regions which is to be expected due to the increased amount of image data used in calculating the cross-correlation functions. The reduction in error associated with increased computational time for SCC with larger windows is the result of greater accuracy in low gradient regions despite the decrease in accuracy in the high gradient region.

The CBC algorithms have values of t'_v = 1.46 and 2.00 for δ_W = 2pix and 8pix respectively which in the case of δ_W = 8pix returns a 23.5% reduction in average calculated displacement error for double the vector computation time. The increase in computation time for greater window displacements can be attributed to programming inefficiencies in the application of the algorithm as sub-windows from the main image pairs are transferred to a new variable before the individual interrogation regions are calculated, if the cross-correlation functions were calculated directly from the main image inputs it is expected that there would be significantly less variation in computation time with window offset due to the reduced amount of data being transferred.

The iterative algorithms, MGRID, PID and HPIDCBC are all much more computationally expensive than single iteration algorithms due to the vector field being calculated twice, in each case with 32x32pix^2 interrogation regions for the first pass. MGRID applied without CBC (MGRID δ_W = 0pix) has t'_v = 3.41 and results in a higher average displacement error than CBC δ_W = 8pix which has a lower computational time of t'_v = 2.00 showing that applying CBC with δ_W = 8pix is both less computationally expensive and more accurate than the two iteration multigrid standard cross-correlation algorithm. When applying MGRID in conjunction with CBC (MGRID δ_W = 2pix, 4pix and 8pix) the computational time is greatly increased mainly due to the much greater overheads of applying CBC in the initial iteration when using 32x32pix^2 windows, the increased

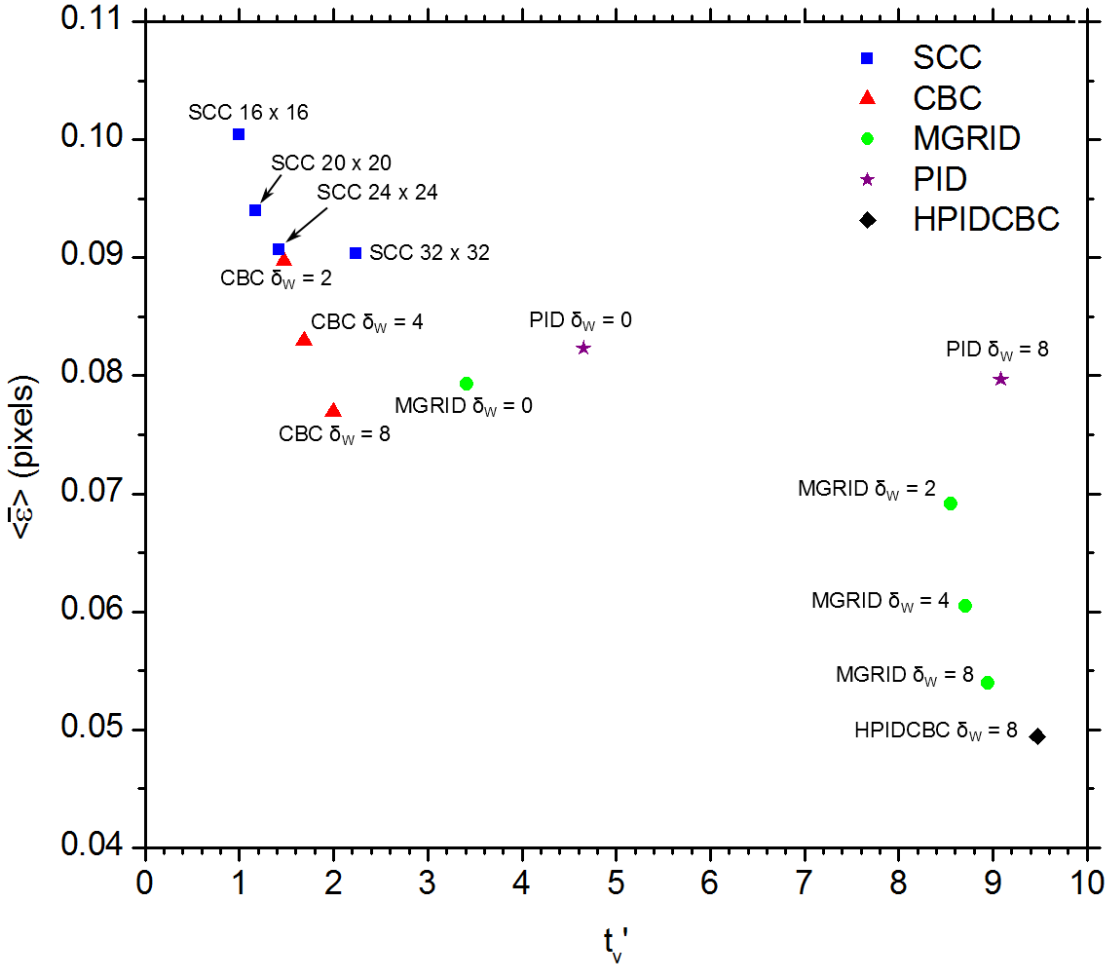

Fig. 5.27 Average spatial displacement vector error against normalised computation time per vector for various vector calculation algorithms employed with varying parameters.

computation time comes with a marked increase in the accuracy of the calculated vectors as has been shown. Applying CBC to the multigrid algorithm, MGRID δ_W = 8pix, the average displacement error is reduced by 29.8% when compared to the single iteration CBC δ_W = 8pix but comes at much greater computational expense with t'_v = 8.95, 4.49 times longer than CBC δ_W = 8pix.

The PID algorithm is computationally expensive due to the sub-pixel reconstruction of the second image frames in the second iteration and as has been previously shown leads to higher overall spatial error in low gradient regions with only improvements in the high gradient regions. The most computationally expensive of all the algorithms tested is the new HPIDCBC algorithm with δ_W = 8pix with t'_v = 9.47 showing that the average error can be reduced by approximately 50% compared to the SCC algorithm but requires almost ten times the amount of time to calculate each vector.

5.7 Summary

In chapter five a number of PIV vector calculation algorithms are investigated using synthetic datasets of an Oseen vortex. It is confirmed that the accuracy of calculated vectors is sensitive to

spatial velocity gradients with higher gradient levels decreasing the accuracy of calculated vectors and it is shown that employing more advanced algorithms such as mulitgrid and image deformation can reduce these errors. Hart's Correlation Based Correction algorithm is fully investigated providing new insight into the performance of the algorithm for small window offsets. It is shown that the amount of spurious data and error in measured velocity vectors can be significantly reduced through the multiplication of neighbouring correlation functions offset by just 2 pixels. New information has been obtained regarding the effect of varying a wide range of PIV image parameters such as particle image diameter, uniformity of particle image size, degree of out of plane displacement and the effect that varying these parameters has on the amount of spurious data and the measurement error for SCC and CBC with varying window offsets.

It was shown that in regions of high spatial gradients particle deformation algorithms provide much superior accuracy in measured vectors when compared to other algorithms, including CBC. However, in regions of low velocity gradient it is shown that the CBC algorithm performs the best offering the lowest error in measured velocity vectors. It was using these two results that a new hybrid algorithm was proposed where after an initial iteration spatial gradients are calculated and then in subsequent iterations vectors located in a region where the local spatial gradient is above a predefined level are calculated using an image deformation algorithm and those in low gradient regions are calculated using the CBC algorithm. The new hybrid algorithm was shown to outperform each of the individual algorithms by minimising the error in calculated vectors at all points in the flow with the average measurement error reduced by approximately half when compared to standard cross-correlation. Finally it was shown that the increased accuracy of the new algorithm comes at a high computational cost, taking approximately ten times longer than the standard cross-correlation algorithm to calculate each vector.

Chapter 6

Flow Structure and Turbulence Properties of a Lab Generated Tornado-Like Vortex

6.1 Experimental Apparatus and Data Analysis

6.1.1 Tornado Vortex Simulator

The tornado vortex simulator (TVS) (Figure 6.1) is a Ward-type simulator based on the Texas Tech University vortex simulator II (TTU-VSII) (Mishra et al., 2008). In a laboratory simulation to produce a tornado-like vortex one needs to apply an updraft and circulation to a body of air. In the TVS updraft is applied by means of an axial fan (manufacturer: Axair, model number: HEP-31-2T single-phase plate mounted axial fan.) extracting air from the convection chamber (height 240mm, diameter 550mm) as can be seen in Figure 6.2 and has a maximum measured flow rate of $0.09 m^3/s$. The manufacturer flow characteristics of the axial fan are displayed in Figure 6.3. To reduce turbulence in the updraft through the updraft orifice aluminium honeycomb measuring 150mm x 150mm and 50mm deep with 7mm diameter holes is placed in the convection chamber covering the top of the updraft orifice.

Circulation is applied to the system via four pipes made from 75mm diameter PVC pipe, each of the four pipes have eight 3mm diameter holes drilled at intervals of 30mm vertically starting 30mm from the floor of the chamber. The design of TVS differs from TTU-VSII in using only four pipes rather than the sixteen used there as the vortex data is to be recorded using PIV meaning optical access for a large light sheet filling the inflow region is required. The four circulation pipes are connected to a plenum (height 240mm, diameter 550mm) with airflow provided by four circulation blowers (manufacturer: EBM-Pabst, model number: RG 125-19/14 N DC centrifugal compact fan) each with a maximum flow rate of $0.024 m^3/s$. The manufacturer flow characteristics of the circulation blowers are shown in Figure 6.4

The floor of the inflow region is constructed from smooth plywood with a glass optical window

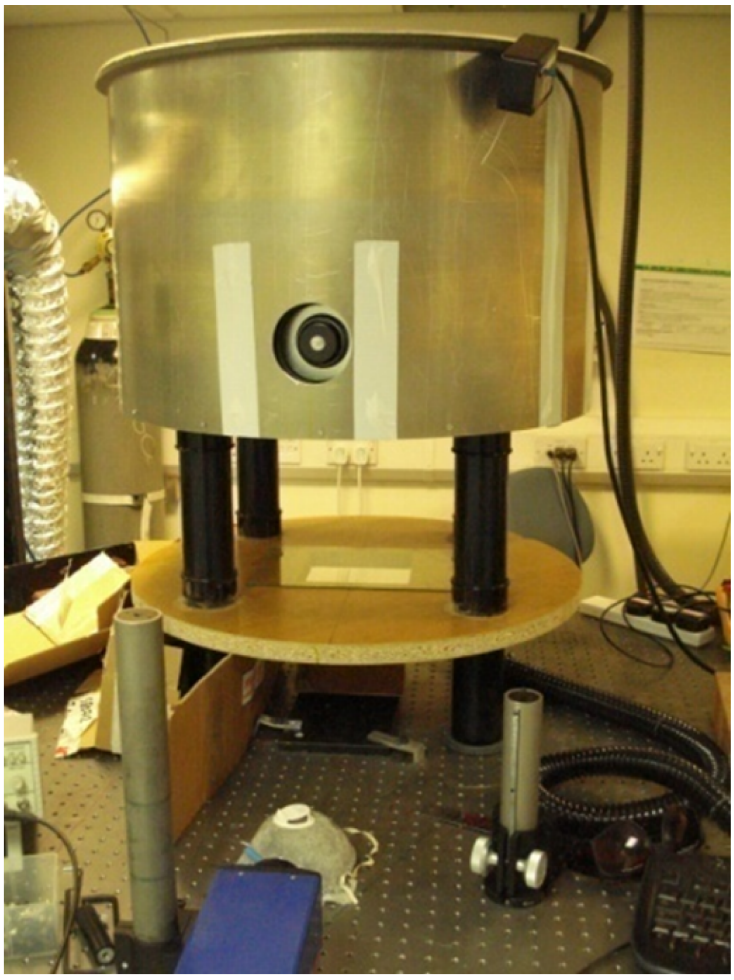

Fig. 6.1 Photograph of the Leeds Tornado Vortex Simulator.

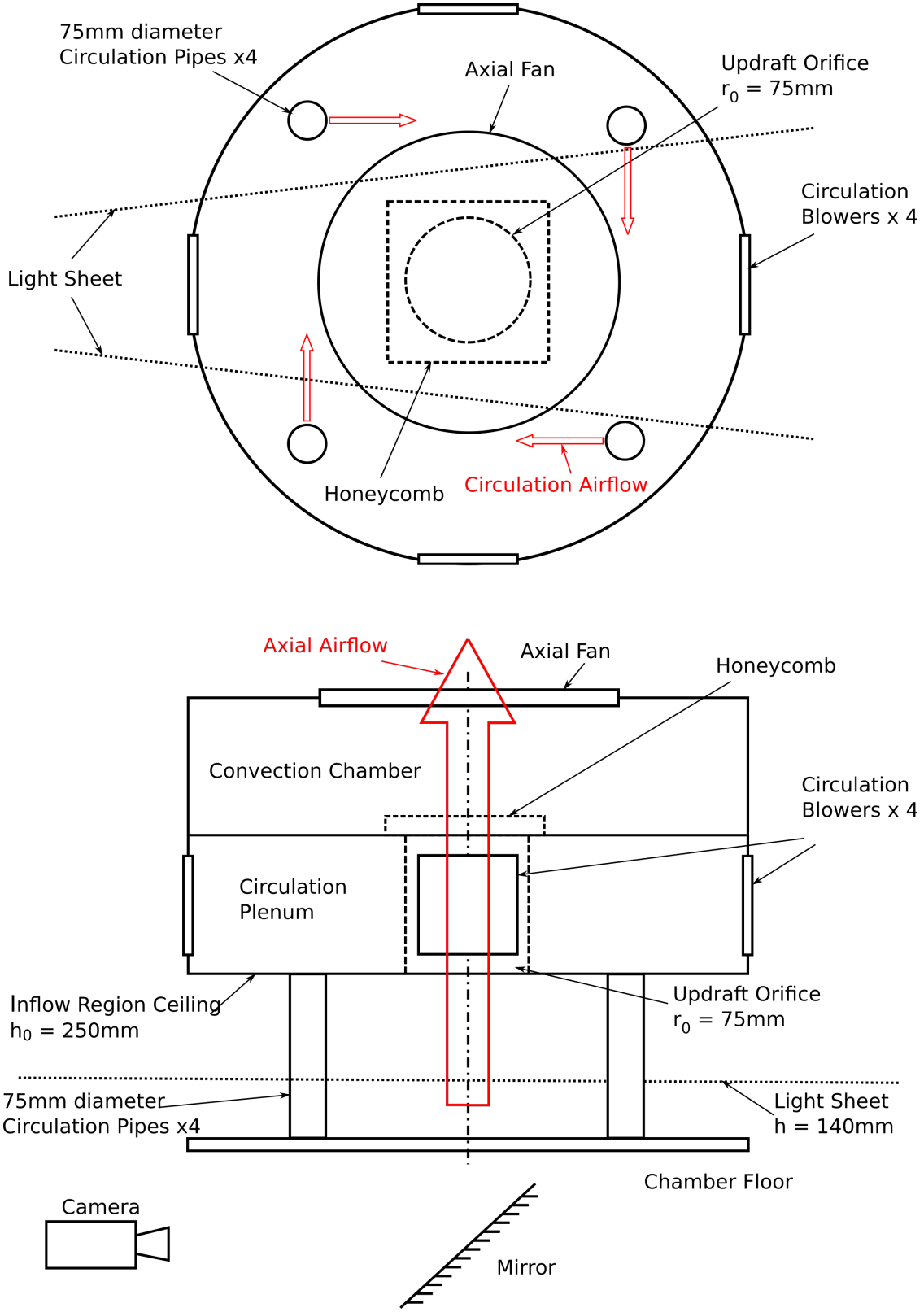

Fig. 6.2 Schematic of the Leeds Tornado Vortex Simulator.

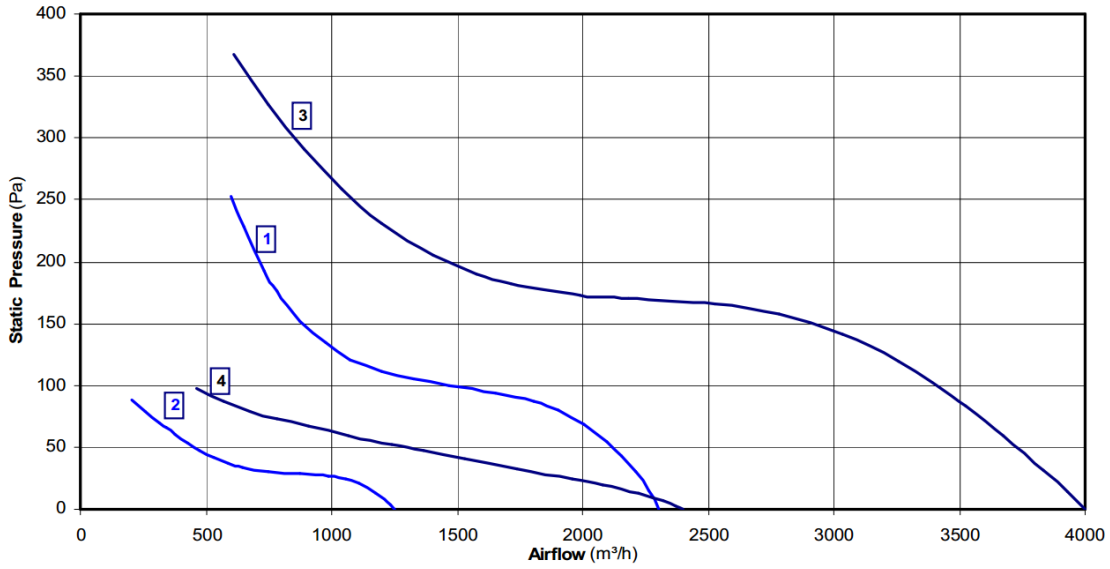

Fig. 6.3 Manufacturer airflow characteristics for Axair HEP-31-2T (curve 3) single-phase plate mounted axial fan. (http://www.axair-fans.co.uk/wp-content/uploads/2015/12/Plate-Cased-Axial-2012-WEB.pdf)

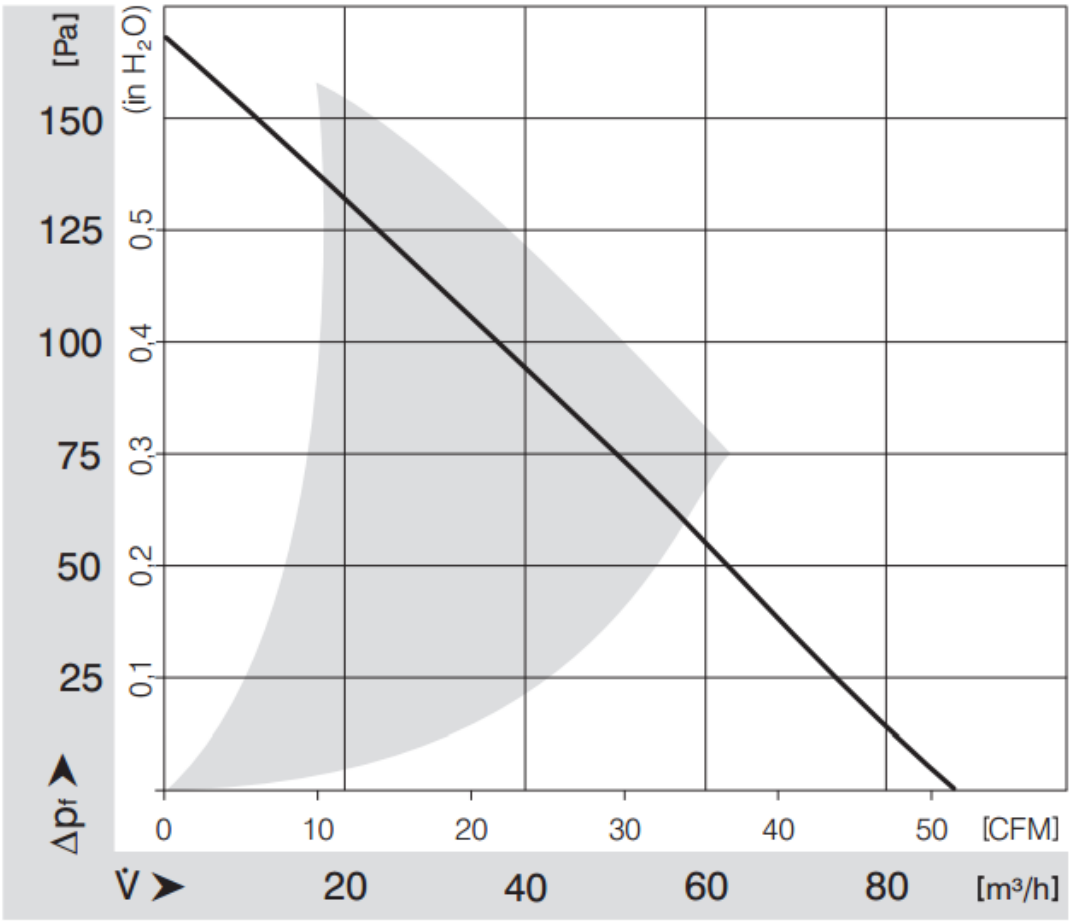

Fig. 6.4 Manufacturer airflow characteristics for EBM-Pabst RG 125-19/14 N circulation blower. (http://img.ebmpapst.com/products/datasheets/DC-centrifugal-fan-RG1251914N-ENU.pdf?_ga=1.155651826.852076993.1463566719)

fitted flush with the floor and centred axially to provide optical access via a mirror below as in Figure 6.2. The height of the inflow region, h_0 from the floor to the chamber ceiling is 0.25m, the updraft orifice r_0 into the convection chamber has radius 75mm and the distance between circulation pipes is 0.36m.

Through independent control of the axial fan and circulation blowers a wide range of swirl ratios can be obtained and in the current study range from 0.0017 to 1.33. The aspect ratio of the simulator $a_0 = h_0/r_0$ for the experiments carried out is fixed at 3.33 though this can be changed by altering the height of the circulation pipes.

6.1.2 PIV Measurements

A light sheet with thickness 0.5mm at the focus is created via a pair of 532nm wavelength Nd:Yag pulse lasers with a pulse energy of 31mJ with the beam expanded using a -50mm focal length plano-concave lens and then shaped into a light sheet with a 300mm focal length cylindrical lens. The measurement plane (x-y) used was set at an axial height of 140mm from the floor of the inflow region. Seeding is added to the system via a smoke generator (Martin Magnum 650), smoke is directed underneath the floor of the inflow region via a pipe and is sucked into the system as part of the inflow. Particles were measured to have a mean diameter of 3.4μm and was measured using interferometric droplet sizing (Damaschke et al., 2005, Glover et al., 1995). Particle images were captured using a LaVision Imager Intense PIV CCD camera with a resolution of 1376 x 1040 pixels with a dynamic range of 12-bit and 6.45 x 6.45μm pixel size fitted with a Sigma 28-80mm lens set to F number 3.5. The interval between image pairs was 10μs - 35μs depending on the flow configuration, this was limited not by the in-plane particle displacements but by loss-of-pairs due to the large axial out-of-plane velocity component. The field of view was 159.63 x 120.65 mm^2 capturing 500 instantaneous image pairs per fan configuration.

The particle images were processed in LaVision DaVis 8.0.2 to generate planar velocity vector fields using the multigrid method with an initial pass using a 32x32 pixel interrogation window with no weighting function and 50% overlap, the final two passes are carried out using 16x16 pixel interrogation windows with a circular weighting function and again a 50% overlap. Using the interrogation windows specified the spatial resolution of the measured velocity field $\Delta x = \Delta y =$ 0.927mm. Spurious vectors were detected using the enhanced normalised median test algorithm as presented in § 5.4.4 and did not exceed 2.5% of the 22360 (172x130 vector grid) vectors calculated from each image pair. Removed spurious vectors were replaced by interpolated vectors using a median filter.

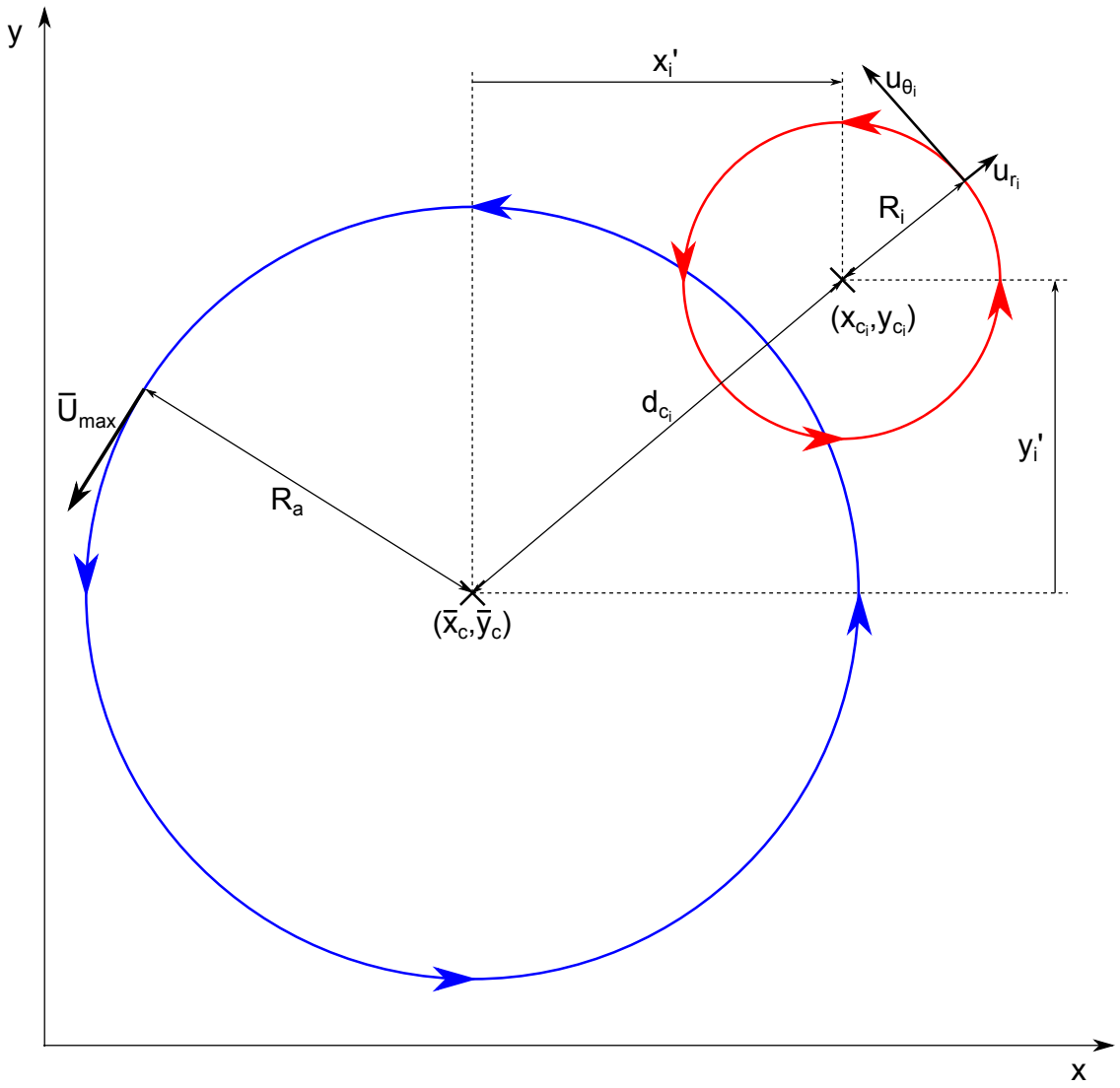

Fig. 6.5 Coordinate system used in tornado vortex PIV experiments. The red circle represents an instantaneous vortex of radius R_i and the blue circle represents the mean flow vortex traced out by the precession of the instantaneous vortices and has radius R_a.

6.2 Results and Discussion

6.2.1 Flow Configurations

To investigate the flow dynamics of the tornado-like vortex a large number of swirl ratios are investigated by using a number of different combinations of axial and circulation fan speeds. The circulation blowers run on a DC power supply and the voltage supplied to these, V_Γ, ranges from 15V to 30V. The axial fan which runs on AC mains has the fan speed regulated with a potentiometer and is set to five different speeds denoted A-E. For example, the data set name A25 refers to axial fan speed A and circulation blower voltage of 25V. A summary of flow parameters which will be calculated throughout this chapter is presented in Table 6.1. The coordinate system that will be used throughout this chapter is presented in Figure 6.5.

Table 6.1 Flow parameters for varying axial and circulation fan configurations

Flow Configuration	S	Re_r	Γ ($\mathrm{m^2s^{-1}}$)	Q ($\mathrm{m^3s^{-1}}$)	$u_{\theta_{max}}$ ($\mathrm{ms^{-1}}$)	R (mm)	R/r_0
A20	0.0041	22772	0.158	0.089	5.409	4.64	0.062
A25	0.0168	21490	0.305	0.084	5.222	9.28	0.124
A30	0.0374	21336	0.450	0.084	5.140	13.92	0.186
B15	0.0017	21551	0.078	0.084	3.354	3.71	0.049
B20	0.0085	19305	0.198	0.076	4.865	6.49	0.086
B25	0.0449	16284	0.413	0.064	4.727	13.90	0.185
B30	0.0978	14201	0.559	0.056	4.574	19.46	0.259
C15	0.0172	16368	0.217	0.064	3.387	10.19	0.136
C20	0.1147	12493	0.457	0.049	2.965	24.56	0.327
C22.5	0.1699	10402	0.515	0.041	3.053	26.87	0.358
C25	0.2133	10402	0.587	0.041	3.148	29.65	0.395
C30	0.3302	8189	0.663	0.032	3.301	31.97	0.426
D15	0.5119	3018	0.344	0.012	1.555	35.21	0.470
D22.5	1.0386	2972	0.466	0.012	1.430	51.90	0.692
D30	1.3284	2832	0.501	0.011	1.356	58.85	0.785
E15	0.0520	11303	0.293	0.044	2.956	15.75	0.210
E20	0.1539	9040	0.444	0.035	2.879	24.56	0.327
E25	0.3487	6571	0.587	0.026	3.057	30.58	0.408
E30	0.4804	5972	0.656	0.023	3.045	34.29	0.457

Flow Rates

For each fan configuration the flow rate through the updraft orifice, Q_V is required for calculation of swirl ratio and the radial Reynolds number. Before measuring the flow rate (and before recording any PIV datasets) the axial and circulation fans were left running for 5 minutes to ensure they had settled to a stable state. The flow rate was measured by measuring the axial flow velocity profile across the updraft orifice using a hotwire probe (Testo 425 Thermal Anemometer), measurements were taken at 10mm intervals across the orifice, each measurement is an ensable average of five time averages with each taken over two minutes with the probe recording at 2Hz, the velocity measurement resolution of the probe is 0.01m/s with an accuracy of 0.03m/s (both the resolution and accuracy are quoted from the probe manual). The velocity profiles were then integrated around a circle to give the full flow rate through the updraft orifice.

Figure 6.6(a) shows the measured flow rate through the updraft orifice, Q_V, for each of the 19 flow configurations. Measurements were taken for 5 axial fan speeds labelled A to E, for these fixed axial fan speeds the voltage supplied to the circulation fans, V_Γ was varied between 15V and 30V. It must be noted that for axial fan flow rates A to D the flow rate decreases with D having the

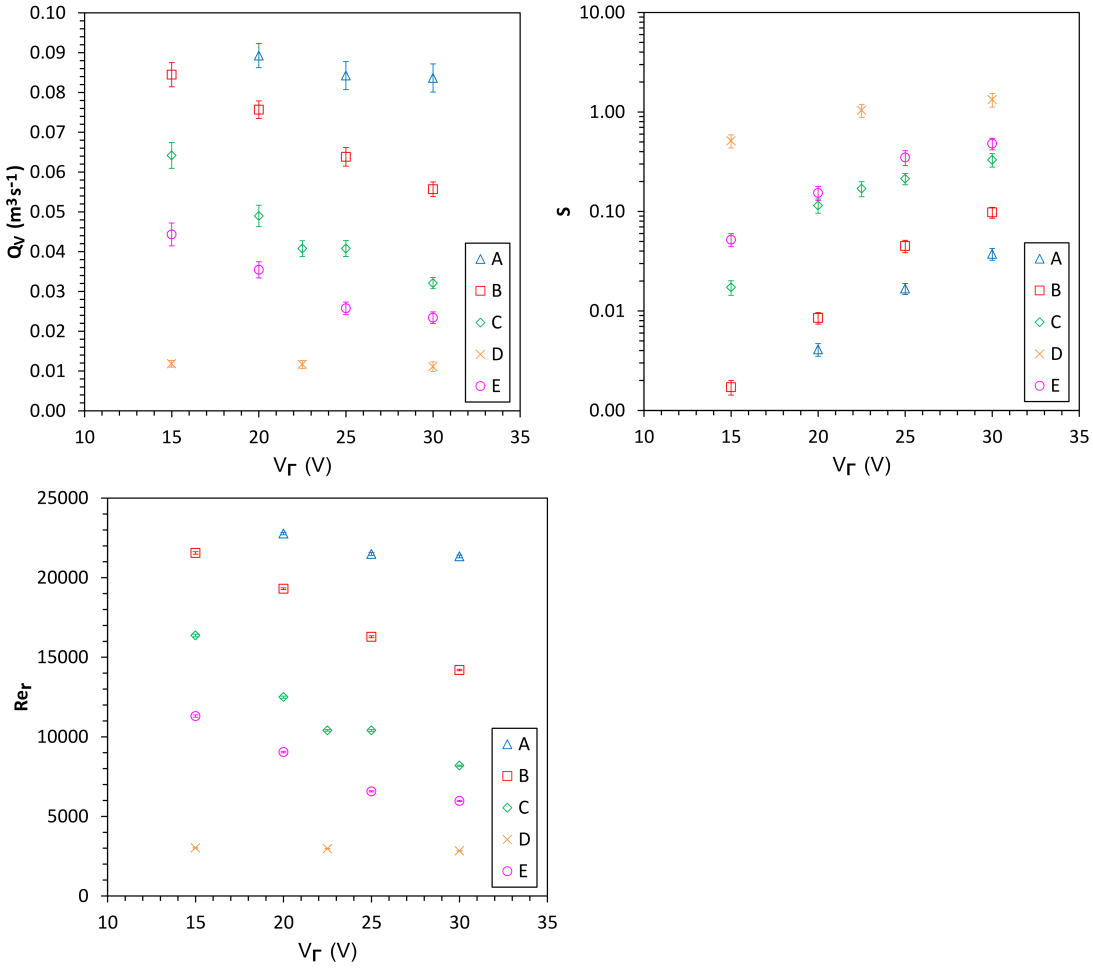

Fig. 6.6 (a) Axial flow rate, Q_V. Error bars indicate +/- one standard deviation of the measured flow rate. (b) swirl ratio, S, and (c) radial Reynolds number, Re_r, for circulation fan speeds A to E and varying axial fan voltage supply, V_Γ.

lowest flow rate, after capturing these initial four datasets configuration E was captured to fill in the gap between C and D and hence the axial flow rate of E is in between C and D. The flow rate through the system varies from a minimum of $0.011\text{m}^3/\text{s}$ for configuration D30 (axial fan speed D, circulation fan voltage, V_Γ = 30V) to a maximum of $0.089\text{m}^3/\text{s}$ for configuration A20. It can be seen that for a fixed axial fan speed the flow rate decreases as the circulation voltage increases with a tight linear trend, though for the lowest axial fan speed (D) the effect of the circulation voltage on flow rate is almost negligible.

Swirl Ratio and Radial Reynolds Number

As highlighted in § 4 the swirl ratio is the parameter that most strongly governs the properties of a tornado-like flow and is defined as the ratio of angular to axial momentum and is calculated as follows:

$$S = \frac{\Gamma R}{2Q_V} \tag{6.1}$$

Where Γ is the circulation, R is the vortex radius and Q_V the flow rate through the system. Here the circulation is calculated at the radius of maximum tangential velocity as follows:

$$\Gamma = 2\pi R u_{\theta_{max}} \tag{6.2}$$

Where R is the radius of the vortex, i.e. the radius at which u_θ is a maximum. Substituting (6.2) into (6.1) the swirl ratio from the PIV data is calculated as:

$$S = \frac{2\pi R^2 u_{\theta_{max}}}{Q_V} \tag{6.3}$$

The radius of the vortex R for a particular flow configuration is the mean distance from the centre of instantaneous vortices to the distance at which $u_{\theta_{max}}$ is observed.

Swirl ratio as a function of circulation fan speed for differing axial fan speed settings is presented in Figure 6.6(b). As expected from (6.3) swirl ratio is heavily dependent on the axial flow rate, Q. With flow configurations (D) with the lowest axial flow rate giving the highest swirl ratios whereas high axial flow rate configurations give the lowest swirl ratios. Swirl ratio ranges from a minimum value of 0.0017 to a maximum of 1.328 for configurations B15 and D30 respectively. With independent control of both the axial fan speed and the circulation fan speeds it is possible to configure the flow to have a similar swirl ratio for different combinations of fan speeds as can be seen for, as an example, configurations A25 and C15 which have flow rates of $0.084\text{m}^3/s$ and $0.064\text{m}^3/\text{s}$ respectively and swirl ratios of 0.0168 and 0.0172 respectively.

The radial Reynolds number, Re_r is defined as:

$$\text{Re}_r = \frac{Q_V}{h_0 \nu} \tag{6.4}$$

Where h_0 is the height of the flow chamber and ν the kinematic viscosity of air (at lab temperature).

$h\nu$ is a constant resulting in Re_r having sole dependence on Q_V resulting in the same trends as in Figure 6.6(a) and Re_r is shown in Figure 6.6(c). Radial Reynolds numbers range from a minimum of 2,832 to a maximum of 22,772 for flow configurations D30 and A20 respectively.

6.2.2 Mean Flow Field

Figure 6.7 and Figure 6.8 present ensemble averaged velocity vectors of instantaneous vector fields for various flow configurations, each containing $N = 500$ individual vector fields, the average velocity vectors are calculated as follows:

$$\overline{u}(x,y) = \frac{1}{N}\sum_{i=1}^{N} u_i(x,y) \tag{6.5}$$

$$\overline{v}(x,y) = \frac{1}{N}\sum_{i=1}^{N} v_i(x,y) \tag{6.6}$$

Where u_i and v_i are the i^{th} instantaneous orthogonal velocity vectors in the x and y directions respectively. The blue circles in Figure 6.7 and Figure 6.8 show the radius of the vortex present in the ensemble average of the instantaneous flow vectors as in (6.5) and (6.6), R_a is the radius (with origin at the mean flow vortex centre) at which the azimuthally averaged velocity profile has maximum velocity.

6.2.3 Instantaneous Vortex Radius

The radius of the vortex produced under certain flow configurations is highly dependent on swirl ratio with low swirl ratio vortices having a small radius and large swirl ratio vortices having a larger radius. The vortex radii range from 3.71mm to 58.85mm for swirl ratios of 0.0017 (B15) and 1.328 (D30) respectively. When plotted on a log-log graph as in Figure 6.9 it can be seen by the straight line nature of the data that the radius of the vortex is related to the swirl ratio by a power law, it was found by regression that vortex radius, R is related to swirl ratio, S by the following relationship:

$$R = 51.75S^{0.417} \tag{6.7}$$

For a more general relationship between vortex radius and swirl ratio the normalized vortex radius, R/r_0 is introduced where the measured vortex radius R is normalized by the tornado chamber updraft radius r_0 with the relationship with swirl ratio shown in Figure 6.9. The normalized vortex radius follows the following relationship with swirl ratio:

$$\left(\frac{R}{r_0}\right) = 0.69S^{0.417} \tag{6.8}$$

The coefficient of determination, R_D^2 for this fit is 0.99 suggesting the data fits very closely to the curves presented in Figure 6.9. The coefficient of determination in literature is usually referred to

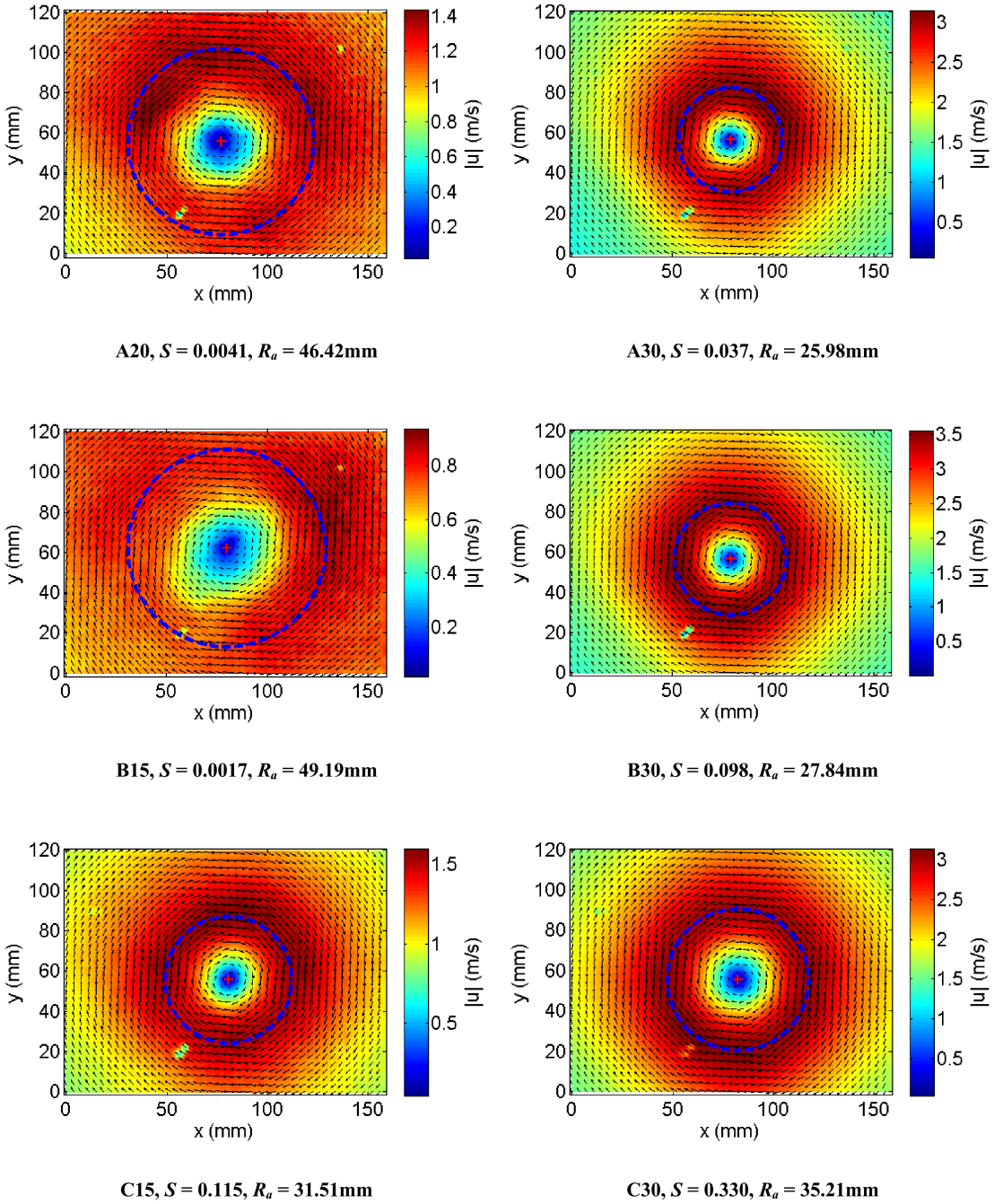

Fig. 6.7 Ensemble average velocity vectors for axial fan settings A-C. Blue circle shows radius of mean flow vortex, R_a. Only every fourth vector shown for clarity.

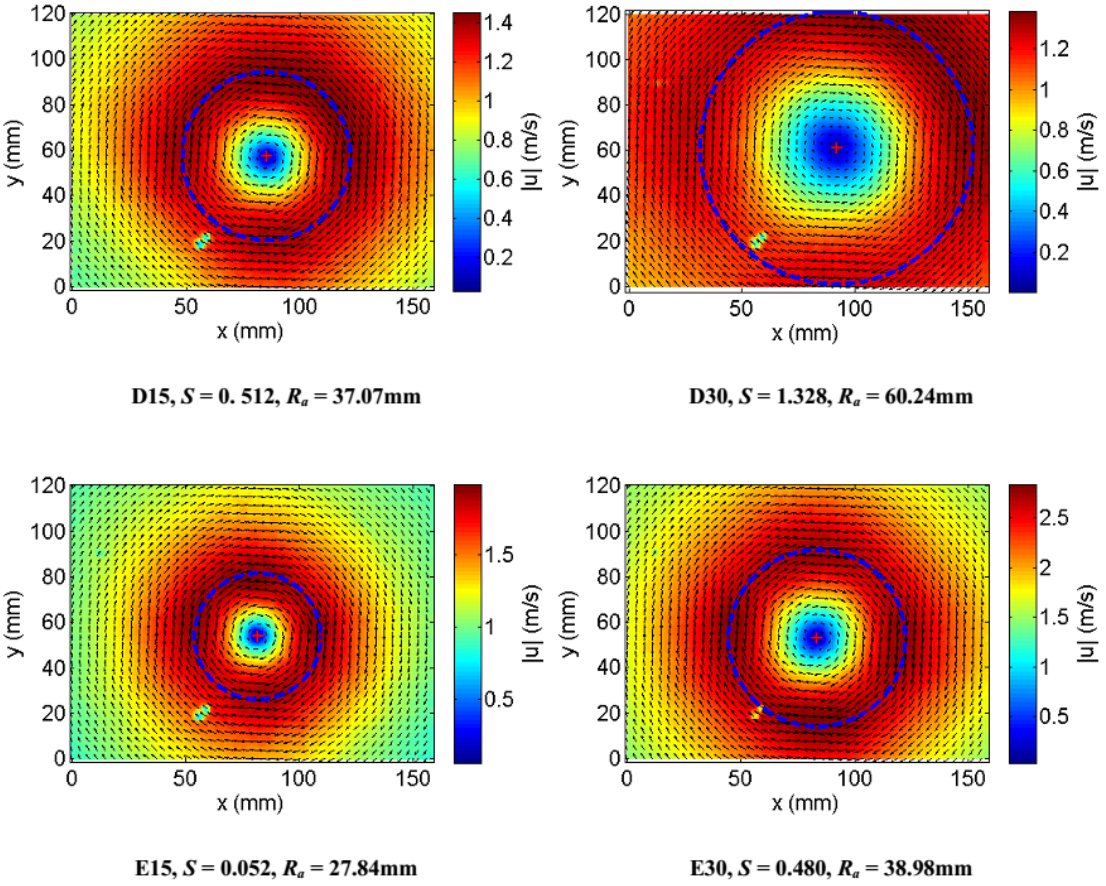

Fig. 6.8 Ensemble average velocity vectors for axial fan settings D and E. Blue circle shows radius of mean flow vortex, R_a. Every fourth vector shown for clarity.

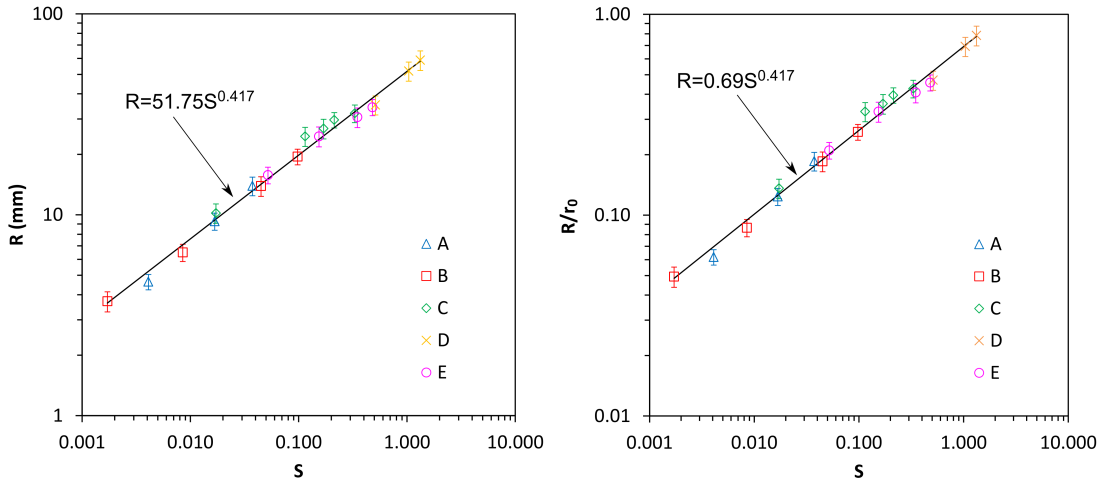

Fig. 6.9 (*left*) Radius of vortex against swirl ratio for axial fan speeds A-E and (*right*) normalised vortex radius. Error bars indicate +/- one standard deviation of instantaneous vortex radii and normalised vortex radii.

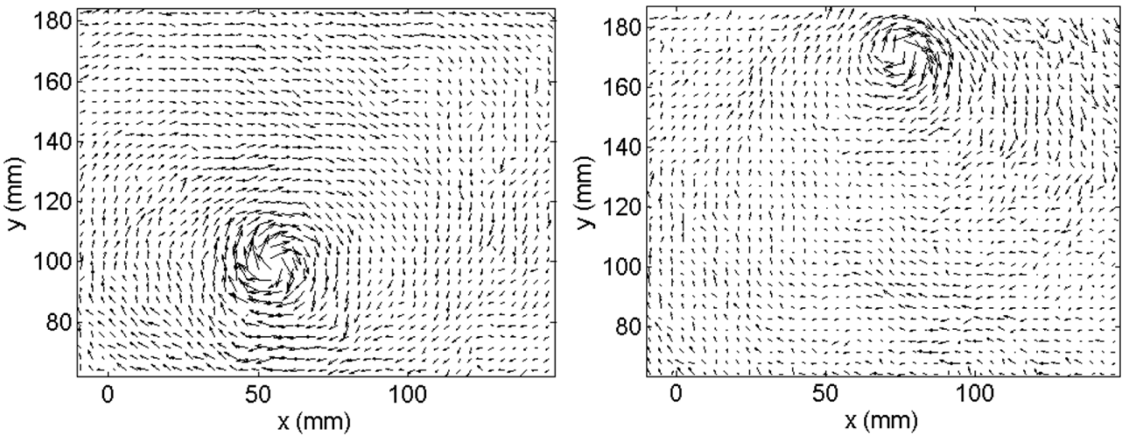

Fig. 6.10 (*left*) Instantaneous velocity vectors for dataset B15, S = 0.0017 vector field number 1 (i = 1) and (*right*) vector field 100 (i = 100).

as R^2 but in this work is referred to as R_D^2 to avoid confusion with the vortex radius R).

6.2.4 Vortex Spatial Stability

The spatial stability of a vortex is an important property of vortex flow. For different applications a vortex that is spatially unstable, i.e. the vortex centre precesses a large amount may be required where other applications require a highly stable vortex that has little precession (vortex centre remains very close to the mean vortex location). An example of vortex precession is shown in Figure 6.10 where it can be seen that for two instantaneous sets of velocity vectors the instantaneous vortex is located at two very different locations within the measurement field. In this work the spatial stability of a vortex, 'vortex spread' is quantified by analysing the statistics of the instantaneous vortex core locations. Here 'vortex spread', σ_c, for a particular flow configuration is defined as the standard deviation (non-gaussian) of the distance of individual vortices from the ensemble average vortex core location. The distance of an instantaneous vortex core, (x_{c_i}, y_{c_i}) from the ensemble average vortex core location $(\overline{x}_c, \overline{y}_c)$ is defined as:

$$d_{c_i} = \sqrt{(x_{c_i} - \overline{x}_c)^2 + (y_{c_i} - \overline{y}_c)^2} \tag{6.9}$$

The standard deviation of d_c, σ_c is then calculated giving a measure of the degree to which the core location deviates from the mean core location thus quantifying 'vortex spread'. Larger values of σ_c indicate that individual vortices are located further away from the mean vortex location suggesting there is more precession (less spatial stability) in the flow whereas low values suggest the instantaneous location of the vortex core is always close to the mean core location and hence indicating low levels of vortex precession (greater vortex spatial stability).

For each instantaneous velocity field with Cartesian vector components $u_i(x,y)$ and $v_i(x,y)$ it is required to find the instantaneous vortex core (x_{c_i}, y_{c_i}) as this precesses around the measurement region through the process of vortex wandering. The vortex identification scheme employed in

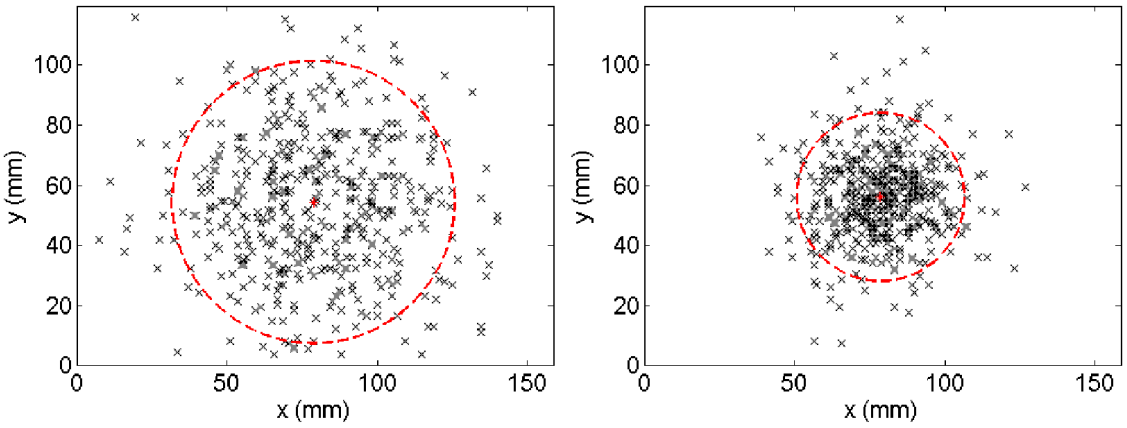

A20, S = 0.0041, σ_c = 14.14mm **A30, S = 0.037, σ_c = 9.89mm**

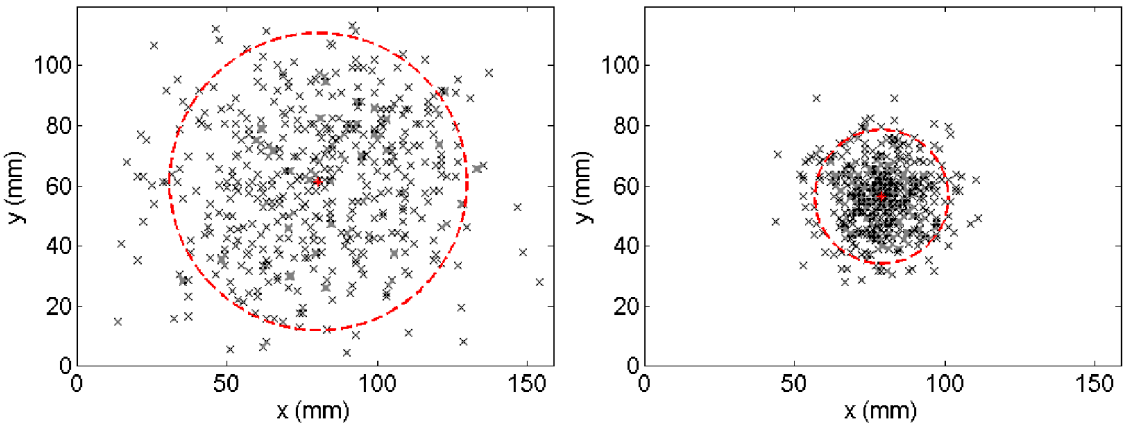

B15, S = 0.0017, σ_c = 14.94mm **B30, S = 0.098, σ_c = 7.50mm**

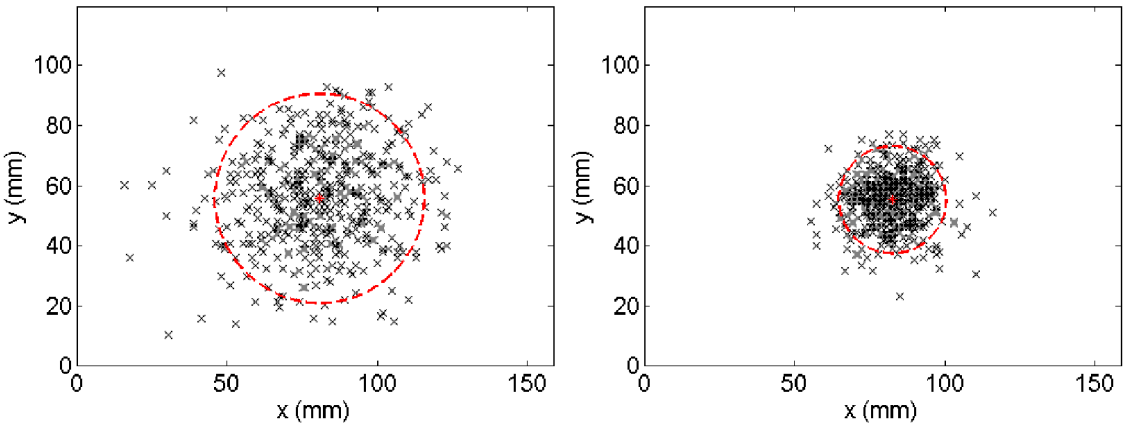

C15, S = 0.115, σ_c = 11.69mm **C30, S = 0.330, σ_c = 5.97mm**

Fig. 6.11 Instantaneous vortex centre plots for axial fan configurations A-C. Red circles are centred on the mean vortex core location and have radius $2\sigma_c$.

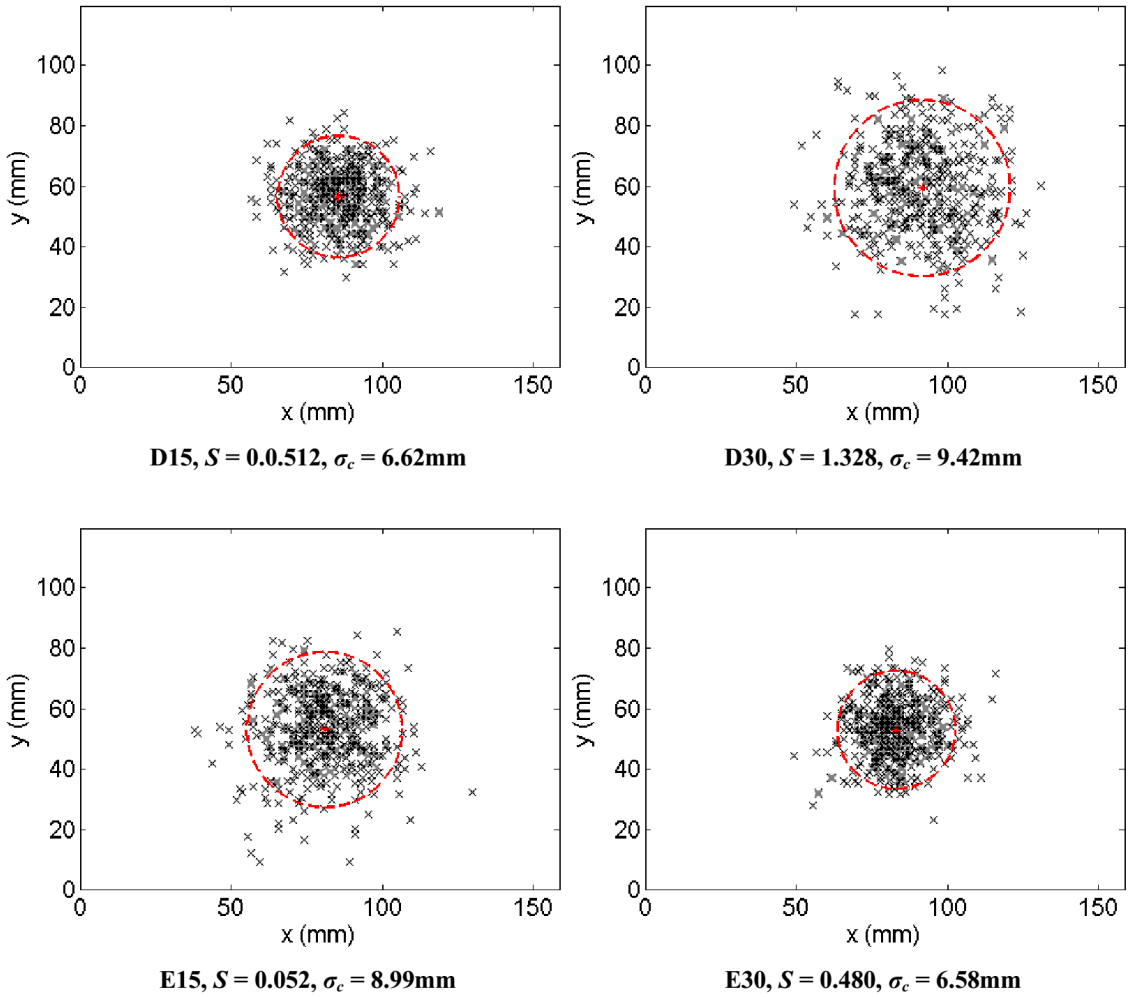

Fig. 6.12 Instantaneous vortex centre plots for axial fan configurations D and E. Red circles are centred on the mean vortex core location and have radius $2\sigma_c$.

this study is the Graftieaux et al. (2001) Γ_1 function (see § 2.50) defined as:

$$\Gamma_1(P) = \frac{1}{S_D} \int_{M \in S_D} \frac{(\overrightarrow{PM} \wedge \mathbf{u}_M) \cdot \hat{z}}{\left\| \overrightarrow{PM} \cdot \mathbf{u}_M \right\|} \mathrm{d}S_D \tag{6.10}$$

Γ_1 is calculated at all vector grid locations in the measurement plane (x, y) and gives a maxima or minima approaching 1 or -1 depending on the direction of rotation, in this case only the main instantaneous vortex core location is required so a large domain, S_D may be used and it is the maxima of $|\Gamma_1|$ that gives the instantaneous vortex core location. For each fan configuration the size of the vortex changes and hence the domain size S_D was varied so that each vortex in each set was identified. For each flow configuration the filter size used in the identification algorithm, the threshold above which vortex centres were identified and the number of vortex cores identifies, N_{Γ_1} for each flow configuration are displayed in Table 6.2. The filter size S_D was varied for each flow configuration due to the changing physical extent of the main vortex core, hence a smaller filter size is used a low swirl ratios (small radius main vortices) and large filter size used for high swirl ratios. The threshold, ε_Γ was also adjusted to give at least one vortex core in the majority of instantaneous vector fields. In some cases, mainly at low swirl ratio, where spatial spread of

Table 6.2 Vortex detection algorithm parameters for each flow configuration

Flow Configuration	Filter Size, S_D	Threshold, ε_{Γ_1}	No. of Cores Detected, N_{Γ_1}
A20	9	0.75	494
A25	11	0.75	498
A30	11	0.75	500
B15	9	0.75	486
B20	9	0.87	496
B25	17	0.85	500
B30	21	0.84	499
C15	17	0.82	496
C20	25	0.82	500
C22.5	25	0.82	499
C25	31	0.8	497
C30	31	0.8	500
D15	35	0.7	500
D22.5	35	0.7	499
D30	35	0.7	499
E15	21	0.82	499
E20	25	0.82	499
E25	31	0.8	499
E30	31	0.8	498

vortices is large some instantaneous vortices were unable to be detected due to residing on the edge of the measurement domain.

Instantaneous vortex core location plots corresponding to the maxima of $|\Gamma_1|$ for different flow configurations are shown in Figure 6.11 and Figure 6.12 with the red circles centred on the mean vortex core location and having a diameter of $2\sigma_c$. In instances where multiple vortices are identified in the instantaneous velocity vectors the main vortex is identified as the one with the greatest $|\Gamma_1|$ value. It can be seen that increasing the swirl ratio has the effect of reducing the area over which instantaneous vortex cores are located (denoted by the red circles), this trend is followed up to swirl ratios of approximately 0.5, above this (axial fan configuration D) the value σ_c increases slightly, this is shown more clearly in Figure 6.13 where σ_c is plotted as a function of swirl ratio. At the lowest swirl ratio (B15, S = 0.0017) the highest value for vortex spread, σ_c is found as having a value of 14.94mm, in Figure 6.11 it can be seen that for this flow configuration instantaneous vortex core locations are spread over a large area with a small number located outside of the field of view (see Table 6.2 for numbers of vortices identified in each dataset) showing that spatially the vortex has a low degree of stability and a high degree of precession. As

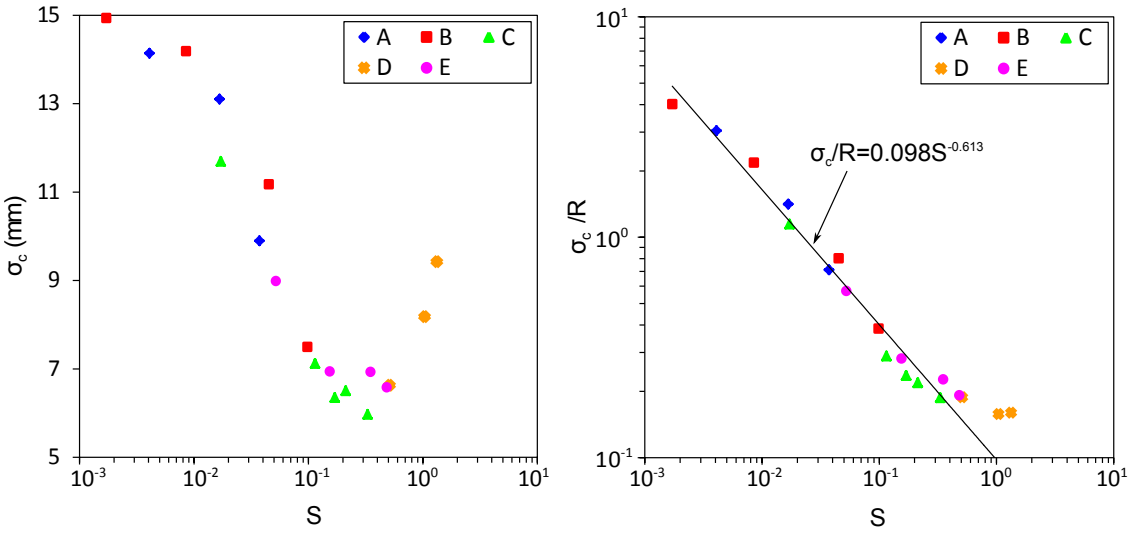

Fig. 6.13 (*left*) Standard deviation of individual vortex distances from mean vortex location for varying swirl ratio and (*right*) normalised by mean vortex radius.

swirl ratio is increased the amount of vortex spread decreases to a minimum of 5.97mm for flow configuration C30, S = 0.330. It can be seen in Figure 6.11 that for this flow configuration all instantaneous vortex core locations are located very close to the mean vortex core location with the vortex displaying high spatial stability and little vortex precession.

It is shown in Figure 6.13 that the amount of vortex spread increases for swirl ratios above approximately 0.35. This can be explained as deviating from the low swirl ratio trend of decreasing vortex spread with increasing swirl ratio by the fact that at higher swirl ratios the size of the vortex is greater. The larger vortices at higher swirl ratios give more variation in location due to the size of the vortex rather than vortex precession as is presented in Figure 6.14 and Figure 6.15 where instantaneous vortex core locations are plotted with the blue dashed circles representing the mean radius of instantaneous vortices centred on the mean instantaneous vortex location. To illustrate this more clearly the vortex spread relative to the size of the vortex (σ_c/R) as a function of swirl ratio is displayed in Figure 6.13. Here it can be clearly seen that the degree of vortex spread relative to the size of the vortex is very closely linked to swirl ratio, when plotted on a log-log graph the straight line trend indicates that (σ_c/R) is related to swirl ratio by a power law relationship. Using regression methods the relationship between (σ_c/R) and swirl ratio was found to be:

$$\left(\frac{\sigma_c}{R}\right) = 0.098S^{-0.613} \tag{6.11}$$

The coefficient of determination, R_D^2 for the data fitting the relationship in (6.11) is 0.977 showing that the data fits very closely. The two data points for $S = 1.039$ (D22.5) and $S = 1.328$ (D30) were not included in calculating the regression as these do not seem to fit the trend of the data for swirl ratio less than 1 indicating that there is a change in the flow regime when swirl ratio exceeds 1.

The graph presented in Figure 6.16 shows the radius of the vortex present in the mean flow vector fields, R_a (averaged over the instantaneous PIV data which includes vortex precession) as a function of swirl ratio, the data shows that the radius of the mean flow vortex is at its highest at

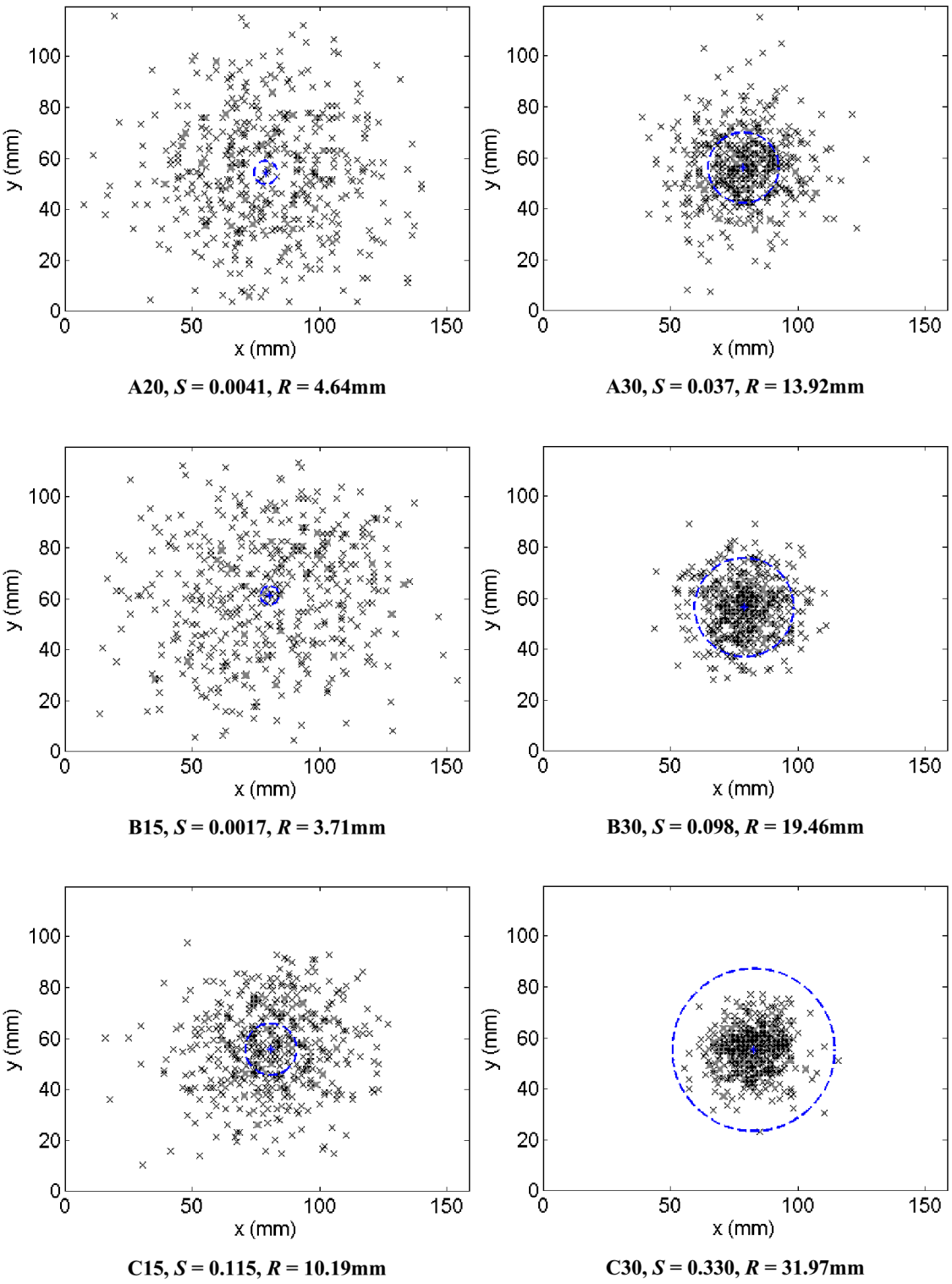

A20, S = 0.0041, R = 4.64mm **A30, S = 0.037, R = 13.92mm**

B15, S = 0.0017, R = 3.71mm **B30, S = 0.098, R = 19.46mm**

C15, S = 0.115, R = 10.19mm **C30, S = 0.330, R = 31.97mm**

Fig. 6.14 Instantaneous vortex centre plots for axial fan configurations A-C. Blue circles are centred on the mean vortex core location and have radius R.

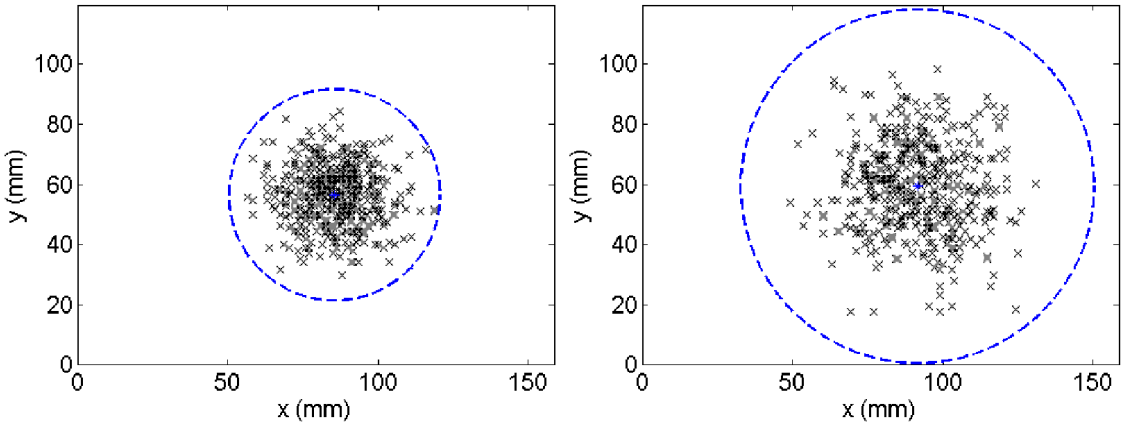

D15, S = 0.0.512, R = 35.22mm **D30, S = 1.328, R = 58.86mm**

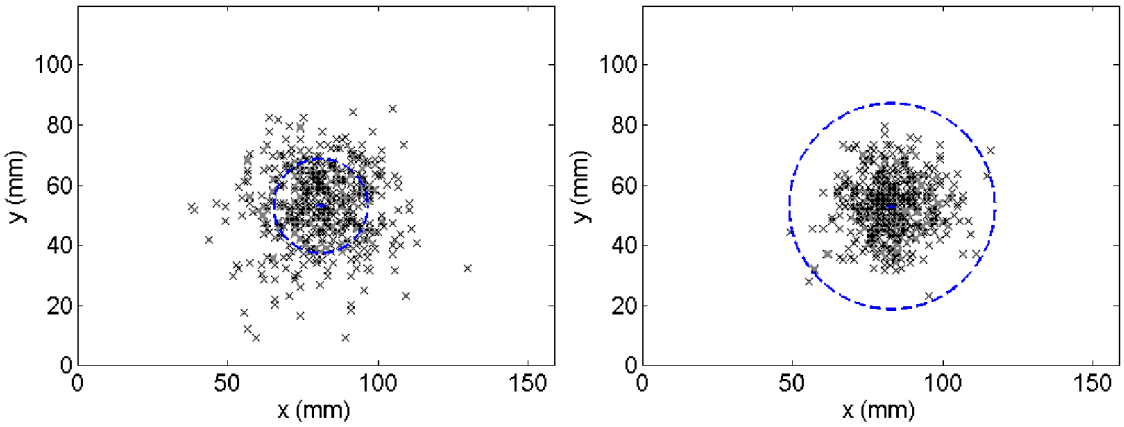

E15, S = 0.052, R = 15.75mm **E30, S = 0.480, R = 34.29mm**

Fig. 6.15 Instantaneous vortex centre plots for axial fan configurations D and E. Blue circles are centred on the mean vortex core location and have radius R.

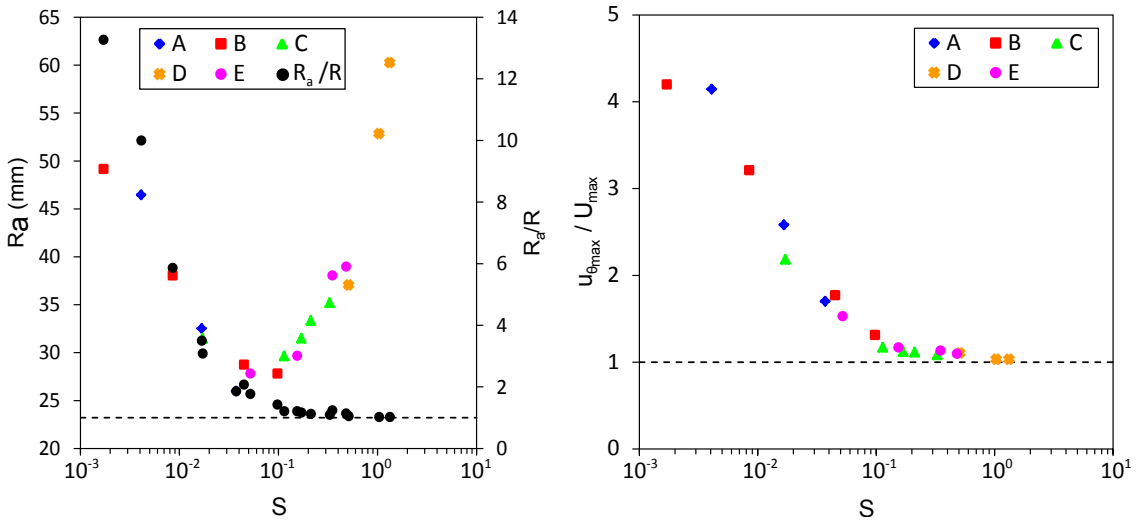

Fig. 6.16 (*left*) Mean flow vortex radius, R_a against swirl ratio, S and ratio of mean flow vortex to mean instantaneous vortex radii (R_a/R) against swirl ratio and (*right*) ratio of maximum mean field vortex speed to maximum tangential velocity of centred velocity vectors for varying swirl ratio.

either limit of the measured range of swirl ratios with a minimum between approximate swirl ratios of 0.04 – 0.1. Also plotted on the graph is the ratio of the mean flow vortex radius and vortex radius with the effects of precession removed, R_a/R (as R is determined from the average instantaneous vortex radius without the effects of precession). At low swirl ratio the mean flow vortex radius is much greater than the radius of the instantaneous vortices which contribute to the mean flow. At the minimum swirl ratio of 0.0017 the mean flow vortex radius is 13.27 times greater than the instantaneous vortex radius suggesting that the structure of the mean flow field is dominated by the effect of the precession of instantaneous vortices at low swirl ratio. The ratio R_a/R continues to decrease with increasing swirl ratio meaning that at higher swirl ratio the structure of the mean flow field more closely represents that of the instantaneous flow field, at a swirl ratio of 0.1 (the value above which R_a begins to increase from the minimum region) the ratio R_a/R is 1.4 which is much smaller than at lower swirl ratios. R_a/R continues to approach a value of 1 as swirl ratio increases further, by swirl ratio 0.15 R_a/R is equal to 1.21 and for the two highest measured swirl ratios, 1.039 and 1.328 the ratio R_a/R is 1.02 highlighting that the size of the mean flow vortex is almost identical to the instantaneous vortices and that precession of the vortex plays little part in the formation of the mean flow field.

Figure 6.16 also shows the ratio of $u_{\theta_{max}}/\overline{U}_{max}$ where $\overline{U}_{max}$ is the absolute maximum speed of the mean flow field vortex (measured at the azimuthally averaged distance R_a from the mean flow field vortex centre) and $u_{\theta_{max}}$ the tangential velocity measured at the radius, R of velocity vectors with the effects of precession removed. At low swirl ratio $u_{\theta_{max}}/\overline{U}_{max}$ is high, with a value of 4.20 at a swirl ratio of 0.0017 showing that the velocities present in the instantaneous vortices are much higher than those depicted in the mean flow field. It is the effects of vortex precession that reduce, through averaging, the velocities measured in the mean flow field. The value of $u_{\theta_{max}}/\overline{U}_{max}$ continues to decrease with increasing swirl ratio, very much in the fashion of R_a/R, approaching

1 at high swirl ratio. At the highest measured swirl ratio of 1.328 $u_{\theta_{max}}/\overline{U}_{max}$ has a value of 1.03, comparing this with a R_a/R value of 1.02 at the same swirl ratio it can be seen that the mean flow vortex is very representative of the instantaneous vortices present in the raw PIV data.

It is shown in Figure 6.13, as previously discussed that the extent of vortex precession with respect to instantaneous vortex size, σ_c/R decreases with increasing swirl ratio, when combining this with the data presented in Figure 6.16 it can be seen that there is a critical region, between swirl ratio of 0.04 and 0.1 where the mean flow field undertakes a transition from being dominated by the effect of vortex precession brought about by the lack of vortex spatial stability at low swirl ratios to a mean flow field where the effects of vortex precession on the mean flow field become negligible and the mean flow field very closely represents that of the instantaneous vortices which constitute the mean.

6.2.5 Vortex Structure

Figure 6.17 to Figure 6.20 show examples of instantaneous velocity fields for varying swirl ratios, streamlines are overlaid to enhance visualisation of the vortex structure. It is clear to see that with increasing swirl ratio the size of the vortex increases but so does the internal structure of the vortex.

It can clearly be seen that the structure of the vortex varies with swirl ratio, at a very low swirl ratio of 0.0041 for configuration A20, presented in Figure 6.17, it can be seen that the structure of the vortex can be split into two regions, there is a small, tight vortex core where the flow is very uniform around the vortex centre and then further away from the vortex centre the flow becomes more disorganised. Increasing swirl ratio it can be seen that the structure of the vortex remains similar at a swirl ratio of 0.33 (flow configuration C30, Figure 6.18) only with larger vortex radius. The flow remains highly organised as a vortex. At swirl ratios greater than unity, where radial momentum becomes more dominant than axial momentum as in Equation (6.3), the structure of the vortex changes as can be seen in Figure 6.19 ($S = 1.04$) and Figure 6.20 ($S = 1.33$). No longer is the vortex a single well-formed vortex but it has secondary smaller vortices which swirl inside of and in the same direction of the main vortex. These multicellular vortices were first presented in laboratory generated tornado-like vortices by Ward (1972) and are also reported more recently by Zhang and Sarkar (2012) and confirm that the tornado-vortex generator is capable of generating flows comparable to those presented in the literature.

To conduct meaningful analysis of instantaneous vortex structure and properties the Cartesian velocity vectors with components $u(x,y)$ and $v(x,y)$ need to be converted to cylindrical coordinates with radial and tangential components $u_r(r,\theta)$ and $u_\theta(r,\theta)$ respectively with origin at the instantaneous vortex core location, (x_{c_i}, y_{c_i}) calculated using (2.50). Once the instantaneous vortex core locations are identified the velocity vectors are converted from Cartesian to cylindrical

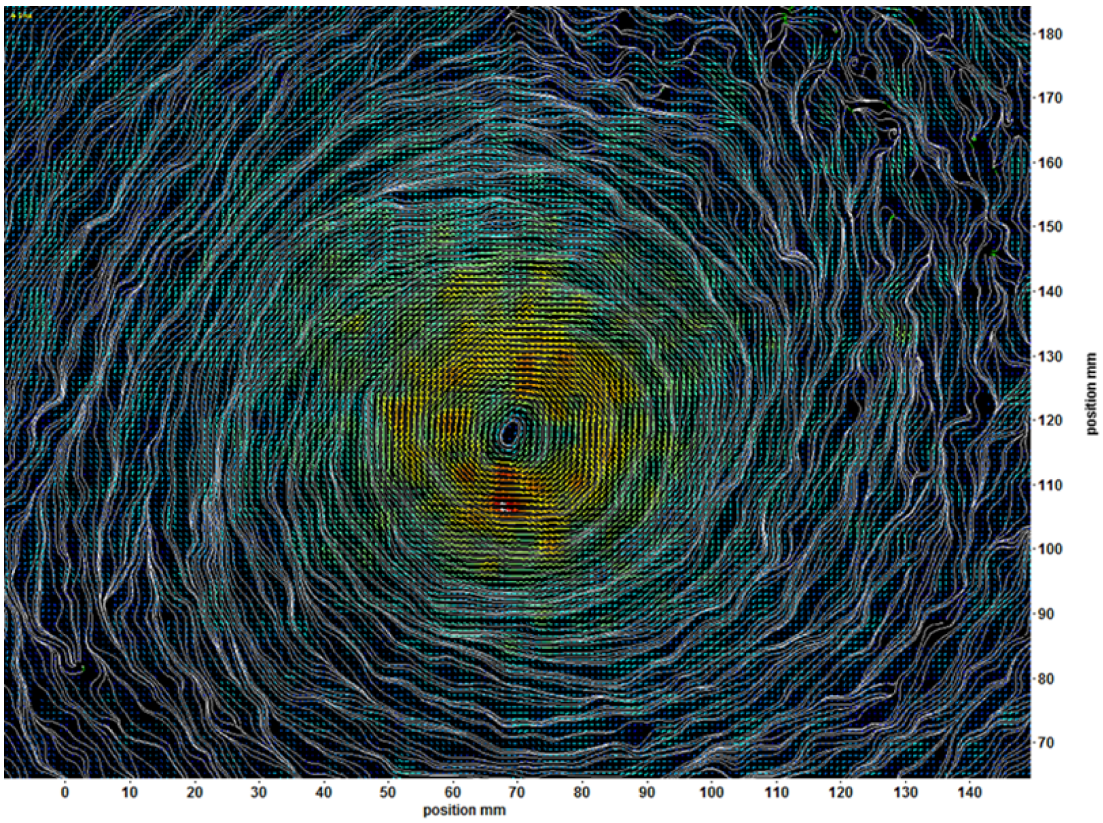

Fig. 6.17 Example of instantaneous velocity vectors for A20, S = 0.0041.

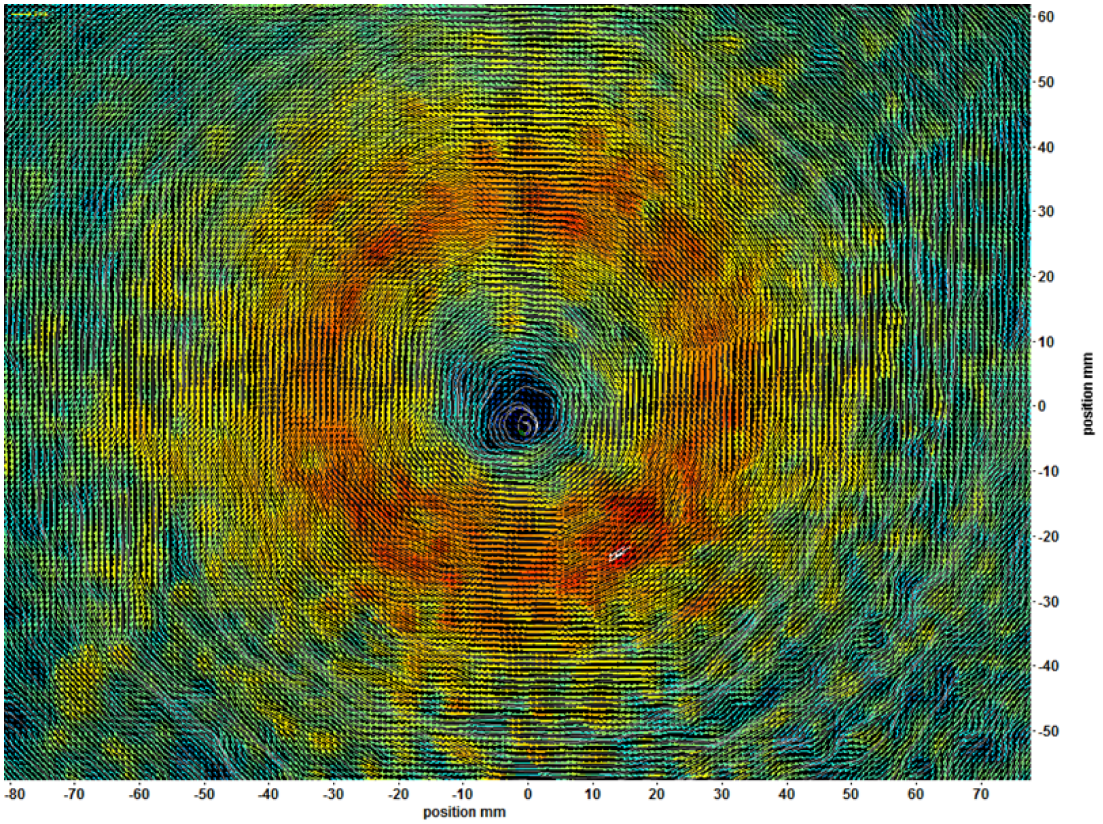

Fig. 6.18 Example of instantaneous velocity vectors for C30, S = 0.330.

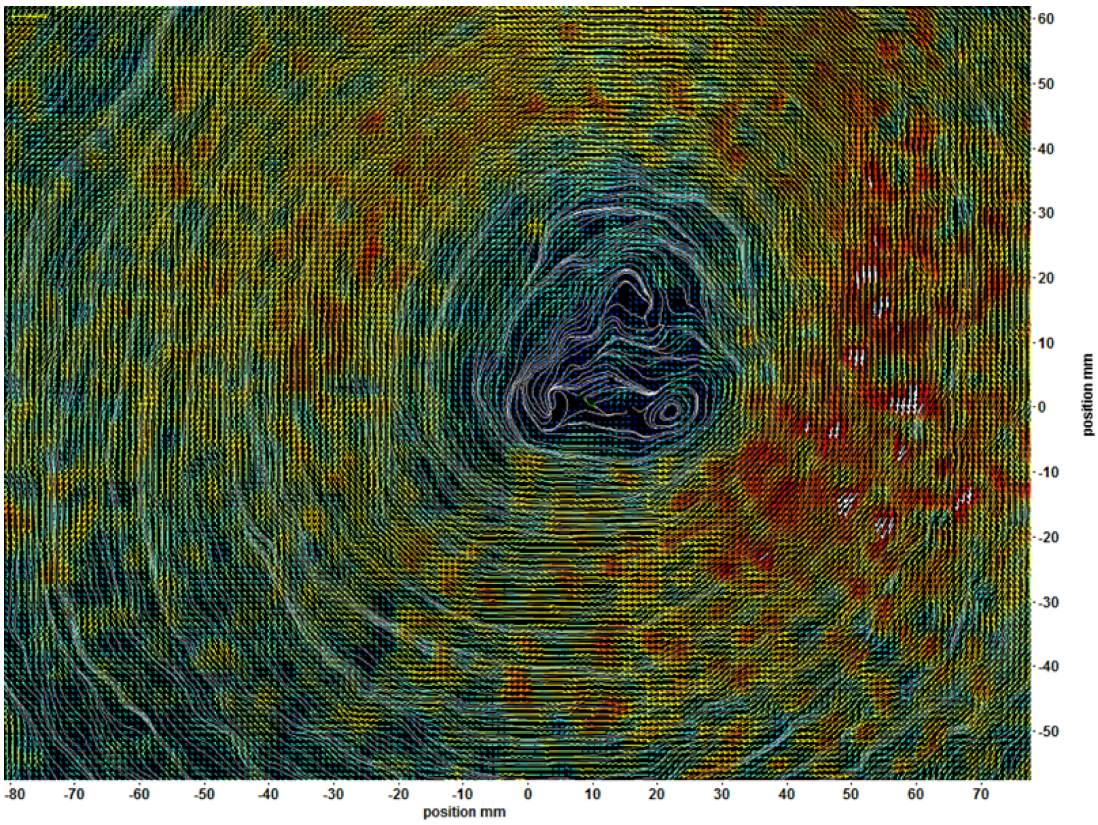

Fig. 6.19 Examples of instantaneous velocity vectors for D22.5, S = 1.039.

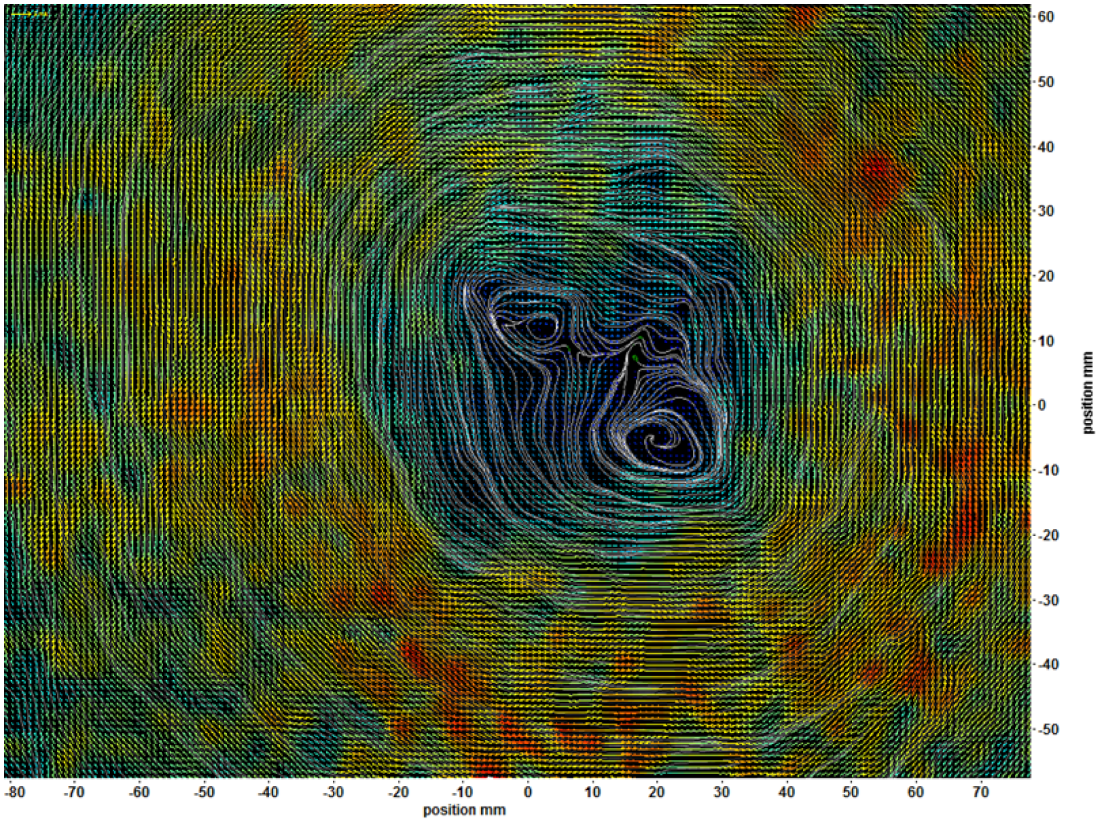

Fig. 6.20 Examples of an instantaneous velocity vectors for D30, S = 1.328.

co-ordinates using the following transformations:

$$u_{\theta_i}(r,\theta) = -u_i \sin\left[\tan^{-1}\left(\frac{y'}{x'}\right)\right] + v_i \cos\left[\tan^{-1}\left(\frac{y'}{x'}\right)\right] \tag{6.12}$$

$$u_{r_i}(r,\theta) = u_i \cos\left[\tan^{-1}\left(\frac{y'}{x'}\right)\right] + v_i \sin\left[\tan^{-1}\left(\frac{y'}{x'}\right)\right] \tag{6.13}$$

Where $x' = x - x_{c_i}$ and $y' = y - y_{c_i}$. From the centred velocity fields azimuthally averaged $u_r(r)$ and $u_\theta(r)$ components are calculated for each radius point from the vortex core, r and it is from these azimuthally averaged profiles that the average vortex radius, R is defined as the radius of maximum tangential velocity, $u_{\theta_{max}}$ and the radius at which circulation for calculating swirl ratio is calculated.

Ensemble averaging after centering each instantaneous velocity vector field for each axial and circumferential flow condition are shown in Figure 6.21 and Figure 6.22 with the background colour indicating velocity magnitude (speed), U. It can clearly be seen that increasing the swirl ratio has the effect of increasing the radius of the vortex as in Figure 6.9.

6.2.6 Comparison of Vortex Structure with an Analytical Oseen Vortex

The vortex tangential velocity profiles, u_θ exhibit the shape of an Oseen vortex. To see how close the averaged velocity profiles fit an Oseen vortex they are plotted next to each other. The Oseen vortex is defined as follows:

$$u_{\theta_{Oseen}}(r,\theta) = \frac{\Gamma}{2\pi r}\left[1 - \exp\left(\frac{-\gamma r^2}{4\nu}\right)\right] \tag{6.14}$$

$$u_{r_{Oseen}}(r,\theta) = 0 \tag{6.15}$$

where Γ is circulation, ν is viscosity and γ a variable governing the size of the vortex. As $u_{\theta_{Oseen}}$ is a function of r and all other parameters act as a scaling with $\Gamma/2\pi$ controlling the velocity magnitude and $-\gamma/4\nu$ controlling the vortex size (6.14) can be rewritten as:

$$u_{\theta_{Oseen}}(r) = \frac{\alpha_v}{r}\left[1 - \exp\left(-\beta_v r^2\right)\right] \tag{6.16}$$

with $\alpha_v = \Gamma/2\pi$ and $\beta_v = \gamma/4\nu$. Fitting the vortex then becomes a question of finding the value β_v which best gives the maximum tangential velocity at the same radius of the azimuthally averaged PIV velocity fields and then selecting an α_v value to match up the peak velocity at that radius. The relationship between R_0 and β_v is $R_0 = 1.1209\beta_v^{-0.5}$.

The ensemble average centred velocity vectors shown in Figure 6.21 and Figure 6.22 show absolute measured velocity magnitudes, from these centred vortex velocity vectors the azimuthally averaged velocity profiles are extracted, these profiles are then normalised by the maximum tangential velocity, $u_{\theta_{max}}$ located at the vortex radius, R. These normalised velocity profiles are pre-

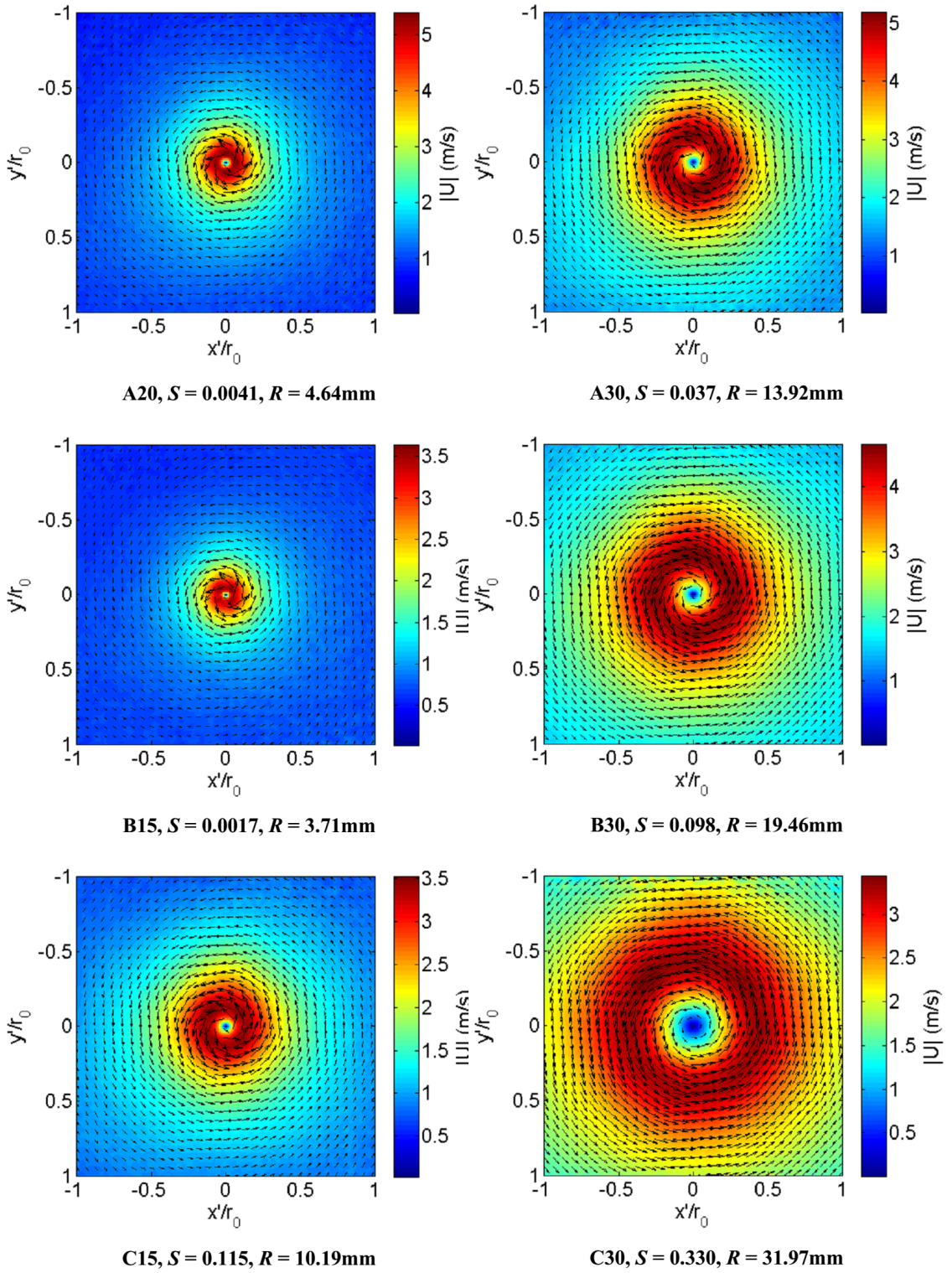

Fig. 6.21 Time average velocity vectors for centred vortices for axial fan settings A-C. Every fourth vector shown for clarity.

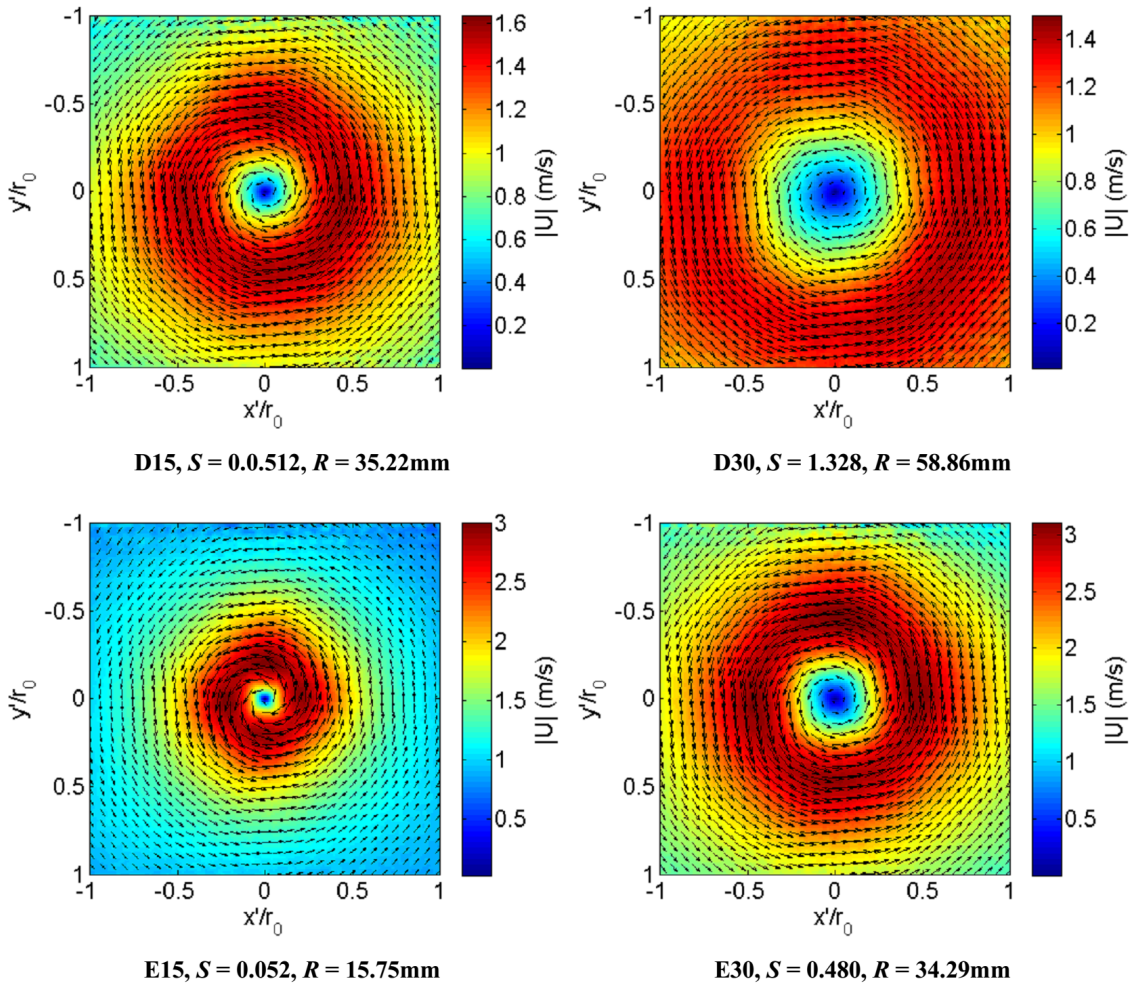

Fig. 6.22 Time average velocity vectors for centred vortices for axial fan settings D and E. Every fourth vector shown for clarity.

sented in Figure 6.23 as a function of the radial distance, r from the vortex centre normalised by the vortex radius R. Also shown as a solid black line is an analytical Oseen vortex velocity profile as previously discussed.

It is apparent from the velocity profile plots that the PIV measured vortices fit very closely to the analytical Oseen vortex in the main vortex region (see Figure 6.23). At lower swirl ratios (axial fan settings A-C) it can be seen that the measured data deviates from the model the further away from the vortex core it is measured. For each fan configuration A-C the measured data fits closer to the model as the circulation is increased (thereby increasing the swirl ratio).

The closeness of fit for the measured data to the Oseen model is good with each measured velocity profile closely resembling the shape of the Oseen vortex profile. Figure 6.24 shows the coefficient of determination, R_D^2 between the tangential velocity profile data and the analytical Oseen model, it is apparent that the data fits the model to a higher degree with increasing swirl ratio. This can be quite misleading though as by looking at the velocity profiles in Figure 6.23 it can be seen that the data fits the model most closely in the region around the radius of the vortex core ($r/R = 1$) and deviates more at increasing radius but the radius range over which data is available decreases at higher swirl ratios owing to the increasing radius of the individual vortices.

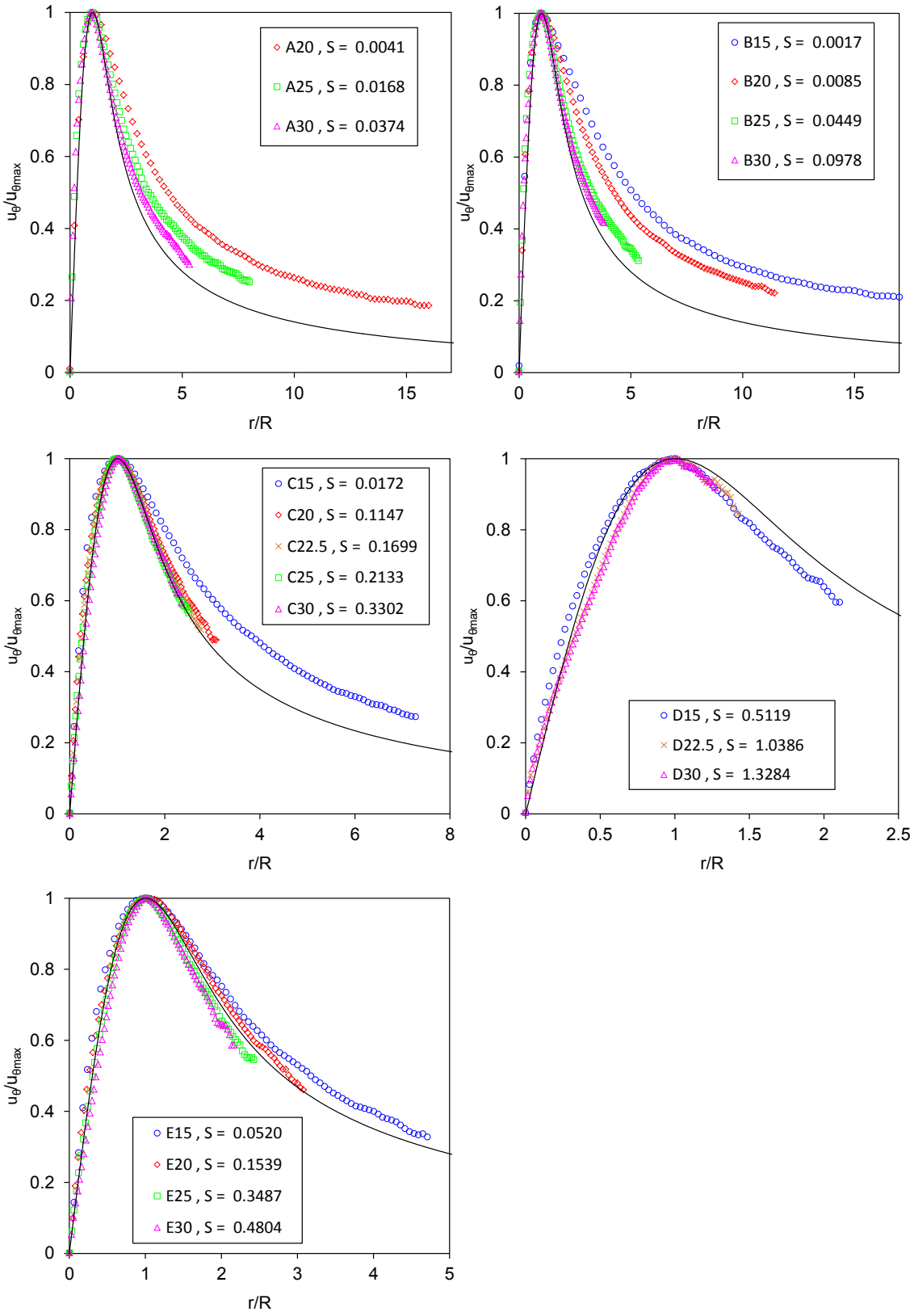

Fig. 6.23 Normalized tangential velocity profiles of ensemble averaged centred instantaneous vortices fitted against an Oseen vortex (black line) for different flow configurations.

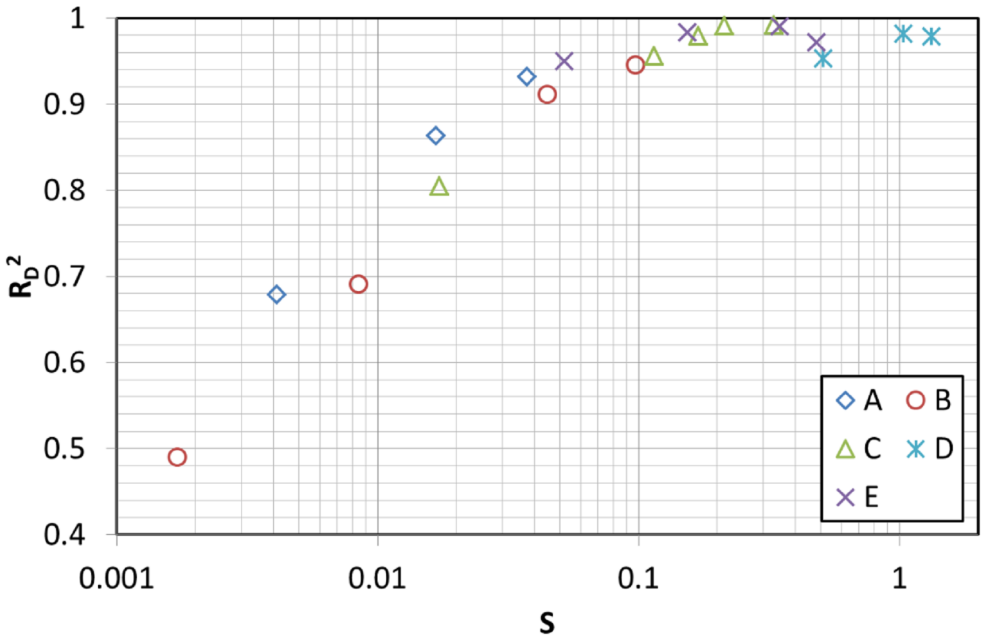

Fig. 6.24 Coefficient of determination against swirl ratio showing the degree to which experimental velocity profile data fits an analytical Oseen model.

To further evaluate the degree to which the measured data fits the Oseen model the fractional error between the measured data and model, ε_{Oseen} was calculated as a function of the radius from the vortex core as follows:

$$\varepsilon_{Oseen}(r) = \frac{\sqrt{(u_{\theta_{Oseen}}(r) - u_\theta(r))^2}}{u_{\theta_{Oseen}}(r)} \tag{6.17}$$

The error plots of ε_{Oseen} shown in Figure 6.25 all show zero error at the vortex radius ($r/R = 1$). This is due to the normalisation of the velocity profiles where $u_\theta/u_{\theta_{max}}$ is equal to one at the vortex radius. In general as the circulation fan speed increases for a fixed axial fan setting the error between the measured and modelled data decreases. Figure 6.26 shows the fractional error, ε_o at a radius of $r/R = 0.5$ (midway between the vortex centre and the radius of the vortex), in this region the PIV data differs from the model by a maximum of 15% at a swirl ratio of 0.017 and the trend of the data shows this decreases with increasing swirl ratio down to a value of 2% at a swirl ratio of 0.213 before increasing again at higher swirl ratios. A similar trend is also shown at a radius of $r/R = 1.5$ where the minimum error between the data and the model is observed at a swirl ratio of 0.33 with a value of 0.2% before increasing at higher swirl ratios. The maximum error at this radius occurs at a swirl ratio of 0.004 with an error value of 8.9%. The magnitude of the errors between the data and the model show that in regions close to the vortex radius the measured tangential velocity profiles more closely fit that of a model Oseen vortex outside the vortex core region at $1.5R$ than at a radius of $0.5R$ which is located inside the vortex core region.

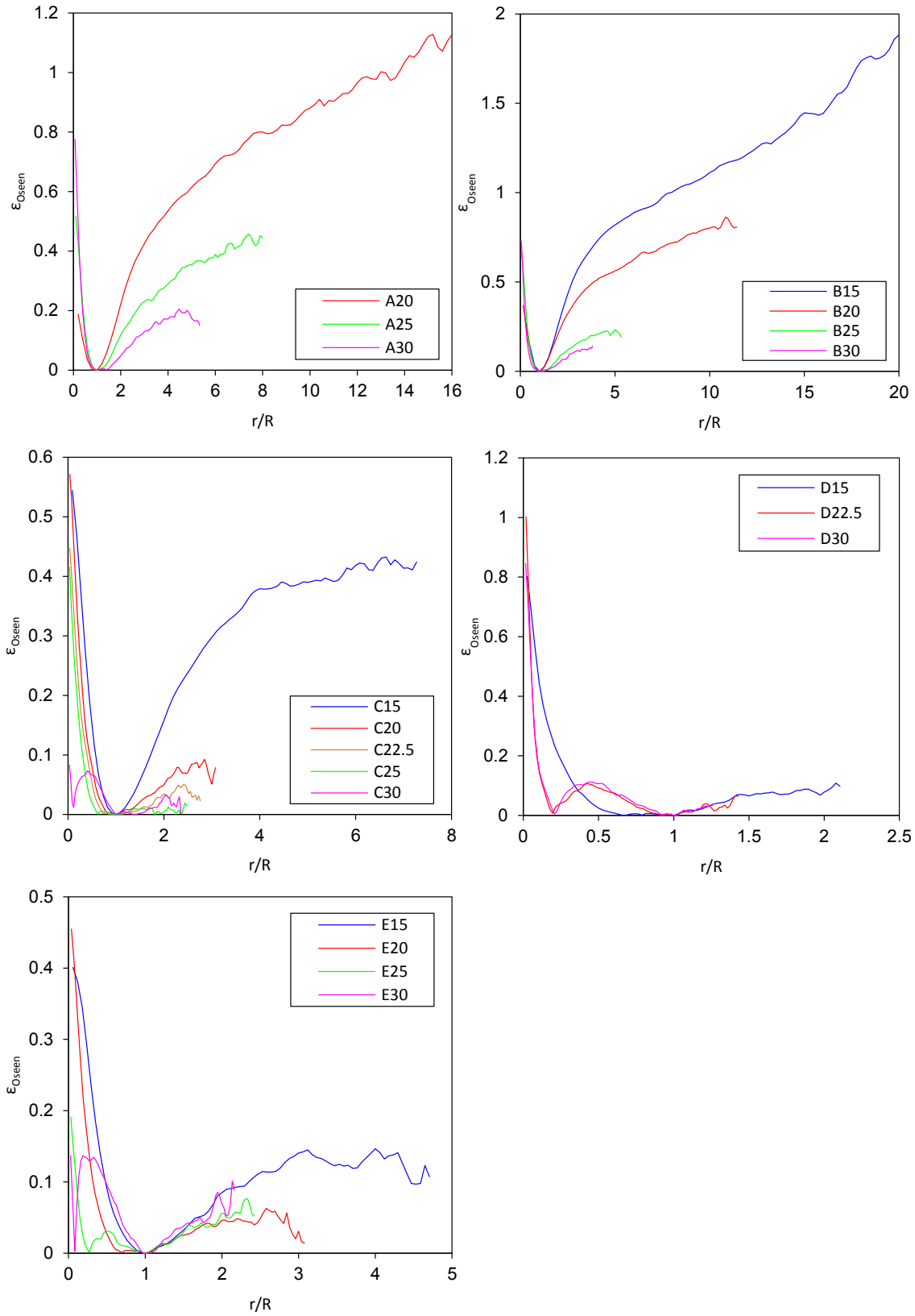

Fig. 6.25 Fractional error ε_{Oseen} between measured velocity profile and Oseen model as a function of normalized radius from the vortex centre.

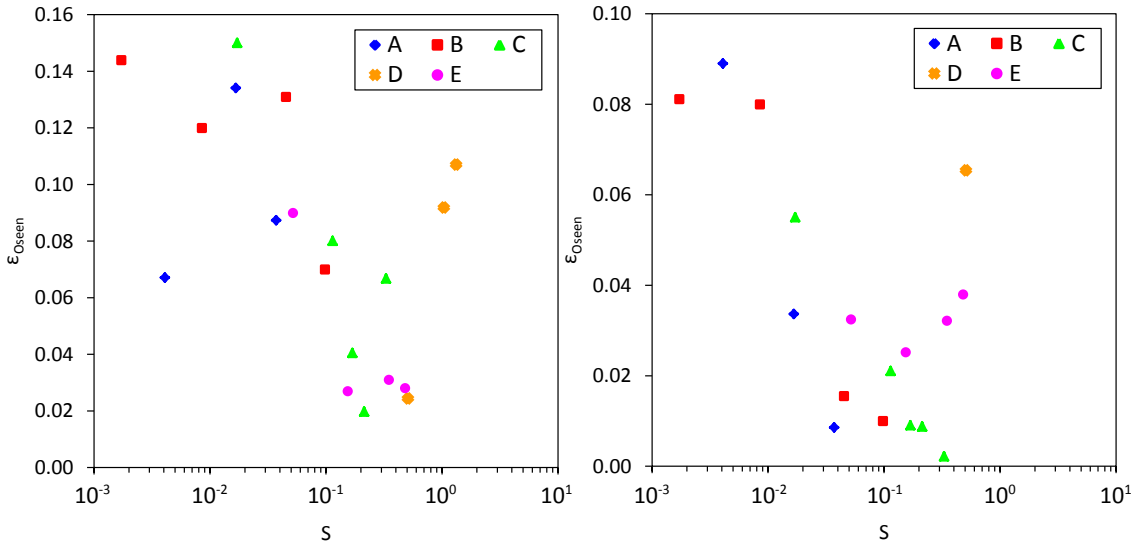

Fig. 6.26 Fractional error ε_{Oseen} between PIV data and Oseen model at a radius (*left*) $r/R = 0.5$ and (*right*) $r/R = 1.5$.

6.2.7 Velocity Variance

Velocity variance (turbulent kinetic energy) was first calculated for the raw data sets, i.e. velocity vectors including the effect of vortex precession. The variance is calculated from the average RMS values of the u' and u' velocity components as follows:

$$k = \frac{1}{2}\left(u_{rms}^2 + v_{rms}^2\right) \tag{6.18}$$

To enable comparison between different flow conditions the turbulence level is normalized by the magnitude of the maximum velocity vector of the mean flow field, $\overline{U}_{max}^2$. Figure 6.27 shows azimuthally averaged plots of $k/\overline{U}_{max}^2$ against radial distance from the mean flow vortex centre. Each turbulence profile shows a maximum value at the mean vortex centre apart from the two highest swirl ratio cases, S = 1.039 and 1.328 which show consistent levels of turbulence from the vortex centre out to a radius of r/R_a of approximately 0.4 before decreasing with increasing radius as with the profiles at lower swirl ratio. The values of $k/\overline{U}_{max}^2$ at the mean flow vortex centre (where peak turbulence occurs) are presented in Figure 6.28 as a function of swirl ratio and generally decrease with increasing swirl ratio. In this presentation of the velocity variance the dominant factor contributing to the turbulence level is the effect of vortex precession. At low swirl ratio vortex precession is high and instantaneous vortices are small meaning that the deviation of instantaneous velocities from the mean flow are much greater than at higher swirl ratios.

Figure 6.29 shows the turbulence characteristics of the vortex flow with the effect of vortex precession removed, removing the effects of vortex precession is beneficial for the analysis of the velocity variance as precession increases the measured variance masking the true turbulence characteristics. The variance for the centered velocity vectors (precession removed) is calculated

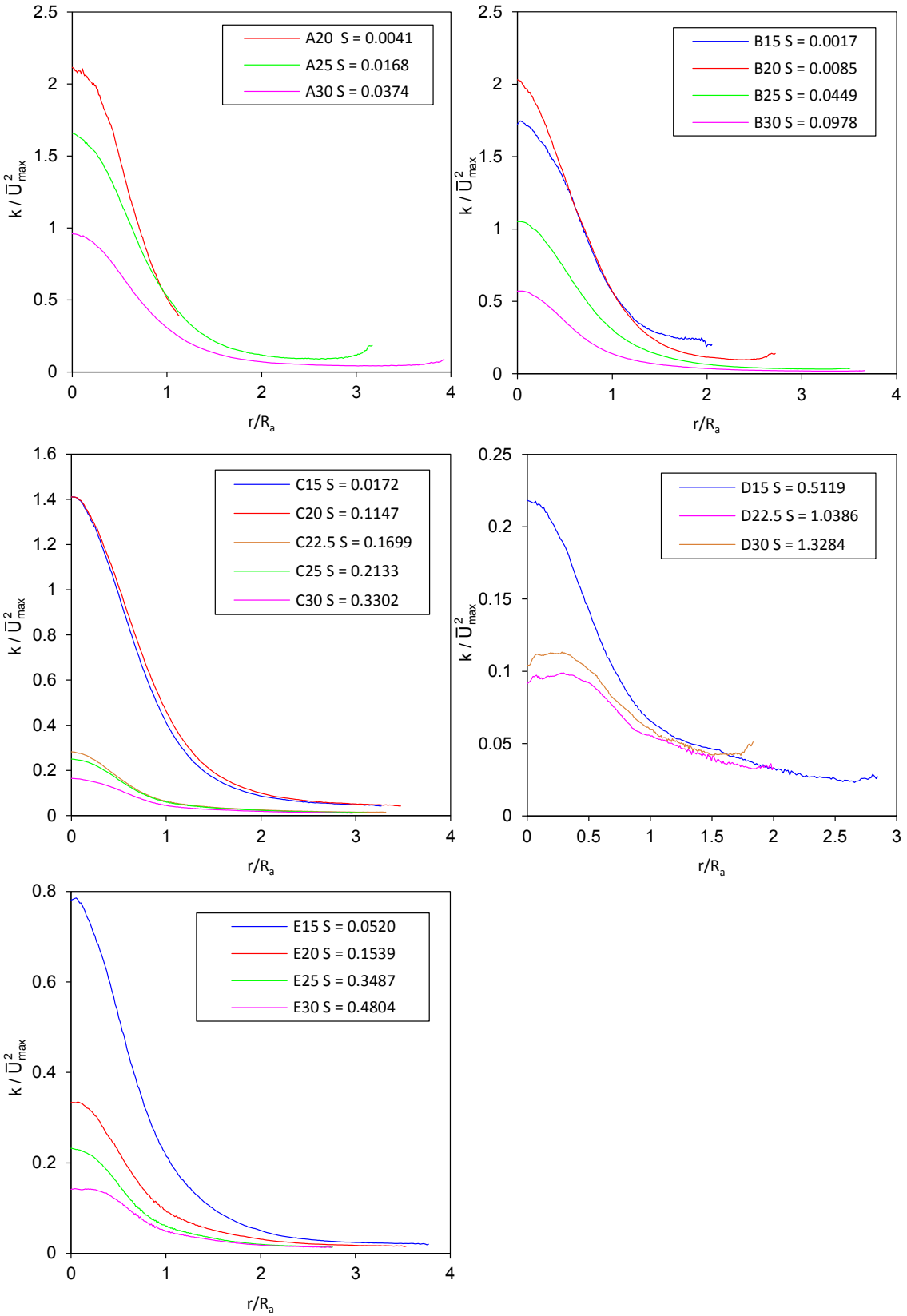

Fig. 6.27 Turbulent kinetic energy, k normalized by mean flow field maximum flow speed $\overline{U}_{max}$ for different flow configurations.

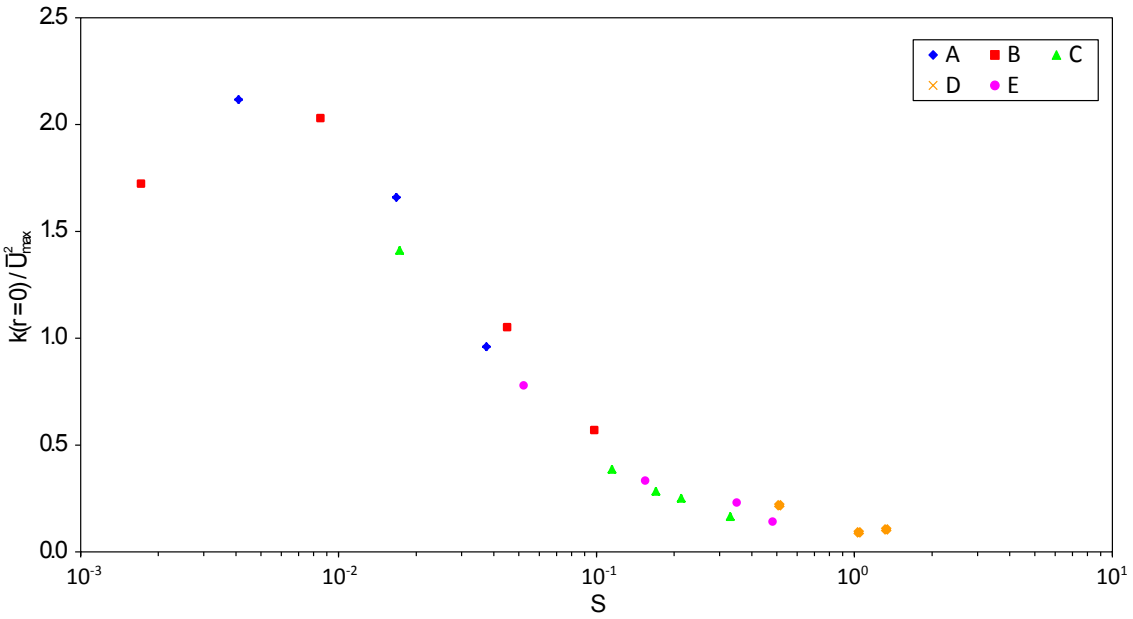

Fig. 6.28 Normalized turbulent kinetic energy at mean flow field swirl centre against swirl ratio.

as the turbulent kinetic energy as follows:

$$k_c = \frac{1}{2}\left(u^2_{\theta_{rms}} + u^2_{r_{rms}}\right) \tag{6.19}$$

The turbulent kinetic energy of the centred velocity vectors is then normalized by $u^2_{\theta_{max}}$ to give a non-dimensional measure. The value of $k_c/u^2_{\theta_{max}}$, plotted as a function of the radius from the vortex core can be seen to increase outwards from the vortex centre before reaching a maximum value inside the vortex core region ($r/R < 1$) before decreasing again. Figure 6.30 shows the radius at which $k_c/u^2_{\theta_{max}}$ reaches a maximum as a function of swirl ratio. It can be seen that between swirl ratios of 0.008 and 0.5 the region of maximum turbulence occurs at a radius of between $r/R = 0.40$ and 0.56. For the two lowest swirl ratios the maximum turbulence intensity occurs at a radius of r/R = 1.06 and 0.80 for swirl ratios of 0.0017 and 0.004 respectively, these results are consistent with the findings of Zhang and Sarkar (2012) who show that the radius of maximum turbulence intensity is greater at a lower swirl ratio though they only present data at two swirl ratios so it is not possible to infer if at beyond a certain swirl ratio the radius of maximum turbulence becomes consistent with little dependence on swirl ratio as Figure 6.30 shows.

The peak velocity variance $(k_c/u^2_{\theta_{max}})_{max}$ of the data in Figure 6.29 is presented in Figure 6.31, as with the radius at which maximum turbulence occurs (Figure 6.30) it can be seen that between swirl ratios of 0.008 and 0.5 the peak turbulence level is largely unaffected by swirl ratios with values across multiple datasets of $(k_c/u^2_{\theta_{max}})_{max}$ lying between 0.025 and 0.036. At swirl ratios above 0.5 the turbulence levels jump significantly to values of 0.067 and 0.075 for swirl ratios of 1.039 and 1.328 respectively which are over double the amount of turbulence in the swirl ratio range 0.008 to 0.5. This increase in turbulence level can be attributed to the more complex flow structure of high swirl ratio vortices which include more complex secondary vortices as can be seen in Figure 6.19 and Figure 6.20. At the other end of the swirl ratio scale, at S = 0.0017 the

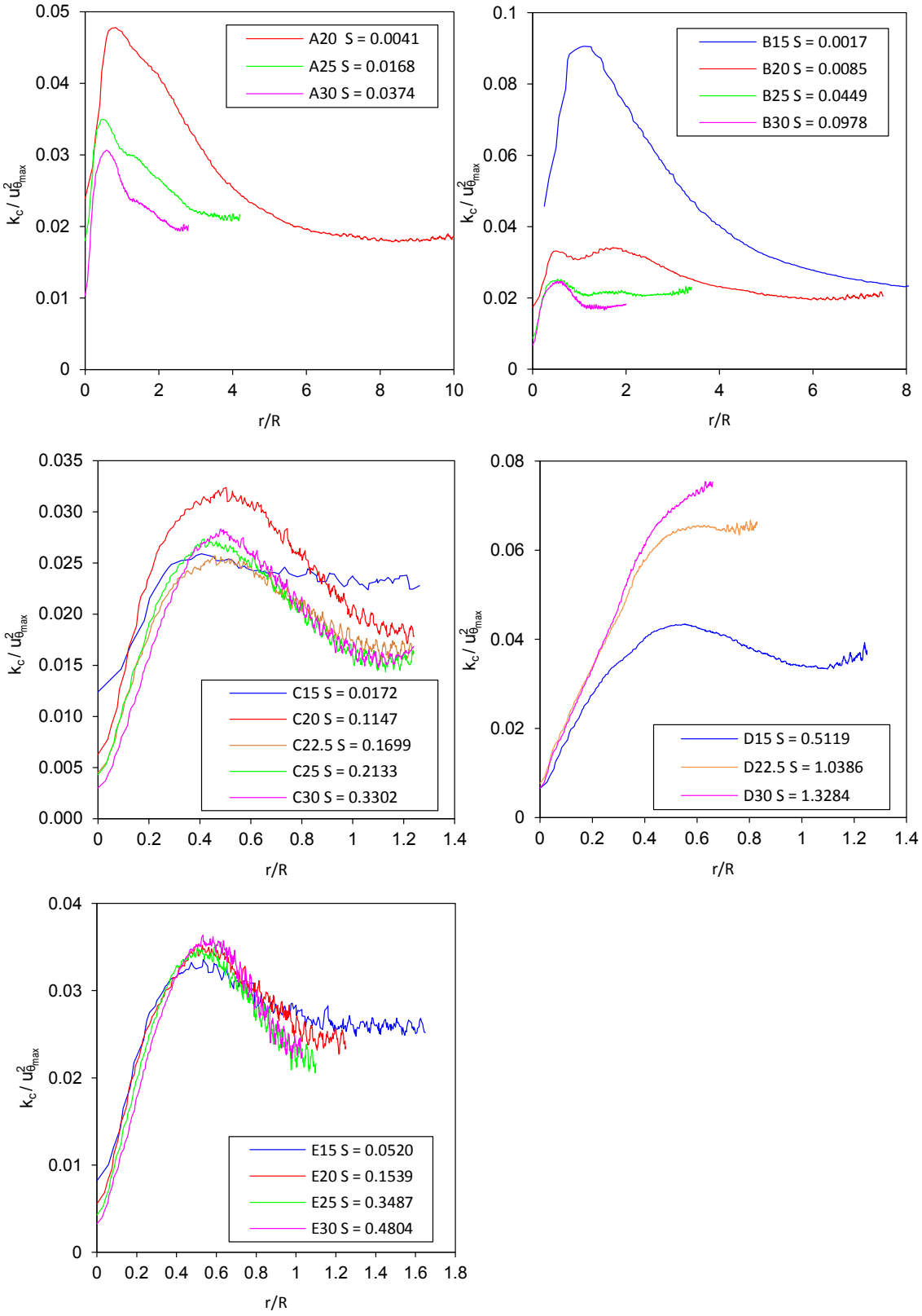

Fig. 6.29 Normalised turbulent kinetic energy profiles with the effect of vortex precession removed.

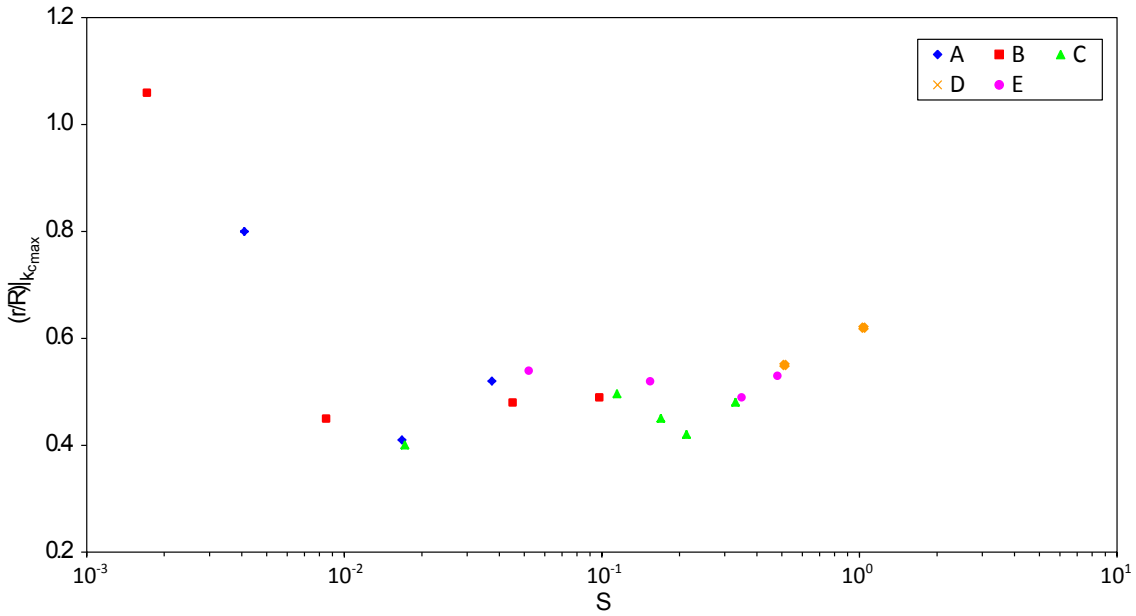

Fig. 6.30 Radius from the vortex centre at which maximum turbulent kinetic occurs for centred velocity vectors.

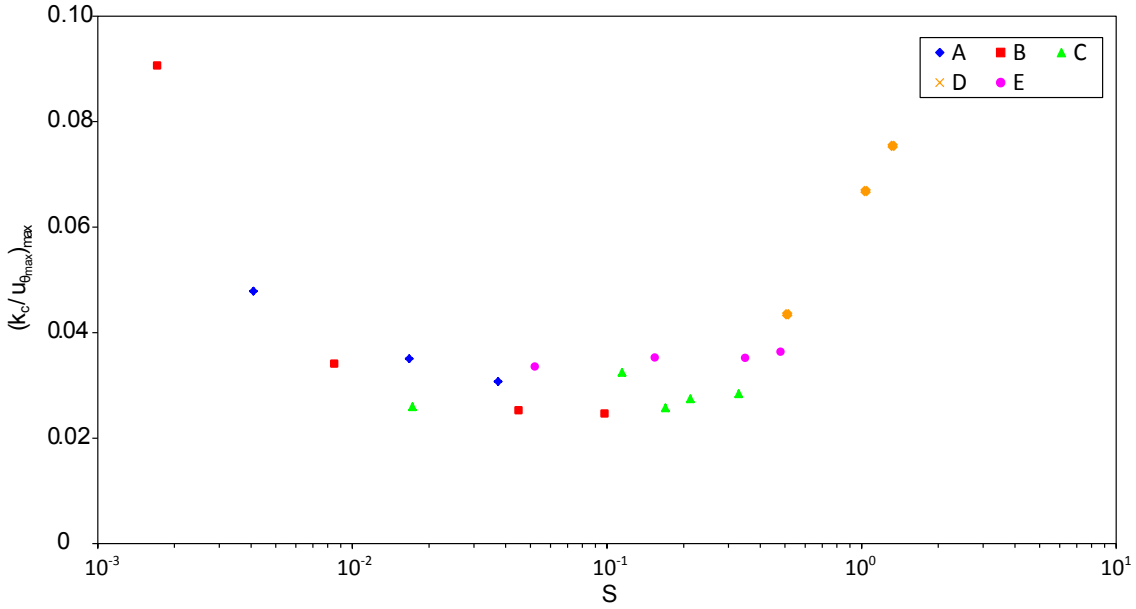

Fig. 6.31 Maximum values of normalised turbulent kinetic energy against swirl ratio for centred velocity vectors.

highest peak turbulence level occurs with a value of 0.090. A contributing factor to this elevated turbulence level could be attributed to the high degree of vortex precession. Instantaneous vortices at this swirl ratio are distributed over a much larger spatial region than at higher swirl ratios which could in turn highlight the different flow conditions due to being close to the circulation pillars or not underneath the updraft orifice which could explain the increased turbulence levels even though the effects of vortex precession are removed.

6.3 Summary

In the work presented in this chapter flow characteristics of a TLV from PIV data are investigated. Through the use of the Grafteaux vortex identification algorithm a robust method of calculating swirl ratio from planar PIV velocity data is presented. This calculated swirl ratio is seen to be a genuine non-dimensional number that characterizes the flow as flows with similar swirl ratios but different axial and circumferential flow rates are seen to be similar.

From the time averaged vortex velocity data it is shown, in agreement with previous literature that the radius of instantaneous vortices increases with increasing swirl ratio. It is show that over the full range of swirl ratios investigated the mean radius of instantaneous vortices follows a strict power law relationship with swirl ratio and is proportional to $S^{0.417}$. The power law relationship between swirl ratio and vortex radius, to the knowledge of the author has not been presented previously.

It is show that over the range of swirl ratios investigated there are three distinct flow regimes:

1. At low swirl ratio $(S < 0.008)$ the flow is dominated by the precession of a small radius single-celled vortex.

2. At intermediate swirl $(0.008 < S < 0.5)$ some vortex precession is evident at the lower swirl end $(0.008 < S < 0.08)$. In this intermediate swirl range, as with the low swirl range the vortex remains single celled in structure.

3. At high swirl ratio $(S > 0.5)$ the effects of vortex precession are minimal with the size of instantaneous vortices approximately equal to that of the mean flow vortex. In this swirl range it is shown that the vortex has a tendency to go multi-cellular with instantaneous double and triple-celled vortices present.

The differentiation between the three aforementioned flow regimes is highlighted through two means; the spread of the instantaneous vortex core centres and the ratio of instantaneous vortex core radius and mean flow vortex radius.

It is shown that the degree of spread of instantaneous vortex cores relative to the mean instantaneous vortex radius decreases with increasing swirl ratio with a tight power law relationship. At low swirl ratios the flow consists of small radius instantaneous vortices with high precession (low spatial stability) and at high swirl ratios large vortices with little precession relative to the instantaneous vortex radius (high spatial stability).

The difference in flow regime between high and low swirl ratio is also illustrated by comparing instantaneous vortex radii and mean flow vortex radii. At low swirl ratio it is shown that, due to precession, the mean flow vortex radius is between 2 and 14 times that of the instantaneous vortex radius. At high swirl ratio it is shown that the mean flow vortex is much more characteristic of the instantaneous flow vortex as both have radius and maximum velocity equal to within 5%.

Mean instantaneous vortex velocity profiles with the effects of vortex precession removed are

shown to closely resemble an analytic Oseen vortex model with increasing accuracy as swirl ratio is increased.

The turbulence intensity of the flow (with precession) is at a maximum at the mean flow vortex centre and is shown to decrease with increasing swirl ratio and spatially with increasing radius.

With the effects of vortex precession removed it is shown that the highest turbulence levels occur within the vortex core radius ($< R$) except for the very lowest swirl ratio. At low swirl ($S < 0.008$) maximum turbulence occurs close to the vortex radius. At intermediate swirl levels the radius of maximum turbulence is at approximately half the vortex radius before increasing slightly at high swirl ratio ($S > 0.5$).

The results presented in this chapter have led to some new understanding of tornado-like vortex flows and the range of swirl ratios over which measurements were taken is greater than in previous studies. Further understanding of the flow regimes can be garnered by performing a decomposition of the flow which is the subject of the next chapter.

Chapter 7

Proper Orthogonal Decomposition of Low Speed PIV Data

7.1 Introductory Remarks

Using the PIV velocity data obtained from a laboratory generated tornado-like vortex (see Chapter § 6) proper orthogonal decomposition (POD) is applied to generate an understanding of the coherent structures present in the flow. By using POD, coherent structures can be educed and their dynamics as a function of swirl ratio are investigated.

In this study the POD is applied to 500 two-component velocity vector fields for each of the swirl ratio and fan configurations resulting in 19 decompositions in total. The dynamics and influence of the coherent structures are investigated by analysing the POD eigenvalues (modal energy content which is directly related to the turbulent kinetic energy contained within that structure), the eigenfunctions (modes/coherent structures) and the reconstruction coefficients.

Lower order modelling of the flow fields is also investigated using reconstructed velocity vectors from a truncated number of POD modes, the aim of this is to educe as much information as possible regarding the large scale flow dynamics whilst neglecting the unstructured turbulent fluctuations and as a tool for data reduction when investigating large data sets of velocity vectors.

7.2 Convergence of Mode Energy

As detailed in § 3 the eigenvalues, $\lambda^{(n)}$ of the POD are related to the energy associated with the corresponding eigenmode $\phi^{(n)}$. Here the eigenvalues (or mode energy), $\lambda^{(n)}$ are normalised to represent the proportion of the total turbulent kinetic energy contained in the modes as a percentage.

Plots of individual and cumulative mode energy against mode number for increasing swirl ratio, S are displayed in Figure 7.1 and Figure 7.2 respectively. Mode energy against swirl ratio is presented in Figure 7.3 and Figure 7.4 and cumulative mode energy against swirl ratio in Figure 7.5 and Figure 7.6 and both as functions of swirl ratio and mode number in Figure 7.7. The

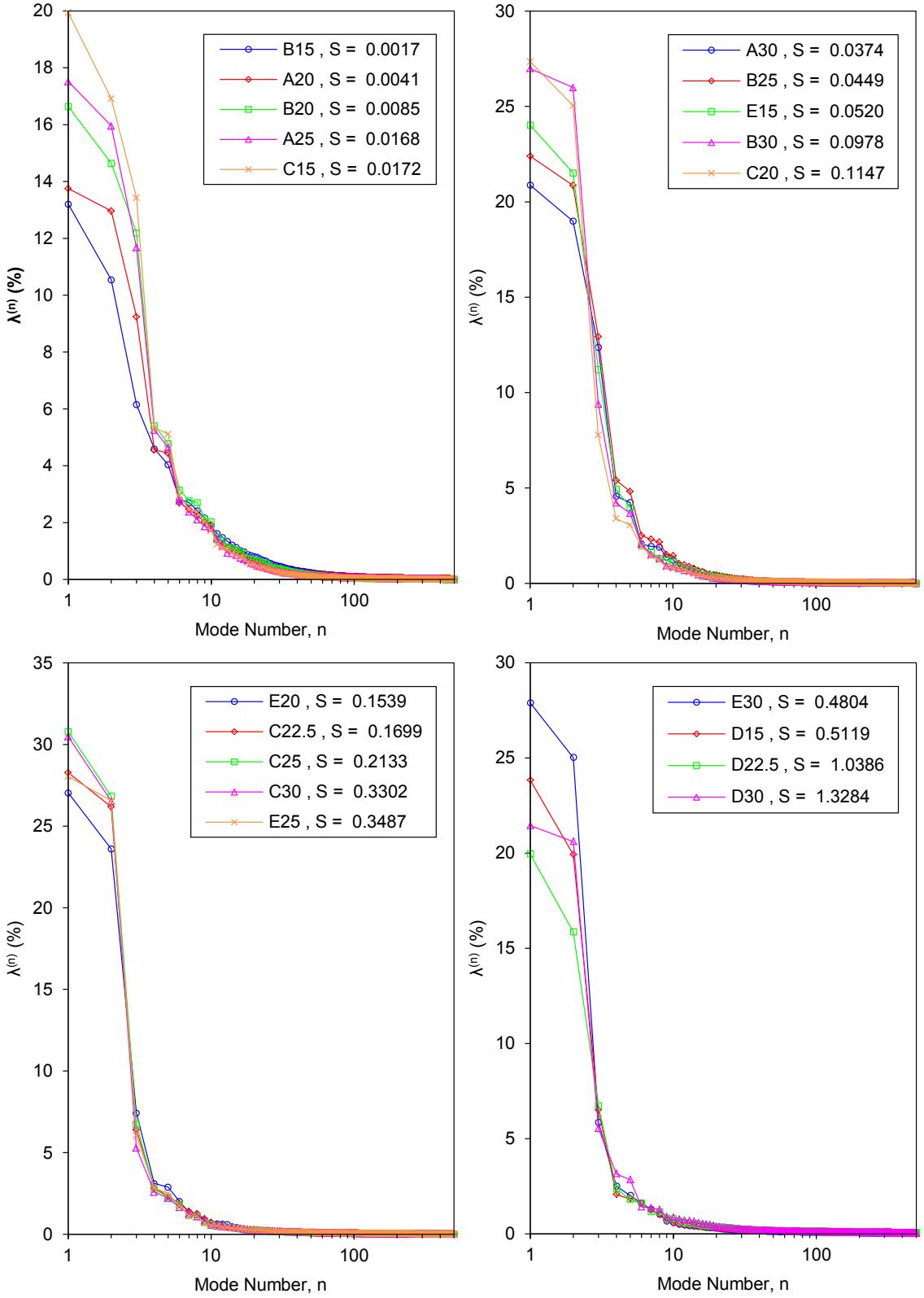

Fig. 7.1 Individual mode energy, $\lambda^{(n)}$ for each flow configuration.

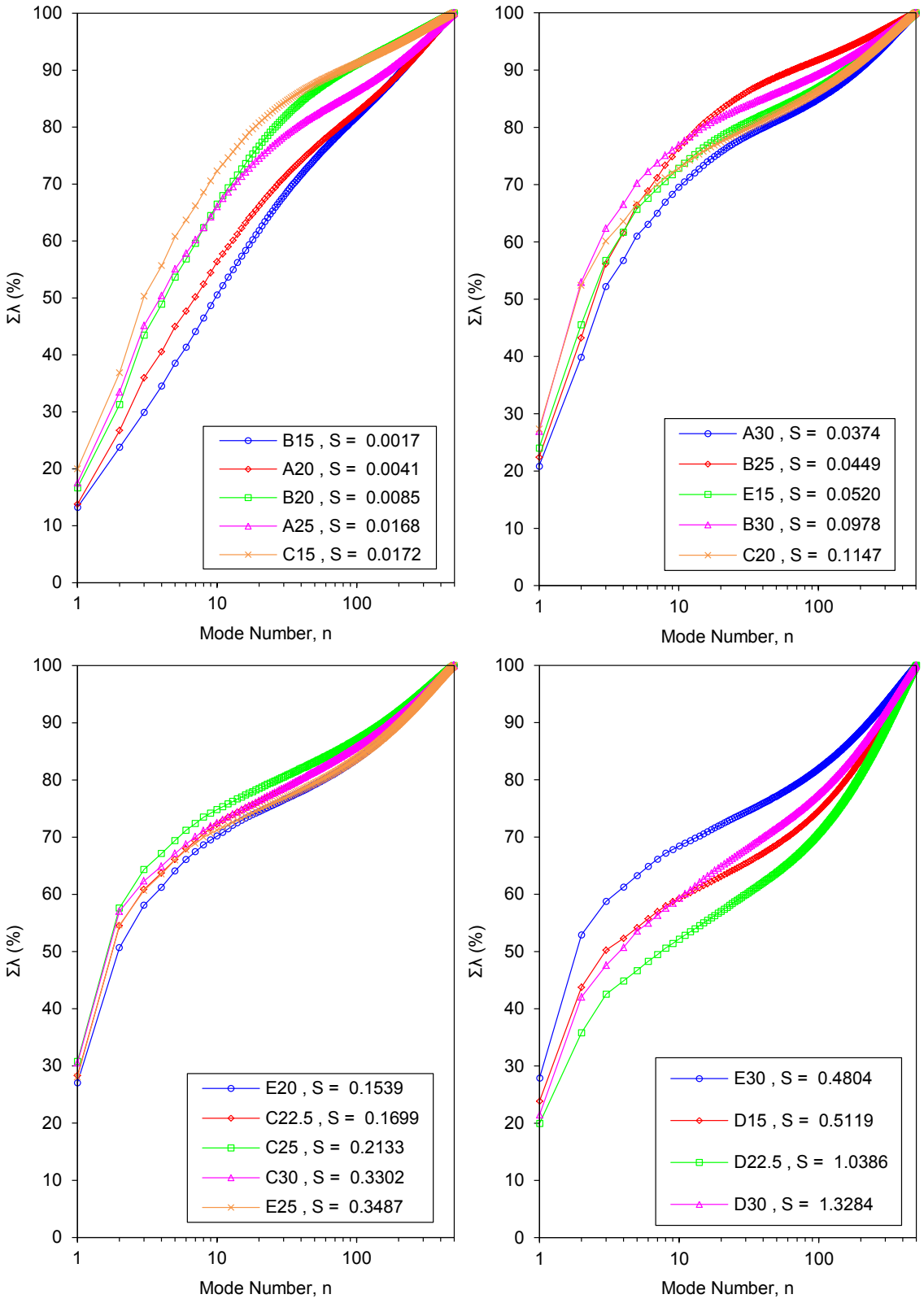

Fig. 7.2 Cumulative mode energy for each flow configuration.

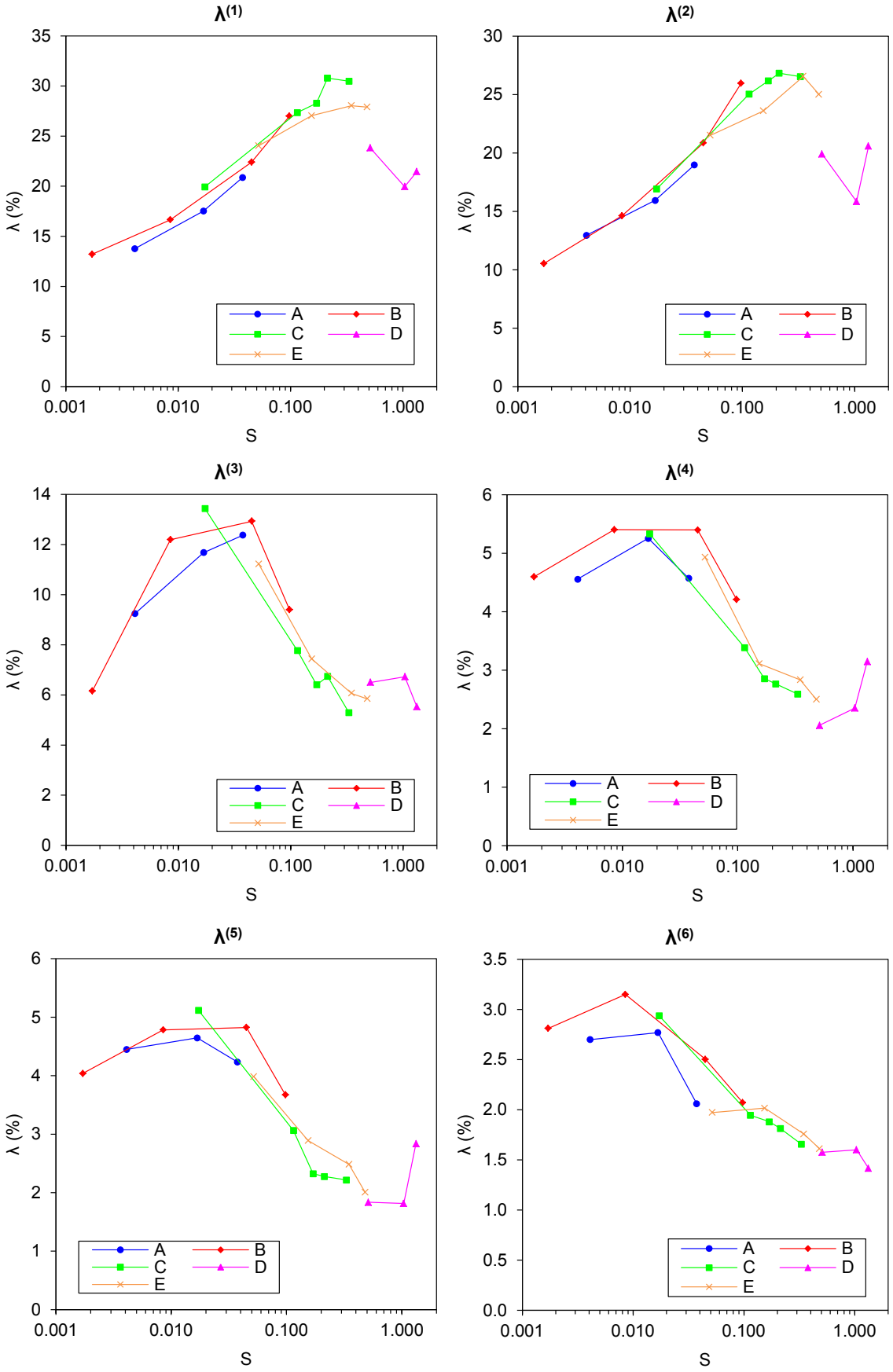

Fig. 7.3 Energy content as a function of swirl ratio for the first 6 POD modes, $\lambda^{(n)}$ for varying axial fan speeds.

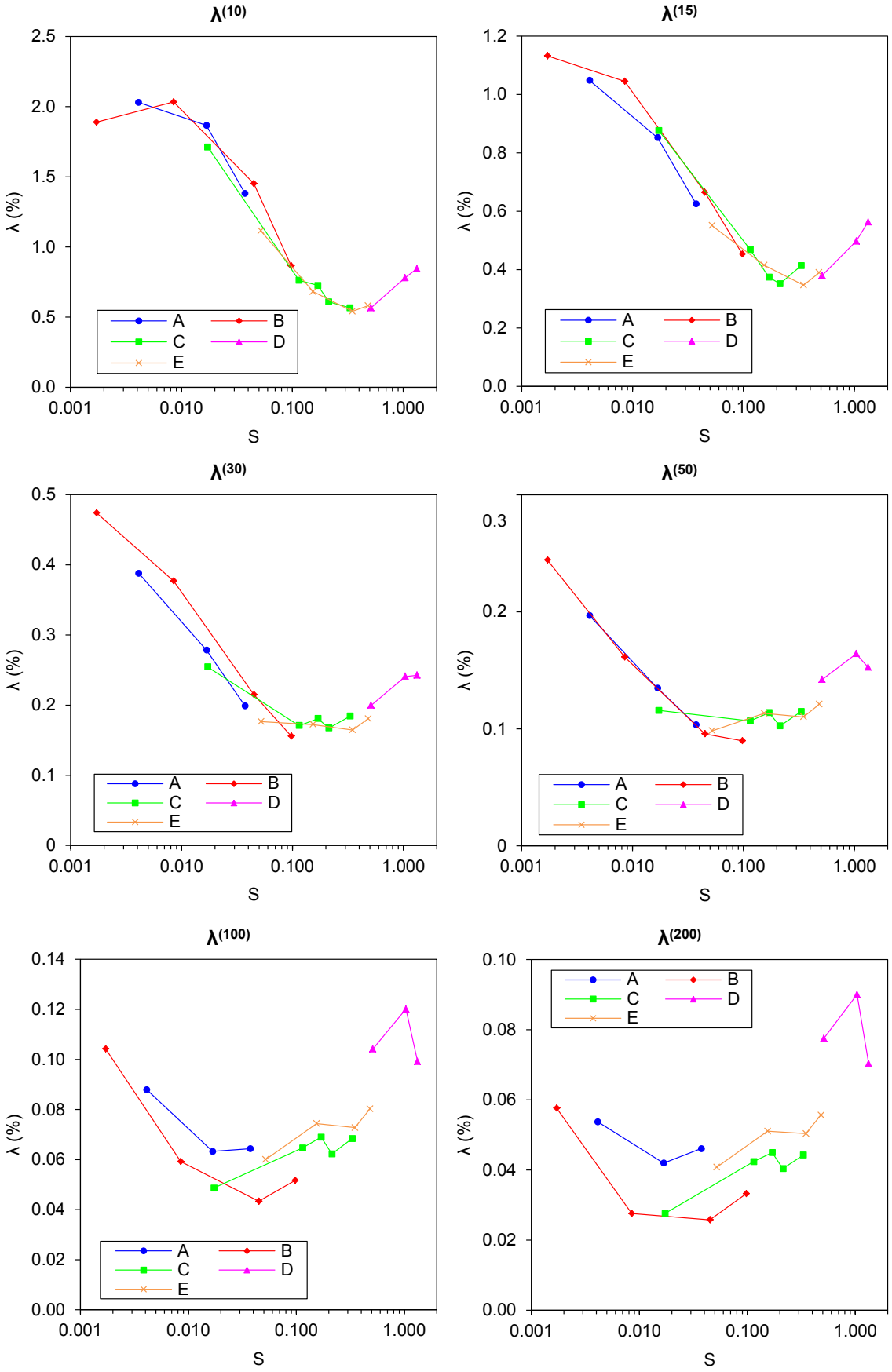

Fig. 7.4 Energy content as a function of swirl ratio for higher order POD modes, $\lambda^{(n)}$ for varying axial fan speeds.

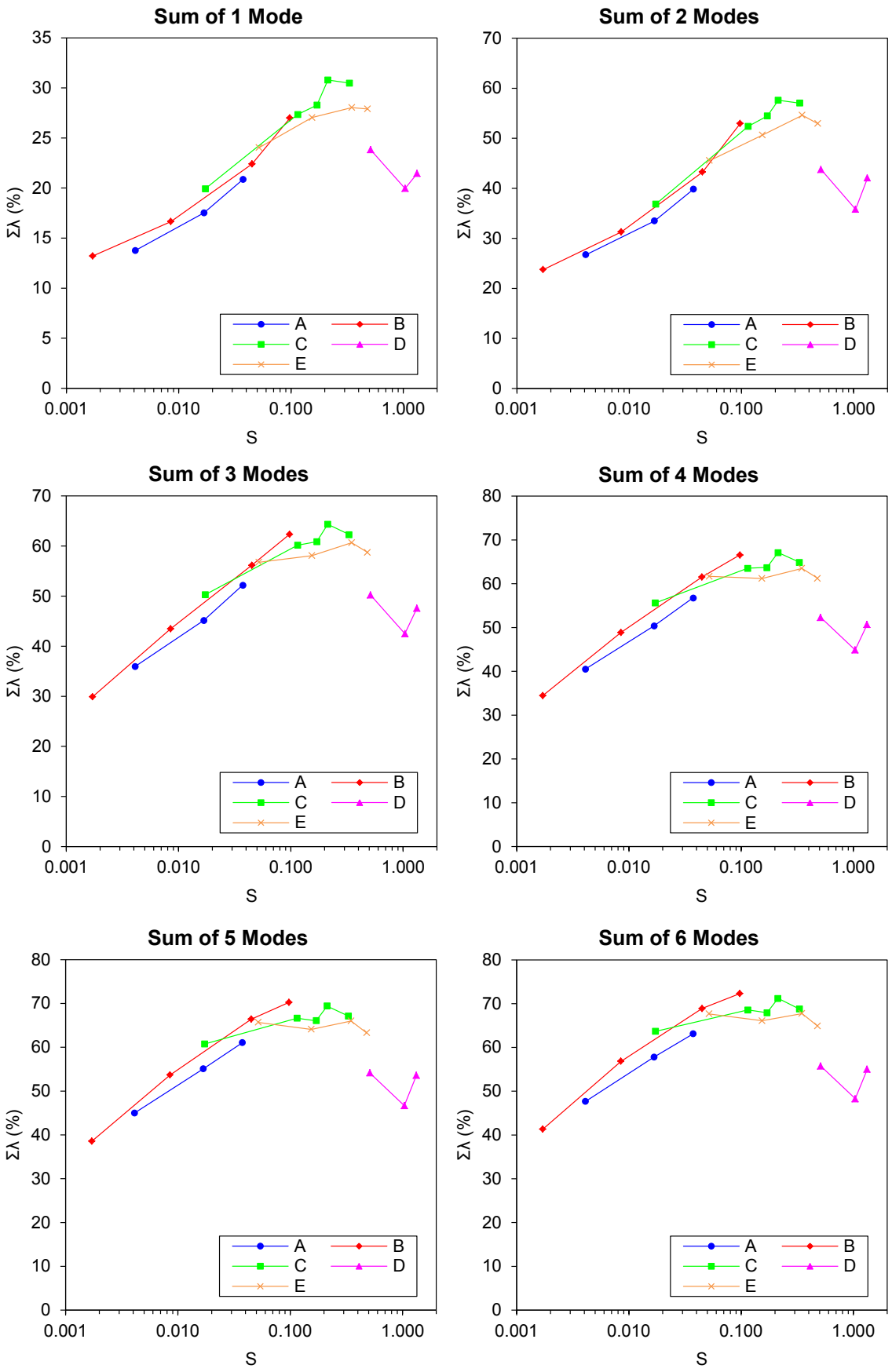

Fig. 7.5 Mode cumulative energy content against swirl ratio for the first 1 - 6 modes for various axial fan speeds.

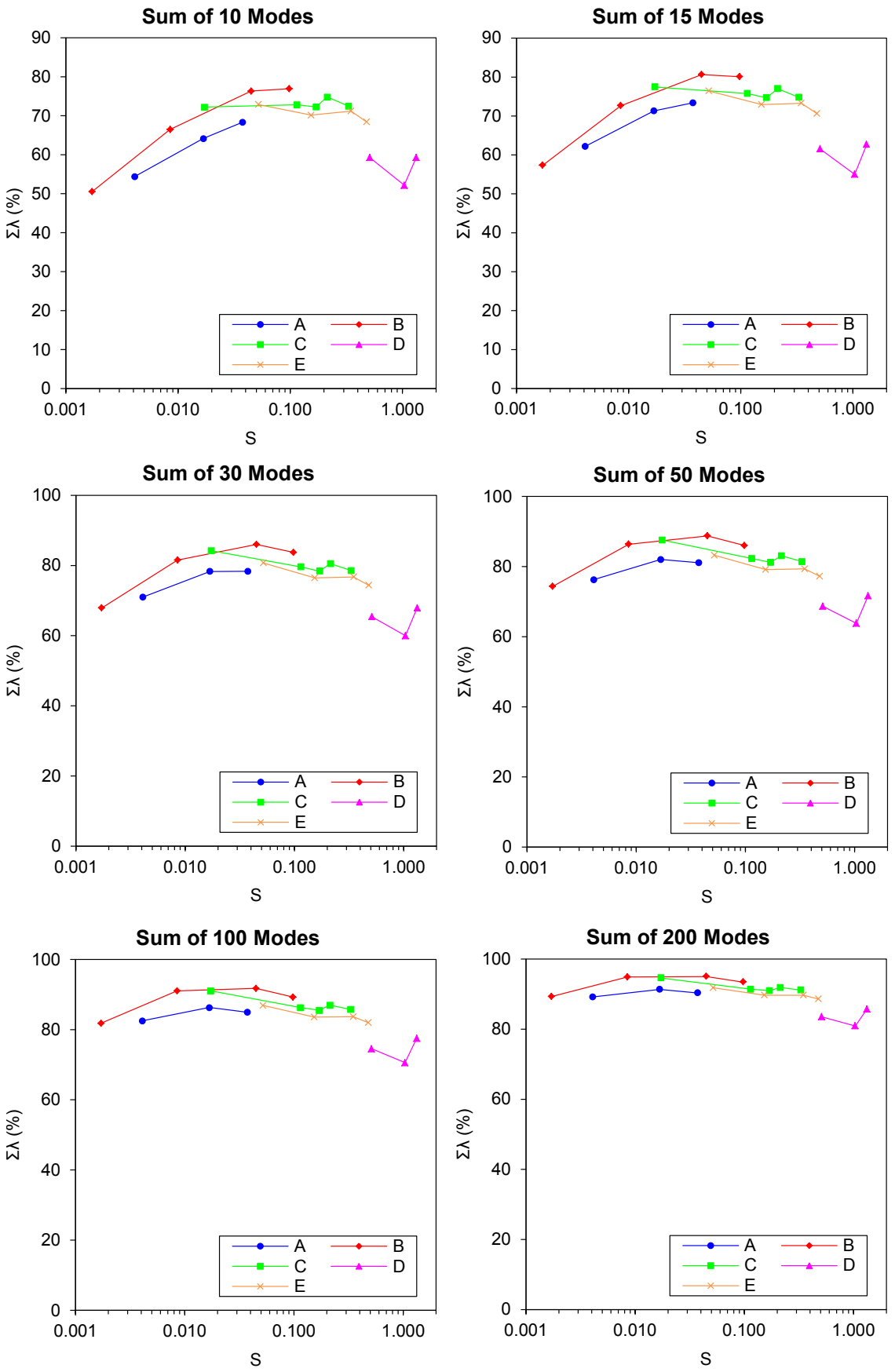

Fig. 7.6 Mode cumulative energy content against swirl ratio for higher cut-off mode numbers for various axial fan speeds.

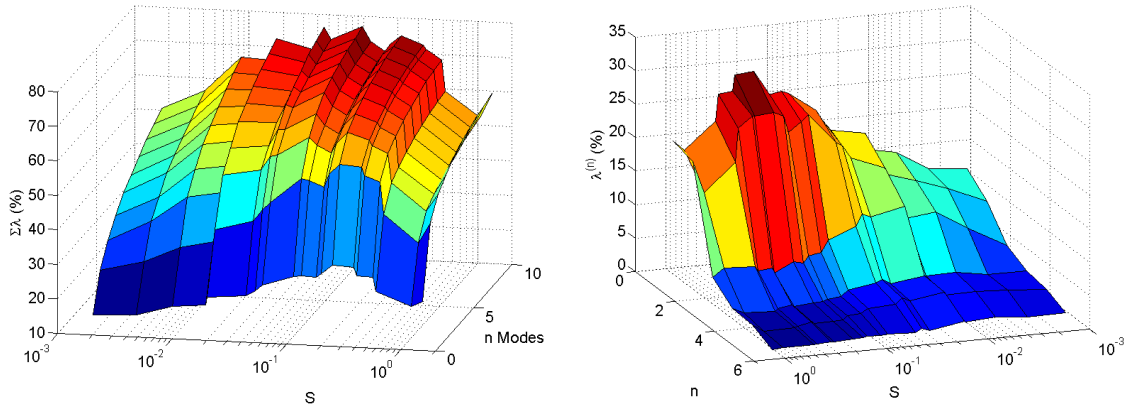

Fig. 7.7 (*Left*) Cumulative mode energy for the first 10 modes against swirl ratio and (*right*) individual mode energy, $\lambda^{(n)}$ against swirl ratio for the first 6 modes.

decompositions of the velocity vectors at each swirl ratio show that it is the first two modes which are dominant in an energy sense. It can be seen in Figure 7.8 that there is a very close trend between swirl ratio and the energy content of the first two modes, $\lambda^{(1)}$ and $\lambda^{(2)}$ with them accounting for 13.21% and 10.54% respectively at the lowest swirl ratio of $S = 0.0017$. The mode one and mode two energy content continues to increase with increasing swirl ratio up to approximately a swirl ratio of $S = 0.3$ to $S = 0.4$ where the energy values flatten out to $\lambda^{(1)}$ and $\lambda^{(2)}$ values of approximately 29% and 27% respectively of the total energy.

As it is the lower order modes that contain the bulk of the energy and the largest spatial coherent structures the higher the percentage energy contained in these modes suggests a more organised flow as it is higher order modes which contain the smaller scale structures and the unorganised turbulence. This observation is backed up by examining the variation in core location from § 6.2.4. At lower swirl ratios the vortex has large variability in where the core centre is located in any snapshot, the extra variability this adds to the ensemble of velocity snapshots is reflected in the lower order mode energy values as higher order modes are required more to describe the flow. Conversely as swirl ratio increases the dominance of the lower order modes increases, this is a reflection of the flow becoming more organised with less variability which is again shown in Figure 6.13 where the variance of the location of the vortex centre is shown to be much lower than at lower swirl ratios. Given the highly reduced variation in core location and the fact that the vortex structure appears to be highly organised with no apparent complexity in the planar velocity vectors within the core the higher order modes have much less variability to account for hence the ability for the flow to be more highly characterised by the lower order modes.

For swirl ratios above $S = 0.5$ the trend between mode energy for $\lambda^{(1)}$ and $\lambda^{(2)}$ and swirl ratios appears to break down with energy content percentages similar to lower swirl ratios. A possible explanation for the reduced energy content of lower order modes at higher swirl ratios is that as swirl ratio increases the size and topography of the vortex changes. As shown in Figure 6.19 and Figure 6.20 the flow inside the vortex is no longer highly organised, tight and approximately perpendicular to the vortex core but exhibits a large core radius with complex internal core flow

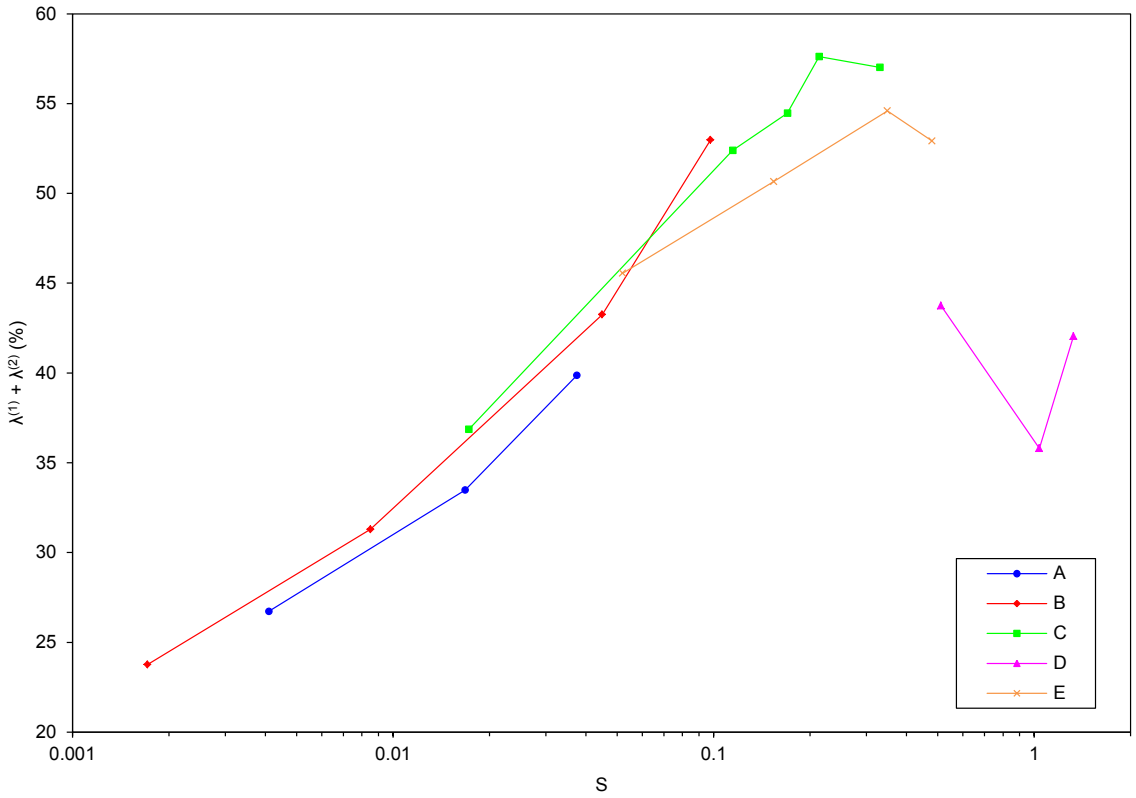

Fig. 7.8 Combined energy content of first two modes against swirl ratio.

structure and overall vortex shape which is constantly changing. The extra complexity added to the flow through the more highly fluctuating core structure means that the variability between different snapshots of the flow requires more modes to be captured. Another explanation for the slower convergence in mode energy could be that the three higher swirl ratios, $S = 0.512$, 1.039 and 1.328 were obtained with a very low axial fan speed (set D, see Table 6.1) resulting in much lower absolute planar velocities than the other data sets, these lower velocities required a larger dt time interval between PIV image pairs to be able to resolve the planar particle displacements and due to the large axial velocity component loss-of-pairs could be increased and thus increasing the amount of measurement noise in the velocity data.

The dominance of the first two modes is illustrated in Figure 7.9 as the ratio between the average energy content of the first two modes, $\lambda^{(1,2)}$ and the third mode, $\lambda^{(3)}$ defined as:

$$\frac{\lambda^{(1,2)}}{\lambda^{(3)}} = \frac{\lambda^{(1)} + \lambda^{(2)}}{2\lambda^{(3)}} \tag{7.1}$$

It can clearly be seen in Figure 7.9 that the dominance of the first two modes over subsequent modes (since $\lambda^{(n-1)} > \lambda^{(n)}$) is a function of swirl ratio. For low values of swirl ratio ($S < 0.05$), the dominance of the first two modes is less pronounced with the average energy content of the first two modes being between approximately 1.3 and 2 times the energy content of the third. For swirl ratios greater than $S = 0.05$ the dominance of the first two modes over the third grows with a maximum ratio of 5.39 at a swirl ratio of $S = 0.33$ meaning the first two modes in this case account for more than ten times the amount of energy contained in the third mode. This again reflects the

variability of the flow with the vortex core becoming more stationary at this range of swirl ratios such that the lower order modes are sufficient to accurately describe the flow.

Figure 7.9 also shows that for the highest swirl ratios, $S > 0.5$ the dominance of the first two modes decreases in accordance with the reduced energy content of the lower order modes as shown in Figure 7.3 (for flow configurations with low axial fan speed - D).

Figure 7.3 shows the mode energy as a function of swirl ratio for the first 6 POD modes. The first two modes show increasing energy content with swirl ratio until there is a discontinuity for data sets D ($S > 0.5$) which have lower mode 1 and 2 energy content. Mode three begins by having low energy content (approximately 6%) at the lowest swirl ratios before increasing with swirl ratio until peaking at approximately 13% for swirl ratios in the range $0.015 < S < 0.05$. At higher swirl ratios, mode three energy decreases again with increasing swirl and levelling off at approximately 6% again for swirl ratios above 0.2.

As mode number, n increases the energy content of the mode begins to uniformly decrease after showing fairly constant energy content for lower swirl ratios. Figure 7.3 shows that for mode n = 4 and 5 the energy content is approximately the same for $S < 0.05$ before decreasing with increasing swirl ratio. At mode n = 6 the energy content begins decreasing at swirl ratios above 0.01. At higher order modes the decreasing trend in mode energy content with increasing swirl ratio becomes even more defined as shown in Figure 7.4, mode 10 for the lowest swirl ratios still account for approximately 2% of the total energy whilst at higher swirl ratios (approximately S = 0.5) the mode contains just over 0.5% of the total energy. This again shows that at higher swirl ratios the flow is characterised by the lower order modes. As mode number increases to 100 the energy content becomes much less dependent on swirl ratio with mode 100 on average containing approximately 0.07% of the total energy with this dropping to approximately 0.045% for mode 200.

The convergence of energy can be seen in Figure 7.5 which shows the cumulative energy content for up to the first six modes. The percentage of the total energy increases with swirl ratio for $S \leq 0.5$. By the time the first three modes are taken into account it can be seen that the total energy content begins to level out above S = 0.09 remaining fairly constant at approximately 60% up to S = 0.5. As the number of modes taken into account increases through four to six modes it can be seen that the point at which swirl ratio has a large effect on the cumulative energy content decreases to approximately S = 0.03. Figure 7.6 shows that the cumulative energy content becomes independent of swirl ratio at lower swirl levels when more modes are taken into account with independence from swirl ratio beginning at $S > 0.015$ for 10 modes where the cumulative energy content remains approximately 73% and for 15 modes energy content is approximately 75% for $S > 0.01$. When the first 30 modes are taken into account the cumulative energy content is between 75% and 85% for $0.008 < S < 0.5$ with only the two lowest swirl ratios, S = 0.0017 and 0.0041 showing lower cumulative energy at 67.9% and 71% respectively. This shows that at lower swirl ratios the flow is more complex, with beyond mode 30 there is significant information

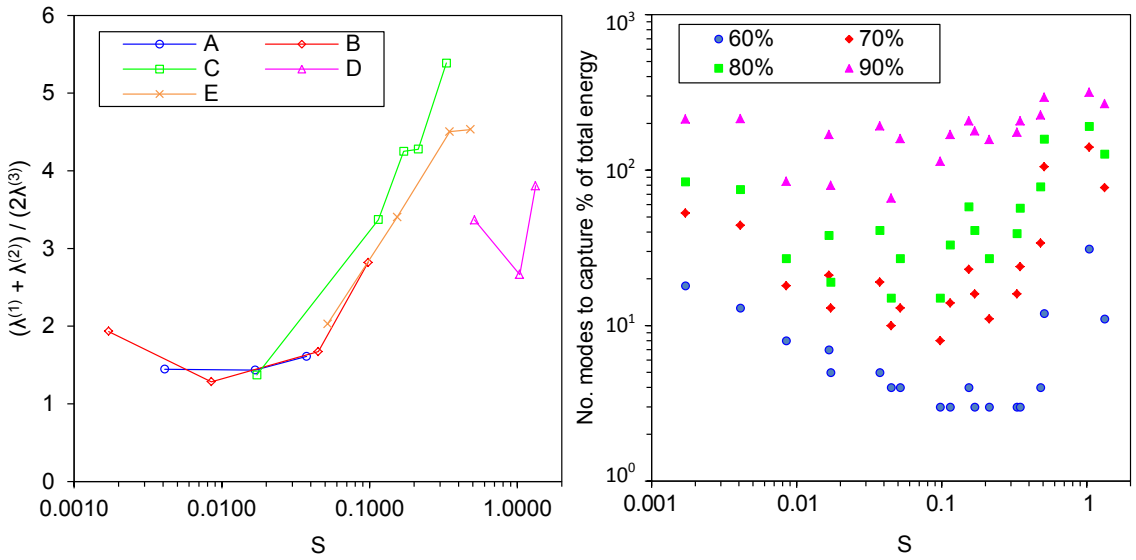

Fig. 7.9 (*left*) Ratio between the average of first two mode energies and third mode energy for varying swirl numberd and (*right*) number of modes required to capture varying percentages of the total energy as a function of swirl ratio.

regarding the flow and these effects are swirl ratio dependent.

By the time the first 100 modes are taken into account the dependence of cumulative energy on swirl ratio is much less pronounced with the cumulative energy content in the range 82-92% for all swirl ratios below 0.5 and increasing to 88-95% for the first 200 modes. This suggests that for mode numbers higher than 100 the energy content is independent of swirl ratio and do not contribute to the large scale dynamics of the vortex and can be explained as containing incoherent turbulent information (similar to the individual mode energy contributions of the higher order modes in Figure 7.4).

By looking at the energy contribution to the total flow of the higher modes it becomes clear that as the flow becomes more stable with increasing swirl ratio the dynamics of the vortex are contained in the lowest order modes with large coherent structure and have a much reduced contribution from the lower energy modes which contain more complex flow structures. Conversely at the lowest swirl ratios whilst the first pair of modes are still dominant the contribution of the higher order modes is more important in containing information about the flow as is shown by the number of modes required to capture certain percentages of the total energy as a function of swirl ratio in Figure 7.9. When mode number increases to mode 100 the dependence on swirl ratio of the energy content appears to disappear suggesting that these modes contain information regarding the incoherent turbulence within the system and do little to describe the bulk motions of the vortex.

7.3 Analysis of Spatial POD Modes

Now that the distribution of energy, $\lambda^{(n)}$, amongst the spatial eigenmodes, $\phi^{(n)}$ has been considered it is useful to investigate the spatial velocity vector structures present as these indicate the

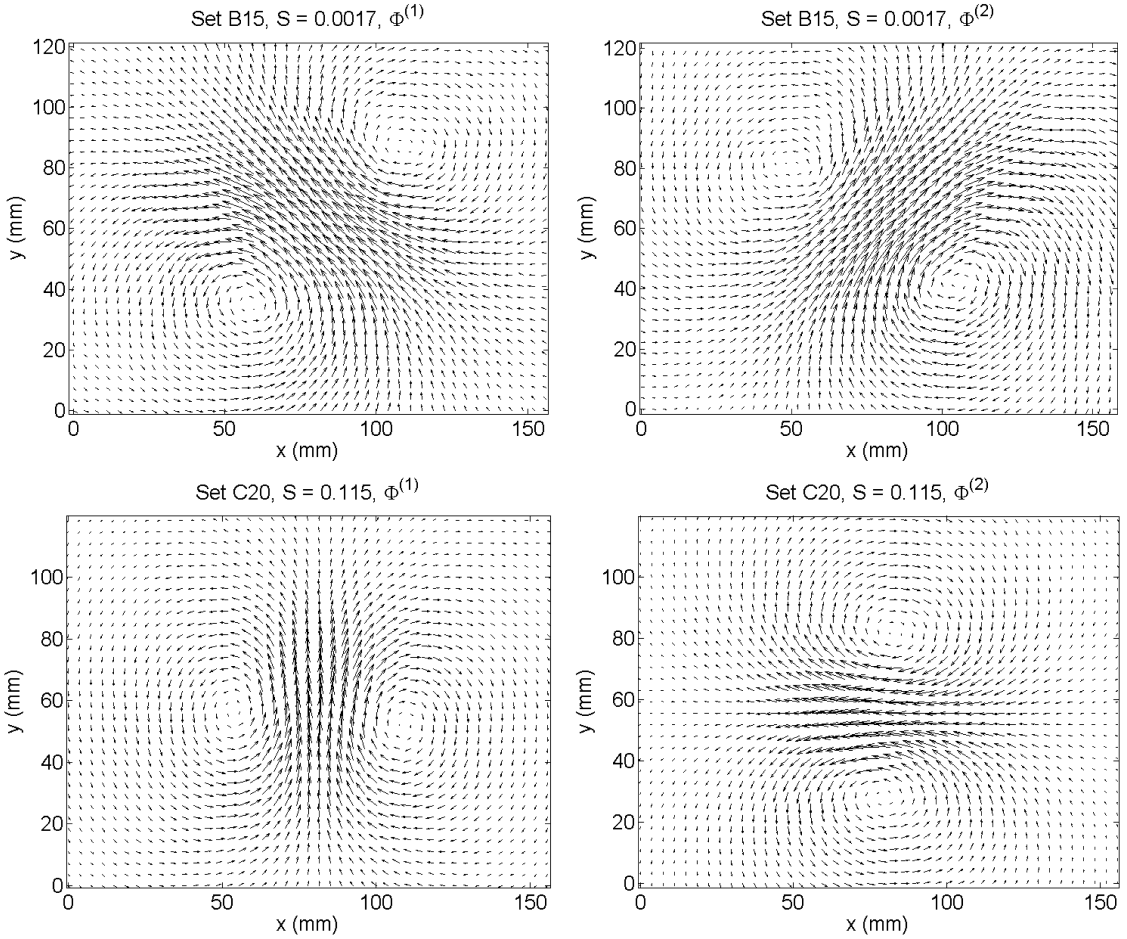

Fig. 7.10 Modes $\phi^{(1)}$ (*left*) and $\phi^{(2)}$ (*right*) for swirl ratios $S = 0.0017$ (*top*) and $S = 0.115$ (*bottom*).

underlying coherent structures which characterize the flow.

The structure of the modes at lower mode order, n, is the same for all swirl ratios with only the size and orientation of the features varying for different swirl ratio data sets. Figure 7.10 and Figure 7.11 shows the first two spatial modes, $\phi^{(1)}$ and $\phi^{(2)}$ for four swirl ratios, $S = 0.0017$, 0.115, 0.349 and 1.328. The similarity in structure between $\phi^{(1)}$ and $\phi^{(2)}$ leads to the assumption that they are both modes contributing to the same coherent structure, this is backed up by consulting the energy associated with the first two modes, $\phi^{(1)}$ and $\phi^{(2)}$ which are almost equal. Structurally these modes contain a pair of counter rotating vortices, where $\phi^{(1)}$ differs from $\phi^{(2)}$ by a rotation of 90°.

Mode 3, $\phi^{(3)}$, as shown in Figure 7.12 consists of a single large vortex centred approximately in the middle of the measurement plane, this mode like the first pair is consistent in type across all swirl ratios.

Modes 4 and 5, $\phi^{(4)}$ and $\phi^{(5)}$ as shown in Figure 7.13 and Figure 7.14 for the two extremes of the swirl ratio range, appear like the first two modes to act as a pair describing the same structure, again this is backed up by the similar energy contributions of $\lambda^{(4)}$ and $\lambda^{(5)}$. The structure of the modes contain two pairs of counter rotating vortices with each vortex approximately evenly spaced around a central point. Mode 5 differs from 4 by a rotation of approximately 45°.

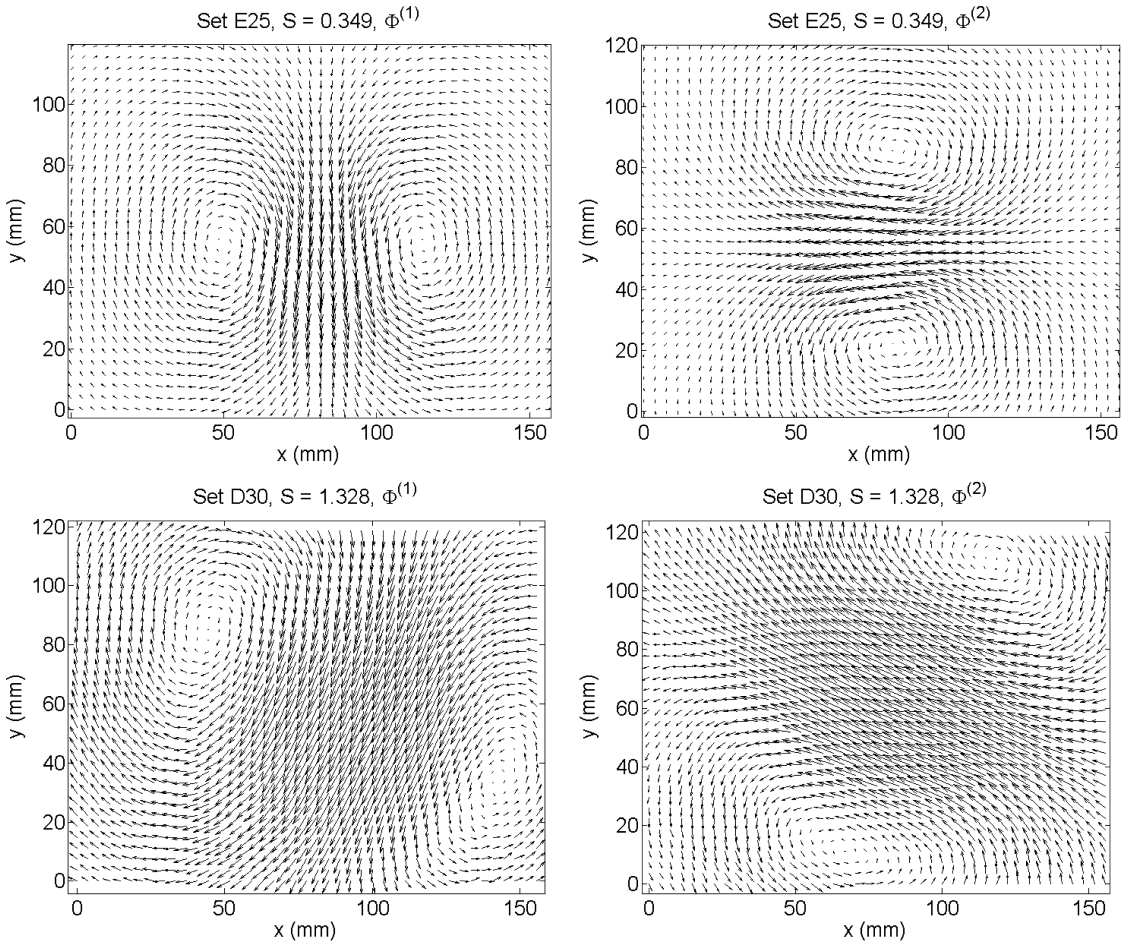

Fig. 7.11 Modes $\phi^{(1)}$ (*left*) and $\phi^{(2)}$ (*right*) for swirl ratios $S = 0.349$ (*top*) and $S = 1.328$ (*bottom*).

When mode 6, $\phi^{(6)}$ is reached the consistency in structure for different flow configurations breaks down with the type of structure varying between different data sets. For lower swirl ratios the modes contain two pairs of counter rotating vortices arranged roughly in a line across the measurement plane. The structure is similar to that of mode 1 but with an extra pair of counter rotating vortices in between the two outer vortices. This topography is common in mode 6 for all swirl ratios lower than $S = 0.0449$ and is shown in Figure 7.15. For swirl ratios $S = 0.0449$ (see Figure 7.16) and above the mode displays a central vortex contained within a large vortex with rotation in the opposite direction and in this sense resembles mode 3 with an added vortex inside the core of the main vortex with opposite rotation. The interaction between the inner and outer counter rotating vortices creates a region of shear which contains typically two smaller vortices. This change in mode structure at a critical swirl ratio is not reflected in the dependence of the energy content $\lambda^{(6)}$ on swirl ratio; as shown in Figure 7.3 there is no change in the relationship between $\lambda^{(6)}$ and swirl ratio in the region where the mode structure changes.

The discussion in the preceding paragraphs about the overall structure of the low order spatial modes shows that the structures contained in the flow are independent of swirl ratio until mode 6 where the structure changes at a critical swirl level. From this information it can be concluded that the largest scale structures that drive the vortex flow are independent of swirl ratio and are

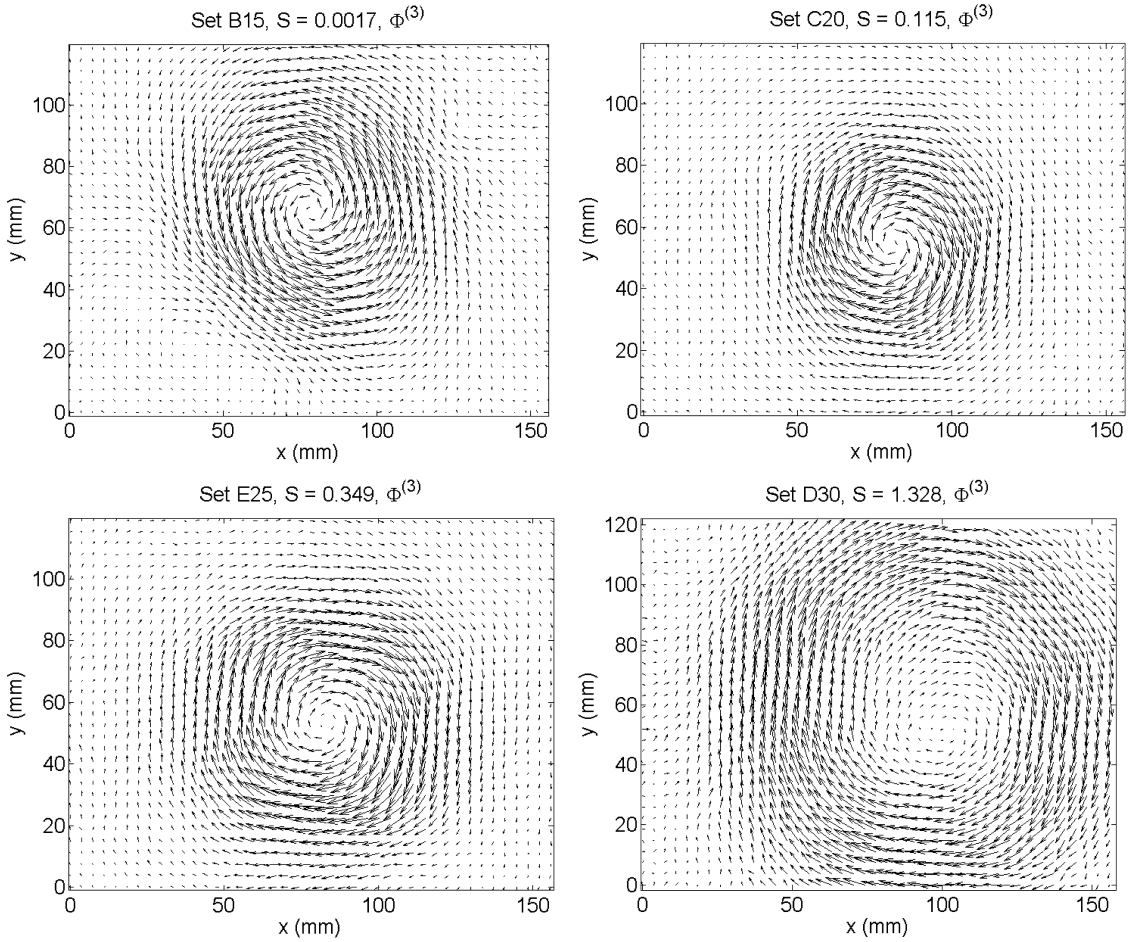

Fig. 7.12 Mode $\phi^{(3)}$ for swirl ratios $S = 0.0017$ (*top left*), $S = 0.115$ (*top right*), $S = 0.349$ (*bottom left*) and $S = 1.328$ (*bottom right*).

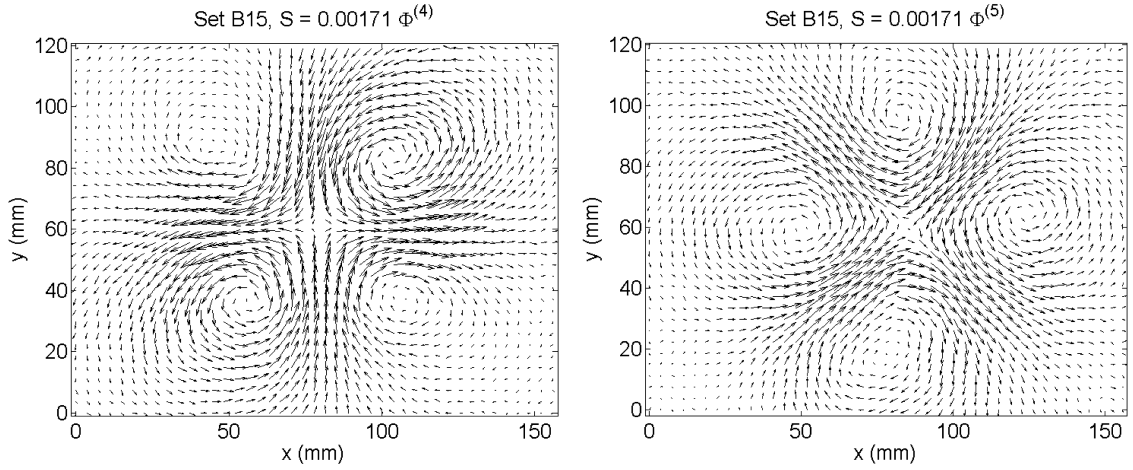

Fig. 7.13 Modes 4 and 5 for flow configuration B15, $S = 0.0017$.

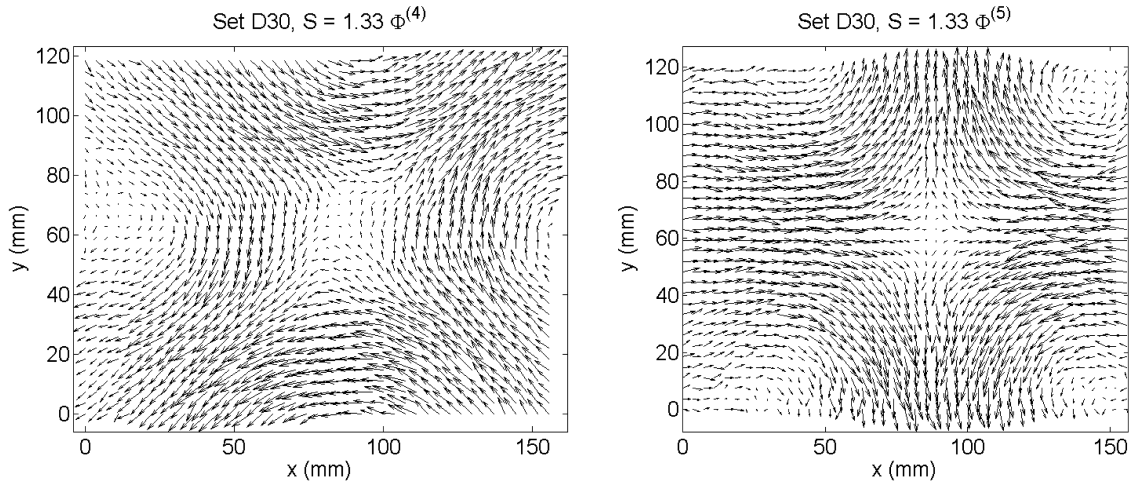

Fig. 7.14 Modes 4 and 5 for flow configuration D30, $S = 1.33$.

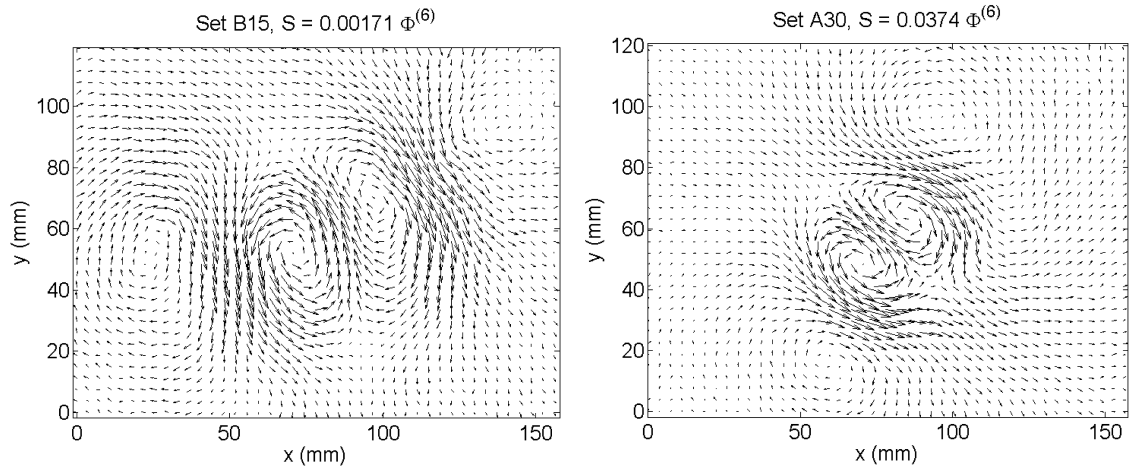

Fig. 7.15 Mode 6 for low swirl ratios.

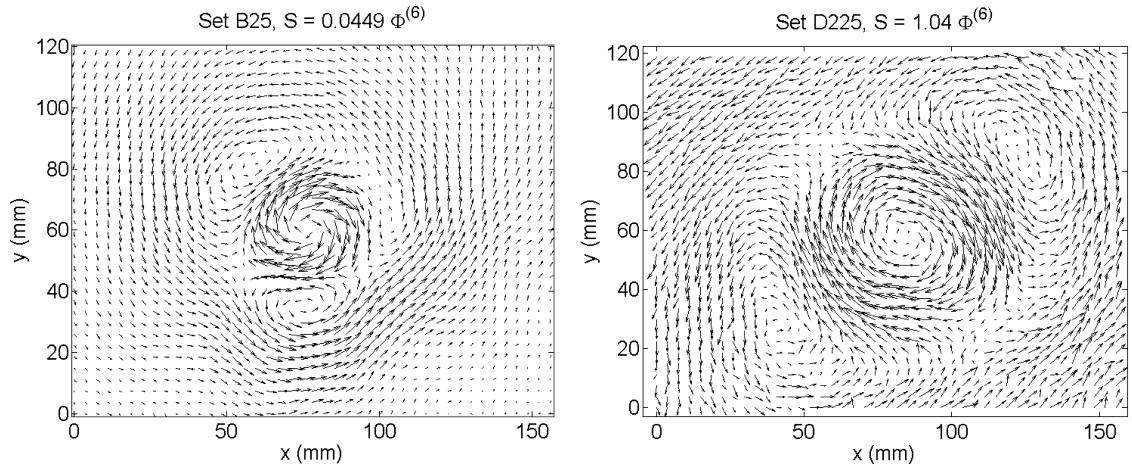

Fig. 7.16 Mode 6 for high swirl ratios.

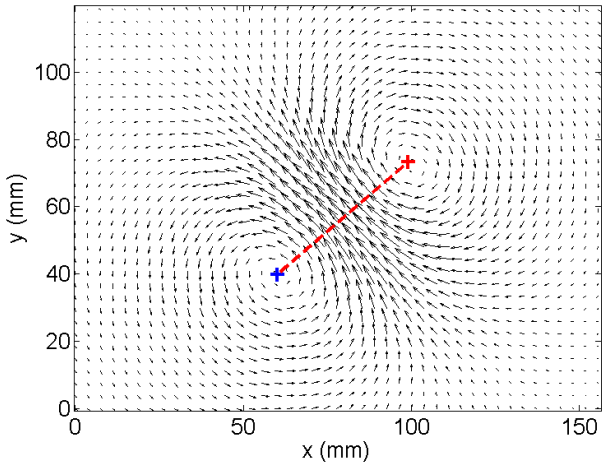

Fig. 7.17 Distance between mode 1 and 2 vortex centres, $d_{v_{12}}$ (shown by the red dashed line).

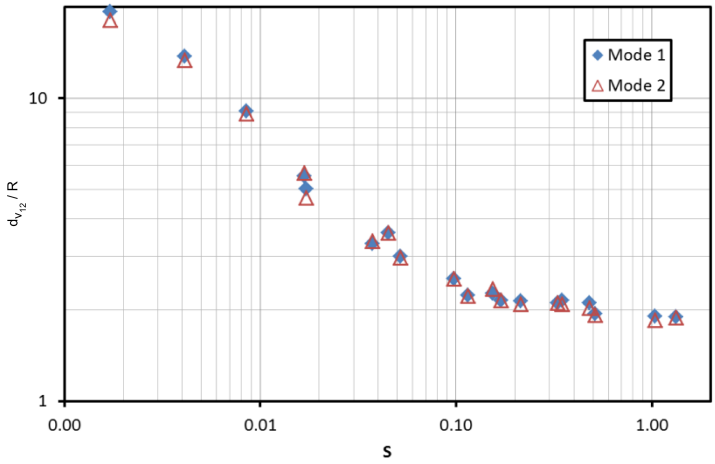

Fig. 7.18 Normalized distance between vortex cores for modes 1 and 2 against swirl ratio.

underlying features of this type of flow. Next an attempt to quantify the spatial properties of the modes is made to investigate their dependence on swirl ratio further by measuring quantities such as vortex radius and spatial distance between vortices.

As already discussed, modes 1 and 2 consist of a pair of counter-rotating vortices. This structure is common across all swirl ratios with only the size of the structure changing. The distance, $d_{v_{12}}$, between the centres of each vortex was calculated as shown by the red dashed line in Figure 7.17.

The distance between the cores of the two vortices in modes 1 and 2, $d_{v_{12}}$, is dependent on swirl ratio as shown in Figure 7.18. For each swirl ratio the vortex size quantified by the radius of the vortex, R, (see Figure 6.9) is used to normalize $d_{v_{12}}$ giving a clear relationship between $d_{v_{12}}/R$ and swirl ratio with $d_{v_{12}}/R$ quickly decreasing in a uniform manner with increasing swirl ratio before the rate of decrease lowers for swirl ratios above $S = 0.1$.

Mode 3 consists of a single centred vortex so it was decided to measure the radius the vortex to quantify this mode. Like modes 1 and 2 the radius of the vortex in mode 3 is closely linked to swirl ratio. Figure 7.19(a) shows the radius of the vortex in mode 3, R_3 normalized by the radius

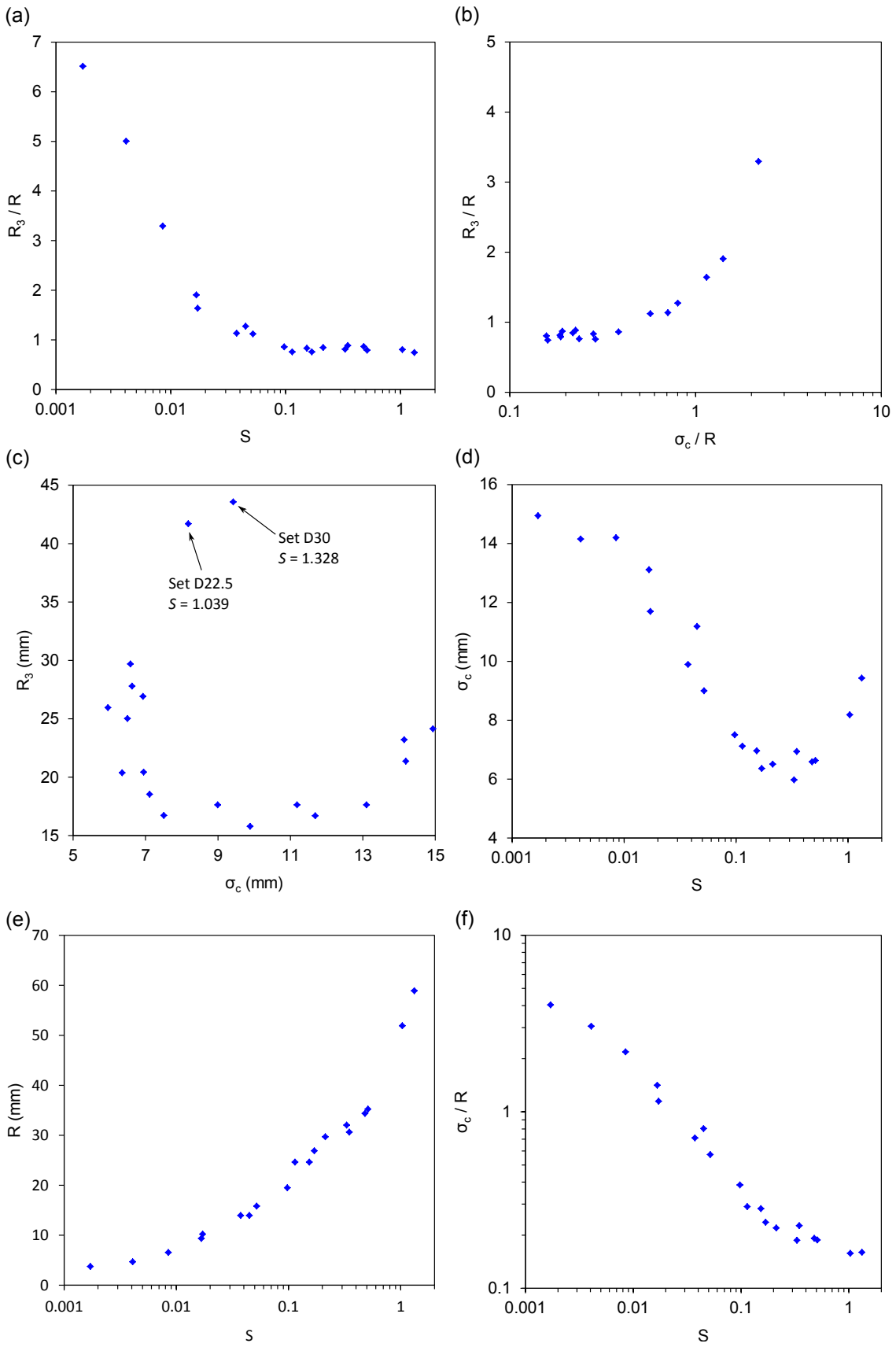

Fig. 7.19 (*a*) Normalized mode 3 vortex radius against swirl ratio and (*b*) normalized mode 3 vortex radius against normalized spatial spread of vortex core locations. (*c*) Radius of mode 3 vortex against spatial spread of vortex core locations and (*d*) spatial spread of vortex core locations against swirl ratio. (*e*) Vortex radius against swirl ratio and (*f*) normalized spread of vortex core locations against swirl ratio.

of the vortex, R, at the particular swirl ratio. The ratio R_3/R decreases with increasing swirl ratio. The normalized radius of the mode 3 vortex, R_3/R is directly related to swirl ratio with the value decreasing monotonically for $S < 0.1$. The dependence of the size of the mode 3 vortex to swirl ratio decreases with increasing swirl ratio, becoming almost constant for $S > 0.1$.

The normalized vortex radius R_3/R also has a close relationship with the extent of the spatial spread of vortex core location, σ_c. As defined in § 6.2.4, σ_c is the standard deviation of the distance d_c of individual vortex cores from the mean vortex core centre giving a measure of the spatial stability of the vortex. High values of σ_c represent vortices with a greater spread of spatial locations. As previously discussed the value σ_c/R gives a measure of the vortex spatial stability with respect to the size of the vortex and it can be seen in Figure 7.19(f) that this value decreases with swirl ratio. The non-normalized vortex spread σ_c decreases with increasing swirl ratio (Figure 7.19(d)) for swirl ratios less than approximately 0.5 after which σ_c increases again, the low swirl high values of σ_c are accounted for by the large amount of vortex precession in the flow whereas the high values at high swirl ratio are due to the much larger vortex size at high swirl ratio (see Figure 7.19(d)). Therefore, the quantity σ_c/R is used to show a measure of vortex precession relative to vortex size. Figure 7.19(b) shows that the radius of the vortex structure which makes up the third spatial POD mode relative to the mean radius of the instantaneous vortices under each flow condition increases the greater the distance over which individual vortex cores are distributed relative to the mean vortex radius.

Investigating R_3/R as a function of σ_c/R and S as shown in Figure 7.20 it can be seen that for swirl ratios less than 0.1 both normalised quantities R_3/R and σ_c/R are useful parameters which characterise the flow for swirl ratios up to 0.1.

Modes 4 and 5 contain two pairs of counter rotating vortices. To quantify the spatial properties of these modes the distances between the two vortices with the same rotational direction were calculated as shown in Figure 7.21. When normalized by the size of the tornado-vortex at a given swirl ratio the distance between the pairs of vortices again shows a very clear decreasing trend with increasing swirl ratio as shown in Figure 7.22. In Figure 7.21 and Figure 7.22 the distances between vortex pairs at the highest swirl ratios could not be calculated as the separation between the individual cores increased to the point where the cores lie outside of the measurement plane.

The trends shown in Figure 7.18, Figure 7.19 and Figure 7.22 for the distance between vortex cores for modes 1, 2, 4 and 5 and the radius of the single vortex in mode 3 show that the size of these structures are dependent on swirl ratio and that the structure size becomes closer to the size of the tornado-vortex at higher swirl ratios whereas for lower swirl ratios the structures are much larger than the individual tornado vortex.

7.4 Autocorrelation Functions of Spatial Modes

To determine the size of the structures contained within the POD modes the normalized spatial autocorrelation of the mode velocity vectors was taken. With the spatial autocorrelation, B_{ij} taken

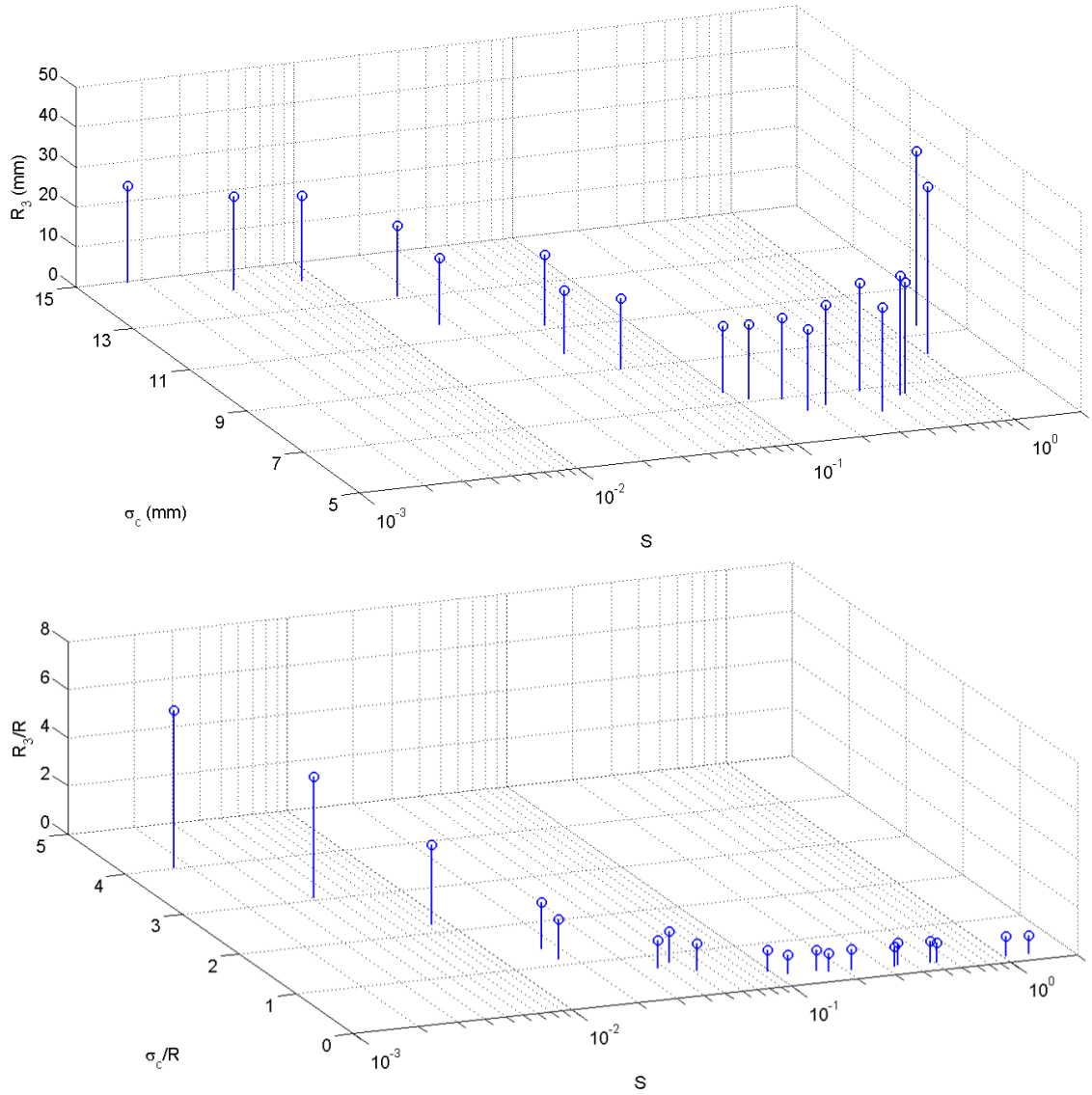

Fig. 7.20 (*top*) Radius of mode 3 vortex against spread of vortex core locations and swirl ratio and (*bottom*) normalised radius of mode 3 vortex against normalised spread of vortex core locations and swirl ratio.

as:

$$B_{ij}(r') = \frac{u_i(x)u_j(x+r')}{u_i'u_j'} \tag{7.2}$$

Where i and j specify the velocity component u or v and r' is a translation vector defining the spatial distance over which the correlation is calculated, for example B_{uv} is the autocorrelation of the u velocity component in the direction of the v velocity component.

Figure 7.23 and Figure 7.24 show the spatial autocorrelation functions of various modes for two flow configurations, B15, S = 0.0017 and E30, S = 0.480 respectively. It can be seen that as mode number increases the distance over which velocity components stay correlated becomes smaller which is to be expected as visual exploration of the spatial modes show the lower, higher energy content modes as containing the largest more organized flow structures. In both cases displayed there is still considerable correlation up to distances of approximately 20mm which

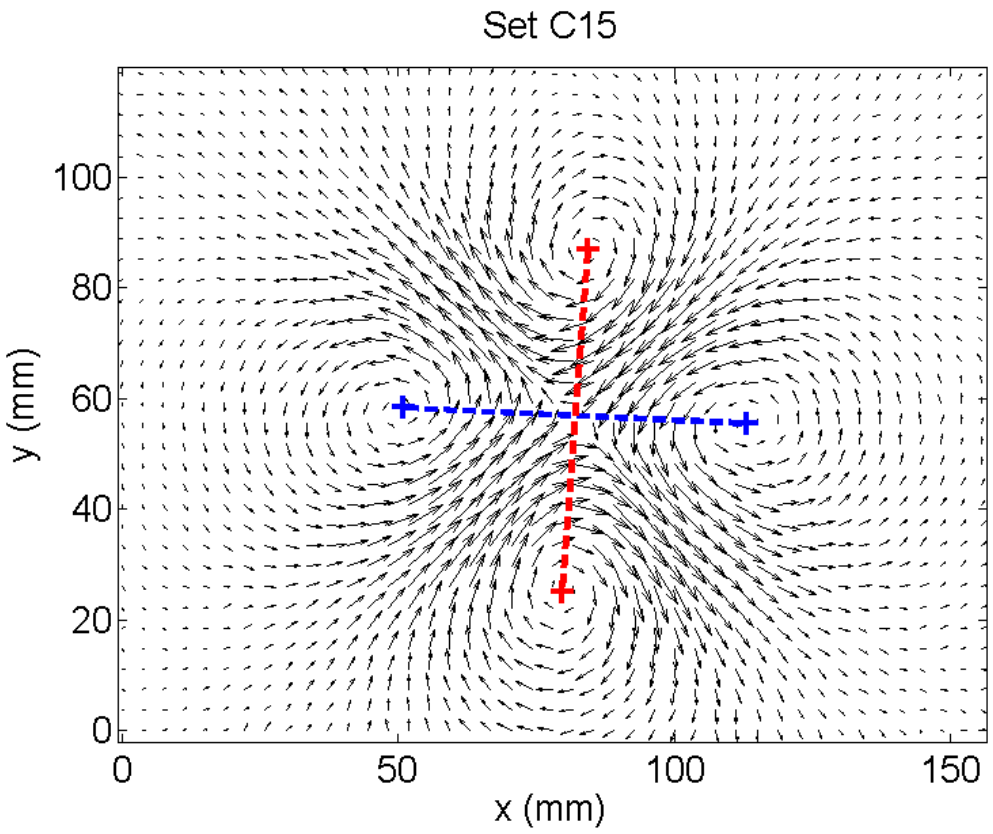

Fig. 7.21 Distance between vortex pairs in modes 4 and 5.

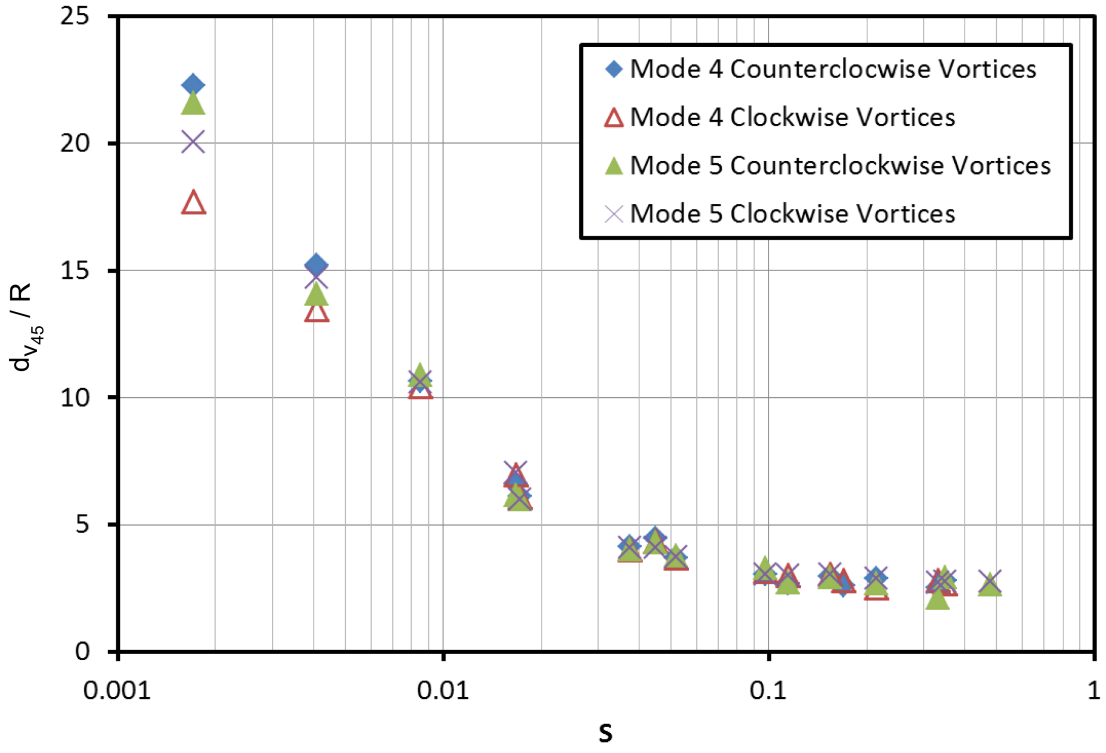

Fig. 7.22 Normalized distance between vortex pairs for modes 4 and 5 against swirl ratio.

with a spatial resolution $\Delta x = \Delta y = 0.9281$mm represents correlation over 22 vector grid points (rounded) up to mode 30. Both cases show by mode 200 that there is very little spatial correlation

between velocity vectors with the correlation function approaching the form of a delta-function with the only significant correlation at zero translation.

To quantify the scale of structures in the modes a distance L is defined as the distance over which the correlation value B drops below a value of $e^{-1} \approx 0.364$. L is taken as the average of the value r' for which B drops below this value for the two streamwise autocorrelation functions B_{uu} and B_{vv} as Figure 7.23 and Figure 7.24 show that these two values are approximately the same.

The correlation length L as a function of mode number for four swirl ratios is displayed in Figure 7.25. It can be seen that up to mode 30 the spatial velocity vector correlations do not vary much with swirl ratio with mode 30 having a correlation length of approximately 15 mm over each swirl ratio. The fact that the correlation length of the modes up to mode 30 are similar for varying swirl ratio suggests that these modes contain information regarding the vortex dynamics of the overall flow.

For modes above 30 Figure 7.25 shows that the correlation length becomes dependent on swirl ratio, with lower swirl ratios containing larger structures. At mode 40 the correlation lengths for $S = 0.480$ and $S = 0.0017$ are 11.1mm and 15.8mm respectively with the correlation length of $S = 0.0017$ taking until mode 70 to decrease to the $S = 0.480$ correlation length at mode 40. By mode 100 the correlation length for $S = 0.480$ decreases to 4.6mm whereas for $S = 0.0017$ the correlation length is 7.4mm. At the higher mode numbers up to $n = 425$ the correlation length converges to a value of 3.71, this value is reached by mode 193 for $S = 0.0017$ but is reached much earlier for $S = 0.480$ at mode 118.

The trends shown in Figure 7.25 are backed up by Figure 7.26 which shows correlation length L as a function of swirl ratio for varying mode number. While up to mode 30 the correlation length is fairly consistent with the amount of variance showing little dependence on swirl ratio. As with Figure 7.25 the modes where a difference in correlation length is observed as a function of swirl ratio are modes 50, 75 and 100 with the correlation length higher for lower swirl ratio.

The lack of spatial correlation at higher mode number is explainable as these modes contain information arising from the randomly fluctuating turbulence and measurement noise in each velocity snapshot. These modes account for a very low proportion of the total flow energy and in the case of investigating the structured dynamics of the vortex flow can be ignored as is shown later in this chapter.

7.5 Lower Order Modeling

As previously stated any individual snapshot velocity field can be approximated using a linear combination of a number of POD modes. Since the decomposition is carried out on the fluctuating velocity component to reproduce the full flow field the modes have to be added to the ensemble average. Thus each full snapshot velocity field, u_i, is recreated as the sum of the ensemble average

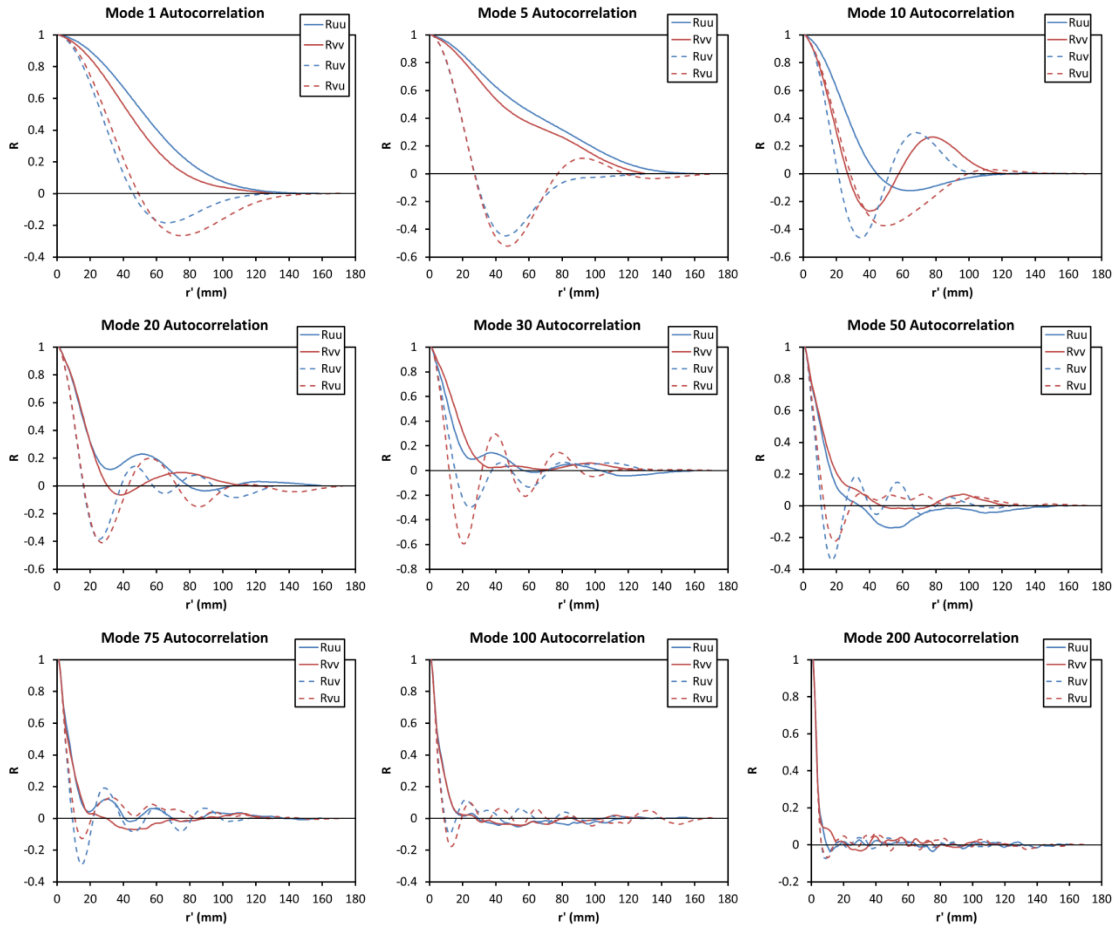

Fig. 7.23 Autocorrelation functions of spatial POD modes for flow configuration B15, $S = 0.0017$.

and a linear combination of each mode:

$$u(\mathbf{x},t_i) \quad = \quad \overline{u}(\mathbf{x}) + \sum_{n=1}^{N_s} a_i^{(n)} \phi^{(n)}(\mathbf{x},t_i) \tag{7.3}$$

The reconstruction of u in (7.3) since it includes all N_s modes contains the full flow information and is exactly equal to the snapshot velocity vectors. If one needs only to consider the large scale flow structures, neglecting the small scale coherent structures and small scale incoherent turbulence the summation to N_s above can be truncated to a cut-off value N_c since it is the first N_c modes that contain the majority of the flow energy associated with the large scale coherent structures. The POD approximation then becomes:

$$u^{(N_c)}(\mathbf{x},t_i) \quad = \quad \overline{u}(\mathbf{x}) + \sum_{n=1}^{N_c} a_i^{(n)} \phi^{(n)}(\mathbf{x},t_i) \tag{7.4}$$

Once the decomposition of the velocity fields has being carried out and the orthonormal basis of eigenfunctions (POD modes) found, the flow can be modelled using only a certain number of the first most important modes. Using a truncated number of modes to recreate the velocity snapshots means that only an approximation is being modelled since not all of the flow information is included but due to the nature of the decomposition the most important energy wise, dominant flow structures are contained in the lower modes whereas the higher modes contain the smaller

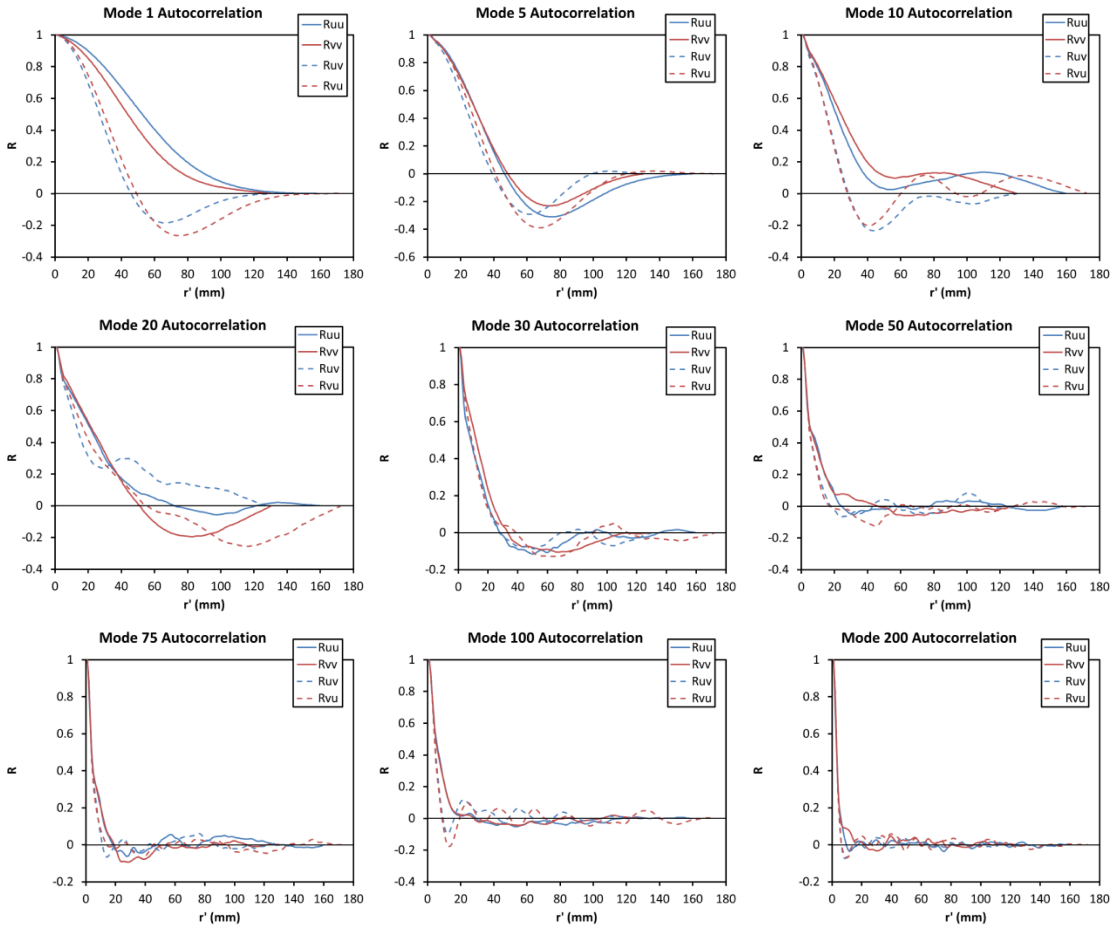

Fig. 7.24 Autocorrelation functions of spatial POD modes for flow configuration E30, $S = 0.480$.

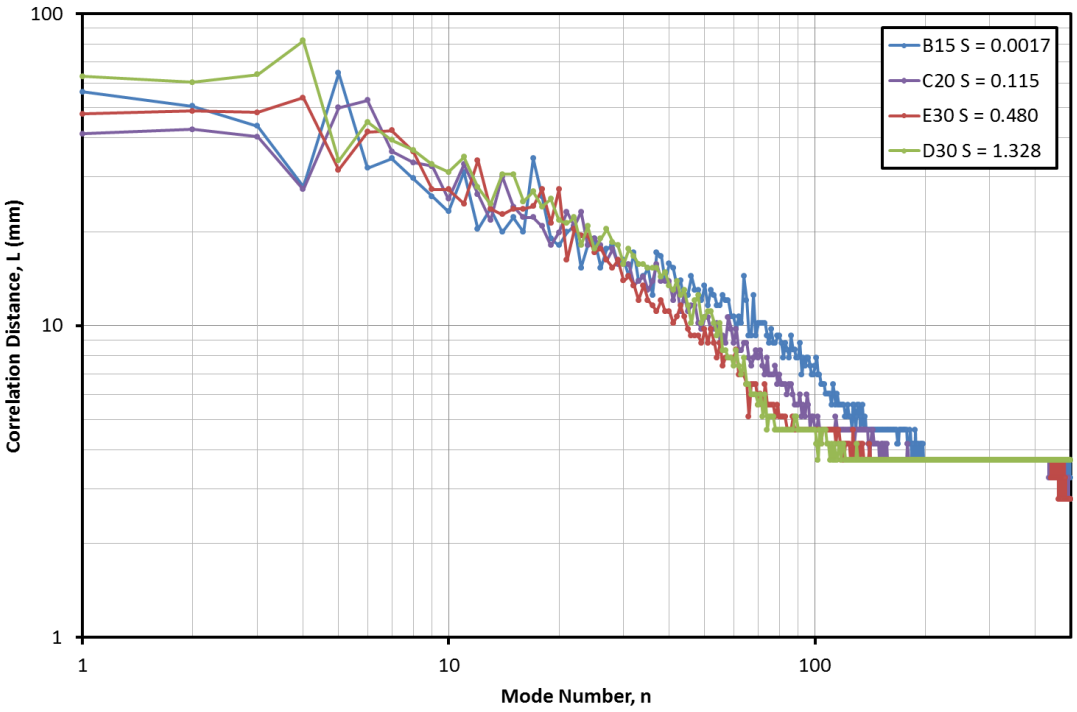

Fig. 7.25 Correlation length, L against mode number for varying swirl ratios.

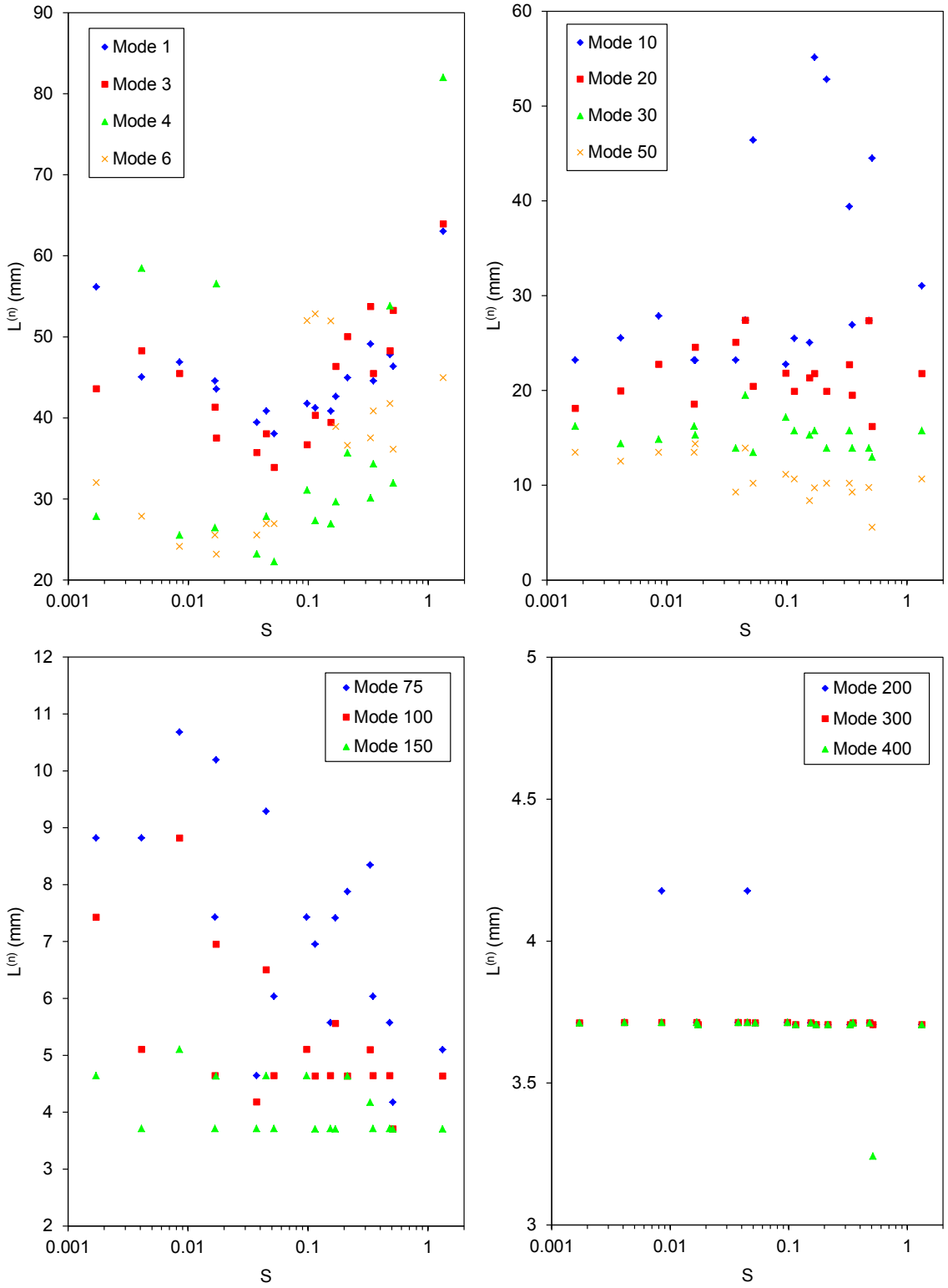

Fig. 7.26 Correlation lengths of varying POD modes against swirl ratio.

scale coherent structures and the even smaller scale incoherent turbulence.

7.5.1 Error in Approximated Velocity Vectors

The most straightforward way of comparing the resemblance between the snapshot data and the truncated POD reconstructions is to consider the difference in the velocity magnitudes. The velocity magnitudes of the i^{th} snapshot $U(\mathbf{x},t_i)$ and POD reconstruction with N_c modes $U^{(N_c)}(\mathbf{x},t_i)$ are defined as:

$$U(\mathbf{x},t_i) = \sqrt{(u(\mathbf{x},t_i))^2+(v(\mathbf{x},t_i))^2} \tag{7.5}$$

$$U^{(N_c)}(\mathbf{x},t_i) = \sqrt{\left(u^{(N_c)}(\mathbf{x},t_i)\right)^2+\left(v^{(N_c)}(\mathbf{x},t_i)\right)^2} \tag{7.6}$$

The percentage error in velocity magnitude, ε_{u_i} at each grid point is then defined as the residual between the snapshot and POD velocity magnitudes divided by the snapshot velocity magnitude:

$$\varepsilon_u(\mathbf{x},t_i) = 100\times\frac{\left|U(\mathbf{x},t_i)-U^{(N_c)}(\mathbf{x},t_i)\right|}{U(\mathbf{x},t_i)} \tag{7.7}$$

With the percentage error in velocity magnitude calculated at each point a spatially averaged percentage error can be calculated $\langle\varepsilon_{u_i}\rangle$ and then to get the spatially averaged ensemble mean percentage error the spatial averages are averaged over each snapshot i:

$$\langle\overline{\varepsilon}_u\rangle = \frac{1}{N_s}\sum_{i=1}^{N_s}\langle\varepsilon_u(t_i)\rangle \tag{7.8}$$

Figure 7.27 shows ε_u for increasing approximation order for a number of different swirl ratios. The percentage error in approximated velocity magnitudes converges to the snapshot values quite slowly, only the E30 data set with $S=0.480$ having less than a 5% error when 300 modes are used in the approximation. In contrast, for the lowest swirl ratio (dataset B15) at 300 modes the error is still 21.5%. Order 1 and 2 approximations show a big difference in the velocity magnitude error with S = 0.0017 having a 45.4% and a 45.0% error respectively compared to 14.6% and 12.8% for S = 0.330. The slower convergence with decreasing swirl ratio is due to the slower convergence of the decomposition energy as shown in Figure 7.5 with the lower swirl ratios having much more variation in the flow and hence a much higher number of modes are required to accurately capture all the flow information.

7.5.2 Comparison of actual and reconstructed vortex velocity profiles

As well as considering the differences in velocity magnitude from the reconstructed velocity vectors, other parameters regarding the structure of the vortices can be investigated. In the current study the centre of each POD approximated vortex with a particular number of modes is located using the methods described in § 6.2.4. From here the mean vortex velocity profiles are extracted

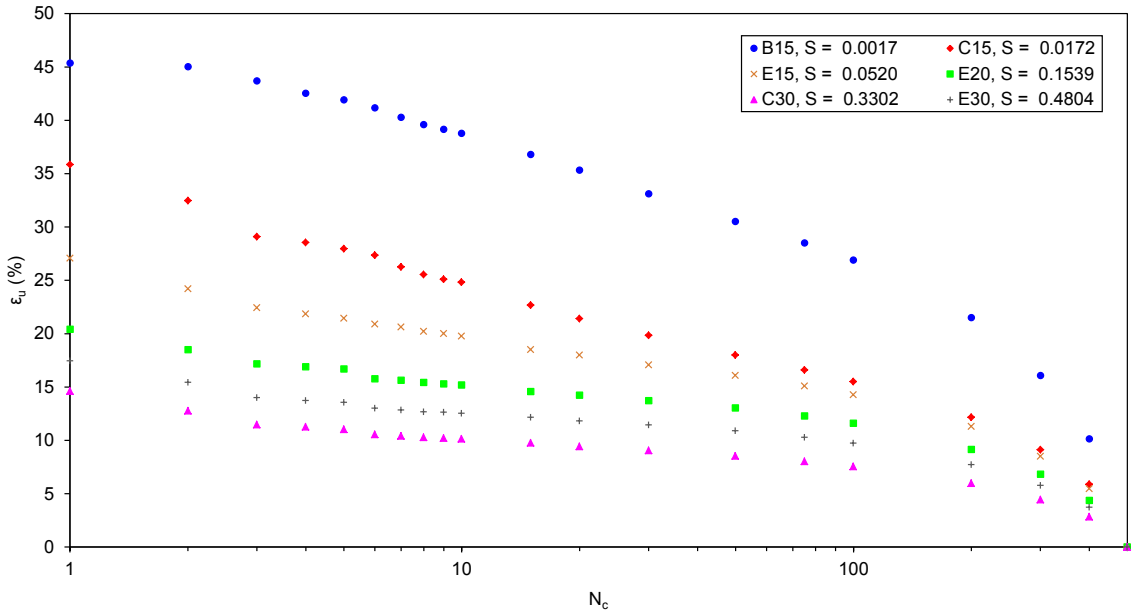

Fig. 7.27 Reconstructed velocity field average percentage error in velocity to snapshot velocities, ε_u for increasing numbers of modes used in reconstruction, N_c.

from which the vortex radius, maximum vortex tangential velocity and swirl ratio are calculated and compared to the values obtained from the snapshot vector fields.

When looking at the similarity between the snapshot vortex structure and that of the POD approximations it can be seen that the level of agreement between the two is highly dependent on both the flow conditions and the number of modes used in the reconstruction. Figure 7.28 shows that for the flow condition B15 at a low swirl ratio of 0.0017 the vortex velocity profiles extracted from the lower order approximations of the vortex are very much different to that obtained from the snapshot data. When a low number of modes are used in the approximation the resulting average vortex profile overestimates the vortex diameter and underestimates the velocities present, at least in the region inside and just outside the radius of maximum velocity. At a radius of approximately 40mm the approximated velocity profile is in strong agreement with the snapshot profile. As the number of modes used in the approximation increases the vortex radius approaches that of the snapshot radius as does the velocity magnitude although the latter approaches and then overtakes the snapshot velocity magnitude before reducing to the snapshot velocity.

For a higher swirl ratio flow configuration, E30, with a swirl ratio of 0.4804 the vortex profile (Figure 7.29) is almost identical to that of the snapshot profile from approximations with only one mode; however as with the previous case the lower mode approximations give an overestimate of the radius and an underestimate of the velocity magnitudes.

As with the case for $S = 0.4804$ at even higher swirl ratio, $S = 1.039$ the lower order approximation vortex profiles are very close to the snapshot vortex profiles using very few modes as shown in Figure 7.29. Visual inspection of the vortex velocity profiles over a range of swirl ratios clearly show that at lower swirl ratios more modes (higher order approximation) are required to model the vortex shape and velocity magnitude to a specific degree of accuracy. For higher swirl

ratios the vortex profiles are much more accurately modelled using only the first 5 modes.

7.5.3 Convergence of Vortex properties

The approximated velocity profiles from the previous figures (Figure 7.28 and Figure 7.29) can be used to determine values of maximum velocity, vortex radius and swirl ratio for the POD mode reconstructions and compared to the values calculated from the snapshot data. The convergence of these measures depend heavily on the number of modes used in the reconstruction and is explored in the following sections.

Convergence of Vortex Maximum Tangential Velocity

The vortex maximum tangential velocity $u_{\theta_{max}}$ is an important property of the vortex as it is used in calculating the swirl ratio and also marks the point from the centre of the vortex to define the radius of the vortex. Figure 7.30 shows the convergence of the POD approximation of maximum tangential velocity using N_c modes, $u^{(N_c)}_{\theta_{max}}$, to the $u_{\theta_{max}}$ calculated from the raw PIV velocity data with increasing approximation order N_c.

Figure 7.30(a) shows that the convergence of $u^{(N_c)}_{\theta_{max}}$ is dependent on both the number of modes used in the approximation and the swirl ratio of the vortex flow with lower swirl ratios requiring a larger number of modes before the approximated maximum tangential velocity converges towards the PIV values. For the lowest swirl ratio case, B15 with $S = 0.0017$ an order 1 and 2 ($N_c = 1$ and $N_c = 2$) approximation for the values of $u^{(N_c)}_{\theta_{max}}$ are only 26.9% and 30.2% of the values from the PIV data; with 15 modes required before this value reaches 50% and to reach a value of 90% approximately 140-160 modes are required in the approximation.

In comparison a higher swirl ratio case E30, $S = 0.480$ with order 1 and 2 approximations give a value of $u^{(N_c)}_{\theta_{max}}$ to an accuracy of 94.8% and 98.6% respectively with 3 modes this increases to 99.4% and converges to a value of 100% after 5 modes. For swirl ratios between $S = 0.0017$ and $S = 0.480$ the convergence of the maximum tangential velocity occurs at lower approximation order N_c with increasing swirl ratio with the lower order approximations giving an underestimate of the actual values.

For the case D225 where the swirl ratio has value $S = 1.039$ an order 1 approximation gives a value of $u^{(N_c)}_{\theta_{max}}$ equal to that of the PIV data, this value then increases with increasing approximation order giving an overestimate for the vortex maximum tangential velocity peaking at a $u^{(N_c)}_{\theta_{max}}$ value 103% that of the PIV value when 5 modes are used in the reconstruction before decreasing again and converging to the actual value by mode 10. This difference in convergence trend to the lower swirl ratios could be due to the difference in the convergence of mode energy for the lowest axial fan speed data set (D15, D225 and D30) shown in Figure 7.6.

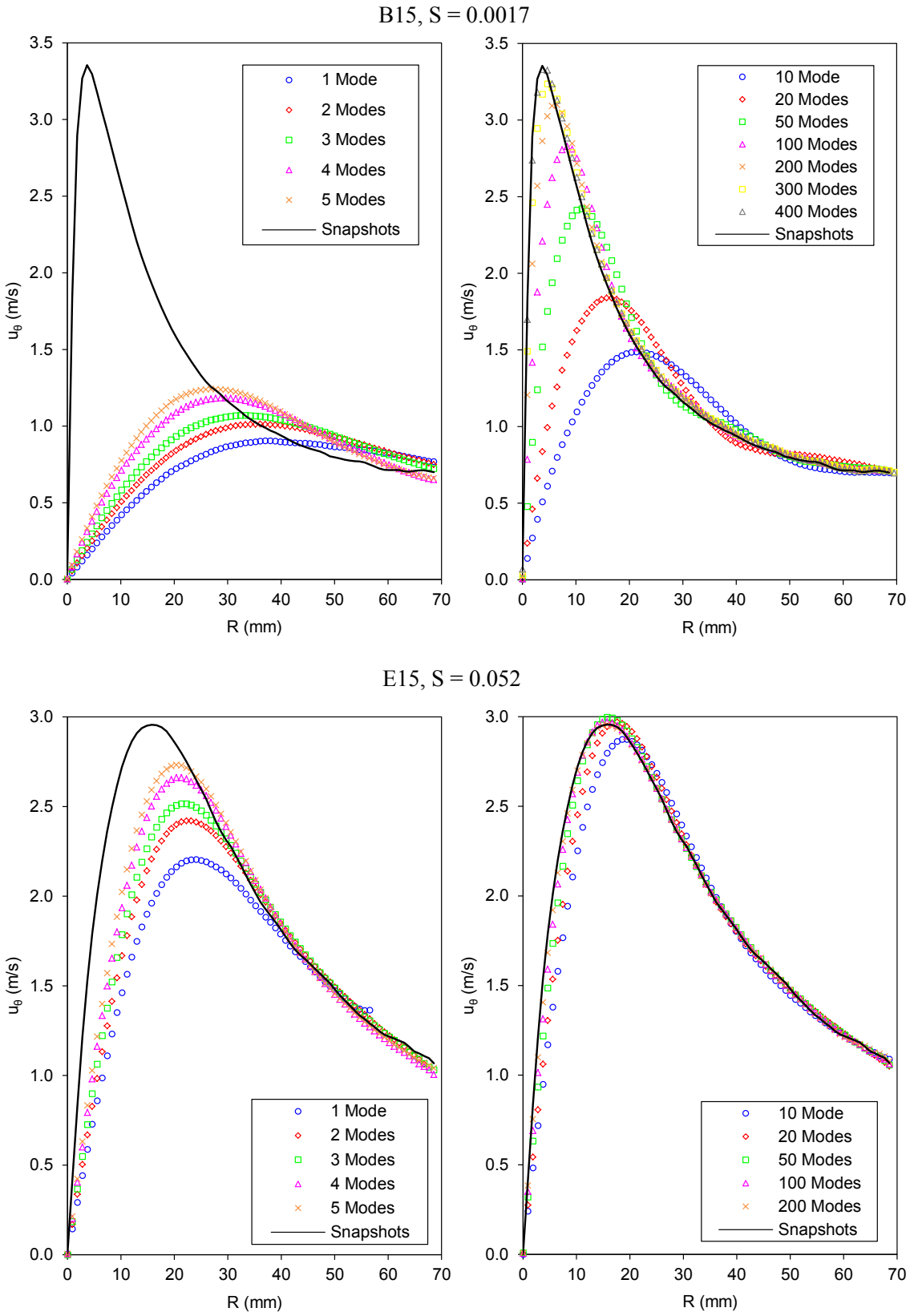

Fig. 7.28 Ensemble averaged vortex velocity profiles for POD reconstructions with varying numbers of modes compared to the snapshot velocity profile (black line) for (*top*) set B15 with a swirl ratio $S = 0.0017$ and (*bottom*) E15 with a swirl ratio $S = 0.052$.

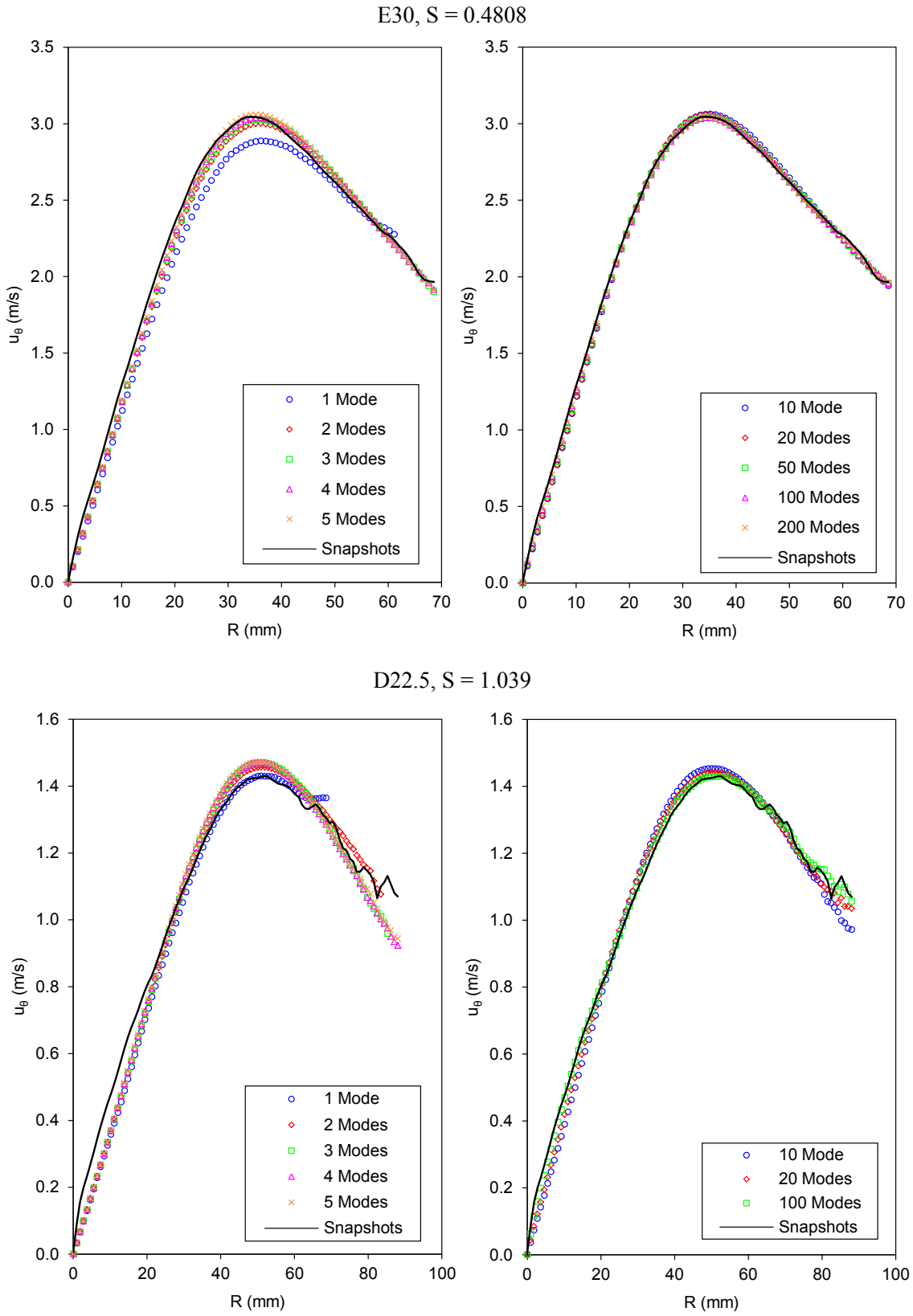

Fig. 7.29 Ensemble averaged vortex velocity profiles for POD approximations with varying numbers of modes compared to the snapshot velocity profile (black line) for (*top*) set E30 with a swirl ratio $S = 0.4804$ and (*bottom*) D22.5 with a swirl ratio $S = 1.039$.

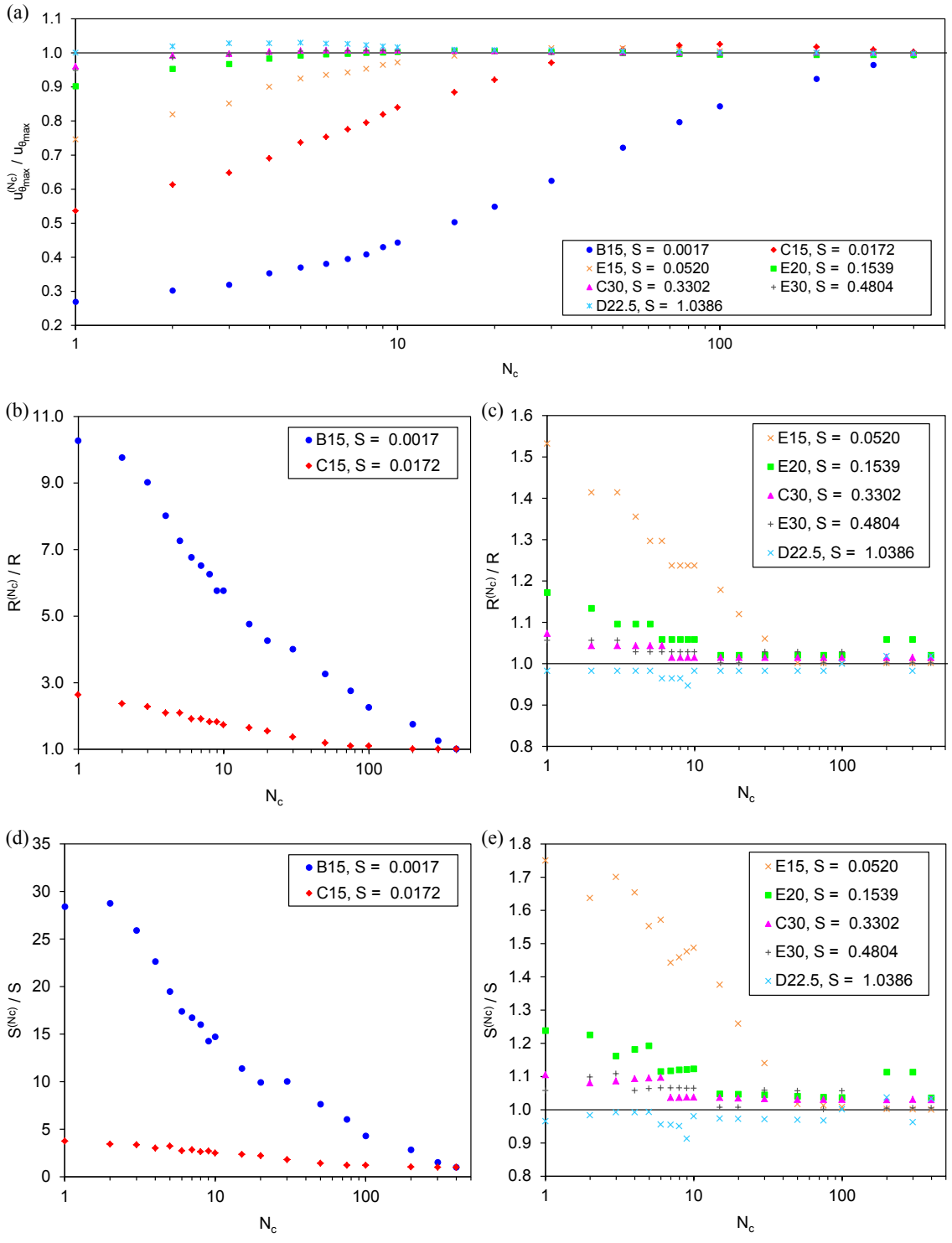

Fig. 7.30 (*a*) Convergence of reconstructed vortex maximum tangential velocity $u_{\theta_{max}}^{(N_c)}$ to snapshot vortex maximum tangential velocity $u_{\theta_{max}}$ with increasing number of modes used for the reconstruction. (*b*) and (*c*) Convergence of reconstructed vortex radius, $R^{(N_c)}$ to snapshot vortex radius, R and (*d*) and (*e*) Convergence of reconstructed vortex swirl ratio, $S^{(N_c)}$ to snapshot vortex swirl ratio, S

Convergence of Vortex Radius

The approximated vortex radius $R^{(N_c)}$ in the flow reconstructed from N_c POD modes and how this value converges as N_c increases is investigated by means of the ratio $R^{(N_c)}/R$ where R is the vortex radius in the original PIV data. The convergence of $R^{(N_c)}/R$ with increasing approximation order N_c is shown in Figure 7.30(b and c) for varying swirl ratios.

As with the maximum vortex tangential velocity, the convergence of the approximated radius to the measured radius $R^{(N_c)}/R$ is a function of both swirl ratio and approximation order with the convergence happening at lower approximation order for increasing swirl ratio.

For low swirl ratios the approximated value of vortex radius is significantly larger than the measured radius from the PIV data when a low approximation order is used. For the lowest swirl ratio, set B15, $S = 0.0017$ order 1 and 2 approximations give an approximated vortex radius of 10.3 and 9.8 times that of the actual radius. Even when the order of the approximation is 200 modes the approximated vortex radius is still nearly twice that of the measured radius ($R^{(200)}/R = 1.75$) with $R^{(N_c)}/R$ falling to 1.25 and 1.0 at N_c = 300 and 400 modes respectively.

The convergence is much quicker for higher swirl ratios with $R^{(N_c)}/R$ for data set E30, S = 0.480 having values of 1.06 for both 1 and 2 mode approximations falling to a value of 1 at an order 15 approximation. In Figure 7.30(c) the discrete nature of the data can be seen in the lack of smoothness of the graph with $R^{(N_c)}/R$ having the same value for a number of successive approximation orders, this is due to the radius being limited to discrete vector grid points. It would be possible to smooth out the radius data, for example by applying a three-point Gaussian fit to the three data points centered on the vortex maximum tangential velocity, however, here the discrete data is plotted and the trends are still observable.

As is the case with the convergence of the tangential velocity data set D225, S= 1.039, shows a different trend for $R^{(N_c)}/R$. While low order approximations for lower swirl ratios show an over estimate in the vortex radius this case shows an underestimate before settling to the measured value.

Convergence of Swirl Ratio

The convergence of the approximated vortex maximum velocity and radius to the snapshot values is of key importance when deciding the truncation order of the approximation as flow parameters such as swirl ratio are a function of these values. The convergence of the approximated swirl ratio to the measured swirl ratio is again shown in the form of the ratio of approximated swirl ratio (from the N_c reconstructed POD modes) to measured swirl ratio $S^{(N_c)}/S$. Figures 7.30(d and e) show that to accurately approximate the swirl ratio of the vortex a much higher number of modes have to be used for a low swirl ratio than for a high swirl ratio as is the case with approximating the vortex radius and vortex maximum velocity.

Figure 7.30(d and e) show that the convergence of $S^{(N_c)}/S$ follows a similar trend to the convergence of the vortex radius rather than the vortex maximum tangential velocity. This is to be

expected as swirl ratio is a function of the radius squared and a linear function of the velocity as in (6.3). At low swirl ratio the approximation of the swirl ratio shows a large error for low approximation order, for data set $S = 0.0017$ order 1 and 2 approximations give values of $S^{(N_c)}/S$ of 28.4 and 28.8 respectively which are vast over estimates. At higher swirl ratios, set E30, $S = 0.480$, give values of $S^{(N_c)}/S$ equal to 1.05 and 1.10 for order 1 and 2 approximations respectively. As is the case with vortex radius and vortex tangential velocity maximum the data set D225, $S = 1.039$ gives an underestimate of the swirl ratio before converging to the actual value.

The convergence of swirl ratio can be thought to be the most important of the three properties discussed in this section as it is swirl ratio that governs many of the other properties of the vortex flow such as turbulence levels, vortex location stability shown in Chapter § 6.

7.6 Vortex Spatial Stability

As well as interest in the properties of the vortex such as radius and maximum velocity the spatial stability of the vortex is also of interest. It is shown in § 6.2.4 that the location of vortex cores from instantaneous velocity vectors is much more varied at lower swirl ratios with a larger number of vortex cores located further from the mean vortex centre than at higher swirl ratio. It is therefore important to investigate the spatial distribution of individual vortex cores from lower order approximations.

From the PIV velocity vectors the location of individual vortex cores (x_{c_i}, y_{c_i}) are found by using (6.10). The location of the vortex core for a lower order approximated vortex $(x_c^{(N_c)}, y_c^{(N_c)})$ is calculated in the same manner. From this the error in the core location ε_d can be calculated. The mean vortex core location $(\overline{x}_c, \overline{y}_c)$ is defined as the mean of all instantaneous core locations. The distance of each instantaneous vortex core from the mean core location is then defined as:

$$d_{c_i} = \sqrt{(x_{c_i} - \overline{x}_c)^2 + (y_{c_i} - \overline{y}_c)^2} \tag{7.9}$$

Likewise, the distance of the approximated vortex centre from the mean vortex centre is defined as:

$$d_{c_i}^{(N_c)} = \sqrt{\left(x_{c_i}^{(N_c)} - \overline{x}_c\right)^2 + \left(y_{c_i}^{(N_c)} - \overline{y}_c\right)^2} \tag{7.10}$$

The error in the distance of the approximated vortex core from the mean can then be calculated as:

$$\varepsilon_d = \left| d_{c_i}^{(N_c)} - d_{c_i} \right| \tag{7.11}$$

Figure 7.31 shows the ensemble averaged error in the distance of the approximated vortex core from the mean vortex core location (the average of ε_d values over all realisations of the flow at a particular axial and tangential flow condition). It can be seen that the error in core location reduces with increasing order of the approximation and also decreases with swirl ratio. For $S = 0.0017$ order 1 and 2 approximations give an error in core location of 22.3mm and 14.9mm respectively

and by 10 modes the error in the core location drops to 7mm, it is not until 200 modes are used in the approximation that the error in the core location becomes less than the spatial resolution of the velocity vector grid points. At a swirl ratio of $S = 0.480$ the error in core location for 1 and 2 order approximations are 8.7mm and 4.4mm respectively but still requires an order 200 mode approximation to reduce the error to less than the spatial resolution of the data. It can be seen that the error in core location for higher swirl ratios at lower order approximations is less than that of high swirl ratios.

The increase in core location accuracy with lower order approximations can be attributed to the fact that at lower swirl ratio there is much more variation in the location of individual vortex cores and the energy convergence of the POD is slower requiring a higher number of modes to take account of this much increased variability in the flow. At higher swirl ratios the vortex is much more stable spatially meaning that similarity between individual snapshots is increased therefore reducing the variability in the flow and requiring a lower number of modes to capture the bulk of the flow information.

Spatial modes 1 and 2 for all data sets are shown to be a pair of orthogonal vector fields containing a pair of counter rotating vortices each as shown in Figure 7.10 and Figure 7.11. Figure 7.32 shows the core locations of reconstructed velocity fields using the first two modes, blue crosses show the core location when the reconstruction is made using only the mean and the first mode, red crosses the mean and only the second mode and the green crosses show the core location using the mean and both the first two modes ($N_c = 2$). It can be seen that modes 1 and 2 both have the effect of linearly translating the vortex core in orthogonal directions though only up to a certain distance. For the lower swirl ratios $S = 0.0017$ and 0.017 it can be seen that the core locations of reconstructed fields using both the first two modes are a combination of the mode 1 and mode 2 individual translations giving a circular distribution of core locations, for these low swirl ratios the circles are largely hollow with a relatively low number of vortex cores inside the circle as the majority of vortices at these swirl ratios lie outside of the limits of the translations of the first two modes meaning higher order modes are required to move the vortex core further away from the mean position.

For the higher swirl ratio case the distribution of vortex cores for an order 2 approximation are again circular but with the majority of the cores located towards the centre, this is due to the vortex at this swirl ratio having much greater spatial stability and more often lie within the limits of the linear translations provided by the first two modes.

The effect of the first two modes on the location of the vortex core can go some way to explaining the quicker convergence of energy in the POD at higher swirl ratios as the vortex can be more accurately placed spatially with fewer modes than is the case for low swirl ratio.

In § 6.2.4 a measure of the vortex spatial stability was presented as the standard deviation, σ_c of the distance of the individual vortex cores from the mean vortex core location. The same is done with approximated vector fields with the approximation of order N_c modes having standard

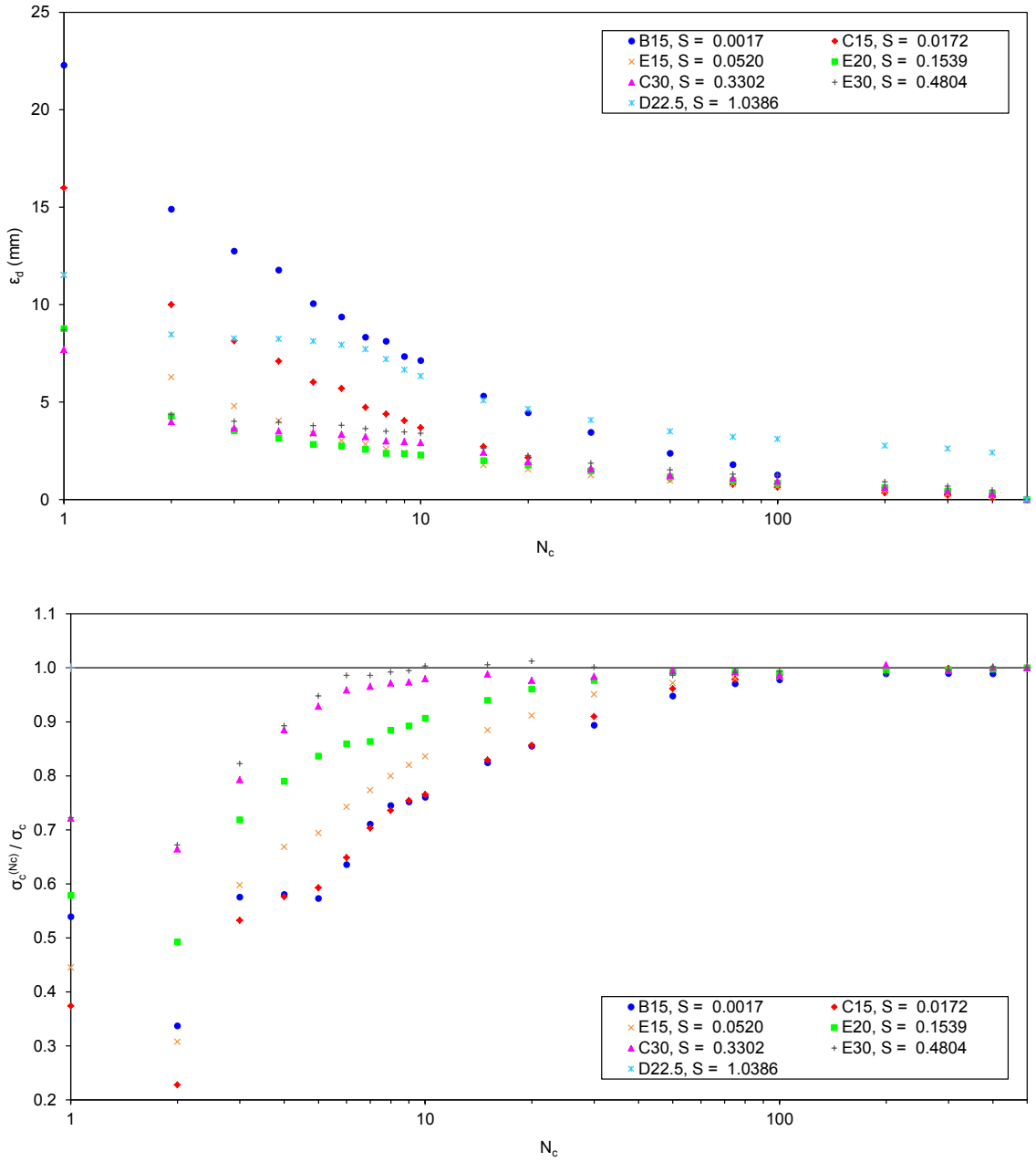

Fig. 7.31 (*top*) Ensemble average error in the location of reconstructed vortex core, ε_d for reconstructed velocity fields containing increasing an increasing number of modes, N_c. (*bottom*) Convergence of the standard deviation of reconstructed vortex core location, $\sigma_c^{(n)}$ to snapshot vortex location standard deviation σ_c

deviation of core locations from mean core location of $\sigma_c^{(N_c)}$. The convergence of the core stability to the PIV core stability is presented as the ratio of the two, $\sigma_c^{(N_c)}/\sigma_c$ in Figure 7.31.

As is the case with other properties of the flow, the convergence of the vortex stability $\sigma_c^{(N_c)}/\sigma_c$ is quicker for higher swirl ratios though the extent of the difference in the convergence is much less for different swirl ratios than other properties such as vortex radius, maximum tangential velocity and swirl ratio. Each swirl ratio shows a decrease in $\sigma_c^{(N_c)}/\sigma_c$ when N_c is 2 before moving towards a value of 1 with increasing approximation order, N_c. For swirl ratios of 0.0017 to 0.052 it takes up to approximately just over 100 modes for the scattering of the cores to converge (to within 5% of the final value), this occurs at 50 modes for $S = 0.154$ and 10 modes for $S = 0.480$.

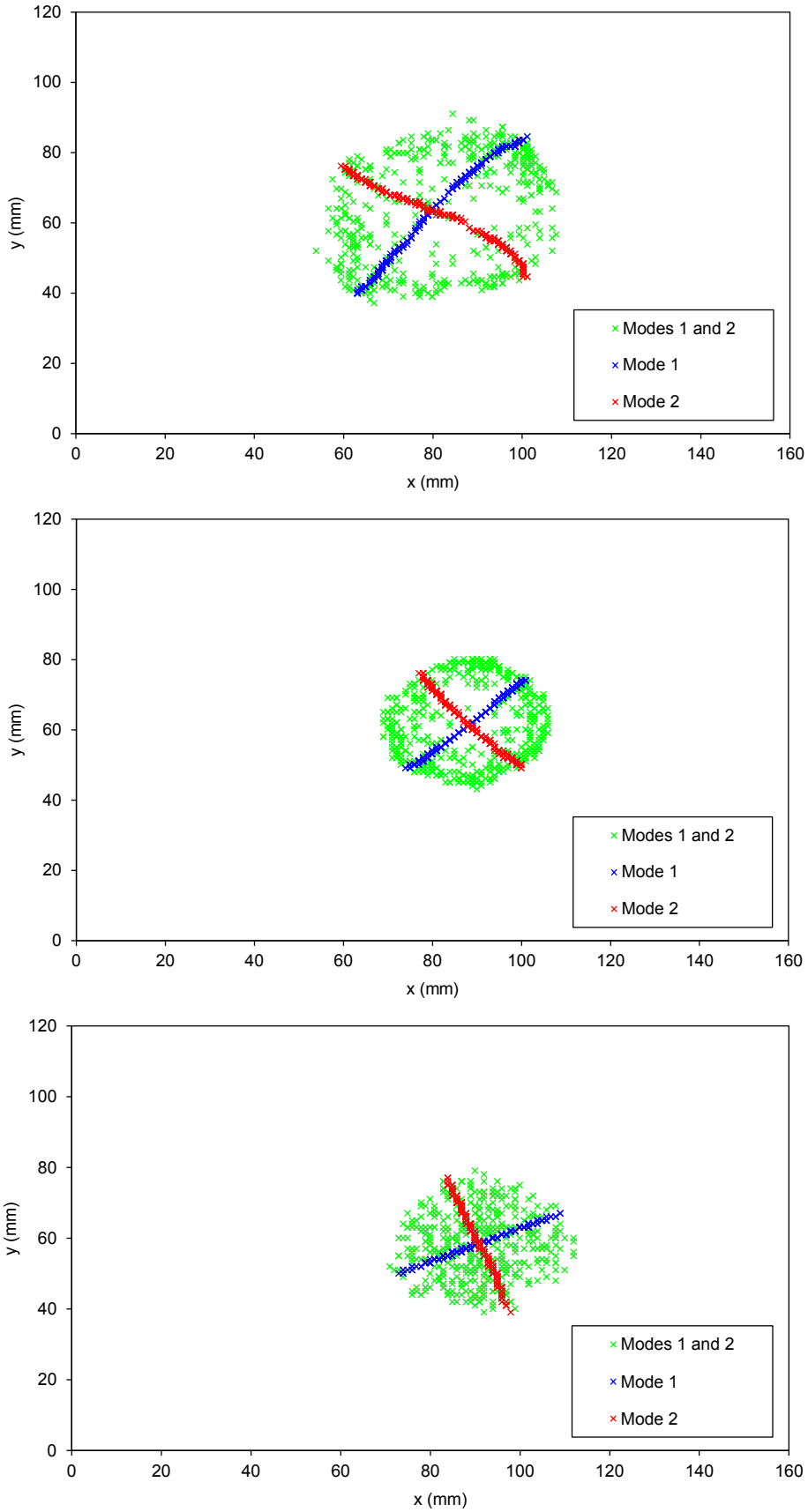

Fig. 7.32 Core locations of reconstruction using only mode 1 (blue crosses), only mode 2 (red crosses) and both modes 1 and 2 (green crosses) for B15, $S = 0.0017$ (*top*), C15, $S = 0.0172$ (*middle*) and E30, $S = 0.481$ (*bottom*)

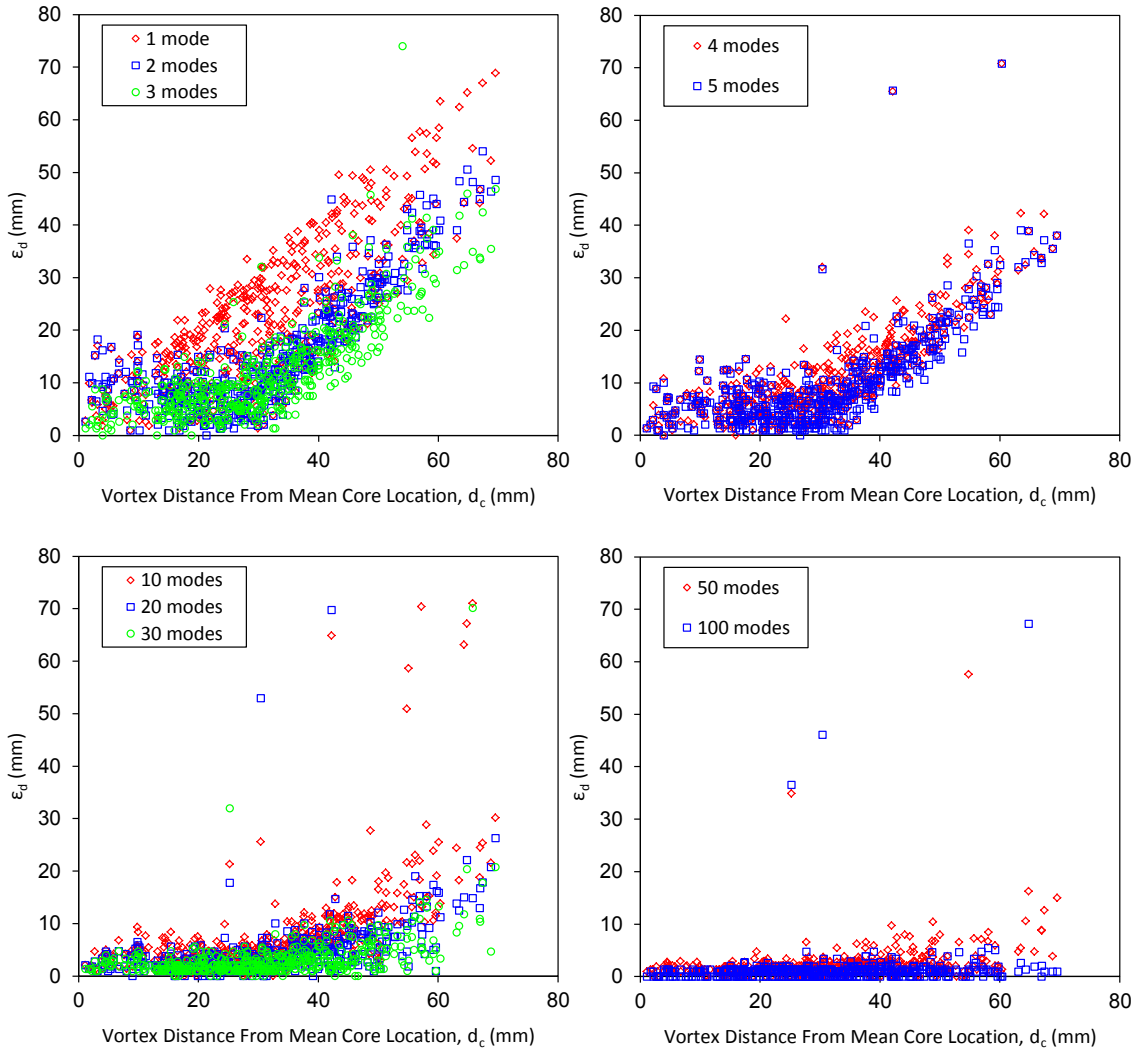

Fig. 7.33 Error in reconstructed core distance from snapshot core distance from the mean snapshot vortex core location for set B15, S = 0.0017.

Further to the average error in the vortex core location from vector fields approximated from the POD Figure 7.33 and Figure 7.34 show that for lower order approximations the error in the location of the vortex core increases the further away the original vortex core is from the mean vortex core location. In the two cases shown, set B15, S = 0.0017 (Figure 7.33) and set E30, S = 0.480 (Figure 7.34) it can be seen that a single mode approximation ($N_c = 1$) the relationship between error in approximated core location ε_d is approximately linear with increasing distance of the vortex core from the mean vortex core location d_c. An explanation of this error can be seen in Figure 7.32 where a single mode approximation only has the effect of translating the vortex core over a straight line. For approximation of order 2, $N_c = 2$, ε_d remains largely the same for values of d_c between 0 and 30mm for S = 0.0017 and between d_c = 0 and 24mm for S = 0.480, whereas for core locations with d_c greater than these values ε_d again increases in a linear fashion. Again referring to Figure 7.32 it can be seen that the limits of the constant error range show the diameter of the approximately circular distribution of vortex cores for a 2nd order approximation, the bunching of vortex cores on the edge of these distributions represent vortices with a core location outside of that which can be modelled using only the first two modes. The trend for a

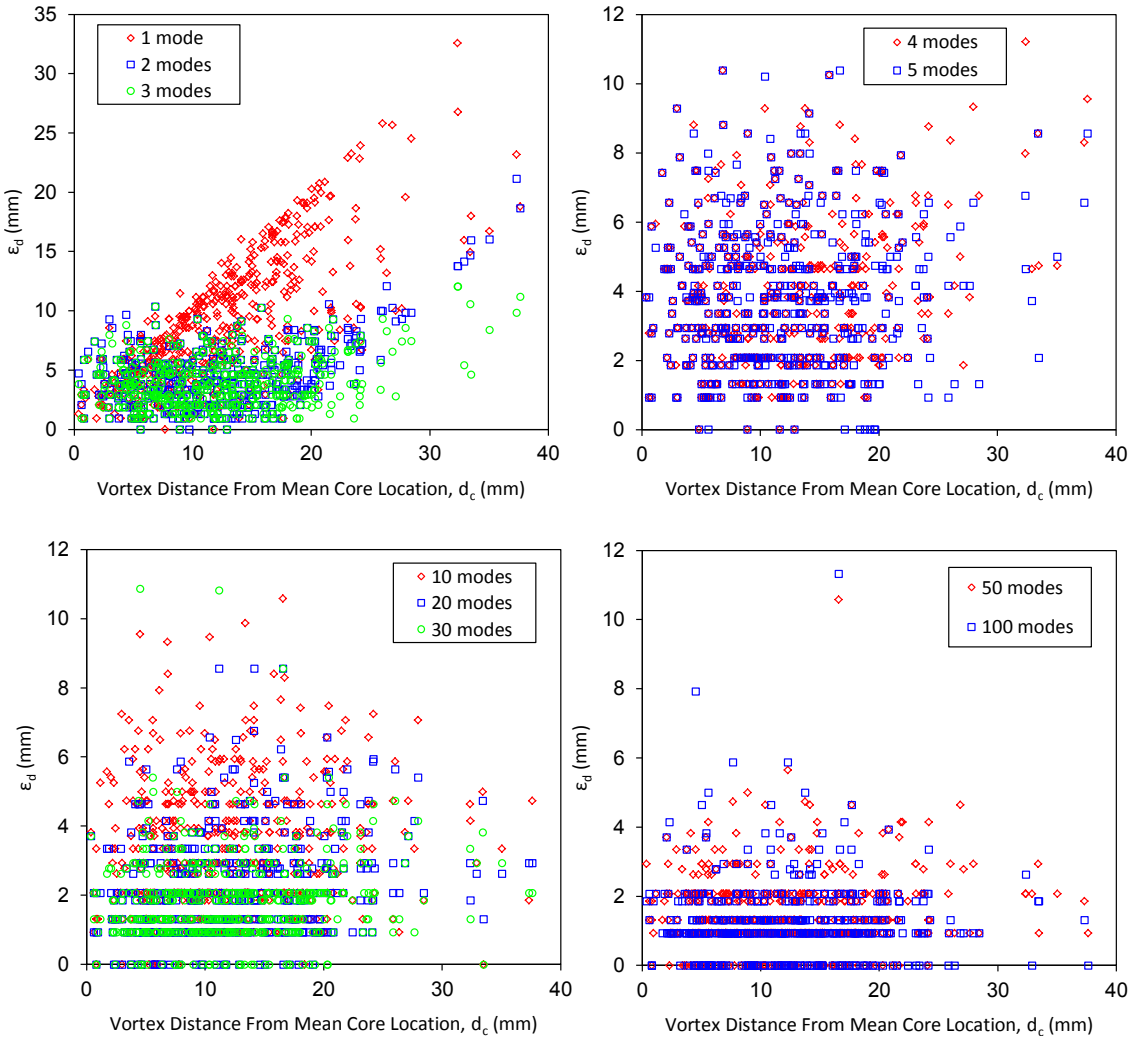

Fig. 7.34 Error in reconstructed core distance from snapshot core distance from the mean snapshot vortex core location for set E30, $S = 0.480$.

3rd order approximation is very similar to that of a 2nd order one only with ε_d having slightly lower values for higher d_c and the error in the core location for the higher swirl ratio is lower for corresponding dc values than the lower swirl ratio indicating that the higher proportional energy content of the lower modes at higher swirl ratio lead to more accurate lower order approximations of the flow.

For the $S = 0.0017$ case increasing the order of approximation still leaves a dependence on the value of dc though the threshold over which the error increases with increasing approximation order with ε_d remaining largely constant for d_c values of up to 40-45mm before increasing for d_c values greater than this. By the time the approximation order is 100 the error in core location is not dependent on the location of the core showing that between 50 and 100 modes are required to accurately locate the vortex core spatially. The dependence on d_c for $S = 0.480$ disappears for approximations of order greater than 4.

7.7 The Effect of Core Location on the Convergence of Turbulent Kinetic Energy

The turbulent kinetic energy, k of an individual two-dimensional velocity vector field is given as:

$$k = \frac{1}{2}\left(u_{rms}^2 + v_{rms}^2\right) \tag{7.12}$$

Similarly the turbulent kinetic energy of an approximated velocity field of approximation order N_c is given as:

$$k = \frac{1}{2}\left(\left(u_{rms}^{(N_c)}\right)^2 + \left(v_{rms}^{(N_c)}\right)^2\right) \tag{7.13}$$

Since the POD breaks the flow into a set of modes on energy terms and velocity fields are represented as a linear combination of these modes the more modes used in an approximation the more of the total energy, k is contained within that approximation. Whilst the value λ gives the relative energy associated with each mode on average across each snapshot vector field it is useful to investigate the energy content of individual order N_c velocity vector fields. The percentage energy content of an individual approximation of order, N_c to the total energy content is then given as the following ratio:

$$\frac{k^{(N_c)}}{k} \tag{7.14}$$

Using the ratio of approximate energy content to total energy content the convergence of energy of the decomposition can be investigated as a function of the spatial location of individual vortices. Figure 7.35 and Figure 7.36 show the convergence of turbulent energy for different order approximations of individual velocity vector fields as a function of the spatial distance of the individual vortex core from the mean vortex core location d_c. For the low swirl ratio case in Figure 7.35 where S = 0.0017 it can be seen that the distance of an individual measured vortex core from the mean vortex location has little bearing on the percentage energy content of approximated velocity fields for approximations of order less than 50. For approximations of order 50, 75 and 100 it can be seen that the total energy content converges quicker (with a linear trend as shown in Figure 7.37) the further away from the mean vortex location an individual vortex is located.

For the higher swirl ratio data set, E30, S = 0.480 the energy content of approximated velocity vectors is heavily dependent on the distance an individual vortex lies from the mean vortex location as shown in Figure 7.36. It can be seen for a vortex close to the mean vortex location approximated velocity vector fields contain a lower proportion of the total turbulent kinetic energy than for vortices further away from the mean vortex location. Figure 7.38 shows that the energy convergence as a function of the distance of a vortex from the mean vortex location closely fits a second order polynomial trend.

Using the fitted data in Figure 7.39 the average proportion of turbulent kinetic energy contained

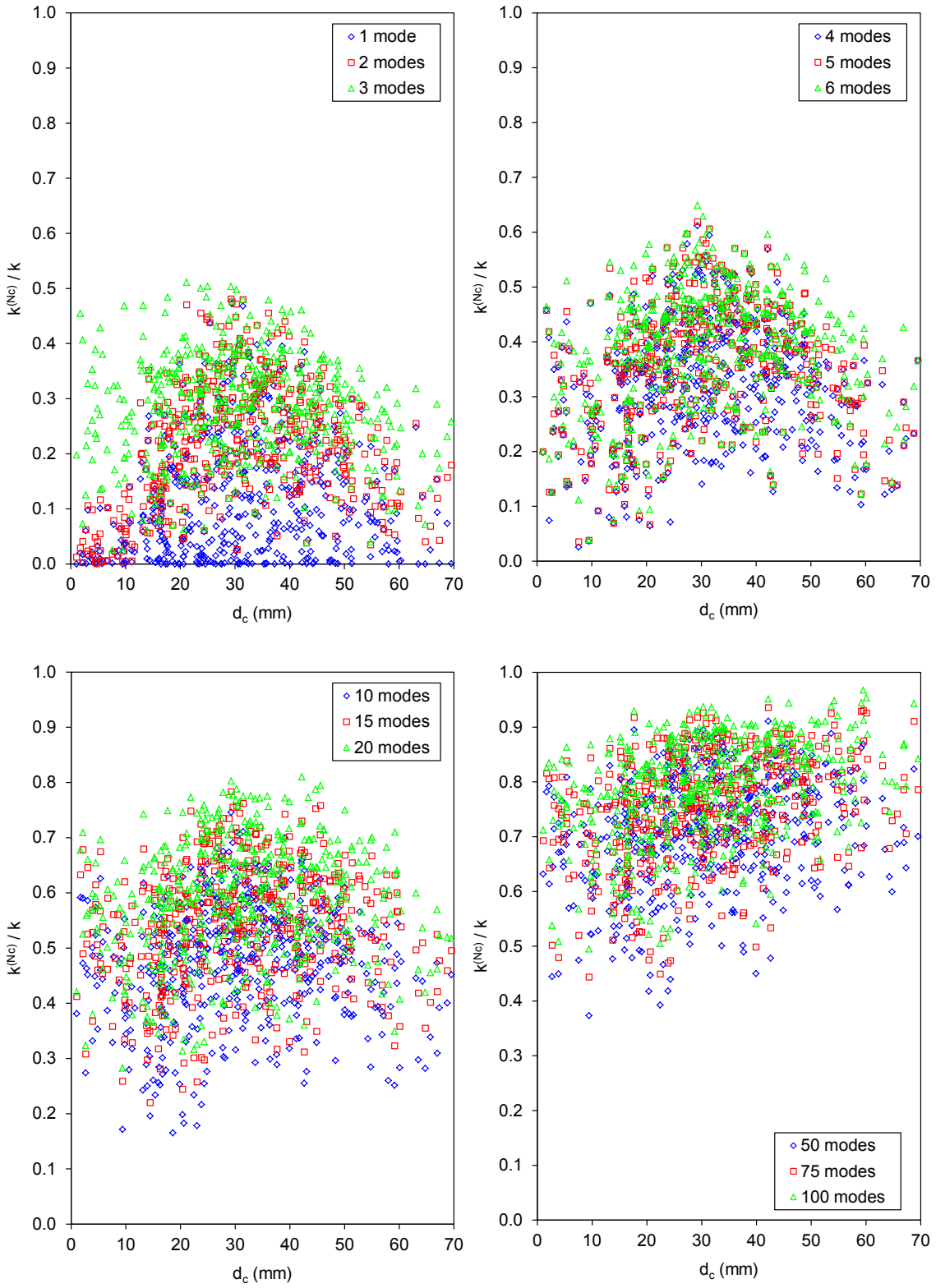

Fig. 7.35 Convergence of turbulent kinetic energy of reconstructed velocity fields as a function of vortex distance from mean vortex location for set B15, $S = 0.0017$.

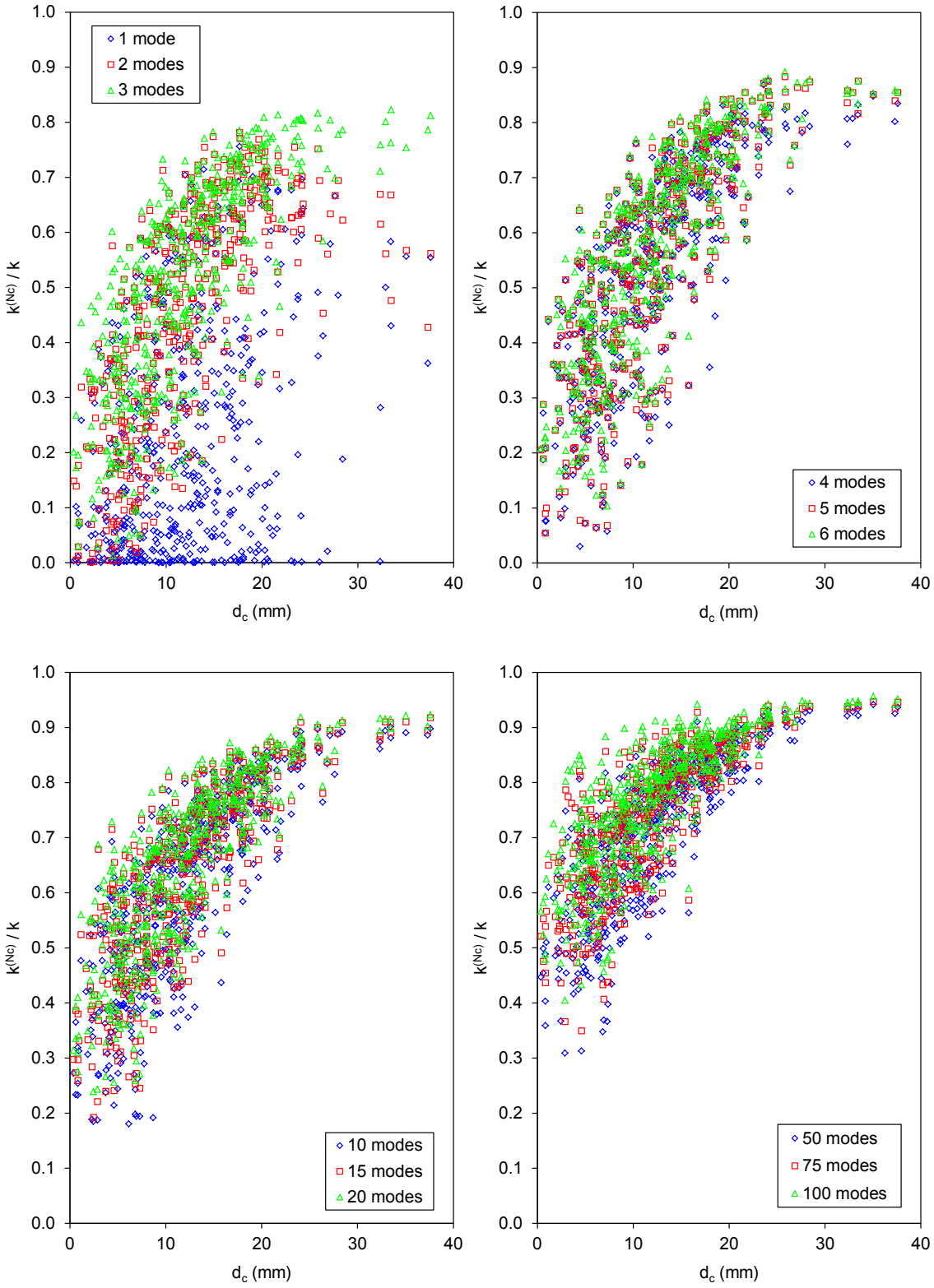

Fig. 7.36 Convergence of turbulent kinetic energy of reconstructed velocity fields as a function of vortex distance from mean vortex location for set E30, $S = 0.480$.

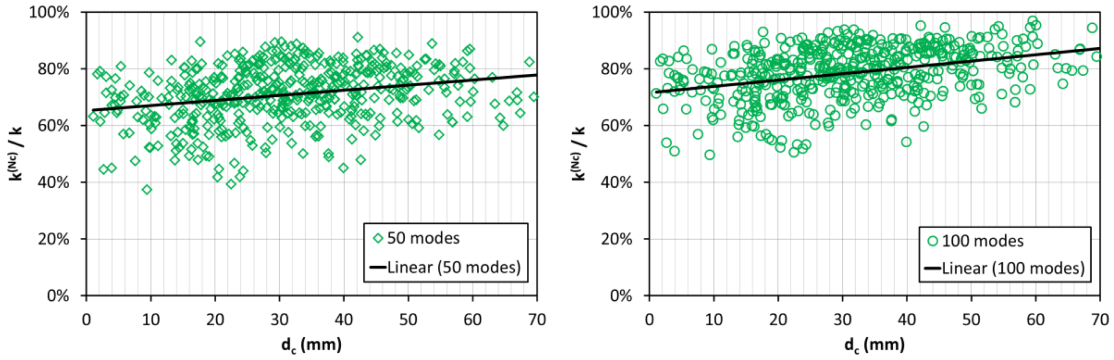

Fig. 7.37 Linear trend fits of turbulent energy convergence as a function of vortex distance from mean vortex location for (*left*) a 50 mode approximation and (*right*) a 100 mode approximation for data set B15, $S = 0.0017$.

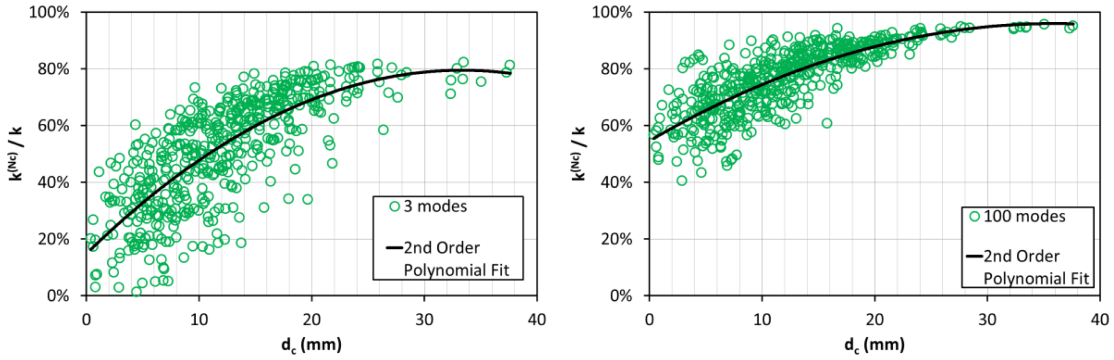

Fig. 7.38 2nd order polynomial fits of turbulent energy convergence as a function of vortex distance from mean vortex location for (*left*) a 3 mode approximation and (*right*) a 100 mode approximation for data set E30, $S = 0.480$.

in approximations of various order as a function of the vortex distance from the mean vortex location can be seen. For a low order approximation of order, $N_c = 3$ for a vortex close to the mean vortex location, $d_c = 0.38$mm, on average only 16% of the total turbulent kinetic energy is accounted for, this increases up to 79% for vortices located at the furthest distance of 37.62mm. This trend holds as the approximation order is increased, for an approximation of order $N_c = 100$ still only 55% of the total energy is captured for vortices a distance 0.38mm from the mean vortex location, again, this increases up to 96% for vortices a distance of 37.62mm away.

A similar trend can be seen in the low swirl ratio case of data set B15, $S = 0.0017$ but the effect of vortex location on energy convergence is not as pronounced as in the E30, $S = 0.480$ case in that vortices close to the mean vortex location contain a higher proportion of the total turbulent kinetic energy than those further away.

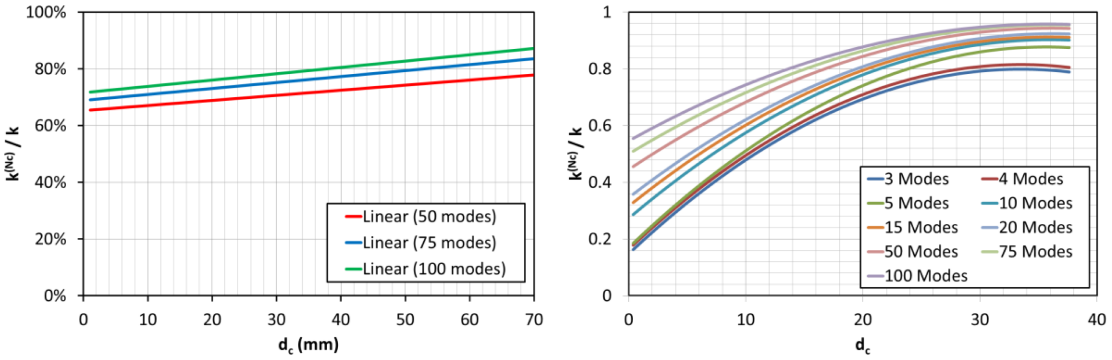

Fig. 7.39 (*left*) Convergence of turbulent kinetic energy for data set B15, S = 0.0017 as a function of vortex distance from the mean vortex location and (*right*) the convergence for data set E30, S = 0.480.

7.8 Summary

Presented in this chapter, to the knowledge of the author, is the first proper orthogonal decomposition of laboratory generated tornado-like vortex flow.

The total turbulent kinetic energy of the flow is distributed among a basis of spatial modes (coherent structures). Energy is more heavily distributed in the lower order modes with subsequent modes accounting for less of the total energy than the previous one.

For each flow configuration the first two modes are the most energetic, the combined energy contained within the first two modes is shown to follow a well defined relationship increasing with swirl ratio ranging from 24% to 58% for swirl ratios less than 0.5. The change in flow regime for high swirl ratios ($S > 0.5$) highlighted in the previous chapter is again evident as the energy content of the first two modes is reduced to approximately 40%.

Mode energy content quickly reduces with increasing mode number for mode 3 and above with mode 3 at most containing only 13% of the total flow energy, by the sixth and 15th modes only a maximum of 3.3% and 1.15% of the total flow energy respectively is contained showing how low order modes dominate the flow.

The individual mode energy content is closely linked to swirl ratio with three distinct regimes for low, intermediate and high swirl levels as identified in the previous chapter. Between modes 4 and 15 modal energy content is greatest at low swirl ($S < 0.008 - 0.01$) where the modal energy varies little with swirl ratio. At intermediate swirl ratios ($0.01<S<0.5$) energy content decreases with swirl ratio before increasing slightly for high swirl ratios ($S > 0.5$) showing how the dominance of certain coherent structures is swirl ratio dependent.

Convergence of mode energy is quickest in the intermediate swirl range which is consistent with the more organised, low precession, well defined vortex structure nature of the flow. Convergence is slower at low swirl ratios owing to increased variation due to vortex precession and slower at high swirl ratio owing to increased variation in structure within the vortex core due to the multi-cellular nature.

Low order spatial modes (coherent structures) comprise of well defined, highly organised vortex structures with some shown to act as pairs. Modes 1 and 2 are made of two counter-rotating vortices with an approximate 90° rotation between the modes and also account for similar percentages of the total energy. The same is observed with modes 4 and 5 which are each made of two pairs of counter rotating vortices and again having similar energy content.

For the low order modes the structure of each mode remains unchanged with varying swirl ratio with only the spatial dimension of the structures changing apart from mode 6 where a clear change of structure is observed between low and intermediate to high swirl ratios.

The spatial dimensions of the structures in the lower order modes such as vortex radius and distance between vortex pairs show well defined relationships to swirl ratio again showing different regimes between low and high swirl ratio.

As modal energy content decreases so does the length scale of the spatial structures present

within them showing that the most energetic lower order modes contain highly organised, structured flow information. Beyond mode 200 there is almost no correlation between spatially separated points which leads to the conclusion that these modes contain the unstructured stochastic turbulence of the flow.

Mean velocity profiles of lower order approximations to the instantaneous PIV vectors are presented showing how at higher swirl ratios the measured velocity profiles are more accurately recreated using a lower number of modes than those at lower swirl ratios. This is reflected in the convergence of vortex radius, vortex maximum tangential velocity and swirl ratio of approximated velocity fields. In general, convergence towards the measured values (with an increasing number of modes used in the approximation) is quicker with increasing swirl ratio owing to the reduced variation in the flow with the decreasing influence of vortex precession.

Lower order approximations are shown to underestimate the level of vortex precession observed in the measured data. Approximations comprising only the first or second modes are shown to translate the vortex along two orthogonal straight lines. It is shown through the slow convergence of approximated vortex core centres to measured values that significant flow information is still contained within higher order modes up to approximately mode 100 and especially for low swirl ratios where precessional effects are greatest.

When vortex precession is high (low swirl ratios) it takes a greater number of modes to accurately spatially position a realisation of a measured vortex the further away from the mean vortex core location it is positioned. At higher swirl ratios where the effect of precession is much reduced the error in vortex core location is independent of position for approximations of order 3 and greater.

At low swirl ratio energy convergence of approximated velocity vectors is quicker the further away from the mean vortex centre a vortex is located suggesting that lower order modes contain significant translational information.

The results presented here provide a new understanding of flows of this type identifying the coherent structures that interact to form the flow we observe. The energy content of these structures identified through POD provide a valuable means of characterising the variability of the flow and its dependence on swirl ratio. POD provides valuable information regarding the spatial structures contained within the flow, in order to investigate the temporal structures velocity data captured at a higher sampling frequency is required and this is carried out in the next chapter.

Chapter 8

High Speed PIV of a Tornado-Like Vortex

8.1 Introduction

The results obtained in Chapters § 6 and § 7 were obtained using low repetition rate PIV. While this provided a good data set for the evaluation of spatial characteristics of the flow in order to evaluate the dynamics of the flow, data captured at a higher sampling frequency is required.

As far as the author is aware this is the first time high temporal resolution full-field velocity measurements of a laboratory tornado-like vortex have been conducted. The aim is to investigate the dynamics of the flow through an evaluation of energy-frequency and energy-wavenumber spectra and temporal and spatial velocity correlations from which length and time scales, characteristic frequencies and wavenumbers and estimations of dissipation rates and Kolmogorov length scales can be made. POD is also applied to the new data sets in which the dynamics of the coherent structures are investigated by analysing the time evolution of the POD coefficients associated with each mode. Finally the chapter concludes with a comparison of POD conducted on a synthetic dataset with that obtained through PIV.

The PIV system used to capture the data in this chapter consists of a high repetition rate laser synchronised to a high speed camera. The laser is a twin cavity 527nm Litron LDY300 PIV laser with a maximum repetition rate of 10kHz per cavity resulting in a maximum repetition rate of 20kHz combining both cavities. The camera is a black and white Photron Fastcam SA1.1 with a resolution of 1024 x 1024 pixels squared and 12-bit greyscale levels with enough onboard memory to store 5400 images at full image resolution or 2700 PIV image pairs.

It is required that both high and low frequency flow features are measured, due to the limitations of the camera storage capacity a compromise on the sampling frequency had to be made. The sampling frequency was chosen to be 125Hz giving a temporal resolution of 0.008 seconds and a recording length of 21.6 seconds (2500 image pairs) ensuring that the full effects of vortex precession could be recorded.

Based on the data presented in Chapter 6 five flow conditions were selected with a swirl ratio range of 0.032<S<0.979 using three different axial fan speeds and two different circulation blower supply voltages (see Table 8.1 for a summary of the flow configurations). Measurements were taken in the same plane as the low repetition rate PIV measurements. The time separation between image pairs was adjusted based on the axial fan flow rate, with a dt value of 2μs for the highest axial fan flow rate and 6μs for the lowest.

8.2 Results

For the five flow configurations the swirl ratio was calculated using the method presented in § 6 where the effect of vortex precession is removed from the flow by finding the instantaneous vortex centre. The mean radius, R of the vortex for each flow configuration is calculated based on this centre point and the azymuthally averaged tangential velocity profile. Combined with the calculation of the flow rate through the rig from hotwire velocity profiles of the axial velocity component through the updraft orifice the swirl ratio is calculated using (6.1). Swirl ratio and vortex radius for each flow configuration are presented in Table 8.1. The datasets are labelled HS-A#. Where HS indicates high speed so not to be confused with data sets from the low speed PIV. A is the axial fan setting which has three values; F for full speed M for a medium fan speed and L for a low fan speed with the number corresponding to the voltage supplied to the circulation blowers.

A range of swirl ratios was obtained, ranging from S = 0.032 up to S = 0.979. The mean radius of the instantaneous vortices is presented as a function of swirl ratio in Figure 8.3. For reference the vortex radius obtained from the low-speed PIV in Figure 6.9 is presented as a dashed red line. The solid black line in Figure 8.3 is a power law trendline fitted using the inbuilt trendline function in MS Excel. The relationship between vortex radius and swirl ratio for the low-speed PIV experiments and the high-speed data presented here are largely in agreement. The relationship between normalised instantaneous vortex radius, R/r_0 and swirl ratio is of the following form:

$$\left(\frac{R}{r_0}\right) = \alpha S^{\beta} \tag{8.1}$$

where α is a constant and β is the power law exponent. It can be seen in Figure 8.3 that for a given swirl ratio the vortex radius is slightly less than that obtained at a corresponding swirl ratio in the low speed PIV experiment with the scaling factor, α having a reduced value of 0.582 in the current study compared to a value of 0.690 in the previous experiment. The power law exponents, β are in close agreement with values of 0.462 for the high-speed data and 0.417 for the low speed. The variation in measured vortex radius between the two experiments can be accounted for by the fact that between the two experiments the rig was dismantled for storage so variation in the exact alignment of the axial fan and the circulation pillars is to be expected. On the whole however the two sets of results are largely in agreement showing reasonable repeatability.

Figure 8.1 and Figure 8.2 show PIV vector sequences at intervals of 1000ms for the lowest

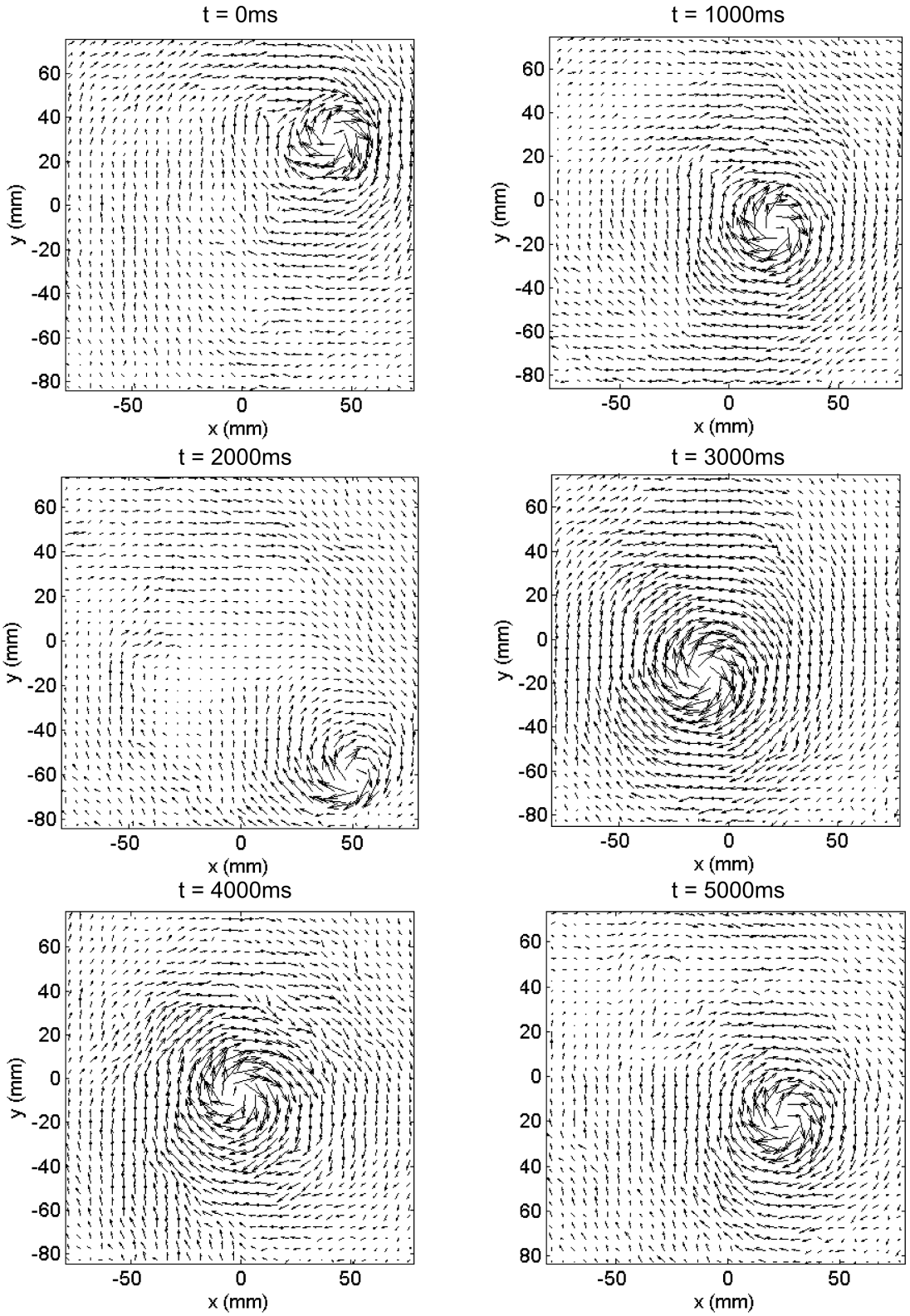

Fig. 8.1 PIV vector sequence at intervals of 1000ms for configuration HS-M17, $S = 0.032$. Every fourth vector shown for clarity.

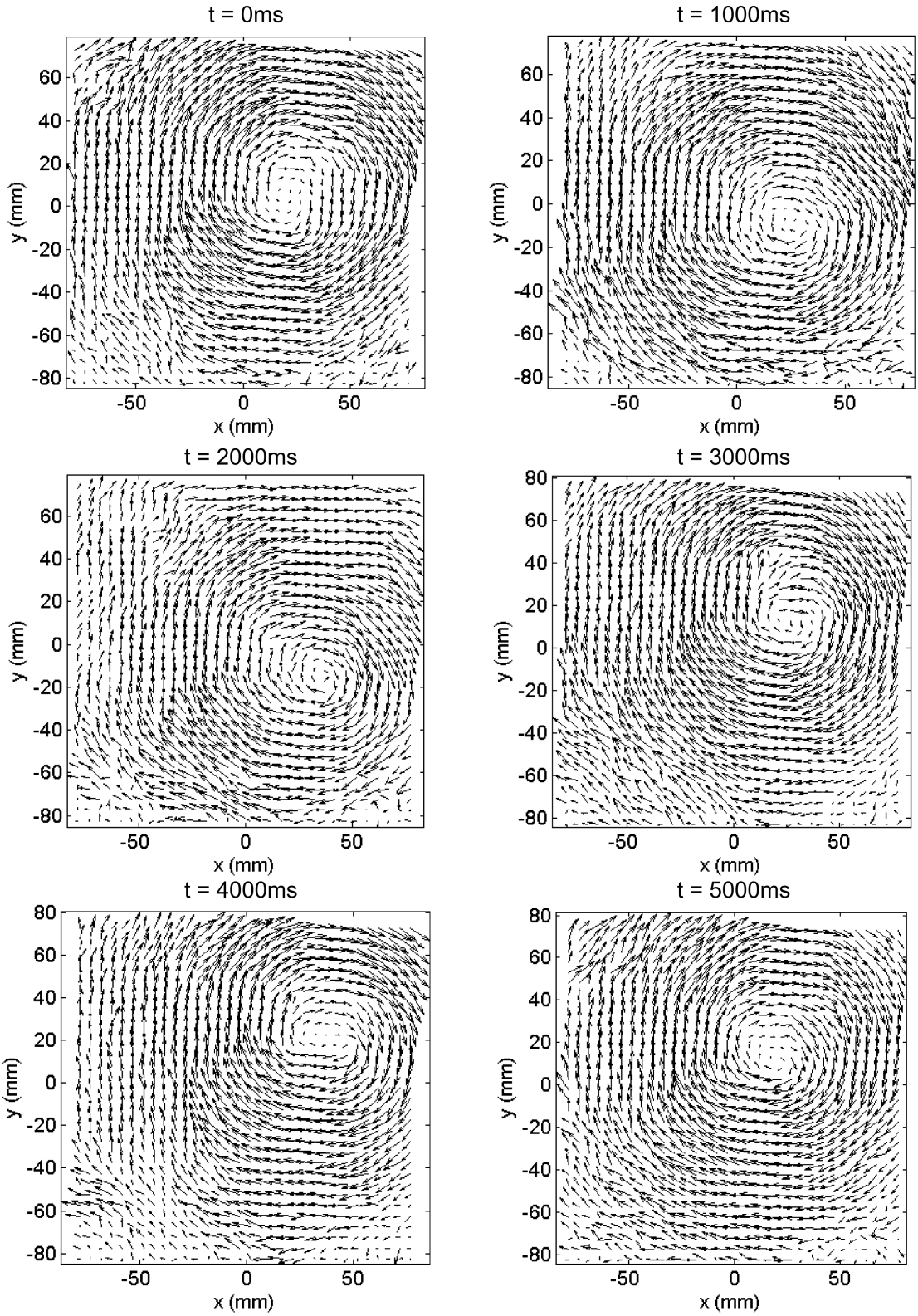

Fig. 8.2 PIV vector sequence at intervals of 1000ms for configuration HS-L30, $S = 0.979$. Every fourth vector shown for clarity.

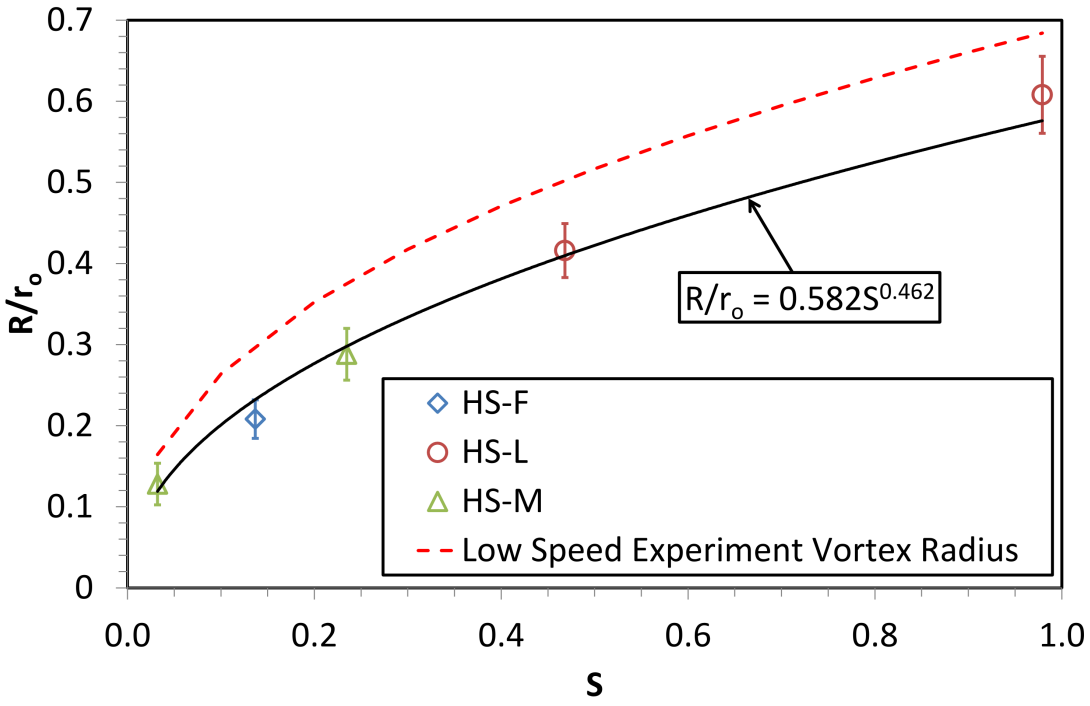

Fig. 8.3 Normalised mean instantaneous vortex core radius as a function of swirl ratio. Error bars indicate +/- one standard deviation in instantaneous R/r_0 values.

swirl ratio configuration, HS-M17, $S = 0.032$ and the highest, HS-L30, $S = 0.979$ respectively. It can be seen that for $S = 0.032$ the vortex is small and exhibits a high degree of precession whereas at high swirl, $S = 0.979$, a large vortex is present and shows little precession. This is consistent with the results presented in Chapter 6.

The extensive analysis carried out in the previous section of the flow data obtained using low-speed PIV will not be revisited here; rather the mean characteristics of the HS-PIV data will be presented and the remaining analysis will focus on the unique understanding that can be gained with high speed velocity realisations.

8.2.1 Mean Flow Characteristics

Time averaged velocity vectors of the PIV data were calculated using (6.5) and (6.6). From the mean flow velocity vectors the radius of the vortex, R_a is calculated as the distance from the mean flow vortex centre to the radius at which maximum wind speed, u_{max} occurs. The radius of the

Table 8.1 Summary of flow vortex characteristics for the five flow configurations used in the high-speed PIV experiments.

	HS-M17	HS-F30	HS-M30	HS-L17	HS-L30
R/r_0	0.128	0.208	0.288	0.416	0.608
Q (m^3/s)	0.066	0.071	0.046	0.015	0.013
S	0.032	0.137	0.235	0.468	0.979

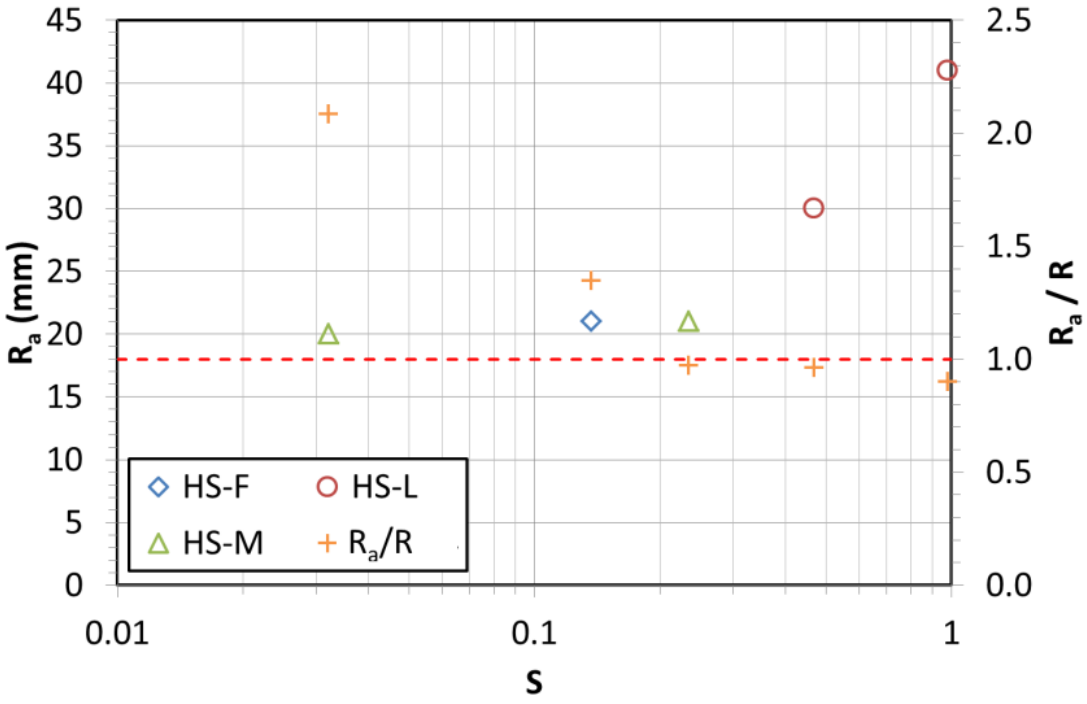

Fig. 8.4 Mean flow vortex radius against swirl ratio and ratio of mean flow vortex to mean instantaneous vortex radii against swirl ratio.

mean flow vortex and the ratio of the mean flow vortex radius to the mean instantaneous vortex radius, R_a/R are presented in Figure 8.4. As with the mean instantaneous vortex radius against swirl ratio the mean flow vortex radius against swirl ratio relationship is in close agreement with the results obtained from the low-speed PIV as presented in Figure 6.16. The current results show that for the range of swirl ratios covered R_a increases with increasing swirl ratio, this is in agreement with the results in Figure 6.16 where R_a also increases with increasing swirl ratio with the only noticeable difference being that R_a for the current results is approximately 5mm lower than those from the previous low-speed results, again, this can be attributed to natural variation arising from the dismantling and rebuilding of the rig between experiments. The values of R_a/R between the two experiments are both in close agreement with R_a/R having a value of between 2 and 2.5 for a swirl ratio in the region of 0.01 and becoming closer to 1 with increasing swirl ratio.

The mean flow properties and relationship with the instantaneous vortices presented here show that the two experiments exhibit closely similar mean flow characteristics and are comparable.

8.2.2 Analysis of Velocity Time-Series

The results obtained in the first experiment were obtained using low-speed PIV with a low temporal frequency of approximately 2-3Hz, the temporal resolution of which is too low to calculate temporal turbulence characteristics and hence the focus on spatial properties of the flow. The current high-speed PIV data was obtained at a much higher temporal resolution of f_s = 125Hz allowing for the investigation of turbulence properties temporally. As it has been shown the bulk flow characteristics between data obtained from both experiments are comparable and for that

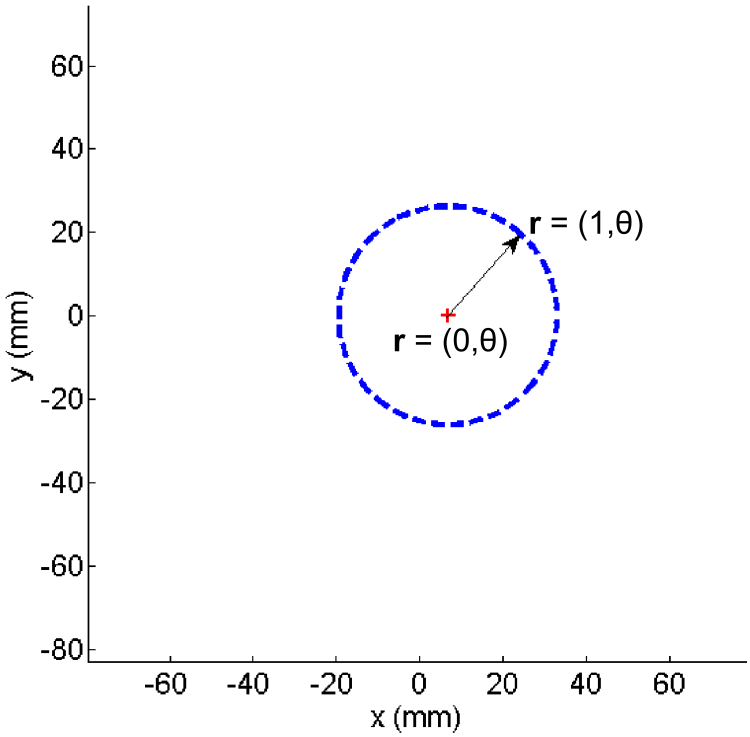

Fig. 8.5 Coordinate system employed for the analysis of time series data. The red cross indicates the mean flow vortex center $(\overline{x_c}, \overline{y_c})$ which becomes the origin for the position vector $r = (\rho, \theta)$. The blue circle has radius R_a.

reason the majority of the spatial analysis will not be repeated on the high-speed data.

When analysing the time-series velocity data it is not practical to do so at each vector location due to the large amount of data contained within each dataset. Each dataset consists of 2700 instantaneous velocity vector fields, each containing 128 x 128 = 16384 velocity vectors so time series analysis will be conducted at a grid of individual points. The limiting factor of 2700 instantaneous velocity fields is based on the on-board memory capacity of the high speed camera which at the sampling frequency chosen at 125Hz gives a recording time of 21.6 seconds.

It was decided to evaluate the velocity vectors using Cartesian components in the x and y direction as the high degree of precession of the vortex make interpretation of instantaneous radial and tangential velocity components somewhat misleading when a fixed origin is used thus leading to steep gradients between positive and negative values as the instantaneous vortex core location moves relative to the origin. The instantaneous velocity u_i is the velocity component in the i^{th} coordinate direction which due to the planar measurements takes the values 1 (parallel to the x-axis) and 2 (parallel to the y-axis).

Although Cartesian velocity components are used polar coordinates are henceforth used to describe the position in the flow field, $r = (\rho, \theta)$ with origin at the centre of the mean flow vortex and normalized radial component $\rho = r/R_a$ and azimuth θ where $\theta = 0$ runs parallel to the y-axis in the positive direction. The coordinate system is shown in Figure 8.5, the position $r = (1, \theta)$ is a point on the circle with origin at the mean flow vortex centre and radius equal to that of the mean flow vortex.

Time series data is evaluated at $\theta = \pi/4, 3\pi/4, 5\pi/4, 7\pi/4$ and ρ from 0 to 2 at intervals of 0.25.

The time-series mean velocity at point r is calculated in the usual manner:

$$\overline{u}(\mathbf{r}) = \frac{1}{N}\sum_{n=1}^{N} u(\mathbf{r}, t_n) \tag{8.2}$$

Where $t_n = (n-1)\Delta t$ with $\Delta t = 1/f_s$ the time between measurements at the sampling frequency f_s=125Hz and N = 2700 instantaneous vector fields. Likewise, using Reynolds Decomposition the fluctuating component of velocity, u_i' is calculated as follows:

$$u'(\mathbf{r}, t) = u(\mathbf{r}, t) - \overline{u}(\mathbf{r}) \tag{8.3}$$

The average velocity magnitude $\overline{U}(r)$ is:

$$\overline{U}(\mathbf{r}) = \sqrt{(\overline{u}(\mathbf{r}))^2 + (\overline{v}(\mathbf{r}))^2} \tag{8.4}$$

The RMS value of velocity fluctuations, u_{rms} is defined as:

$$u_{rms}(\mathbf{r}) = \sqrt{\frac{1}{N}\sum_{n=1}^{N} (u'(\mathbf{r}, t_n))^2} \tag{8.5}$$

with total velocity fluctuation over both u and v velocity components, $u_{rms_{uv}}$:

$$u_{rms_{uv}} = \sqrt{\frac{1}{2}(u_{rms}^2 + v_{rms}^2)} \tag{8.6}$$

From here on, unless explicitly specified u' will refer to the RMS value of the velocity fluctuations. Many of the flow properties investigated in the rest of this chapter are functions of radius with respect to the location of the centre of the mean flow vortex, taking this into account flow properties are azymuthully averaged becoming spatially a function only of normalised radius, ρ rather than radial position vector $\mathbf{r} = (\rho, \theta)$.

Turbulence intensity, I, the ratio of the size of the velocity fluctuations to the mean flow value is defined as:

$$I = \frac{u_{rms_{uv}}}{\overline{U}} \tag{8.7}$$

The time averaged mean flow properties defined above are presented in Figure 8.6 as a function of ρ for the five different flow configurations. The plots of velocity magnitude show that at ρ = 0 the mean velocity is approximately zero, this is characteristic of the centre point of a vortex and increases radially up to the point $\rho = 1$ before decreasing again outside of the core region $\rho > 1$. The magnitude of the velocity fluctuations, u' are at a maximum at ρ = 0 and decrease with increasing radial position, this is characteristic of a vortex showing precession, the instantaneous vortex is smaller than the vortex swept out in the mean flow (see Figure 8.4) the variation in

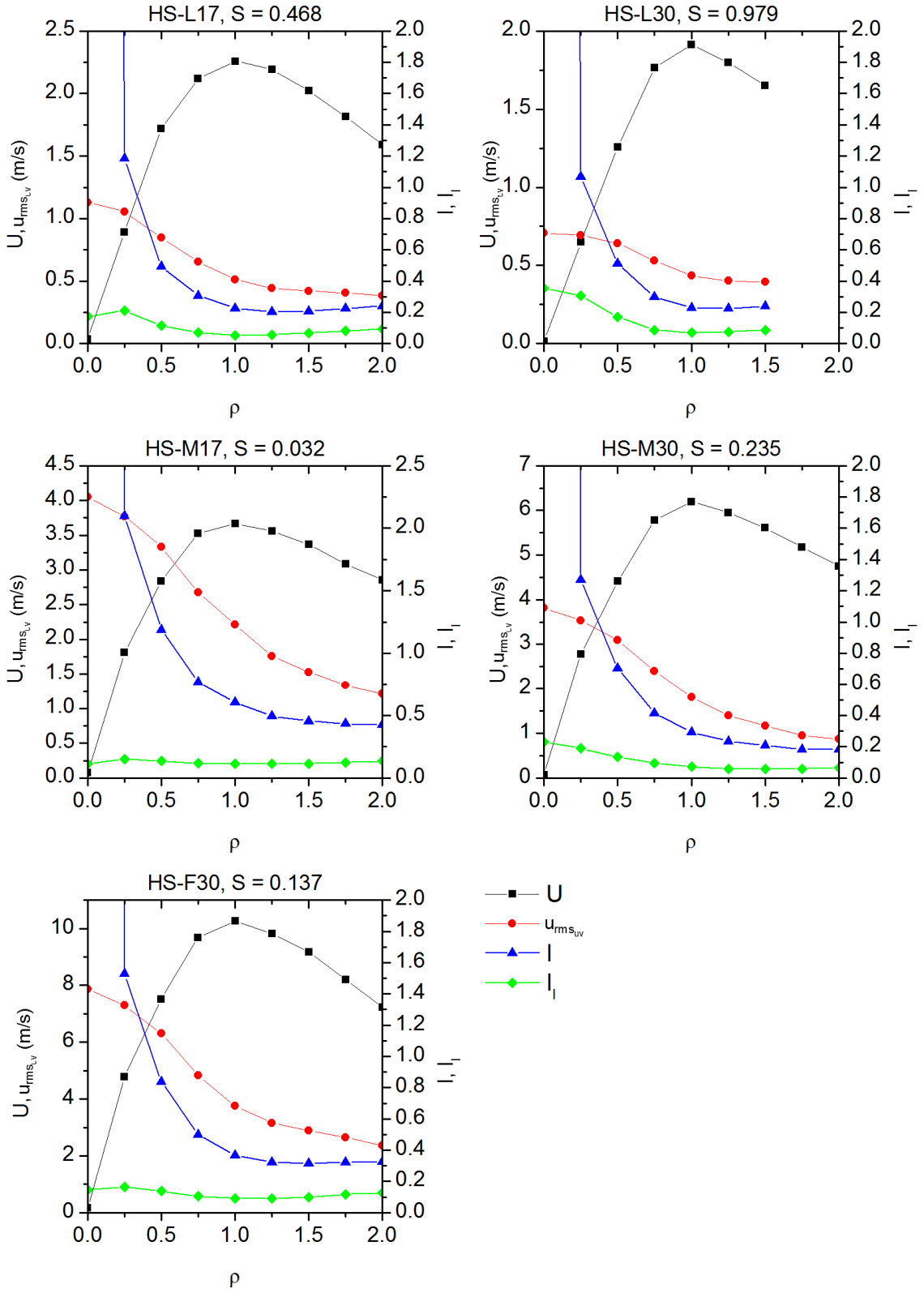

Fig. 8.6 Radial plots of time series mean velocity magnitude $\overline{U}$, the RMS value of velocity fluctuations $u_{rms_{uv}}$, the turbulence intensity, I and the local turbulence intensity I_l.

velocity from the mean is much greater towards the centre of the mean flow whereas in the region outside of the mean flow vortex the instantaneous flow is much closer to that of the mean flow and hence the decrease in fluctuating velocity.

The turbulence intensity, I (Figure 8.6 and Figure 8.7 as a function of swirl ratio) decreases outwards for $\rho > 0$. On the plots I is not shown for $\rho = 0$ as the approximately zero mean flow velocity at this point results in turbulence intensity tending to infinity. The turbulence intensity is very strongly a function of both the radial location within the flow and of swirl ratio. In Figure 8.7 it can be seen within the mean flow vortex core region ($\rho < 1$) the intensity increases as the centre of the core is approached and the intensity is greater for lower swirl ratios. Outside the core region ($\rho > 0$) the intensity collapses as a function of radial position and varies only with swirl ratio. In all regions of the flow the intensity value is very high, this is due to the fluctuating component of velocity being calculated using classical Reynolds decomposition which means that it includes the large scale coherent variations caused by the precession of the vortex. To measure the intensity of the turbulence without the contribution of the large scale coherent fluctuations one would have to remove the effects of precession when calculating the fluctuating velocity component. Precession of the instantaneous vortex is much greater at low swirl ratio than that at high swirl ratio as was shown in the previous section giving rise to the very large turbulence intensity values in the inner core region at low swirl ratio. At ρ = 0.25 the intensity is approximately 210% for the lowest swirl ratio (S = 0.032) indicating that the mean flow does not at all give an accurate estimate of what is happening at any instant in time, at the highest swirl ratio (S = 0.979) where the effects of precession are much reduced the intensity value drops to 60% which is still significantly high. The lowest recorded intensities occur outside the core region for swirl ratios above 0.235 where the intensity values range from approximately 18-24%.

The high values of turbulence intensity recorded owing to large scale coherent fluctuations are an indication that small scale eddies in the inertial range are not convected by a constant velocity but by a convection velocity which varies in time. This is an important point as when dealing with data in a *Eulerian* frame of reference (fixed in space, varying in time) one is often required to convert from a temporal to a spatial series (fixed in time, varying in space) in order to calculate certain properties of the flow such as length scales and wavenumber-energy spectra. The conversion from temporal to spatial series is classically conducted using Taylor's hypothesis of frozen turbulence (Taylor, 1928) where the spatial fluctuating velocity $u'(x)$ can be educed from $u'(t = x/\overline{u})$, however this requires a well defined convection velocity $\overline{u}$ and that the velocity fluctuations are much smaller than $\overline{u}$ i.e. $\overline{u} \gg u'$ (small intensity).

In the current flow data it is clear that any turbulence at a specific location is not convected at a constant velocity, the time series plots of u'_1 in Figure 8.8 show two different situations, one for a low swirl ratio flow (S = 0.036) at ρ = 0.25 and the other for S = 0.979 at $\rho = 1.25$, the corresponding turbulence intensity values are 2.09 and 0.22 respectively. It is immediately noticeable that in the high intensity case the magnitude of the fluctuations are considerably larger

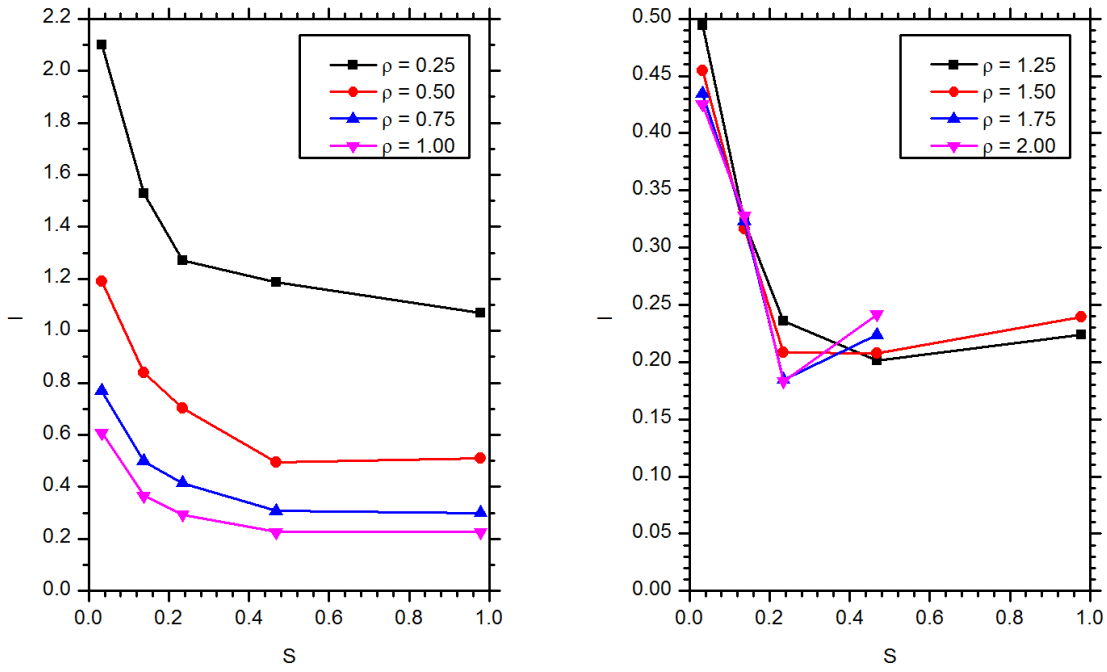

Fig. 8.7 Turbulence intensity as a function of swirl ratio for different radial locations.

than the low intensity case with the high intensity case fluctuations having a maximum deviation from the mean of approximately $\pm$ 11m/s compared to an approximate maximum deviation of $\pm$1m/s at low intensity. The black lines in Figure 8.8 are locally averaged fluctuating velocity averaged over 25 data points (in time). The quasi-periodicity exhibited in the fluctuating velocity are characteristic of large scale coherent structures and not true turbulence. It is this behaviour that makes the application of Taylor's hypothesis on this data invalid as the convective velocity associated with these structures is not constant.

To overcome the limitations of Taylor's hypothesis Pinton and Labbé (1995) employ a correction using a local time average as the convection velocity. Using their correction the velocity at time t is related to the velocity at location x by:

$$u(t) \rightarrow u(x), x \quad = \quad \int_0^t \overline{u}(\tau) \mathrm{d}\tau \tag{8.8}$$

Where $\overline{u}$ is the local average velocity defined in the usual way by:

$$\overline{u}(\tau) \quad = \quad \frac{1}{T_A} \int_{\tau - \frac{T_A}{2}}^{\tau + \frac{T_A}{2}} u(t) \mathrm{d}t \tag{8.9}$$

Where T_A is the time over which the local average is calculated and is generally in the region of the integral time scale T_{Int}. The proposed correction to Taylor's hypothesis was applied by Pinton and Labbé to a confined vortex flow and has more recently been used by several groups in the analysis of vortex time series velocity data (Baroud et al., 2003; Simand et al., 2000; Sun et al., 2005). Using the correction to Taylor's hypothesis the local intensity level I_l (see Figure 8.9) is greatly reduced (averaged over the full time series), using a local averaging time T_A equal to that of the integral time T_{Int}. At a radial distance $\rho \geq 0.5$ all local turbulence intensity values are

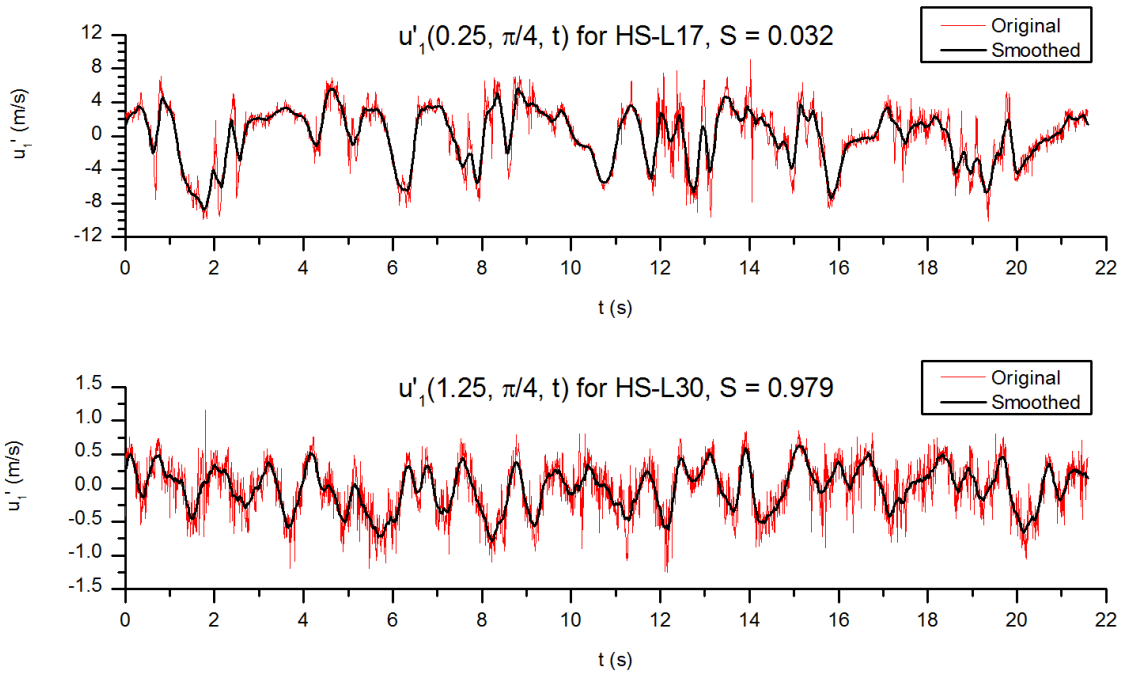

Fig. 8.8 Time series fluctuating velocity component u_1' for (*top*) $S = 0.032$ at $\rho = 0.25$ and (*bottom*) $S = 0.979$ at $\rho = 1.25$. Black line is a local average of 25 datapoints.

below approximately 13% and above 4% with the exception of $S = 0.979$ when the intensity is approximately 17% in the region of the vortex core position and at $\rho = 0.25$ the local intensity values increase with greater variation depending on swirl ratio with the most extreme case again $S = 0.979$ with a local intensity of a little over 35%. For the points where the local intensity is above 15% the corrected Taylor's hypothesis is still used but it must be regarded with caution when interpreting spatial values calculated from time series data.

The integral time scale of the fluctuating velocity T_{Int} is a characteristic timespan over which the time series signal becomes decorrelated with it self thus giving a temporal description of the size of the largest flow structures in the same way the integral length scale Λ provides a spatial measure of the largest flow structures (see § 2.4.2). T_{Int} is calculated by integrating the fluctuating velocity auto-correlation function (in time) as follows:

$$T_{Int_i} = \int_0^{\tau|_{B=0}} B_i(\tau)\mathrm{d}t \tag{8.10}$$

Where B_i is the time-series autocorrelation of the i^{th} fluctuating velocity component (essentially x or y) and the limit of the integration is the first zero crossing of B_i. B_i at point r is calculated as follows:

$$B_i(\boldsymbol{\zeta},t) = \frac{\overline{u_i'(\boldsymbol{\zeta},t)u_i'(\boldsymbol{\zeta},t+\tau)}}{\overline{u_i'^2(\boldsymbol{\zeta})}} \tag{8.11}$$

With the overbar denoting (as usual) a temporal average and $\boldsymbol{\zeta} = (\zeta_1, \zeta_2)$ is the spatial separation vector. In this work both spatial and temporal autocorrelation functions are denoted by B. For autocorrelations in time there is a single subscript, e.g. B_i as time only has one direction, spatial

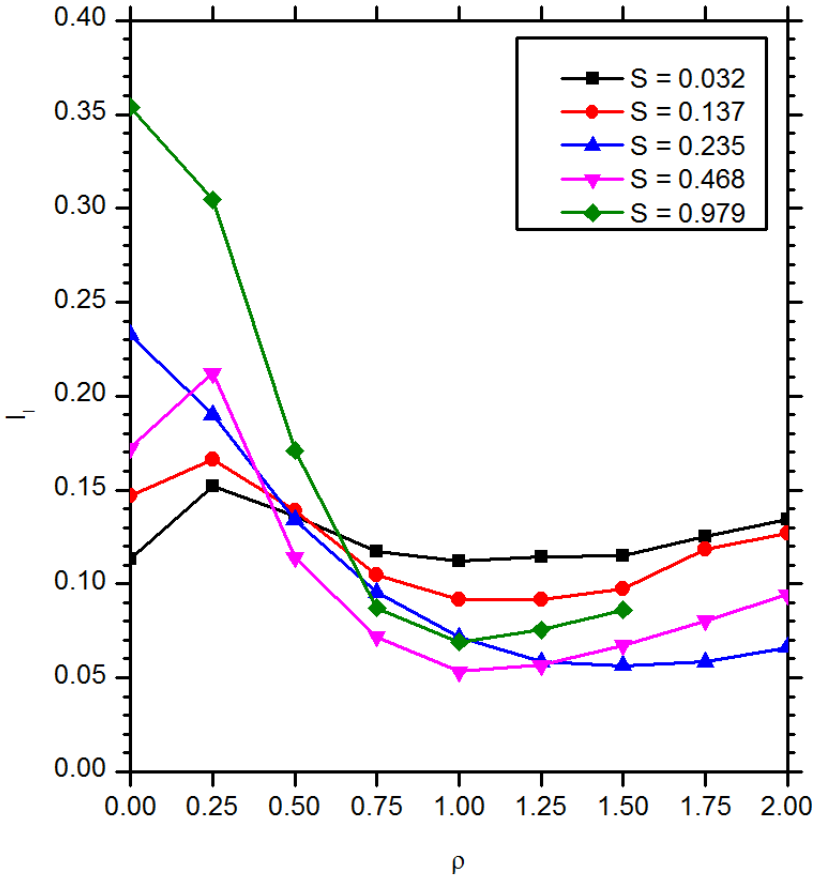

Fig. 8.9 Local turbulent intensity I_l after applying the correction to Taylor's hypothesis.

correlation functions are of the form B_{ij} which is the autocorrelation of the i^{th} fluctuating velocity component in the direction of j. As B is non-dimensional the units of T_{Int} obtained from the integral in (8.10) are seconds.

As with many of the other properties of the flow the integral scales calculated are a function of radial position and do not vary with azimuth hence for each radial location $T_{Int}(\rho)$ is taken as the average of T_{Int} as calculated at each azimuth. T_{Int} is approximately equal for both velocity components so again T_{Int} is given as the average of T_{Int_1} and T_{Int_2} and is presented in Figure 9 8 as a function of both radial position and swirl ratio. It is observable that the integral time scale only has a loose relationship with swirl ratio and is more dependent on the strength of the circulation fed to the system, at swirl ratios of $S = 0.032$ and $S = 0.468$ the integral time scale is considerably larger than the other three, this can be explained by the fact that at those two swirl ratios the circulation blowers are set to 17V whereas the others are set to 30V. This reduction in energy has the effect of reducing the in-plane velocities meaning that any flow structures are convected more slowly resulting in the fixed point velocity signal staying correlated with its self over a longer time period. This behaviour is also visible when the integral time scale is plotted as a function of ρ. T_{Int} decreases with radial distance away from the centre of the vortex for all cases except $S = 0.032$ which sees a slight increase up to approximately $\rho = 1$ before decreasing again. The range of T_{Int} spans from 0.23s for $S = 0.468$ at the centre of the vortex down to 0.076s for $S = 0.235$ and in each

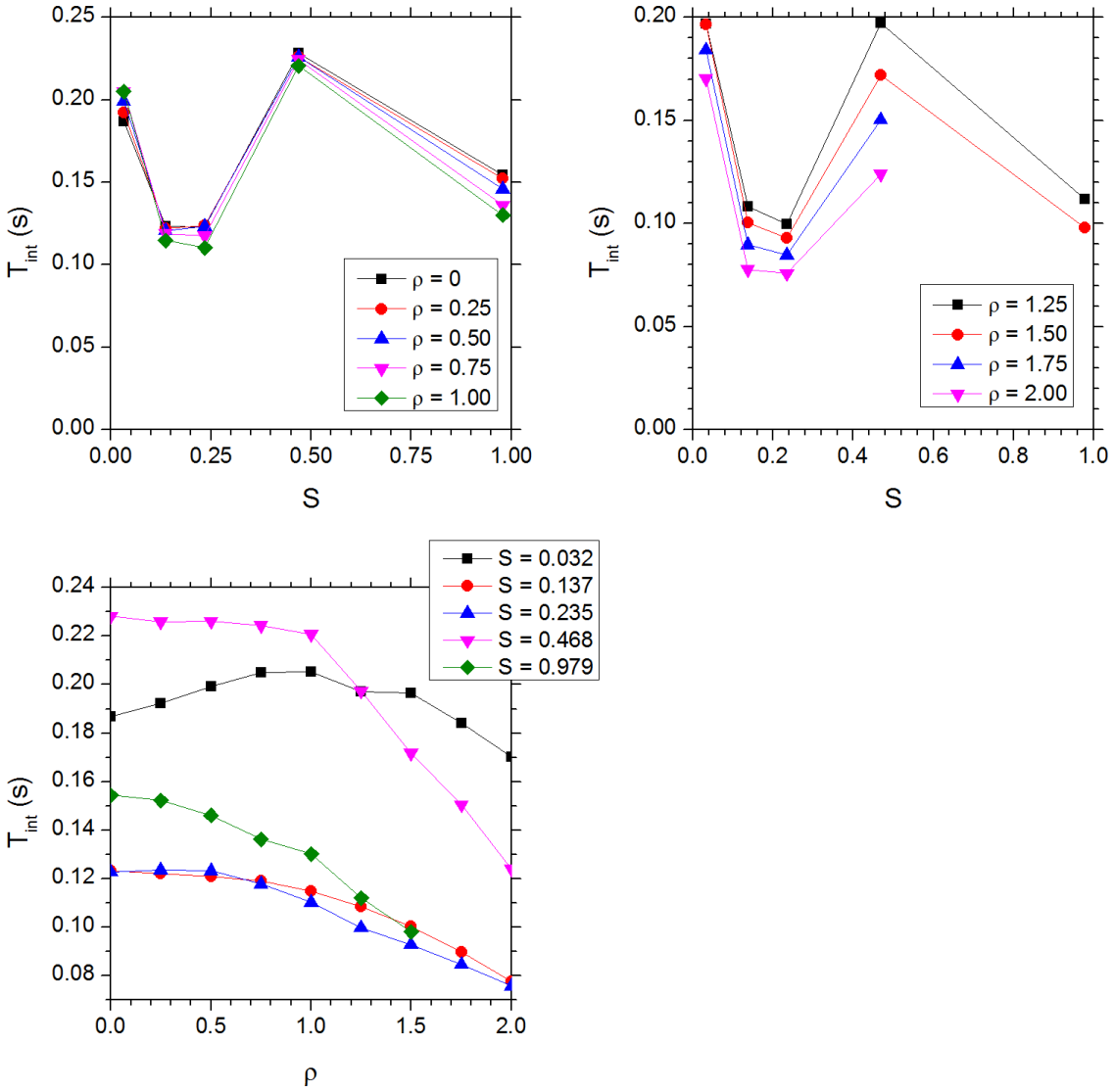

Fig. 8.10 Integral time scale as calculated from the time autocorrelation function as a function of swirl ratio and ρ.

case the rate of change of T_{Int} with radial position is low in the region $\rho < 1$ where T_{Int} remains at a fairly constant level apart from the two cases at the extremes of the swirl ratio range. Outside of the core region T_{Int} shows a more rapid decline with increasing radial position.

In order to gain a more physical understanding, the integral time scale fluctuating velocity time series are presented in Figure 8.11 at the extremes of the integral scale. The top time-series is that of u'_1 at $r = (2, \pi/4)$ for $S = 0.137$ which has time-scale $T_{Int} = 0.078$s and the second time-series is for $S = 0.468$ captured at the centre of the mean flow vortex core and has an integral time of $T_{Int} = 0.23$s. It can be seen that the frequency of the large scale structures is much higher in the low integral time-scale time-series showing that the velocity fluctuations become decorrelated over a shorter time period than the high integral time case where the frequency of the large scale structures is much lower.

The autocorrelation functions relating to these time series are presented in Figure 8.12. The oscillatory nature of the correlation functions is a reflection of the oscillations shown in the time-series and shows that the fluctuating velocity is on the largest scales periodic and therefore indica-

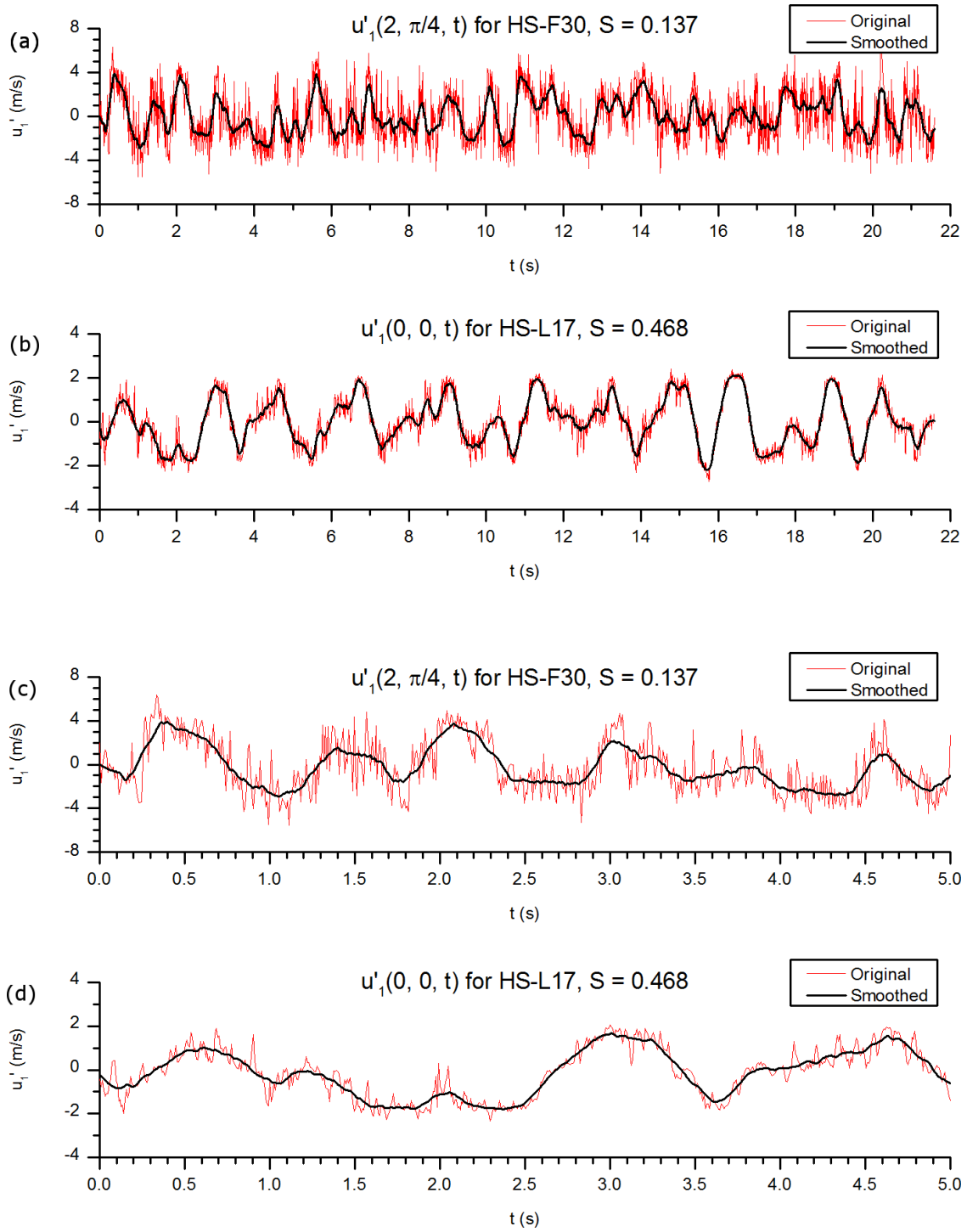

Fig. 8.11 Fluctuating velocity time series with a low integral time (*a*) and a long integral time (*b*). (*c*) and (*d*) are the same time series as in (*a*) and (*d*) but zoomed in on the first five seconds. The black lines are a local moving average of 25 data points.

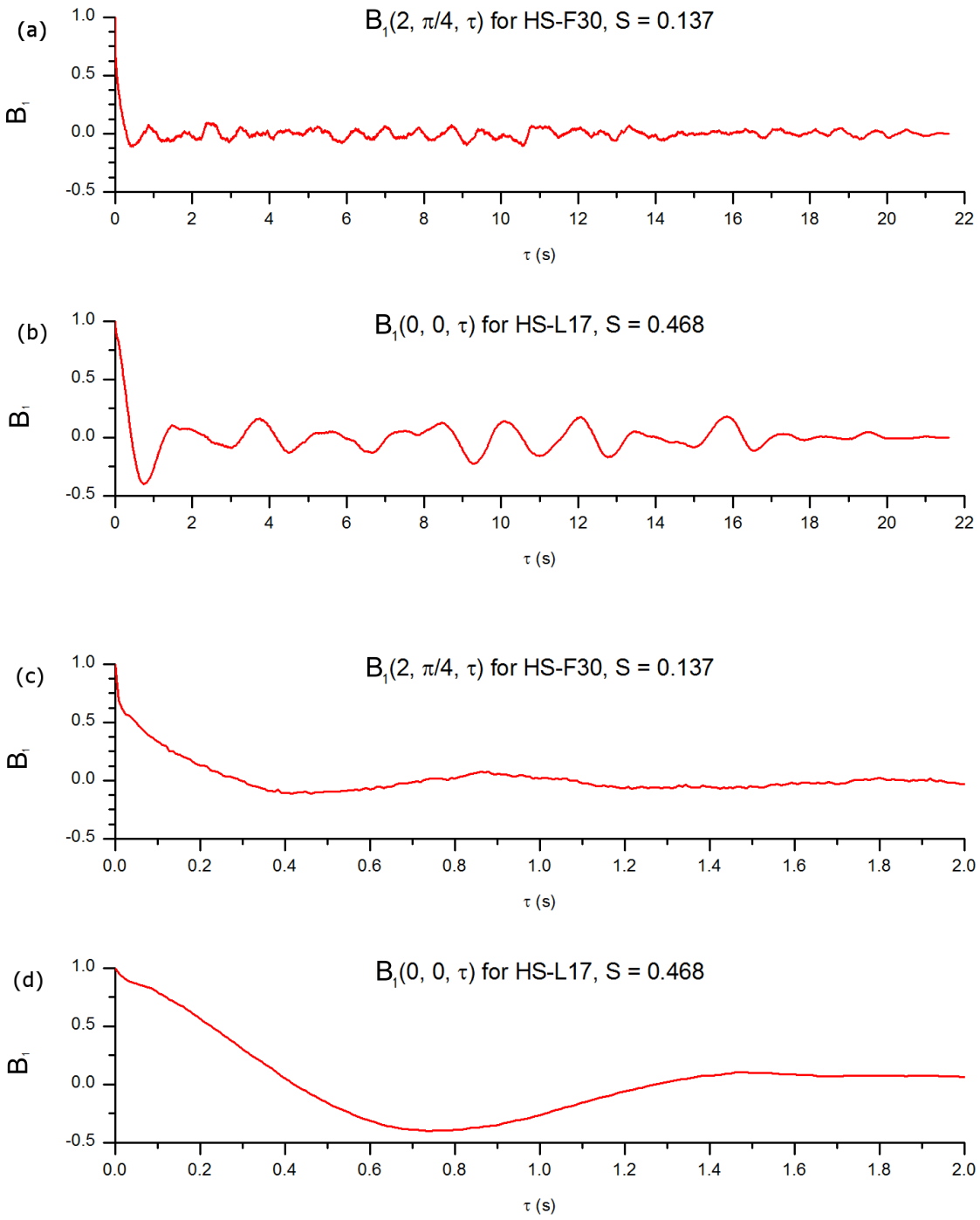

Fig. 8.12 Autocorrelation functions of the fluctuating velocity time-series in Figure 8.11, (*a*) and (*b*) full (one-sided) autocorrelation functions and (*c*) and (*d*) zoomed in autocorrelation functions.

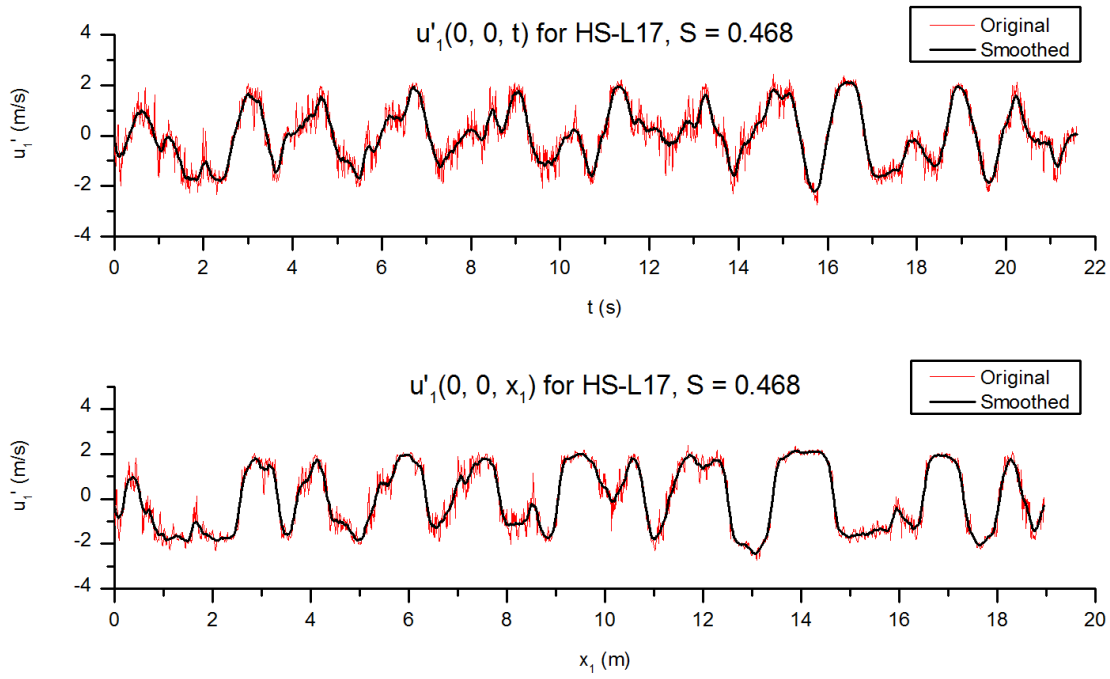

Fig. 8.13 Conversion of fluctuating velocity time-series (*top*) to a spatial series using the correction to Taylor's hypothesis (*bottom*).

tive of organized coherent structures. If the structures were non-coherent and purely turbulent one would see the correlation function quickly approach zero without periodic features. It can be seen as an example from the autocorrelation at $S = 0.468$ that the integral up to the first zero crossing is approximately the area of a triangle of unit height and length of 0.45s which is very close to the calculated value of $T_{Int} = 0.23$s. The steep initial decline of the autocorrelation function for $S = 0.137$ (which is not present in the $S = 0.468$ case) is down to the large high frequency fluctuations around the large scale motions.

The integral length scale, Λ is calculated from the time series fluctuating velocities converted to a function of space using the correction to Taylor's hypothesis, an example of which is shown in Figure 8.13. If the time-series was converted using the traditional implementation of Taylor's hypothesis where a constant convective velocity is utilized the spatial velocity signal would hold exactly the same shape as the time-series only dilated or stretched on the space axis. Using the correction based on a locally averaged convective velocity. Whilst the features present in both signals remain constant the degree of dilationstretching varies along the space axis. It is noticed that the peaks and minima present in the time signal are broadened when converted to a spatial series and is explained by the greater magnitude of the velocity in the time series at these points which indicates that the local convective velocity is greater. The distance spanned by the interpreted spatial series is consistent with the distance travelled by a fluid particle travelling at the time-average mean velocity at that point.

From the spatial fluctuating velocity time series the autocorrelation B_{ij}, (of the i^{th} fluctuating velocity component in the j^{th} direction) is calculated in a similar way to the time series autocorre-

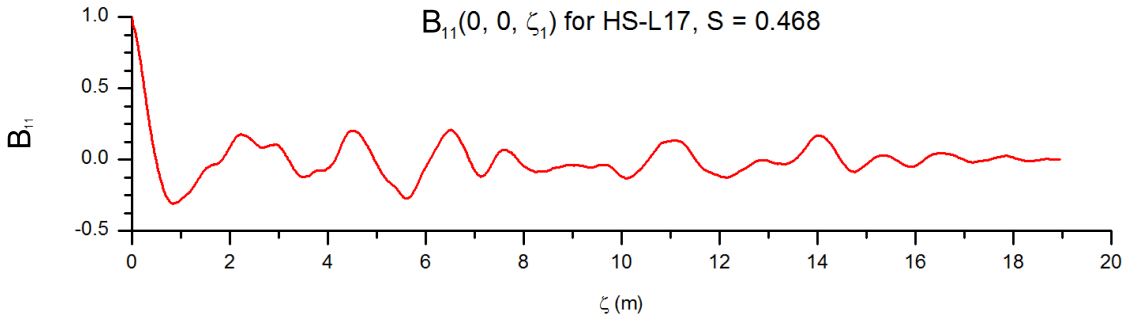

Fig. 8.14 Spatial autocorrelation function of the $u_1'(0,0)$ for $S = 0.468$.

lation:

$$B_{ij}(\zeta_i) = \frac{\langle u_i'(x_j)u_i'(x_j+\zeta_i)\rangle}{\langle u_i'(x_j)u_i'(x_j)\rangle} \tag{8.12}$$

Where $\langle\cdot\rangle$ indicates averaging over all spatial points and ζ_i is a spatial shift in the i^{th} coordinate direction. In this work only longitudinal correlation functions, B_{ii} are considered. From the spatial autocorrelation function the integral length scale Λ_i is calculated as:

$$\Lambda_i = \int_0^{\zeta_i|_{B=0}} B_{ii}(\zeta_i)\mathrm{d}\zeta_i \tag{8.13}$$

The spatial autocorrelation of the spatial series in Figure 8.13 is presented in Figure 8.14 and the calculated integral length scales in Figure 8.15. The radial plots of Λ show that at a given radial location Λ decreases with increasing swirl ratio apart from the two lowest swirl ratios, $S = 0.032$ and 0.137 where $S = 0.137$ is initially greater before crossing at $\rho = 0.75$. The integral length is greatest at $\rho = 0$ and ranges from 0.98m for $S = 0.137$ down to 0.19m for $S = 0.979$. As the integral length scale is a measure of the size of the largest structures that make up the fluctuating velocity, which for the current flow is dominated by the precession of the vortex, which is to be expected as at the low swirl ratios there is much more vortex precession than for the more stable high swirl vortices. All flow configurations show a decline in integral length scale with increasing radial position with the rate of decrease being greater at lower swirl ratio. For the outer core region ($\rho > 1$) the integral length scale is smaller than the inner core region as one would expect as the flow is less affected by the precession of the vortex and the flow is more uniform as is indicated from the turbulence intensity in the outer core region (Figure 8.7) where the turbulent fluctuations are closer in strength to those caused by precession of the vortex.

Integral Scale Reynolds Number

The Reynolds number, as described in § 2.2.3 is the ratio of inertial to viscous forces contained within a flow and is given by:

$$\mathrm{Re} = \frac{ul}{\nu} \tag{8.14}$$

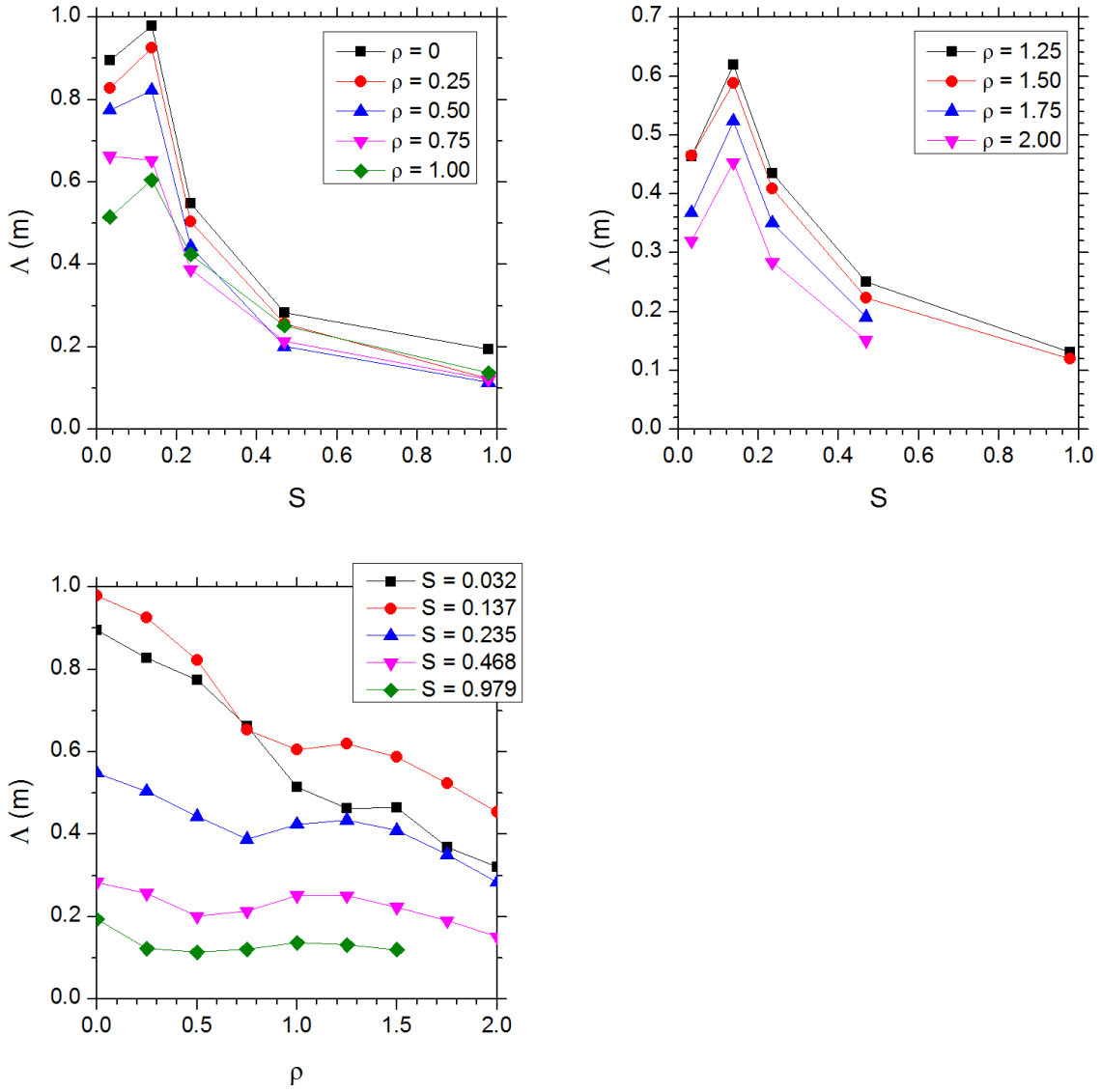

Fig. 8.15 Integral length scale as calculated from fluctuating velocity time-series using the correction to Taylor's hypothesis.

Where u and l are a characteristic velocity and length scale of the flow. In the current work the system is unbounded so a characteristic length based on the dimensions of the tornado vortex chamber cannot be defined as flow structures may (and do as seen in Figure 8.15) exceed the dimensions of the chamber, also in the current flow a characteristic velocity is difficult to define as some regions of the flow have zero mean velocity and others a highly variable mean velocity. It is for these reasons that a Reynolds number defined by the integral length and time scales, Re_{Int} will be used:

$$\mathrm{Re}_{Int} = \frac{u_{Int}\Lambda}{\nu} = \frac{\frac{\Lambda}{T_{Int}}\Lambda}{\nu} = \frac{\Lambda^2}{T_{Int}\nu} \tag{8.15}$$

In homogeneous turbulence one would expect the Reynolds number to be constant with varying location within the flow as the integral length and time scales are constant (Saddoughi and Veeravalli, 1994), this is not the case with the current flow which exhibits inhomogeneity as shown by the positional variation in integral time and length scales (Figure 8.10 and Figure 8.15). The same

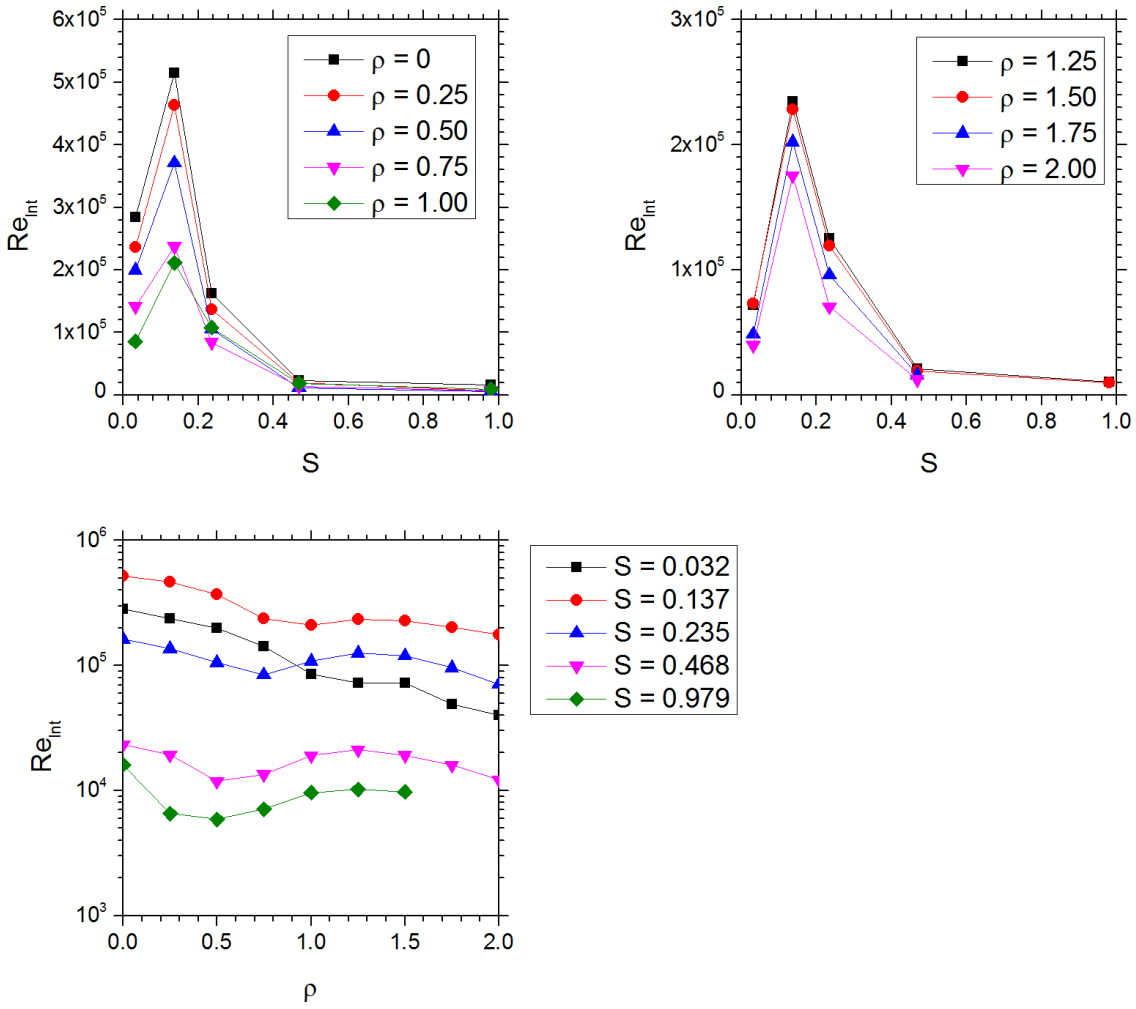

Fig. 8.16 Integral scale Reynlods number, Re_{Int} as functions of swirl ratio and radial position.

inhomogeneity is also observed in the Reynolds number when presented as a function of radial position as in Figure 8.16. The Reynolds number of the flow, invariant of swirl ratio has a maximum Reynolds number at the location of the mean flow vortex core and ranges from a peak value of Re_{Int} = 16084 to Re_{Int} = 515090 for swirl ratios of S = 0979 and 0.137 respectively. Figure 8.16 shows that the Reynolds number does not have a clear relationship with the swirl ratio, this is to be expected as the Reynolds number is the ratio of inertial to viscous forces within the flow and it can be seen that the swirl ratio is more closely linked to the flow rate through the system. The configuration with the highest Reynolds numbers, S = 0.137 is the configuration HS-F30 which has the highest axial fan speed which indicates a greater energy input into the system which drives the inertial structures, likewise the two swirl ratios corresponding to the lowest axial fan speed, S = 0.468 and 0.979 (HS-L17 and HS-L30) have a much lower energy input which is reflected in the lower value of Reynolds number as the inertial forces are closer in scale to the viscous forces.

Energy-Frequency Spectra

As detailed in the review chapter turbulent energy is distributed between different scale structures within the flow which each have a unique frequency and corresponding wavenumber. To avoid

confusion the turbulent energy spectrum taken in energy-frequency space from the time-series data is denoted $F(f)$ with frequency, f. In energy-wavenumber space obtained from the converted spatial series the energy contained by structures of wavenumber $\kappa = 2\pi/l$, where l, the corresponding wavelength in the spatial domain is denoted as $E(\kappa)$. $F_i(f)$ is obtained by taking the Fourier transform of the corresponding temporal autocorrelation as obtained from (8.10) as follows:

$$\hat{B}_i(f) = \int_{-\infty}^{\infty} B_i(\tau) e^{-2\pi i f \tau} \mathrm{d}\tau \tag{8.16}$$

The factor 2π in the exponent of (8.16) gives the frequency f in Hertz as opposed to angular frequency $\omega = 2\pi f$. $F(f)$ represents the amount of the total fluctuating kinetic energy, k at the associated frequency f and as previously defined:

$$k_i = \frac{1}{2}u_i'^2 = \int_0^{\infty} F_i(f)\mathrm{d}f \tag{8.17}$$

Using Parseval's theorem which states that the energy contained within a signal is equal to that contained in its transform then the normalized version of the autocorrelation function $F(f)$ is related to $\hat{B}_i(f)$ as follows:

$$F_i(f) = 2u_i'^2 \hat{B}_i(f) \tag{8.18}$$

Likewise the distribution of turbulent energy as a function of wavenumber, κ is calculated from the spatial autocorrelation function B_{ii}:

$$\tilde{B}_{ii}(\kappa_1) = \int_{-\infty}^{\infty} B_{ii}(\zeta_1) e^{-2\kappa_i \zeta_i} \mathrm{d}\zeta_i \tag{8.19}$$

Noting the absence of the factor 2π in the exponent the resulting transform is a function of wavenumber, κ. In the same manner as the frequency domain transform the energy spectrum $E_{ii}(\kappa)$ is:

$$E_{ii}(\kappa_i) = 2u_i'^2 \tilde{B}_{ii}(\kappa) \tag{8.20}$$

Dealiasing and the Welch Method

Due to the limits on the sampling frequency f_s the energy spectra $F(f)$ and $E(\kappa)$ show signs of aliasing as can be seen in Figure 8.15. The original spectrum (black line) shows signs of aliasing for frequency f greater than approximately 10Hz, this increase in energy contained in the higher frequencies of the energy spectrum is an artefact of the limited sampling frequency which moves energy contained in higher unresolved frequencies into the lower, resolved frequencies. It can be seen that the spectrum exhibits a clear inertial range following the -5/3 power law until aliasing begins to feature at approximately 10Hz. In an attempt to remove the excess energy at high frequencies caused by aliasing a filter proposed by Gobbi et al. (2006) is applied, the effect

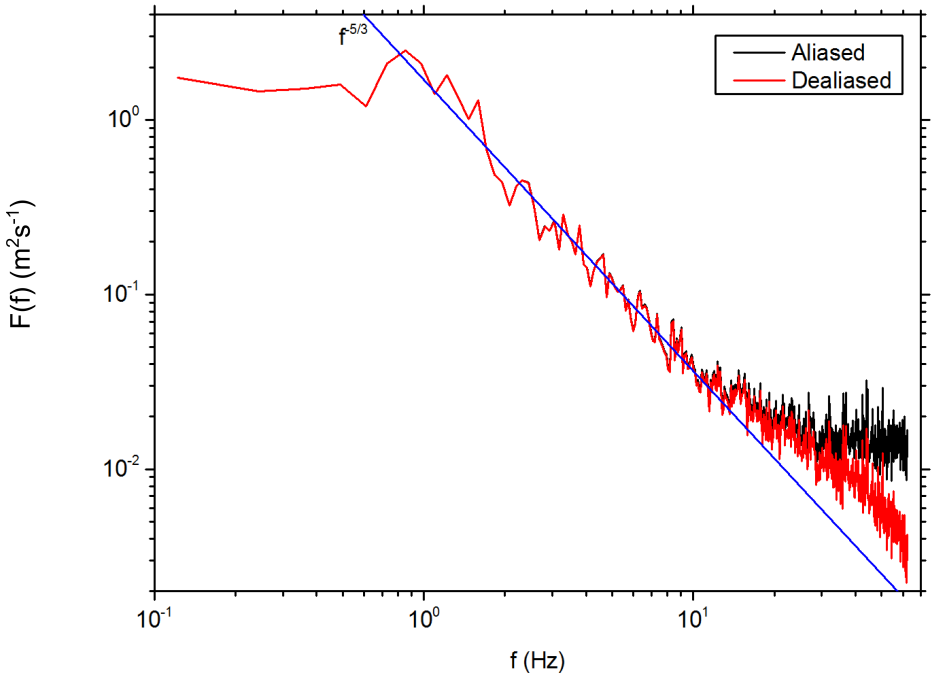

Fig. 8.17 Effect of dealiasing the energy spectrum $F(f)$ using the Gobbi filter.

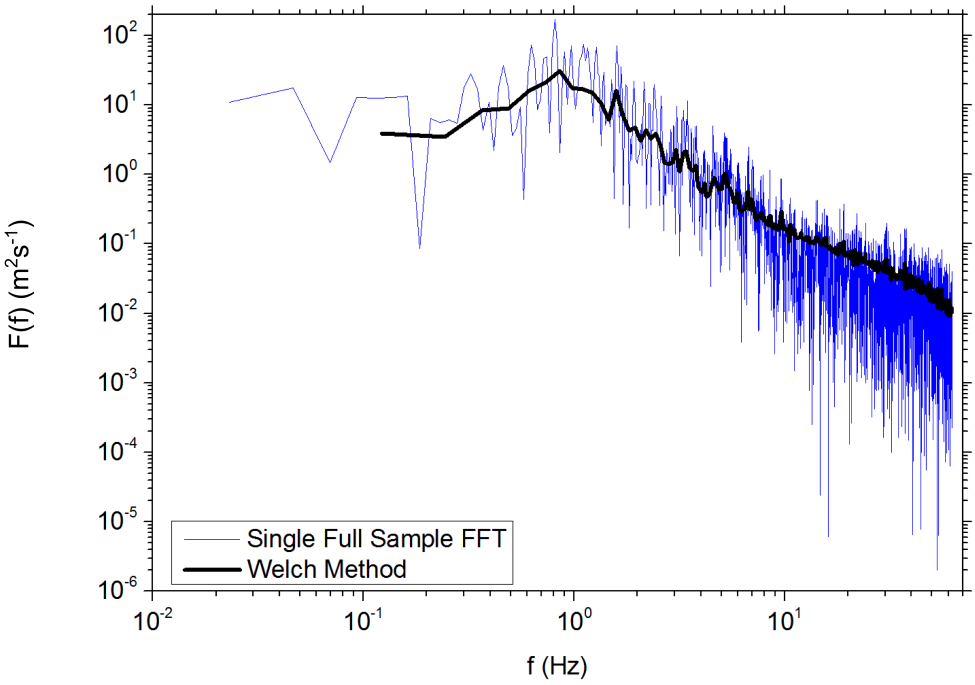

Fig. 8.18 Reducing spectral noise by employing the Welch method (black line) to compute energy spectra compared to a single full signal FFT (blue line).

of which is seen in the red line in Figure 8.17. Whilst the filter does not remove all the effects of aliasing it is a marked improvement on the original spectrum. The filter is defined as follows:

$$\hat{z}(f) = \frac{[1+\cos(\pi f \delta t)]^2}{4}\hat{x}(f) \tag{8.21}$$

where $\hat{z}$ is the filtered spectrum, $\hat{x}$ is the raw frequency of wavebumber specra, $F(f)$ or $E(\kappa)$, f is frequency (or wavenumber) and Δt the temporal resolution of the velocity measurements.

To further reduce noise in the energy spectra the Welch method is used as opposed to a traditional single FFT over the full range of the data (Welch, 1967). The Welch method reduces noise in the spectrum at the expense of some resolution at low frequencies. A time (or spatial) data series is truncated into several subsamples on which a traditional FFT is carried out. For a stationary signal (or periodic signal sampled over a long enough time frame) the spectra of the sub-samples contains the same spectral features as the full signal meaning that the FFTs can be averaged to give a spectrum with much reduced noise. In the work carried out the spectrum is generated from the double sided autocorrelation functions which have a signal length $(2N-1) = 5399$ data points, the Welch method was applied using a sub-sample length of 1024 data points and an overlap of 256 data points with an example displayed in Figure 8.18. It can be seen in Figure 8.18 that by using the Welch method the noise levels of the spectrum are greatly reduced at the expense of losing the ability to resolve the lower frequencies. However, using the stated window size it can be seen that frequencies in the integral range (frequencies below approximately 1Hz) are still resolved.

In a further attempt to reduce noise in the energy spectra the spectra $F_1(f)$ and $F_2(f)$ are averaged to give $F(f)$ and likewise with $E_{11}(\kappa)$ and $E_{22}(\kappa)$. The validity of taking the average spectrum for the two velocity components is displayed in Figure 8.19 which shows that the spectra of both velocity components are very similar, showing the same spectral features. The similarity between the spectra of the different velocity components is a good indication that the turbulence is isotropic (the same in each direction) at least in the measured plane. Likewise with the averaging of the spectra between the two velocity components the spectra obtained from velocity measurements at fixed radius, ρ but varying azimuth θ are strikingly similar as shown in Figure 8.19 so they are again averaged to give the spectra at radius ρ, $F(\rho, f)$ and $E(\rho, \kappa)$.

Energy Spectra

For reference azimuthally averaged frequency and wavenumber spectra for each flow configuration are provided in Appendix 1. The azimuthally averaged energy-frequency spectra for $S = 0.032$ and $S = 0.979$ presented in Figure 8.20 and Figure 8.21 respectively. The dashed red lines represent $F(f) \propto f^{-5/3}$ and represent the inertial range following Kolmogorov (1941b) and the blue dashed vertical lines correspond to the frequency, f_{Int} associated with the integral time-scale, T_{Int} where $f_{Int} = 1/(2\pi T_{Int})$. Azimuthally averaged energy-wavenumber spectra, $E(\kappa)$ are presented in Figure 8.22 to Figure 8.23 with the red dashed lines indicating $E(\kappa) \propto \kappa^{-5/3}$ and the vertical blue dashed lines the wavenumber, κ_{Int} which is related to the integral length scale Λ by $\kappa_{Int} = 1/\Lambda$.

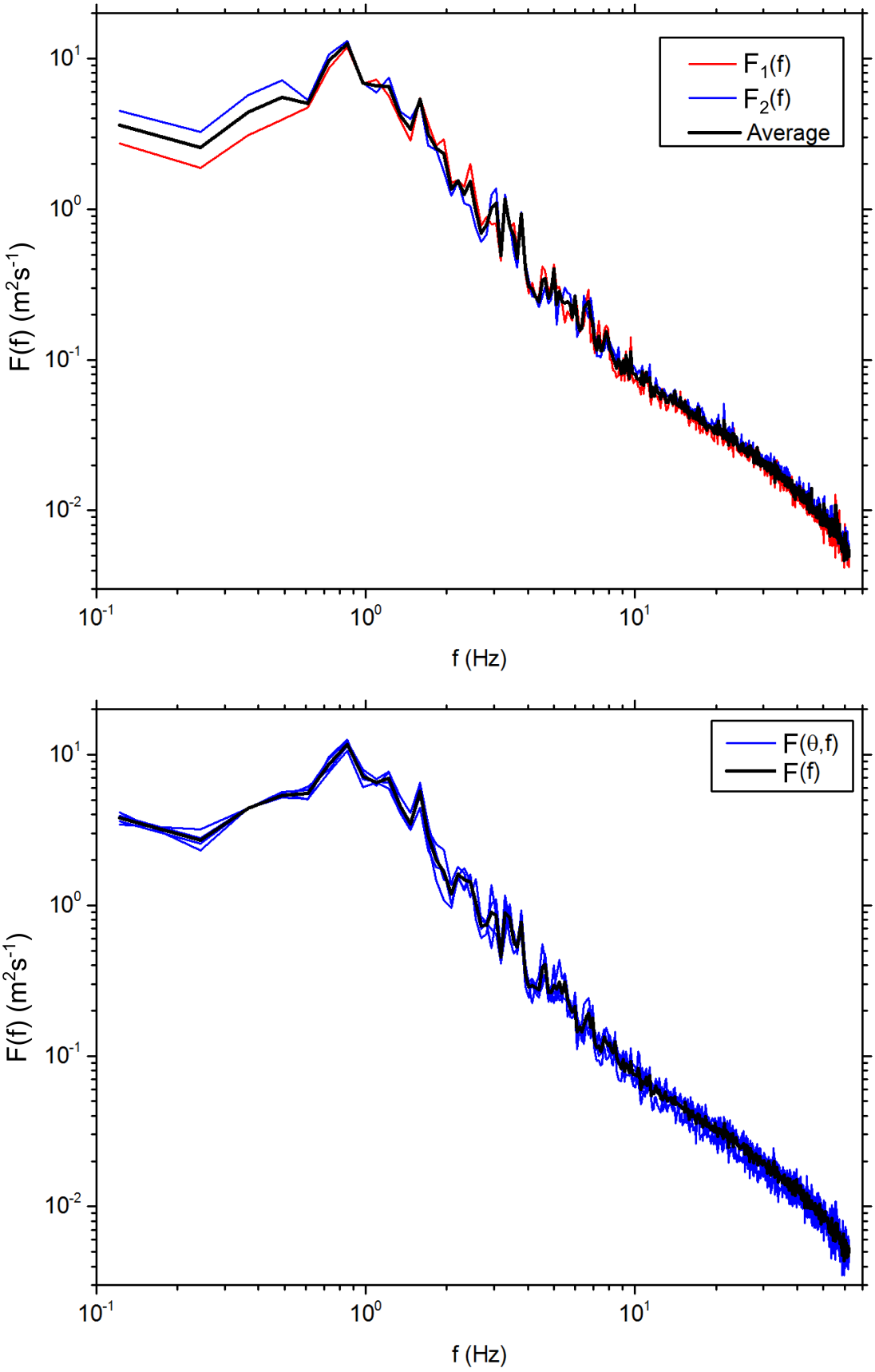

Fig. 8.19 (*top*) Averaging of energy spectra between the two velocity components and (*bottom*) azimuthal averaging of spectra.

For the energy-frequency and energy-wavenumber spectra presented in Figure 8.20 to Figure 8.21 it can be seen that the total energy contained within the spectra decreases with increasing radial position from the vortex centre as is consistent with calculated turbulence intensity at each radial position as presented in Figure 8.6. For the low swirl ratio case, $S = 0.032$ both the energy-frequency and energy-wavenumber spectra show an inertial subrange which closely fits Kolmogorov's -5/3 power law until the effects of aliasing deviate the spectra from this trend at higher frequency/wavenumber. The high swirl ratio case, $S = 0.979$ shows the spectra having a -5/3 gradient over a much shorter frequency/wavenumber band due to the higher peak frequency of the spectra and the effects of aliasing.

Frequency and Wavenumber of Integral Scale Structures

It has already been shown from the temporal and spatial autocorrelation functions the largest coherent structures that make up the fluctuating velocity component have an integral time and length scale and from these a corresponding frequency and wavenumber can be calculated. A structure with integral time scale T_{Int} has corresponding integral frequency, $f_{Int} = 1/(2\pi T_{Int})$ and likewise a structure with integral length scale Λ has the characteristic integral wavenumber $\kappa = 1/\Lambda$.

The integral frequency as a function of swirl ratio and radial position is presented in Figure 8.24 and can immediately be seen to be proportional to the inverse of T_{Int} as presented in Figure 8.10. One observes that the driving factor behind the frequency of the velocity fluctuations is the strength of the circulation supplied to the system via the circulation blowers. The two swirl ratios which exhibit lower integral frequencies both have 17V supplied to the circulation blowers whereas the other three swirl ratios with higher integral frequencies all have 30V supplied to the circulation blowers. The reduced circulation has the effect of reducing the rotation velocity of the vortex which results in the slower advection of structures within the flow which correspond to lower frequencies. Again, as with the integral time scale the integral frequency is near constant in the inner core region of the mean flow vortex before increasing in the outer core region as the flow structures become smaller and therefore more frequent which is shown by the increase in integral wavenumber (smaller structures) in Figure 8.25.

Dissipation Rate

The dissipation rate, ε is the rate at which energy is dissipated from large integral scale flow structures to smaller scale structures as outlined in § 2.4.5. The dissipation rate from one-dimensional energy-wavenumber spectra (Figure 8.22 and Figure 8.23) can be calculated as follows (Tennekes and Lumley, 1972):

$$\varepsilon = 2\nu \int_0^\infty \kappa^2 E(\kappa) \mathrm{d}\kappa \tag{8.22}$$

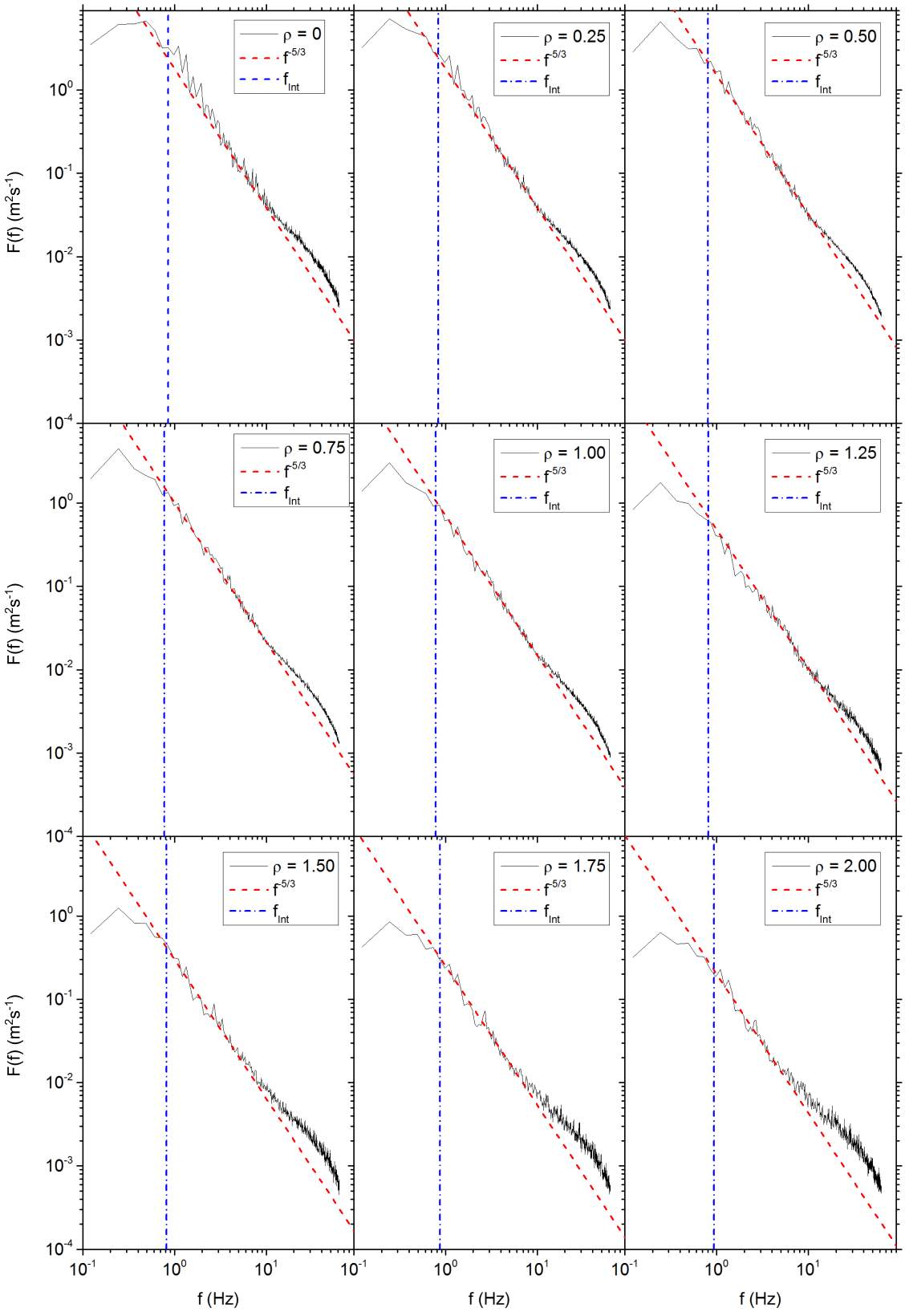

Fig. 8.20 Energy-frequency spectra $F(f)$ for HS-M17, $S = 0.032$ at varying radial positions ρ.

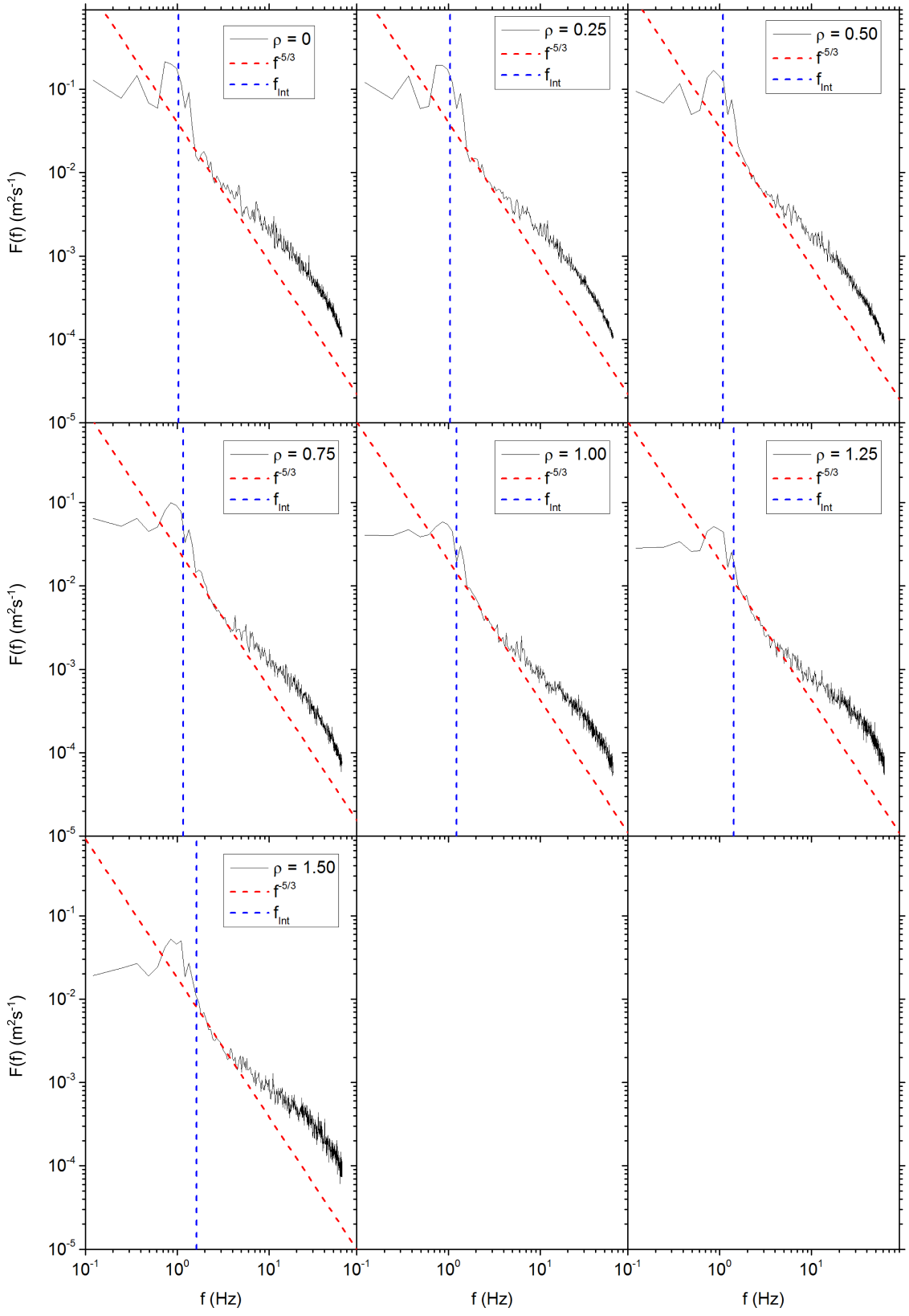

Fig. 8.21 Energy-frequency spectra $F(f)$ for HS-L30, $S = 0.979$ at varying radial positions ρ.

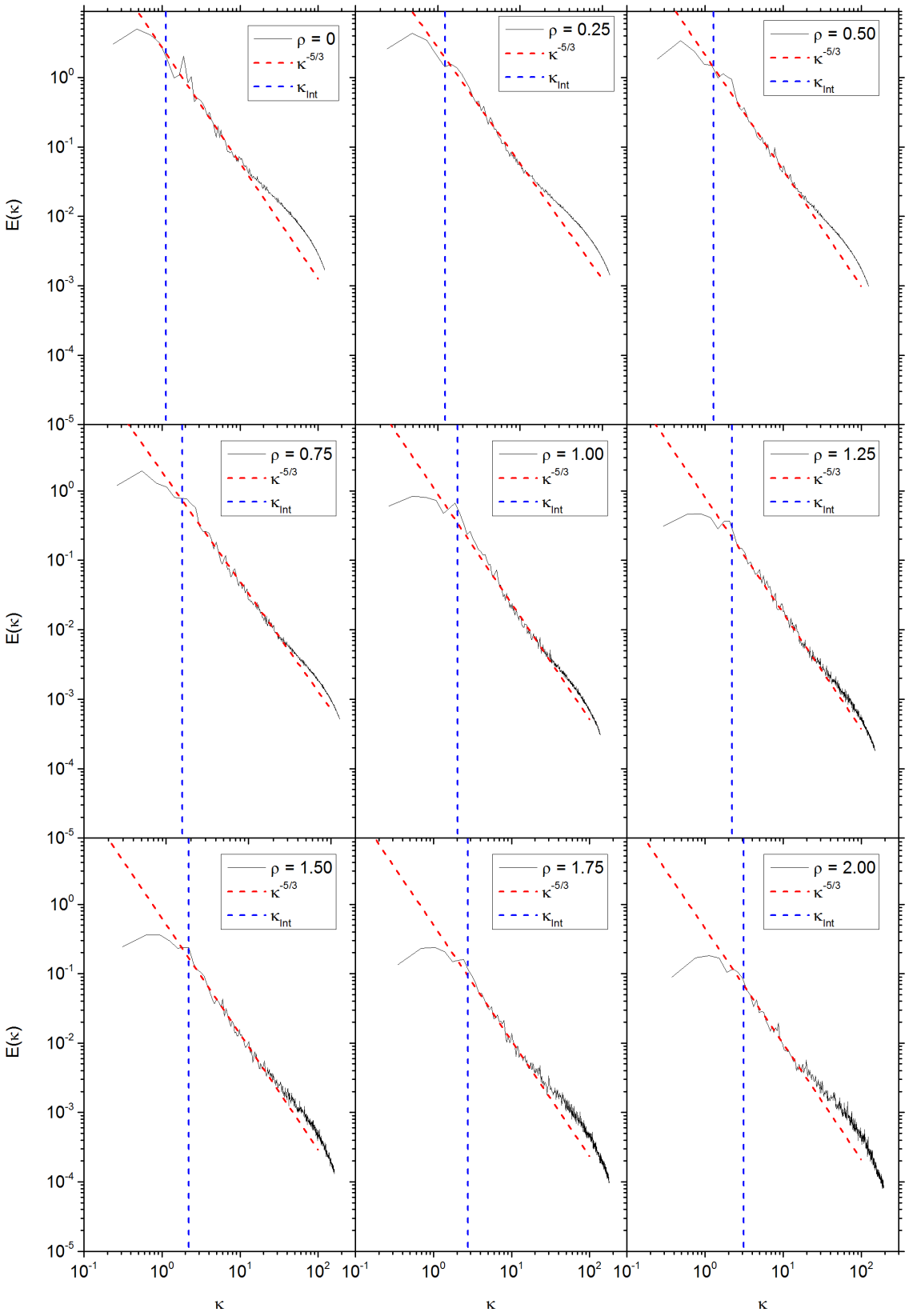

Fig. 8.22 Energy-wavenumber spectra $E(\kappa)$ for HS-M17, $S = 0.032$ at varying radial positions ρ.

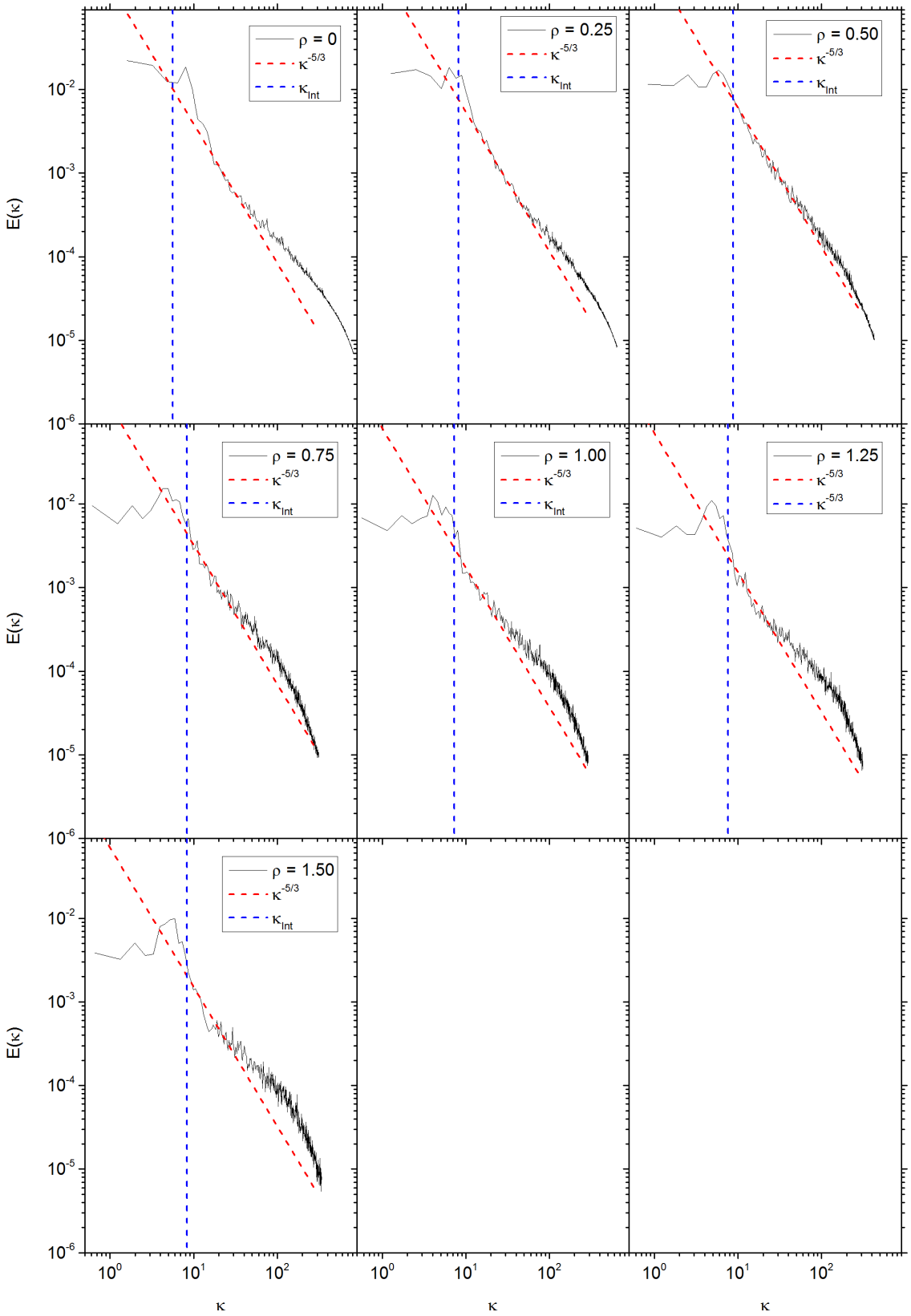

Fig. 8.23 Energy-wavenumber spectra $E(\kappa)$ for HS-L30, $S = 0.979$ at varying radial positions ρ.

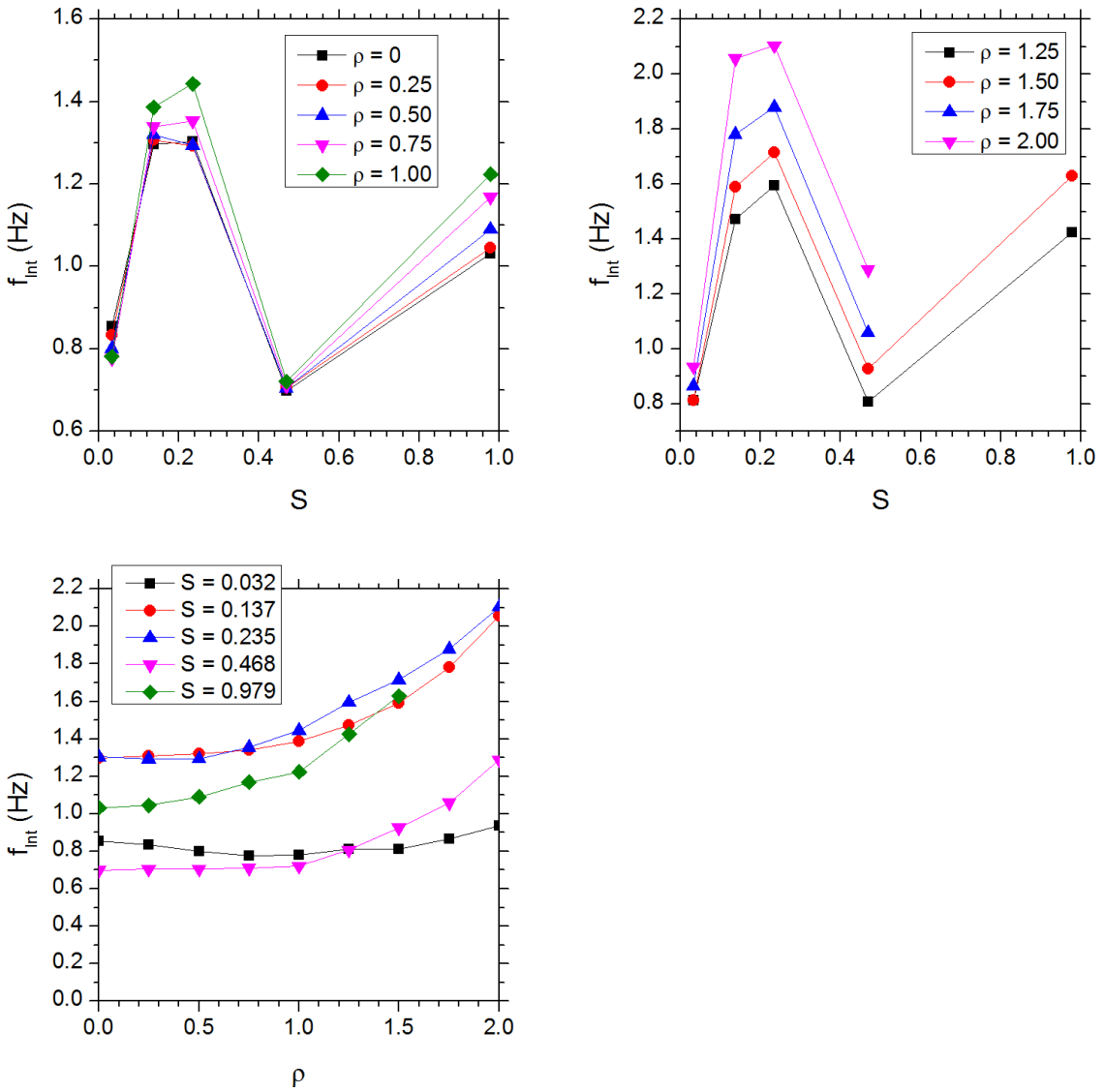

Fig. 8.24 Frequency associated with the integral time scale as a function of swirl ratio and radial position.

Here the dissipation rate is an estimate from the one dimensional longitudinal energy spectrum so gives the streamwise rate of energy dissipation. For isotropic and homogeneous flows the full dissipation rate can be calculated as $\varepsilon = 15\nu \int_0^\infty \kappa^2 E(\kappa) \mathrm{d}\kappa$ but it is already shown that the flow is inhomogeneous and with only two velocity components available it will be assumed, due to the highly three dimensional nature of the flow that isotropy is not present.

Using the estimated values of dissipation rate the Kolmogorov lengthscale, *eta* is calculated as follows:

$$\eta = \left(\frac{\nu^3}{\varepsilon}\right)^{1/4} \tag{8.23}$$

The estimate of the longitudinal dissipation rate is presented in Figure 8.26, it is once more clear that the flow shows strong inhomogeneity as the dissipation rate is heavily dependent on the position within the flow. In terms of the dissipation rate the flow can be broken down into two distinct regions, for the inner core region, $\rho \leq 1$ the dissipation rate is at a maximum when $\rho = 0$ and

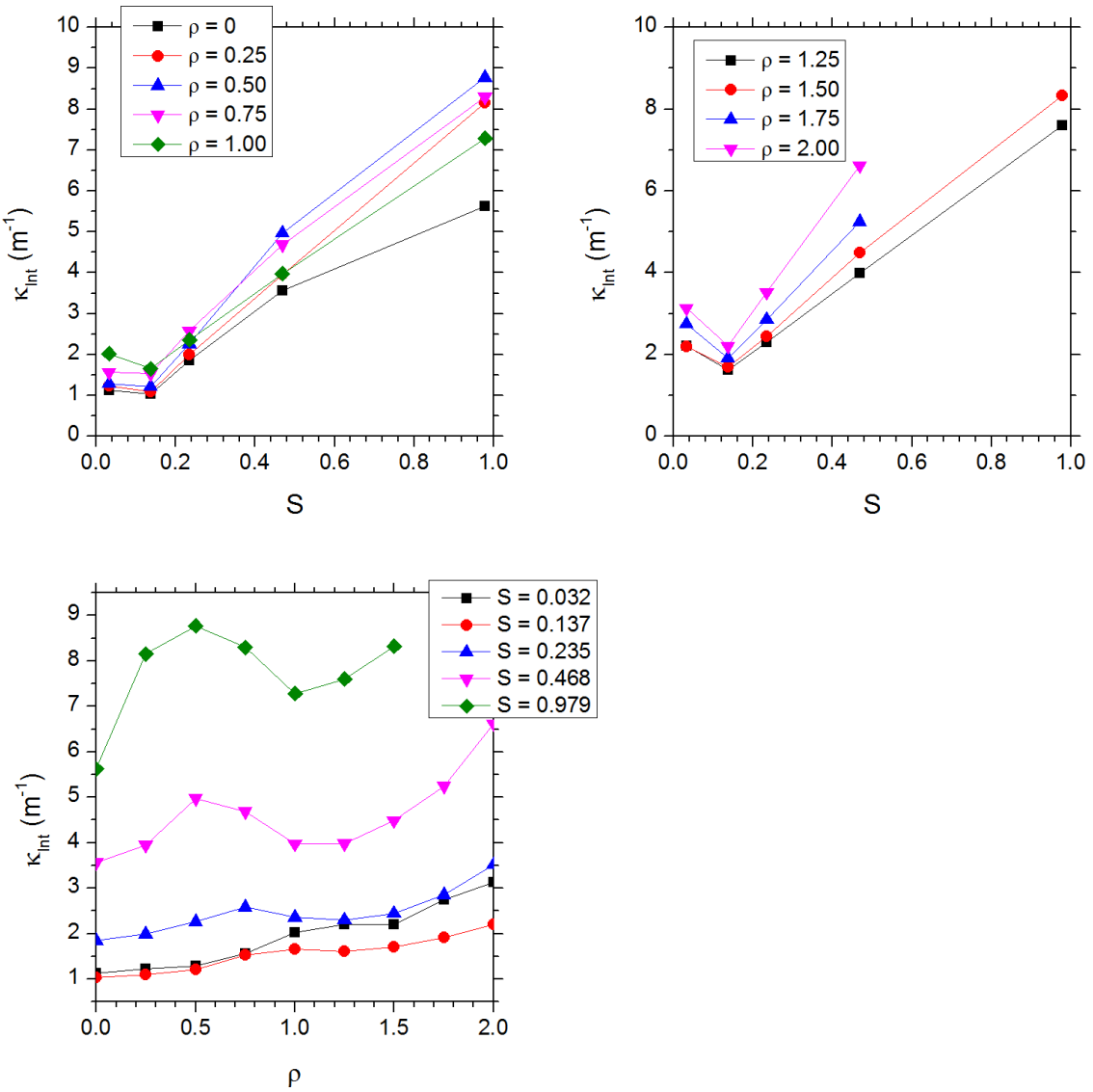

Fig. 8.25 Wavenumber associated with the integral length scale of the flow as a function of swirl ratio and radial position.

decreases radially outwards up to $\rho = 1$, outside the core region for $\rho > 1$ the dissipation rate remains approximately constant. The Kolmogorov lengthscale calculated from the dissipation rate is presented in Figure 8.27 where it can be seen that the Kolmogorov scale, the lengthscale at which energy is dissipated to heat through viscosity is larger in the outer core region than in the inner core region. The Kolmogorov lengthscale ranges from approximately 0.45mm at the location of the mean flow vortex core up to a maximum of approximately 0.95mm in the outer core region for $S = 0.235$.

Referring to Figure 8.6 it can be noticed that the rate of dissipation of turbulent energy and the magnitude of the velocity fluctuations are linked as they both have considerably higher values at lower radial position ρ where the size of the large energy containing structures of the integral scale are also largest. From this one can say that the larger, higher energy content flow structures dissipate their energy to smaller scale structures at a quicker rate than in the outer core region where the dominant flow structures are smaller and contain much less turbulent energy.

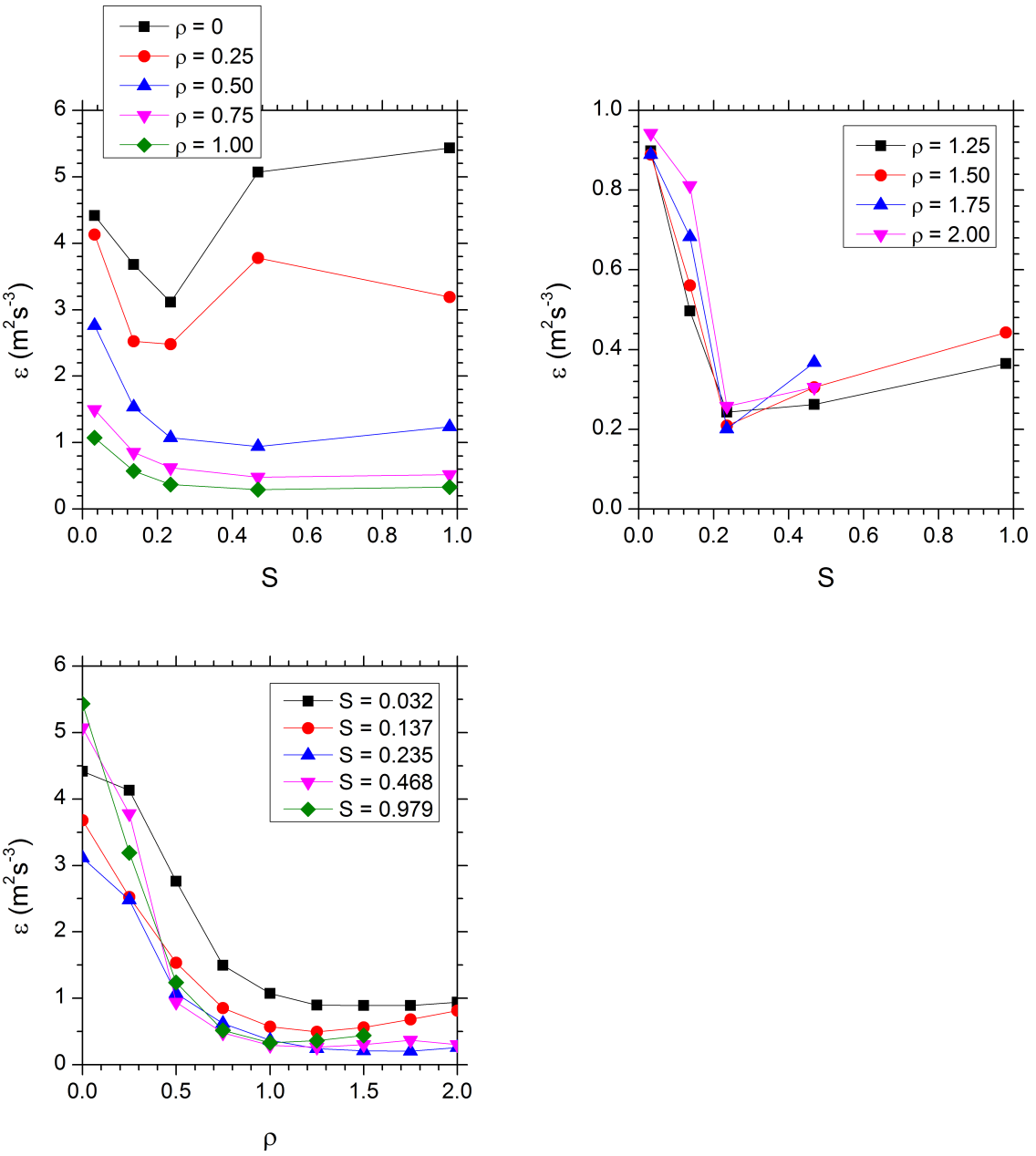

Fig. 8.26 Turbulent dissipation rate as a function of swirl ratio and radial location.

It can be seen that in the outer core region $\rho \geq 1$ the dissipation rate becomes almost independent of radial location and becomes singularly a function of the swirl ratio in which there are two different regimes apparent. For low swirl ratios between $S = 0.032$ and 0.235 the dissipation rate reduces in value by approximately a factor of 4 from values of $0.019 \mathrm{m}^2\mathrm{s}^{-3}$ to $0.005 \mathrm{m}^2\mathrm{s}^{-3}$. For Swirl ratios above 0.235 the dissipation rate slowly increases with swirl ratio. The change in behaviour of the dissipation rate could be explained by the changing of the mean flow from precession dominated to a more spatially stationary vortex with a greater degree of internal structure variation.

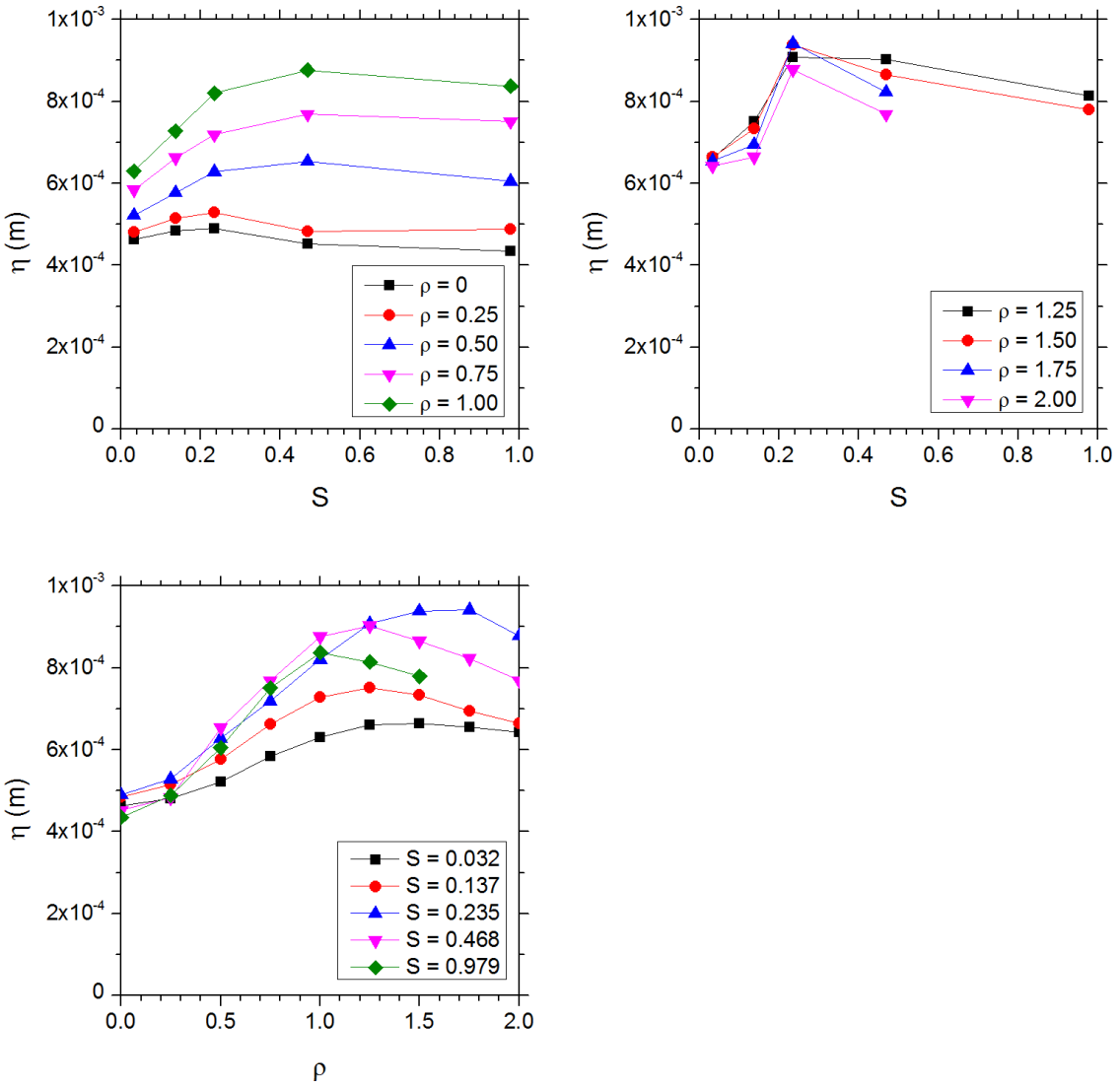

Fig. 8.27 Turbulent dissipation rate as a function of swirl ratio and radial location.

8.3 Proper Orthogonal Decomposition

8.3.1 Convergence of Mode Energy and Comparison with the Low Speed Data

Proper orthogonal decomposition was applied to the high speed PIV datasets in the same manner as the low speed data. As to be expected the structure of the spatial modes is consistent with the previous low speed data showing the same flow structures in corresponding modes. Furthermore the distribution of mode energy, λ is consistent between the low speed and high speed data sets. Figure 8.28 shows the percentage energy content and cumulative energy content of the first six modes as a function of swirl ratio. The individual mode energy of the first six modes is consistent with the energy distribution from the low speed data with the first two modes, which are related, containing an increasing proportion of the total energy with increasing swirl ratio until the energy content reduces at the highest swirl ratio, $S = 0.979$ which as with the low speed data can be attributed to a change in the nature of the flow from precession dominated to a more spatially stable large vortex exhibiting more complex multicellular vortex structure. The total energy contained

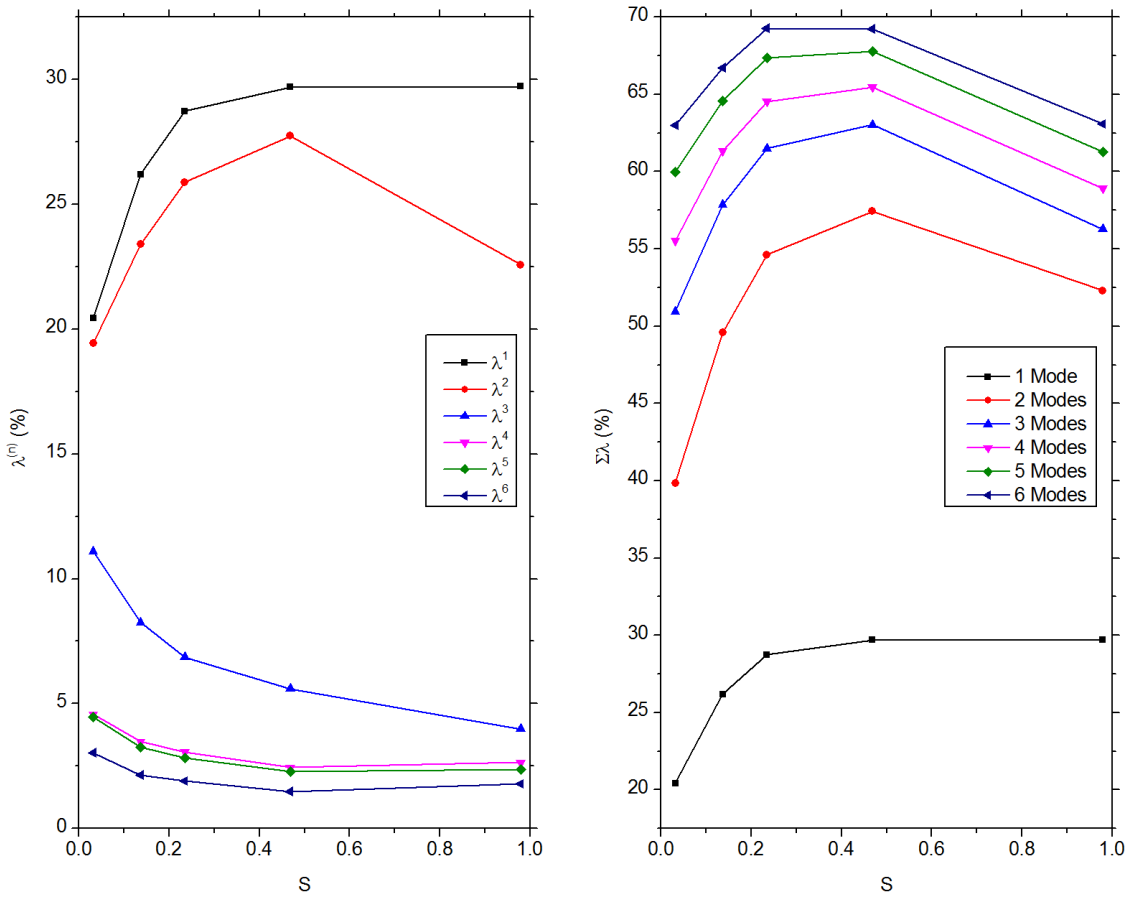

Fig. 8.28 (*left*) Percentage energy content, λ of the first six modes and (*right*) cumulative energy of the first 6 modes as functions of swirl ratio.

in the first two modes ranges between approximately 39% at $S = 0.032$ and 54% at $S = 0.468$ which is almost identical to the low speed data energy distribution as presented in Figure 8 15 the only difference being in the amount of energy contained at high swirl ratio $(S \approx 1)$, which is reduced compared to lower swirl levels (consistent with the low speed data) but the energy content is slightly higher at 54% compared to 40%.

The energy content of modes 3 and higher are again consistent with the low speed data showing decreasing energy content with increasing swirl ratio with almost identical values between the two datasets. It can again be seen that modes 4 and 5 can be considered a pair of modes identified with the same structure as they contain approximately the same amount of the total flow energy. Due to the similarities in the energy content and mode structure between the two datasets the analysis carried out on the low speed data will not be repeated and it shows that the recording period chosen for the high speed experiment was long enough to capture the long time-scale dynamics of the flow.

8.3.2 Spectral Properties of the POD

In order to compare the distribution of turbulent energy between POD and Fourier decomposition the Fourier transform was applied to a temporal autocorrelation function of the fluctuating velocity

components averaged over both velocity components and each spatial coordinate, B_{all} as follows:

$$B_{all}(\tau) = \frac{1}{2N_xN_y}\sum_{i=1}^{2}\sum_{j=1}^{N_x}\sum_{k=1}^{N_y}\int_{-\infty}^{\infty}u_i'(x_j,y_k,t)u_i'(x_j,y_k,t+\tau)\mathrm{d}\tau \tag{8.24}$$

Where i indicates the two fluctuating velocity components, N_x and N_y the number of velocity vectors in the x and y directions respectively and the integral is the standard temporal autocorrelation function.

Figure 8.29 shows the convergence of cumulative energy with increasing numbers of POD and Fourier modes. Like the POD the Fourier decomposition decomposes the total energy among 2700 Fourier modes where the Fourier modes are frequency bands. It is clearly visible that the conversion of energy is much quicker with POD than Fourier which is to be expected as the POD decomposes the flow information onto a set of basis functions that are optimal in the energy sense (Chatterjee, 2000). An accelerated rate of energy convergence occurs in the Fourier decomposition for frequencies above approximately 10Hz (approximately the 600^{th} Fourier mode) and is a result of aliasing as the sampling frequency at which the data was captured is too low to account for all high frequency components as discussed previously in this chapter. It is seen that the bulk of the energy is contained between approximately the 10th and 100th Fourier modes corresponding to a 0.2Hz to 2Hz band of frequencies.

Figure 8.30 shows the percentage of the total modes (2700) required to capture 80% and 90% of the total turbulent energy for both POD and Fourier decomposition as a function of swirl ratio. It can be seen that the number of modes required to capture both 80% and 90% of the energy increases with increasing swirl ratio whereas with the Fourier decomposition, apart from the lowest swirl ratio case $S = 0.032$, the number of modes required to capture 80% of the energy remains approximately constant with increasing swirl ratio with only a slight increase at $S = 0.979$, and for 90% of the total energy does not vary with swirl ratio above $S = 0.032$. This shows that the proportion of energy associated with the higher frequencies is approximately the same irrespective of swirl ratio. Unfortunately more low swirl ratio flows would have to be recorded in order to conclude that the lower number of Fourier modes required to capture 80% or 90% of the energy at $S = 0.032$ is part of a larger trend or is an outlier from the trend displayed for swirl ratios above 0.032.

The ratio of the number of Fourier modes to number of POD modes required to capture 80% of the energy increases with swirl ratio as one would expect as the POD converges more slowly at high swirl. To capture 80% of the energy 4 times the number of Fourier modes are required at the lowest recorded swirl ratio and this increases to 17 times at the highest swirl ratio.

Comparing the energy convergence between the two methods of decomposition it is shown that the flow is much more accurately described, in terms of turbulent energy, by the POD rather than the Fourier decomposition at low mode number showing that POD is much more efficient in extracting dominant flow structures.

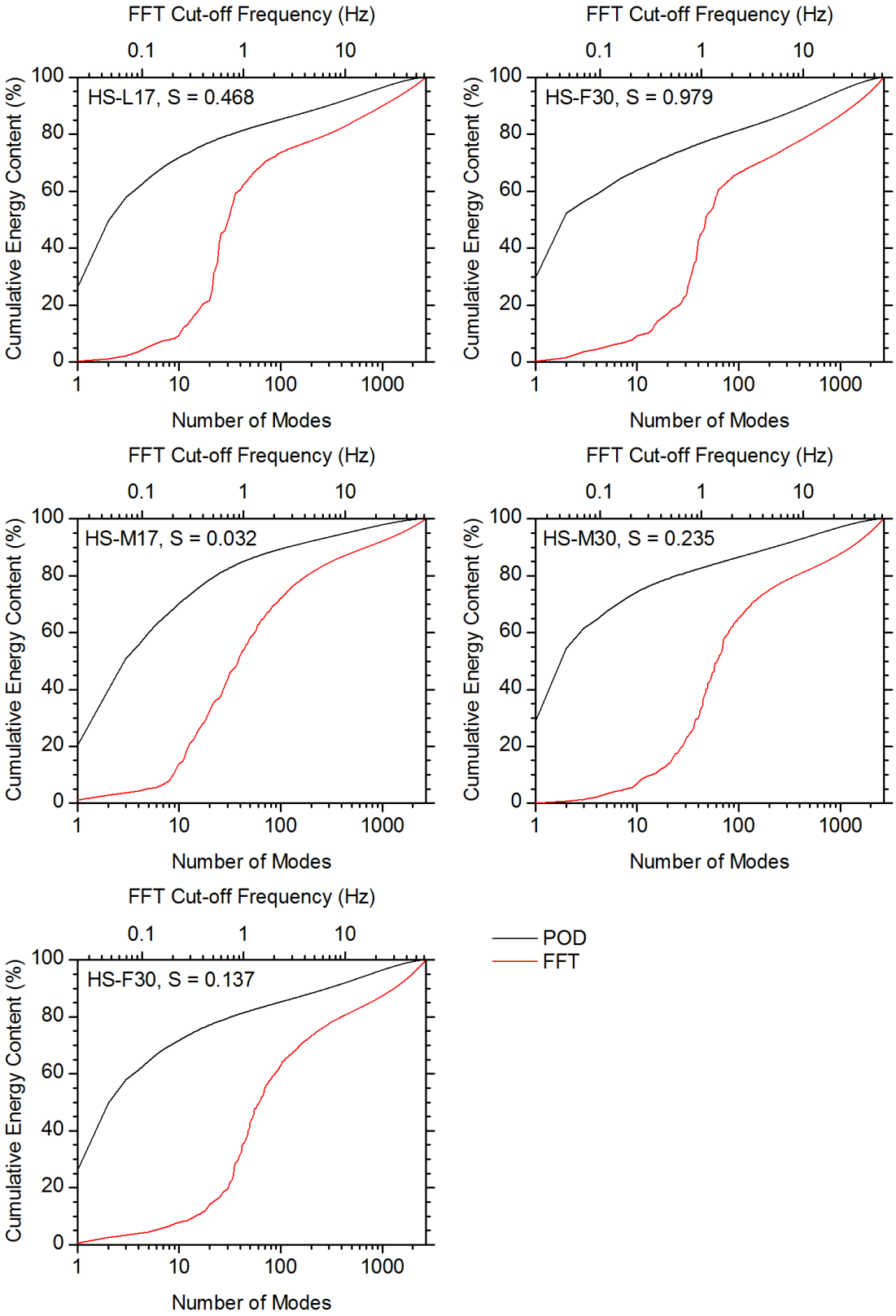

Fig. 8.29 Convergence of turbulence energy among POD modes and Fourier modes (frequency bands).

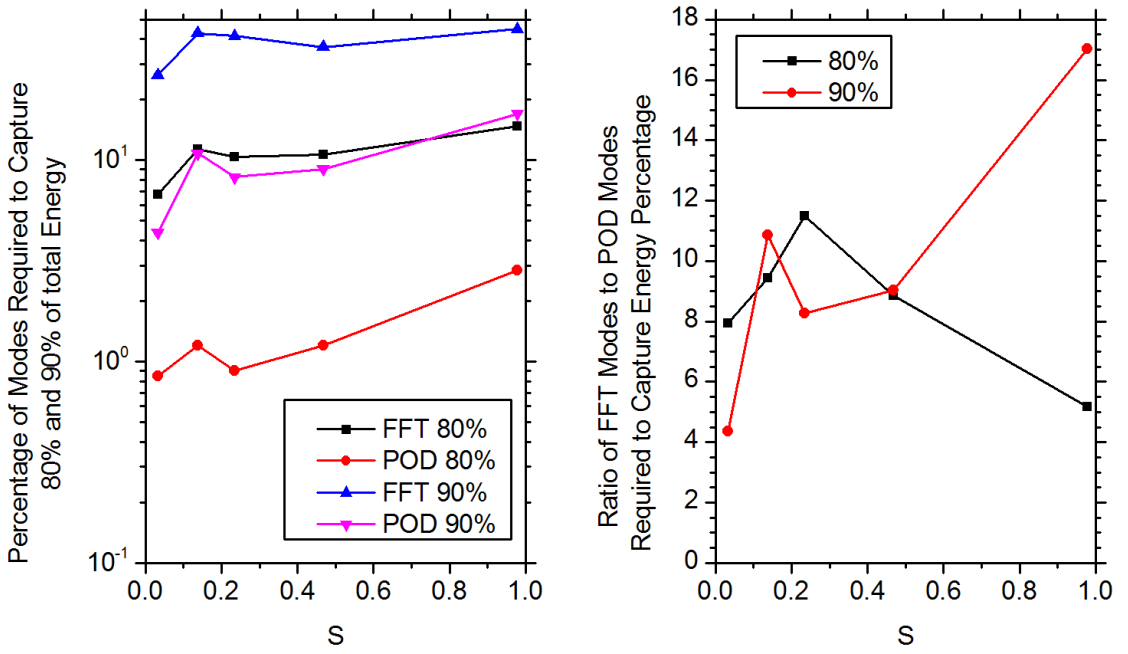

Fig. 8.30 (*left*) Percentage of modes required to capture 80% and 90% of the total flow energy for POD and Fourier decomposition and (*right*) The ratio of Fourier to POD modes required to capture 80% and 90% of the energy.

8.3.3 Analysis of Temporal Coefficients

Fluctuating velocity vectors at an instant in time are recreated through a linear summation of spatial POD modes ϕ multiplied by the corresponding temporal coefficient a as follows:

$$u'(t) = \sum_{n=1}^{N_s} a^{(n)}(t)\phi^{(n)} \tag{8.25}$$

Where N_s is the number of modes which is equal to the number of snapshots which equal 2700 for the high speed PIV data. The POD modes $\phi^{(n)}$ describe the spatial flow structures associated with mode n and the dynamics of these structures are contained within the temporally evolving POD coefficients $a^{(n)}$. An example of the temporal evolution of $a^{(1)}$ for dataset HS-F30 is presented in Figure 8.31 which displays a strong low frequency oscillatory motion (shown by the red line representing a moving average of 25 datapoints) centred around zero as well as higher frequency fluctuations (represented by the black line, the raw coefficients), Figure 8.31 is primarily presented to show the effect of smoothing the data as subsequent plots present smoothed data for clarity.

The temporal evolution of the POD coefficients associated with modes 1 to 6 for dataset HS-F30 are presented in Figure 8.32, again the data is presented as a moving average of window size 25 data points for greater clarity. The coefficients as presented are normalized by their energy content λ. As previously stated certain pairs of modes were identified as having similar energy content and spatial structure, this link between pairs of modes is visible in the evolution of their respective coefficients. The coefficients of modes 1 and 2 both display oscillations of approximately equal period separated by a phase difference in that peaks in one coefficient lag peaks in the other by a certain time difference, the same behaviour is displayed in the coefficients for the 4^{th} and 5^{th}

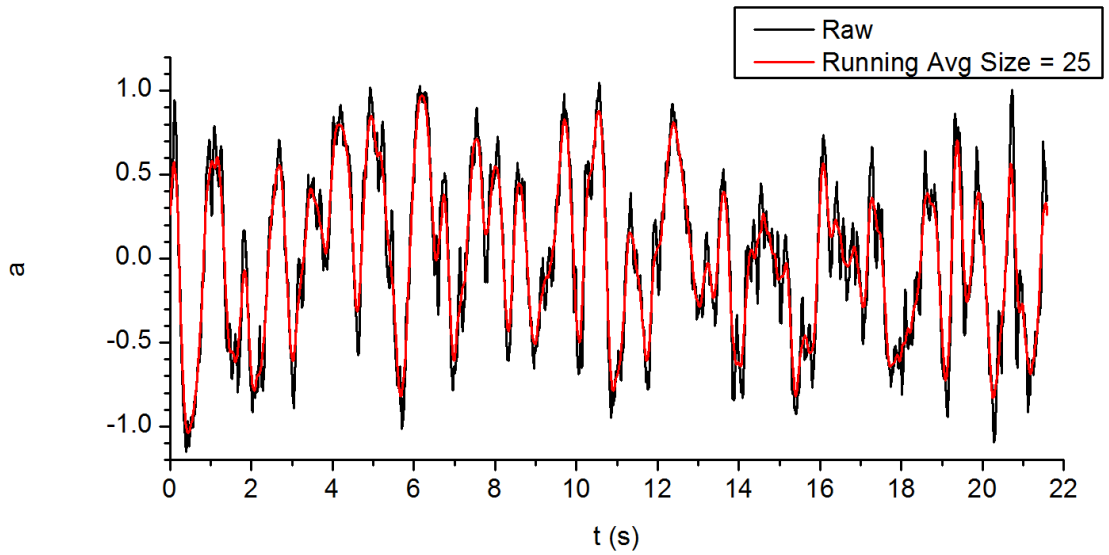

Fig. 8.31 Temporal evolution of the first mode POD temporal coefficients for data set HS-F30.

modes. Modes 3 and 6 are not associated with neighbouring modes in either spatial structure or energy content and it can be seen by the longer period of the major oscillations of the coefficients associated with these modes (coherent structures) that they describe lower frequency dynamics of the flow than mode pairs 1 and 2 and 4 and 5.

The temporal structure of the POD coefficients is more clearly identified by looking at their autocorrelation functions displayed in Figure 8.33 to Figure 8.35. Also displayed in these figures is the temporal correlation function of the fluctuating component of the total velocity vectors as defined by (8.24). It is observed that the periodicity of autocorrelation functions of the first two modes is very closely linked to that of the total fluctuating velocity autocorrelation function highlighting that the dominant temporal structures contributing to the full fluctuating velocity field are described by the first mode coefficients. The pseudo-periodic nature of the higher order modes is also evident in the autocorrelation functions of higher order coefficients with the mode-pair 4 and 5 showing shorter period dominant oscillations whereas modes 3 and 6 correspond to spatial structures that vary again pseudo-periodically but with a noticeably longer period linking them to lower frequency variations in the flow.

The integral timescale of the POD coefficients was calculated from their autocorrelation functions to obtain the integral frequency f_{Int} in the same manner the velocity integral timescale was calculated using (8.10). The integral frequency data are presented for each dataset in Figure 8.36. It can be seen that for each dataset the integral frequency increases in a linear fashion with mode number before levelling off to values between 40Hz and 44Hz above a certain mode number. As the integral frequency can be interpreted as the average frequency based on energy content across all frequency bands, individual normalized spectra of the POD coefficients for mode 1 and mode 1000 for dataset HS-F30 are presented in Figure 8.37. The integral frequencies of the coefficient spectra plotted in Figure 8.37 are 1.12Hz and 41.16 Hz for the first and 1000th modes respectively. It can be seen for the first mode that the majority of the spectral energy is concentrated in the band

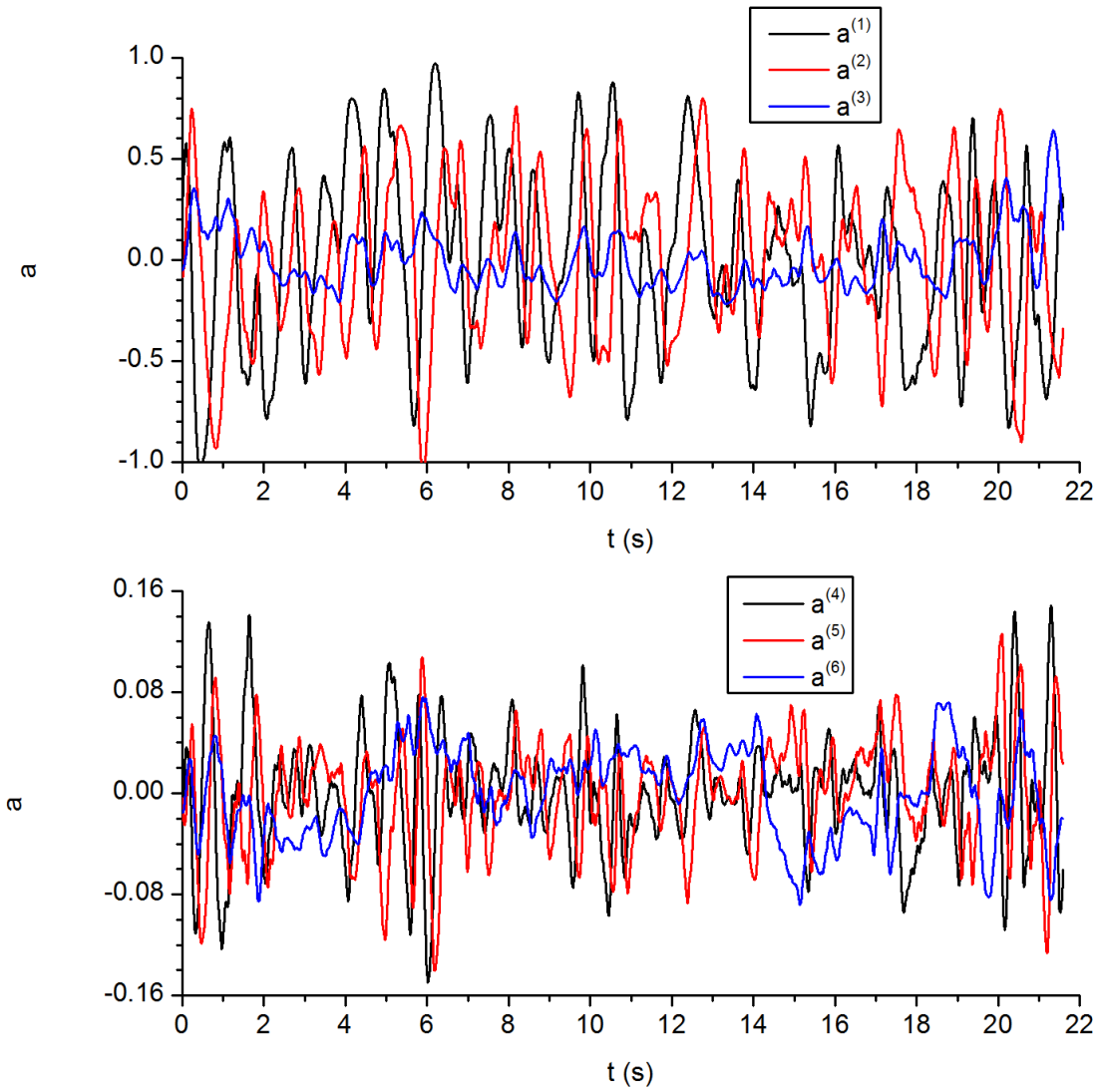

Fig. 8.32 Temporal evolution of POD coefficients $a^{(n)}$ for dataset HS-F30 for the first 6 modes. Data is smoothed using a running average of window size 25 data points.

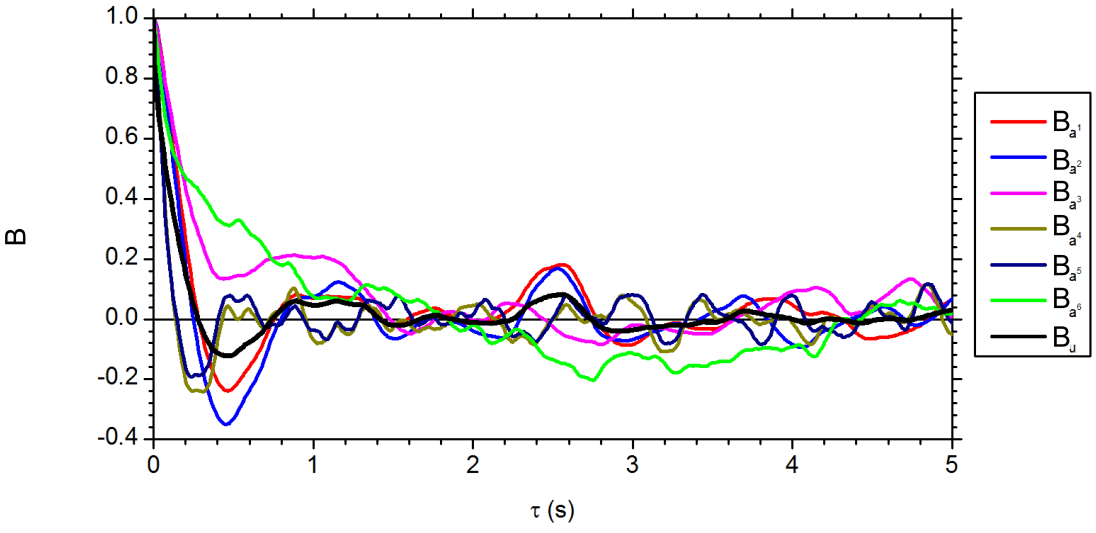

Fig. 8.33 Autocorrelation functions of the first 6 POD coefficients for dataset HS-F30.

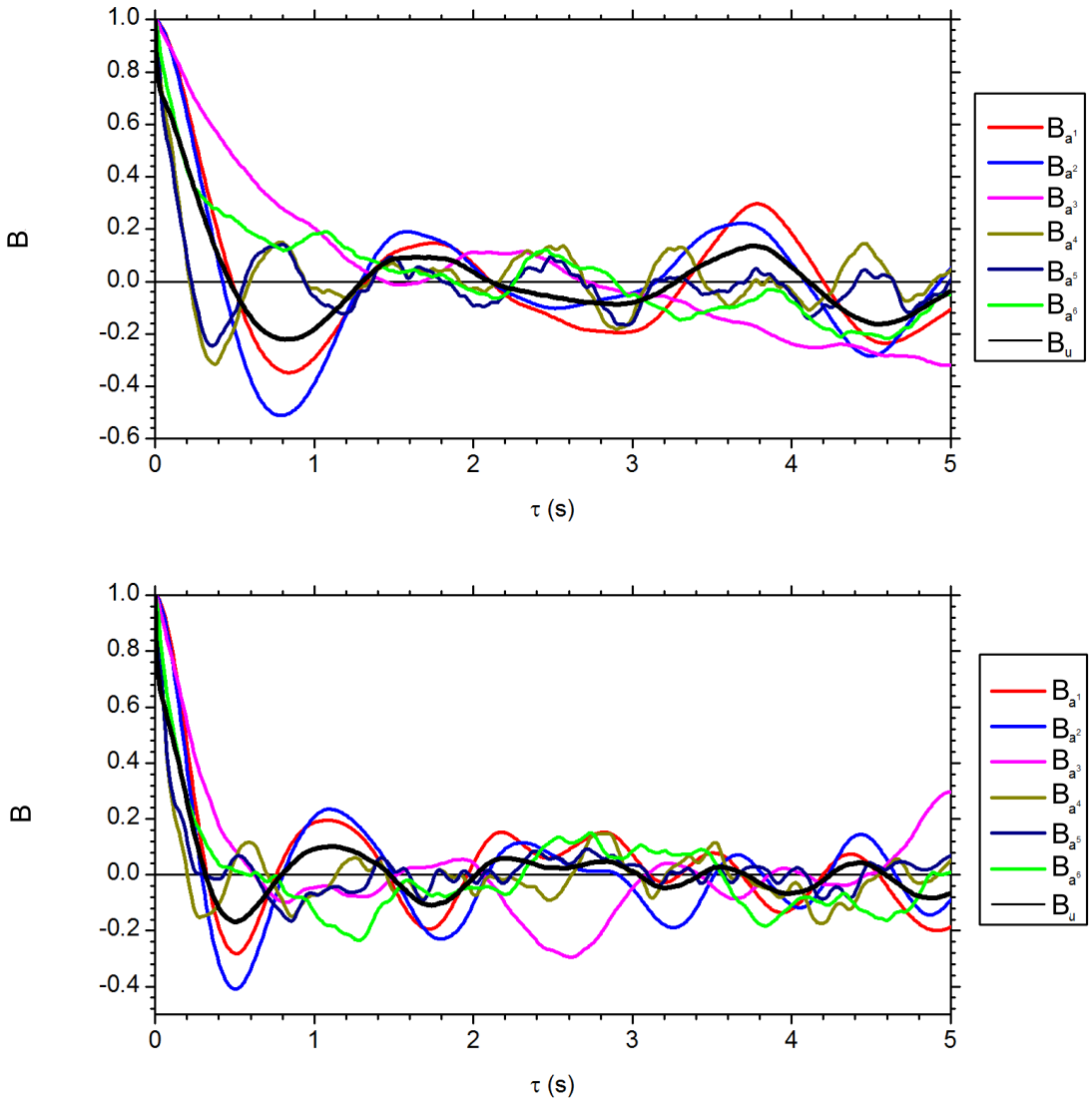

Fig. 8.34 Autocorrelation functions of the first 6 POD coefficients for dataset HS-L17 (*top*) and HS-L30 (*bottom*).

of frequencies below 2 Hz whereas for the 1000th mode the spectral energy is more evenly distributed among frequencies above approximately 1Hz showing that there are no dominant low frequency structures and this mode is typical of random or turbulent fluctuations.

Referring back to Figure 8.36 it can be seen that the mode number at which the integral frequency levels off to the 40-44Hz range differs between flow configurations which have a circulation blower supply of 30 and 17 volts. For the three datasets at which 30V is supplied the integral frequency begins to level off at approximately mode 200 whereas for the 17V configurations the cut-off increases to approximately mode 300. This suggests that structured temporal features of the flow are contained in a greater number of modes when the circulation supplied to the flow is lower.

Whilst the POD decomposes the velocity data in terms of the energy content of the spatial structures (modes) with the highest energy content modes being the lower modes and subsequent

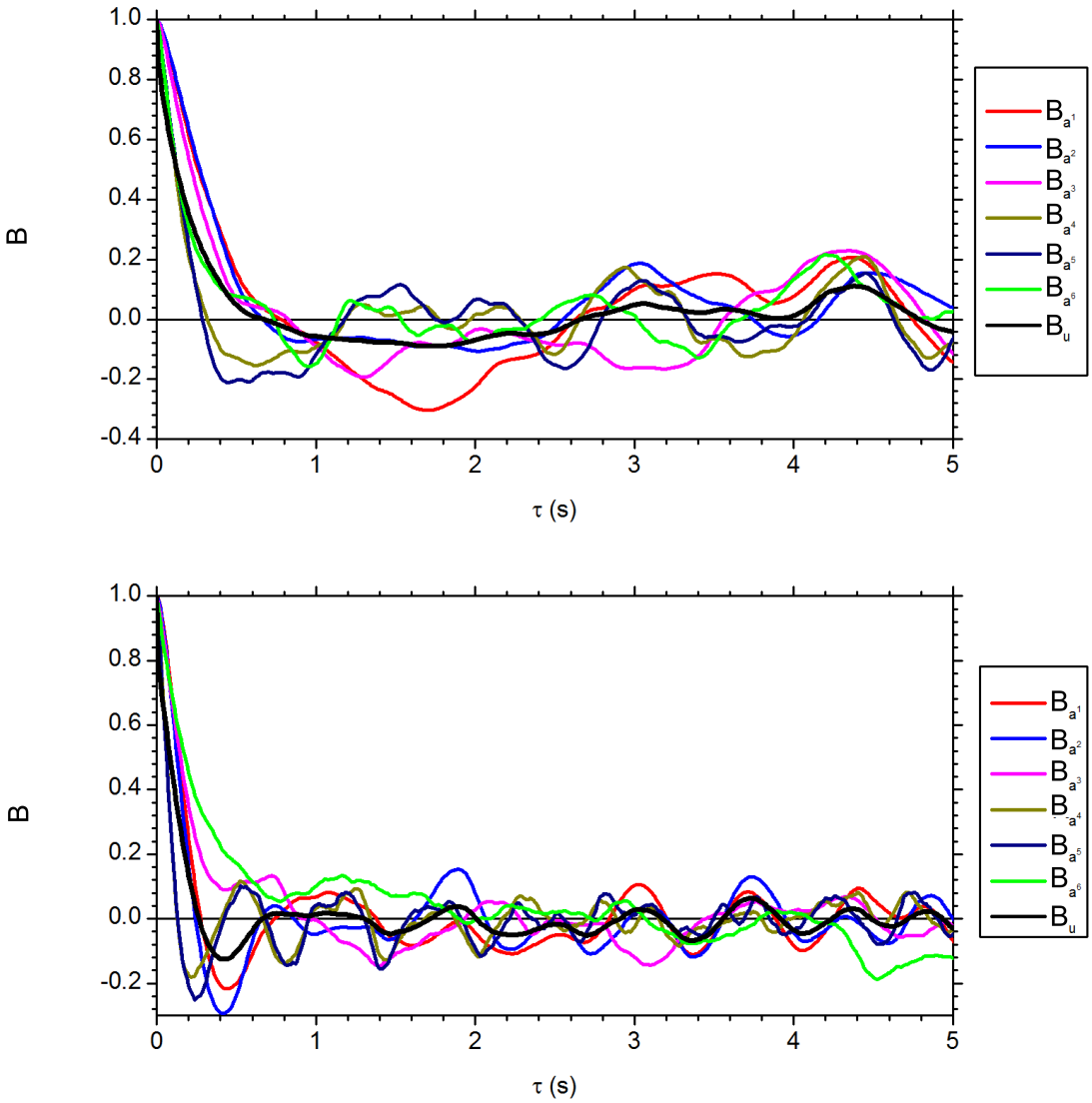

Fig. 8.35 Autocorrelation functions of the first 6 POD coefficients for dataset HS-M17 (*top*) and HS-M30 (*bottom*).

modes containing less of the total energy it can be seen through the integral frequencies of the coefficients that these energetic modes also contain the structured low frequency dynamics of the flow and the higher order modes the unstructured turbulent variations. Referring back to Figure 8.29 and Figure 8.36 it can be seen that using Fourier decomposition flow information in the frequency range below 40 Hz is distributed among approximately the first 1800 Fourier modes, this same range of temporal frequencies are contained in only the first 200-300 POD modes depending on the flow configuration. This shows that POD is a much more efficient method than Fourier decomposition in reducing the flow and capturing the structured dynamics.

A spectral analysis of POD coefficients was carried out by computing the Fourier transforms of the autocorrelation functions of the coefficients and for comparison, of the spatially averaged fluctuating velocity autocorrelation function as defined by (8.24). The spectra presented in Figure 8.38 to Figure 8.40 are normalized by the total energy of the transform so that the value at

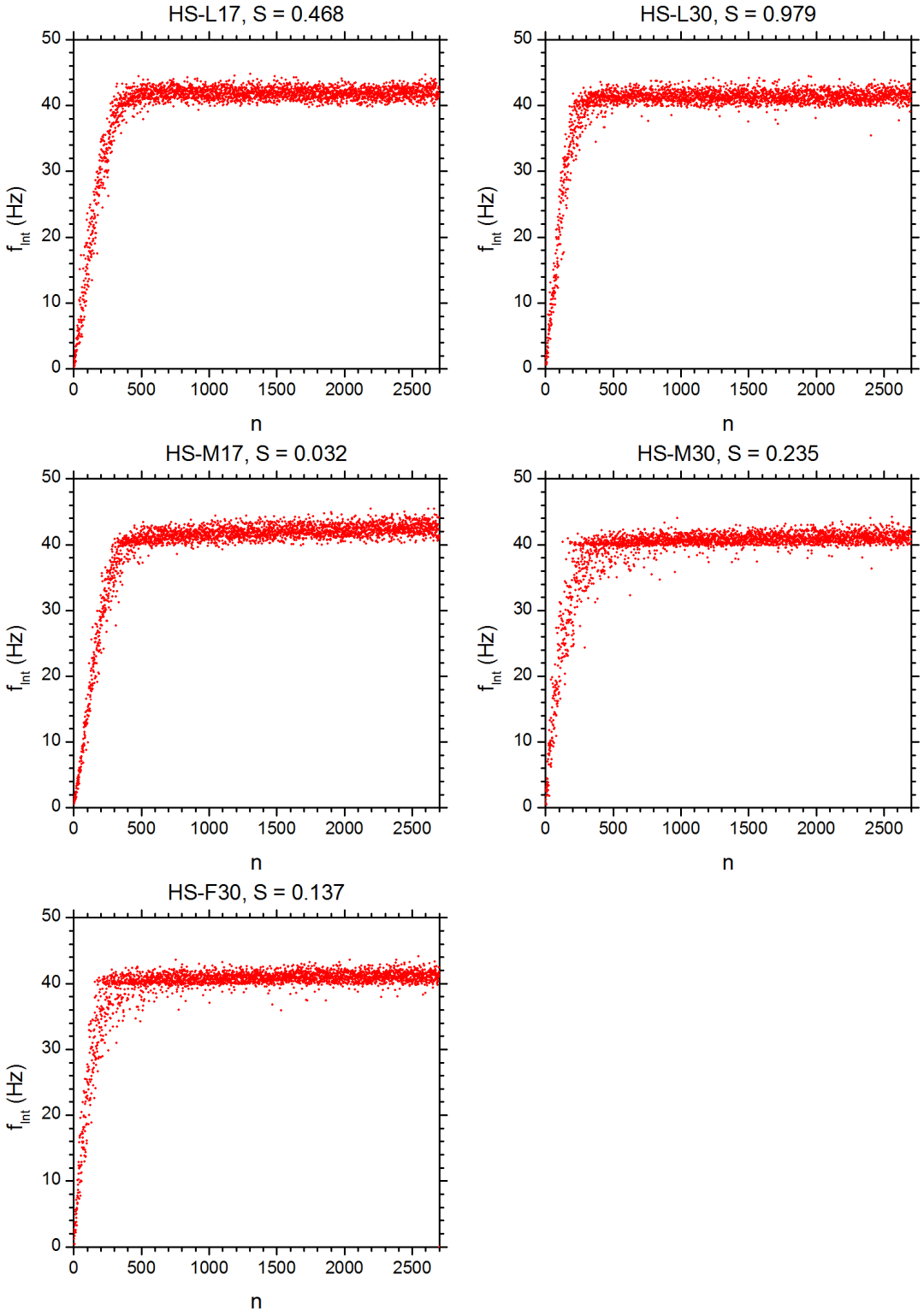

Fig. 8.36 Integral frequency of POD coefficients.

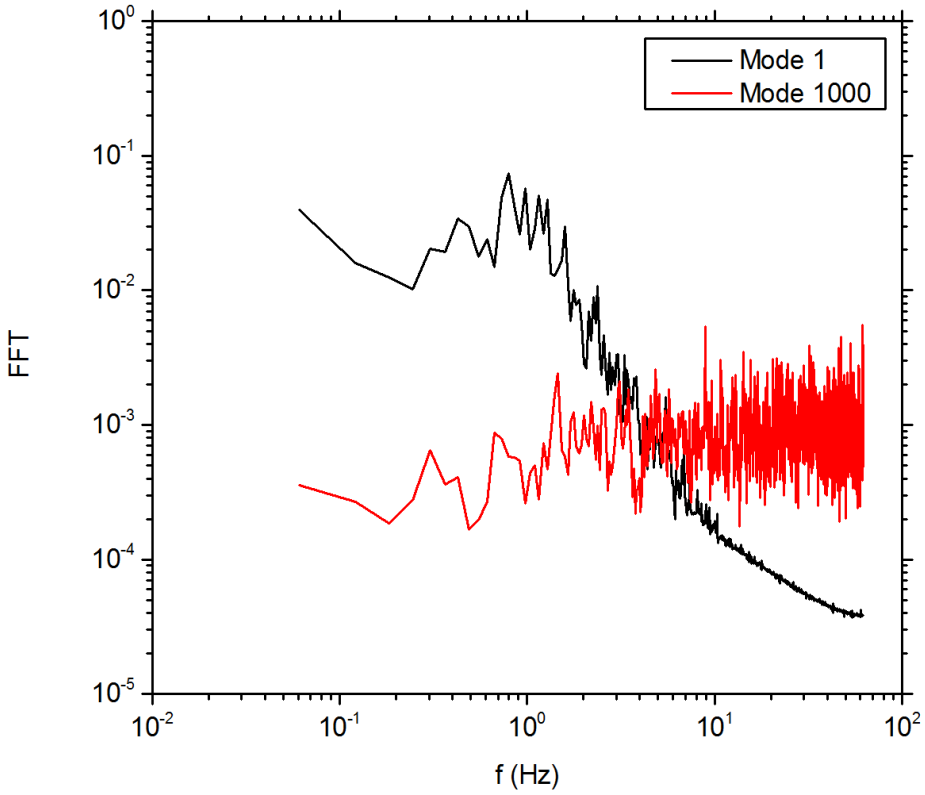

Fig. 8.37 Normalized spectra of the first and 1000th POD coefficients for dataset HS-F30.

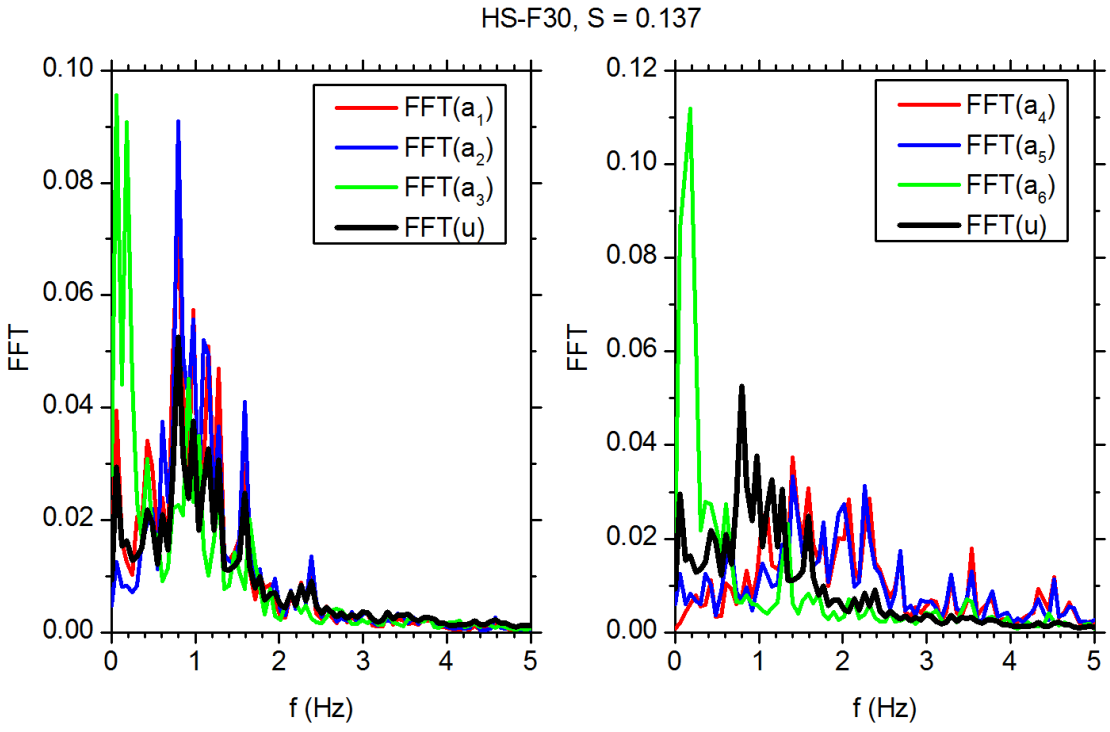

Fig. 8.38 Normalized spectra of POD temporal coefficients and spatially averaged velocity data for dataset HS-F30.

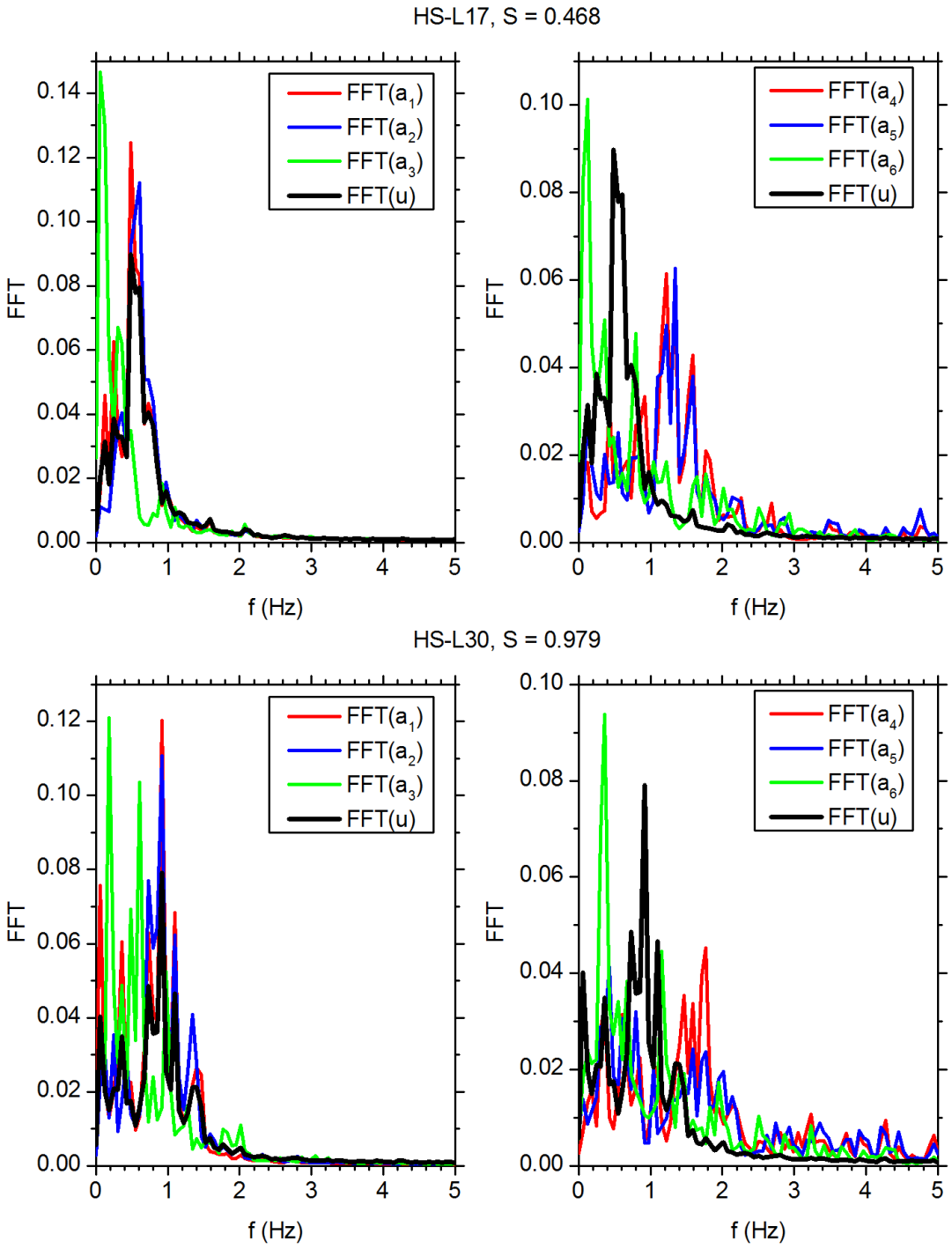

Fig. 8.39 Normalized spectra of POD temporal coefficients and spatially averaged velocity data for dataset HS-L17 (*top*) and HS-L30 (*bottom*).

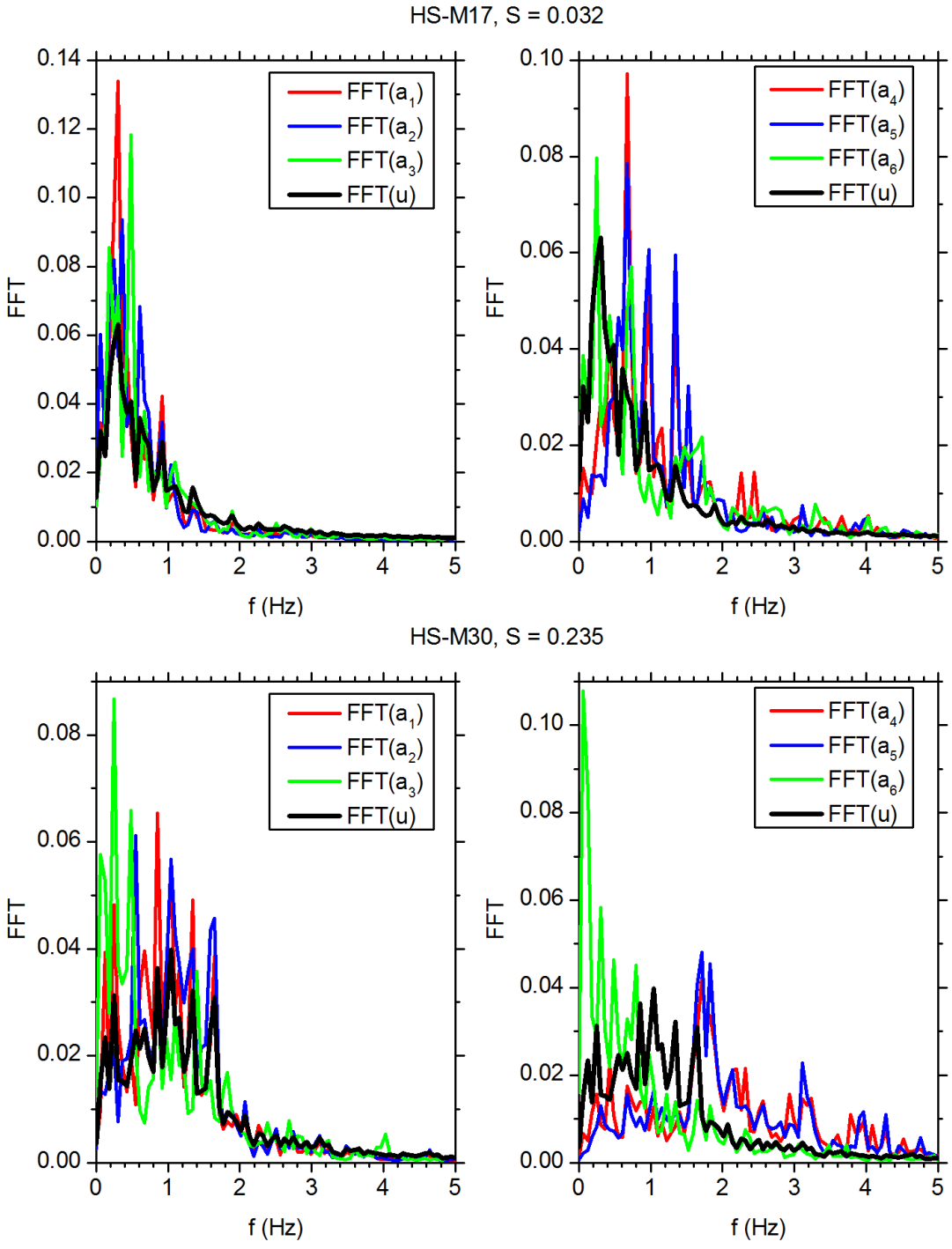

Fig. 8.40 Normalized spectra of POD temporal coefficients and spatially averaged velocity data for dataset HS-M17 (*top*) and HS-M30 (*bottom*).

each data point is the fraction of the signal energy contained within that frequency band (integrating over all frequencies gives a value of 1). The peak frequency f_0 of the spectra is identified as the frequency containing the most energy and is plotted in Figure 8.41. It can be seen in the spectra plots and Figure 8.41 that the peak frequency of the first two POD coefficients is very closely match to the frequency of the velocity fluctuations which further as one would expect due to the similarity between the autocorrelation functions of these coefficients and the velocity fluctuations which shows that as well as the spatially dominant flow structures the dominant dynamics of the velocity fluctuations are also contained within these modes. As well as the similarity in the peak frequencies of the first two modes the distribution of low frequency energy (<5Hz) shows a close similarity to the velocity spectra with spectral peaks at the same frequencies which shows that the dynamics of the lower order modes contain a broad range of frequencies related to those of the overall flow.

The fourth and fifth mode coefficient peak frequencies are if not exactly, very close to twice the peak frequency of the first two modes which suggest that dynamically the structures described by the fourth and fifth modes are a harmonic of the first two modes with the exception of the fifth mode coefficients at the highest swirl ratio where the peak frequency does not follow the trend and is much lower at 0.4Hz. The third and sixth mode coefficient peak frequencies are consistent with less energetic spectra peaks in the velocity signal in the <0.35Hz range for all datasets apart from the lowest swirl case (HS-M17) where the third mode peak frequency is greater than that of the first two modes. In this case the spectra of the velocity fluctuations differs from the other datasets in that the majority of the spectral energy is contained in a relatively narrow band of low frequencies below approximately 1Hz.

8.4 Comparison of POD between PIV and synthetic data

In order to develop a further understanding of the POD of the PIV velocity data the decomposition was carried out on synthetic datasets. The synthetic datasets consist of a uniform grid measuring 129 x 129 on which two-component velocity vectors were imposed of an Oseen vortex with randomly placed centre (x_0, y_0):

$$u_\theta = \frac{\Gamma}{r}\left[1 - \exp\left(\frac{-r^2}{r_c^2}\right)\right] \tag{8.26}$$

Where r is the radial coordinate from the origin which is located at the centre of the grid at grid coordinate (64, 64), r_c is the radius of the vortex which is set to 10 grid units and Γ the circulation which in this case will be set to unity. The degree of simulated precession is controlled by adjusting the standard deviation of normally distributed instantaneous vortex core locations which in this case is set to 20.

The first four randomly placed Oseen vortex vector fields and the instantaneous vortex core locations for 1000 snapshots are presented in Figure 8.42 and Figure 8.43 respectively with the

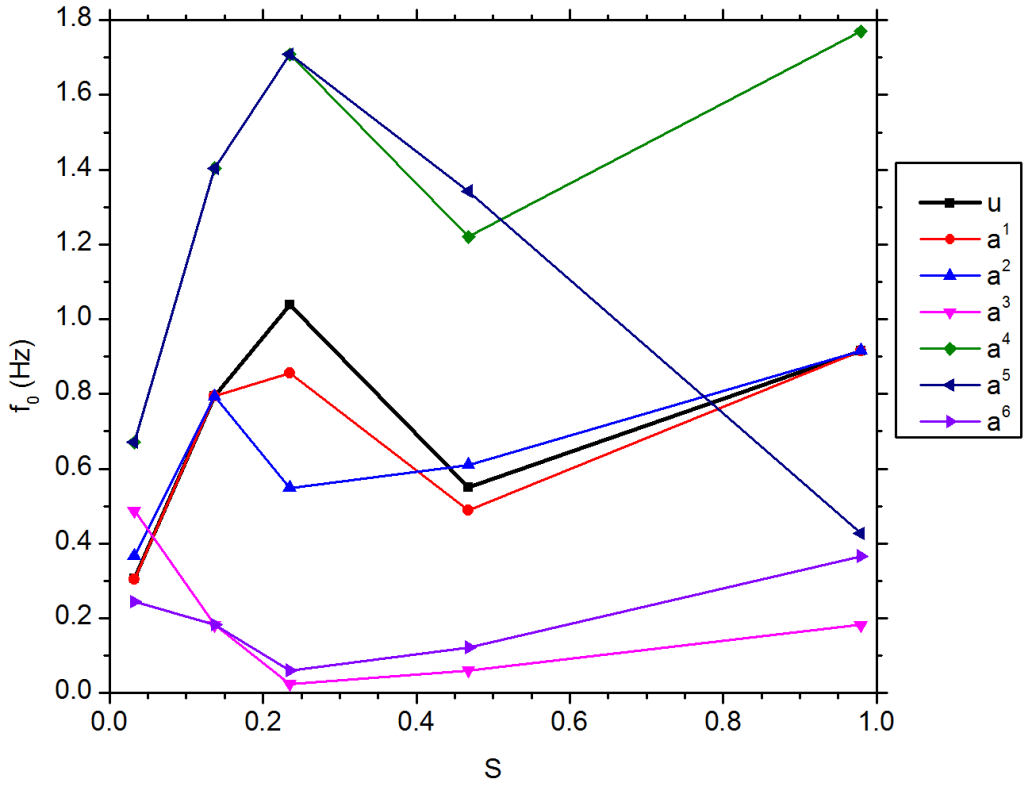

Fig. 8.41 Peak frequency f_0 of the first six POD temporal coefficients and the peak frequency of the velocity spectra (black line) as a function of swirl ratio.

mean vector field presented in Figure 8.44

In Figure 8.45 the percentage mode energy $\lambda^{(i)}$ for the first 20 modes and the convergence of λ over all modes is shown. It can be seen that the first two modes, $\lambda^{(1)}$ and $\lambda^{(2)}$ contain almost 50% of the total energy of the fluctuating velocity fields with the third mode, $\lambda^{(3)}$ containing 12.8% and modes four and five, $\lambda^{(4)}$ and $\lambda^{(5)}$ containing 7.1% and 6.5% respectively. The energy convergence is very quick with the first ten modes containing 88.7% of the total energy, the first 15 modes containing 94% and the first 20 modes containing 96.5% of the energy. The very quick convergence of the mode energy can be attributed to a number of factors. Firstly there is no randomly fluctuating 'turbulent' element in the velocity data which is often featured in the higher order modes in experimental data. Secondly the individual vortices have uniform shape and size, in experimental data the size of the vortex fluctuates around a mean size and is often not perfectly circular. It is these unordered random fluctuations that are present in the PIV datasets that attribute the higher order mode energy content.

Looking at the energy distribution in Figure 8.45. it can be seen that modes 1 and 2 have a similar energy content to that of the PIV data (Figure 8.28) and it can be assumed that these modes describe the same structure. The same is apparent with modes 4 and 5 and to a lesser extent modes 6 and 7, these features are consistent with the PIV datasets previously discussed.

The first five spatial POD modes, $\phi(1)$ to $\phi(5)$ are shown in Figure 8.46 and Figure 8.47, it can be seen that the mode structure is equivalent to the structure of the related modes from the PIV data as presented in § 7 with the first two modes showing a pair of counter rotating vortices, the third mode showing a singular vortex and the fourth and fifth modes showing two pairs of counter-rotating vortices each.

As a final comparison three different synthetic data sets of 1000 instantaneous vector fields were constructed representing high, low and medium swirl ratios. The low swirl ratio case consists of a small instantaneous vortex radius of 5 units with a high degree of precession (standard deviation of core location equal to 20), the high swirl ratio case is a large spatially stable vortex with radius 20 and positional standard deviation of 5 and the medium case falls in-between with radius and standard deviation of 12.5. The distribution of energy among the first twenty modes is presented in Figure 8.45, it can be seen that at higher swirl ratio, for a more stable large vortex a higher percentage of the total energy is contained within the first two modes and is consistent with the PIV data.

Figure 8.48: Distribution of POD mode energy for the first 10 modes for synthetic datasets representing high, medium and low swirl ratios. The similarity in the distribution of mode energy and spatial structure of the lower order modes between the synthetic and PIV data shows that the large scale energy containing structures can, to a certain degree of accuracy be modelled by a randomly distributed Oseen vortex and that the results are not an artefact of the methods used in the capturing of the PIV data.

8.5 Summary

Presented in this chapter are the first known high temporal resolution full field velocity measurements of a laboratory generated tornado like vortex. Due to hardware limitations (mainly camera storage memory) and the requirement to account for large scale flow variations due to precession as well as small scale turbulence a compromise on the temporal resolution of the measurements had to be made. To account for the large scale temporal structures it was not possible to record down to the Kolmogorov scale.

Initial results confirm the repeatability of configuring the flow as the relationships between swirl ratio and instantaneous vortex radius and mean flow vortex radius agree, to a reasonable degree with those obtained from the low speed data as presented in § 6.

Due to the periodic nature of the flow, single point temporally resolved velocity measurements do not have a well defined mean and have large RMS values of velocity fluctuations which in turn lead to very high turbulence intensity levels. Turbulence intensity is greatest at the mean flow vortex centre (as is also shown in § 6 - Low Speed tornado-vortex PIV) reducing in value as the radial position increases to the boundary of the vortex core region, outside of the vortex core turbulence intensity is shown to be independent of spatial position. It is shown how applying a correction to Taylor's hypothesis based on a local mean (temporal) velocity value can return much

lower local turbulence intensity values making it viable to apply Taylor's hypothesis to convert velocity time-series data to a function of space.

The integral time scale of the vortex is shown to be influenced little by swirl ratio but predominantly by the flow rate of the circulation blowers. When induced circulation was low (17V supply voltage) the integral time scale is significantly longer than when induced circulation is high (30V supply voltage). Integral time scale is shown to be at a maximum and approximately constant at all locations within the vortex core region (though differing depending on the flow configuration) for swirl ratios below 0.5. At swirl ratio close to 1 the integral time scale is shown to decrease approximately linearly from the mean vortex centre outwards. As the flow domain is unbounded the integral scale (spatial) structures extend beyond the size of the measurement domain. However, by applying the correction to Taylor's hypothesis it became possible to calculate integral length scales from the time series velocity measurements. Unlike the integral time scale the integral length scale is shown to have a much more defined relationship with swirl ratio with a maximum length scale of 0.8m – 1.0m for $S < 0.2$ down to 10cm – 20cm for $S = 0.979$. Integral length scale is at a maximum at the mean flow vortex centre reducing with increasing radial position.

Due to the compromise in temporal resolution of the velocity measurements there were considerable artefacts due to aliasing in velocity spectra, it is shown how a filter can be applied to the spectra to reduce, if not negate, the effect of aliasing.

Velocity spectra of both temporal and spatial (Taylor's hypothesis) velocity measurements at a single point are shown to vary only with radial position enabling the azimuthal averaging of velocity spectra at a particular radius and thus reducing the noise levels in the spectra.

Both energy-frequency and energy-wavenumber spectra resemble traditional one-dimensional energy spectra with the majority of the turbulent energy contained at low frequency/wavenumber integral scale structures. A distinct inertial subrage is present in each spectra which in parts follow Kolmogorov's -5/3 law before departing at higher frequency/wavenumber due to aliasing of the signal.

The frequency of the integral scale structures is linked to the integral time scale and therefore is dependent on the fan configuration. The integral frequency is shown to be approximately constant in the region within the mean flow vortex core before increasing outside suggesting outside of the mean flow vortex core the flow is less organised.

Integral wavenumber is, like integral length scale, closely dependant on swirl ratio with low values at low swirl ratio. There is little variation in wavenumber for swirl ratios below 0.2 and above this value the integral wavenumber increases with increasing swirl ratio.

The dissipation rate of the flow is shown to have well defined relationships with both swirl ratio and radial position. As to be expected the dissipation rate is at a maximum at the mean flow vortex centre where turbulence intensity is greatest. From the centre of the core dissipation rate decreases radially outwards up to the mean flow vortex radius outside of which the dissipation rate remains constant for any given swirl ratio.

Calculated Kolmogorov length scales had a maximum value of approximately 0.95mm (S = 0.979) which is considerably below the spatial resolution of the PIV vector data which was set at 1.25mm. The Kolmogorov length scale is shown to be at a minimum in the centre of the mean vortex core and at this point varies little with swirl ratio and having a minimum value of approximately 0.42mm. The Kolmogorov length scale increases radially outwards to the vortex core radius and once outside varies little with increasing radius.

The results of POD on the high speed data show the same trends for mode energy content and energy convergence as those presented in Chapter 7 (Low speed tornado-vortex POD) with similar values at similar swirl ratios.

Energy convergence of the POD is shown to be much quicker than Fourier decomposition with 10% of the total POD modes containing approximately 90% of the total energy and 10% of the total Fourier modes containing only approximately 80% of the total energy.

Investigation of the POD coefficients shows that the large scale spatial structures contained within the low order modes (as identified in Chapter 7) have distinct frequency spectra. Peaks in the spectra of individual mode coefficients are shown to match certain spectral features of the full velocity data showing that certain flow structures, POD modes, are associated with certain spectral features of the whole flow.

The integral frequency was calculated for each set of mode coefficients and shows that lower order modes contain low frequency structures which are characteristic of organised coherent structures. The integral frequency of the coefficients peaks at approximately 40-42Hz for approximately mode 300 and greater (out of a total of 2700), it is shown that at high mode number energy is distributed approximately equally among frequencies above 1Hz and much lower values below this level, characteristic of unorganised purely turbulent flow variations.

Finally POD is conducted on a synthetic data set of an Oseen vortex with simulated precession and the structure of the spatial modes and patterns in the mode energy levels are shown to closely match those from the results of the high and low speed PIV velocity measurements.

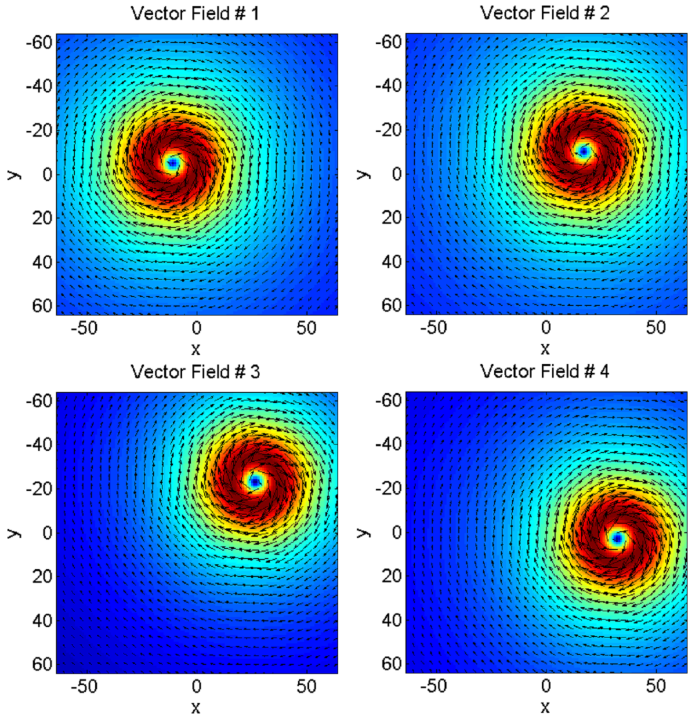

Fig. 8.42 Distribution of vortex core locations for synthetic vector fields..

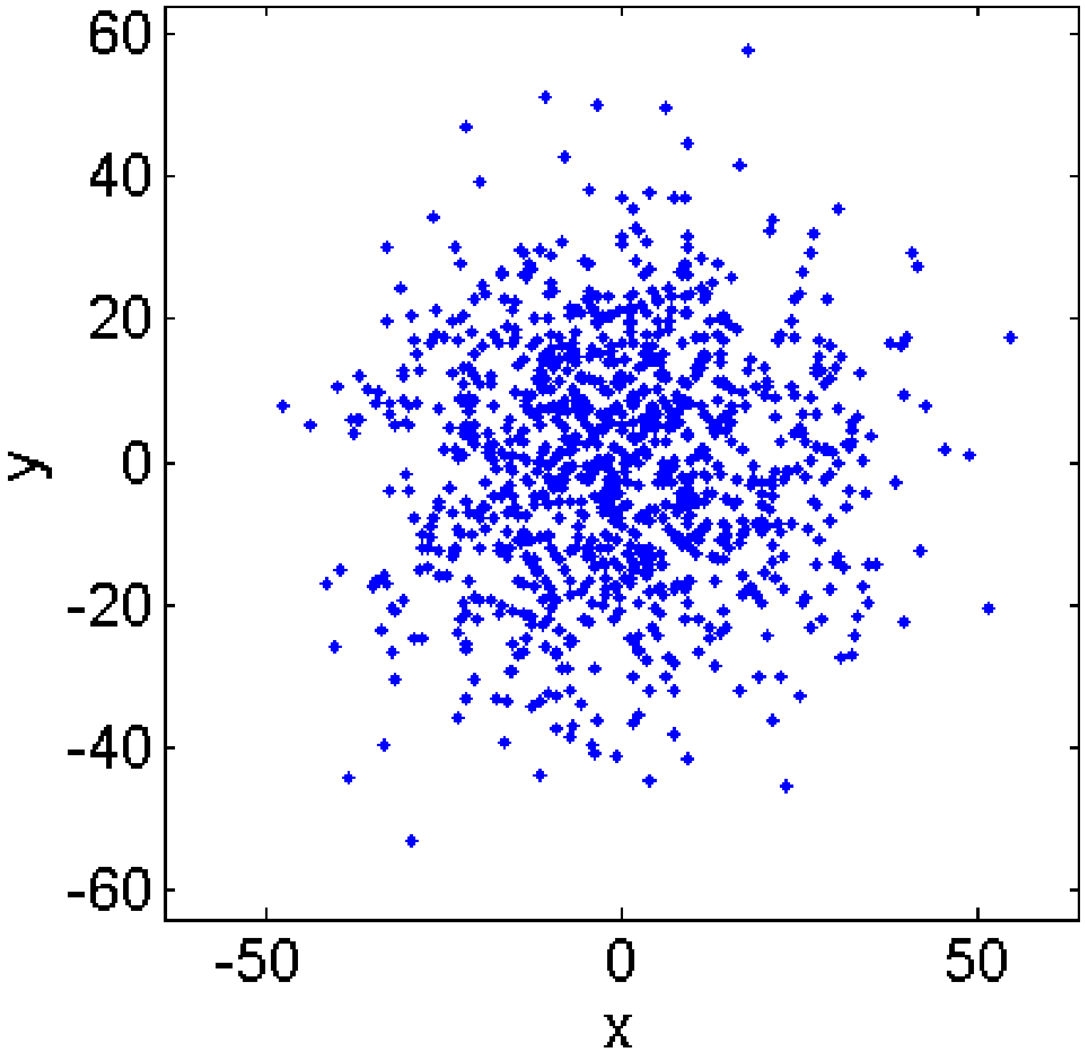

Fig. 8.43 First four Oseen vortex vector fields with randomly Gaussian distributed vortex centres. Only one in four vectors shown for clarity and background colour indicates velocity magnitude (arbitrary units).

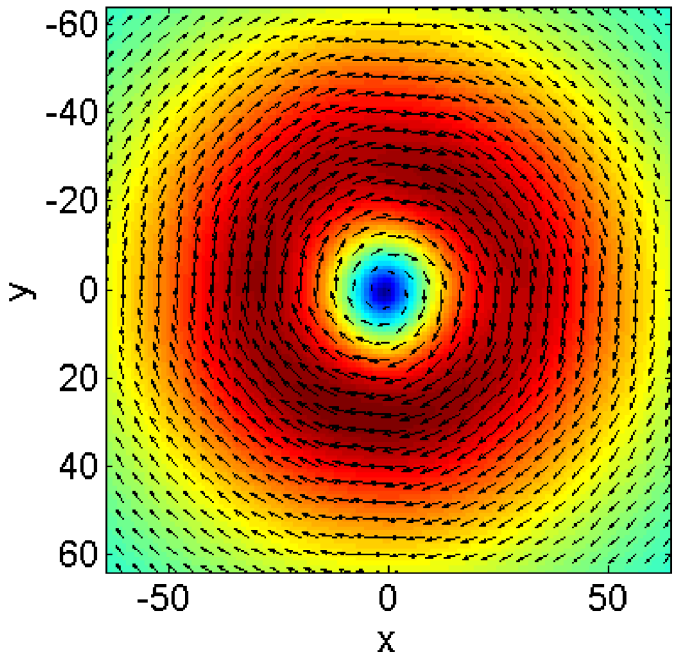

Fig. 8.44 Mean vector field of synthetic dataset. Only one in four vectors shown for clarity.

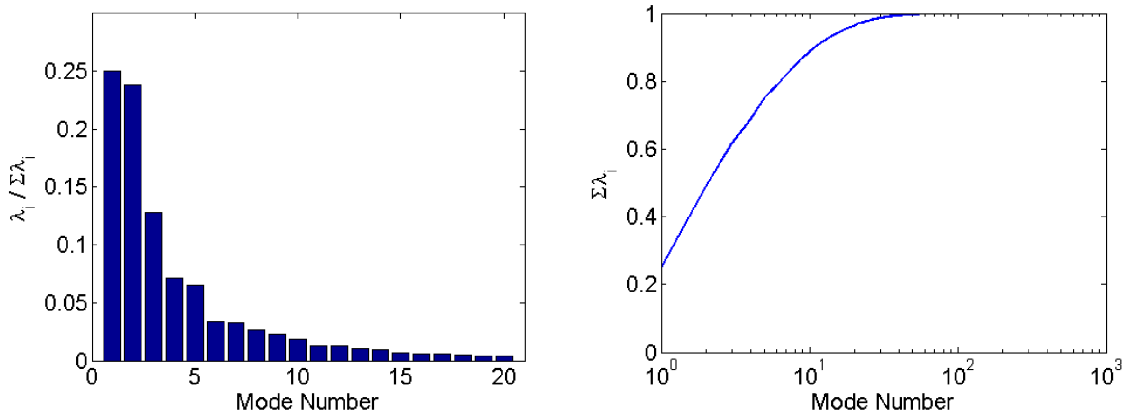

Fig. 8.45 (*left*) Percentage mode energy for the first 20 modes and (*right*) the convergence of mode energy.

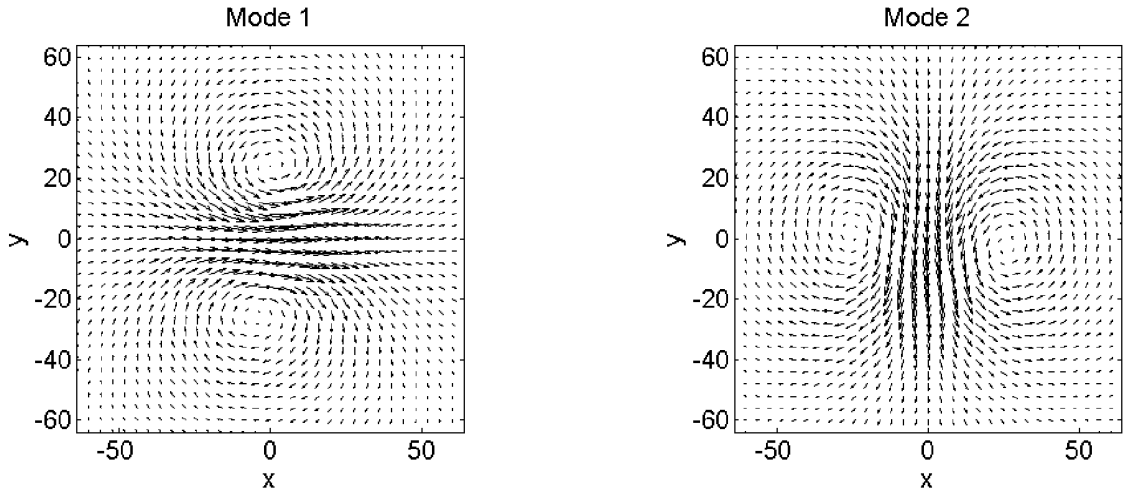

Fig. 8.46 First two synthetic data POD modes $\phi^{(1)}$ and $\phi^{(2)}$. Only every fourth vector shown for clairy.

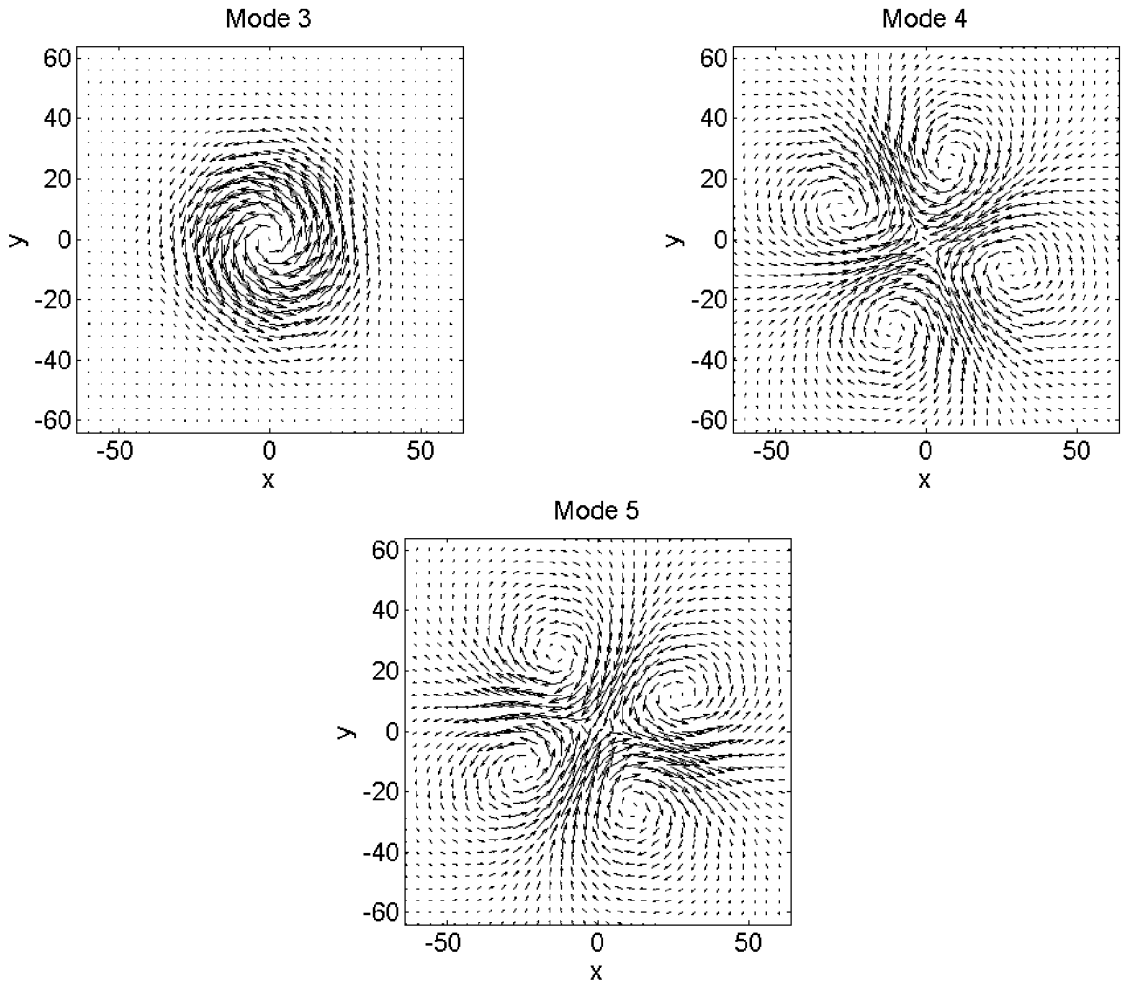

Fig. 8.47 Synthetic data POD modes $\phi^{(3)}$, $\phi^{(4)}$ and $\phi^{(5)}$. Only every fourth vector shown for clairy.

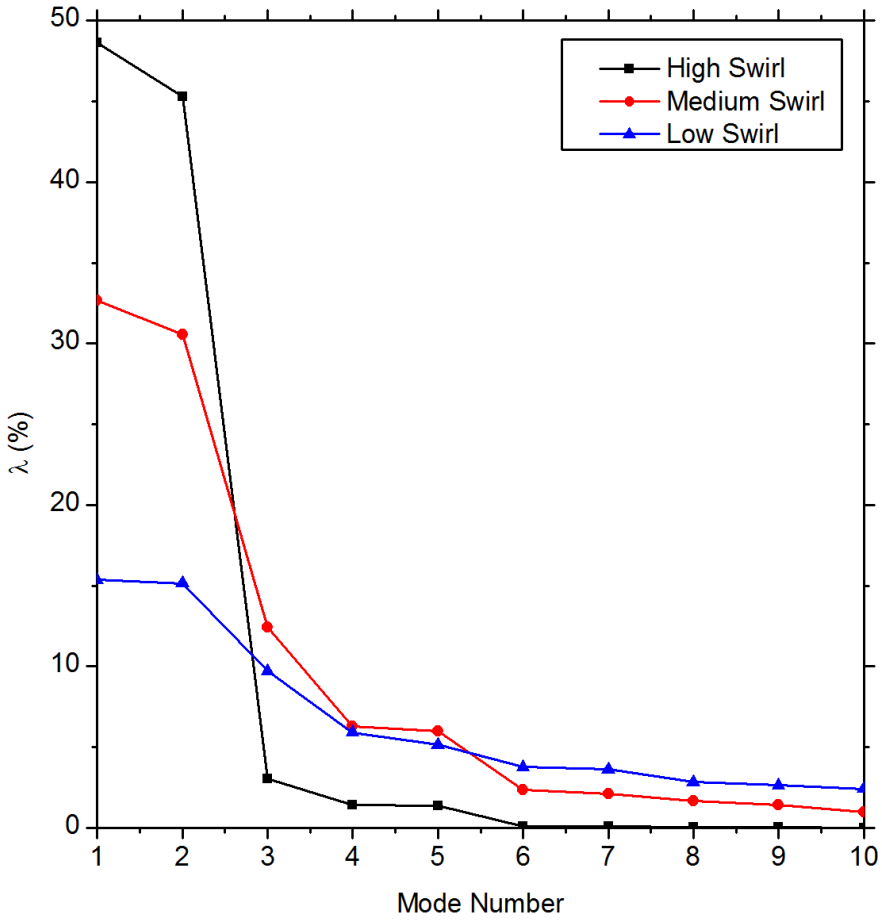

Fig. 8.48 Distribution of POD mode energy for the first 10 modes for synthetic datasets representing high, medium and low swirl ratios.

Chapter 9

Conclusions and Future Work

9.1 Conclusions

The first part of this study focuses on evaluating cross-correlation based PIV vector calculation algorithms. Algorithms were tested against synthetic images depicting Oseen vortex flow enabling the comparison between imposed and measured particle image displacements. The synthetic image parameters were varied to investigate the sensitivities of each algorithm to each parameter. The methods evaluated were standard cross-correlation (SCC), multigrid (MGRID), the products of adjacent correlation functions (CBC), particle image deformation (PID) and an original method combining PID methods and CBC methods (HPIDCBC). The major conclusions regarding the investigation into vector calculation algorithms are as follows.

- It was shown that in regions of high spatial gradients the PID algorithms provide much superior accuracy in calculated vectors when compared to the SCC, MGRID and CBC algorithms. This is due to the deformations of the interrogation regions which compensates for linear gradients in the particle image displacements.

- In regions of low velocity gradient it is shown that the CBC algorithm performs best offering the lowest error in measured velocity vectors. This is due to the final correlation function being generated by a greater number of particle image pairs owing to the offsets of the individual interrogation regions and the near elimination of random noise signals in individual correlation functions through the element-wise multiplication of adjacent correlation functions.

- Combining the results of CBC and PID a new iterative algorithm was developed (HPIDCBC) where CBC is utilised in regions of low spatial displacement gradients and PID in regions of high spatial gradients. The new HPIDCBC method is shown to return displacement vectors with a reduced level of error across the full Oseen vortex, and not just in regions of low or high spatial gradients, when compared to existing methods.

- The new HPIDCBC algorithm, while offering greater accuracy in calculating displacement

vectors, comes with a high computational cost; taking approximately ten times longer to calculate individual vectors than SCC.

The second part of the study focusses on applying planar low repetition rate particle image velocimetry (PIV) and high speed time resolved PIV to the study of vortex flow in a laboratory generated tornado like vortex (TLV). New analysis methods were developed providing original data on the structure, spatial stability and turbulence characteristics and their dependence on swirl ratio of laboratory generated tornado-like vortices. The application of high speed time resolved PIV gives for the first time, to the author's knowledge, full field high speed planar velocity measurements where previously high speed time resolved measurements have only been captured at single points using hot wire anemometry. Also as far as the author is aware, the thesis presents the first use of the proper orthogonal decomposition (POD) technique to investigate the spatial and temporal structures of laboratory generated TLVs. The major fluid-mechanical conclusions of the investigation into laboratory generated TLVs are as follows.

- Swirl ratio is seen to be a genuine non-dimensional number that characterizes the flow as flows with similar swirl ratios but different axial and circumferential flow rates are seen to be similar; exhibiting comparable vortex radius and degree of vortex precession.
- It is shown that over the range of swirl ratios investigated there are three distinct flow regimes:
  - At low swirl ratio ($S <= 0.008$) the flow is dominated by the precession (low spatial stability) of a small radius single-celled vortex.
  - At intermediate swirl ($0.008 < S < 0.5$) some vortex precession is evident at the lower swirl end ($0.008 < S < 0.08$), in this intermediate swirl range, as with the low swirl range the vortex remains single celled in structure.
  - At high swirl ratio ($S > 0.5$) the effects of vortex precession are minimal (high spatial stability) with the size of instantaneous vortices approximately equal to that of the mean flow vortex. In this swirl range it is shown that the vortex has a tendency to go multi-cellular with instantaneous double and triple-celled vortices present that are increasingly prevalent at the high swirl end of the range investigated.
- The difference in flow regime between high and low swirl ratios is measured through the spread of instantaneous vortex core locations and by comparing instantaneous vortex radii and mean flow vortex radii. At low swirl ratio it is shown that, due to precession, the mean flow vortex radius is between 2 and 14 times that of the instantaneous vortex radius. At high swirl ratio it is shown that the mean flow vortex is much more characteristic of the instantaneous flow vortex as the radius and maximum velocity are equal to within 5%.
- Mean instantaneous vortex velocity profiles with the effects of vortex precession removed

are shown to closely resemble an analytic Oseen vortex model with increasing accuracy as swirl ratio is increased.

- Due to the periodic nature of the flow, single point temporally resolved velocity measurements do not have a well defined mean and have large RMS values of velocity fluctuations which in turn lead to very high turbulence intensity levels. Turbulence intensity is greatest at the mean flow vortex centre reducing in value as the radial position increases to the boundary of the vortex core region. Outside of the vortex core turbulence intensity is shown to not vary with spatial position. It is shown how applying a correction to Taylor's hypothesis based on a local temporal mean velocity value, much lower local turbulence intensity values are obtained making it viable to apply Taylor's hypothesis to convert velocity time-series data to a function of space and thus allowing the calculation of the integral length scale, which, due to the TVS being unbounded, cannot be calculated from the spatial velocity vector data owing to the limited measurement domain. Unlike the integral time scale the integral length scale is shown to have a much more defined relationship with swirl ratio with a maximum length scale of 0.8m – 1.0m for $S < 0.2$ down to 10cm – 20cm for $S = 0.979$. Integral length scale is at a maximum at the mean flow vortex centre reducing with increasing radial position.

- The integral time scale of the vortex is shown to be influenced little by swirl ratio but predominantly by the flow rate of the circulation blowers. When induced circulation was low (17V supply voltage) the integral time scale is significantly longer than when induced circulation is high (30V supply voltage). Integral time scale is shown to be at a maximum and approximately constant at all locations within the vortex core region (though differing depending on the flow configuration) for swirl ratios below 0.5. At swirl ratios close to 1 the integral time scale is shown to decrease approximately linearly from the mean vortex centre outwards.

- Velocity spectra of both temporal and spatial (Taylor's hypothesis) velocity measurements at a single point are shown to vary only with radial position enabling the azimuthal averaging of velocity spectra at a particular radius and thus reducing the noise levels in the spectra.

- The frequency of the integral scale structures is linked to the integral time scale and therefore is dependent on the fan configuration. The integral frequency is shown to be approximately constant in the region within the mean flow vortex core before increasing outside suggesting outside of the mean flow vortex core the flow is less organised.

- Integral wavenumber is, like integral length scale, closely dependant on swirl ratio with low values at low swirl ratio. There is little variation in wavenumber for swirl ratios below 0.2 and above this value the integral wavenumber increases with increasing swirl ratio.

- The dissipation rate of the flow is shown to have well defined relationships with both swirl

ratio and radial position. As expected the dissipation rate is at a maximum at the mean flow vortex centre where turbulence intensity is greatest. From the centre of the core, dissipation rate decreases radially outwards up to the mean flow vortex radius outside of which the dissipation rate remains constant for any given swirl ratio.

- Calculated Kolmogorov length scales had a maximum value of approximately 0.95mm ($S = 0.979$) which is considerably below the spatial resolution of the PIV vector data which was set at 1.25mm. The Kolmogorov length scale is shown to be at a minimum in the centre of the mean vortex core and at this point varies little with swirl ratio and having a minimum value of approximately 0.42mm. The Kolmogorov length scale increases radially outwards to the vortex core radius and once outside varies little with increasing radius.

- POD analysis of a tornado-like vortex was conducted using both low speed and high speed time resolved PIV data showing well defined relationships between POD mode energy and mode cumulative energy.

  - Mode cumulative energy exhibits distinct flow regimes for low swirl ($S < 0.5$) and high swirl ($S > 0.5$). Individual mode energy content is closely linked to swirl ratio with three distinct regimes for low, intermediate and high swirl levels.

  - Between mode 4 and 15 modal energy content is greatest at low swirl ($S < 0.008 - 0.01$) where the modal energy varies little with swirl ratio. At intermediate swirl ratios ($0.01 < S < 0.5$) modal energy content decreases with swirl ratio before increasing slightly for high swirl ratios ($S > 0.5$) showing how the dominance of certain coherent structures is swirl ratio dependent.

  - Energy convergence of the POD is shown to be faster than Fourier decomposition with 80% of POD modes containing comparable energy to 90% of Fourier modes.

  - Investigation of the temporal POD coefficients shows that the large scale spatial structures contained within the low order modes have distinct frequency spectra. Peaks in the spectra of individual mode coefficients are shown to match certain spectral features of the full velocity data showing that certain flow structures are associated with certain spectral features of the whole flow. The integral frequency was calculated for each set of mode coefficients and shows that lower order modes contain low frequency structures which are characteristic of organised coherent structures. The integral frequency of the coefficients peak at approximately 40-42Hz for approximately mode 300 and greater (out of a total of 2700), it is shown that at high mode number energy is distributed approximately equally among frequencies above 1Hz and much lower values below this level, characteristic of disorganised purely turbulent flow variations.

9.2 Future Work

In the present study it was not possible to use the new HPIDCBC algorithm for calculating velocity vectors from the TLV PIV images due to the processing time required. HPIDCBC showed improved accuracy in calculating displacement vectors from synthetic particle image images. This algorithm should be made viable, for the analysis of large high-resolution datasets through reprogramming in a compiled language rather than in MATLAB as presented.

Further improvements to HPIDCBC could be made by investigating a wider range of image interpolation algorithms and windowing functions.

The performance of the enhanced normalised median test spurious vector detection algorithm presented in Chapter 5 should comprehensibly analysed to see if it outperforms the original (Westerweel) algorithm in increasing sensitivity to spurious data and reducing the number of false positives.

In the work presented all TLV PIV measurements were recorded in the same vertically located horizontal plane. The height from the chamber floor from which velocity data is recorded should be varied to investigate different regions of the flow. Of particular interest is the ground plane where it is shown in the literature that most of the inflow (significant radial velocity component) into the vortex occurs. By taking PIV measurements at different locations in the flow and by applying the analytical techniques presented in this work further insights and a more complete understanding of the structure and turbulence properties of the TLV will be obtained.

With improved camera storage capacity the temporal resolution of high speed PIV measurements can be increased to capture both low frequency flow information and all information including the Kolmogorov scale dissipation range removing the effect of aliasing and increasing the accuracy of calculated dissipation rates and Kolmogorov length scales. By employing stereo-PIV three component velocity vectors could be calculated in which the out of plane velocities can be investigated, this is of high interest as the flow has a significant axial component and this has remained uninvestigated in the work presented here.

References

Adrian, R. J. (1988). Statistical properties of properties of particle image velocimetry measurements in turbulent flow. *Laser Anemometry in Fluid Mechanics III*.

Adrian, R. J. (1991). Particle-imaging techniques for experimental fluid mechanics. *Annual Review of Fluid Mechanics*, 23(1):261–304.

Adrian, R. J., Christensen, K. T., and Liu, Z. C. (2000). Analysis and interpretation of instantaneous turbulent velocity fields. *Experiments in Fluids*, 29(3):275–290.

Alan, K., Charlotte, D., and Philippe, G. (2010). Aerodynamic control inside an internal combustion engine. *Measurement Science and Technology*, 21(12):125404.

Alim, A. (2006). A physical comprehensive definition of a vortex based on the lamb vector. *Algerian Journal of Applied Fluid Mechanics*, 1:1–5.

AMS (2012). Inertial Subrange. American Meteorological Society Glossary of Meteorology [online]. *http://glossary.ametsoc.org/wiki/Inertial_subrange*. Accessed 10 November 2013.

Astarita, T. (2007). Analysis of weighting windows for image deformation methods in piv. *Experiments in Fluids*, 43(6):859–872.

Astarita, T. (2008). Analysis of velocity interpolation schemes for image deformation methods in piv. *Experiments in Fluids*, 45(2):257–266.

Astarita, T. (2009). Adaptive space resolution for piv. *Experiments in Fluids*, 46(6):1115–1123.

Astarita, T. and Cardone, G. (2005). Analysis of interpolation schemes for image deformation methods in piv. *Experiments in Fluids*, 38(2):233–243.

Awwal, A. A. S., Munir, S. M., and Islam, M. K. (2000). Particle velocity computation using a phase-only filter. In *Proc. SPIE: Photonic Devices and Algorithms for Computing II*, pages 36–43.

Baroud, C. N., Plapp, B. B., Swinney, H. L., and She, Z.-S. (2003). Scaling in three-dimensional and quasi-two-dimensional rotating turbulent flows. *Physics of Fluids*, 15(8):2091–2104.

Batchelor, G. (1953). *The Theory of Homogeneous Turbulence*. Cambridge University Press, Cambridge, England.

Benedict, L, H. and Gould, R, D. (1998). Concerning time and length scale estimates made from burst-mode lda autocorrelation measurements. *Experiments in Fluids*, 24(3):246–253.

Bernard, P. S. and Wallace, J. M. (2002). *Turbulent Flow: Analysis, Measurement, and Prediction*. John Wiley & Sons, New york, USA.

Bewley, G, P., Kelken, C., Eberhard, B., and Research, I. C. f. T. (2012). On integral length scales in anisotropic turbulence. *Physics of Fluids*, 24(6):061702–7.

Bizon, K., Continillo, G., Mancaruso, E., Merola, S, S., and Vaglieco, B, M. (2010). Pod-based analysis of combustion images in optically accessible engines. *Combustion and Flame*, 157(4):632–640.

Borée, J. (2003). Extended proper orthogonal decomposition: a tool to analyse correlated events in turbulent flows. *Experiments in Fluids*, 35(2):188–192.

Breuer, S., Oberlack, M., and Peters, N. (2005). *Non-isotropic length scales during the compression stroke of a motored piston engine*, volume 74. Springer, Dordrecht, PAYS-BAS.

Bruno, R. and Carbone, V. (2005). The solar wind as a turbulence laboratory. *Living Reviews in Solar Physics*, 2(4).

Bussiere, M., Nobes, D, S., and Koch, C, R. (2012). A combinatorial vortex detection and characterization algorithm for 2c2d piv data. In *16th Int Symp on Applications of Laser Techniques to Fluid Mechanics, pp. 5*, Lisbon, Portugal.

Cameron, S. M. (2011). Piv algorithms for open-channel turbulence research: Accuracy, resolution and limitations. *Journal of Hydro-environment Research*, 5(4):247–262.

Cantwell, B. J. (1981). Organized motion in turbulent flow. *Annual Review of Fluid Mechanics*, 13(1):457–515.

Cebeci, T. (2004). *Analysis of Turbulent Flows*. Elsevier Science, Amsterdam, The Netherlands.

Chanson, H. and Carosi, G. (2007). Turbulent time and length scale measurements in high-velocity open channel flows. *Experiments in Fluids*, 42(3):385–401.

Chapman, G. T. and Tobak, M. (1985). *Observations, Theoretical Ideas, and Modeling of Turbulent Flows—Past, Present, and Future*, volume 58 of *Applied Mathematical Sciences*, chapter 2, pages 19–49. Springer New York.

Chatterjee, A. (2000). An introduction to the proper orthogonal decomposition. *Current science*, 78(7):808–817.

Chen, J. and Katz, J. (2005). Elimination of peak-locking error in piv analysis using the correlation mapping method. *Measurement Science and Technology*, 16(8):1605.

Cholemari, M, R. (2007). Modelling and correction of peak-locking in digital piv. *Experiments in Fluids*, 42(6):913–922.

Chong, P., Hongping, W., and Jinjun, W. (2013). Phase identification of quasi-periodic flow measured by particle image velocimetry with a low sampling rate. *Measurement Science and Technology*, 24(5):055305.

Chong, M, S., Perry, A, E., and Cantwell, B, J. (1990). A general classification of three-dimensional flow fields. *Physics of Fluids A: Fluid Dynamics*, 2(5):765–777.

Christensen, K, T. (2004). The influence of peak-locking errors on turbulence statistics computed from piv ensembles. *Experiments in Fluids*, 36(3):484–497.

Church, C. R., Snow, J. T., and Agee, E. M. (1977). Tornado vortex simulation at purdue university. *Bulletin of the American Meteorological Society*, 58(9):900–908.

Church, C, R., Snow, J, T., Baker, G, L., and Agee, E, M. (1979). Characteristics of tornado-like vortices as a function of swirl ratio: A laboratory investigation. *Journal of the Atmospheric Sciences*, 36(9):1755–1776.

Cosadia, I., Borée, J., Charnay, G., and Dumont, P. (2006). Cyclic variations of the swirling flow in a diesel transparent engine. *Experiments in Fluids*, 41(1):115–134.

Cosadia, I., Boree, J., and Dumont, P. (2007). Coupling time-resolved piv flow-fields and phase-invariant proper orthogonal decomposition for the description of the parameters space in a transparent diesel engine. *Experiments in Fluids*, 43(2-3):357–370.

Davidson, P. A. (2004). *Turbulence: An Introduction for Scientists and Engineers: An Introduction for Scientists and Engineers*. Oxford University Press, Oxford, UK.

Davies-Jones, R. P. (1973). The dependence of core radius on swirl ratio in a tornado simulator. *Journal of the Atmospheric Sciences*, 30(7):1427–1430.

Davies-Jones, R. P. (1986). *Tornado Dynamics*, volume 2. University of Oklahoma Press, Oklahoma, USA.

Doulgerakis, Z., Yianneskis, M., and Ducci, A. (2011). On the manifestation and nature of macroinstabilities in stirred vessels. *AIChE Journal*, 57(11):2941–2954.

Druault, P., Delville, J., and Bonnet, J. P. (2005a). Proper orthogonal decomposition of the mixing layer flow into coherent structures and turbulent gaussian fluctuations. *Comptes Rendus de l'Academie des Sciences Serie II*.

Druault, P., Guibert, P., and Alizon, F. (2005b). Use of proper orthogonal decomposition for time interpolation from piv data. *Experiments in Fluids*, 39(6):1009–1023.

Duncan, J., Bryce, T., Thomsen, H., Dabiri, D., Hove, J. R., and Gharib, M. (2009). An extended study of a generalized digital particle image velocimetry (dpiv) processing technique. *Measurement Science and Technology*, 20(7):075401.

Duwig, C. and Iudiciani, P. (2010). Extended proper orthogonal decomposition for analysis of unsteady flames. *Flow, Turbulence and Combustion*, 84(1):25–47.

Eckstein, A., Charonko, J., and Vlachos, P. P. (2008). Phase correlation processing for dpiv measurements. *Experiments in Fluids*, 45(3):485–500.

Eckstein, A. and Vlachos, P. P. (2009a). Assessment of advanced windowing techniques for digital particle image velocimetry (dpiv). *Measurement Science and Technology*, 20(7).

Eckstein, A. and Vlachos, P. P. (2009b). Digital particle image velocimetry (dpiv) robust phase correlation. *Measurement Science and Technology*, 20(5):055401.

Feng, L.-H., Wang, J.-J., and Pan, C. (2011). Proper orthogonal decomposition analysis of vortex dynamics of a circular cylinder under synthetic jet control. *Physics of Fluids*, 23(1):014106–13.

Fincham, A. and Delerce, G. (2000). Advanced optimization of correlation imaging velocimetry algorithms. *Experiments in Fluids*, 29(1):S013–S022.

Fogleman, M., Lumley, J., Rempfer, D., and Haworth, D. (2004). Application of the proper orthogonal decomposition to datasets of internal combustion engine flows. *Journal of Turbulence*, 5:N23.

Fore, L. B., Tung, A. T., Buchanan, J. R., and Welch, J. W. (2005). Nonlinear temporal filtering of time-resolved digital particle image velocimetry data. *Experiments in Fluids*, 39(1):22–31.

Glickman, T. S. (2000). *Glossary of Meteorology*. American Meteorological Society, Boston, Mass., USA, 2 edition.

Gobbi, M. F., Chamecki, M., and Dias, N. L. (2006). Application of digital filtering for minimizing aliasing effects in atmospheric turbulent surface layer spectra. *Water Resources Research*, 42(3):W03405.

Gonzalez, R. C. and Woods, R. E. (2001). *Digital Image Processing*. Addison-Wesley Longman Publishing Co., Inc.

Graftieaux, L., Michard, M., and Grosjean, N. (2001). Combining piv, pod and vortex identification algorithms for the study of unsteady turbulent swirling flows. *Meas. Sci. Tech.*, 12:1422.

Grant, I. (1997). Particle image velocimetry: a review. *Proc. Instn. Mech. Engrs*, 211(C):55–76.

Gui, L. and Merzkirch, W. (2000). A comparative study of the mqd method and several correlation-based piv evaluation algorithms. *Exp Fluids*, 28(1):36–44.

Gui, L. and Wereley, S, T. (2002). A correlation-based continuous window-shift technique to reduce the peak-locking effect in digital piv image evaluation. *Exp Fluids*, 32:506–17.

Gui, L. M. W. (1998). Generating arbitrarily sized interrogation windows for correlation-based analysis of particle image velocimetry recordings. *Experiments in Fluids*, 24(1):66–69.

Gurka, R., Liberzon, A., and Hetsroni, G. (2006). Pod of vorticity fields: A method for spatial characterization of coherent structures. *International Journal of Heat and Fluid Flow*, 27(3):416–423.

Haan Jr, F. L., Sarkar, P. P., and Gallus, W. A. (2008). Design, construction and performance of a large tornado simulator for wind engineering applications. *Engineering Structures*, 30(4):1146–1159.

Hangan, H., Hashemi-Tari, P., and Kim, J. (2008). Modeling of high intensity winds. In *Structures Congress 2008: 18th Analysis and Computation Specialty Conference*, pages 1–6.

Hariharan, P. (1984). *Optical holography : principles, techniques and applications*. Cambridge monographs on physics. Cambridge University Press, Cambridge.

Hart, D. P. (2000). Piv error correction. *Experiments in Fluids*, 29(1):13–22.

Hasal, P., Montes, J.-L., Boisson, H.-C., and Fořt, I. (2000). Macro-instabilities of velocity field in stirred vessel:: detection and analysis. *Chemical Engineering Science*, 55(2):391–401.

Hashemi-Tari, P., Gurka, R., and Hangan, H. (2010). Experimental investigation of tornado-like vortex dynamics with swirl ratio: The mean and turbulent flow fields. *Journal of Wind Engineering and Industrial Aerodynamics*, 98(12):936–944.

Haworth, D. C. and Jansen, K. (2000). Large-eddy simulation on unstructured deforming meshes: towards reciprocating ic engines. *Computers & Fluids*, 29(5):493–524.

Hinze, J. O. (1975). *Turbulence*. McGraw-Hill.

Hoecker, W. H. (1960). Wind speed and air flow patterns in the dallas tornado of april 2, 1957. *Monthly Weather Review*, 88(5):167–180.

Holmes, P., Lumley, J. L., and Berkooz, G. (1998). *Turbulence, coherent structures, dynamical systems and symmetry*. Cambridge University Press, Cambridge, England.

Hu, H., Yang, Z., Sarkar, P., and Haan, F. (2011). Characterization of the wind loads and flow fields around a gable-roof building model in tornado-like winds. *Experiments in Fluids*, 51(3):835–851.

Huang, H., Dabiri, D., and Gharib, M. (1997). On errors of digital particle image velocimetry. *Measurement Science and Technology*, 8(12):1427.

Huang, H. T., Fielder, H. F., and Wang, J. J. (1993). Limitation and improvement of piv, part ii. particle image distortion, a novel technique. *Exp Fluids*, 15:263–273.

Huera-Huarte, F. J. and Vernet, A. (2010). Vortex modes in the wake of an oscillating long flexible cylinder combining pod and fuzzy clustering. *Experiments in Fluids*, 48(6):999–1013.

Hulst, H. C. v. d. (1957). *Light Scattering by Small Particles*. Dover Books on Physics Series. Dover Publications, New York.

Hunt, J. C. R., Wray, A. A., and Moin, P. (1988). Eddies, stream, and convergence zones in turbulent flows. *Center For Turbulence Research*, Report CTR-S88.

Jambunathan, K., Ju, X. Y., Dobbins, B. N., and Ashforth-Frost, S. (1995). An improved cross correlation technique for particle image velocimetry. *Measurement Science and Technology*, 6(5):507.

Jeong, J. and Hussain, F. (1995). On the identification of a vortex. *Journal of Fluid Mechanics*, 285:69–94.

Jiang, M., Machiraju, R., and Thompson, D. (2005). Detection and visualization of vortices. In Hansen, C. D. and Johnson, C. R., editors, *Visualization Handbook*, pages 295 – XXVIII. Butterworth-Heinemann, Burlington.

Jischke, M. C. and Parang, M. (1974). Properties of simulated tornado-like vortices. *Journal of the Atmospheric Sciences*, 31(2):506–512.

Keane, R. D. and Adrian, R. J. (1992). Theory of cross-correlation analysis of piv images. *Applied Scientific Research*, 49(3):191–215.

Kim, B. J. and Sung, H. J. (2006). A further assessment of interpolation schemes for window deformation in piv. *Experiments in Fluids*, 41(3):499–511.

Kim, J. S., Kim, S. M., Kim, H. D., Ji, H. S., and Kim, K. C. (2012). Dynamic structures of bubble-driven liquid flows in a cylindrical tank. *Experiments in Fluids*, 53(1):21–35.

Kolmogorov, A. N. (1941a). Dissipation of energy in the locally isotropic turbulence. *Proceedings of the Royal Society of London. Series A: Mathematical and Physical Sciences*, 434(1890):15–17.

Kolmogorov, A. N. (1941b). The local structure of turbulence in incompressible viscous fluid for very large reynolds numbers. *Proceedings of the Royal Society of London. Series A: Mathematical and Physical Sciences*, 434(1890):9–13.

Kostas, J., Soria, J., and Chong, M, S. (2005). A comparison between snapshot pod analysis of piv velocity and vorticity data. *Experiments in Fluids*, 38(2):146–160.

Kourentis, L. and Konstantinidis, E. (2012). Uncovering large-scale coherent structures in natural and forced turbulent wakes by combining piv, pod, and ftle. *Experiments in Fluids*, 52(3):749–763.

Li, Y., Zhao, H., and N, L. (2002). Analysis of large-scale flow characteristics in a four-valve spark ignition engine. *Proc. Instn. Mech. Engrs*, 216(C).

Liang, D., Jiang, C., and Li, Y. (2003). Cellular neural network to detect spurious vectors in piv data. *Experiments in Fluids*, 34(1):52–62.

Liang, Y. C., Lee, H. P., Lim, S. P., Lin, W. Z., Lee, K. H., and Wu, C. G. (2002). Proper orthogonal decomposition and its applications—part i: Theory. *Journal of Sound and Vibration*, 252(3):527–544.

Liné, A., Gabelle, J.-C., Morchain, J., Anne-Archard, D., and Augier, F. (2013). On {POD} analysis of {PIV} measurements applied to mixing in a stirred vessel with a shear thinning fluid. *Chemical Engineering Research and Design*, 91(11):2073 – 2083. Mixing.

Liu, Z., Jia, L., Zheng, Y., and Zhang, Q. (2008). Flow-adaptive data validation scheme in piv. *Chemical Engineering Science*, 63(1):1–11.

Liu, Y, Z., Shi, L, L., and Zhang, Q, S. (2011). Proper orthogonal decomposition of wall-pressure fluctuations under the constrained wake of a square cylinder. *Experimental Thermal and Fluid Science*, 35(7):1325–1333.

Lugt, H. J. (1972). *Vortex Flow in Nature and Technology*. John Wiley & Sons Inc, New York, USA.

Lumley, J. L. (1967). *The Structure of Inhomogeneous Turbulent Flows*, pages 166–178. Nauka.

Lumley, J, L. (2001). Early work on fluid mechanics in the ic engine. *Annual Review of Fluid Mechanics*, 33(1):319–338.

Lund, D. E. and Snow, J. T. (1993). *Laser doppler velocimetry measurements in tornado like vortices*, page 297–306. Amer. Geophys. Union.

Maurel, S., Borée, J., and Lumley, J. L. (2001). Extended proper orthogonal decomposition: Application to jet/vortex interaction. *Flow, Turbulence and Combustion*, 67(2):125–136.

Meyer, K. E., Cavar, D., and Pedersen, J. M. (2007). *POD as tool for comparison of PIV and LES data*. Faculty of Engineering, University “La Sapienza”, Rome, Italy.

Mishra, A, R., James, D, L., and Letchford, C, W. (2008a). Physical simulation of a single-celled tornado-like vortex, part a: Flow field characterization. *Journal of Wind Engineering and Industrial Aerodynamics*, 96(8–9):1243–1257.

Mishra, A, R., James, D, L., and Letchford, C, W. (2008b). Physical simulation of a single-celled tornado-like vortex, part b: Wind loading on a cubical model. *Journal of Wind Engineering and Industrial Aerodynamics*, 96(8–9):1258–1273.

Müller, E.-A. and Obermeier, F. (1988). Vortex sound. *Fluid Dynamics Research*, 3(1–4):43–51.

Navier, C. L. M. H. (1823). Mémoire sur les lois du mouvement des fluids. *Mem. Acad. Sci. Inst. Fr.*, 6:389–416.

NOAA (2012). Annual U.S. Killer Tornado Statistics. National Oceanic and Atmospheric Administration - Storm Prediction Center [online]. *http://www.spc.noaa.gov/climo/torn/fatalmap.php?yr=2011*. Accessed 10 July 2012.

Nogueira, J., Lecuona, A., and Rodríguez, P, A. (1997). Data validation, false vectors correction and derived magnitudes calculation on piv data. *Measurement Science and Technology*, 8(12):1493.

Nogueira, J., Lecuona, A., and Rodríguez, P. A. (1999). Local field correction piv: on the increase of accuracy of digital piv systems. *Experiments in Fluids*, 27(2):107–116.

Nogueira, J., Lecuona, A., and Rodríguez, P. A. (2001). Local field correction piv, implemented by means of simple algorithms, and multigrid versions. *Measurement Science and Technology*, 12(11):1911.

Nogueira, J., Lecuona, A., Ruiz-Rivas, U., and Rodriguez, P, A. (2002). Analysis and alternatives in two dimensional multigrid particle image velocimetry methods: Application of a dedicated weighting function and symmetric direct correlation. *Measurement Science and Technology*, 13:963–974.

O'Neill, P., Nicolaides, D., Honnery, D., and Soria, J. (2004). Autocorrelation functions and the determination of integral length with reference to experimental and numerical data. *15th Australasian Fluid Mechanics Conference. The University of Sydney, Sydney, Australia*.

Patte-Rouland, B., Lalizel, G., Moreau, J., and Rouland, E. (2001). Flow analysis of an annular jet by particle image velocimetry and proper orthogonal decomposition. *Measurement Science and Technology*, 12(9):1404.

Pickering, C. J. D. and Halliwell, N. A. (1984). Speckle photography in fluid flows: signal recovery with two-step processing. *Appl. Opt.*, 23(8):1128–1129.

Pinton, J.-F. and Labbé, R. (1995). *Correction to Taylor's Hypothesis in Swirling Flows*, volume 24 of *Fluid Mechanics and Its Applications*, chapter 76, pages 418–422. Springer Netherlands.

Pope, S. B. (2000). *Turbulent flows*. Cambridge University Press, Cambridge, UK.

Portela, L, M. (1998). *On the identification and charaterisation of vortices in the turbulent boundary layer*. PhD thesis, Stanford University, USA.

Prabhu, R. D., Collis, S. S., and Yong, C. (2001). The influence of control on proper orthogonal decomposition of wall-bounded turbulent flows. *Physics of Fluids*, 13(2):520–537.

Pratt, W. K. (2001). *Digital Image Processing: PIKS Inside*. John Wiley & Sons, Inc., New York, NY, USA, 3rd edition.

Pun, C. S., Susanto, A., and Dabiri, D. (2007). Mode-ratio bootstrapping method for piv outlier correction. *Measurement Science and Technology*, 18(11):3511.

Pust, O. (2000). Piv: Direct cross-correlation compared with fft-based cross-correlation. *University of the Federal Armed Forces Hamburg, D–22039 Hamburg, Germany*.

Raffel, M., Willert, C. E., and Kompenhans, J. (1998). *Particle Image Velocimetry: A Practical Guide*. Experimental fluid mechanics. Springer, Berlin, Germany; New York, USA.

Regert, T., Rambaud, P., and Reithmuller M, L. (2005). Investigation of the link between physics and pod modes. (Belgium).

Richardson, L. F. (1922). *Weather prediction by numerical process*. Cambridge University Press, Cambridge, England.

Robinson, S. K. (1991). Coherent motions in the turbulent boundary layer. *Annual Review of Fluid Mechanics*, 23(1):601–639.

Roesgen, T. (2003). Optimal subpixel interpolation in particle image velocimetry. *Experiments in Fluids*, 35(3):252–256.

Rohály, J., Frigerio, F., and Hart, D. P. (2002). Reverse hierarchical piv processing. *Measurement Science and Technology*, 13(7):984.

Rotunno, R. (1979). A study in tornado-like vortex dynamics. *Journal of the Atmospheric Sciences*, 36(1):140–155.

Roudnitzky, S., Druault, P., and Guibert, P. (2006). Proper orthogonal decomposition of in-cylinder engine flow into mean component, coherent structures and random gaussian fluctuations. *Journal of Turbulence*, 7:N70.

Rowley, C. W., Colonius, T., and Murray, R. M. (2000). Pod based models of self-sustained oscillations in the flow past an open cavity. *AIAA paper*, 1969:2000.

Saarenrinne, P. and Piirto, M. (2000). Turbulent kinetic energy dissipation rate estimation from piv velocity vector fields. *Experiments in Fluids*, 29(1):S300–S307.

Saarenrinne, P., Piirto, M., and Eloranta, H. (2001). Experiences of turbulence measurement with piv. *Measurement Science and Technology*, 12(11):1904.

Sadarjoen, I. A. and Post, F. H. (1999). *Geometric Methods for Vortex Extraction*, chapter 6, pages 53–62. Eurographics. Springer Vienna.

Saddoughi, S. G. and Veeravalli, S. V. (1994). Local isotropy in turbulent boundary layers at high reynolds number. *Journal of Fluid Mechanics*, 268:333–372.

Sapkota, A. and Ohmi, K. (2008). Detection of piv outliers using rule-based fuzzy logic. In *Fuzzy Systems, 2008. FUZZ-IEEE 2008. (IEEE World Congress on Computational Intelligence). IEEE International Conference on*, pages 1655–1659.

Sarkar, P. F., Haan, W., Gallus Jr, W., Le, K., and Wurman, J. (2005). Velocity measurements in a laboratory tornado simulator and their comparison with numerical and full-scale data. In *Proceedings of the 37th Joint Meeting Panel on Wind and Seismic Events*, Tsukuba, Japan.

Scarano, F. (2002). Iterative image deformation methods in piv. *Measurement Science and Technology*, 13(1):R1.

Scarano, F. (2003). Theory of non-isotropic spatial resolution in piv. *Experiments in Fluids*, 35(3):268–277.

Scarano, F. and Riethmuller, M. L. (1999). Iterative multigrid approach in piv image processing with discrete window offset. *Experiments in Fluids*, 26(6):513–523.

Scarano, F. and Riethmuller, M. L. (2000). Advances in iterative multigrid piv image processing. *Experiments in Fluids*, 29(1):S051–S060.

Schram, C. and Riethmuller, M, L. (2001). Vortex ring evolution in an impulsively started jet using digital particle image velocimetry and continuous wavelet analysis. *Measurement Science and Technology*, 12(9):1413.

Shavit, U., Lowe, R. J., and Steinbuck, J. V. (2007). Intensity capping: a simple method to improve cross-correlation piv results. *Experiments in Fluids*, 42(2):225–240.

Sheng, J., Meng, H., and Fox, R, O. (2000). A large eddy piv method for turbulence dissipation rate estimation. *Chemical Engineering Science*, 55(20):4423–4434.

Shinneeb, A.-M. (2006). *Confinement effects in shallow water jets*. PhD thesis, University of Saskatchewan.

Shinneeb, A.-M., Balachandar, R., and Bugg, J. D. (2008). Analysis of coherent structures in the far-field region of an axisymmetric free jet identified using particle image velocimetry and proper orthogonal decomposition. *Journal of Fluids Engineering*, 130:9.

Shinneeb, A. M., Bugg, J. D., and Balachandar, R. (2004). Variable threshold outlier identification in piv data. *Measurement Science and Technology*, 15(9):1722.

Simand, C., Chillà, F., and Pinton, J. F. (2000). Inhomogeneous turbulence in the vicinity of a large-scale coherent vortex. *EPL (Europhysics Letters)*, 49(3):336.

Sirovich, L. (1987). Turbulence and the dynamics of coherent structures: Part i-iii. *Quarterly of Applied Mathematics*, 45.

Stanislas, M. and Monnier, J. C. (1997). Practical aspects of image recording in particle image velocimetry. *Measurement Science and Technology*, 8(12):1417–1426.

Stanislas, M., Okamoto, K., and Kähler, C. (2003). Main results of the first international piv challenge. *Measurement Science and Technology*, 14(10):R63.

Stelmach, J. and Kuncewicz, C. (2012). Analysis of methods for measuring energy dissipation rates in the tank with the use of a piv system. In *14th European Conference on Mixing*, pages 443–448, Warsaw, Poland.

Stokes, G. G. (1848). On the theories of the internal friction of fluids in motion, and of the equilibrium and motion of elastic solids. *Transactions of the Cambridge Philosophical Society*, 8.

Strawn, R. C., Kenwright, D. N., and Ahmad, J. (1999). Computer visualization of vortex wake systems. *AIAA Journal*, 37(4):511–512.

Sun, C., Xia, K.-Q., and Tong, P. (2005). Three-dimensional flow structures and dynamics of turbulent thermal convection in a cylindrical cell. *Physical Review E*, 72(2):026302. PRE.

Swamy, N. V. C., Gowda, B. H. L., and Lakshminath, V. R. (1979). Auto-correlation measurements and integral time scales in three-dimensional turbulent boundary layers. *Applied Scientific Research*, 35(4):237–249.

Tamura, Y., Suganuma, S., Kikuchi, H., and Hibi, K. (1999). Proper orthogonal decomposition of random wind pressure field. *Journal of Fluids and Structures*, 13(7–8):1069–1095.

Taylor, G. I. (1928). The energy of a body moving in an infinite fluid, with an application to airships. *Proceedings of the Royal Society of London. Series A*, 120(784):13–21.

Taylor, G. I. (1935). Statistical theory of turbulence. *Proceedings of the Royal Society of London. Series A - Mathematical and Physical Sciences*, 151(873):421–444.

Tennekes, H. and Lumley, J. L. (1972). *A First course in turbulence*. MIT Press, Cambridge, Maassachusetts, USA.

Thacker, A., Loyer, S., and Aubrun, S. (2010). Comparison of turbulence length scales assessed with three measurement systems in increasingly complex turbulent flows. *Experimental Thermal and Fluid Science*, 34(5):638–645.

Timmerman, B. H., Skeen, A. J., Bryanston-Cross, P. J., and J, G. M. (2009). Large-scale time-resolved digital particle image velocimetry (tr-dpiv) for measurement of high subsonic hot coaxial jet exhaust of a gas turbine engine. *Measurement Science and Technology*, 20(7):074002.

Towers, D. P. and Towers, C. E. (2004). Cyclic variability measurements of in-cylinder engine flows using high-speed particle image velocimetry. *Measurement Science and Technology*, 15(9):1917.

Towers, D. P. and Towers, C. E. (2008). *High-Speed PIV: Applications in Engines and Future Prospects*, volume 112 of *Topics in Applied Physics*, chapter 18, pages 345–361. Springer Berlin Heidelberg.

Tritton, D. J. (1988). *Physical Fluid Dynamics*. Clarendon Press.

Tropea, C., Yarin, A. L., and Foss, J. F. (2007). *Springer Handbook of Experimental Fluid Mechanics*. Springer, Berlin, Germany.

Uruba, V. (2012). Decomposition methods in turbulence research. *EPJ Web of Conferences*, 25.

Vincent, A. and Meneguzzi, M. (1991). The spatial structure and statistical properties of homogeneous turbulence. *J. Fluid Mech.*, 225:1–20.

von Kármán, T. (1937). *Turbulence*. 25th Wilbur Wright memorial lecture. Royal Aeronautical Society.

Vu, T.-T. and Guibert, P. (2012). Proper orthogonal decomposition analysis for cycle-to-cycle variations of engine flow. effect of a control device in an inlet pipe. *Experiments in Fluids*, 52(6):1519–1532.

Wan, C. A. and Chang, C. C. (1972). Measurement of the velocity field in a simulated tornado-like vortex using a three-dimensional velocity probe. *Journal of the Atmospheric Sciences*, 29(1):116–127.

Ward, N. B. (1972). The exploration of certain features of tornado dynamics using a laboratory model. *Journal of the Atmospheric Sciences*, 29(6):1194–1204.

Wernet, M. P. (2005). Symmetric phase only filtering: a new paradigm for dpiv data processing. *Measurement Science and Technology*, 16(3):601.

Wernet, M, P. (2007). Temporally resolved piv for space–time correlations in both cold and hot jet flows. *Measurement Science and Technology*, 18(5):1387.

Westerweel, J. (1994). Efficient detection of spurious vectors in particle image velocimetry data. *Experiments in Fluids*, 16(3-4):236–247.

Westerweel, J. (1997). Fundamentals of digital particle image velocimetry. *Measurement Science and Technology*, 8(12):1379.

Westerweel, J. (2008). On velocity gradients in piv interrogation. *Exp Fluids*, 44:831–842.

Westerweel, J., Dabiri, D., and Gharib, M. (1997). The effect of a discrete window offset on the accuracy of cross-correlation analysis of digital piv recordings. *Experiments in Fluids*, 23(1):20–28.

Westerweel, J. and Scarano, F. (2005). Universal outlier detection for piv data. *Experiments in Fluids*, 39(6):1096–1100.

Willert, C. E. and Gharib, M. (1991). Digital particle image velocimetry. *Experiments in Fluids*, 10(4):181–193.

Yang, Z., Sarkar, P., and Hu, H. (2011). An experimental study of a high-rise building model in tornado-like winds. *Journal of Fluids and Structures*, 27(4):471–486.

Ying, S. J. and Chang, C. C. (1970). Exploratory model study of tornado-like vortex dynamics. *Journal of the Atmospheric Sciences*, 27(1):3–14.

Young, C. N., Johnson, D. A., and Weckman, E. J. (2004). A model-based validation framework for piv and ptv. *Experiments in Fluids*, 36(1):23–35.

Zhang, W. and Sarkar, P. P. (2012). Near-ground tornado-like vortex structure resolved by particle image velocimetry (piv). *Experiments in Fluids*, 52(2):479–493.

Appendix A

Energy Spectra of High-Speed Tornado-Like Vortex PIV Velocity Data

A.1 Energy-Frequency Spectra

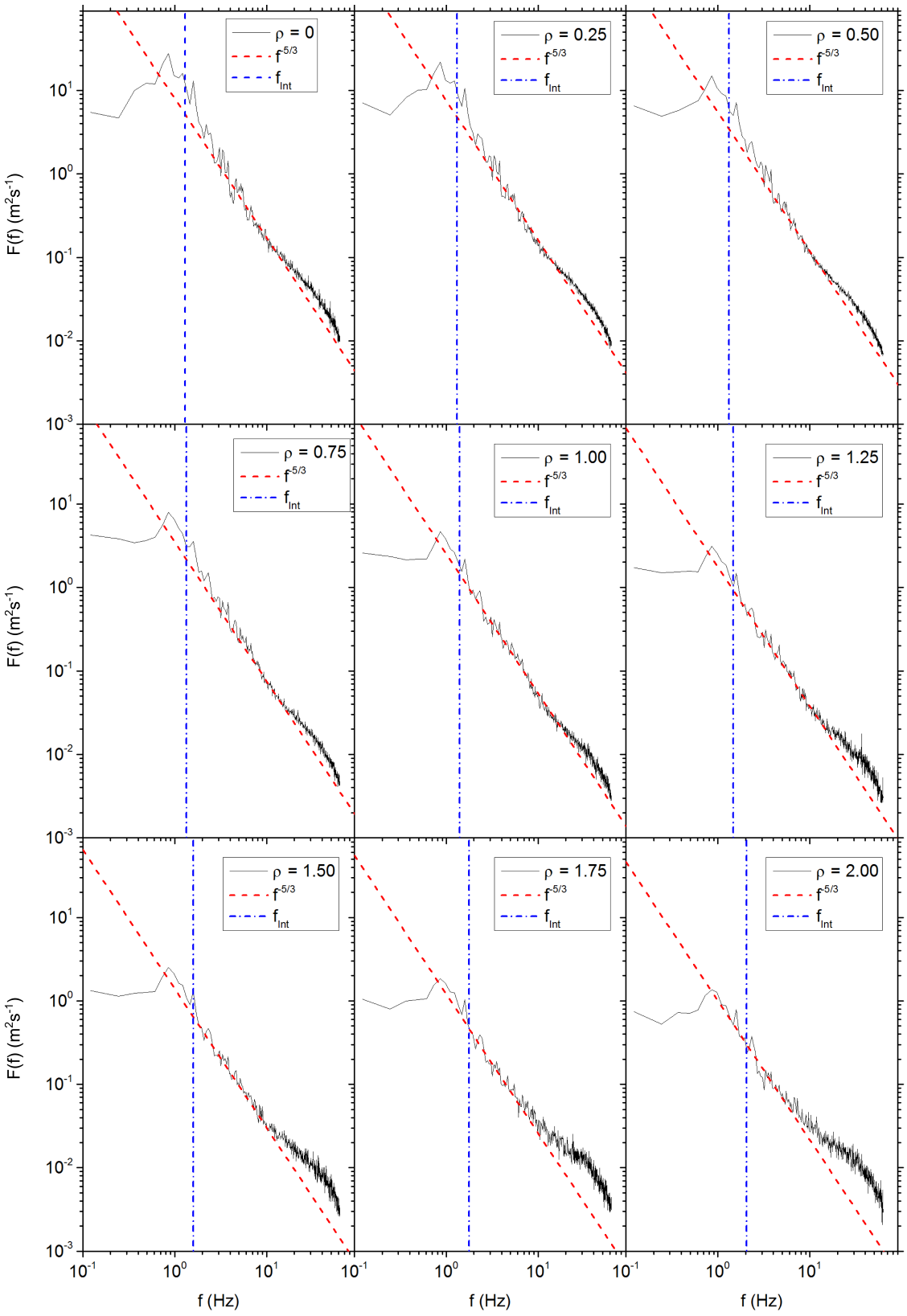

Fig. A.1 Energy-frequency spectra $F(f)$ for HS-F30, $S = 0.137$ at varying radial positions ρ.

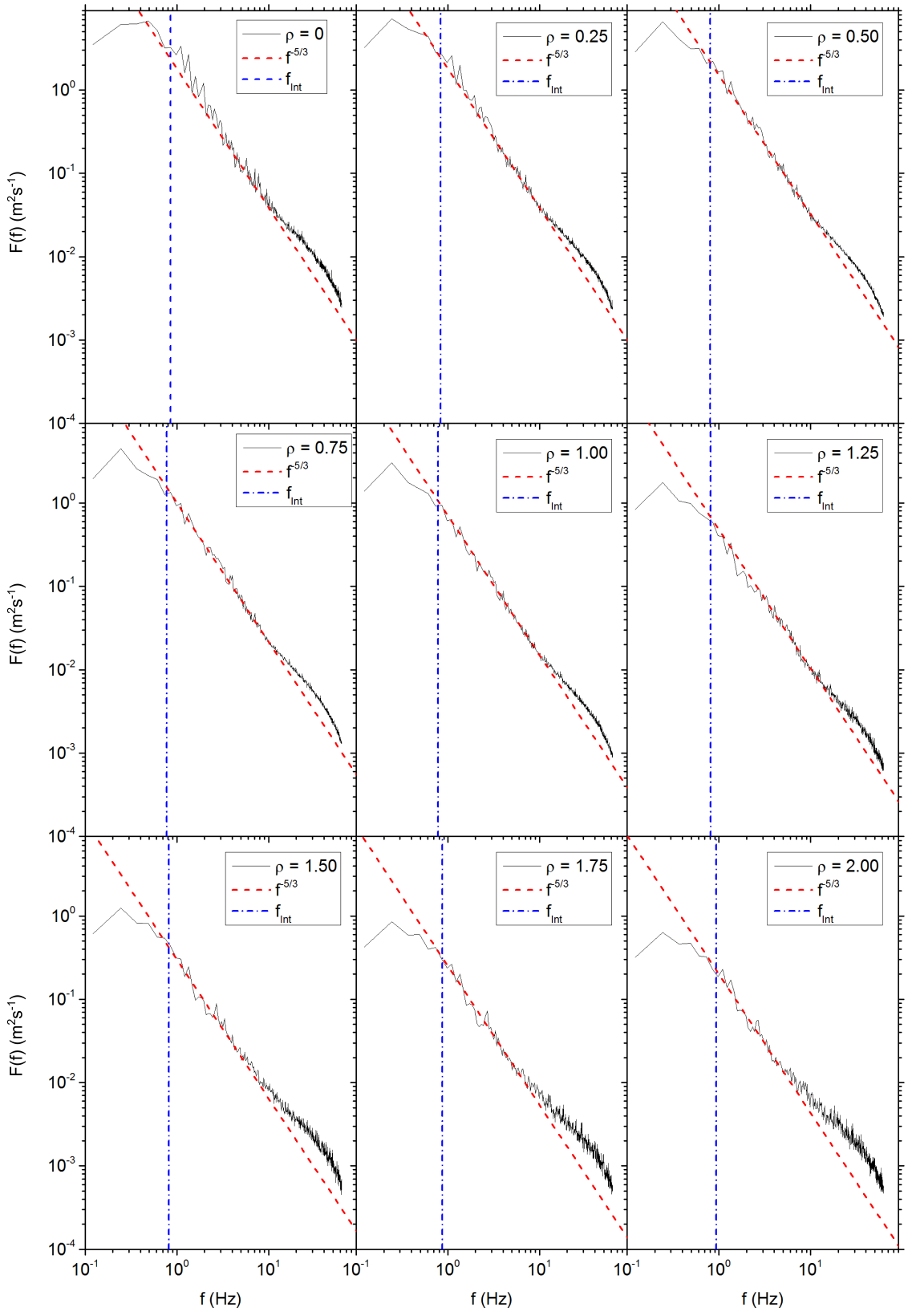

Fig. A.2 Energy-frequency spectra $F(f)$ for HS-M17, $S = 0.032$ at varying radial positions ρ.

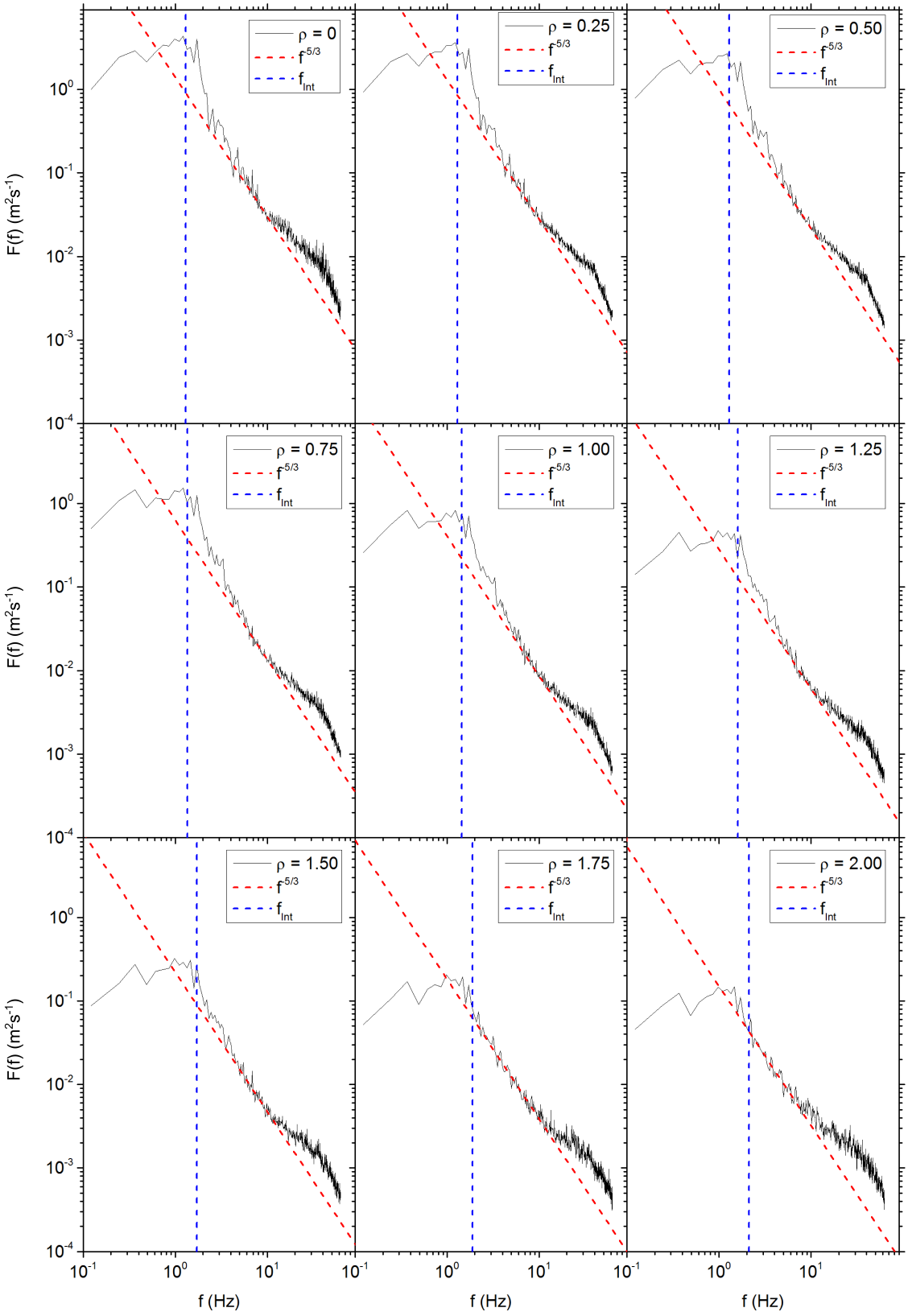

Fig. A.3 Energy-frequency spectra $F(f)$ for HS-M30, $S = 0.235$ at varying radial positions ρ.

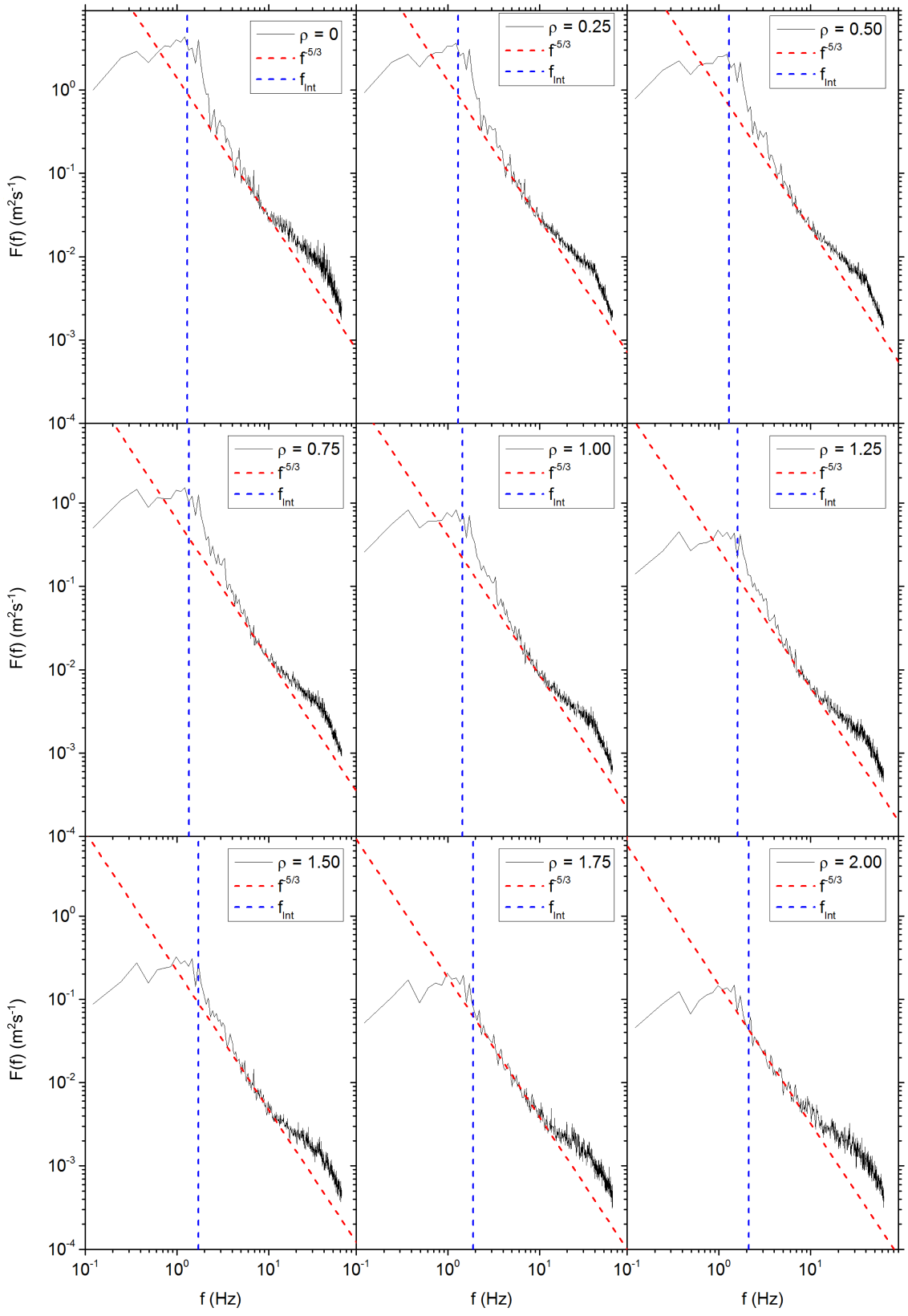

Fig. A.4 Energy-frequency spectra $F(f)$ for HS-L17, $S = 0.468$ at varying radial positions ρ.

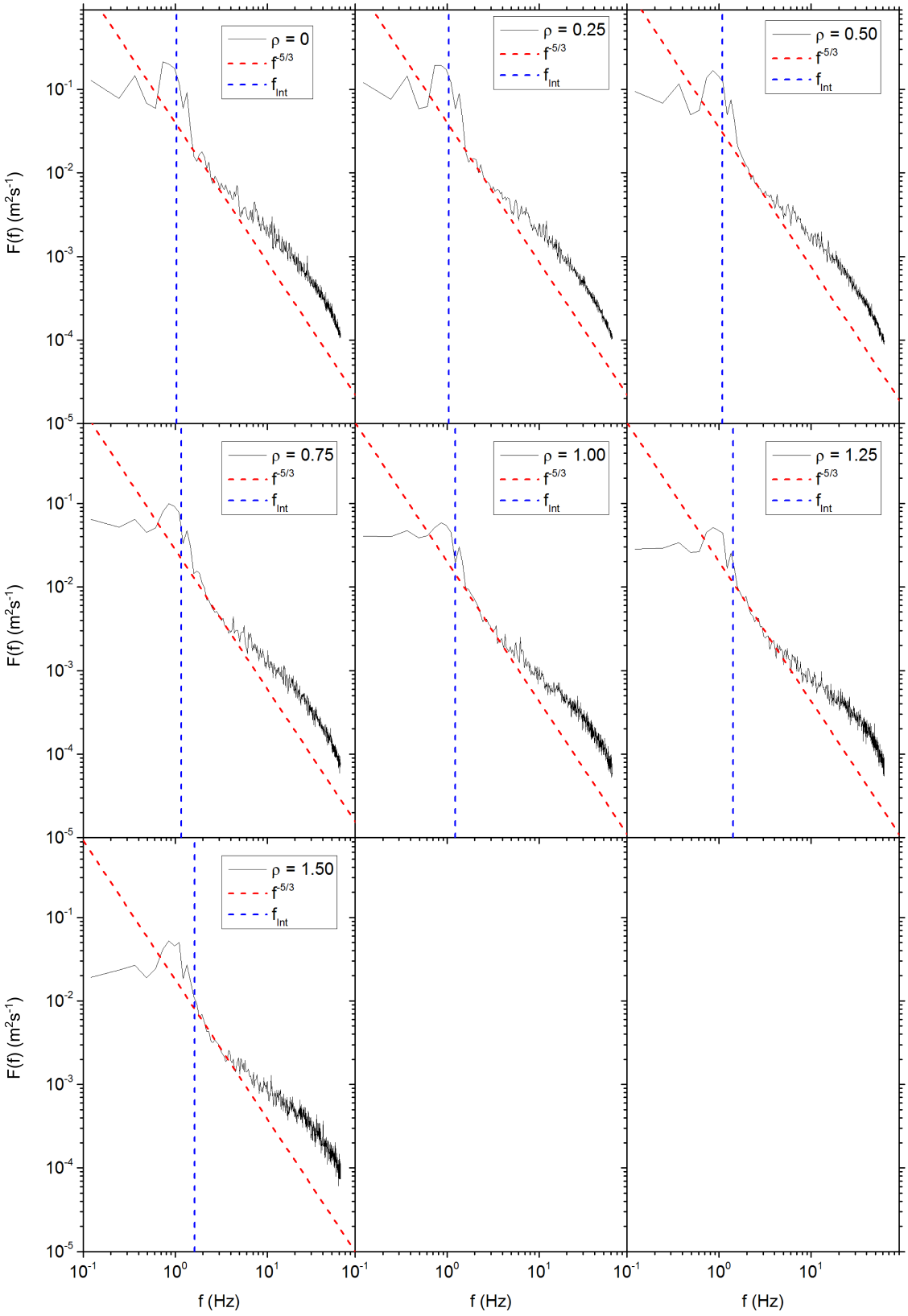

Fig. A.5 Energy-frequency spectra $F(f)$ for HS-L30, $S = 0.979$ at varying radial positions ρ.

A.2 Energy-Wavenumber Spectra

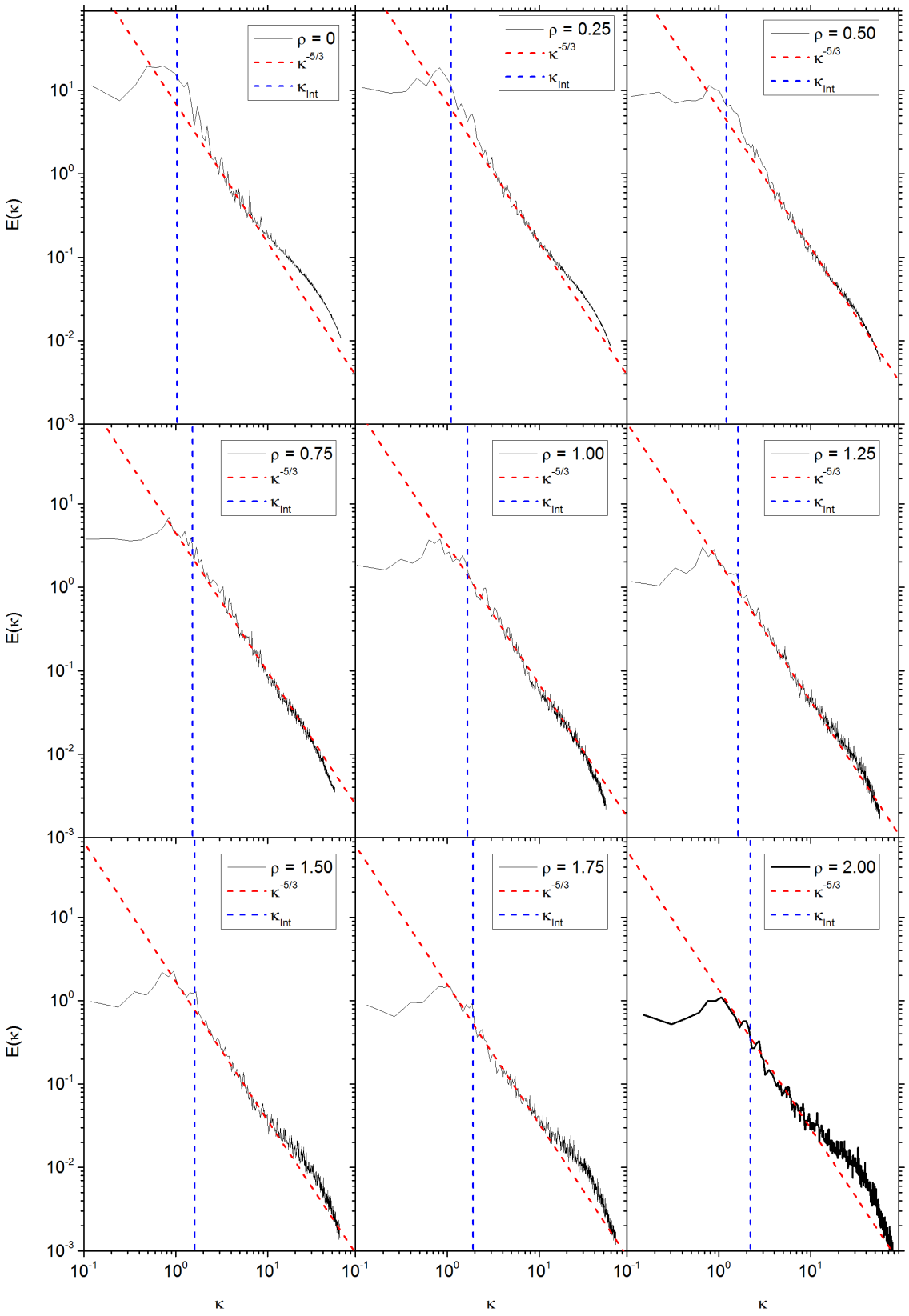

Fig. A.6 Energy-wavenumber spectra $E(\kappa)$ for HS-F30, $S = 0.137$ at varying radial positions ρ.

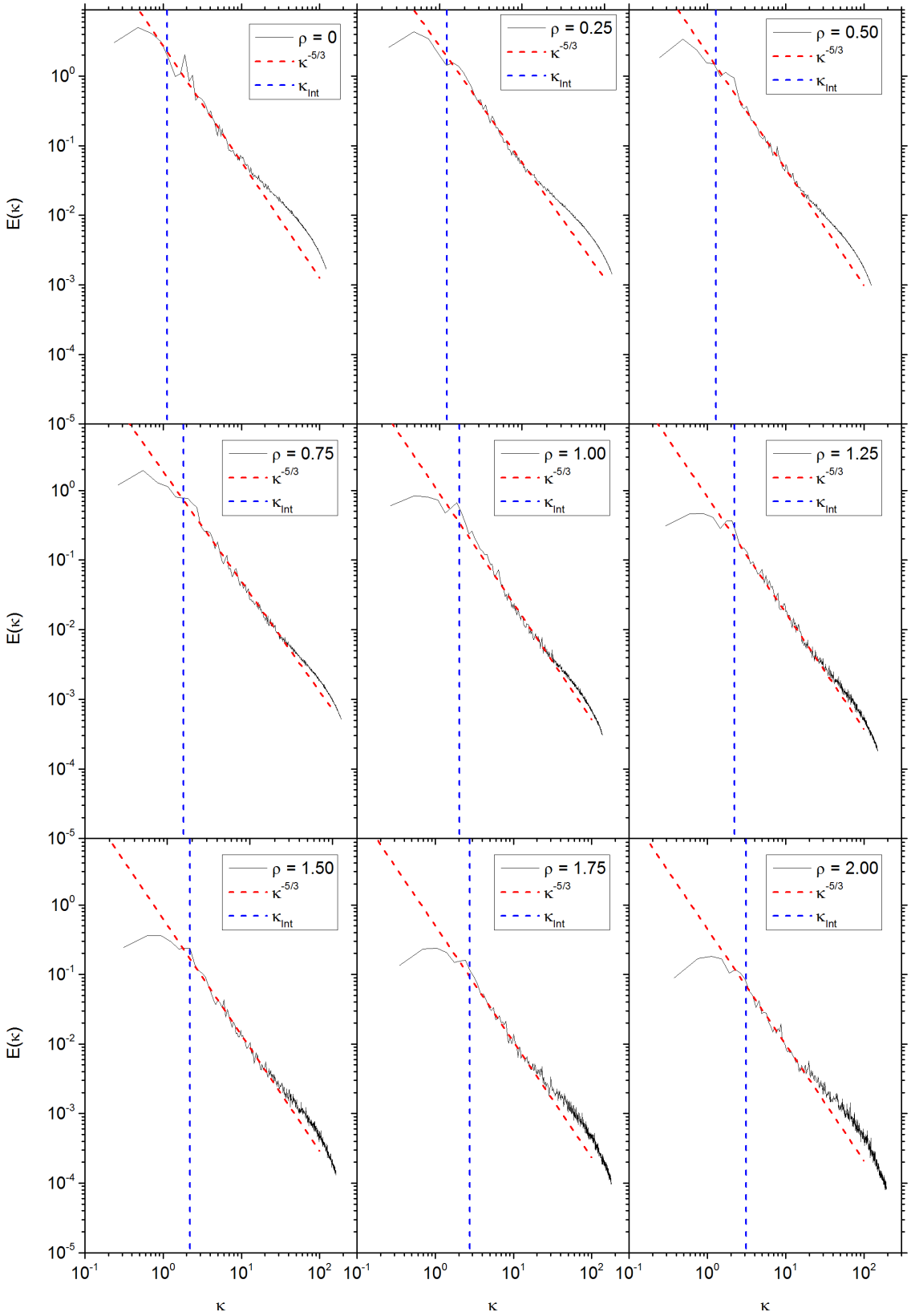

Fig. A.7 Energy-wavenumber spectra $E(\kappa)$ for HS-M17, $S = 0.032$ at varying radial positions ρ.

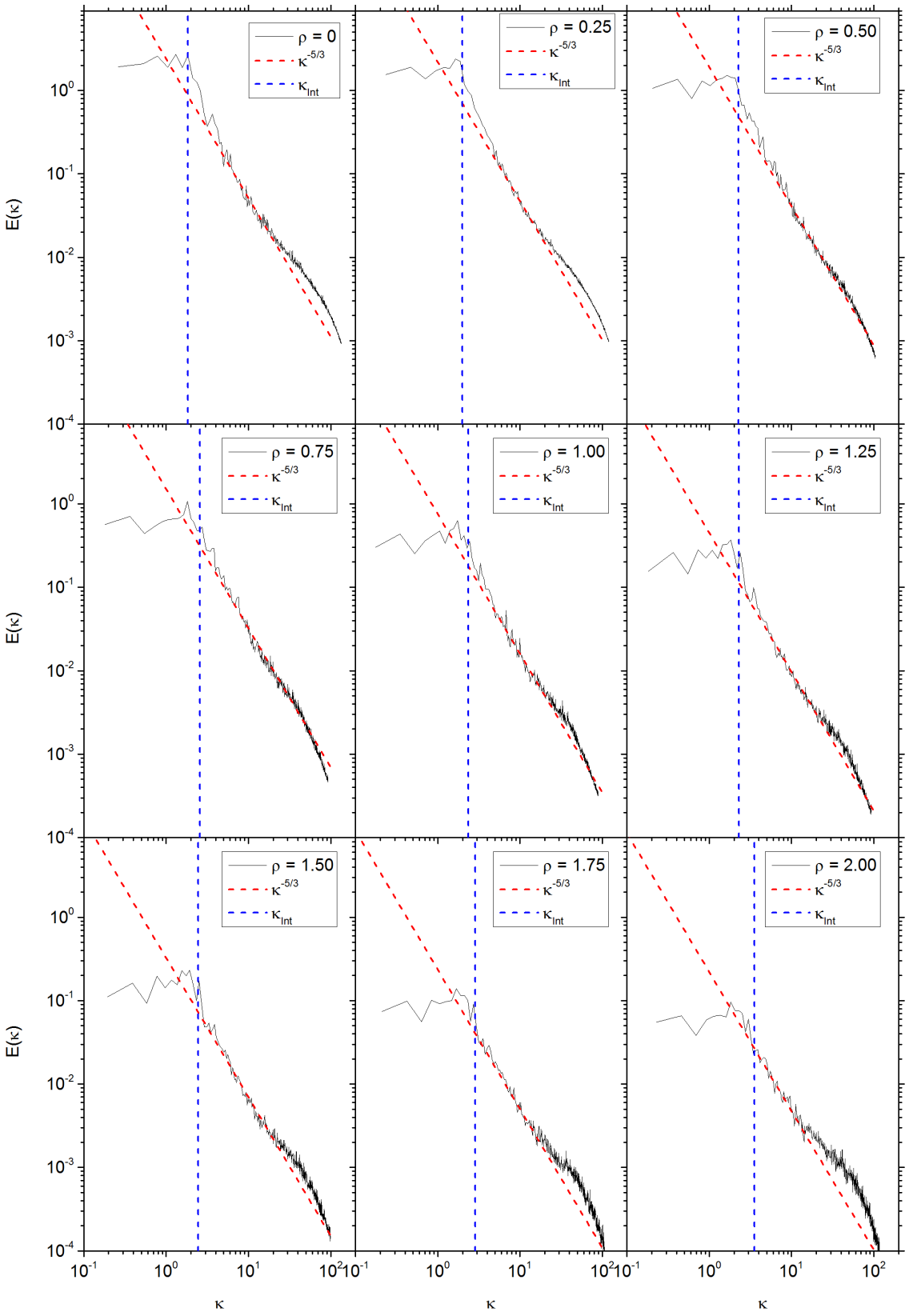

Fig. A.8 Energy-wavenumber spectra $E(\kappa)$ for HS-M30, $S = 0.235$ at varying radial positions ρ.

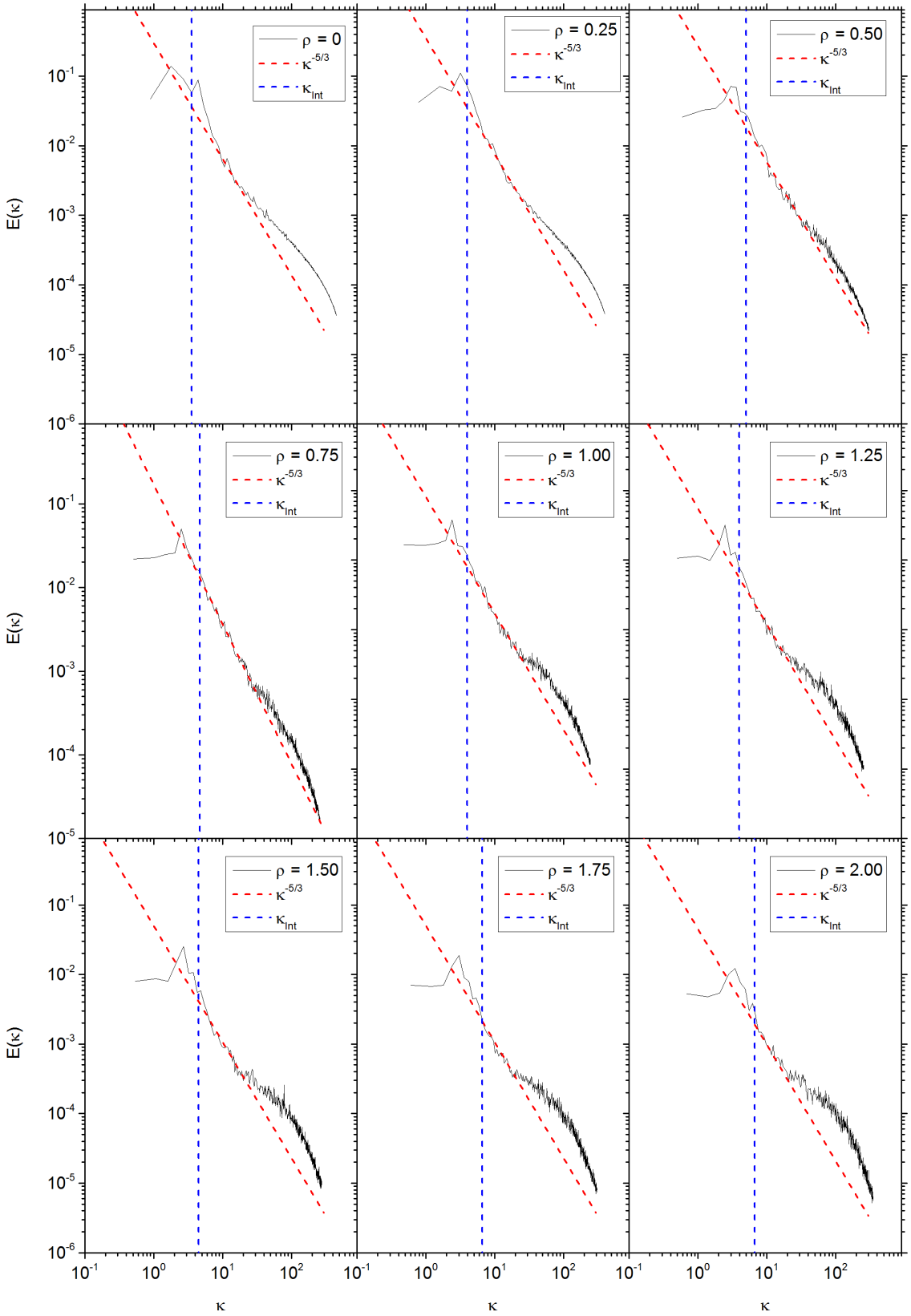

Fig. A.9 Energy-wavenumber spectra $E(\kappa)$ for HS-L17, $S = 0.468$ at varying radial positions ρ.

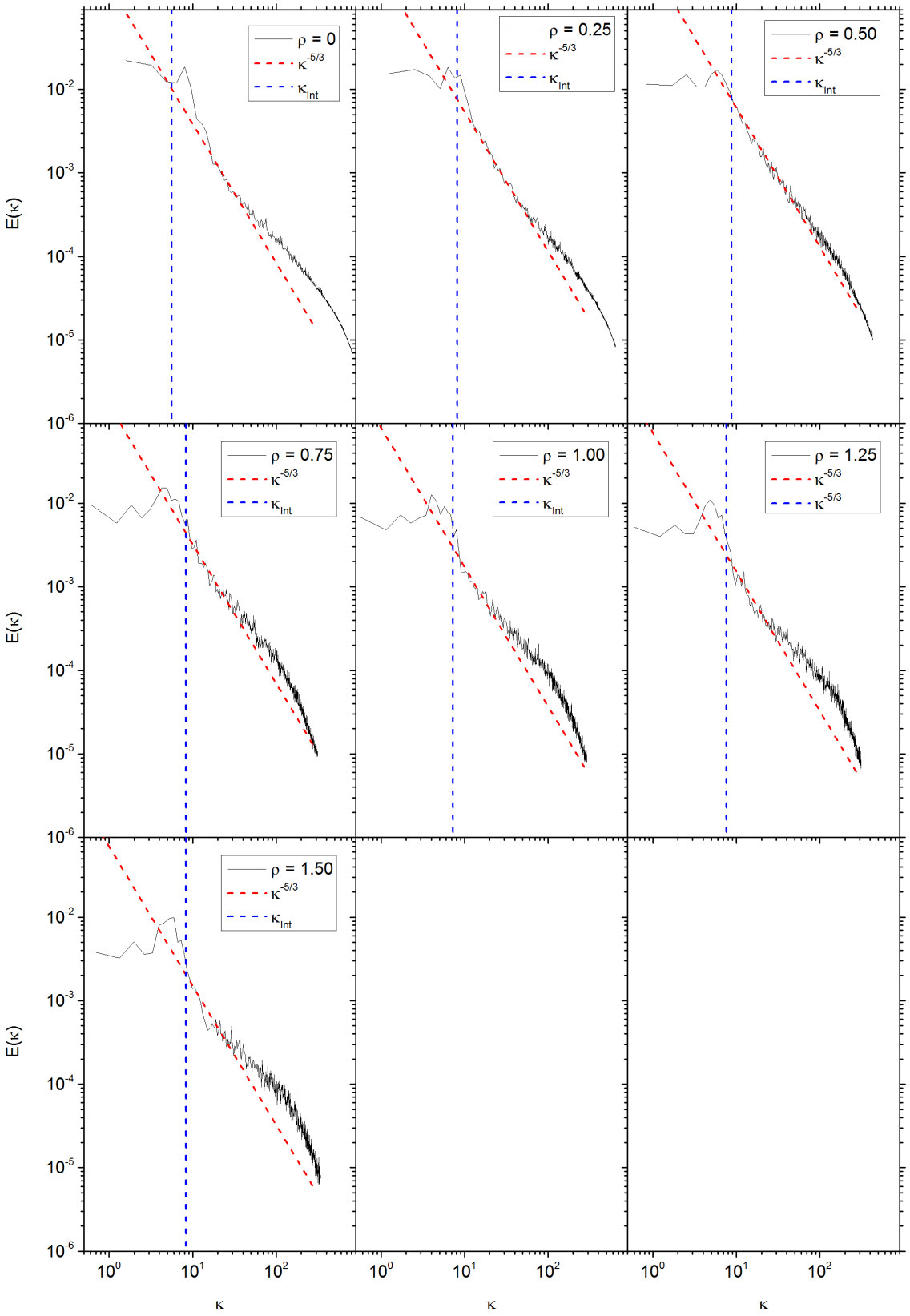

Fig. A.10 Energy-wavenumber spectra $E(\kappa)$ for HS-L30, $S = 0.979$ at varying radial positions ρ.